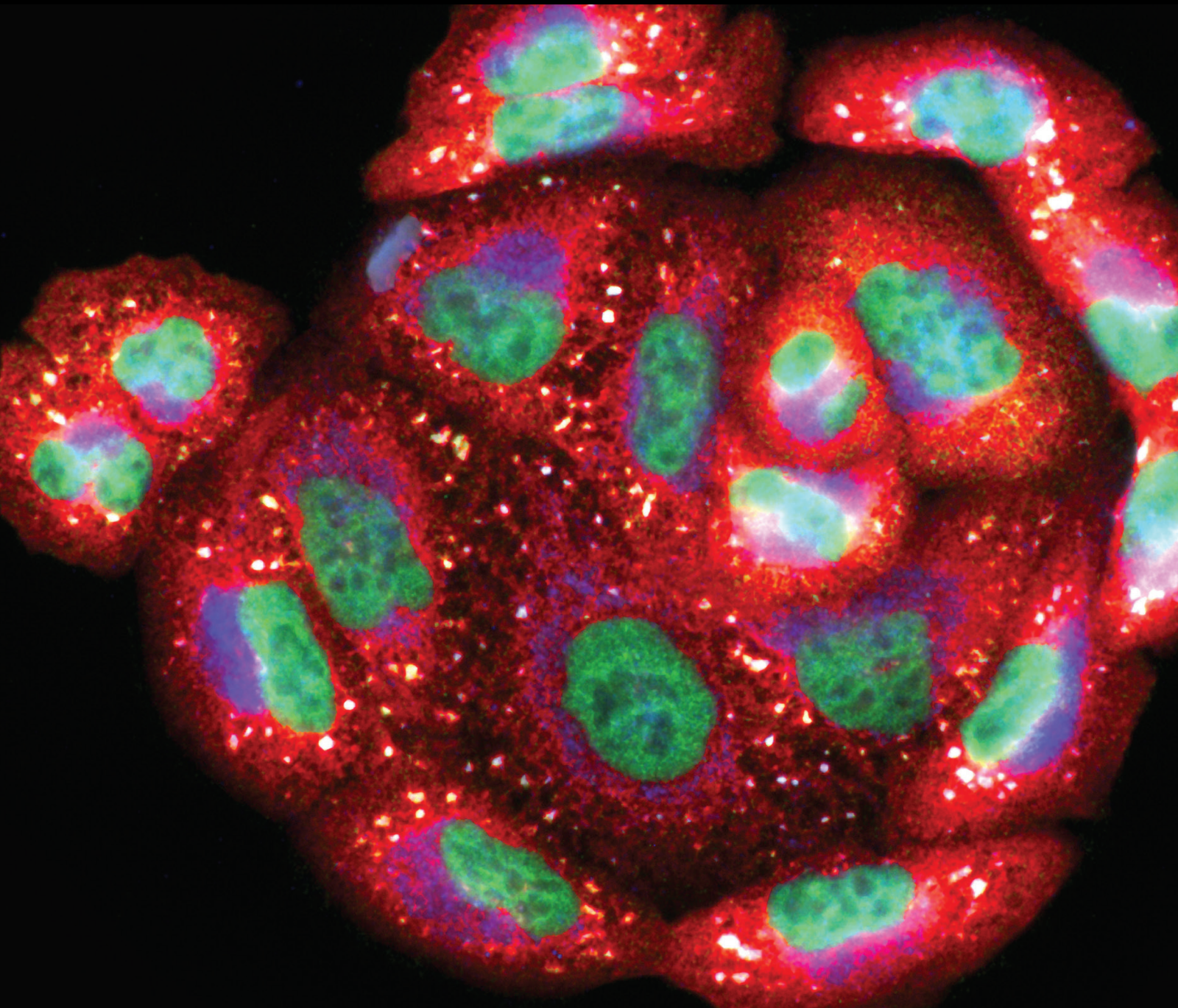


# Glial Cells and Oxidative Stress in Stroke

Lead Guest Editor: Anwen Shao

Guest Editors: Yujie Chen, Yuanjian Fang, Hansen Chen, and Yue He





---

# **Glial Cells and Oxidative Stress in Stroke**

Oxidative Medicine and Cellular Longevity

---

## **Glial Cells and Oxidative Stress in Stroke**

Lead Guest Editor: Anwen Shao

Guest Editors: Yujie Chen, Yuanjian Fang, Hansen  
Chen, and Yue He



---

Copyright © 2024 Hindawi Limited. All rights reserved.

This is a special issue published in "Oxidative Medicine and Cellular Longevity" All articles are open access articles distributed under the Creative Commons Attribution License, which permits unrestricted use, distribution, and reproduction in any medium, provided the original work is properly cited.

# Chief Editor

Jeannette Vasquez-Vivar, USA

## Associate Editors

Amjad Islam Aqib, Pakistan  
Angel Catalá , Argentina  
Cinzia Domenicotti , Italy  
Janusz Gebicki , Australia  
Aldrin V. Gomes , USA  
Vladimir Jakovljevic , Serbia  
Thomas Kietzmann , Finland  
Juan C. Mayo , Spain  
Ryuichi Morishita , Japan  
Claudia Penna , Italy  
Sachchida Nand Rai , India  
Paola Rizzo , Italy  
Mithun Sinha , USA  
Daniele Vergara , Italy  
Victor M. Victor , Spain

## Academic Editors

Ammar AL-Farga , Saudi Arabia  
Mohd Adnan , Saudi Arabia  
Ivanov Alexander , Russia  
Fabio Altieri , Italy  
Daniel Dias Rufino Arcanjo , Brazil  
Peter Backx, Canada  
Amira Badr , Egypt  
Damian Bailey, United Kingdom  
Rengasamy Balakrishnan , Republic of Korea  
Jiaolin Bao, China  
Ji C. Bihl , USA  
Hareram Birla, India  
Abdelhakim Bouyahya, Morocco  
Ralf Braun , Austria  
Laura Bravo , Spain  
Matt Brody , USA  
Amadou Camara , USA  
Marcio Carochio , Portugal  
Peter Celec , Slovakia  
Giselle Cerchiaro , Brazil  
Arpita Chatterjee , USA  
Shao-Yu Chen , USA  
Yujie Chen, China  
Deepak Chhangani , USA  
Ferdinando Chiaradonna , Italy

Zhao Zhong Chong, USA  
Fabio Ciccarone, Italy  
Alin Ciobica , Romania  
Ana Cipak Gasparovic , Croatia  
Giuseppe Cirillo , Italy  
Maria R. Ciriolo , Italy  
Massimo Collino , Italy  
Manuela Corte-Real , Portugal  
Manuela Curcio, Italy  
Domenico D'Arca , Italy  
Francesca Danesi , Italy  
Claudio De Lucia , USA  
Damião De Sousa , Brazil  
Enrico Desideri, Italy  
Francesca Diomede , Italy  
Raul Dominguez-Perles, Spain  
Joël R. Drevet , France  
Grégory Durand , France  
Alessandra Durazzo , Italy  
Javier Egea , Spain  
Pablo A. Evelson , Argentina  
Mohd Farhan, USA  
Ioannis G. Fatouros , Greece  
Gianna Ferretti , Italy  
Swaran J. S. Flora , India  
Maurizio Forte , Italy  
Teresa I. Fortoul, Mexico  
Anna Fracassi , USA  
Rodrigo Franco , USA  
Juan Gambini , Spain  
Gerardo García-Rivas , Mexico  
Husam Ghanim, USA  
Jayeeta Ghose , USA  
Rajeshwary Ghosh , USA  
Lucia Gimeno-Mallench, Spain  
Anna M. Giudetti , Italy  
Daniela Giustarini , Italy  
José Rodrigo Godoy, USA  
Saeid Golbidi , Canada  
Guohua Gong , China  
Tilman Grune, Germany  
Solomon Habtemariam , United Kingdom  
Eva-Maria Hanschmann , Germany  
Md Saquib Hasnain , India  
Md Hassan , India

Tim Hofer , Norway  
John D. Horowitz, Australia  
Silvana Hrelia , Italy  
Dragan Hrnčić, Serbia  
Zebo Huang , China  
Zhao Huang , China  
Tariq Hussain , Pakistan  
Stephan Immenschuh , Germany  
Norsharina Ismail, Malaysia  
Franco J. L. , Brazil  
Sedat Kacar , USA  
Andleeb Khan , Saudi Arabia  
Kum Kum Khanna, Australia  
Neelam Khaper , Canada  
Ramoji Kosuru , USA  
Demetrios Kouretas , Greece  
Andrey V. Kozlov , Austria  
Chan-Yen Kuo, Taiwan  
Gaocai Li , China  
Guoping Li , USA  
Jin-Long Li , China  
Qiangqiang Li , China  
Xin-Feng Li , China  
Jialiang Liang , China  
Adam Lightfoot, United Kingdom  
Christopher Horst Lillig , Germany  
Paloma B. Liton , USA  
Ana Lloret , Spain  
Lorenzo Loffredo , Italy  
Camilo López-Alarcón , Chile  
Daniel Lopez-Malo , Spain  
Massimo Lucarini , Italy  
Hai-Chun Ma, China  
Nageswara Madamanchi , USA  
Kenneth Maiese , USA  
Marco Malaguti , Italy  
Steven McAnulty, USA  
Antonio Desmond McCarthy , Argentina  
Sonia Medina-Escudero , Spain  
Pedro Mena , Italy  
V́ctor M. Mendoza-Núñez , Mexico  
Lidija Milkovic , Croatia  
Alexandra Miller, USA  
Sara Missaglia , Italy

Premysl Mladenka , Czech Republic  
Sandra Moreno , Italy  
Trevor A. Mori , Australia  
Fabiana Morroni , Italy  
Ange Mouithys-Mickalad, Belgium  
Iordanis Mourouzis , Greece  
Ryoji Nagai , Japan  
Amit Kumar Nayak , India  
Abderrahim Nemmar , United Arab Emirates  
Xing Niu , China  
Cristina Nocella, Italy  
Susana Novella , Spain  
Hassan Obied , Australia  
Pál Pacher, USA  
Pasquale Pagliaro , Italy  
Dilipkumar Pal , India  
Valentina Pallottini , Italy  
Swapnil Pandey , USA  
Mayur Parmar , USA  
Vassilis Paschalis , Greece  
Keshav Raj Paudel, Australia  
Ilaria Peluso , Italy  
Tiziana Persichini , Italy  
Shazib Pervaiz , Singapore  
Abdul Rehman Phull, Republic of Korea  
Vincent Pialoux , France  
Alessandro Poggi , Italy  
Zsolt Radak , Hungary  
Dario C. Ramirez , Argentina  
Erika Ramos-Tovar , Mexico  
Sid D. Ray , USA  
Muneeb Rehman , Saudi Arabia  
Hamid Reza Rezvani , France  
Alessandra Ricelli, Italy  
Francisco J. Romero , Spain  
Joan Roselló-Catafau, Spain  
Subhadeep Roy , India  
Josep V. Rubert , The Netherlands  
Sumbal Saba , Brazil  
Kunihiro Sakuma, Japan  
Gabriele Saretzki , United Kingdom  
Luciano Saso , Italy  
Nadja Schroder , Brazil

Anwen Shao , China  
Iman Sherif, Egypt  
Salah A Sheweita, Saudi Arabia  
Xiaolei Shi, China  
Manjari Singh, India  
Giulia Sita , Italy  
Ramachandran Srinivasan , India  
Adrian Sturza , Romania  
Kuo-hui Su , United Kingdom  
Eisa Tahmasbpour Marzouni , Iran  
Hailiang Tang, China  
Carla Tatone , Italy  
Shane Thomas , Australia  
Carlo Gabriele Tocchetti , Italy  
Angela Trovato Salinaro, Italy  
Rosa Tundis , Italy  
Kai Wang , China  
Min-qi Wang , China  
Natalie Ward , Australia  
Grzegorz Wegrzyn, Poland  
Philip Wenzel , Germany  
Guangzhen Wu , China  
Jianbo Xiao , Spain  
Qiongming Xu , China  
Liang-Jun Yan , USA  
Guillermo Zalba , Spain  
Jia Zhang , China  
Junmin Zhang , China  
Junli Zhao , USA  
Chen-he Zhou , China  
Yong Zhou , China  
Mario Zoratti , Italy

# Contents

---

**Retracted: Molecular Evolution of the Activating Transcription Factors Shapes the Adaptive Cellular Responses to Oxidative Stress**

Oxidative Medicine and Cellular Longevity

Retraction (1 page), Article ID 9875345, Volume 2024 (2024)

**Retracted: Microglia Involves in the Immune Inflammatory Response of Poststroke Depression: A Review of Evidence**

Oxidative Medicine and Cellular Longevity

Retraction (1 page), Article ID 9860462, Volume 2024 (2024)

**Retracted: Role of Glial Cell-Derived Oxidative Stress in Blood-Brain Barrier Damage after Acute Ischemic Stroke**

Oxidative Medicine and Cellular Longevity

Retraction (1 page), Article ID 9859161, Volume 2024 (2024)

**Retracted: Clinical Effect of Digital Subtraction Angiography Combined with Neurointerventional Thrombolysis for Acute Ischemic Cerebrovascular Disease and Its Influence on Vascular Endothelial Function and Oxidative Stress**

Oxidative Medicine and Cellular Longevity

Retraction (1 page), Article ID 9851637, Volume 2024 (2024)

**Retracted: Automatic Detection of Epilepsy Based on Entropy Feature Fusion and Convolutional Neural Network**

Oxidative Medicine and Cellular Longevity

Retraction (1 page), Article ID 9847185, Volume 2024 (2024)

**Retracted: Long Noncoding RNA TUG1 Aggravates Cerebral Ischemia/Reperfusion Injury by Acting as a ceRNA for miR-3072-3p to Target St8sia2**

Oxidative Medicine and Cellular Longevity

Retraction (1 page), Article ID 9832607, Volume 2024 (2024)

**Retracted: Aquaporin 4 Depolarization-Enhanced Transferrin Infiltration Leads to Neuronal Ferroptosis after Subarachnoid Hemorrhage in Mice**

Oxidative Medicine and Cellular Longevity

Retraction (1 page), Article ID 9830698, Volume 2024 (2024)

**Retracted: Influence Factors and Predictive Models for the Outcome of Patients with Ischemic Stroke after Intravenous Thrombolysis: A Multicenter Retrospective Cohort Study**

Oxidative Medicine and Cellular Longevity

Retraction (1 page), Article ID 9813785, Volume 2024 (2024)

**Retracted: Asymmetric Dimethylarginine Protects Neurons from Oxygen Glucose Deprivation Insult by Modulating Connexin-36 Expression**

Oxidative Medicine and Cellular Longevity

Retraction (1 page), Article ID 9785874, Volume 2024 (2024)



**Retracted: Delivery of miR-654-5p via SonoVue Microbubble Ultrasound Inhibits Proliferation, Migration, and Invasion of Vascular Smooth Muscle Cells and Arterial Thrombosis and Stenosis through Targeting TCF21**

Oxidative Medicine and Cellular Longevity

Retraction (1 page), Article ID 9757393, Volume 2024 (2024)

**Retracted: Radioanatomical Study of the Skull Base and Septum in Chinese: Implications for Using the HBF for Endoscopic Skull Base Reconstruction**

Oxidative Medicine and Cellular Longevity

Retraction (1 page), Article ID 9872861, Volume 2023 (2023)

**Pathophysiology of Ischemic Stroke: Noncoding RNA Role in Oxidative Stress**

Zhongzhou Su [ID](#), Yingze Ye [ID](#), Chengen Shen [ID](#), Sheng Qiu [ID](#), Yao Sun [ID](#), Siping Hu [ID](#), Xiaoxing Xiong [ID](#), Yuntao Li [ID](#), Liqin Li [ID](#), and Hongfa Wang [ID](#)

Review Article (12 pages), Article ID 5815843, Volume 2022 (2022)

**[Retracted] Role of Glial Cell-Derived Oxidative Stress in Blood-Brain Barrier Damage after Acute Ischemic Stroke**

Xiaoyan Hu [ID](#), Yanping Wang [ID](#), Weihong Du [ID](#), Li-Jun Liang [ID](#), Wei Wang [ID](#), and Xinchun Jin [ID](#)

Review Article (14 pages), Article ID 7762078, Volume 2022 (2022)

**[Retracted] Influence Factors and Predictive Models for the Outcome of Patients with Ischemic Stroke after Intravenous Thrombolysis: A Multicenter Retrospective Cohort Study**

Jin Hu [ID](#), Zhixian Fang [ID](#), Xia Lu [ID](#), Fei Wang [ID](#), Ningyuan Zhang [ID](#), Wenliang Pan [ID](#), Xinzheng Fu [ID](#), Gongchun Huang [ID](#), Xiaoli Tan [ID](#), and Wenyu Chen [ID](#)

Research Article (18 pages), Article ID 3363735, Volume 2022 (2022)

**[Retracted] Clinical Effect of Digital Subtraction Angiography Combined with Neurointerventional Thrombolysis for Acute Ischemic Cerebrovascular Disease and Its Influence on Vascular Endothelial Function and Oxidative Stress**

Xuna Wang, Xuesong Zhang, Qingbo Guan, and Kuiyang Wang [ID](#)

Research Article (8 pages), Article ID 2777865, Volume 2022 (2022)

**[Retracted] Microglia Involves in the Immune Inflammatory Response of Poststroke Depression: A Review of Evidence**

Weili Xia, Yong Xu, Yuandong Gong, Xiaojing Cheng, Tianguai Yu [ID](#), and Gongchang Yu [ID](#)

Review Article (11 pages), Article ID 2049371, Volume 2022 (2022)



**[Retracted] Delivery of miR-654-5p via SonoVue Microbubble Ultrasound Inhibits Proliferation, Migration, and Invasion of Vascular Smooth Muscle Cells and Arterial Thrombosis and Stenosis through Targeting TCF21**

Tao Wang, Xiaoqiang Tang, Yong Zhang, Xiaoqin Wang, Haifeng Shi, Ruohan Yin, and Changjie Pan [ID](#)







Research Article (24 pages), Article ID 4757081, Volume 2022 (2022)

## Contents











**[Retracted] Molecular Evolution of the Activating Transcription Factors Shapes the Adaptive Cellular Responses to Oxidative Stress**

Hafiz Ishfaq Ahmad , Asia Iqbal, Nabeel Ijaz, Muhammad Irfan Ullah, Akhtar Rasool Asif, Abdur Rahman, Tahir Mehmood, Ghulam Haider, Shakeel Ahmed, Samy F. Mahmoud, Fatimah Othman Alghamdi, Hala Abdulrahman Al Amari, Mario Juan Simirgiotis, and Jinping Chen   
Research Article (13 pages), Article ID 2153996, Volume 2022 (2022)




**[Retracted] Asymmetric Dimethylarginine Protects Neurons from Oxygen Glucose Deprivation Insult by Modulating Connexin-36 Expression**

Kun Fang , Shufen Chen , Yi Wang , Fangzhe Chen , Mei Cui , and Qiang Dong   
Research Article (8 pages), Article ID 5339361, Volume 2022 (2022)

**[Retracted] Aquaporin 4 Depolarization-Enhanced Transferrin Infiltration Leads to Neuronal Ferroptosis after Subarachnoid Hemorrhage in Mice**

Yuan Liu , Zongqi Wang , Chang Cao , Zhongmou Xu , Jinxin Lu , Haitao Shen , Xiang Li , Haiying Li , Jiang Wu , and Gang Chen   
Research Article (14 pages), Article ID 8808677, Volume 2022 (2022)




**Inhibiting Microglia-Derived NLRP3 Alleviates Subependymal Edema and Cognitive Dysfunction in Posthemorrhagic Hydrocephalus after Intracerebral Hemorrhage via AMPK/Beclin-1 Pathway**

Zhaoqi Zhang , Peiwen Guo, Suna Huang, Zhengcai Jia, Tunan Chen, Xin Liu, Hua Feng , and Yujie Chen   
Research Article (17 pages), Article ID 4177317, Volume 2022 (2022)

**[Retracted] Automatic Detection of Epilepsy Based on Entropy Feature Fusion and Convolutional Neural Network**

Yongxin Sun  and Xiaojuan Chen   
Research Article (13 pages), Article ID 1322826, Volume 2022 (2022)


**[Retracted] Long Noncoding RNA TUG1 Aggravates Cerebral Ischemia/Reperfusion Injury by Acting as a ceRNA for miR-3072-3p to Target St8sia2**

Miao Chen , Feng Wang, Limin Fan, Hairong Wang , and Shuo Gu   
Research Article (20 pages), Article ID 9381203, Volume 2022 (2022)



**[Retracted] Radioanatomical Study of the Skull Base and Septum in Chinese: Implications for Using the HBF for Endoscopic Skull Base Reconstruction**

Dongsheng Gu   
Research Article (11 pages), Article ID 9940239, Volume 2022 (2022)

**The Novel Nrf2 Activator Omaveloxolone Regulates Microglia Phenotype and Ameliorates Secondary Brain Injury after Intracerebral Hemorrhage in Mice**

Libin Hu, Yang Cao, Huaijun Chen, Lei Xu, Qiguo Yang, Hang Zhou, Jianru Li, Qian Yu, Zhangqi Dou, Yin Li, Feng Yan, Fuyi Liu , and Gao Chen   
Research Article (18 pages), Article ID 4564471, Volume 2022 (2022)

**Luteolin Confers Cerebroprotection after Subarachnoid Hemorrhage by Suppression of NLPR3  
Inflammasome Activation through Nrf2-Dependent Pathway**

Zi-Huan Zhang, Jia-Qiang Liu, Cheng-Di Hu, Xin-Tong Zhao, Fei-Yun Qin, Zong Zhuang , and Xiang-Sheng Zhang 

Research Article (18 pages), Article ID 5838101, Volume 2021 (2021)

## *Retraction*

# **Retracted: Molecular Evolution of the Activating Transcription Factors Shapes the Adaptive Cellular Responses to Oxidative Stress**

### **Oxidative Medicine and Cellular Longevity**

Received 8 January 2024; Accepted 8 January 2024; Published 9 January 2024

Copyright © 2024 Oxidative Medicine and Cellular Longevity. This is an open access article distributed under the Creative Commons Attribution License, which permits unrestricted use, distribution, and reproduction in any medium, provided the original work is properly cited.

This article has been retracted by Hindawi following an investigation undertaken by the publisher [1]. This investigation has uncovered evidence of one or more of the following indicators of systematic manipulation of the publication process:

- (1) Discrepancies in scope
- (2) Discrepancies in the description of the research reported
- (3) Discrepancies between the availability of data and the research described
- (4) Inappropriate citations
- (5) Incoherent, meaningless and/or irrelevant content included in the article
- (6) Manipulated or compromised peer review

The presence of these indicators undermines our confidence in the integrity of the article's content and we cannot, therefore, vouch for its reliability. Please note that this notice is intended solely to alert readers that the content of this article is unreliable. We have not investigated whether authors were aware of or involved in the systematic manipulation of the publication process.

Wiley and Hindawi regrets that the usual quality checks did not identify these issues before publication and have since put additional measures in place to safeguard research integrity.

We wish to credit our own Research Integrity and Research Publishing teams and anonymous and named external researchers and research integrity experts for contributing to this investigation.

The corresponding author, as the representative of all authors, has been given the opportunity to register their agreement or disagreement to this retraction. We have kept a record of any response received.

### **References**

- [1] H. I. Ahmad, A. Iqbal, N. Ijaz et al., "Molecular Evolution of the Activating Transcription Factors Shapes the Adaptive Cellular Responses to Oxidative Stress," *Oxidative Medicine and Cellular Longevity*, vol. 2022, Article ID 2153996, 13 pages, 2022.

## *Retraction*

# **Retracted: Microglia Involves in the Immune Inflammatory Response of Poststroke Depression: A Review of Evidence**

### **Oxidative Medicine and Cellular Longevity**

Received 8 January 2024; Accepted 8 January 2024; Published 9 January 2024

Copyright © 2024 Oxidative Medicine and Cellular Longevity. This is an open access article distributed under the Creative Commons Attribution License, which permits unrestricted use, distribution, and reproduction in any medium, provided the original work is properly cited.

This article has been retracted by Hindawi, as publisher, following an investigation undertaken by the publisher [1]. This investigation has uncovered evidence of systematic manipulation of the publication and peer-review process. We cannot, therefore, vouch for the reliability or integrity of this article.

Please note that this notice is intended solely to alert readers that the peer-review process of this article has been compromised.

Wiley and Hindawi regret that the usual quality checks did not identify these issues before publication and have since put additional measures in place to safeguard research integrity.

We wish to credit our Research Integrity and Research Publishing teams and anonymous and named external researchers and research integrity experts for contributing to this investigation.

The corresponding author, as the representative of all authors, has been given the opportunity to register their agreement or disagreement to this retraction. We have kept a record of any response received.

### **References**

- [1] W. Xia, Y. Xu, Y. Gong, X. Cheng, T. Yu, and G. Yu, "Microglia Involves in the Immune Inflammatory Response of Poststroke Depression: A Review of Evidence," *Oxidative Medicine and Cellular Longevity*, vol. 2022, Article ID 2049371, 11 pages, 2022.

## *Retraction*

# **Retracted: Role of Glial Cell-Derived Oxidative Stress in Blood-Brain Barrier Damage after Acute Ischemic Stroke**

### **Oxidative Medicine and Cellular Longevity**

Received 8 January 2024; Accepted 8 January 2024; Published 9 January 2024

Copyright © 2024 Oxidative Medicine and Cellular Longevity. This is an open access article distributed under the Creative Commons Attribution License, which permits unrestricted use, distribution, and reproduction in any medium, provided the original work is properly cited.

This article has been retracted by Hindawi, as publisher, following an investigation undertaken by the publisher [1]. This investigation has uncovered evidence of systematic manipulation of the publication and peer-review process. We cannot, therefore, vouch for the reliability or integrity of this article.

Please note that this notice is intended solely to alert readers that the peer-review process of this article has been compromised.

Wiley and Hindawi regret that the usual quality checks did not identify these issues before publication and have since put additional measures in place to safeguard research integrity.

We wish to credit our Research Integrity and Research Publishing teams and anonymous and named external researchers and research integrity experts for contributing to this investigation.

The corresponding author, as the representative of all authors, has been given the opportunity to register their agreement or disagreement to this retraction. We have kept a record of any response received.

### **References**

- [1] X. Hu, Y. Wang, W. Du, L.-J. Liang, W. Wang, and X. Jin, "Role of Glial Cell-Derived Oxidative Stress in Blood-Brain Barrier Damage after Acute Ischemic Stroke," *Oxidative Medicine and Cellular Longevity*, vol. 2022, Article ID 7762078, 14 pages, 2022.

## *Retraction*

# **Retracted: Clinical Effect of Digital Subtraction Angiography Combined with Neurointerventional Thrombolysis for Acute Ischemic Cerebrovascular Disease and Its Influence on Vascular Endothelial Function and Oxidative Stress**

### **Oxidative Medicine and Cellular Longevity**

Received 8 January 2024; Accepted 8 January 2024; Published 9 January 2024

Copyright © 2024 Oxidative Medicine and Cellular Longevity. This is an open access article distributed under the Creative Commons Attribution License, which permits unrestricted use, distribution, and reproduction in any medium, provided the original work is properly cited.

This article has been retracted by Hindawi, as publisher, following an investigation undertaken by the publisher [1]. This investigation has uncovered evidence of systematic manipulation of the publication and peer-review process. We cannot, therefore, vouch for the reliability or integrity of this article.

Please note that this notice is intended solely to alert readers that the peer-review process of this article has been compromised.

Wiley and Hindawi regret that the usual quality checks did not identify these issues before publication and have since put additional measures in place to safeguard research integrity.

We wish to credit our Research Integrity and Research Publishing teams and anonymous and named external researchers and research integrity experts for contributing to this investigation.

The corresponding author, as the representative of all authors, has been given the opportunity to register their agreement or disagreement to this retraction. We have kept a record of any response received.

## **References**

- [1] X. Wang, X. Zhang, Q. Guan, and K. Wang, "Clinical Effect of Digital Subtraction Angiography Combined with Neurointerventional Thrombolysis for Acute Ischemic Cerebrovascular Disease and Its Influence on Vascular Endothelial Function and Oxidative Stress," *Oxidative Medicine and Cellular Longevity*, vol. 2022, Article ID 2777865, 8 pages, 2022.

## Retraction

# Retracted: Automatic Detection of Epilepsy Based on Entropy Feature Fusion and Convolutional Neural Network

### Oxidative Medicine and Cellular Longevity

Received 8 January 2024; Accepted 8 January 2024; Published 9 January 2024

Copyright © 2024 Oxidative Medicine and Cellular Longevity. This is an open access article distributed under the Creative Commons Attribution License, which permits unrestricted use, distribution, and reproduction in any medium, provided the original work is properly cited.

This article has been retracted by Hindawi following an investigation undertaken by the publisher [1]. This investigation has uncovered evidence of one or more of the following indicators of systematic manipulation of the publication process:

- (1) Discrepancies in scope
- (2) Discrepancies in the description of the research reported
- (3) Discrepancies between the availability of data and the research described
- (4) Inappropriate citations
- (5) Incoherent, meaningless and/or irrelevant content included in the article
- (6) Manipulated or compromised peer review

The presence of these indicators undermines our confidence in the integrity of the article's content and we cannot, therefore, vouch for its reliability. Please note that this notice is intended solely to alert readers that the content of this article is unreliable. We have not investigated whether authors were aware of or involved in the systematic manipulation of the publication process.

In addition, our investigation has also shown that one or more of the following human-subject reporting requirements has not been met in this article: ethical approval by an Institutional Review Board (IRB) committee or equivalent, patient/participant consent to participate, and/or agreement to publish patient/participant details (where relevant).

Wiley and Hindawi regrets that the usual quality checks did not identify these issues before publication and have since put additional measures in place to safeguard research integrity.

We wish to credit our own Research Integrity and Research Publishing teams and anonymous and named external researchers and research integrity experts for contributing to this investigation.

The corresponding author, as the representative of all authors, has been given the opportunity to register their agreement or disagreement to this retraction. We have kept a record of any response received.

### References

- [1] Y. Sun and X. Chen, "Automatic Detection of Epilepsy Based on Entropy Feature Fusion and Convolutional Neural Network," *Oxidative Medicine and Cellular Longevity*, vol. 2022, Article ID 1322826, 13 pages, 2022.



## Retraction

# Retracted: Long Noncoding RNA TUG1 Aggravates Cerebral Ischemia/Reperfusion Injury by Acting as a ceRNA for miR-3072-3p to Target St8sia2

### Oxidative Medicine and Cellular Longevity

Received 8 January 2024; Accepted 8 January 2024; Published 9 January 2024

Copyright © 2024 Oxidative Medicine and Cellular Longevity. This is an open access article distributed under the Creative Commons Attribution License, which permits unrestricted use, distribution, and reproduction in any medium, provided the original work is properly cited.

This article has been retracted by Hindawi, as publisher, following an investigation undertaken by the publisher [1]. This investigation has uncovered evidence of systematic manipulation of the publication and peer-review process. We cannot, therefore, vouch for the reliability or integrity of this article.

Please note that this notice is intended solely to alert readers that the peer-review process of this article has been compromised.

Wiley and Hindawi regret that the usual quality checks did not identify these issues before publication and have since put additional measures in place to safeguard research integrity.

We wish to credit our Research Integrity and Research Publishing teams and anonymous and named external researchers and research integrity experts for contributing to this investigation.

The corresponding author, as the representative of all authors, has been given the opportunity to register their agreement or disagreement to this retraction. We have kept a record of any response received.

### References

- [1] M. Chen, F. Wang, L. Fan, H. Wang, and S. Gu, "Long Noncoding RNA TUG1 Aggravates Cerebral Ischemia/Reperfusion Injury by Acting as a ceRNA for miR-3072-3p to Target St8sia2," *Oxidative Medicine and Cellular Longevity*, vol. 2022, Article ID 9381203, 20 pages, 2022.

## *Retraction*

# **Retracted: Aquaporin 4 Depolarization-Enhanced Transferrin Infiltration Leads to Neuronal Ferroptosis after Subarachnoid Hemorrhage in Mice**

### **Oxidative Medicine and Cellular Longevity**

Received 8 January 2024; Accepted 8 January 2024; Published 9 January 2024

Copyright © 2024 Oxidative Medicine and Cellular Longevity. This is an open access article distributed under the Creative Commons Attribution License, which permits unrestricted use, distribution, and reproduction in any medium, provided the original work is properly cited.

This article has been retracted by Hindawi, as publisher, following an investigation undertaken by the publisher [1]. This investigation has uncovered evidence of systematic manipulation of the publication and peer-review process. We cannot, therefore, vouch for the reliability or integrity of this article.

Please note that this notice is intended solely to alert readers that the peer-review process of this article has been compromised.

Wiley and Hindawi regret that the usual quality checks did not identify these issues before publication and have since put additional measures in place to safeguard research integrity.

We wish to credit our Research Integrity and Research Publishing teams and anonymous and named external researchers and research integrity experts for contributing to this investigation.

The corresponding author, as the representative of all authors, has been given the opportunity to register their agreement or disagreement to this retraction. We have kept a record of any response received.

### **References**

- [1] Y. Liu, Z. Wang, C. Cao et al., “Aquaporin 4 Depolarization-Enhanced Transferrin Infiltration Leads to Neuronal Ferroptosis after Subarachnoid Hemorrhage in Mice,” *Oxidative Medicine and Cellular Longevity*, vol. 2022, Article ID 8808677, 14 pages, 2022.

## *Retraction*

# **Retracted: Influence Factors and Predictive Models for the Outcome of Patients with Ischemic Stroke after Intravenous Thrombolysis: A Multicenter Retrospective Cohort Study**

### **Oxidative Medicine and Cellular Longevity**

Received 8 January 2024; Accepted 8 January 2024; Published 9 January 2024

Copyright © 2024 Oxidative Medicine and Cellular Longevity. This is an open access article distributed under the Creative Commons Attribution License, which permits unrestricted use, distribution, and reproduction in any medium, provided the original work is properly cited.

This article has been retracted by Hindawi following an investigation undertaken by the publisher [1]. This investigation has uncovered evidence of one or more of the following indicators of systematic manipulation of the publication process:

- (1) Discrepancies in scope
- (2) Discrepancies in the description of the research reported
- (3) Discrepancies between the availability of data and the research described
- (4) Inappropriate citations
- (5) Incoherent, meaningless and/or irrelevant content included in the article
- (6) Manipulated or compromised peer review

The presence of these indicators undermines our confidence in the integrity of the article's content and we cannot, therefore, vouch for its reliability. Please note that this notice is intended solely to alert readers that the content of this article is unreliable. We have not investigated whether authors were aware of or involved in the systematic manipulation of the publication process.

Wiley and Hindawi regrets that the usual quality checks did not identify these issues before publication and have since put additional measures in place to safeguard research integrity.

We wish to credit our own Research Integrity and Research Publishing teams and anonymous and named external researchers and research integrity experts for contributing to this investigation.

The corresponding author, as the representative of all authors, has been given the opportunity to register their agreement or disagreement to this retraction. We have kept a record of any response received.

### **References**

- [1] J. Hu, Z. Fang, X. Lu et al., "Influence Factors and Predictive Models for the Outcome of Patients with Ischemic Stroke after Intravenous Thrombolysis: A Multicenter Retrospective Cohort Study," *Oxidative Medicine and Cellular Longevity*, vol. 2022, Article ID 3363735, 18 pages, 2022.

## Retraction

# Retracted: Asymmetric Dimethylarginine Protects Neurons from Oxygen Glucose Deprivation Insult by Modulating Connexin-36 Expression

### Oxidative Medicine and Cellular Longevity

Received 8 January 2024; Accepted 8 January 2024; Published 9 January 2024

Copyright © 2024 Oxidative Medicine and Cellular Longevity. This is an open access article distributed under the Creative Commons Attribution License, which permits unrestricted use, distribution, and reproduction in any medium, provided the original work is properly cited.

This article has been retracted by Hindawi following an investigation undertaken by the publisher [1]. This investigation has uncovered evidence of one or more of the following indicators of systematic manipulation of the publication process:

- (1) Discrepancies in scope
- (2) Discrepancies in the description of the research reported
- (3) Discrepancies between the availability of data and the research described
- (4) Inappropriate citations
- (5) Incoherent, meaningless and/or irrelevant content included in the article
- (6) Manipulated or compromised peer review

The presence of these indicators undermines our confidence in the integrity of the article's content and we cannot, therefore, vouch for its reliability. Please note that this notice is intended solely to alert readers that the content of this article is unreliable. We have not investigated whether authors were aware of or involved in the systematic manipulation of the publication process.

Wiley and Hindawi regrets that the usual quality checks did not identify these issues before publication and have since put additional measures in place to safeguard research integrity.

We wish to credit our own Research Integrity and Research Publishing teams and anonymous and named external researchers and research integrity experts for contributing to this investigation.

The corresponding author, as the representative of all authors, has been given the opportunity to register their agreement or disagreement to this retraction. We have kept a record of any response received.

### References

- [1] K. Fang, S. Chen, Y. Wang, F. Chen, M. Cui, and Q. Dong, "Asymmetric Dimethylarginine Protects Neurons from Oxygen Glucose Deprivation Insult by Modulating Connexin-36 Expression," *Oxidative Medicine and Cellular Longevity*, vol. 2022, Article ID 5339361, 8 pages, 2022.

## Retraction

# Retracted: Delivery of miR-654-5p via SonoVue Microbubble Ultrasound Inhibits Proliferation, Migration, and Invasion of Vascular Smooth Muscle Cells and Arterial Thrombosis and Stenosis through Targeting TCF21

### Oxidative Medicine and Cellular Longevity

Received 8 January 2024; Accepted 8 January 2024; Published 9 January 2024

Copyright © 2024 Oxidative Medicine and Cellular Longevity. This is an open access article distributed under the Creative Commons Attribution License, which permits unrestricted use, distribution, and reproduction in any medium, provided the original work is properly cited.

This article has been retracted by Hindawi following an investigation undertaken by the publisher [1]. This investigation has uncovered evidence of one or more of the following indicators of systematic manipulation of the publication process:

- (1) Discrepancies in scope
- (2) Discrepancies in the description of the research reported
- (3) Discrepancies between the availability of data and the research described
- (4) Inappropriate citations
- (5) Incoherent, meaningless and/or irrelevant content included in the article
- (6) Manipulated or compromised peer review

The presence of these indicators undermines our confidence in the integrity of the article's content and we cannot, therefore, vouch for its reliability. Please note that this notice is intended solely to alert readers that the content of this article is unreliable. We have not investigated whether authors were aware of or involved in the systematic manipulation of the publication process.

Wiley and Hindawi regrets that the usual quality checks did not identify these issues before publication and have since put additional measures in place to safeguard research integrity.

We wish to credit our own Research Integrity and Research Publishing teams and anonymous and named external researchers and research integrity experts for contributing to this investigation.

The corresponding author, as the representative of all authors, has been given the opportunity to register their

agreement or disagreement to this retraction. We have kept a record of any response received.

### References

- [1] T. Wang, X. Tang, Y. Zhang et al., "Delivery of miR-654-5p via SonoVue Microbubble Ultrasound Inhibits Proliferation, Migration, and Invasion of Vascular Smooth Muscle Cells and Arterial Thrombosis and Stenosis through Targeting TCF21," *Oxidative Medicine and Cellular Longevity*, vol. 2022, Article ID 4757081, 24 pages, 2022.

## Retraction

# Retracted: Radioanatomical Study of the Skull Base and Septum in Chinese: Implications for Using the HBF for Endoscopic Skull Base Reconstruction

### Oxidative Medicine and Cellular Longevity

Received 26 September 2023; Accepted 26 September 2023; Published 27 September 2023

Copyright © 2023 Oxidative Medicine and Cellular Longevity. This is an open access article distributed under the Creative Commons Attribution License, which permits unrestricted use, distribution, and reproduction in any medium, provided the original work is properly cited.

This article has been retracted by Hindawi following an investigation undertaken by the publisher [1]. This investigation has uncovered evidence of one or more of the following indicators of systematic manipulation of the publication process:

- (1) Discrepancies in scope
- (2) Discrepancies in the description of the research reported
- (3) Discrepancies between the availability of data and the research described
- (4) Inappropriate citations
- (5) Incoherent, meaningless and/or irrelevant content included in the article
- (6) Peer-review manipulation

The presence of these indicators undermines our confidence in the integrity of the article's content and we cannot, therefore, vouch for its reliability. Please note that this notice is intended solely to alert readers that the content of this article is unreliable. We have not investigated whether authors were aware of or involved in the systematic manipulation of the publication process.

In addition, our investigation has also shown that one or more of the following human-subject reporting requirements has not been met in this article: ethical approval by an Institutional Review Board (IRB) committee or equivalent, patient/participant consent to participate, and/or agreement to publish patient/participant details (where relevant).

Wiley and Hindawi regrets that the usual quality checks did not identify these issues before publication and have since put additional measures in place to safeguard research integrity.

We wish to credit our own Research Integrity and Research Publishing teams and anonymous and named external

researchers and research integrity experts for contributing to this investigation.

The corresponding author, as the representative of all authors, has been given the opportunity to register their agreement or disagreement to this retraction. We have kept a record of any response received.

### References

- [1] D. Gu, "Radioanatomical Study of the Skull Base and Septum in Chinese: Implications for Using the HBF for Endoscopic Skull Base Reconstruction," *Oxidative Medicine and Cellular Longevity*, vol. 2022, Article ID 9940239, 11 pages, 2022.

## Review Article

# Pathophysiology of Ischemic Stroke: Noncoding RNA Role in Oxidative Stress

Zhongzhou Su <sup>1,2</sup>, Yingze Ye <sup>3</sup>, Chengen Shen <sup>1,2</sup>, Sheng Qiu <sup>1,2</sup>, Yao Sun <sup>1,2</sup>,  
Siping Hu <sup>2,4</sup>, Xiaoxing Xiong <sup>1,2,3</sup>, Yuntao Li <sup>1,2,3</sup>, Liqin Li <sup>1</sup>, and Hongfa Wang <sup>5</sup>

<sup>1</sup>Department of Neurosurgery, The Affiliated Huzhou Hospital, Zhejiang University School of Medicine (Huzhou Central Hospital), Huzhou, China

<sup>2</sup>Huzhou Key Laboratory of Basic Research and Clinical Translation for Neuro Modulation, Huzhou, China

<sup>3</sup>Department of Neurosurgery, Renmin Hospital of Wuhan University, Wuhan, China

<sup>4</sup>Department of Anesthesiology, The Affiliated Huzhou Hospital, Zhejiang University School of Medicine (Huzhou Central Hospital), Huzhou, China

<sup>5</sup>Rehabilitation Medicine Center, Department of Anesthesiology, Zhejiang Provincial People's Hospital, Affiliated People's Hospital, Hangzhou Medical College, Hangzhou, China

Correspondence should be addressed to Yuntao Li; [lyta722@live.com](mailto:lyta722@live.com), Liqin Li; [liliqin@hzhospital.com](mailto:liliqin@hzhospital.com), and Hongfa Wang; [whf033@163.com](mailto:whf033@163.com)

Received 8 June 2022; Revised 12 July 2022; Accepted 20 August 2022; Published 12 September 2022

Academic Editor: Yujie Chen

Copyright © 2022 Zhongzhou Su et al. This is an open access article distributed under the Creative Commons Attribution License, which permits unrestricted use, distribution, and reproduction in any medium, provided the original work is properly cited.

Stroke is a neurological disease that causes significant disability and death worldwide. Ischemic stroke accounts for 75% of all strokes. The pathophysiological processes underlying ischemic stroke include oxidative stress, the toxicity of excitatory amino acids, ion disorder, enhanced apoptosis, and inflammation. Noncoding RNAs (ncRNAs) may have a vital role in regulating the pathophysiological processes of ischemic stroke, as confirmed by the altered expression of ncRNAs in blood samples from acute ischemic stroke patients, animal models, and oxygen-glucose-deprived (OGD) cell models. Due to specific changes in expression, ncRNAs can potentially be biomarkers for the diagnosis, treatment, and prognosis of ischemic stroke. As an important brain cell component, glial cells mediate the occurrence and progression of oxidative stress after ischemic stroke, and ncRNAs are an irreplaceable part of this mechanism. This review highlights the impact of ncRNAs in the oxidative stress process of ischemic stroke. It focuses on specific ncRNAs that underlie the pathophysiology of ischemic stroke and have potential as diagnostic biomarkers and therapeutic targets.

## 1. Introduction

Globally, stroke is the cause of the second-highest deaths and the most disability-adjusted life years (DALYs). Stroke is a significant economic burden and stress on society worldwide [1, 2]. Nearly 60% of all strokes occur in people under 70 years old, and stroke incidence rates have shown a sharp and steady increase among young people aged 15 to 49 years [3]. Strokes can be classified into hemorrhagic or ischemic strokes, and the latter accounts for nearly 87% of all stroke cases [4]. A cerebral artery embolism leads to ischemic stroke with ischemia and hypoxia in the infraction of the corresponding brain areas,

resulting in neuronal death and irreversible neurological deficits. After ischemia, neurons can immediately not maintain their normal transmembrane ion gradient and homeostasis. This triggers several processes that lead to cell death, such as excitotoxicity, oxidative and nitrative stress, inflammation, and apoptosis. These pathophysiological processes are highly detrimental to neurons, glial, and endothelial cells [5–7]. They are interrelated and continuously trigger each other in a positive feedback loop that destroys neurons [8]. Furthermore, ischemia-reperfusion injury (IRI) that occurs once blood flow is restored may exacerbate these processes [9]. During rapid blood flow recanalization, the demand for sugars and oxygen

increases rapidly, oxidase is activated in large amounts, and the degree of tissue oxidation increases greatly. These changes result in a cellular “oxidative burst” and excessive formation of reactive oxygen species (ROS), leading to secondary cerebral ischemia and reperfusion brain damage. As the most basic and critical pathological progression of brain injury, oxidative stress causes neuronal apoptosis, activation of inflammatory signaling pathways, and impairment of the blood-brain barrier (BBB) [10–12].

ncRNAs are a class of functional RNAs. While they cannot code for proteins, ncRNAs regulate gene expression in a posttranscriptional manner, including microRNAs (miRNAs), long noncoding RNAs (lncRNAs), and circular RNAs (circRNAs) [13, 14]. ncRNAs have been reported to be abundantly expressed in the mammalian brain. Additionally, recent studies have depicted that cerebral ischemia alters the expression profiles of ncRNAs [15, 16]. According to many studies, ncRNAs are involved in oxidative stress by controlling transcription and translation, thereby affecting neuronal cell survival [17–19].

Despite the unfavorable results of clinical trials, pre-clinical studies have suggested that oxidative stress damage may be a potential therapeutic target in ischemic stroke. Dysregulation of ncRNAs is a known mechanism contributing to cerebral ischemia, and potential biomarkers and therapeutic targets for treating cerebral ischemia have been identified. However, none of these breakthroughs have been successfully implemented in clinical practice. This review is aimed at discussing the role of noncoding RNA in oxidative stress in postischemic stroke brain injuries to lay the foundation for therapy and prophylaxis.

## 2. Oxidative Stress in Ischemic Stroke and Ischemia-Reperfusion Injury

The brain accounts for 20% of the total oxygen consumption. Accordingly, it has poor tolerance to hypoxia. When blood flow is interrupted, the ischemic area of the brain cannot maintain redox homeostasis and ion balance due to the lack of oxygen and glucose, which affects cell electrochemistry, metabolism, and the release of toxic products. Anoxic depolarization and various processes are triggered by the massive efflux of  $K^+$  and influx of  $Na^+$ , water, and  $Ca^{2+}$ . These result in oxidative and nitrosative stress, excitotoxicity, inflammation, and apoptosis, eventually injuring neurons, glia, and endothelial cells [5, 7, 20–22]. During this process, numerous free radicals are formed, including reactive oxygen species (ROS) and reactive nitrogen species (RNS), which participate in the breakdown of antioxidant systems and lead to brain damage caused by ischemic stroke as well as cerebral ischemia-reperfusion injury [23]. However, two phases of ischemia and reperfusion have differences with regard to the source of free radicals and state of oxidative stress.

*2.1. Oxidative Stress in the Phases of Ischemia.* During the ischemic period, restricted oxygen availability is associated with acidosis, energy deficiency, and changes in ion homeostasis, leading to compensatory brain dysfunction and even-

tually neuronal death [24, 25]. In the presence of residual oxygen, e.g., in low-flow ischemia, ROS is produced mainly in mitochondria. Under physiological conditions, superoxide dismutase (SOD), glutathione peroxidase (GPX), catalase, and other antioxidant enzymes can aid in maintaining a neutral balance and catalytically protect brain tissues from the cytotoxicity of reactive oxygen species [26]. In addition, ROS play a physiological role by regulating immune system function, maintaining redox homeostasis, and participating in various metabolic pathways, even as second messengers [27, 28]. Endothelial cells rich in mitochondria are efficient sources of ROS. Due to their inherent characteristics and environmental factors, they are especially vulnerable to oxidative stress-induced damage. The effects of ROS include excessive lipid peroxidation and alterations in the functions of receptors, ion channels, and other membrane proteins, subsequently affecting the fluidity and permeability of cell membranes [29–31]. These pathologies cause damage to the blood-brain barrier (BBB) and often lead to leukocyte infiltration and edema [32, 33]. Furthermore, neuronal function relies on the continuous availability of ATP. As ischemic stroke depletes oxygen in the brain, neurons can no longer maintain their transmembrane gradient, and neuronal signaling is impaired [34]. In addition, glucose and oxygen deprivation inhibits ATP synthesis and blocks Na/K-ATPase activity. As a result, calcium ions flow into the cell [29–31]. Increased  $Ca^{2+}$  concentration activates cyclases (cox-1 and cox-2) and phospholipase A2, which not only increases ROS production but also enhances glutamergic neurotransmission [32, 35]. Increased levels of sodium, calcium, and adenosine diphosphate (ADP) also contribute to the overproduction of mitochondrial ROS (mROS) [36, 37], inducing neuron apoptosis and death [38, 39].

Nitric oxide (NO) is another substance that promotes oxidative stress. NO peaks rapidly at 0.5 h after MCAO and immediately decreases to a low level at 4 h together with eNOS/Nnos. Then, NO gradually increased with the increase in iNOS and peaked at 46 h [40]. In studies of ischemic stroke patients, increases in NO metabolites from day 1 to day 2 were beneficial for neurological function, while sharp increases in NO metabolites from days 2 to 7 were associated with a doubling of infarct volume [40]. NO displays cytotoxicity by destroying cellular DNA, blocking mitochondrial activity, and enhancing nitrifying damage by forming peroxynitrite ( $ONOO^-$ ) [41, 42]. NO is usually produced by endothelial nitric oxide synthase (eNOS). However, under inflammatory conditions, smooth muscle cells and macrophages overexpress inducible nitric oxide synthase (iNOS), thus producing large amounts of NO [43]. Moreover, NO is also produced by neuronal nitric oxide synthase (nNOS) [32, 40]. When it collides with NO, both molecules react quickly to form highly reactive  $ONOO^-$  [44]. Superoxide anions can also be dismutated into the more stable  $H_2O_2$  through a reaction catalyzed by superoxide dismutase (SOD). In the central nervous system,  $O_2^-$  is one of the most important reactive oxygen species as it damages ROS-producing cells and neighboring cells [43, 45]. Superoxide,



a byproduct of mitochondrial respiratory chain reactions, is the product of xanthine oxidase (XO) and nicotinamide adenine dinucleotide phosphate (NADPH) oxidase (NOX) activities [43, 46–48]. Interestingly, as the levels of superoxide increase, the NO radical has a dual effect. To be specific, NO interferes with SOD by reducing the antioxidant effect of SOD [43].

**2.2. Oxidative Stress in the Phases of Reperfusion.** The reperfusion of ischemic tissue has long been thought to be beneficial for tissue injury recovery. However, in the 1970s, reports of paradoxical enhancement of the injury response after ischemic (or hypoxic) tissue reperfusion (or reoxygenation) appeared, and the assumed beneficial effects of early reperfusion on tissue recovery after ischemia were questioned [49]. The question was solved when it was first found that the sudden resupply of molecular oxygen to energy- (and oxygen-) deficient tissues resulted in a special injury response not seen in hypoxic stress [50]. The discovery of this reoxygenation-dependent injury response, now known as “reperfusion injury,” established a new field of scientific research that has since grown rapidly and continuously.

During reperfusion, the overproduction of ROS originates from four pathways: mitochondrial respiratory chain, cyclooxygenase-2-catalyzed arachidonic acid reaction, NADPH oxidase, and xanthine and hypoxanthine via xanthine oxidase (Figure 1). In the stage of early reperfusion, when microglia and other peripheral immune cells infiltrate, activation of NADPH oxidase in these immune cells contributes to the production of ROS, a phenomenon known as the “oxygen burst.” NADPH oxidase also produces ROS in other cells, such as vascular endothelial cells [51]. When the blood flow is reinstated, a large amount of oxygen arrives and accelerates oxidative damage. Furthermore, oxidative stress during ischemia and reperfusion is known to activate proapoptotic signaling pathways such as cytochrome c signaling, induce DNA damage, alter protein structure and function, and induce lipid peroxidation [52–54]. In addition, oxidative stress can directly regulate important molecules in cellular signaling circuits, such as ion channels and protein kinases [55]. Over the past 25 years, researchers have found that hydrogen peroxide and possibly superoxide play a physiological role in cell signaling and transcriptional regulation [56]. Later research revealed that hydrogen peroxide is also produced under physiological conditions, e.g., in response to growth signals, and it can be overproduced in transformed cells expressing oncogenic mutant Ras [57]. ROS is produced in response to various ligands, including growth factors, cytokines, and G protein-coupled receptors [58, 59]. Therefore, during the recovery phase of reperfusion, low ROS concentrations play a key role in biotransduction signaling, which may be an important reason for promoting recovery from brain tissue damage during the recovery phase.

As displayed in Figure 1, NO and ONOO<sup>-</sup> are two common types of RNS frequently reported in cerebral ischemia-reperfusion injury. Low levels of NO, produced by endothelial nitric oxide synthase, have physiological functions; conversely, high levels of NO, produced by inducible nitric

oxide synthase (NOS) and neuronal nitric oxide synthase (nNOS), have effects on ischemic brain tissue. iNOS and nNOS are known to lead to inflammation, cell death, increased blood-brain barrier permeability, and increased infarct size. During cerebral ischemia or cerebral ischemia-reperfusion injury, NO is produced simultaneously with superoxide anion (O<sup>2-</sup>) and rapidly reacts with O<sup>2-</sup> at a diffusion-limited rate to generate ONOO<sup>-</sup>. Peroxynitrite readily penetrates the lipid bilayer. It then impairs cell signaling by causing lipid peroxidation of the membrane, mediates nitration of tyrosine residues, and inhibits tyrosine phosphorylation. Peroxynitrite inactivates aconitase and superoxide dismutase, mediates NO-induced BBB damage, and triggers apoptotic cell death (Figure 1).

### 3. Roles of ncRNAs in Ischemia Stroke-Induced Oxidative Stress

**3.1. miRNA Involved in Oxidative Stress following Ischemia Stroke.** miRNAs, small noncoding RNA superfamily members, are endogenous single-stranded RNA molecules of about 18–25 nucleotides [60]. They act as negative regulators for more than 60% of protein-coding gene expressions by degrading or translationally inhibiting target mRNAs [61–63]. miRNAs can simultaneously modulate targets involved in the pathophysiological process of cerebral ischemia. Therefore, they are considered to have potential as diagnostic and prognostic biomarkers and promising therapeutics in treating ischemic stroke [64, 65]. miRNAs are produced as long primary transcripts (pri-miRNAs) and cleaved by Drosha RNase III endonuclease to result in dry ring intermediates (pre-miRNAs) of approximately 60 to 70 nucleotides [66]. The pre-miRNAs are then exported from the nucleus to the cytoplasm, where they are treated by Dicer RNase II endonucleases to form mature miRNAs of approximately 22–25 nucleotides [67]. Next, the mature miRNAs bind to multiprotein complexes called RNA-induced silencing complexes (RISC), which then bind to the 3'-untranslated region (UTR) of their respective target mRNAs to inhibit translation [68]. Previous studies have found that miRNAs can be potential targets and modulators of oxidative stress-related pathways [69]. miRNAs associated with oxidative stress-related pathways are known as oxidative stress-responsive miRNAs [70]. Intracellular ROS can inhibit or promote miRNA expression and thus produce subsequent biological effects by regulating their direct target genes [71] (Figure 2).

The transient expression of miRNA was observed in blood and brain samples in the MCAO model after reperfusion. Additionally, miR-124a and -290 were upregulated after IR, targeted VSNL1 [72], encoded neuronal calcium sensor proteins in cerebellar granulos cells, and regulated intracellular signaling pathways directly or indirectly by regulating cyclic nucleotide and MAPK pathways [73], therefore playing an active role in cell death, migration, and neuronal plasticity under pathological conditions such as stroke [74, 75]. Furthermore, miR30a-3p, -99a, -99b, -100, -223, and -383 were upregulated after IR and targeted

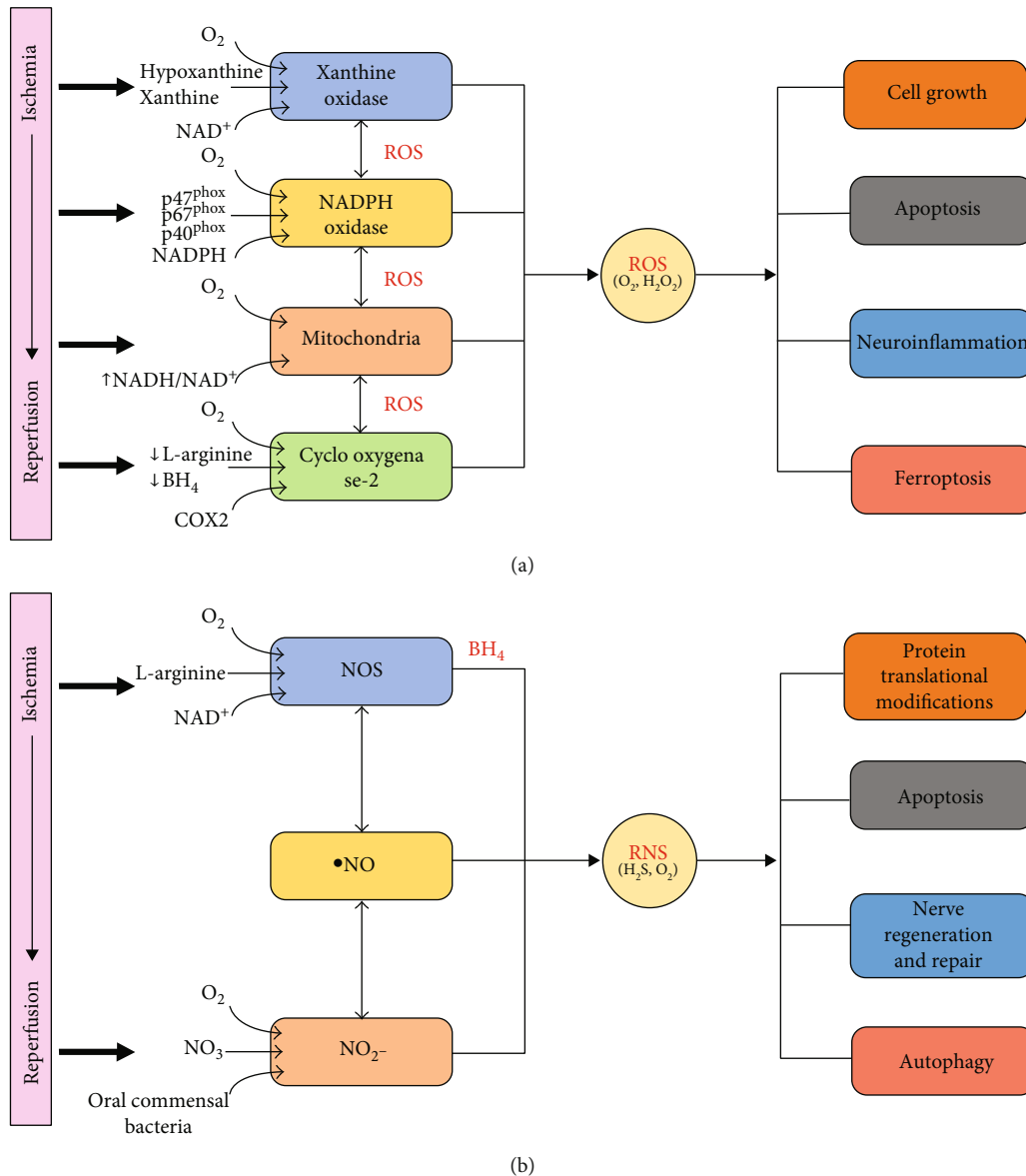


FIGURE 1: The sources of ROS and RNS during cerebral ischemia-reperfusion injury. During reperfusion, the overproduction of ROS originates from four pathways: mitochondrial respiratory chain, cyclooxygenase-2-catalyzed arachidonic acid reaction, NADPH oxidase, and xanthine and hypoxanthine via xanthine oxidase. In addition, NO and ONOO<sup>-</sup> are two common types of RNS that have been frequently reported in cerebral ischemia-reperfusion injury.

AQP4 [72], which was speculated to reduce cerebral edema due to its action as a water-selective channel in the plasma membrane of many cells and maintains cerebral hydrohomeostasis [76, 77]. miR-132 and -664 were downregulated after IR and targeted MMP9 [72], which disrupted the blood-brain barrier and caused cerebral edema. In addition, serum MMP-9 level was noted to be correlated with the severity of clinical stroke [78–80].

Based on transcriptome analysis, mitochondrial dysfunction and increased oxidative stress were the molecular mechanisms of miR-210 blockade, leading to increased tissue damage. While miR-210 can alleviate the decreased oxidative metabolism caused by tissue hypoxia, miR-210 also increases the accumulation of ROS, causing cell death and tissue damage [81–83]. However, in ischemic rats, the neu-

roprotective effects of decreased apoptosis and antioxidant stress response to vagus stimulation were associated with increased miR-210 expression. Protection decreased when miR-210 was blocked, thus suggesting that miR-210 is a neuroprotective factor against ischemia/reperfusion injury [84].

miR-124 is preferentially expressed in the cerebral cortex and cerebellum, initially at low levels in neural progenitors and subsequently at high levels in differentiated and mature neurons [85, 86]. In addition, miR-124 has been reported to protect PC12 cells from OGD/R-induced apoptosis by reducing oxidative stress via the PI3K/AKT/Nrf2 pathway [87]. Moreover, miR-124 enhances neurological recovery in various neurological illnesses by reducing oxidative stress after spinal cord damage via Bax [88, 89]. miR-124 inhibits inflammatory activation under oxidative stress and thereby

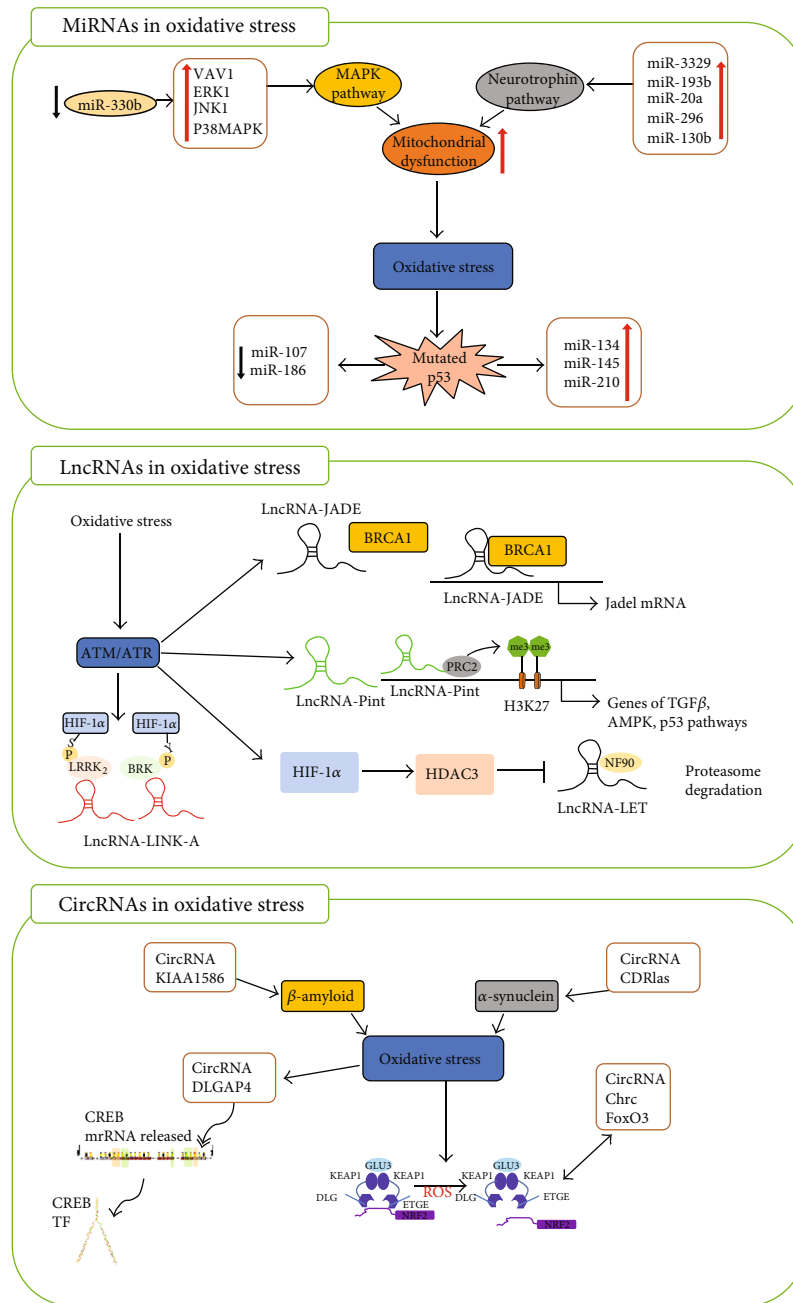


FIGURE 2: A mechanistic diagram of representative ncRNAs involved in oxidative stress under cerebral ischemia-reperfusion injury. Three different types of ncRNAs are involved in the mechanism of oxidative stress regulation in ischemic stroke, including oxidative stress induction, regulation, and effect. The ncRNAs in figure are taken as examples.

delays the progression of Alzheimer’s disease (AD) [90]. These findings suggest that miR-124 is an important therapeutic target for inhibiting oxidative stress in ischemic stroke.

miR-217 is highly expressed in MCAO rats and the OGD cell model, and its expression level positively correlates with cognitive impairment in MCAO rats. miR-217 also deregulates MEF2D, regulates HDAC5 and ND6 expression, and promotes mitochondrial ROS production, thus leading to enhanced neuronal damage in ischemic stroke and IR [91].

**3.2. lncRNAs Involved in Oxidative Stress following Ischemia Stroke.** lncRNAs of more than 200 nucleotides are cell- and tissue-specific. These may be classified based on the genomic placement between the coding areas of their functional genes (long intergenic ncRNAs) or by coding gene overlap in either the consensus or antisense direction [92, 93]. As guides for chromatin modification complexes or transcription factors in the nucleus, cytoplasmic lncRNAs typically regulate mRNA translation by acting as competing endogenous RNA (ceRNA) or controlling mRNA stability [94]. Also, the lncRNA expression profile in the ischemic

penumbra was significantly altered after 1 h reperfusion in MCAO rats [95] (Figure 2).

In patients with ischemic stroke, lncRNA ZFAS1 is significantly downregulated [96, 97]. However, upregulated lncRNA-ZFAS1 can ameliorate brain injury in MCAO rats. It directly sponges miR-582 by promoting NOS3 expression and attenuating I/R-induced inflammation and cell apoptosis via oxidative stress. Studies have also mentioned that lncRNA-ZFAS1 can scavenge miR-186-5p by increasing the expression of the apoptosis regulator MCL1 and rescuing OGD-induced apoptosis of N2a cells [98].

lncRNA-H19 is a maternally derived gene on human chromosome 11. It is associated with stroke susceptibility in the Chinese population [99]. A previous study found that lncRNA-H19 was upregulated within 3 h after stroke, whereas levels of lncRNA-H19 were positively correlated with NIHSS scores of stroke patients within 3 h after stroke onset [100]. It demonstrated antioxidant capacity in metformin-mediated neuronal protection in ischemic stroke [101]. In the OGD/R model, inhibited lncRNA-H19 could reverse metformin-mediated SOD accumulation and MDA elimination [101]. This function was enabled by direct targeting of miR-148a-3p to regulate Rock2/HO-1/Nrf2 [101]. lncRNA-H19 also inhibited miR-19a and upregulated the inhibitor of DNA binding/differentiation 2 (Id2) that led to neuronal apoptosis induced by hypoxia [100].

lncRNA-SNHG14, also known as UBE3A-ATS, is an inhibitor of UBE3A, a brain-specific gene associated with neuronal development. It is involved in neuroinflammation after stroke [102]. lncRNA-SNHG14 promotes the accumulation of NO in microglia, leading to continuous activation of microglia, which causes apoptosis of neurons via the miR-145-5p/PLA2G4A axis [102]. Moreover, inhibition of lncRNA-SNHG14 SOD inhibits MDA accumulation and degradation in the BV-2 OGD model by regulating the miR-199b/AQP4 axis [103].

In lncRNA PVT1-inhibited MCAO rats, oxidative stress and neuron apoptosis were limited, and neurological impairments improved. In MCAO rats, the lncRNA PVT1 was activated by the sex-determining region Y-box 2 (SOX), sponged miR-24-3p, and regulated STAT3 expression [104].

In the SH-SY5Y OGD/R model, lncRNA SNHG15 was highly expressed and promoted the activation of oxidative stress signaling pathways by directly targeting miR-141/SIRT1 [105]. Moreover, miR-183-5p reversed lncRNA SNHG15-induced ROS accumulation in OGD/R-treated SH-SY5Y by directly targeting FOXO1 [106]. Furthermore, lncRNA SNHG15 retention reduced ROS accumulation in PC12 cells treated with OGD/R via the miR-455-3p/TP53INP1 axis [107].

Next, lncRNA OIP5-AS1 was downregulated in ischemic stroke patients, MCAO/R rats, and OGD/R-treated BV2 cells. Overexpression of OIP5-AS1 significantly decreased MDA accumulation, GSH, and overconsumption of SOD, thus counteracting neuroinflammation and oxidative stress and protecting neuronal injury by activating CTRP3 via sponging of miR-186-5p [108].

**3.3. circRNA Involves in Oxidative Stress after Ischemia Stroke.** circRNAs (single-stranded and conserved RNA molecules) are formed by the cleavage of many primary RNA transcripts that synthesize mRNA [109]. As they lack a well-defined 50- and 30-terminus [110], circRNAs can remain stable under the stress of RNase. circRNA regulates gene expression by various mechanisms, including functioning as a cornea through spongy miRNAs, forming ternary complexes with proteins, and encoding proteins [111–113]. circRNAs are abundant in brain tissue and involved in the development of vascular disease. Accordingly, they have been associated with neurological function [114] and acute ischemic stroke [115] (Figure 2).

Based on gene sequencing and KEGG analysis, circRyr2\_23, circGucy1a2\_7, circCamta1\_9, circSmad4\_4, and circDlga3\_1 play important roles in regulating oxidative stress by accessing Hif-1, Nrf, and VEGF signaling pathways [116]. The downregulation of circGucy1a2\_7 and circRyr2\_36 that occurs after stroke should spontaneously resist oxidative stress by adsorbing miR-7a5p to regulate Keap1/NRF-2 signaling [116–118].

circCCDC9 was downregulated in MCAO mice and remained at a low level for 72 h [119]. The upregulated circCCDC9 could restore eNOS expression, reduce oxidative stress, and protect the blood-brain barrier [119–121].

In patients with acute cerebral ischemic stroke, blood levels of circPHKA2 were downregulated. The same results were noted in human brain microvascular endothelial cells (HBMECs) treated with OGD [122]. Further studies confirmed that the upregulation of circPHKA2 decreased the accumulation of ROS and MDA, as well as increased SOD and GSH in OGD-HBMECs, which was due to the competitive binding of miR-574-5p to modulate SOD2 [122].

Various studies on microarrays and sequencing analyses have reported abnormal circRNA expression in ischemic stroke. Furthermore, analyses of Gene Ontology (GO) and Kyoto Encyclopaedia of Genes and Genomes (KEGG) recalled these circRNAs to be prominent in neuroinflammation, apoptosis, and oxidative stress [123]. However, a few studies have explained the mechanism of circRNA involvement in oxidative stress after ischemic stroke, which has also been explored in other diseases [124] (Table 1).

#### 4. Noncoding RNA Therapy for Ischemic Stroke

It is extremely important to find objective and effective biomarkers for stroke, because these indicators can not only help the early diagnosis and prognosis assessment of stroke but also serve as therapeutic targets to assist the development of new drugs. Universality, stroke can cause cascade changes of chemicals and transcripts in brain tissue, while conserved expression, defined specificity, high stability, and abundance are the main characteristics of ncRNAs that render them very attractive diagnostic tools for assessing diseases. Thus far, studies have demonstrated the potential of ncRNAs as a cancer diagnostic marker, and recently, studies have shown that ncRNA is also a potential diagnostic marker for neurodegenerative diseases [92, 125, 126].

TABLE 1: A list of ncRNAs involved in oxidative stress under cerebral ischemia-reperfusion injury.

ncRNAs	Functions	References
<b>miRNA</b>		
miR-124a	Encoding neuronal calcium sensor proteins in cerebellar granulosa cells	[68, 70]
miR-290	Regulating cyclic nucleotide and MAPK pathways	[69, 71]
miR30a-3p	Migration and neuronal plasticity	[72]
miR-99	Regulates AQP4	[73]
miR-100	Connects the DNA damage response to histone H4 acetylation	[74]
miR-223	Regulates serum MMP-9 level	[75]
miR-383	Regulates AQP4 and causes cerebral edema	[76]
FmiR-132	Involves the blood-brain barrier disruption	[70]
miR-210	Alleviates the decreased oxidative metabolism caused by tissue hypoxia	[79–81]
miR-124	Protects PC12 cells from OGD/R-induced apoptosis by reducing oxidative stress via the PI3K/AKT/Nrf2 pathway	[83–85]
miR-217	Deregulates MEF2D, regulates the expression of HDAC5 and ND6, and promotes mitochondrial ROS production	[89]
<b>lncRNAs</b>		
lncRNA ZFAS1	Downregulated by oxidative stress	[93, 94]
ANRIL	Represses the expression of INK4A-ARF-INK4B	[96]
lncRNA-H19	Reverses metformin-mediated SOD accumulation and MDA elimination	[98, 99]
lncRNA-SNHG14	Promotes accumulation of NO in microglia, leading to continuous activation of microglia	[99, 100]
lncRNA PVT1	Regulated STAT3 expression and activated by the sex-determining region Y-box 2 (SOX)	[101]
lncRNA SNHG15	Reduces ROS accumulation of PC12 cells treated with OGD/R via the miR-455-3p/TP53INP1 axis	[102–104]
lncRNA OIP5-AS1	Protecting neuronal injury by activating CTRP3 via sponging miR-186-5p	[105]
<b>circRNAs</b>		
circCCDC9	Restores eNOS expression, reduces oxidative stress, and protects the blood-brain barrier	[106–108]
circPHKA2	Decreases the accumulation of ROS and MDA and increases SOD by competitive binding miR-574-5p	[109]

In the past few years, several *in vivo* and *in vitro* studies have demonstrated that certain ncRNAs change over time after ischemic stroke, and they are expected to be widely used as biomarkers in clinical practice. The observed variations in ncRNA amounts in blood samples could be helpful biomarkers that reflect the pathophysiological state of the brain, thus implying that circulating ncRNAs have potential prospects. In addition, Dykstra-Aiello et al. [127] discovered aberrant ncRNA expression in peripheral blood of stroke patients with sex differences, suggesting that certain ncRNAs may be useful biomarkers for stroke development. Wang et al. [128] investigated patients with ischemic stroke and reported that mutations in the H19 gene increased the risk of ischemic stroke. Another independent study revealed that lncRNA H19 levels were significantly increased in the blood and cytoplasm of stroke patients, with high diagnostic sensitivity and specificity levels. This indicates that lncRNA H19 may be a novel diagnostic and therapeutic target for ischemic stroke. Moreover, Mehta et al. [129] suggested that lncRNA FosDT could reduce the loss of motor function after cerebral infarction and stroke via the regulation of REST downstream genes.

In clinical practice, noncoding RNAs are abnormally expressed in the blood of ischemic stroke patients and are closely related to patient prognosis. In whole blood, studies

have found that miR-122, miR-148a, let-7i, miR-19a, miR-320d, and miR-4429 are downregulated, while miR-363 and miR-487b are upregulated [130]. Moreover, Lu et al. [131] put forward the idea of noncoding RNAs as potential clinical biomarkers for disorders in the CNS. They suggest that noncoding RNAs can regulate CNS function and many diseases and can be used as a potential biomarker for the diagnosis and prognosis of CNS diseases, as well as combined with other biomarkers and imaging tools to improve the diagnostic power. Subsequently, Mehta et al. [16] conducted a comprehensive circRNA expression profile analysis on male tMCAO mice. microRNA-binding sites, transcription factor binding and gene ontology of circRNAs altered after ischemia were determined under cerebral ischemia. In their study, a total of 1322 detectable circRNAs were comprehensively analysed, of which 283 had significant changes. Their research shows that these noncoding RNAs altered after stroke may be controlled by a set of transcription factors. These noncoding RNAs are involved in many processes and functions such as biological regulation, metabolism, cell communication, and binding with proteins, ions, and nucleic acids. Liu et al. [132] also studied the expression profile of ncRNAs in ischemic stroke and confirmed that noncoding RNA is a potential target for diagnosis and treatment of stroke.

Current research has discovered the role of certain functional ncRNAs such as lncRNA H19 and MALAT1 in ischemic stroke. However, research on ncRNAs still faces many challenges. For example, it is difficult to study their molecular mechanisms due to the complexity of the various functions of ncRNAs. Furthermore, many ncRNAs are expressed only in primates. Even though a significant part of the molecular mechanism has been identified, there is still a long way to go before it can be implemented in clinical use.

## 5. Conclusion

In this review, the mechanisms of oxidative stress in ischemic stroke and reperfusion injury were discussed, alongside the involvement of ncRNAs in the pathological process. Additionally, the potential of three types of ncRNAs for treating stroke was explored. With advances in clinical and experimental techniques, continued research into ncRNAs and their pathways could likely lead to developing a new treatment for ischemic stroke.

## Conflicts of Interest

The authors declare that they have no competing interests.

## Authors' Contributions

Zhongzhou Su and Yingze Ye contributed equally to this work.

## Acknowledgments

This work was supported by the Fundamental Research Funds for the Central Universities (2042022kf1216).

## References

- [1] V. L. Feigin, E. Nichols, T. Alam et al., "Global, regional, and national burden of neurological disorders, 1990-2016: a systematic analysis for the Global Burden of Disease Study 2016," *Lancet Neurology*, vol. 18, pp. 459-480, 2019.
- [2] V. L. Feigin, A. A. Abajobir, K. H. Abate et al., "Global, regional, and national burden of neurological disorders during 1990-2015: a systematic analysis for the Global Burden of Disease Study 2015," *Lancet Neurology*, vol. 16, pp. 877-897, 2017.
- [3] V. L. Feigin, "Anthology of stroke epidemiology in the 20th and 21st centuries: assessing the past, the present, and envisioning the future," *International Journal of Stroke*, vol. 14, no. 3, pp. 223-237, 2019.
- [4] V. L. Feigin, M. H. Forouzanfar, R. Krishnamurthi et al., "Global and regional burden of stroke during 1990-2010: findings from the Global Burden of Disease Study 2010," *Lancet*, vol. 383, no. 9913, pp. 245-255, 2014.
- [5] E. Besancon, S. Guo, J. Lok, M. Tymianski, and E. H. Lo, "Beyond NMDA and AMPA glutamate receptors: emerging mechanisms for ionic imbalance and cell death in stroke," *Trends in Pharmacological Sciences*, vol. 29, no. 5, pp. 268-275, 2008.
- [6] Y. B. Ouyang, L. A. Voloboueva, L. J. Xu, and R. G. Giffard, "Selective dysfunction of hippocampal CA1 astrocytes contributes to delayed neuronal damage after transient forebrain ischemia," *The Journal of Neuroscience*, vol. 27, no. 16, pp. 4253-4260, 2007.
- [7] L. Xu, J. F. Emery, Y. B. Ouyang, L. A. Voloboueva, and R. G. Giffard, "Astrocyte targeted overexpression of Hsp72 or SOD2 reduces neuronal vulnerability to forebrain ischemia," *Glia*, vol. 58, no. 9, pp. 1042-1049, 2010.
- [8] B. K. Siesjö, "Pathophysiology and treatment of focal cerebral ischemia: Part II: mechanisms of damage and treatment," *Journal of Neurosurgery*, vol. 77, no. 3, pp. 337-354, 1992.
- [9] R. Khatri, A. M. McKinney, B. Swenson, and V. Janardhan, "Blood-brain barrier, reperfusion injury, and hemorrhagic transformation in acute ischemic stroke," *Neurology*, vol. 79, no. 13, Supplement 1, pp. S52-S57, 2012.
- [10] T. Kahles, P. Luedike, M. Endres et al., "NADPH oxidase plays a central role in blood-brain barrier damage in experimental stroke," *Stroke*, vol. 38, no. 11, pp. 3000-3006, 2007.
- [11] C. Kleinschnitz, H. Grund, K. Wingerl et al., "Post-stroke inhibition of induced NADPH oxidase type 4 prevents oxidative stress and neurodegeneration," *PLoS Biology*, vol. 8, no. 9, article e1000479, 2010.
- [12] H. J. Zhang, Y. Q. Xing, W. Jin, D. Li, K. Wu, and Y. Lu, "Effects of curcumin on interleukin-23 and interleukin-17 expression in rat retina after retinal ischemia-reperfusion injury," *International Journal of Clinical and Experimental Pathology*, vol. 8, no. 8, pp. 9223-9231, 2015.
- [13] G. Romano, D. Veneziano, M. Acunzo, and C. M. Croce, "Small non-coding RNA and cancer," *Carcinogenesis*, vol. 38, no. 5, pp. 485-491, 2017.
- [14] F. J. Slack and A. M. Chinnaiyan, "The role of non-coding RNAs in oncology," *Cell*, vol. 179, no. 5, pp. 1033-1055, 2019.
- [15] A. Dharap, K. Bowen, R. Place, L. C. Li, and R. Vemuganti, "Transient focal ischemia induces extensive temporal changes in rat cerebral microRNAome," *Journal of Cerebral Blood Flow and Metabolism*, vol. 29, no. 4, pp. 675-687, 2009.
- [16] S. L. Mehta, G. Pandi, and R. Vemuganti, "Circular RNA expression profiles alter significantly in mouse brain after transient focal ischemia," *Stroke*, vol. 48, no. 9, pp. 2541-2548, 2017.
- [17] T. Kim, Y. J. Jeon, R. Cui et al., "Role of MYC-regulated long noncoding RNAs in cell cycle regulation and tumorigenesis," *Journal of the National Cancer Institute*, vol. 107, no. 4, 2015.
- [18] B. R. Iyengar, A. Choudhary, M. A. Sarangdhar, K. V. Venkatesh, C. J. Gadgil, and B. Pillai, "Non-coding RNA interact to regulate neuronal development and function," *Frontiers in Cellular Neuroscience*, vol. 8, p. 47, 2014.
- [19] S. Memczak, M. Jens, A. Elefsinioti et al., "Circular RNAs are a large class of animal RNAs with regulatory potency," *Nature*, vol. 495, no. 7441, pp. 333-338, 2013.
- [20] T. M. Woodruff, J. Thundiyil, S. C. Tang, C. G. Sobey, S. M. Taylor, and T. V. Arumugam, "Pathophysiology, treatment, and animal and cellular models of human ischemic stroke," *Molecular Neurodegeneration*, vol. 6, no. 1, p. 11, 2011.
- [21] R. Rama and J. C. García, "Excitotoxicity and oxidative stress in acute stroke," in *Ischemic Stroke*, B. Schaller, Ed., pp. 17-33, IntechOpen, Rijeka, 2016.
- [22] Y. Li and G.-Y. Yang, "Pathophysiology of ischemic stroke," in *Translational Research in Stroke*, P. A. Lapchak and G.-Y. Yang, Eds., pp. 51-75, Springer, Singapore, 2017.
- [23] M. S. Sun, H. Jin, X. Sun et al., "Free radical damage in ischemia-reperfusion injury: an obstacle in acute ischemic

- stroke after revascularization therapy," *Oxidative Medicine and Cellular Longevity*, vol. 2018, Article ID 3804979, 17 pages, 2018.
- [24] J. Levraut, H. Iwase, Z. H. Shao, T. L. Vanden Hoek, and P. T. Schumacker, "Cell death during ischemia: relationship to mitochondrial depolarization and ROS generation," *American Journal of Physiology. Heart and Circulatory Physiology*, vol. 284, no. 2, pp. H549–H558, 2003.
- [25] T. L. Vanden Hoek, C. Li, Z. Shao, P. T. Schumacker, and L. B. Becker, "Significant levels of oxidants are generated by isolated cardiomyocytes during ischemia prior to reperfusion," *Journal of Molecular and Cellular Cardiology*, vol. 29, no. 9, pp. 2571–2583, 1997.
- [26] M. Yoshioka, K. Tanaka, I. Miyazaki et al., "The dopamine agonist cabergoline provides neuroprotection by activation of the glutathione system and scavenging free radicals," *Neuroscience Research*, vol. 43, no. 3, pp. 259–267, 2002.
- [27] M. Valko, D. Leibfritz, J. Moncol, M. T. Cronin, M. Mazur, and J. Telser, "Free radicals and antioxidants in normal physiological functions and human disease," *The International Journal of Biochemistry & Cell Biology*, vol. 39, no. 1, pp. 44–84, 2007.
- [28] L. Wu, X. Xiong, X. Wu et al., "Targeting oxidative stress and inflammation to prevent ischemia-reperfusion injury," *Frontiers in Molecular Neuroscience*, vol. 13, p. 28, 2020.
- [29] J. H. Heo, S. W. Han, and S. K. Lee, "Free radicals as triggers of brain edema formation after stroke," *Free Radical Biology & Medicine*, vol. 39, no. 1, pp. 51–70, 2005.
- [30] R. Ye, M. Shi, Q. Liu, and J. Chen, "Redox imbalance and stroke," *Oxidative Medicine and Cellular Longevity*, vol. 2016, Article ID 3065263, 2 pages, 2016.
- [31] S. M. de la Monte, "Brain insulin resistance and deficiency as therapeutic targets in Alzheimer's disease," *Current Alzheimer Research*, vol. 9, no. 1, pp. 35–66, 2012.
- [32] R. Rodrigo, M. Libuy, F. Feliú, and D. Hasson, "Oxidative stress-related biomarkers in essential hypertension and ischemia-reperfusion myocardial damage," *Disease Markers*, vol. 35, no. 6, Article ID 974358, p. 790, 2013.
- [33] R. P. Durbin, "Letter: acid secretion by gastric mucous membrane," *The American Journal of Physiology*, vol. 229, no. 6, p. 1726, 1975.
- [34] T. P. Obrenovitch, J. Urenjak, D. A. Richards, Y. Ueda, G. Curzon, and L. Symon, "Extracellular neuroactive amino acids in the rat striatum during ischaemia: comparison between penumbral conditions and ischaemia with sustained anoxic depolarisation," *Journal of Neurochemistry*, vol. 61, no. 1, pp. 178–186, 1993.
- [35] P. Gerreth, M. Maciejczyk, A. Zalewska, K. Gerreth, and K. Hojan, "Comprehensive evaluation of the oral health status, salivary gland function, and oxidative stress in the saliva of patients with subacute phase of stroke: a case-control study," *Journal of Clinical Medicine*, vol. 9, no. 7, p. 2252, 2020.
- [36] M. Maciejczyk, P. Gerreth, A. Zalewska, K. Hojan, and K. Gerreth, "Salivary gland dysfunction in stroke patients is associated with increased protein glycooxidation and nitrosative stress," *Oxidative Medicine and Cellular Longevity*, vol. 2020, Article ID 6619439, 14 pages, 2020.
- [37] L. Ramiro, A. Simats, T. García-Berrocso, and J. Montaner, "Inflammatory molecules might become both biomarkers and therapeutic targets for stroke management," *Therapeutic Advances in Neurological Disorders*, vol. 11, 2018.
- [38] A. Jana, E. L. Hogan, and K. Pahan, "Ceramide and neurodegeneration: susceptibility of neurons and oligodendrocytes to cell damage and death," *Journal of the Neurological Sciences*, vol. 278, no. 1–2, pp. 5–15, 2009.
- [39] B. R. S. Broughton, D. C. Reutens, and C. G. Sobey, "Apoptotic mechanisms after cerebral ischemia," *Stroke*, vol. 40, no. 5, pp. e331–e339, 2009.
- [40] M. Bladowski, J. Gawrys, D. Gajeci, E. Szahidewicz-Krupska, A. Sawicz-Bladowska, and A. Doroszko, "Role of the platelets and nitric oxide biotransformation in ischemic stroke: a translative review from bench to bedside," *Oxidative Medicine and Cellular Longevity*, vol. 2020, Article ID 2979260, 18 pages, 2020.
- [41] Z. Q. Chen, R. T. Mou, D. X. Feng, Z. Wang, and G. Chen, "The role of nitric oxide in stroke," *Medical Gas Research*, vol. 7, no. 3, pp. 194–203, 2017.
- [42] L. Adams, M. C. Franco, and A. G. Estevez, "Reactive nitrogen species in cellular signaling," *Experimental Biology and Medicine (Maywood, N.J.)*, vol. 240, no. 6, pp. 711–717, 2015.
- [43] Y. C. Cheng, J. M. Sheen, W. L. Hu, and Y. C. Hung, "Polyphenols and oxidative stress in atherosclerosis-related ischemic heart disease and stroke," *Oxidative Medicine and Cellular Longevity*, vol. 2017, Article ID 8526438, 16 pages, 2017.
- [44] F. X. Guix, I. Uribealago, M. Coma, and F. J. Muñoz, "The physiology and pathophysiology of nitric oxide in the brain," *Progress in Neurobiology*, vol. 76, no. 2, pp. 126–152, 2005.
- [45] P. Pacher, J. S. Beckman, and L. Liaudet, "Nitric oxide and peroxynitrite in health and disease," *Physiological Reviews*, vol. 87, no. 1, pp. 315–424, 2007.
- [46] M. Maciejczyk, E. Żebrowska, and A. Chabowski, "Insulin resistance and oxidative stress in the brain: What's new?," *International Journal of Molecular Sciences*, vol. 20, no. 4, p. 874, 2019.
- [47] L. Zhang, J. Wu, X. Duan et al., "NADPH oxidase: a potential target for treatment of stroke," *Oxidative Medicine and Cellular Longevity*, vol. 2016, Article ID 5026984, 9 pages, 2016.
- [48] J. Duan, S. Gao, S. Tu, C. Lenahan, A. Shao, and J. Sheng, "Pathophysiology and therapeutic potential of NADPH oxidases in ischemic stroke-induced oxidative stress," *Oxidative Medicine and Cellular Longevity*, vol. 2021, Article ID 6631805, 11 pages, 2021.
- [49] K. A. Reimer, J. E. Lowe, M. M. Rasmussen, and R. B. Jennings, "The wavefront phenomenon of ischemic cell death. 1. Myocardial infarct size vs duration of coronary occlusion in dogs," *Circulation*, vol. 56, no. 5, pp. 786–794, 1977.
- [50] D. J. Hearse, S. M. Humphrey, and E. B. Chain, "Abrupt reoxygenation of the anoxic potassium-arrested perfused rat heart: a study of myocardial enzyme release," *Journal of Molecular and Cellular Cardiology*, vol. 5, no. 4, pp. 395–407, 1973.
- [51] D. N. Granger and P. R. Kvietys, "Reperfusion injury and reactive oxygen species: the evolution of a concept," *Redox Biology*, vol. 6, pp. 524–551, 2015.
- [52] O. Peters, T. Back, U. Lindauer et al., "Increased formation of reactive oxygen species after permanent and reversible middle cerebral artery occlusion in the rat," *Journal of Cerebral Blood Flow and Metabolism*, vol. 18, no. 2, pp. 196–205, 1998.

- [53] M. Yamato, T. Egashira, and H. Utsumi, "Application of in vivo ESR spectroscopy to measurement of cerebrovascular ROS generation in stroke," *Free Radical Biology & Medicine*, vol. 35, no. 12, pp. 1619–1631, 2003.
- [54] T. Kalogeris, C. P. Baines, M. Krenz, and R. J. Korthuis, "Ischemia/reperfusion," *Comprehensive Physiology*, vol. 7, no. 1, pp. 113–170, 2016.
- [55] K. Raedschelders, D. M. Ansley, and D. D. Chen, "The cellular and molecular origin of reactive oxygen species generation during myocardial ischemia and reperfusion," *Pharmacology & Therapeutics*, vol. 133, no. 2, pp. 230–255, 2012.
- [56] J. D. Lambeth and A. S. Neish, "Nox enzymes and new thinking on reactive oxygen: a double-edged sword revisited," *Annual Review of Pathology*, vol. 9, no. 1, pp. 119–145, 2014.
- [57] K. Irani, Y. Xia, J. L. Zweier et al., "Mitogenic signaling mediated by oxidants in Ras-transformed fibroblasts," *Science*, vol. 275, no. 5306, pp. 1649–1652, 1997.
- [58] M. Sundaresan, Z. X. Yu, V. J. Ferrans, K. Irani, and T. Finkel, "Requirement for generation of H<sub>2</sub>O<sub>2</sub> for platelet-derived growth factor signal transduction," *Science*, vol. 270, no. 5234, pp. 296–299, 1995.
- [59] R. L. Ibsen and X. Y. Yu, "Establishing cuspid-guided occlusion with bonded porcelain," *Journal of Esthetic Dentistry*, vol. 1, no. 3, pp. 80–85, 1989.
- [60] J. Cao, C. Zhao, L. Gong et al., "MiR-181 enhances proliferative and migratory potentials of retinal endothelial cells in diabetic retinopathy by targeting KLF6," *Current Eye Research*, vol. 47, no. 6, pp. 882–888, 2022.
- [61] G. Li, K. C. Morris-Blanco, M. S. Lopez et al., "Impact of microRNAs on ischemic stroke: from pre- to post-disease," *Progress in Neurobiology*, vol. 163–164, pp. 59–78, 2018.
- [62] D. P. Bartel, "MicroRNAs: genomics, biogenesis, mechanism, and function," *Cell*, vol. 116, no. 2, pp. 281–297, 2004.
- [63] A. S. Flynt and E. C. Lai, "Biological principles of microRNA-mediated regulation: shared themes amid diversity," *Nature Reviews Genetics*, vol. 9, no. 11, pp. 831–842, 2008.
- [64] B. P. Lewis, C. B. Burge, and D. P. Bartel, "Conserved seed pairing, often flanked by adenosines, indicates that thousands of human genes are microRNA targets," *Cell*, vol. 120, no. 1, pp. 15–20, 2005.
- [65] S. E. Khoshnam, W. Winlow, Y. Farbood, H. F. Moghaddam, and M. Farzaneh, "Emerging roles of microRNAs in ischemic stroke: as possible therapeutic agents," *Journal of Stroke*, vol. 19, no. 2, pp. 166–187, 2017.
- [66] Y. Lee, C. Ahn, J. Han et al., "The nuclear RNase III Drosha initiates microRNA processing," *Nature*, vol. 425, no. 6956, pp. 415–419, 2003.
- [67] M. I. Almeida, R. M. Reis, and G. A. Calin, "MicroRNA history: discovery, recent applications, and next frontiers," *Mutation Research*, vol. 717, no. 1–2, pp. 1–8, 2011.
- [68] A. Eulalio, E. Huntzinger, and E. Izaurralde, "Getting to the root of miRNA-mediated gene silencing," *Cell*, vol. 132, no. 1, pp. 9–14, 2008.
- [69] N. Engedal, E. Žerovnik, A. Rudov et al., "From oxidative stress damage to pathways, networks, and autophagy via microRNAs," *Oxidative Medicine and Cellular Longevity*, vol. 2018, Article ID 4968321, 16 pages, 2018.
- [70] Y. Wan, R. Cui, J. Gu et al., "Identification of four oxidative stress-responsive microRNAs, miR-34a-5p, miR-1915-3p, miR-638, and miR-150-3p, in hepatocellular carcinoma," *Oxidative Medicine and Cellular Longevity*, vol. 2017, Article ID 5189138, 12 pages, 2017.
- [71] H. Bu, S. Wedel, M. Cavinato, and P. Jansen-Dürr, "MicroRNA regulation of oxidative stress-induced cellular senescence," *Oxidative Medicine and Cellular Longevity*, vol. 2017, Article ID 2398696, 12 pages, 2017.
- [72] K. Jeyaseelan, K. Y. Lim, and A. Armugam, "MicroRNA expression in the blood and brain of rats subjected to transient focal ischemia by middle cerebral artery occlusion," *Stroke*, vol. 39, no. 3, pp. 959–966, 2008.
- [73] K. H. Braunewell and A. J. Klein-Szanto, "Visinin-like proteins (VSNLs): interaction partners and emerging functions in signal transduction of a subfamily of neuronal Ca<sup>2+</sup>-sensor proteins," *Cell and Tissue Research*, vol. 335, no. 2, pp. 301–316, 2009.
- [74] N. F. Olde Loohuis, A. Kos, G. J. Martens, H. Van Bokhoven, N. Nadif Kasri, and A. Aschrafi, "MicroRNA networks direct neuronal development and plasticity," *Cellular and Molecular Life Sciences*, vol. 69, no. 1, pp. 89–102, 2012.
- [75] C. W. Lin, L. C. Chang, G. C. Tseng, C. M. Kirkwood, E. L. Sibille, and R. A. Sweet, "VSNL1 co-expression networks in aging include calcium signaling, synaptic plasticity, and Alzheimer's disease pathways, Front," *Frontiers in Psychiatry*, vol. 6, p. 30, 2015.
- [76] Q. Guo, I. Sayeed, L. M. Baronne, S. W. Hoffman, R. Guennoun, and D. G. Stein, "Progesterone administration modulates AQP4 expression and edema after traumatic brain injury in male rats," *Experimental Neurology*, vol. 198, no. 2, pp. 469–478, 2006.
- [77] M. C. Papadopoulos and A. S. Verkman, "Aquaporin-4 and brain edema," *Pediatric Nephrology*, vol. 22, no. 6, pp. 778–784, 2007.
- [78] S. Horstmann, P. Kalb, J. Koziol, H. Gardner, and S. Wagner, "Profiles of matrix metalloproteinases, their inhibitors, and laminin in stroke patients: influence of different therapies," *Stroke*, vol. 34, no. 9, pp. 2165–2170, 2003.
- [79] J. Montaner, J. Alvarez-Sabín, C. Molina et al., "Matrix metalloproteinase expression after human cardioembolic stroke: temporal profile and relation to neurological impairment," *Stroke*, vol. 32, no. 8, pp. 1759–1766, 2001.
- [80] A. Rosell, A. Ortega-Aznar, J. Alvarez-Sabín et al., "Increased brain expression of matrix metalloproteinase-9 after ischemic and hemorrhagic human stroke," *Stroke*, vol. 37, no. 6, pp. 1399–1406, 2006.
- [81] G. Zaccagnini, F. Martelli, P. Fasanaro et al., "p66ShcA modulates tissue response to hindlimb ischemia," *Circulation*, vol. 109, no. 23, pp. 2917–2923, 2004.
- [82] Y. Jiang, L. Li, X. Tan, B. Liu, Y. Zhang, and C. Li, "miR-210 mediates vagus nerve stimulation-induced antioxidant stress and anti-apoptosis reactions following cerebral ischemia/reperfusion injury in rats," *Journal of Neurochemistry*, vol. 134, no. 1, pp. 173–181, 2015.
- [83] S. Hu, M. Huang, Z. Li et al., "MicroRNA-210 as a novel therapy for treatment of ischemic heart disease," *Circulation*, vol. 122, 11\_Supplement\_1, pp. S124–S131, 2010.
- [84] P. Fuschi, B. Maimone, C. Gaetano, and F. Martelli, "Non-coding RNAs in the vascular system response to oxidative stress," *Antioxidants & Redox Signaling*, vol. 30, no. 7, pp. 992–1010, 2019.



- [85] M. Deo, J. Y. Yu, K. H. Chung, M. Tippens, and D. L. Turner, "Detection of mammalian microRNA expression by in situ hybridization with RNA oligonucleotides," *Developmental Dynamics*, vol. 235, no. 9, pp. 2538–2548, 2006.
- [86] M. Åkerblom, R. Sachdeva, I. Barde et al., "MicroRNA-124 is a subventricular zone neuronal fate determinant," *The Journal of Neuroscience*, vol. 32, no. 26, pp. 8879–8889, 2012.
- [87] K. Shu and Y. Zhang, "Protodioscin protects PC12 cells against oxygen and glucose deprivation-induced injury through miR-124/AKT/Nrf2 pathway," *Cell Stress & Chaperones*, vol. 24, no. 6, pp. 1091–1099, 2019.
- [88] G. Gong, Y. Gu, Y. Zhang, W. Liu, L. Li, and J. Li, "RETRACTED: tanshinone IIA alleviates oxidative damage after spinal cord injury in vitro and in vivo through up-regulating miR-124," *Life Sciences*, vol. 216, pp. 147–155, 2019.
- [89] Z. Xu, K. Zhang, Q. Wang, and Y. Zheng, "MicroRNA-124 improves functional recovery and suppresses Bax-dependent apoptosis in rats following spinal cord injury," *Molecular Medicine Reports*, vol. 19, no. 4, pp. 2551–2560, 2019.
- [90] C. Z. Feng, J. B. Yin, J. J. Yang, and L. Cao, "Regulatory factor X1 depresses ApoE-dependent A $\beta$  uptake by miRNA-124 in microglial response to oxidative stress," *Neuroscience*, vol. 344, pp. 217–228, 2017.
- [91] L. Shi, Z. Tian, Q. Fu et al., "miR-217-regulated MEF2D-HDAC5/ND6 signaling pathway participates in the oxidative stress and inflammatory response after cerebral ischemia," *Brain Research*, vol. 1739, article 146835, 2020.
- [92] M. Esteller, "Non-coding RNAs in human disease," *Nature Reviews. Genetics*, vol. 12, no. 12, pp. 861–874, 2011.
- [93] M. Wang, S. Gan, B. Li, and Y. Wang, "Long non-coding RNA-ATB attenuates the angiotensin II-induced injury of vascular endothelial cell," *Annals of Clinical and Laboratory Science*, vol. 50, no. 3, pp. 378–382, 2020.
- [94] L. Li, M. Wang, Z. Mei et al., "lncRNAs HIF1A-AS2 facilitates the up-regulation of HIF-1 $\alpha$  by sponging to miR-153-3p, whereby promoting angiogenesis in HUVECs in hypoxia," *Biomedicine & Pharmacotherapy*, vol. 96, pp. 165–172, 2017.
- [95] A. Dharap, V. P. Nakka, and R. Vemuganti, "Effect of focal ischemia on long noncoding RNAs," *Stroke*, vol. 43, no. 10, pp. 2800–2802, 2012.
- [96] Y. Zhang and Y. Zhang, "lncRNA ZFAS1 improves neuronal injury and inhibits inflammation, oxidative stress, and apoptosis by sponging miR-582 and upregulating NOS3 expression in cerebral ischemia/reperfusion injury," *Inflammation*, vol. 43, no. 4, pp. 1337–1350, 2020.
- [97] J. Wang, J. Ruan, M. Zhu et al., "Predictive value of long non-coding RNA ZFAS1 in patients with ischemic stroke," *Clinical and Experimental Hypertension*, vol. 41, no. 7, pp. 615–621, 2019.
- [98] B. Shen, L. Wang, Y. Xu, H. Wang, and S. He, "Long non-coding RNA ZFAS1 exerts a protective role to alleviate oxygen and glucose deprivation-mediated injury in ischemic stroke cell model through targeting miR-186-5p/MCL1 axis," *Cytotechnology*, vol. 73, no. 4, pp. 605–617, 2021.
- [99] P. Wan, W. Su, and Y. Zhuo, "The role of long noncoding RNAs in neurodegenerative diseases," *Molecular Neurobiology*, vol. 54, no. 3, pp. 2012–2021, 2017.
- [100] Z. Xiao, Y. Qiu, Y. Lin et al., "Blocking lncRNA H19-miR-19a-1d2 axis attenuates hypoxia/ischemia induced neuronal injury," *Aging (Albany NY)*, vol. 11, no. 11, pp. 3585–3600, 2019.
- [101] J. Zeng, L. Zhu, J. Liu et al., "Metformin protects against oxidative stress injury induced by ischemia/reperfusion via regulation of the lncRNA-H19/miR-148a-3p/Rock2 axis," *Oxidative Medicine and Cellular Longevity*, vol. 2019, Article ID 8768327, 18 pages, 2019.
- [102] X. Qi, M. Shao, H. Sun, Y. Shen, D. Meng, and W. Huo, "Long non-coding RNA SNHG14 promotes microglia activation by regulating miR-145-5p/PLA2G4A in cerebral infarction," *Neuroscience*, vol. 348, pp. 98–106, 2017.
- [103] G. Zhang, T. Li, X. Chang, and J. Xing, "Long noncoding RNA SNHG14 promotes ischemic brain injury via regulating miR-199b/AQP4 Axis," *Neurochemical Research*, vol. 46, no. 5, pp. 1280–1290, 2021.
- [104] Z. Chen, T. Fan, X. Zhao, and Z. Zhang, "Depleting SOX2 improves ischemic stroke via lncRNA PVT1/microRNA-24-3p/STAT3 axis," *Molecular Medicine*, vol. 27, no. 1, p. 107, 2021.
- [105] M. Kang, F. Ji, X. Sun, H. Liu, and C. Zhang, "lncRNA SNHG15 promotes oxidative stress damage to regulate the occurrence and development of cerebral ischemia/reperfusion injury by targeting the miR-141/SIRT1 axis," *Journal of Healthcare Engineering*, vol. 2021, Article ID 6577799, 7 pages, 2021.
- [106] Y. Wen, X. Zhang, X. Liu, Y. Huo, Y. Gao, and Y. Yang, "Suppression of lncRNA SNHG15 protects against cerebral ischemia-reperfusion injury by targeting miR-183-5p/FOXO1 axis," *American Journal of Translational Research*, vol. 12, no. 10, pp. 6250–6263, 2020.
- [107] Y. Fan, L. Wei, S. Zhang et al., "lncRNA SNHG15 knock-down protects against OGD/R-induced neuron injury by downregulating TP53INP1 expression via binding to miR-455-3p," *Neurochemical Research*, vol. 46, no. 4, pp. 1019–1030, 2021.
- [108] Y. Chen, W. Liu, M. Chen, Q. Sun, H. Chen, and Y. Li, "Up-regulating lncRNA OIP5-AS1 protects neuron injury against cerebral hypoxia-ischemia induced inflammation and oxidative stress in microglia/macrophage through activating CTRP3 via sponging miR-186-5p," *International Immunopharmacology*, vol. 92, article 107339, 2021.
- [109] A. Rybak-Wolf, C. Stottmeister, P. Glazar et al., "Circular RNAs in the mammalian brain are highly abundant, conserved, and dynamically expressed," *Molecular Cell*, vol. 58, no. 5, pp. 870–885, 2015.
- [110] W. R. Jeck, J. A. Sorrentino, K. Wang et al., "Circular RNAs are abundant, conserved, and associated with ALU repeats," *RNA*, vol. 19, no. 2, pp. 141–157, 2013.
- [111] R. Huang, Y. Zhang, B. Han et al., "Circular RNA HIPK2 regulates astrocyte activation via cooperation of autophagy and ER stress by targeting MIR124-2HG," *Autophagy*, vol. 13, no. 10, pp. 1722–1741, 2017.
- [112] W. W. Du, W. Yang, E. Liu, Z. Yang, P. Dhaliwal, and B. B. Yang, "Foxo3 circular RNA retards cell cycle progression via forming ternary complexes with p21 and CDK2," *Nucleic Acids Research*, vol. 44, no. 6, pp. 2846–2858, 2016.
- [113] Y. Yang, X. Gao, M. Zhang et al., "Novel role of FBXW7 circular RNA in repressing glioma tumorigenesis," *Journal of the National Cancer Institute*, vol. 110, no. 3, pp. 304–315, 2018.
- [114] L. S. Kristensen, M. S. Andersen, L. V. W. Stagsted, K. K. Ebbesen, T. B. Hansen, and J. Kjems, "The biogenesis, biology and characterization of circular RNAs," *Nature Reviews. Genetics*, vol. 20, no. 11, pp. 675–691, 2019.

- [115] Y. F. Song, L. Zhao, B. C. Wang et al., "The circular RNA TLK1 exacerbates myocardial ischemia/reperfusion injury via targeting miR-214/RIPK1 through TNF signaling pathway," *Free Radical Biology & Medicine*, vol. 155, pp. 69–80, 2020.
- [116] C. Wang, Y. Yang, M. Xu et al., "Deep sequencing of the rat MCAO cortexes reveals crucial circRNAs involved in early stroke events and their regulatory networks," *Neural Plasticity*, vol. 2021, Article ID 9942537, 17 pages, 2021.
- [117] M. Patel, "Targeting oxidative stress in central nervous system disorders," *Trends in Pharmacological Sciences*, vol. 37, no. 9, pp. 768–778, 2016.
- [118] J. W. Kaspar, S. K. Niture, and A. K. Jaiswal, "Nrf2:INrf2 (Keap1) signaling in oxidative stress," *Free Radical Biology & Medicine*, vol. 47, no. 9, pp. 1304–1309, 2009.
- [119] L. Wu, H. Xu, W. Zhang, Z. Chen, W. Li, and W. Ke, "Circular RNA circCCDC9 alleviates ischaemic stroke ischaemia/reperfusion injury via the notch pathway," *Journal of Cellular and Molecular Medicine*, vol. 24, no. 24, pp. 14152–14159, 2020.
- [120] Z. H. Zhang, Y. R. Wang, F. Li et al., "Circ-camk4 involved in cerebral ischemia/reperfusion induced neuronal injury," *Scientific Reports*, vol. 10, no. 1, p. 7012, 2020.
- [121] Z. Zhang, J. He, and B. Wang, "Circular RNA circ\_HECTD1 regulates cell injury after cerebral infarction by miR-27a-3p/FSTL1 axis," *Cell Cycle*, vol. 20, no. 9, pp. 914–926, 2021.
- [122] X. Yang, X. Li, C. Zhong et al., "Circular RNA circPHKA2 relieves OGD-induced human brain microvascular endothelial cell injuries through competitively binding miR-574-5p to modulate SOD2," *Oxidative Medicine and Cellular Longevity*, vol. 2021, Article ID 3823122, 17 pages, 2021.
- [123] Y. Y. Wang, Y. Z. Wang, H. Y. Zhang, and Z. Y. He, "The role of circular RNAs in brain and stroke," *Frontiers in Bioscience-Landmark*, vol. 26, no. 5, pp. 36–50, 2021.
- [124] Y. Zhang, Y. Chen, Y. Wan et al., "Circular RNAs in the regulation of oxidative stress," *Frontiers in Pharmacology*, vol. 12, article 697903, 2021.
- [125] R. Rupaimoole and F. J. Slack, "MicroRNA therapeutics: towards a new era for the management of cancer and other diseases," *Nature Reviews. Drug Discovery*, vol. 16, no. 3, pp. 203–222, 2017.
- [126] M. Matsui and D. R. Corey, "Non-coding RNAs as drug targets," *Nature Reviews. Drug Discovery*, vol. 16, no. 3, pp. 167–179, 2017.
- [127] C. Dykstra-Aiello, G. C. Jickling, B. P. Ander et al., "Altered expression of long noncoding RNAs in blood after ischemic stroke and proximity to putative stroke risk loci," *Stroke*, vol. 47, no. 12, pp. 2896–2903, 2016.
- [128] W. Wang, B. Jiang, H. Sun et al., "Prevalence, incidence, and mortality of stroke in China: results from a nationwide population-based survey of 480 687 adults," *Circulation*, vol. 135, no. 8, pp. 759–771, 2017.
- [129] S. L. Mehta, T. Kim, and R. Vemuganti, "Long noncoding RNA FosDT promotes ischemic brain injury by interacting with REST-associated chromatin-modifying proteins," *The Journal of Neuroscience*, vol. 35, no. 50, pp. 16443–16449, 2015.
- [130] G. C. Jickling, B. P. Ander, X. Zhan, D. Noblett, B. Stamova, and D. Liu, "microRNA expression in peripheral blood cells following acute ischemic stroke and their predicted gene targets," *PLoS One*, vol. 9, no. 6, article e99283, 2014.
- [131] D. Lu, A. D. Xu, and X. Ad, "Mini review: circular RNAs as potential clinical biomarkers for disorders in the central nervous system," *Frontiers in Genetics*, vol. 7, no. 53, 2016.
- [132] C. Liu, C. Zhang, J. Yang et al., "Screening circular RNA expression patterns following focal cerebral ischemia in mice," *Oncotarget*, vol. 8, no. 49, pp. 86535–86547, 2017.

## *Retraction*

# **Retracted: Role of Glial Cell-Derived Oxidative Stress in Blood-Brain Barrier Damage after Acute Ischemic Stroke**

### **Oxidative Medicine and Cellular Longevity**

Received 8 January 2024; Accepted 8 January 2024; Published 9 January 2024

Copyright © 2024 Oxidative Medicine and Cellular Longevity. This is an open access article distributed under the Creative Commons Attribution License, which permits unrestricted use, distribution, and reproduction in any medium, provided the original work is properly cited.

This article has been retracted by Hindawi, as publisher, following an investigation undertaken by the publisher [1]. This investigation has uncovered evidence of systematic manipulation of the publication and peer-review process. We cannot, therefore, vouch for the reliability or integrity of this article.

Please note that this notice is intended solely to alert readers that the peer-review process of this article has been compromised.

Wiley and Hindawi regret that the usual quality checks did not identify these issues before publication and have since put additional measures in place to safeguard research integrity.

We wish to credit our Research Integrity and Research Publishing teams and anonymous and named external researchers and research integrity experts for contributing to this investigation.

The corresponding author, as the representative of all authors, has been given the opportunity to register their agreement or disagreement to this retraction. We have kept a record of any response received.

### **References**

- [1] X. Hu, Y. Wang, W. Du, L.-J. Liang, W. Wang, and X. Jin, "Role of Glial Cell-Derived Oxidative Stress in Blood-Brain Barrier Damage after Acute Ischemic Stroke," *Oxidative Medicine and Cellular Longevity*, vol. 2022, Article ID 7762078, 14 pages, 2022.

## Review Article

# Role of Glial Cell-Derived Oxidative Stress in Blood-Brain Barrier Damage after Acute Ischemic Stroke

Xiaoyan Hu <sup>1</sup>, Yanping Wang <sup>2</sup>, Weihong Du <sup>1</sup>, Li-Jun Liang <sup>3</sup>, Wei Wang <sup>4</sup>,  
and Xinchun Jin <sup>1</sup>

<sup>1</sup>Beijing Key Laboratory of Cancer Invasion and Metastasis Research, Department of Histology and Embryology, School of Basic Medical Sciences, Advanced Innovation Center for Human Brain Protection, Capital Medical University, Beijing 100069, China

<sup>2</sup>Department of Neurology, The Second Hospital of Jiaxing City, Jiaxing, 314000 Zhejiang, China

<sup>3</sup>Children's Hospital of Shanxi Province, Taiyuan, Shanxi Province, China

<sup>4</sup>Department of Physiology and Pathophysiology, School of Basic Medical Sciences, Capital Medical University, Beijing 100069, China

Correspondence should be addressed to Yanping Wang; [ypwang93@163.com](mailto:ypwang93@163.com) and Xinchun Jin; [xinchunjin@gmail.com](mailto:xinchunjin@gmail.com)

Received 10 June 2022; Accepted 13 August 2022; Published 2 September 2022

Academic Editor: Anwen Shao

Copyright © 2022 Xiaoyan Hu et al. This is an open access article distributed under the Creative Commons Attribution License, which permits unrestricted use, distribution, and reproduction in any medium, provided the original work is properly cited.

The integrity of the blood-brain barrier (BBB) is mainly maintained by endothelial cells and basement membrane and could be regulated by pericytes, neurons, and glial cells including astrocytes, microglia, oligodendrocytes (OLs), and oligodendrocyte progenitor cells (OPCs). BBB damage is the main pathological basis of hemorrhage transformation (HT) and vasogenic edema after stroke. In addition, BBB damage-induced HT and vasogenic edema will aggravate the secondary brain tissue damage. Of note, after reperfusion, oxidative stress-initiated cascade plays a critical role in the BBB damage after acute ischemic stroke (AIS). Although endothelial cells are the target of oxidative stress, the role of glial cell-derived oxidative stress in BBB damage after AIS also should receive more attention. In the current review, we first introduce the physiology and pathophysiology of the BBB, then we summarize the possible mechanisms related to BBB damage after AIS. We aim to characterize the role of glial cell-derived oxidative stress in BBB damage after AIS and discuss the role of oxidative stress in astrocytes, microglia cells and oligodendrocytes in after AIS, respectively.

## 1. Introduction

Stroke, a common acute cerebrovascular disease, accounts for approximately 9% of all death worldwide and is the second leading cause of death in addition to cardiovascular disease [1]. Stroke is prevalent in the middle-aged and elderly population and is receiving increasing attention in an increasingly ageing society [2]. Stroke is characterized by high morbidity, disability, and mortality rates and can be divided into hemorrhagic stroke and ischemic stroke, the latter of which accounts for 87% of stroke patients [3]. For treatment of acute ischemic stroke (AIS), tissue plasminogen activator (tPA) is the only thrombolytic drug approved by the Food and Drug Adminis-

tration (FDA), but its clinical use is limited by a strict time window (within 4.5 hours of stroke onset), the high risk of cerebral hemorrhage transformation (HT) after thrombolysis, and high death rate following HT [4]. Because of these limitations, thrombolytic therapy is given to only 3% of patients suffering from AIS [5].

After the onset of cerebral ischemia, a series of pathological events are triggered, including energy depletion, excitotoxicity, oxidative stress, inflammation, BBB disruption, and cell death [6]. HT caused by BBB damage aggravate the secondary brain tissue damage [7]. In addition, there is evidence that 25-30% of ischemic stroke survivors develop immediate or delayed vascular cognitive impairment (VCI)

or vascular dementia (VaD) [8, 9]. It is therefore crucial to investigate the mechanisms underlying BBB damage after AIS and develop the strategies to protect BBB integrity to reduce secondary brain damage.

The BBB prevents harmful neurotoxic plasma components, blood cells, and pathogens from entering the brain. In addition, BBB also regulates the transport of molecules in and out of the central nervous system (CNS) to maintain its normal function. BBB integrity is mainly maintained by the tight junction proteins (TJPs) between endothelial cells and the basement membrane covering the endothelial cell surface. Meanwhile, BBB integrity is also regulated by other cells in the CNS, such as glial cells [9, 10]. In recent years, glial cells have gradually attracted interests of scientists and doctors. They not only support cells in the CNS but also participates in the progression of related neuropathology such as ischemia-reperfusion injury. The new perspective regards microglia, astrocytes, OLs, and OPCs as exciting therapeutic targets for the treatment of AIS [6, 11]. However, the specific roles of glial cells as well as the underlying mechanisms after AIS need further investigation.

As mentioned above, the current treatments for AIS are intravenous thrombolysis and endovascular mechanical thrombectomy which would induce recanalization. However, reperfusion results in the production of large amounts of reactive oxygen species (ROS), which are responsible for most of the ischemia-reperfusion injury, resulting in brain tissue damage. In addition, oxidative stress can lead to apoptosis, autophagy, and necrosis of brain cells [12]. Therefore, it is crucial to fully understand the mechanisms by which oxidative stress is generated after AIS. Because of the high oxygen consumption, previous research and reviews addressing oxidative stress-induced damage have mainly focused on the neurons within the brain. This review is aimed at summarizing how glial cells influence both the integrity of the BBB and the development of oxidative stress after stroke, providing new ideas for future stroke treatment from the perspective of glial cells.

## 2. Physiology and Pathophysiology of the Blood-Brain Barrier (BBB)

**2.1. Endothelial Cells and Basement Membrane in the BBB.** BBB is a highly selective semipermeable membrane barrier that separates blood circulating in the brain from brain tissue. The BBB is a highly differentiated endothelial cell structure of the neurovascular system, consisting mainly of brain microvascular endothelial cells (BMECs), basement membrane (BM), astrocytes end feet surrounding the microvasculature, and pericytes (Figure 1(a)) [13].

Endothelial cells (ECs), joined by tight junctions and adherent junctions, form the first barrier of the BBB for selective passage of intra- and extravascular substances [14–16]. In addition, ECs produce and release various vascular regulatory factors such as endothelin, nitric oxide (NO), and vascular endothelial growth factor (VEGF) to regulate brain microcirculation [17].

The basement membrane (BM) that surrounds ECs forms a second barrier to the BBB. The BM is a complex

layer of extracellular matrix proteins that provides support for epithelial and endothelial cells, separating these cells from the brain tissue, thereby contributing to the development, formation, and maintenance of the BBB [18, 19].

**2.2. Regulation of BBB Integrity by Astrocytes, Pericytes, and Neurons.** Astrocytes play an important role in maintaining the integrity of the BBB. It has been shown that the brain microvasculature can maintain its integrity in the presence of massive astrocyte loss, suggesting that astrocytes are not directly involved in the maintaining the integrity of the BBB [20]. Astrocytes are primarily involved in maintaining the integrity of the BBB through releasing certain active substances, in particular growth factors such as VEGF and glial cell-derived neurotrophic factor. In addition, astrocytes are also able to influence the integrity of the BBB by regulating the expression of intracellular cyclic adenosine monophosphate (cAMP) and other proteins [17].

Pericytes are flat, undifferentiated, contractile connective tissue cells that surround the capillary wall [21]. Pericytes synthesize and secrete albumin as an important step in maintaining the integrity of the BBB [22]. During stroke, pericytes migrate away from the vasculature, thereby contributing to increased BBB permeability [23, 24].

Neurons are the most basic structural and functional units of the nervous system, which play the role of connecting and integrating input information and outputting information [25]. BBB regulation in response to neural activity is possibly a direct action of neurotransmitters on cells of the BBB. Of note, acute increases in neural activity in adult animals have also been implicated in changes in BBB function [26], and aberrantly, high neural activity has also been correlated with BBB high permeability [27]. In addition, Lacoste et al. showed that neuronal activity modulates vascular plasticity in the postnatal brain. Moreover, deprivation of sensory input from the barrel cortex of mice, either by surgical deafferent or by genetic inhibition of neurotransmitter release, results in reduced blood vessel density after birth [9]. Neuronal regulation of the BBB and neurovascular coupling has been reviewed by Kaplan et al. [28].

**2.3. Regulation of BBB Integrity by Microglia, Oligodendrocytes (OLs), and Oligodendrocyte Progenitor Cells (OPCs).** Microglia, the resident macrophages of the CNS, numbering 10–15% of the total cell population of the brain, are extremely responsive to changes in the CNS microenvironment and are involved in the homeostatic regulation of the CNS [29]. Microglia are brain microvessel-associated cells. They alter tight junction assembly and BBB permeability by releasing vasoactive substances and cytokines [30, 31]. Normally, microglia are in a quiescent state. Under pathological condition, microglia are activated to either M1 or M2 type [32]. M1 microglia have proinflammatory and prokilling functions. In contrast, M2 microglia are involved in immune regulation, control of inflammatory mechanisms, and repair of damage resolution [33]. Studies have shown that microglia activation is directly related to BBB integrity [34]. Microglia activation may be triggered by microorganisms (e.g., bacteria and virus) or neurodegenerative diseases such as Alzheimer's disease

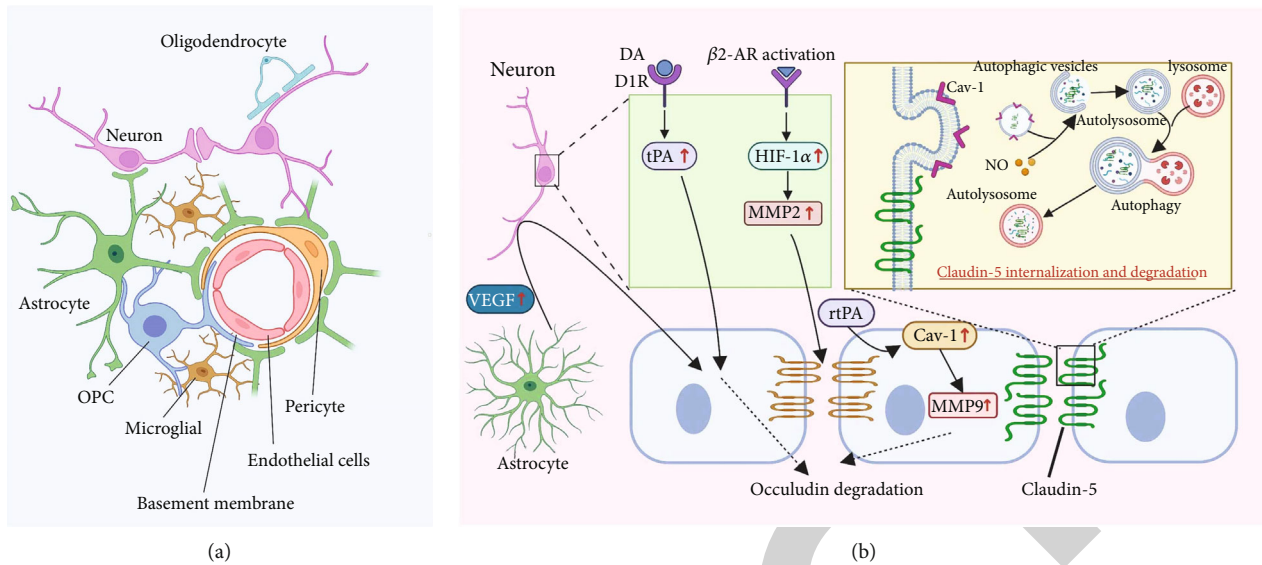


FIGURE 1: Components of blood-brain barrier and the mechanisms underlying BBB damage after acute ischemic stroke. (a) Schematic diagram of the BBB structure and other neural cells in the CNS that interact with the BBB. (b) Molecular mechanisms of BBB disruption in the acute phase of ischemia. (1) VEGF produced by activated astrocyte after stroke acts on neurons and causes occludin degradation between endothelial cells. (2) Dopamine receptor activation elevates endogenous tPA in neurons, which causes occludin degradation. (3) The upregulation of HIF-1 $\alpha$  in neurons increases the expression of MMP-2 in endothelial cells and leads to the degradation of occludin. (4) Caveolin-1 mediates tPA-induced MMP-9 upregulation in cultured brain microvascular endothelial cells. (5) Nitric oxide interacts with caveolin-1 to facilitate autophagy-lysosome-mediated claudin-5 degradation in endothelial cells.

(AD), Parkinson's disease (PD), or stroke. Microglia activation is one of the earliest events in cerebral ischemic events, occurring within minutes to hours after AIS [6, 35]. Therefore, microglia activity is crucial for prognostic and mechanistic investigation after AIS.

Oligodendrocytes (OLs) are myelinating cells of the CNS derived from oligodendrocyte progenitor cells (OPCs), which are widely distributed in the CNS and account for 5%-8% of glial cells [36]. Abnormal oligodendrocyte function underlies the pathology of a range of diseases including stroke, multiple sclerosis (MS), schizophrenia, and AD [37]. After AIS, the function of OLs is impaired, leading to impaired myelin formation on the surface of neurons, followed by impaired neurological function and brain tissue damage [37]. Recent studies have shown that under physiological or pathological conditions, OLs release extracellular vesicles (EVs) into neurons. EVs carry proteins including myelin-associated proteins, which can modulate BBB integrity by regulating neuronal function and neurovascular coupling [38]. Niu et al. showed that in AD patients, interactions between OLs and vascular are disrupted. This interferes with the integrity of endothelial tight junctions and astrocytes end feet, thereby disrupting the BBB and increasing vascular permeability [39]. When white matter is damaged, inflammation and oxidative stress stimulate the release of large amounts of matrix metalloproteinase 9 (MMP-9) from OLs and OPCs, resulting the disruption of the structure of blood vessels and inhibition of the restoration of the BBB [40].

**2.4. BBB Damage in Neurological Diseases.** The crucial role of the BBB impairment in the pathological processes of neurological diseases (VCI, VaD, AD, PD, ischemic stroke, MS,

and amyotrophic lateral sclerosis (ALS)) received special attention just for a few years [41, 42]. BBB dysfunction begins in the hippocampus in early stage of AD detected with magnetic resonance imaging, and BBB damage may initiate a range of tissue damage, lead to synaptic and neuronal dysfunction and cognitive impairment, end with AD [43]. Notably, BBB breakdown and vascular dysfunction are hallmarks of AD, and targeting BBB has great translational potential in AD therapy [44].

BBB disruption also plays an important role in the pathogenesis of PD, which is characterized by progressive degeneration of dopaminergic neurons in the substantia nigra (SN) [45]. For example, the expression of TJPs decreased, along with increased vascular permeability and accumulation of oligomeric  $\alpha$ -syn in activated astrocytes of mice brain [46]. In addition, astrocytic VEGFA has been shown to be an essential mediator in BBB disruption in PD [47]. Of note, BBB dysfunction could be detected in PD patients accompanied by the decrease of the function of P-glycoprotein (P-gp), a special protein in the blood vessels of the brain [48]. Therefore, BBB disruption precedes the loss of numerous dopaminergic neurons in the SN and has been hypothesized to contribute to the progression of PD [49].

BBB disruption after stroke was induced by inflammation-driven injury including oxidative stress, increased production of matrix metalloproteinases (MMP), activation of microglia, and infiltration of peripheral immune cells into ischemic tissues [50]. Aging-related vulnerability of the BBB increases the risk and exacerbates the severity of AIS [51]. The role of BBB in aging and neurodegeneration has been reviewed by Knox et al. [52], and BBB impairment is a cause rather than a consequence in aging-related neurodegenerative diseases

[53]. Therefore, treatment that could maintain the integrity of BBB would have important roles in preventing aging-related neurological diseases.

### 3. Possible Mechanisms Related to BBB Damage after Acute Ischemic Stroke

**3.1. BBB Damage Induced by Acute Ischemia.** After AIS, thrombolysis with tPA within the time window is the only FDA-approved drug. However, its clinical use is limited because of the risk of BBB damage-related vasogenic edema and HT. Jin et al. found that BBB injury occurred firstly in the striatum and preoptic area within 3 hours of cerebral ischemia. The BBB damage area coincides with the brain sites where HT occurred after tPA thrombolysis [54–56]. The mechanisms have been explored, and several signal pathway was involved, such as rapid MMP-2 secretion-mediated occludin degradation and caveolin-1-mediated claudin-5 redistribution [56, 57], neuronal-astroglial cell interactions [58], NO production, and autophagy activation [59]. The BBB damage after AIS is also associated with the neuronal apoptosis induced by neuregulin receptor degradation protein-1, an E3 ubiquitin ligase [60]. The mechanism of BBB injury after AIS is summarized in Figure 1(b). Notably, clinical trials targeting related signaling pathways after AIS are summarized in Table 1.

**3.2. BBB Damage Induced by Acute Ischemia and Reperfusion.** Current treatment for AIS focus on revascularization. However, once blood flow is restored, a series of ischemia-reperfusion injuries will be induced. These include biochemical events, ionic imbalance, oxidative stress, and inflammation, ultimately leading to cellular necrosis and apoptosis. These processes cause massive ROS production, resulting in oxidative stress injury and ultimately brain tissue damage and impaired neurological functions [12].

**3.2.1. Inflammation.** Inflammatory stimulation is a key mediator of BBB disruption after AIS. Previous studies have shown that inflammation after AIS is mediated by the proinflammatory factors tumor necrosis factor alpha (TNF- $\alpha$ ) and interleukin-1 $\beta$  (IL-1 $\beta$ ), which are produced between 2 and 6 h after ischemic injury [61]. In addition, proinflammatory factors induce subsequent migration of adhesion molecules, activated neutrophils, lymphocytes, and monocytes into the brain parenchyma [62, 63]. In particular, infiltration of neutrophils plays a key role in enhancing BBB permeability and worsening stroke prognosis [62, 63]. Adhesion molecules such as intercellular adhesion molecule-1 (ICAM-1) and vascular cellular adhesion molecule-1 (VCAM-1), which are expressed at low levels in the BBB, are significantly increased after AIS [64]. It has been shown that inhibition of adhesion molecules or neutrophil integrin proteins may prevent BBB disruption by reducing the number of neutrophils that enter the brain after AIS [65]. In addition, high expression of proinflammatory factors increases the chance of stroke recurrence [66]. The neuroinflammatory response associated with leukocyte infiltration plays an important role

in BBB destruction and HT. Inflammatory factors which are released from the ischemic area attract the leukocytes to cross the BBB and enter the brain [67], and leukocyte infiltration may damage the BBB and cause HT by disrupting microvascular endothelial cells. Notably, injection of matrix metalloproteinase 9 (MMP-9) inhibitors can reduce inflammation and the risk of HT during thrombolysis [68].

Brain tissue contains lipids with high amounts of unsaturated fatty acids and high concentrations of iron, which make the brain more susceptible to free radicals [69]. Free radicals are divided into two categories: ROS and reactive nitrogen species (RNS). The accumulation of a large number of free radicals plays a key role in many pathological processes of ischemia-reperfusion. Neuronal nitric oxide synthase (nNOS) mediates the production of large amounts of NO in neurons during ischemia, and NO may inhibit the mitochondrial respiratory chain and also react with superoxide radical anion to form highly active peroxynitrite, which increases brain damage. NO reacts with or transforms important biological compounds to generate ROS such as hydroxyl radicals and RNS [70–72].

**3.2.2. Oxidative Stress.** After cerebral ischemia-reperfusion, the inflammatory response induces the production of a large number of ROS, which eventually leads to oxidative stress [73]. The source of ROS consists of two main ways (Figure 2): (1) enzymatic (products of the mitochondrial electron transport chain, which is the primary way to generate ROS [74], and (2) nonenzymatic, the process requires the production of ROS in the presence of free iron [75].

ROS in the CNS are mainly produced by astrocytes and microglia. Superoxide, one of the most important ROS in the CNS, is produced by enzymes such as xanthine oxidase (XO), nicotinamide adenine dinucleotide phosphate (NADPH), or as a by-product of the respiratory chain [76]. ROS include peroxy radical (HO<sub>2</sub>), hydroxyl radical (OH $\cdot$ ), superoxide anion (O<sub>2</sub> $\cdot^-$ ), hydrogen peroxide (H<sub>2</sub>O<sub>2</sub>), hypochlorous acid, and ozone [12]. The neuronal oxidative stress after AIS is mainly divided into three stages. The first stage occurs immediately after ischemia, during which oxygen glucose deprivation (OGD) induces mitochondrial depolarization and uncoupling of mitochondrial respiratory chain in neurons. Intermediates accumulated in the respiratory chain interact with oxygen to generate ROS [77]. The second stage is between 25 and 35 minutes characterized by hypoglycemia and hypoxia. At this time, the intracellular ATP is depleted, and a large amount of XO is activated. The third stage is the reperfusion stage where the oxygenation level increases, producing a large amount of ROS [78]. ROS can act on the basement membrane and cell membrane to cause damage to basement membrane and endothelial cells, eventually leading to BBB damage [79]. Studies have shown that AIS leads to a large amount of ROS production which could regulate the expression of claudin-5 and occludin in the BBB to increase paracellular solute leakage and decrease BBB integrity [31, 80, 81].

TABLE 1: Clinical trials targeting signaling pathways related to blood-brain barrier damage.

Signaling pathways	Reference
Autophagy, IL-1, CREB1, mTOR, BER (base extension repair), interferon, relaxin, RAN, estrogen receptor, gas signaling pathway	[147]
AMPK/mTOR signaling pathway	[148]
RBP4/Lp-PLA2/Netrin-1 signaling pathway	[149]
Zinc as a signaling medium	[150]

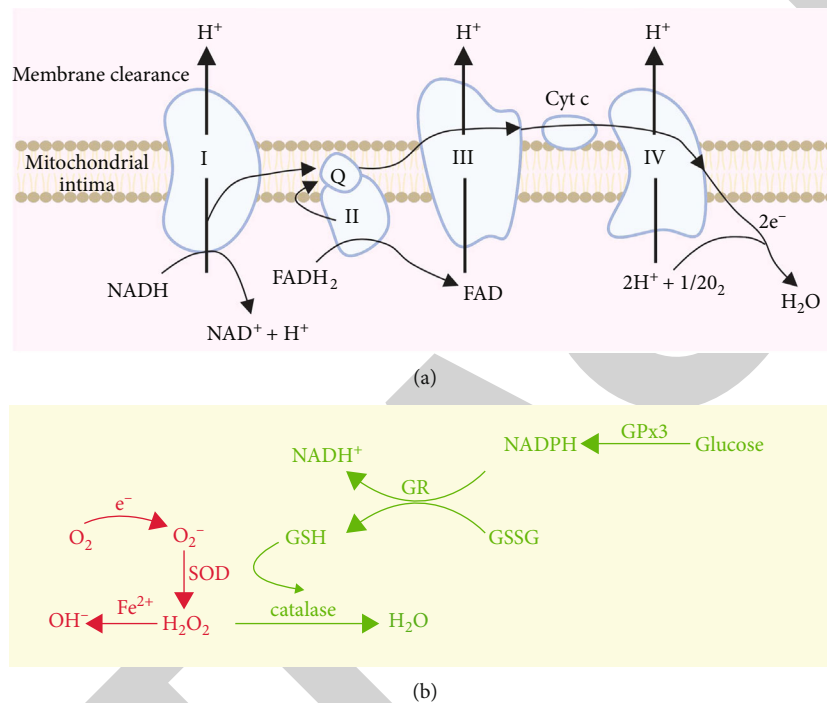


FIGURE 2: The mitochondrial electron transport chain under normal conditions and production of ROS. (a) Physiological conditions, electrons are sequentially transferred on complex I, coenzyme Q, complex III, cytochrome C, and complex IV on the inner mitochondrial membrane and finally produce  $H_2O$  and  $O_2$ . (b) The production process of ROS (red). Under pathological conditions, electrons leave the ETC and directly combine with  $O_2$  to form super oxide radicals- $O_2^-$ .  $O_2^-$  can generate  $H_2O_2$  under the catalysis of SOD.  $H_2O_2$  catalyzes the formation of  $OH^-$  in the presence of metallic  $Fe^{2+}$ . On the other hand, there are antioxidative pathways in cells (green).  $H_2O_2$  can be reduced to  $H_2O$  under the action of GSH via the pentose phosphate pathway. ETC: electron transport chain;  $NAD^+$ : nicotinamide adenine dinucleotide;  $FADH_2$ : flavin adenine dinucleotide; FAD: flavinadeninedinucleotide; Cyt C: cytochrome C; GPx3: glutathione peroxidase 3; GSH: glutathione; GSSG: oxidized glutathione; GR: glutathione reductase.

## 4. Role of Glial Cell-Derived Oxidative Stress in the BBB Damage after Acute Ischemic Stroke

### 4.1. Astrocytes in Stroke

**4.1.1. Oxidative Stress in Astrocytes.** Astrocytes are critically involved in maintaining the integrity of the BBB. Under physiological conditions, there are clear and distinct boundaries between resting astrocytes. When mild injury occurs, astrocytes begin to proliferate, with hypertrophy of cell bodies and processes accompanied by upregulated expression of GFAP. When the injury was aggravated, astrocytes proliferated massively, and the expression of GFAP was significantly upregulated. The cell body is markedly enlarged, and there is overlap between the cells [82]. There are three main ways of

oxidative stress after astrocytes activation: mitochondria-derived oxidative stress, NADPH-derived oxidative stress, and RNS production (Figure 3) [83]. Disrupted mitochondrial function leads to an increase of ROS in astrocytes, resulting in astrocytes proliferation [83]. There is a significant increase of cytoplasmic  $Ca^{2+}$  concentration when astrocytes are exposed to OGD.  $Ca^{2+}$  accumulates excessively into the mitochondria via voltage-dependent anion channels (VDAC) and mitochondrial calcium unidirectional transporters (MCU), triggering the activation of the mitochondrial permeability transition pore (MPTP). Upon MPTP activation, small molecules are excreted from the mitochondria without selectivity. The discharge of small molecules leads to the dissipation of mitochondrial membrane potential, which ultimately leads to impaired antioxidant



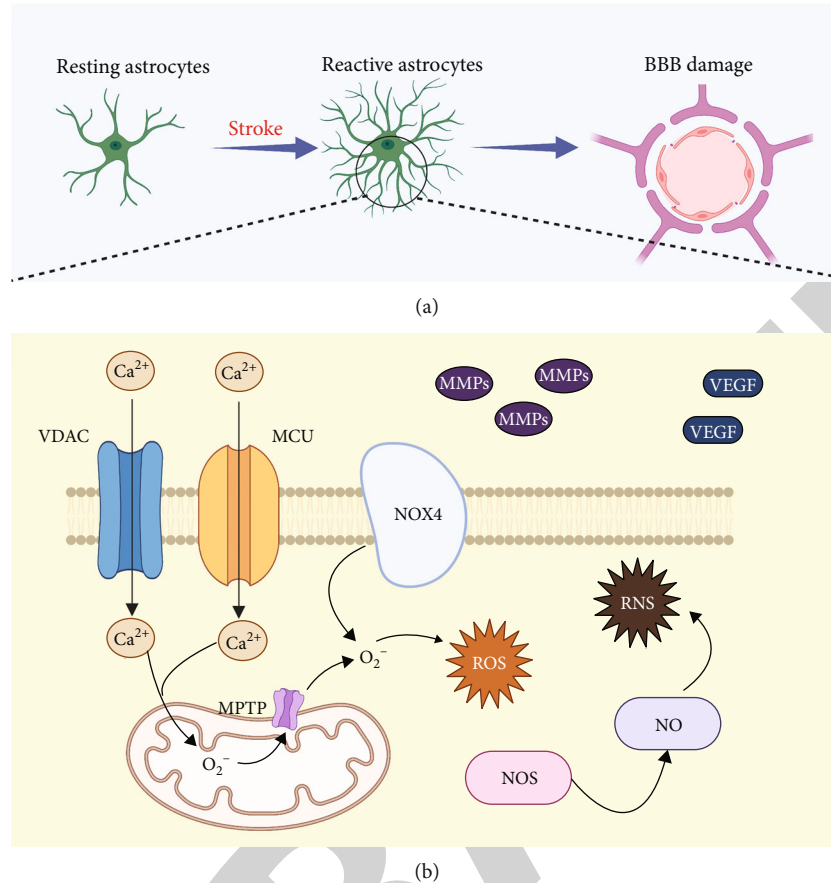


FIGURE 3: Schematic illustration of the mechanism by which astrocytes activation disrupts BBB integrity after stroke. (a) Astrocytes activation disrupts BBB integrity after stroke. (b) Activated astrocytes allow a large amount of  $Ca^{2+}$  to enter mitochondria through VDAC and MCU to generate  $O_2^-$ .  $O_2^-$  exits mitochondria through MPTP to cause oxidative stress. NOX4 promotes oxidative stress in astrocytes. In addition, NOS in astrocytes catalyzes the production of NO to cause RNS. On the other hand, activated astrocytes secrete VEGF and MMPs causing BBB dysfunction.

pathways and ROS production [74]. In addition, the physiological function of astrocytes is influenced by NADPH-derived oxidative stress. NOX2 and NOX4 are the most abundantly expressed NOX isoforms of the NADPH oxidase (NOX) family in the CNS. Studies have shown that NOX4 is expressed in astrocytes, and its expression regulates oxidative stress in astrocytes [84, 85]. RNS production is another mode of endogenous oxidative stress in astrocytes. All the three isoforms of NOS that are expressed in the CNS are expressed in astrocytes,  $Ca^{2+}$ /calmodulin-dependent nNOS, endothelial NOS (eNOS), and  $Ca^{2+}$ -independent inducible NOS (iNOS). NO produced by activated astrocytes can cause the dysfunction of neuron mitochondrial membrane complexes II, III, and IV [86]. NO can enhance S-nitrosylation of protein disulfide isomerase, followed by superoxide dismutase 1 (SOD1) aggregation in astrocytes and enhanced ischemia-reperfusion injury [87].

After AIS, activated astrocytes also have positive effects besides their damaging effects. As an important antioxidant and free radical scavenger, glutathione participates in redox reactions and can combine with peroxides and free radicals to reduce ROS toxicity. Astrocytes are rich in glutathione

and enzymes related to glutathione metabolism, which play a key role in reducing oxidative stress toxicity and preventing aggravation of ischemic injury [69, 88–91].

**4.1.2. Regulation of BBB Permeability by Astrocytes.** Astrocytes play an important role in BBB injury after AIS. Endothelial cells and astrocytes were cocultured to mimic *in vitro* BBB and endothelial cells exposed to 24h OGD caused astrocytes apoptosis by secreting microvesicles accompanied by increased BBB permeability and degradation of the tight junction proteins occludin and claudin-5 [92]. In addition, after AIS, neurons stimulate VEGF production by astrocytes, leading to degradation of the tight junction proteins occludin and claudin-5 and increased permeability of the BBB [93]. In addition, astrocytes can release MMPs and glutamate. MMPs disrupt endothelial TJPs and some kinds of extracellular matrix [94]. Glutamate activates N-methyl-D-aspartate (NMDA) receptors on endothelial cells, inducing vasodilation and increasing BBB permeability [95, 96]. Indeed, astrocytes also produce NO and increase the permeability of the BBB through the cyclic guanosine monophosphate pathway [97, 98]. Moreover, astrocytes produce ET-

1 after AIS, an endogenous long-acting vasoconstrictor which overexpression can increase BBB permeability and aggravate brain injury [99, 100].

Astrocytes can produce some cytokines to maintain BBB function. Astrocytes can produce angiotensin-1 (Ang-1) and Sonic Hedgehog (SHH) and increase endothelial tight junction protein expression and angiogenesis to protect the BBB [101, 102]. Under ischemic conditions, astrocytes can produce insulin-like growth factor-1 (IGF-1) which could stabilize the microvascular cytoskeleton to maintain normal permeability of the BBB [103, 104]. Taken together, astrocytes have a dual role in regulating BBB permeability. How to regulate the secretion of protective factors by astrocytes and to protect the integrity of the BBB requires further research.

#### 4.2. Microglia in Stroke

**4.2.1. Microglia and Oxidative Stress.** After AIS, microglia are firstly activated (Figure 4). 24 h after AIS, microglia activation can be detected in the core and peri-infarct areas of ischemic hemisphere [105, 106]. On one hand, activated microglia produce cytokines and chemokines that promote leukocyte infiltration and aggravate the disruption of the BBB and brain tissue [107]. On the other hand, activated microglia may play a beneficial role by phagocytosing cellular debris and suppressing inflammatory responses [17]. The activated microglia can be defined by the expression of surface markers, Iba1, IB4, F4/80, CD11b, and CD68, and increased CD11b expression could indicate the severity of microglia activation [108]. Activated microglia after AIS are polarized into a proinflammatory M1 phenotype or an anti-inflammatory M2 phenotype that produces immunomodulatory molecules such as cytokines and chemokines. It has been shown that M1 microglia promote secondary brain injury, whereas M2 microglia promote recovery after AIS [109, 110]. Inducible nitric oxide synthase (iNOS) and arginase-1 (Arg1) represent a relatively straightforward set of markers to follow M1 versus M2 phenotypes [111]. Roy et al. showed that stimulation of mouse BV-2 microglia and primary microglia with lipopolysaccharide (LPS) promoted upregulation of CD11b expression. Meanwhile, the elevated CD11b expression in microglia was blocked by antioxidants such as N-acetylcysteine and pyrrolidine dithiocarbamate [112]. Inhibition of ROS prevents the proliferation and activation of microglia [113], suggesting that ROS are involved in microglia activation. Mander et al. reported that the proinflammatory cytokines IL-1 $\beta$  or TNF- $\alpha$  stimulated microglia proliferation, which could be inhibited by a NADPH oxidase inhibitor oleuropein, suggesting that NADPH oxidase-derived hydrogen peroxide mediated the microglia proliferation after AIS [114]. Microglia NADPH oxidase can be rapidly activated by LPS and interferon-gamma (IFN- $\gamma$ ), followed by the expression upregulation of iNOS and NO that are induced by ROS release in rat. NADPH oxidase inhibitors blocked the upregulation, indicating that NADPH oxidase is involved in the proinflammatory response of microglia, further supporting that NADPH oxidase-derived ROS are essential for proinflammatory gene expression in glial cells [115].

Studies have shown that nuclear factor erythroid 2-related factor 2 (Nrf2) plays a critical role in promoting the transition of microglia to the M2 phenotype. In a Parkinson's disease model, microglia in Nrf2-deficient mice have an increased M1 and a decreased M2 phenotype [116]. In the presence of ROS, microglia may tend to polarize toward M1 and reduce the activation of M2, thus playing an important role in inflammation. It is important to note that M2 microglia have three subtypes, M2a, M2b, and M2c, which are related to the timing of stimulation [117]. The exact role of these three subtypes of M2 microglia in neurological diseases needs further investigation.

#### 4.2.2. The Role of Microglia in Maintaining the BBB Integrity.

It has been shown that loss of microglia increases vascular permeability and cerebral hemorrhage, with detrimental effects on vascular density in a neonatal stroke model. Growing evidence demonstrate that the dual roles of microglia exhibited in BBB damage after AIS may depend on the phenotype of microglia. Microglia/macrophages are activated into a proinflammatory or an anti-inflammatory phenotype when they are stimulated [118–120]. After stroke, proinflammatory cytokines such as IL-1 $\beta$ , TNF- $\alpha$ , and IL-6 are upregulated in M1-type microglia and disrupt BBB integrity by altering cytoskeletal organization, TJP expression, and MMP production [121]. In addition, M1-type microglia increase brain endothelial cell permeability by NADPH oxidase activation-induced P-glycoprotein dysfunction, which leads to the accumulation of neurotoxic molecules in the brain [122]. Inhibiting microglia activation by minocycline, an inhibitor of inflammation, promotes long-term neurovascular remodeling and neurological recovery after ischemia [123]. On the other hand, the complexity of retinal vasculature is reduced if macrophage-colony stimulating factor is deficit in mice, suggesting a potential role for microglia in angiogenesis [124]. After stroke, microglia aggregate around the vascular system, resulting in vascular disintegration and upregulation of phagocytic CD68 expression in the penumbra [125]. Subsequently, microglia released the proangiogenic factor VEGF, suggesting that microglia can promote cerebral vascular remodeling after ischemic stroke [126]. Since microglia play a dual role after stroke, further study are needed to explore how to activate the microglia into an anti-inflammatory phenotype to promote neural recovery after stroke.

#### 4.3. Oligodendrocytes and OPC in Stroke

**4.3.1. Oligodendrocytes, OPC, and Oxidative Stress.** Oligodendrocytes (OLs), the cells responsible for axon myelin formation in the CNS, are deficit in neurological diseases including multiple sclerosis (MS), schizophrenia, and AD [37]. So far, most of ischemia stroke-related studies focus on gray matter, and the role of white matter has been ignored. Actually, white matter damage accounts for about half of the infarction area after cerebral ischemia [127, 128]. In animal models of stroke, the degree of white matter damage is strongly correlated with the age of the animals. It was shown that juvenile animals are more resistant to

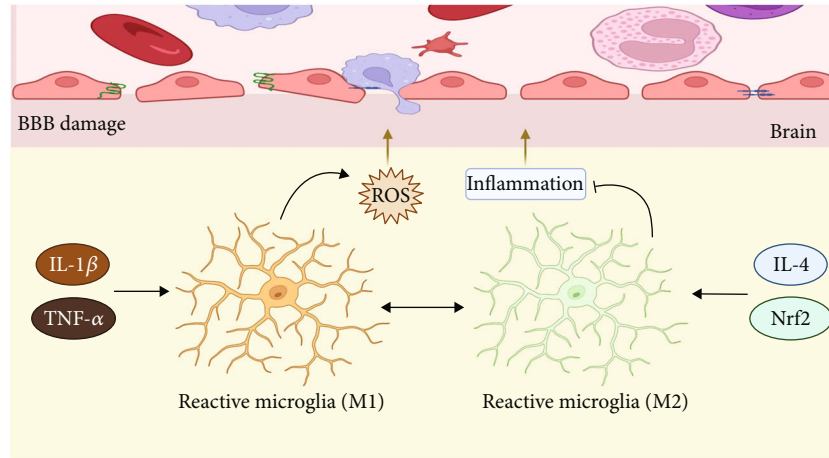


FIGURE 4: Schematic representation of the effect of microglia activation on BBB integrity after stroke. Microglia are activated to either M1 or M2 type after stroke. They have different effects on BBB integrity. IL-1 $\beta$  and TNF- $\alpha$  promote M1 microglia activation. IL-4 and Nrf2 promote M2 microglia activation.

cerebral ischemia compared to perinatal and old [129, 130], suggesting that white matter damage mechanisms are associated with age.

In the early stages of cerebral ischemia, there is an increase in oxidative stress, especially after reperfusion, which leads to OL damage and consequent demyelination, followed by severe long-term sensorimotor and cognitive deficits [131]. During cerebral ischemia, OLs produce large amounts of superoxide radicals, lipid peroxidation, and iron oxidation (Figure 5) [132]. Pantoni et al. showed that 30 minutes after arterial occlusion, OLs, and astrocytes were significantly swollen and 3 h later, a large number of OLs were fatally injured [133]. OPCs are more vulnerable to stimuli than neurons or astrocytes during early reperfusion after stroke [134]. Delayed treatment with the antioxidant ebselenolide significantly reduced transient ischemia-induced gray and white matter injury and neurological deficits, suggesting that oxidative stress plays an important role in the white matter injury after cerebral ischemia [135].

During ischemia, extracellular levels of the neurotransmitters glutamate and ATP are significantly elevated, which triggers OL injury [136, 137]. Excess neurotransmitters over-activate the receptors and cause damage to OLs through excitotoxicity [138]. Glutamate receptor antagonists partially protect against oligodendrocyte damage and reduce white matter injury [139].

**4.3.2. The Role of Oligodendrocytes and OPC on BBB Permeability and Angiogenesis.** OLs are involved in the regulation of the integrity of the BBB by interacting with endothelial cells. After stroke, OLs secrete MMP-9 which could accelerate the angiogenic response after white matter injury. Primary OLs treated with the proinflammatory cytokine IL-1 $\beta$  induces upregulation and secretion of MMP-9. Tube formation was significantly increased if brain endothelial cells were treated with IL-1 $\beta$ -conditioned medium of OLs. MMP inhibitor GM6001 was able to inhibit angiogenesis around the injury zone. It is shown that MMP-9 produced by OLs can promote angiogenesis

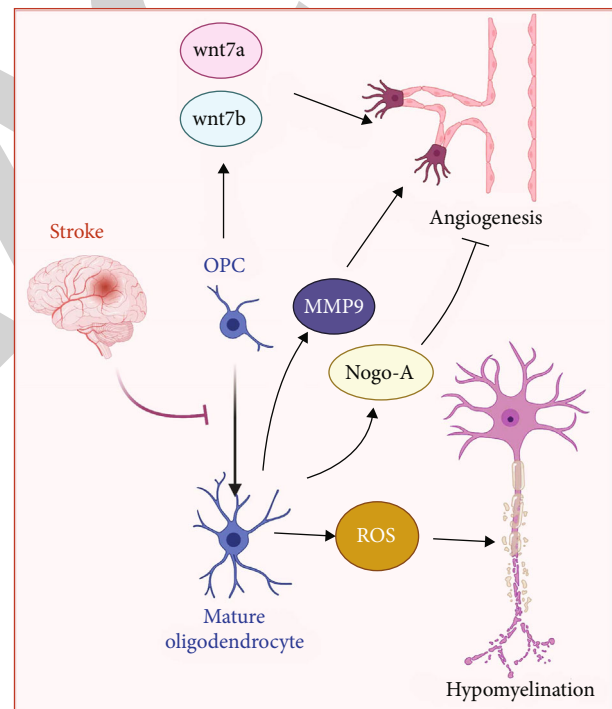


FIGURE 5: Schematic representation of the effects of OLs and OPCs on BBB integrity and angiogenesis after stroke. After stroke, the differentiation of OPCs into OLs is blocked. Oxidative stress in damaged OLs causes neuronal demyelination. High expression of Nogo-A in OLs inhibits angiogenesis. Poststroke oligodendrocytes secrete MMP-9, which accelerates angiogenesis following white matter injury. On the other hand, OPCs secrete Wnt7a and Wnt7b to promote angiogenesis after stroke.

*in vitro* [140, 141]. OPCs secrete the soluble factor TGF- $\beta$ 1 that maintains the integrity of the BBB. In an *in vitro* BBB model, OPC-conditioned medium increased tight junction protein expression and decreased BBB permeability by activating the TGF- $\beta$  receptor-MEK/ERK signaling pathway [142]. In neonatal mouse brain, OPCs

attached to brain endothelial cells via basement membrane, indicating that OPCs also play a key role in promoting BBB integrity [143]. In addition, OPCs play an important role in facilitating angiogenesis in the brain. Hypoxia causes OPCs to secrete Wnt7a and Wnt7b, which directly stimulate endothelial cell proliferation and promote angiogenesis [144]. Nogo-A is a membrane protein expressed on the surface of OLs and neurons. It is a growth inhibitory, antiadhesion, and growth cone collapse factor. In the postnatal mouse brain, high expression of Nogo-A inhibits angiogenesis, and decreased expression of Nogo-A increases angiogenesis *in vivo* [145]. Therefore, OPCs may improve neurological recovery by modulating poststroke angiogenesis which is positively associated with the recovery of neurological function after stroke [146].

## 5. Conclusion

There is an urgent need to understand the pathophysiological mechanisms after AIS and the interactions between the various components of the brain. In this review, we discuss the mechanisms of BBB dysfunction after stroke, in particular, the impact of oxidative stress on the BBB. Subsequently, we discuss the important roles of glial cells such as astrocytes, microglia, OPCs, and OLs in oxidative stress after stroke, as well as their impact on the BBB and angiogenesis. Future studies could explore the specific mechanisms of glial cell-mediated oxidative stress, the functional differences between different glial cell types, and the differential effects of different glial cells on the integrity of BBB, which would be a very promising target for the treatment of AIS.

## 6. Literature Search Criteria

Relevant research articles and reviews before June 2022 were retrieved on PubMed using glia, BBB, oxidative stress, and stroke as keywords. References to included studies were manually screened for 150 articles based on the relevance of the title/abstract to the keywords.

## Abbreviations

AD:	Alzheimer's disease
Ang-1:	Angiopoietin-1
AIS:	Acute ischemic stroke
Arg1:	Arginase-1
BBB:	Blood-brain barrier
cAMP:	Cyclic adenosine monophosphate
CNS:	Central nervous system
Cyt C:	Cytochrome C
ETC:	Electron transport chain
EVs:	Extracellular vesicles
FADH2:	Flavin adenine dinucleotide
FAD:	Flavin adenine dinucleotide
FDA:	Food and Drug Administration
GR:	Glutathione reductase
GSH:	Glutathione
GSSG:	Oxidized glutathione

H2O2:	Hydrogen peroxide
HO2·:	Peroxy radical
HT:	Hemorrhagic transformation
ICAM-1:	Intercellular adhesion molecule-1
IGF-1:	Insulin-like growth factor-1
IL-1 $\beta$ :	Interleukin-1 $\beta$
iNOS:	Inducible nitric oxide synthase
LPS:	Lipopolysaccharide
MCU:	Mitochondrial calcium unidirectional transporters
MMP-2:	Matrix metalloproteinase 2
MMP-9:	Matrix metalloproteinase 9
MPTP:	Mitochondrial permeability transition pore
MS:	Multiple sclerosis
NAD <sup>+</sup> :	Nicotinamide adenine dinucleotide
NADPH:	Nicotinamide adenine dinucleotide phosphate
NO:	Nitric oxide
NOX:	NADPH oxidase
Nrf2:	Nuclear factor erythroid 2-related factor 2
O2·:	Superoxide anion
OGD:	Oxygen glucose deprivation
OH·:	Hydroxyl radical
OLs:	Oligodendrocytes
OPCs:	Oligodendrocyte progenitor cells
RNS:	Reactive nitrogen species
ROS:	Reactive oxygen species
SHH:	Sonic Hedgehog
SN:	Substantia nigra
SOD1:	Superoxide dismutase 1
TJPs:	Tight junction proteins
TNF- $\alpha$ :	Tumor necrosis factor alpha
tPA:	Tissue plasminogen activator
VCAM-1:	Vascular cellular adhesion molecule-1
VCI:	Vascular cognitive impairment
VDAC:	Voltage-dependent anion channels
VD:	Vascular dementia
XO:	Xantine oxidase.

## Data Availability

No data were used to support this study.

## Conflicts of Interest

The authors declare that they have no conflicts of interest.

## Authors' Contributions

Xiaoyan Hu and Yanping Wang contributed equally to this work.

## Acknowledgments

This work was supported by the National Natural Science Foundation of China (81870973 and 81671145). This work was also supported by grants from the Jiaying Plan of Science and Technology under grant no. 2022AY30028.

## References

- [1] P. Boursin, S. Paternotte, B. Dercy, C. Sabben, and B. Maier, "Semantics, epidemiology and semiology of stroke," *Soins*, vol. 63, no. 828, pp. 24–27, 2018.
- [2] V. L. Feigin, G. A. Mensah, B. Norrving, C. J. L. Murray, G. A. Roth, and GBD 2013 Stroke Panel Experts Group, "Atlas of the global burden of stroke (1990-2013): the GBD 2013 study," *Neuroepidemiology*, vol. 45, no. 3, pp. 230–236, 2015.
- [3] D. Mozaffarian, E. J. Benjamin, A. S. Go et al., "Heart disease and stroke statistics–2015 update: a report from the American Heart Association," *Circulation*, vol. 131, no. 4, pp. e29–322, 2015.
- [4] R. S. Marshall, "Progress in intravenous thrombolytic therapy for acute stroke," *JAMA Neurology*, vol. 72, no. 8, pp. 928–934, 2015.
- [5] T. Knecht, J. Story, J. Liu, W. Davis, C. Borlongan, and I. dela Peña, "Adjunctive therapy approaches for ischemic stroke: innovations to expand time window of treatment," *International journal of molecular sciences*, vol. 18, no. 12, p. 2756, 2017.
- [6] I. H. Hernández, M. Villa-González, G. Martín, M. Soto, and M. J. Pérez-Álvarez, "Glial cells as therapeutic approaches in brain ischemia-reperfusion injury," *Cell*, vol. 10, no. 7, p. 1639, 2021.
- [7] Y. Yang and G. A. Rosenberg, "Matrix metalloproteinases as therapeutic targets for stroke," *Brain Research*, vol. 1623, pp. 30–38, 2015.
- [8] R. N. Kalaria, R. Akinyemi, and M. Ihara, "Stroke injury, cognitive impairment and vascular dementia," *Biochimica et Biophysica Acta*, vol. 1862, no. 5, pp. 915–925, 2016.
- [9] M. D. Sweeney, Z. Zhao, A. Montagne, A. R. Nelson, and B. V. Zlokovic, "Blood-brain barrier: from physiology to disease and back," *Physiological Reviews*, vol. 99, no. 1, pp. 21–78, 2019.
- [10] X. Jiang, A. V. Andjelkovic, L. Zhu et al., "Blood-brain barrier dysfunction and recovery after ischemic stroke," *Progress in Neurobiology*, vol. 163–164, pp. 144–171, 2018.
- [11] S. Xu, J. Lu, A. Shao, J. H. Zhang, and J. Zhang, "Glial cells: role of the immune response in ischemic stroke," *Frontiers in Immunology*, vol. 11, p. 294, 2020.
- [12] S. Orellana-Urzúa, I. Rojas, L. Libano, and R. Rodrigo, "Pathophysiology of ischemic stroke: role of oxidative stress," *Current Pharmaceutical Design*, vol. 26, no. 34, pp. 4246–4260, 2020.
- [13] B. V. Zlokovic, "The blood-brain barrier in health and chronic neurodegenerative disorders," *Neuron*, vol. 57, no. 2, pp. 178–201, 2008.
- [14] G. Bazzoni and E. Dejana, "Endothelial cell-to-cell junctions: molecular organization and role in vascular homeostasis," *Physiological Reviews*, vol. 84, no. 3, pp. 869–901, 2004.
- [15] P. M. Carvey, B. Hendey, and A. J. Monahan, "The blood-brain barrier in neurodegenerative disease: a rhetorical perspective," *Journal of Neurochemistry*, vol. 111, no. 2, pp. 291–314, 2009.
- [16] L. González-Mariscal, A. Domínguez-Calderón, A. Raya-Sandino, J. M. Ortega-Olvera, O. Vargas-Sierra, and G. Martínez-Revollar, "Tight junctions and the regulation of gene expression," *Seminars in Cell & Developmental Biology*, vol. 36, pp. 213–223, 2014.
- [17] W. Li, R. Pan, Z. Qi, and K. J. Liu, "Current progress in searching for clinically useful biomarkers of blood-brain barrier damage following cerebral ischemia," *Brain circulation*, vol. 4, no. 4, pp. 145–152, 2018.
- [18] W. M. Pardridge, "Molecular biology of the blood-brain barrier," *Molecular Biotechnology*, vol. 30, no. 1, pp. 057–070, 2005.
- [19] A. W. Morris, M. M. G. Sharp, N. J. Albarogthy et al., "Vascular basement membranes as pathways for the passage of fluid into and out of the brain," *Acta Neuropathologica*, vol. 131, no. 5, pp. 725–736, 2016.
- [20] C. L. Willis, C. C. Nolan, S. N. Reith et al., "Focal astrocyte loss is followed by microvascular damage, with subsequent repair of the blood-brain barrier in the apparent absence of direct astrocytic contact," *Glia*, vol. 45, no. 4, pp. 325–337, 2004.
- [21] Y. Persidsky, S. H. Ramirez, J. Haorah, and G. D. Kammogne, "Blood-brain barrier: structural components and function under physiologic and pathologic conditions," *Journal of Neuroimmune Pharmacology*, vol. 1, no. 3, pp. 223–236, 2006.
- [22] P. Dore-Duffy, A. Katychev, X. Wang, and E. van Buren, "CNS microvascular pericytes exhibit multipotential stem cell activity," *Journal of Cerebral Blood Flow and Metabolism*, vol. 26, no. 5, pp. 613–624, 2006.
- [23] E. Gonul, B. Duz, S. Kahraman, H. Kayali, A. Kubar, and E. Timurkaynak, "Early pericyte response to brain hypoxia in cats: an ultrastructural study," *Microvascular Research*, vol. 64, no. 1, pp. 116–119, 2002.
- [24] P. Dore-Duffy, C. Owen, R. Balabanov, S. Murphy, T. Beaumont, and J. A. Rafols, "Pericyte migration from the vascular wall in response to traumatic brain injury," *Microvascular Research*, vol. 60, no. 1, pp. 55–69, 2000.
- [25] A. Azarfar, N. Calcini, C. Huang, F. Zeldenrust, and T. Celikel, "Neural coding: a single neuron's perspective," *Neuroscience and Biobehavioral Reviews*, vol. 94, pp. 238–247, 2018.
- [26] U. Vazana, R. Veksler, G. S. Pell et al., "Glutamate-mediated blood-brain barrier opening: implications for neuroprotection and drug delivery," *The Journal of Neuroscience*, vol. 36, no. 29, pp. 7727–7739, 2016.
- [27] I. E. Andrés, M. A. Deli, S. Veszelka, K. Hayashi, B. Hennig, and M. Toborek, "The NMDA and AMPA/KA receptors are involved in glutamate-induced alterations of occludin expression and phosphorylation in brain endothelial cells," *Journal of Cerebral Blood Flow and Metabolism*, vol. 27, no. 8, pp. 1431–1443, 2007.
- [28] L. Kaplan, B. W. Chow, and C. Gu, "Neuronal regulation of the blood-brain barrier and neurovascular coupling," *Nature Reviews. Neuroscience*, vol. 21, no. 8, pp. 416–432, 2020.
- [29] K. Picard, M. K. St-Pierre, H. A. Vecchiarelli, M. Bordeleau, and M. É. Tremblay, "Neuroendocrine, neuroinflammatory and pathological outcomes of chronic stress: a story of microglial remodeling," *Neurochemistry International*, vol. 145, p. 104987, 2021.
- [30] M. L. Rennels, T. F. Gregory, and K. Fujimoto, "Innervation of capillaries by local neurons in the cat hypothalamus: a light microscopic study with horseradish peroxidase," *Journal of Cerebral Blood Flow and Metabolism*, vol. 3, no. 4, pp. 535–542, 1983.

- [31] N. J. Abbott, L. Rönnbäck, and E. Hansson, "Astrocyte-endothelial interactions at the blood-brain barrier," *Nature Reviews. Neuroscience*, vol. 7, no. 1, pp. 41–53, 2006.
- [32] A. Nimmerjahn, F. Kirchhoff, and F. Helmchen, "Resting microglial cells are highly dynamic surveillants of brain parenchyma In Vivo," *Science*, vol. 308, no. 5726, pp. 1314–1318, 2005.
- [33] S. R. Subramaniam and H. J. Federoff, "Targeting microglial activation states as a therapeutic avenue in Parkinson's disease," *Frontiers in Aging Neuroscience*, vol. 9, p. 176, 2017.
- [34] W. Abdullahi, D. Tripathi, and P. T. Ronaldson, "Blood-brain barrier dysfunction in ischemic stroke: targeting tight junctions and transporters for vascular protection," *American Journal of Physiology. Cell Physiology*, vol. 315, no. 3, pp. C343–c356, 2018.
- [35] R. Jin, G. Yang, and G. Li, "Inflammatory mechanisms in ischemic stroke: role of inflammatory cells," *Journal of Leukocyte Biology*, vol. 87, no. 5, pp. 779–789, 2010.
- [36] M. R. Dawson, A. Polito, J. M. Levine, and R. Reynolds, "NG2-expressing glial progenitor cells: an abundant and widespread population of cycling cells in the adult rat CNS," *Molecular and Cellular Neurosciences*, vol. 24, no. 2, pp. 476–488, 2003.
- [37] S. Kuhn, L. Gritti, D. Crooks, and Y. Dombrowski, "Oligodendrocytes in development, myelin generation and beyond," *Cell*, vol. 8, no. 11, p. 1424, 2019.
- [38] D. Rufino-Ramos, P. R. Albuquerque, V. Carmona, R. Perfeito, R. J. Nobre, and L. Pereira de Almeida, "Extracellular vesicles: novel promising delivery systems for therapy of brain diseases," *Journal of Controlled Release*, vol. 262, pp. 247–258, 2017.
- [39] J. Niu, H. H. Tsai, K. K. Hoi et al., "Aberrant oligodendroglial-vascular interactions disrupt the blood-brain barrier, triggering CNS inflammation," *Nature Neuroscience*, vol. 22, no. 5, pp. 709–718, 2019.
- [40] G. Hamanaka, R. Ohtomo, H. Takase, J. Lok, and K. Arai, "Role of oligodendrocyte-neurovascular unit in white matter repair," *Neuroscience Letters*, vol. 684, pp. 175–180, 2018.
- [41] F. Erdo, L. Denes, and E. de Lange, "Age-associated physiological and pathological changes at the blood-brain barrier: a review," *Journal of Cerebral Blood Flow and Metabolism*, vol. 37, no. 1, pp. 4–24, 2017.
- [42] G. A. Rosenberg, "Neurological diseases in relation to the blood-brain barrier," *Journal of Cerebral Blood Flow and Metabolism*, vol. 32, no. 7, pp. 1139–1151, 2012.
- [43] G. Barisano, A. Montagne, K. Kisler, J. A. Schneider, J. M. Wardlaw, and B. V. Zlokovic, "Blood-brain barrier link to human cognitive impairment and Alzheimer's disease," *Nature Cardiovascular Research*, vol. 1, no. 2, pp. 108–115, 2022.
- [44] C. S. B. Singh, K. B. Choi, L. Munro, H. Y. Wang, C. G. Pfeifer, and W. A. Jefferies, "Reversing pathology in a preclinical model of Alzheimer's disease by hacking cerebrovascular neoangiogenesis with advanced cancer therapeutics," *eBioMedicine*, vol. 71, p. 103503, 2021.
- [45] W. Poewe, K. Seppi, C. M. Tanner et al., "Parkinson disease," *Nature Reviews. Disease Primers*, vol. 3, no. 1, p. 17013, 2017.
- [46] Z. Ruan, D. Zhang, R. Huang et al., "Microglial activation damages dopaminergic neurons through MMP-2/-9-mediated increase of blood-brain barrier permeability in a Parkinson's disease mouse model," *International Journal of Molecular Sciences*, vol. 23, no. 5, p. 2793, 2022.
- [47] G. Lan, P. Wang, R. B. Chan et al., "Astrocytic VEGFA: an essential mediator in blood-brain-barrier disruption in Parkinson's disease," *Glia*, vol. 70, no. 2, pp. 337–353, 2022.
- [48] R. Kortekaas, K. L. Leenders, J. C. H. van Oostrom et al., "Blood-brain barrier dysfunction in parkinsonian midbrain in vivo," *Annals of Neurology*, vol. 57, no. 2, pp. 176–179, 2005.
- [49] I. Rite, A. Machado, J. Cano, and J. L. Venero, "Blood-brain barrier disruption induces in vivo degeneration of nigral dopaminergic neurons," *Journal of Neurochemistry*, vol. 101, no. 6, pp. 1567–1582, 2007.
- [50] E. Candelario-Jalil, R. M. Dijkhuizen, and T. Magnus, "Neuroinflammation, stroke, blood-brain barrier dysfunction, and imaging modalities," *Stroke*, vol. 53, no. 5, pp. 1473–1486, 2022.
- [51] J. A. Mohawk, C. B. Green, and J. S. Takahashi, "Central and peripheral circadian clocks in mammals," *Annual Review of Neuroscience*, vol. 35, no. 1, pp. 445–462, 2012.
- [52] E. G. Knox, M. R. Aburto, G. Clarke, J. F. Cryan, and C. M. O'Driscoll, "The blood-brain barrier in aging and neurodegeneration," *Molecular Psychiatry*, vol. 27, no. 6, pp. 2659–2673, 2022.
- [53] W. Cai, K. Zhang, P. Li et al., "Dysfunction of the neurovascular unit in ischemic stroke and neurodegenerative diseases: an aging effect," *Ageing Research Reviews*, vol. 34, pp. 77–87, 2017.
- [54] X. Jin, J. Liu, Y. Yang, K. J. Liu, Y. Yang, and W. Liu, "Spatio-temporal evolution of blood brain barrier damage and tissue infarction within the first 3 h after ischemia onset," *Neurobiology of Disease*, vol. 48, no. 3, pp. 309–316, 2012.
- [55] W. Liu, J. Hendren, X. J. Qin, and K. J. Liu, "Normobaric hyperoxia reduces the neurovascular complications associated with delayed tissue plasminogen activator treatment in a rat model of focal cerebral ischemia," *Stroke*, vol. 40, no. 7, pp. 2526–2531, 2009.
- [56] J. Liu, X. Jin, K. J. Liu, and W. Liu, "Matrix metalloproteinase-2-mediated occludin degradation and caveolin-1-mediated claudin-5 redistribution contribute to blood-brain barrier damage in early ischemic stroke stage," *The Journal of Neuroscience*, vol. 32, no. 9, pp. 3044–3057, 2012.
- [57] W. Liu, R. Sood, Q. Chen et al., "Normobaric hyperoxia inhibits NADPH oxidase-mediated matrix metalloproteinase-9 induction in cerebral microvessels in experimental stroke," *Journal of Neurochemistry*, vol. 107, no. 5, pp. 1196–1205, 2008.
- [58] Y. N. Li, R. Pan, X. J. Qin et al., "Ischemic neurons activate astrocytes to disrupt endothelial barrier via increasing VEGF expression," *Journal of Neurochemistry*, vol. 129, no. 1, pp. 120–129, 2014.
- [59] J. Liu, J. Weaver, X. Jin et al., "Nitric oxide interacts with caveolin-1 to facilitate autophagy-lysosome-mediated claudin-5 degradation in oxygen-glucose deprivation-treated endothelial cells," *Molecular Neurobiology*, vol. 53, no. 9, pp. 5935–5947, 2016.
- [60] Y. Zhang, K. Yang, T. Wang, W. Li, X. Jin, and W. Liu, "Nrdp1 increases ischemia induced primary rat cerebral cortical neurons and pheochromocytoma cells apoptosis via downregulation of HIF-1 $\alpha$  protein," *Frontiers in Cellular Neuroscience*, vol. 11, p. 293, 2017.

- [61] X. Wang, F. C. Barone, N. V. Aiyar, and G. Z. Feuerstein, "Interleukin-1 receptor and receptor antagonist gene expression after focal stroke in rats," *Stroke*, vol. 28, no. 1, pp. 155–162, 1997, discussion 161-2.
- [62] M. Gelderblom, F. Leyppoldt, K. Steinbach et al., "Temporal and spatial dynamics of cerebral immune cell accumulation in stroke," *Stroke*, vol. 40, no. 5, pp. 1849–1857, 2009.
- [63] G. C. Jickling, D. Z. Liu, B. P. Ander, B. Stamova, X. Zhan, and F. R. Sharp, "Targeting neutrophils in ischemic stroke: translational insights from experimental studies," *Journal of Cerebral Blood Flow and Metabolism*, vol. 35, no. 6, pp. 888–901, 2015.
- [64] M. A. Petty and E. H. Lo, "Junctional complexes of the blood-brain barrier: permeability changes in neuroinflammation," *Progress in Neurobiology*, vol. 68, no. 5, pp. 311–323, 2002.
- [65] E. Y. Choi, S. Santoso, and T. Chavakis, "Mechanisms of neutrophil transendothelial migration," *Frontiers in bioscience: a journal and virtual library*, vol. 14, no. 5, pp. 1596–1605, 2009.
- [66] P. Welsh, G. D. O. Lowe, J. Chalmers et al., "Associations of proinflammatory cytokines with the risk of recurrent stroke," *Stroke*, vol. 39, no. 8, pp. 2226–2230, 2008.
- [67] Y. Xing, Z. N. Guo, S. Yan, H. Jin, S. Wang, and Y. Yang, "Increased globulin and its association with hemorrhagic transformation in patients receiving intra-arterial thrombolysis therapy," *Neuroscience Bulletin*, vol. 30, no. 3, pp. 469–476, 2014.
- [68] Y. Murata, A. Rosell, R. H. Scannevin, K. J. Rhodes, X. Wang, and E. H. Lo, "Extension of the thrombolytic time window with minocycline in experimental stroke," *Stroke*, vol. 39, no. 12, pp. 3372–3377, 2008.
- [69] R. Dringen, "Metabolism and functions of glutathione in brain," *Progress in Neurobiology*, vol. 62, no. 6, pp. 649–671, 2000.
- [70] D. S. Warner, H. Sheng, and I. Batinić-Haberle, "Oxidants, antioxidants and the ischemic brain," *The Journal of Experimental Biology*, vol. 207, no. 18, pp. 3221–3231, 2004.
- [71] M. H. Selim and R. R. Ratan, "The role of iron neurotoxicity in ischemic stroke," *Ageing Research Reviews*, vol. 3, no. 3, pp. 345–353, 2004.
- [72] Z. Q. Chen, R. T. Mou, D. X. Feng, Z. Wang, and G. Chen, "The role of nitric oxide in stroke," *Medical Gas Research*, vol. 7, no. 3, pp. 194–203, 2017.
- [73] C. L. Allen and U. Bayraktutan, "Oxidative stress and its role in the pathogenesis of ischaemic stroke," *International Journal of Stroke*, vol. 4, no. 6, pp. 461–470, 2009.
- [74] D. B. Zorov, M. Juhaszova, and S. J. Sollott, "Mitochondrial reactive oxygen species (ROS) and ROS-induced ROS release," *Physiological Reviews*, vol. 94, no. 3, pp. 909–950, 2014.
- [75] B. Halliwell and J. M. Gutteridge, "Biologically relevant metal ion-dependent hydroxyl radical generation: An update," *FEBS letters*, vol. 307, no. 1, pp. 108–112, 1992.
- [76] D. Hu, F. Serrano, T. D. Oury, and E. Klann, "Aging-dependent alterations in synaptic plasticity and memory in mice that overexpress extracellular superoxide dismutase," *The Journal of Neuroscience*, vol. 26, no. 15, pp. 3933–3941, 2006.
- [77] A. Y. Abramov, A. Scorziello, and M. R. Duchon, "Three distinct mechanisms generate oxygen free radicals in neurons and contribute to cell death during anoxia and reoxygenation," *The Journal of Neuroscience*, vol. 27, no. 5, pp. 1129–1138, 2007.
- [78] J. F. Turrens, "Mitochondrial formation of reactive oxygen species," *The Journal of Physiology*, vol. 552, no. 2, Part 2, pp. 335–344, 2003.
- [79] J. J. Lochhead, G. McCaffrey, C. E. Quigley et al., "Oxidative stress increases blood-brain barrier permeability and induces alterations in occludin during hypoxia-reoxygenation," *Journal of Cerebral Blood Flow and Metabolism*, vol. 30, no. 9, pp. 1625–1636, 2010.
- [80] G. Schreiberl, G. Kooij, A. Reijerkerk et al., "Reactive oxygen species alter brain endothelial tight junction dynamics via RhoA, PI3 kinase, and PKB signaling," *The FASEB Journal*, vol. 21, no. 13, pp. 3666–3676, 2007.
- [81] G. W. Kim, A. Lewén, J. C. Copin, B. D. Watson, and P. H. Chan, "The cytosolic antioxidant, copper/zinc superoxide dismutase, attenuates blood-brain barrier disruption and oxidative cellular injury after photothrombotic cortical ischemia in mice," *Neuroscience*, vol. 105, no. 4, pp. 1007–1018, 2001.
- [82] X. Y. Shen, Z. K. Gao, Y. Han, M. Yuan, Y. S. Guo, and X. Bi, "Activation and role of astrocytes in ischemic stroke," *Frontiers in Cellular Neuroscience*, vol. 15, p. 755955, 2021.
- [83] E. K. Shih and M. B. Robinson, "Role of astrocytic mitochondria in limiting ischemic brain injury?," *Physiology*, vol. 33, no. 2, pp. 99–112, 2018.
- [84] Z. Nayernia, V. Jaquet, and K. H. Krause, "New insights on NOX enzymes in the central nervous system," *Antioxidants & Redox Signaling*, vol. 20, no. 17, pp. 2815–2837, 2014.
- [85] M. W. Park, H. W. Cha, J. Kim et al., "NOX4 promotes ferroptosis of astrocytes by oxidative stress-induced lipid peroxidation via the impairment of mitochondrial metabolism in Alzheimer's diseases," *Redox Biology*, vol. 41, p. 101947, 2021.
- [86] M. Moriyama, S. Fujitsuka, K. Kawabe, K. Takano, and Y. Nakamura, "Zinc potentiates lipopolysaccharide-induced nitric oxide production in cultured primary rat astrocytes," *Neurochemical Research*, vol. 43, no. 2, pp. 363–374, 2018.
- [87] X. Chen, T. Guan, C. Li et al., "SOD1 aggregation in astrocytes following ischemia/reperfusion injury: a role of NO-mediated S-nitrosylation of protein disulfide isomerase (PDI)," *Journal of Neuroinflammation*, vol. 9, no. 1, p. 237, 2012.
- [88] T. Mizui, H. Kinouchi, and P. H. Chan, "Depletion of brain glutathione by buthionine sulfoximine enhances cerebral ischemic injury in rats," *The American Journal of Physiology*, vol. 262, no. 2, pp. H313–H317, 1992.
- [89] R. Dringen, M. Brandmann, M. C. Hohnholt, and E. M. Blumrich, "Glutathione-dependent detoxification processes in astrocytes," *Neurochemical Research*, vol. 40, no. 12, pp. 2570–2582, 2015.
- [90] S. Griffin, J. B. Clark, and L. Canevari, "Astrocyte-neurone communication following oxygen-glucose deprivation," *Journal of Neurochemistry*, vol. 95, no. 4, pp. 1015–1022, 2005.
- [91] Y. Chen, N. E. Vartiainen, W. Ying, P. H. Chan, J. Koistinaho, and R. A. Swanson, "Astrocytes protect neurons from nitric oxide toxicity by a glutathione-dependent mechanism," *Journal of Neurochemistry*, vol. 77, no. 6, pp. 1601–1610, 2001.
- [92] Q. Pan, C. He, H. Liu et al., "Microvascular endothelial cells-derived microvesicles imply in ischemic stroke by modulating astrocyte and blood brain barrier function and cerebral blood flow," *Molecular Brain*, vol. 9, no. 1, p. 63, 2016.

- [93] Y. Shen, J. Gu, Z. Liu et al., "Inhibition of HIF-1 $\alpha$  reduced blood brain barrier damage by regulating MMP-2 and VEGF during acute cerebral ischemia," *Frontiers in Cellular Neuroscience*, vol. 12, p. 288, 2018.
- [94] S. Zhang, Q. An, T. Wang, S. Gao, and G. Zhou, "Autophagy and MMP-2/9-mediated reduction and redistribution of ZO-1 contribute to hyperglycemia-increased blood-brain barrier permeability during early reperfusion in stroke," *Neuroscience*, vol. 377, pp. 126–137, 2018.
- [95] C. D. Sharp, I. Hines, J. Houghton et al., "Glutamate causes a loss in human cerebral endothelial barrier integrity through activation of NMDA receptor," *American Journal of Physiology. Heart and Circulatory Physiology*, vol. 285, no. 6, pp. H2592–H2598, 2003.
- [96] L. Lu, A. D. Hogan-Cann, A. K. Globa et al., "Astrocytes drive cortical vasodilatory signaling by activating endothelial NMDA receptors," *Journal of Cerebral Blood Flow and Metabolism*, vol. 39, no. 3, pp. 481–496, 2019.
- [97] Y. Gu, G. Zheng, M. Xu et al., "Caveolin-1 regulates nitric oxide-mediated matrix metalloproteinases activity and blood-brain barrier permeability in focal cerebral ischemia and reperfusion injury," *Journal of Neurochemistry*, vol. 120, no. 1, pp. 147–156, 2012.
- [98] Z. Jiang, C. Li, D. M. Arrick, S. Yang, A. E. Baluna, and H. Sun, "Role of nitric oxide synthases in early blood-brain barrier disruption following transient focal cerebral ischemia," *PLoS One*, vol. 9, no. 3, article e93134, 2014.
- [99] A. C. Lo, A. Y. S. Chen, V. K. L. Hung et al., "Endothelin-1 overexpression leads to further water accumulation and brain edema after middle cerebral artery occlusion via aquaporin 4 expression in astrocytic end-feet," *Journal of Cerebral Blood Flow and Metabolism*, vol. 25, no. 8, pp. 998–1011, 2005.
- [100] V. K. Hung, P. K. K. Yeung, A. K. W. Lai et al., "Selective astrocytic endothelin-1 overexpression contributes to dementia associated with ischemic stroke by exaggerating astrocyte-derived amyloid secretion," *Journal of Cerebral Blood Flow and Metabolism*, vol. 35, no. 10, pp. 1687–1696, 2015.
- [101] H. Yu, P. Wang, P. An, and X. Yixue, "Recombinant human angiopoietin-1 ameliorates the expressions of ZO-1, occludin, VE-cadherin, and PKC $\alpha$  signaling after focal cerebral ischemia/reperfusion in rats," *Journal of Molecular Neuroscience*, vol. 46, no. 1, pp. 236–247, 2012.
- [102] S. A. Hill, M. Fu, and A. D. R. Garcia, "Sonic Hedgehog signaling in astrocytes," *Cellular and Molecular Life Sciences*, vol. 78, no. 4, pp. 1393–1403, 2021.
- [103] S. Bake, A. Okoreeh, H. Khosravian, and F. Sohrabji, "Insulin-like growth factor (IGF)-1 treatment stabilizes the microvascular cytoskeleton under ischemic conditions," *Experimental Neurology*, vol. 311, pp. 162–172, 2019.
- [104] J. Pitt, K. C. Wilcox, V. Tortelli et al., "Neuroprotective astrocyte-derived insulin/insulin-like growth factor 1 stimulates endocytic processing and extracellular release of neuron-bound A $\beta$  oligomers," *Molecular Biology of the Cell*, vol. 28, no. 20, pp. 2623–2636, 2017.
- [105] C. Qin, L. Q. Zhou, X. T. Ma et al., "Dual functions of microglia in ischemic stroke," *Neuroscience Bulletin*, vol. 35, no. 5, pp. 921–933, 2019.
- [106] O. Garaschuk and A. Verkhratsky, "Physiology of microglia," *Methods in Molecular Biology*, vol. 2034, pp. 27–40, 2019.
- [107] A. C. da Fonseca, D. Matias, C. Garcia et al., "The impact of microglial activation on blood-brain barrier in brain diseases," *Frontiers in Cellular Neuroscience*, vol. 8, p. 362, 2014.
- [108] H. W. Morrison and J. A. Filosa, "A quantitative spatiotemporal analysis of microglia morphology during ischemic stroke and reperfusion," *Journal of Neuroinflammation*, vol. 10, p. 4, 2013.
- [109] J. Wang, H. Xing, L. Wan, X. Jiang, C. Wang, and Y. Wu, "Treatment targets for M2 microglia polarization in ischemic stroke," *Biomedicine & Pharmacotherapy*, vol. 105, pp. 518–525, 2018.
- [110] H. L. Meng, X. X. Li, Y. T. Chen et al., "Neuronal soluble Fas ligand drives M1-microglia polarization after cerebral ischemia," *CNS Neuroscience & Therapeutics*, vol. 22, no. 9, pp. 771–781, 2016.
- [111] J. D. Cherry, J. A. Olschowka, and M. K. O'Banion, "Neuroinflammation and M2 microglia: the good, the bad, and the inflamed," *Journal of Neuroinflammation*, vol. 11, no. 1, p. 98, 2014.
- [112] A. Roy, A. Jana, K. Yatish et al., "Reactive oxygen species up-regulate CD11b in microglia via nitric oxide: implications for neurodegenerative diseases," *Free Radical Biology & Medicine*, vol. 45, no. 5, pp. 686–699, 2008.
- [113] C. G. Zou, Y. S. Zhao, S. Y. Gao et al., "Homocysteine promotes proliferation and activation of microglia," *Neurobiology of Aging*, vol. 31, no. 12, pp. 2069–2079, 2010.
- [114] P. K. Mander, A. Jekabsone, and G. C. Brown, "Microglia proliferation is regulated by hydrogen peroxide from NADPH oxidase," *Journal of Immunology*, vol. 176, no. 2, pp. 1046–1052, 2006.
- [115] S. Pawate, Q. Shen, F. Fan, and N. R. Bhat, "Redox regulation of glial inflammatory response to lipopolysaccharide and interferon $\gamma$ ," *Journal of Neuroscience Research*, vol. 77, no. 4, pp. 540–551, 2004.
- [116] A. I. Rojo, N. G. Innamorato, A. M. Martin-Moreno, M. L. de Ceballos, M. Yamamoto, and A. Cuadrado, "Nrf 2 regulates microglial dynamics and neuroinflammation in experimental Parkinson's disease," *Glia*, vol. 58, no. 5, pp. 588–598, 2010.
- [117] V. Chhor, T. le Charpentier, S. Lebon et al., "Characterization of phenotype markers and neuronotoxic potential of polarised primary microglia *in vitro*," *Brain, Behavior, and Immunity*, vol. 32, pp. 70–85, 2013.
- [118] X. Hu, R. K. Leak, Y. Shi et al., "Microglial and macrophage polarization—new prospects for brain repair," *Nature Reviews. Neurology*, vol. 11, no. 1, pp. 56–64, 2015.
- [119] X. Jiang, H. Pu, X. Hu et al., "A post-stroke therapeutic regimen with Omega-3 polyunsaturated fatty acids that promotes white matter integrity and beneficial microglial responses after cerebral ischemia," *Translational Stroke Research*, vol. 7, no. 6, pp. 548–561, 2016.
- [120] X. Y. Xiong, L. Liu, and Q. W. Yang, "Functions and mechanisms of microglia/macrophages in neuroinflammation and neurogenesis after stroke," *Progress in Neurobiology*, vol. 142, pp. 23–44, 2016.
- [121] W. Pan and A. J. Kastin, "Tumor necrosis factor and stroke: role of the blood-brain barrier," *Progress in Neurobiology*, vol. 83, no. 6, pp. 363–374, 2007.
- [122] J. Matsumoto, S. Dohgu, F. Takata et al., "Lipopolysaccharide-activated microglia lower P-glycoprotein function in brain microvascular endothelial cells," *Neuroscience Letters*, vol. 524, no. 1, pp. 45–48, 2012.



## *Retraction*

# **Retracted: Influence Factors and Predictive Models for the Outcome of Patients with Ischemic Stroke after Intravenous Thrombolysis: A Multicenter Retrospective Cohort Study**

### **Oxidative Medicine and Cellular Longevity**

Received 8 January 2024; Accepted 8 January 2024; Published 9 January 2024

Copyright © 2024 Oxidative Medicine and Cellular Longevity. This is an open access article distributed under the Creative Commons Attribution License, which permits unrestricted use, distribution, and reproduction in any medium, provided the original work is properly cited.

This article has been retracted by Hindawi following an investigation undertaken by the publisher [1]. This investigation has uncovered evidence of one or more of the following indicators of systematic manipulation of the publication process:

- (1) Discrepancies in scope
- (2) Discrepancies in the description of the research reported
- (3) Discrepancies between the availability of data and the research described
- (4) Inappropriate citations
- (5) Incoherent, meaningless and/or irrelevant content included in the article
- (6) Manipulated or compromised peer review

The presence of these indicators undermines our confidence in the integrity of the article's content and we cannot, therefore, vouch for its reliability. Please note that this notice is intended solely to alert readers that the content of this article is unreliable. We have not investigated whether authors were aware of or involved in the systematic manipulation of the publication process.

Wiley and Hindawi regrets that the usual quality checks did not identify these issues before publication and have since put additional measures in place to safeguard research integrity.

We wish to credit our own Research Integrity and Research Publishing teams and anonymous and named external researchers and research integrity experts for contributing to this investigation.

The corresponding author, as the representative of all authors, has been given the opportunity to register their agreement or disagreement to this retraction. We have kept a record of any response received.

### **References**

- [1] J. Hu, Z. Fang, X. Lu et al., "Influence Factors and Predictive Models for the Outcome of Patients with Ischemic Stroke after Intravenous Thrombolysis: A Multicenter Retrospective Cohort Study," *Oxidative Medicine and Cellular Longevity*, vol. 2022, Article ID 3363735, 18 pages, 2022.

## Research Article

# Influence Factors and Predictive Models for the Outcome of Patients with Ischemic Stroke after Intravenous Thrombolysis: A Multicenter Retrospective Cohort Study

Jin Hu <sup>1</sup>, Zhixian Fang <sup>2</sup>, Xia Lu <sup>1</sup>, Fei Wang <sup>3</sup>, Ningyuan Zhang <sup>4</sup>, Wenliang Pan <sup>5</sup>, Xinzheng Fu <sup>6</sup>, Gongchun Huang <sup>7</sup>, Xiaoli Tan <sup>2</sup> and Wenyu Chen <sup>2</sup>

<sup>1</sup>Department of Neurology, The Affiliated Hospital of Jiaxing University, Jiaxing, China

<sup>2</sup>Department of Respiration, The Affiliated Hospital of Jiaxing University, Jiaxing, China

<sup>3</sup>Department of Neurology, The First People's Hospital of Jiashan County, Jiaxing, China

<sup>4</sup>Department of Neurology, The First People's Hospital of Tongxiang, Jiaxing, China

<sup>5</sup>Department of Neurology, The People's Hospital of Haiyan, Jiaxing, China

<sup>6</sup>Department of Neurology, The People's Hospital of Haining, Jiaxing, China

<sup>7</sup>Department of Neurology, The First People's Hospital of Pinghu, Jiaxing, China

Correspondence should be addressed to Xiaoli Tan; 381848306@qq.com and Wenyu Chen; 00135116@zjxu.edu.cn

Jin Hu, Zhixian Fang, and Xia Lu contributed equally to this work.

Received 11 May 2022; Revised 24 June 2022; Accepted 28 July 2022; Published 17 August 2022

Academic Editor: Anwen Shao

Copyright © 2022 Jin Hu et al. This is an open access article distributed under the Creative Commons Attribution License, which permits unrestricted use, distribution, and reproduction in any medium, provided the original work is properly cited.

**Objective.** Intravenous thrombolysis (IVT) is currently the main effective treatment for patients with ischemic stroke. This study aimed to analyze the factors affecting the early neurological recovery and prognosis of thrombolytic therapy after surgery and to construct predictive models. **Materials and Methods.** A total of 849 patients with ischemic stroke who received IVT treatment at six centers from June 2017 to March 2021 were included. Patients were divided into the training cohort and the validation cohort. Based on the independent factors that influence the early recovery of neurological function and the prognosis, the respective predictive nomograms were established. The predictive accuracy and discrimination ability of the nomograms were evaluated by ROC and calibration curve, while the decision curve and clinical impact curve were adopted to evaluate the clinical applicability of the nomograms. **Results.** The nomogram constructed based on the factors affecting the prognosis in 3 months had ideal accuracy as the AUC (95% CI) was 0.901 (0.874~0.927) in the training cohort and 0.877 (0.826~0.929) in the validation cohort. The accuracy of the nomogram is required to be improved, since the AUC (95% CI) of the training cohort and the validation cohort was 0.641 (0.597~0.685) and 0.627 (0.559~0.696), respectively. **Conclusions.** Based on this ideal and practical prediction model, we can early identify and actively intervene in patients with ischemic stroke after IVT to improve their prognosis. Nevertheless, the accuracy of predicting nomograms for the recovery of early neurological function after IVT still needs improvement.

## 1. Introduction

The Global Burden of Diseases, Injuries, and Risk Factors (GBD) study estimates rank stroke as the second most common cause of death in the world [1, 2] and the third most common cause of disability-adjusted life years (DALYs) [3], with

75% of stroke deaths and 81% of disability-adjusted life years occur in low- and middle-income countries [4]. Stroke can be divided into ischemic stroke and hemorrhagic stroke. Ischemic stroke is caused by the sudden loss of function led by the interruption of blood supply to part of the brain, and hemorrhagic stroke is caused by angiorrhesis or abnormal

TABLE 1: The prognosis of included cases.

Group	All (N = 849)	Training cohort (N = 594)	Verification cohort (N = 255)
Age	70.07 ± 12.54	70.12 ± 12.45	69.95 ± 12.77
Poor early neurological function recovery	452 (53.2%)	320 (53.9%)	132 (51.8%)
Poor prognosis at 3 months	294 (34.6%)	209 (35.2%)	85 (33.3%)

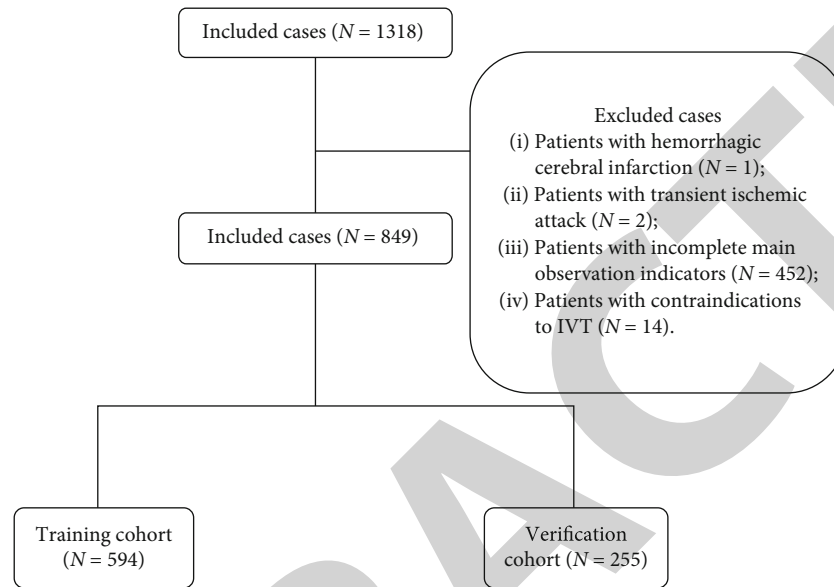


FIGURE 1: The cases selecting process.

blood vessel structure [5]. In general, ischemic stroke accounts for about 80% of stroke cases, and hemorrhagic stroke accounts for about 20%, but the actual proportion of stroke types depends on different patients [6]. According to data from the Chinese Hospital Quality Monitoring System, in 2018, China's 1853 tertiary A hospitals admitted a total of 3,010,204 stroke inpatients, of which 2,466,785 were ischemic stroke patients, accounting for 81.9% [7]. On a global scale, the burden of stroke has increased significantly in the past few decades due to the increase in population size and aging population and the prevalence of changeable risk factors for stroke [8, 9]. Studies have shown that at the beginning of the twenty-first century, about 1.1 million Europeans suffer from stroke each year, and it is predicted that by 2025, 1.5 million Europeans will suffer from stroke each year, and the incidence of young people will gradually increase [10].

Acute reperfusion therapy is by far the most effective method for the treatment of patients with acute ischemic stroke [11]. However, after thrombolytic therapy, the early neurological function of a large number of patients has not been effectively improved. Some patients have poor prognosis after 90 days of treatment. The situation is not optimistic. This part of patients tends to bring an increasingly huge burden to the family and society [12]. This study aims to analyze the factors affecting the early neurological function of patients with acute ischemic stroke (intravenous thrombolysis, IVT) and the prognosis at 3 months after surgery and to establish a predictive model to improve the safety and effectiveness of thrombolytic therapy.

## 2. Materials and Methods

We included ischemic stroke patients undergoing IVT treatment from six centers (the First People's Hospital of Pinghu, the First Hospital of Jiaxing, the First People's Hospital of Jiashan, the First People's Hospital of Tongxiang, the People's Hospital of Haiyan, and the People's Hospital of Haining from June 2017 to March 2021). According to the inclusion and exclusion criteria, the cases that fit this study were selected.

The inclusion criteria are as follows: (1) 18 years old or older; (2) patients treated with alteplase thrombolysis and whose symptom onset time (referring to the time from symptom onset to thrombolytic treatment)  $\leq 4.5$  hours, while patients treated with urokinase and whose symptom onset time  $\leq 6$  hours; (3) cerebral infarction is diagnosed, and there is a certain neurological deficit; and (4) the patient or his family members agree to sign an informed consent.

The exclusion criteria are as follows: (1) patients with hemorrhagic cerebral infarction; (2) patients with transient ischemic attack; (3) patients with cerebral venous sinus thrombosis; (4) patients with brain tumors; (5) patients whose main observation indicators are incomplete due to various reasons; and (6) patients with contraindications to IVT (such as intracranial hemorrhage, history of intracranial hemorrhage, intracranial tumor, giant intracranial aneurysm, active visceral hemorrhage, platelets less than  $100 \times 10^9/L$ , oral anticoagulant and  $INR > 1.7$  or  $PT > 15$  seconds, and intracranial or intraspinal surgery within 3 months before IVT).

TABLE 2: The univariate analysis of prognosis of patients with ischemic stroke at 3 months after IVT.

No.	Factors	All (N = 594)	Group 1 (N = 209)	Group 0 (N = 385)	$t/z/\chi^2$	P
1	Gender (male)	337 (56.7%)	101 (48.3%)	236 (61.3%)	9.288	0.003
2	Ages (year)	70.12 ± 12.45	76.31 ± 11.06	66.76 ± 11.88	9.585	<0.001
3	BMI (kg/m <sup>2</sup> )	22.73 ± 3.52	21.96 ± 3.53	23.15 ± 3.44	-3.977	<0.001
4	BNIHSS (score)	5 (2.75, 12.00)	12 (7, 19)	3 (2, 7)	-12.688	<0.001
5	Smoking (yes)	173 (29.1%)	47 (22.5%)	126 (32.7%)	6.880	0.009
6	SecondThrombolysis (yes)	13 (2.2%)	5 (2.4%)	9 (2.1%)	0.630	0.820
7	Hypertension (yes)	409 (68.9%)	156 (74.6%)	253 (65.7%)	5.034	0.025
8	preAF (yes)	95 (16.0%)	55 (26.3%)	40 (10.4%)	25.574	<0.001
9	preIHD (yes)	36 (6.1%)	17 (8.1%)	19 (4.9%)	2.435	0.119
10	NewAF (yes)	28 (4.7%)	15 (7.2%)	13 (3.4%)	4.356	0.037
11	DM (yes)	89 (15.0%)	39 (18.7%)	50 (13.0%)	3.423	0.064
12	HL (yes)	18 (3.0%)	6 (2.9%)	12 (3.1%)	0.028	0.867
13	CHD (yes)	47 (7.9%)	20 (9.6%)	27 (7.0%)	1.215	0.270
14	CHF (yes)	17 (2.9%)	10 (4.8%)	7 (1.8%)	4.288	0.038
15	PreStrokeHistory (yes)	87 (14.6%)	42 (20.1%)	45 (11.7%)	7.659	0.006
16	CHDHistory (yes)	3 (0.5%)	1 (0.5%)	2 (0.5%)	0.005	0.946
17	HHcy (yes)	33 (5.6%)	14 (6.7%)	19 (4.9%)	0.803	0.370
18	Aspirin (yes)	77 (13.0%)	31 (14.8%)	46 (11.9%)	0.999	0.318
19	Clopidogrel (yes)	17 (2.9%)	10 (4.8%)	7 (1.8%)	4.288	0.038
20	Warfarin (yes)	8 (1.3%)	5 (2.4%)	3 (0.8%)	2.653	0.103
21	Atorvastatin (yes)	27 (4.5%)	9 (4.3%)	18 (4.7%)	0.043	0.837
22	Rosuvastatin (yes)	25 (4.2%)	14 (6.7%)	11 (2.9%)	4.958	0.026
23	PreSBP (mmHg)	154.81 ± 20.18	157.09 ± 19.58	153.57 ± 20.42	2.034	0.029
24	PreDBP (mmHg)	84.9 ± 12.72	84.14 ± 12.96	85.31 ± 12.59	-1.073	0.513
25	Hb (g/L)	139.41 ± 17.03	135.23 ± 18.96	141.68 ± 15.45	-4.214	<0.001
26	RBC (∗10 <sup>12</sup> /L)	4.58 (4.26, 4.93)	4.46 (4.03, 4.84)	4.66 (4.35, 5.00)	-4.745	<0.001
27	WBC (∗10 <sup>9</sup> /L)	7.65 ± 3.41	7.79 ± 2.99	7.57 ± 3.63	0.779	0.436
28	N (%)	63.01 ± 12.44	64.61 ± 13.2	62.14 ± 11.94	2.254	0.025
29	PLT (∗10 <sup>9</sup> /L)	186.53 ± 58.31	181.31 ± 55.71	189.37 ± 59.55	-1.610	0.108
30	K+ (mmol/L)	3.76 ± 0.48	3.77 ± 0.5	3.75 ± 0.46	0.353	0.725
31	Na+ (mmol/L)	141.17 ± 4.3	141.11 ± 4.64	141.2 ± 4.11	-0.240	0.811
32	UN (mmol/L)	6.03 (4.90, 7.20)	6.30 (5.00, 7.70)	5.90 (4.90, 6.99)	-2.473	0.013
33	Cr (μmol/L)	77.1 ± 26.35	79.64 ± 32.42	75.72 ± 22.3	1.556	0.121
34	PT (s)	11.43 ± 1.06	11.55 ± 1.17	11.37 ± 1.00	1.955	0.051
35	APTT (s)	30.22 ± 4.96	29.51 ± 4.92	30.61 ± 4.94	-2.609	0.009
36	INR	1 ± 0.09	1.01 ± 0.09	0.99 ± 0.09	2.498	0.013
37	Fg (g/L)	3.38 (2.69,4.03)	3.50 (2.77,4.22)	3.29 (2.65,3.88)	-2.754	0.006
38	Time (min)	154.7 ± 60.1	161.58 ± 61.75	150.97 ± 58.92	2.061	0.040
39	Drug (u-PA)	49 (8.2%)	25 (12.0%)	24 (6.2%)	5.872	0.015
40	24hNIHSS (score)	3 (1, 9)	11 (6, 22)	2 (1, 4)	15.251	<0.001

Note: Group 1 is poor neurological function recovery group, and group 0 is good neurological function recovery group.

2.1. Patient and Public Involvement. No patient was involved

2.2. Data Collection and Prognosis Classification. The data collected in this study were mainly patient baseline data and outcome indicators, including general information (gender,

age, BMI, NIHSS score at admission, and smoking), some past medical history (secondary thrombolysis, hypertension, previous atrial fibrillation and previous ischemic heart disease, etc.), previous medication history (aspirin, clopidogrel, warfarin, atorvastatin, and rosuvastatin), laboratory test results (systolic

TABLE 3: Logistic regression analysis on prognosis of patients with ischemic stroke at 3 months after IVT.

Factors	B	S.E.	Wald	P	OR	OR 95% CI	
						Low	Up
Ages (year)	0.048	0.011	18.792	0.001	1.050	1.027	1.073
DM (yes)	0.821	0.303	7.333	0.007	2.272	1.254	4.115
APTT (s)	-0.050	0.025	4.036	0.045	0.952	0.906	0.999
Drug (u-PA)	1.100	0.409	7.237	0.007	3.003	1.348	6.693
V24hNIHSS (score)	0.263	0.027	95.063	0.001	1.301	1.234	1.371
Constant	-5.603	1.113	25.328	0.001	0.004		

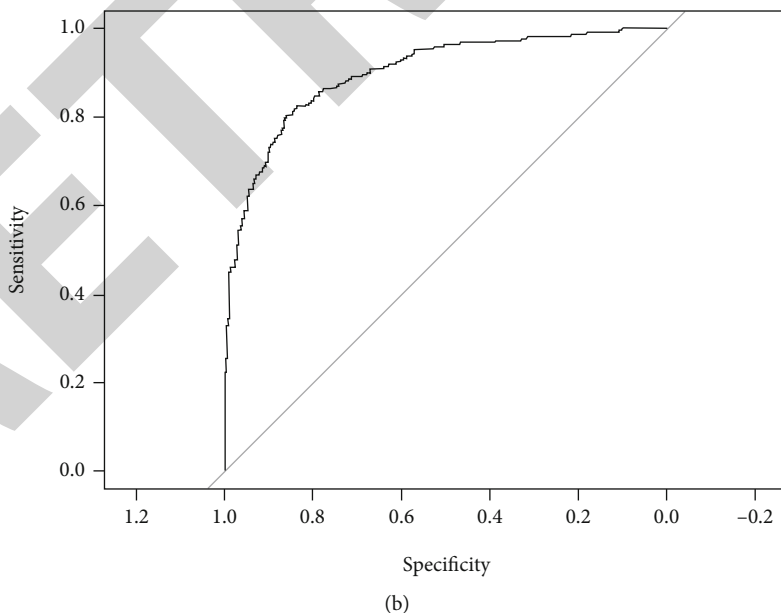
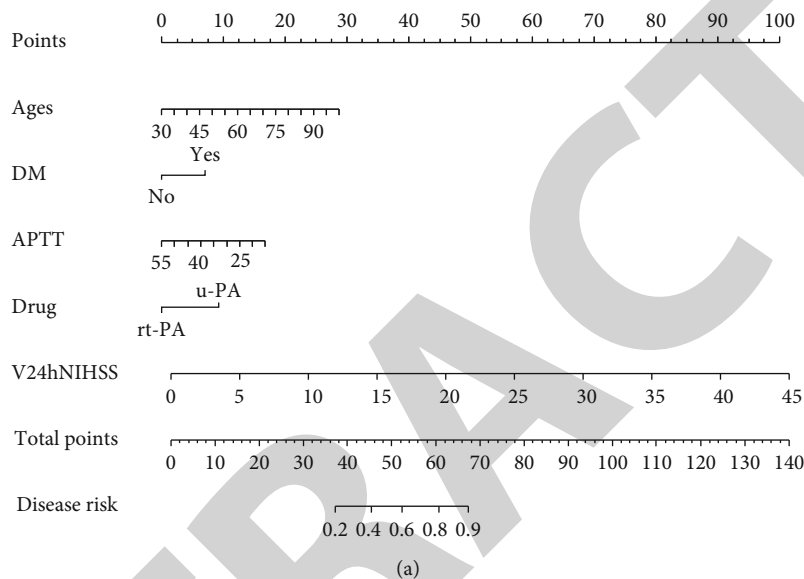


FIGURE 2: Continued.

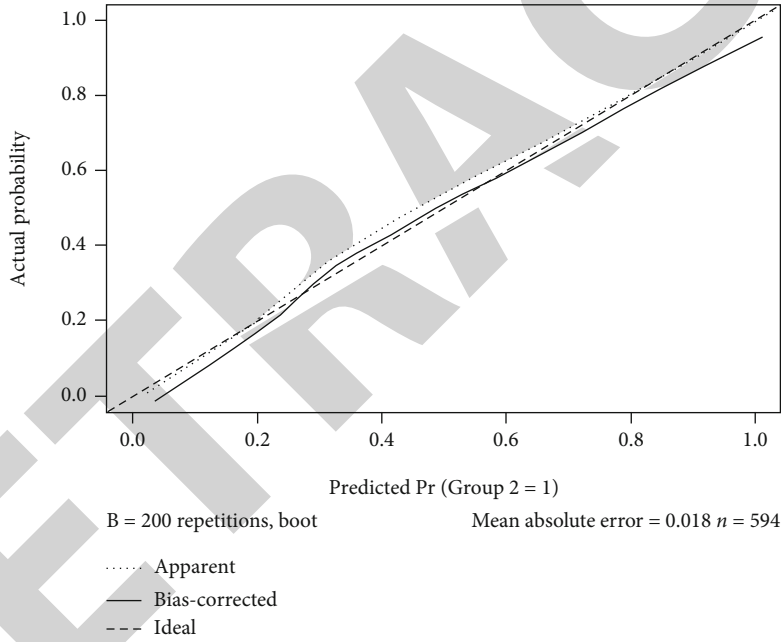
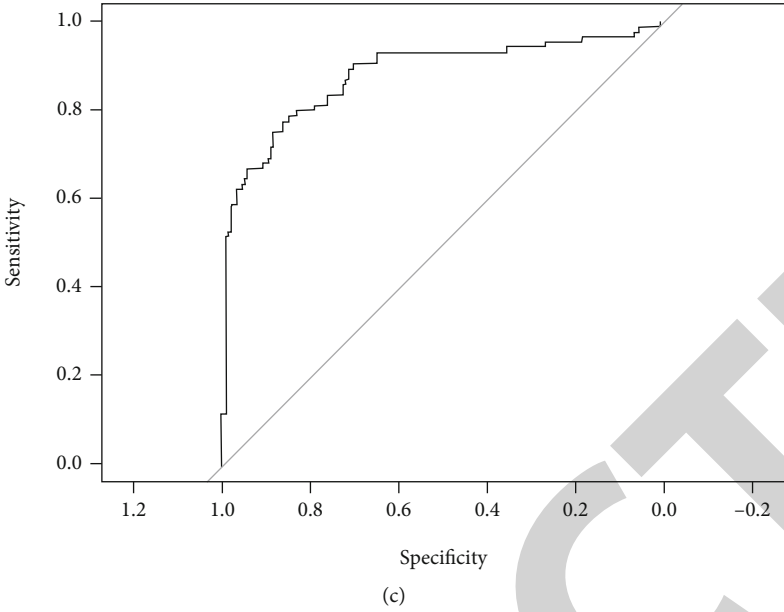


FIGURE 2: Continued.

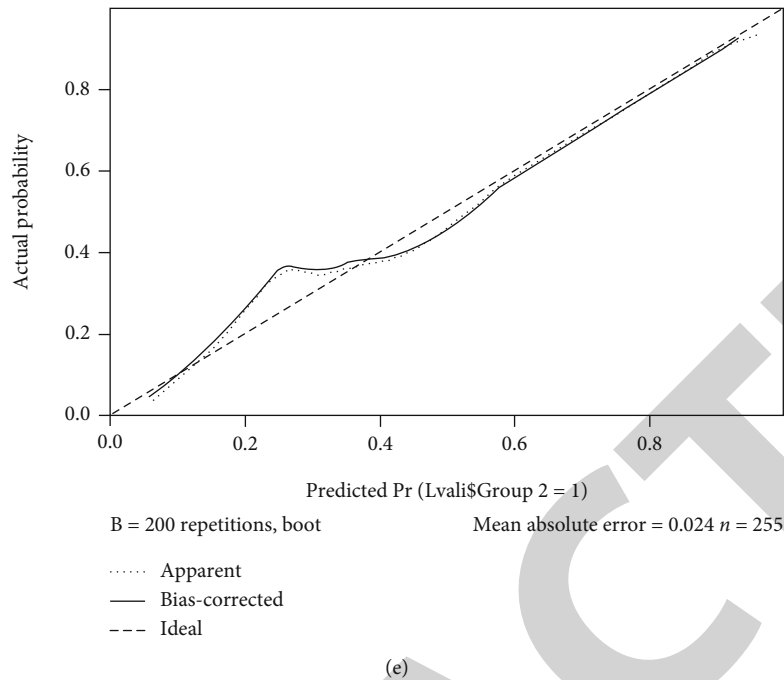


FIGURE 2: The predictive nomogram and ROC curve and calibration curve of nomogram predicting the prognosis at 3 months after IVT. (a) Predictive nomogram of prognosis at 3 months after IVT; (b) the ROC curve of nomogram predicting the prognosis at 3 months after IVT in training cohort; (c) the ROC curve of nomogram predicting the prognosis at 3 months after IVT in verification cohort; (d) the calibration curve of nomogram predicting the prognosis at 3 months after IVT in training cohort; (e) the calibration curve of nomogram predicting the prognosis at 3 months after IVT in verification cohort. Note: In the calibration curve, the abscissa represents the predicted probability for the poor prognosis, and the ordinate represents the actual probability for the poor prognosis. “Apparent” indicates the predicted probability of the risk model for the whole queue; “Bias-corrected” indicates the predicted probability corrected by bias-corrected approach Bootstrapping; “Ideal” indicates the ideal predicted probability. The better the coincidence of the three indicators is, the better the prediction performance of the nomogram is.

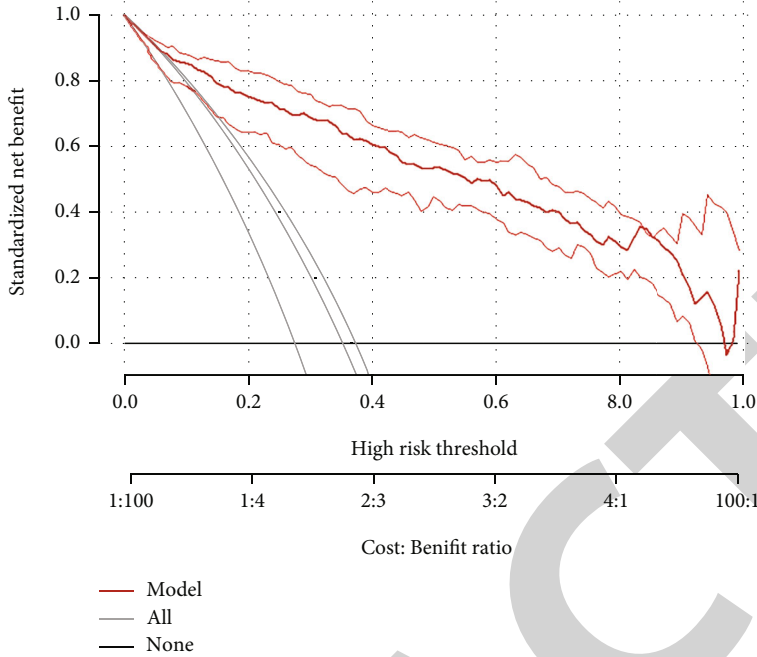
pressure before thrombolysis, diastolic pressure before thrombolysis, hemoglobin, red blood cell count, etc.), treatment information (thrombolysis time and thrombolytic medication), and outcome indicators (24-hour NIHSS score and mRS score at 3 months after surgery). This study discussed the early neurological function recovery after thrombolytic therapy and the prognosis at 3 months. Among them, the early recovery of neurological function was assessed by the National Institutes of Health Stroke Scale (NIHSS) [13], and the prognosis at 3 months after the operation was assessed by the modified Rankin scale. The specific groups are as follows:

- (1) Early neurological function recovery [14].  $\delta \geq 4$  or 24-hour NIHSS  $\leq 1$  was defined as the good early neurological function recovery group (group 0), and  $\delta < 4$  and 24-hour NIHSS  $> 1$  was the poor early neurological function recovery group (group 1). Besides,  $\delta =$  NIHSS at admission 24-hour NIHSS
- (2) Prognosis at 3 months after surgery [15]. The prognosis at 3 months after surgery was measured by mRS score at 3 months after surgery, and the specific definition is as follows: mRS score at 3 months after surgery  $\leq 2$  was defined as the good prognosis group (group 0), and mRS score  $> 2$  at 3 months after sur-

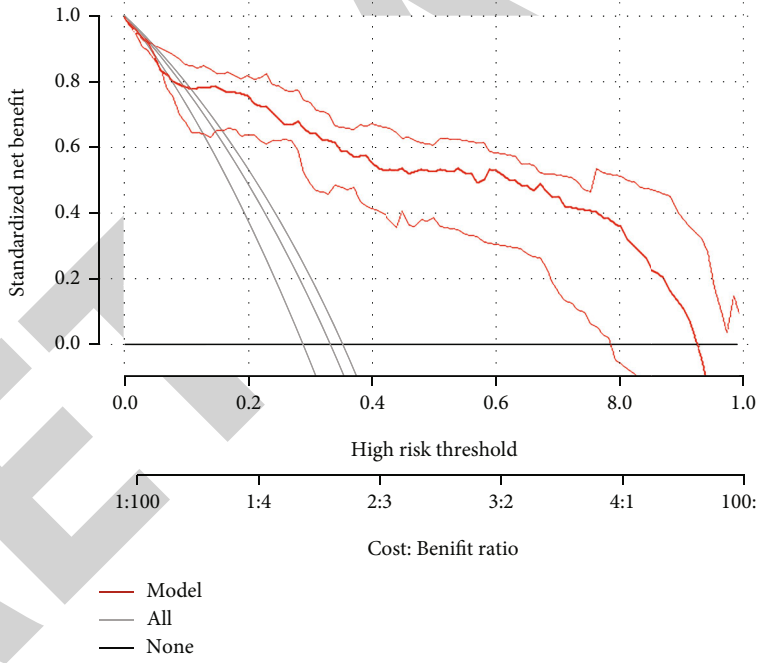
gery was considered as the short-term poor prognosis group (group 1).

**2.3. Model Construction and Verification.** The samples included in this study were divided into training cohorts and verification cohorts at a ratio of 7:3 by nonrepeated random sampling. Variables with  $P < 0.1$  based on the univariate analysis in the training cohort were used as predictors [16] and included them in the multivariate binary logistic regression. The entry method was Forward: LR. Then we analyzed the independent influencing factors that affected the early recovery of neurological function and the prognosis at 3 months after the surgery and established the predictive nomograms, respectively. In the training cohort and verification cohort, ROC curve and calibration curve were used to evaluate the predictive accuracy and discrimination ability of the nomogram, and the decision curve analysis (DCA) and clinical impact curve analysis (CICA) were used to evaluate the nomogram and the clinical applicability of [17, 18].

**2.4. Statistical Analysis.** SPSS 23 statistical software (IBM, Armonk, NY) was used to support univariate analysis and multivariate binary logistic. Continuous data is demonstrated as mean  $\pm$  standard deviation or median (lower quartile and upper quartile), and  $t$ -test or Mann-Whitney  $U$  test



(a)



(b)

FIGURE 3: Continued.



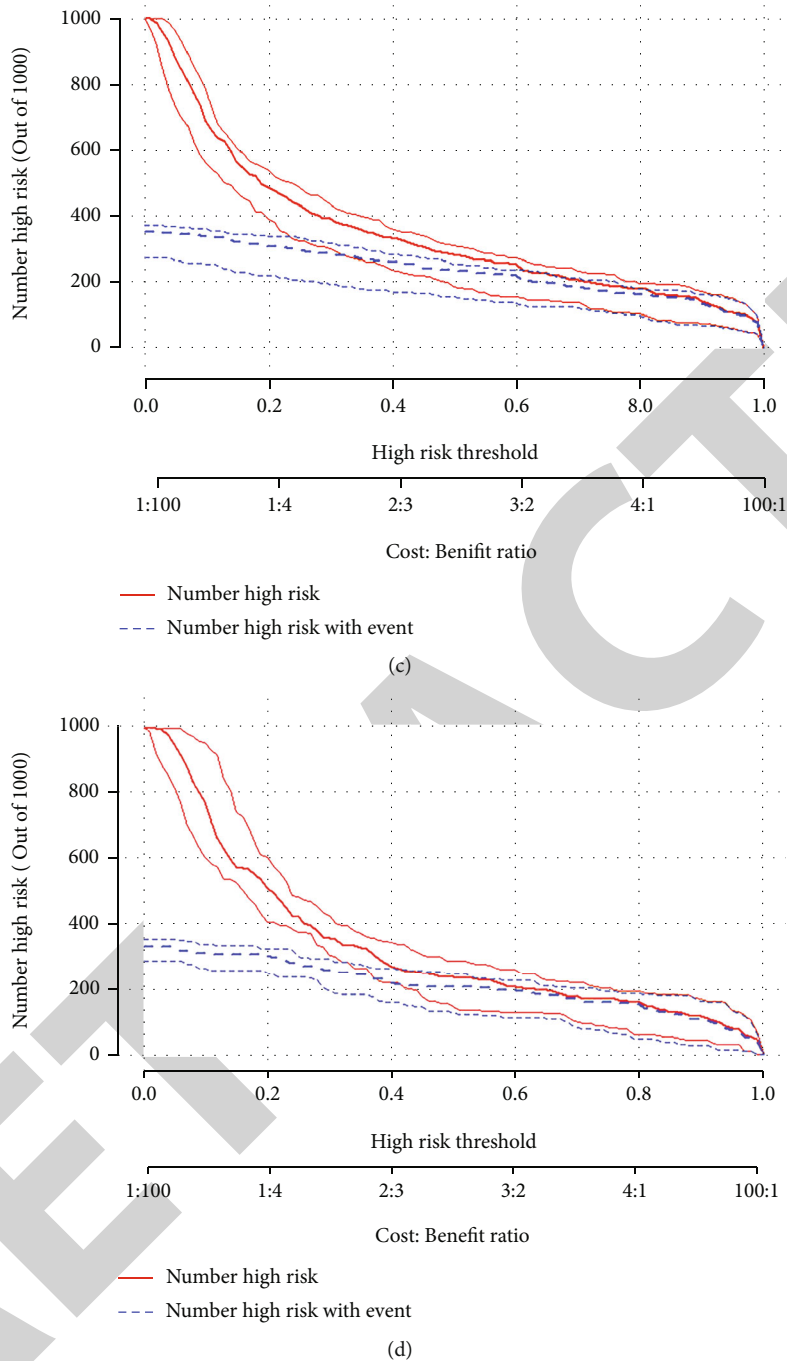


FIGURE 3: The decision curve and clinical impact curve analysis of nomogram predicting the prognosis at 3 months after IVT. (a) The decision curve of nomogram predicting the prognosis at 3 months after IVT in training cohort; (b) the decision curve of nomogram predicting the prognosis at 3 months after IVT cohort; (c) the nomogram predicting the CICA of the prognosis at 3 months after IVT in training cohort; (d) the nomogram predicting the CICA of the prognosis at 3 months after IVT in verification cohort. Note: (1) In the decision curve, the abscissa represents the high-risk threshold probability to predict poor prognosis, and the ordinate represents net benefit. “Model” refers to the net benefit brought by intervention through predicting high-risk patients with poor prognosis under different threshold probabilities according to the risk model; “All” and “None” represent two extreme cases. “All” refers to the net benefit brought by intervention when all patients were at high risk with poor prognosis. “None” refers to no intervention when all patients were at low risk, and under this condition, the net benefit was 0. DCA was used to analyze and compare two extreme cases, the net benefit of the risk model and the corresponding threshold probability. (2) As to the CICA, we assumed that 1000 patients were applied to our model under simulated examination conditions. “Number high risk” represents the number of high-risk patients with poor prognosis predicted by the model at different threshold probabilities. “Number high-risk event” represents the actual number of high-risk patients with poor prognosis.

TABLE 4: Univariate analysis of early neurological recovery after IVT of patients with ischemic stroke.

No.	Factors	All (N = 594)	Group 1 (N = 320)	Group 0 (N = 274)	t/z/ $\chi^2$	P
1	Gender (male)	337 (56.7%)	171 (53.4%)	166 (60.6%)	3.071	0.080
2	Ages (year)	70.12 ± 12.45	71.93 ± 12.35	68.01 ± 12.26	3.873	<0.001
3	BMI (kg/m <sup>2</sup> )	22.73 ± 3.52	22.38 ± 3.53	23.15 ± 3.46	-2.701	0.007
4	BNIHSS (score)	5 (2.75, 12.00)	6 (3, 13)	4 (2, 11)	-4.939	<0.001
5	Smoking (yes)	173 (29.1%)	94 (29.4%)	79 (28.8%)	0.021	0.885
6	SecondThrombolysis (yes)	13 (2.2%)	4 (1.3%)	9 (3.3%)	2.855	0.091
7	Hypertension (yes)	409 (68.9%)	232 (72.5%)	177 (64.6%)	4.297	0.038
8	preAF (yes)	95 (16.0%)	60 (18.8%)	35 (12.8%)	3.924	0.048
9	preIHD (yes)	36 (6.1%)	19 (5.9%)	17 (6.2%)	0.018	0.892
10	NewAF (yes)	28 (4.7%)	11 (3.4%)	17 (6.2%)	2.516	0.113
11	DM (yes)	89 (15.0%)	57 (17.8%)	32 (11.7%)	4.360	0.037
12	HL (yes)	18 (3.0%)	7 (2.2%)	11 (4.0%)	1.677	0.195
13	CHD (yes)	47 (7.9%)	28 (8.8%)	19 (6.9%)	0.668	0.414
14	CHF (yes)	17 (2.9%)	7 (2.2%)	10 (3.6%)	1.135	0.287
15	PreStrokeHistory (yes)	87 (14.6%)	50 (15.6%)	37 (13.5%)	0.531	0.466
16	CHDHistory (yes)	3 (0.5%)	1 (0.3%)	2 (0.7%)		0.598 *
17	HHcy (yes)	33 (5.6%)	21 (6.6%)	12 (4.4%)	1.341	0.247
18	Aspirin (yes)	77 (13.0%)	38 (11.9%)	39 (14.2%)	0.728	0.394
19	Clopidogrel (yes)	17 (2.9%)	11 (3.4%)	6 (2.2%)	0.827	0.363
20	Warfarin (yes)	8 (1.3%)	5 (1.6%)	3 (1.1%)		0.731 *
21	Atorvastatin (yes)	27 (4.5%)	18 (5.6%)	9 (3.3%)	1.863	0.172
22	Rosuvastatin (yes)	25 (4.2%)	12 (3.8%)	13 (4.7%)	0.362	0.547
23	PreSBP (mmHg)	154.81 ± 20.18	156.34 ± 19.16	153.02 ± 21.21	2.003	0.046
24	PreDBP (mmHg)	84.9 ± 12.72	84.91 ± 12.97	84.89 ± 12.44	0.015	0.988
25	Hb (g/L)	139.41 ± 17.03	138.51 ± 17.71	140.46 ± 16.17	-1.395	0.164
26	RBC ( $\diamond 10^{12}/L$ )	4.58 (4.26, 4.93)	4.54 (4.14, 4.89)	4.65 (4.35, 4.98)	-2.717	0.007
27	WBC ( $\diamond 10^9/L$ )	7.65 ± 3.41	7.86 ± 3.62	7.4 ± 3.14	1.629	0.104
28	N (%)	63.01 ± 12.44	64.16 ± 13.14	61.67 ± 11.45	2.462	0.014
29	PLT ( $\diamond 10^9/L$ )	186.53 ± 58.31	186.97 ± 59.26	186.02 ± 57.28	0.198	0.843
30	K+ (mmol/L)	3.76 ± 0.48	3.75 ± 0.48	3.76 ± 0.47	-0.339	0.735
31	Na+ (mmol/L)	141.17 ± 4.3	141 ± 4.15	141.36 ± 4.47	-0.999	0.318
32	UN (mmol/L)	6.03 (4.90, 7.20)	6.10 (4.93, 7.47)	6.00 (4.90, 7.00)	-0.924	0.355
33	Cr ( $\mu$ mol/L)	77.1 ± 26.35	78.42 ± 30.5	75.56 ± 20.42	1.358	0.175
34	PT (s)	11.43 ± 1.06	11.4 ± 1	11.48 ± 1.14	-0.953	0.341
35	APTT (s)	30.22 ± 4.96	29.82 ± 4.95	30.7 ± 4.93	-2.157	0.031
36	INR	1 ± 0.09	0.99 ± 0.09	1 ± 0.09	-0.948	0.343
37	Fg (g/L)	3.38 (2.69, 4.03)	3.46 (2.73, 4.11)	3.30 (2.68, 3.91)	-1.681	0.093
38	Time (min)	154.7 ± 60.1	160.47 ± 60.24	147.96 ± 59.33	2.541	0.011
39	Drug (u-PA)	49 (8.2%)	36 (11.3%)	13 (4.7%)	8.254	0.004

Note: (1) Group 1 is the poor early neurological function recovery group; group 0 is the good early neurological function recovery group; (2) \*P represents the P value calculated by Fisher's exact probability method.

was used for the comparison between the two groups; categorical data was demonstrated as  $n$  (%), and the chi-square test was used for comparison between groups. The construction of the nomogram and the drawing of ROC, decision curve, and clinical impact curve were completed in R4.0.4. Bilateral  $P < 0.05$  was considered statistically significant.

### 3. Results

**3.1. Patient Information.** We enrolled 1,318 stroke patients who received IVT treatment from six hospital centers from June 2017 to March 2021 and excluded patients with hemorrhagic stroke, transient cerebral ischemia, complemented main

TABLE 5: Multivariate logistic regression analysis of early neurological recovery after IVT in patients with ischemic stroke.

Factors	B	S.E.	Wald	P	OR	OR 95% CI	
						Low	Up
Ages (year)	0.022	0.007	8.654	0.003	1.022	1.007	1.037
BNIHSS (score)	0.029	0.011	6.492	0.011	1.030	1.007	1.053
DM (yes)	0.516	0.244	4.477	0.034	1.675	1.039	2.701
N (yes)	0.014	0.007	4.154	0.042	1.014	1.001	1.028
Drug (u-PA)	0.971	0.345	7.917	0.005	2.641	1.343	5.194
Constant	-3.535	0.762	21.524	0.001	0.029		

indicators, and contraindications to IVT, and finally 849 patients were included in this study. Among the samples, 452 patients had poor recovery of neurological function in the early stage, and 294 patients had a poor prognosis at 3 months postoperatively. We use nonrepetitive random sampling at a ratio of 7:3, and draw the training cohort (594 cases) and the verification cohort (255 cases). In the training cohort, 320 patients had poor recovery of early neurological function, and 209 patients had a poor prognosis at 3 months postoperatively. In the verification cohort, 132 patients had poor recovery of neurological function early, and 85 patients had poor prognosis at 3 months after surgery (Table 1 and Figure 1).

### 3.2. Prognosis Prediction Model at 3 Months after Surgery

**3.2.1. Univariate Analysis.** The univariate analysis of the prognosis of patients with ischemic stroke at 3 months after IVT showed that gender, age, BMI, NIHSS score at admission (BNIHSS), smoking, hypertension, previous atrial fibrillation (preAF), new-onset atrial fibrillation (NewAF), congestive heart failure (CHF), previous stroke history (PreStrokeHistory), clopidogrel history (Clopidogrel), rosuvastatin history (Rosuvastatin), pre-thrombolysis systolic blood pressure (PreSBP), hemoglobin (Hb), red blood cell count (RBC), neutrophils (N), APTT, INR, fibrinogen (Fg), medication time (Time), thrombolytic medication (Drug), and 24-hour NIHSS score (24hNIHSS) were significantly different between the two groups ( $P < 0.05$ ). Although diabetes (DM) and PT were not significantly different between the two groups ( $P > 0.05$ ), they were close to 0.05. The above factors may affect the prognosis of patients with ischemic stroke at 3 months after IVT (Table 2).

**3.3. Model Construction.** The above-mentioned possible influencing factors were used as independent variables, and the prognosis at 3 months after IVT was used as the dependent variable. Multivariate binary logistic regression analysis was used, and the Forward: LR was used as the independent variable entry method. We analyzed the independent influencing factors that affect the prognosis of patients with ischemic stroke at 3 months after IVT. The analysis results show that age, diabetes DM, APTT, thrombolytic medication (Drug), and 24-hour NIHSS score (24hNIHSS) were independent factors influencing the prognosis of patients with ischemic stroke at 3 months after IVT, and a nomogram of the prognosis was constructed (Table 3).

**3.3.1. Model Verification.** The accuracy of the nomogram predicting the prognosis at 3 months after IVT was analyzed by the ROC curve, and the AUC (95% CI) in the training cohort was 0.901 (0.874~0.927), the AUC in the verification cohort (95% CI) is 0.877 (0.826~0.929), which shows that the prognosis at 3 months after surgery can be well predicted. The calibration curve based on the training and verification cohort shows that the predicted value of the nomogram for the poor prognosis is in good accordance with the actual value (Figure 2).

Decision curve analysis (DCA) and clinical impact curve analysis (CICA) were used to evaluate the clinical applicability of nomogram predicting the prognosis of patients with ischemic stroke at 3 months after IVT. Both showed that the model had a large practical threshold probability range  $P_t > 0.3$ , and the benefit was higher. The figure showed that when the threshold probability  $P_t = 0.4$ , the cost/benefit = 2 : 3. CICA hypothesized that if the prognosis of 1000 people was evaluated, and we compared the model evaluation results with the actual results, when  $P_t = 0.4$ , the two curves came to be very close (that is, the number of high-risk patients predicted by the model was very close to the actual number of high-risk patients). In summary, this model had a very ideal effect on the prognosis of 3 months after IVT (Figure 3).

### 3.4. Predictive Model of Early Neurological Function Recovery

**3.4.1. Univariate Analysis.** The results of univariate analysis of the early recovery of neurological function of patients with ischemic stroke after IVT showed that age, BMI, NIHSS score at admission (BNIHSS), hypertension, previous atrial fibrillation (preAF), diabetes (DM), systolic blood pressure before thrombolysis (PreSBP), red blood cell count (RBC), neutrophils (N%), APTT, treatment time ONT (Time), and thrombolytic medication (Drug) were significantly different between the two groups ( $P < 0.05$ ), although gender, second thrombolysis (SecondThrombolysis), and fibrinogen (FG) are not significantly different ( $P > 0.05$ ) but less than 0.1. The above factors may be the influencing factors of early neurological function after IVT in patients with ischemic stroke (Table 4).

**3.4.2. Model Construction.** The above-mentioned possible influencing factors were used as independent variables, and the early neurological function recovery after IVT was used

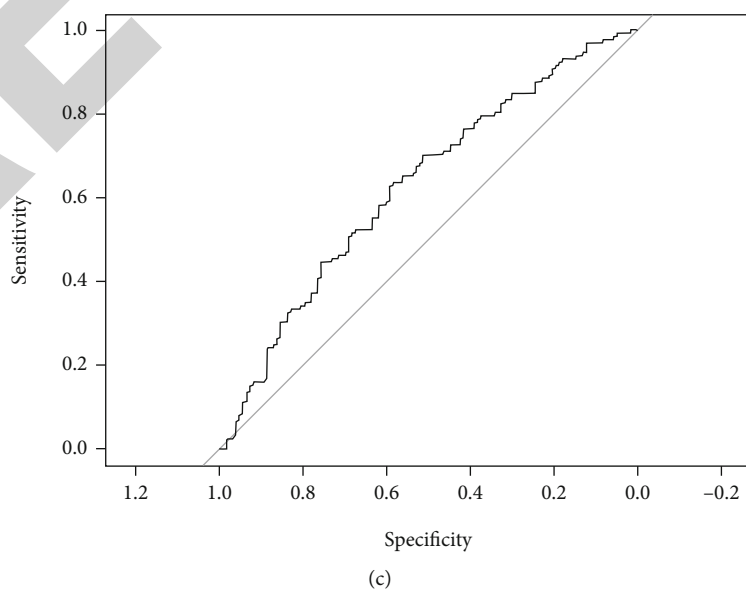
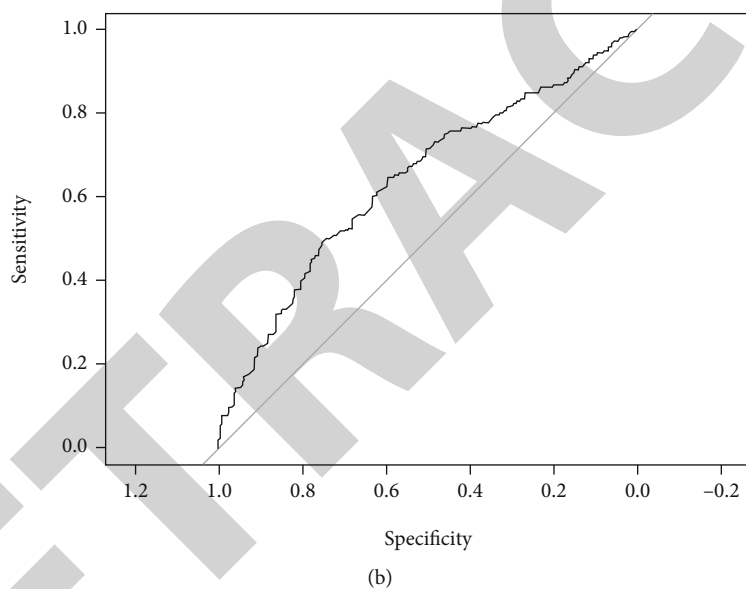
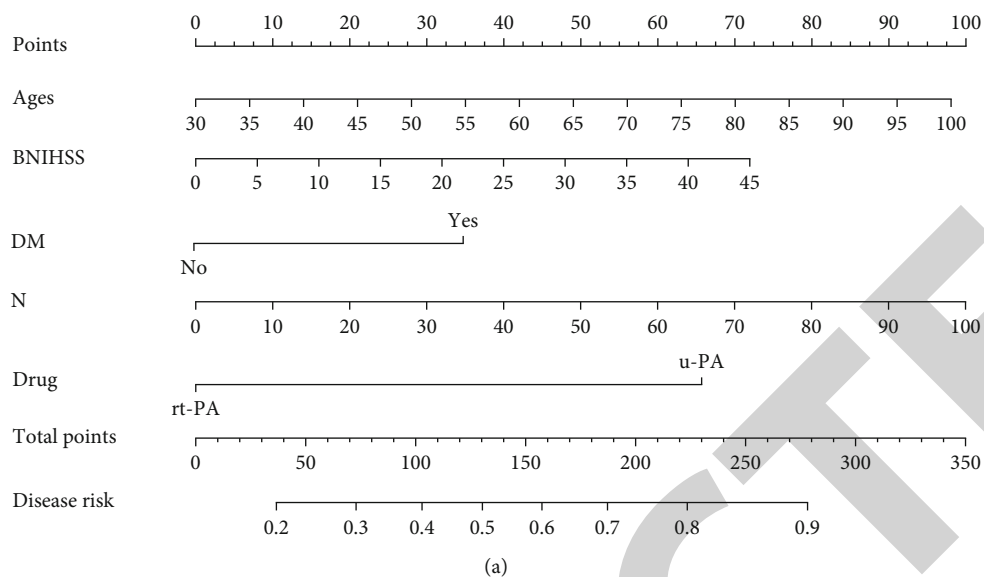


FIGURE 4: Continued.

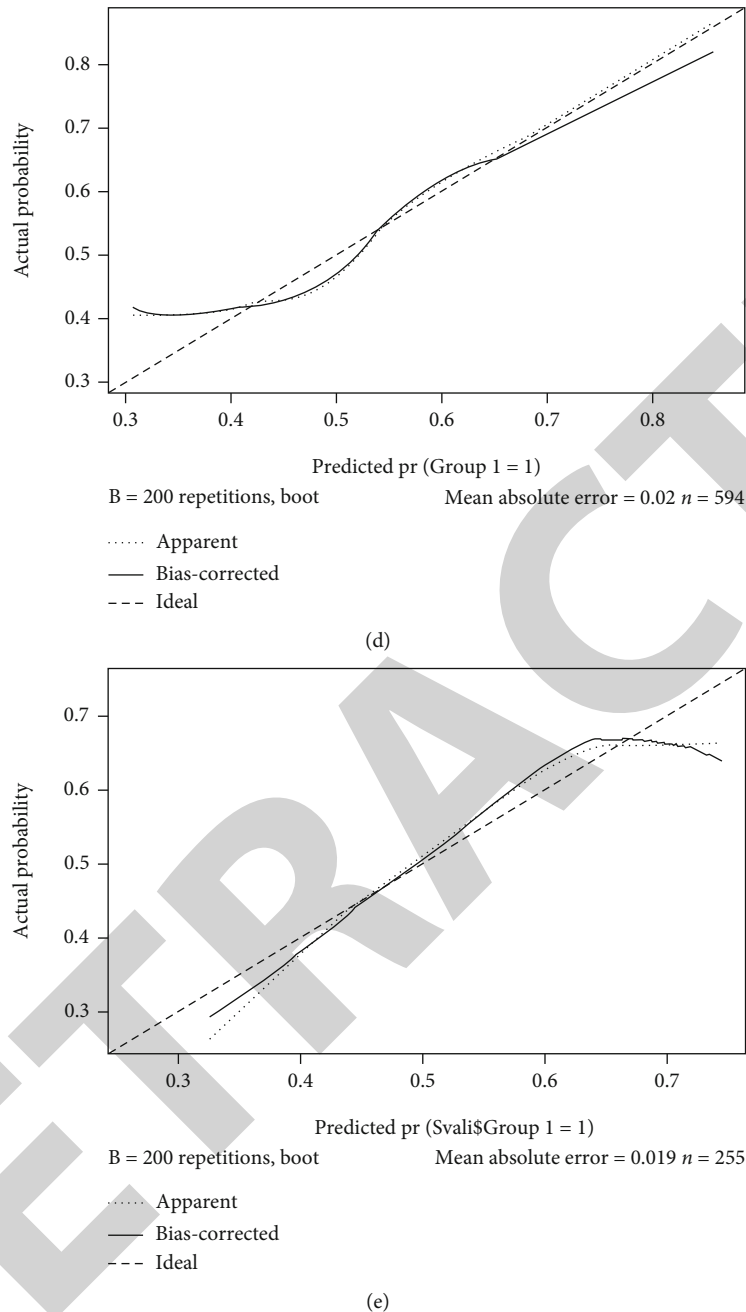
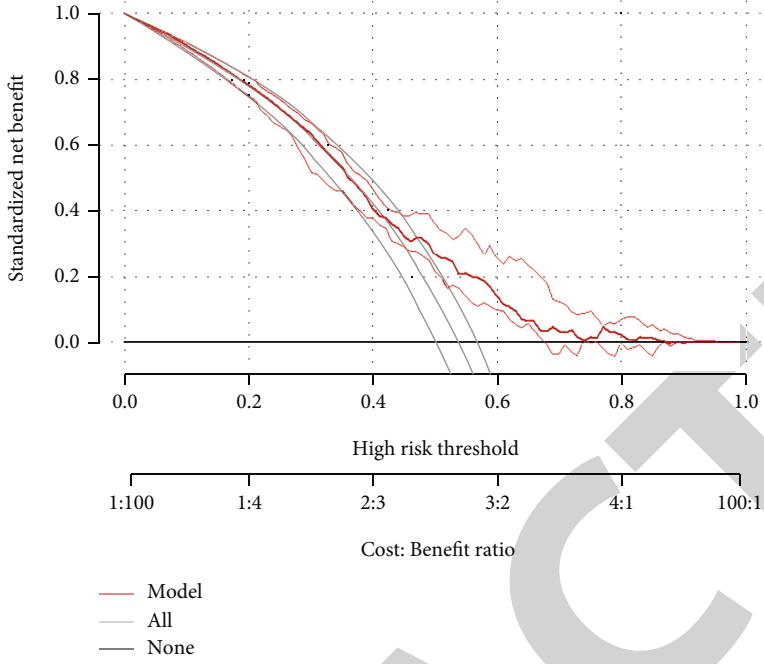


FIGURE 4: The predictive nomogram and ROC curve and calibration curve of nomogram predicting the early neurological recovery after IVT. (a) Predictive nomogram of early neurological recovery after IVT; (b) the ROC curve of the nomogram predicting the early neurological recovery after in training cohort; (c) the ROC curve of the nomogram predicting the early neurological recovery after in verification cohort; (d) the calibration curve of nomogram predicting the early neurological recovery after IVT in training cohort; (e) the calibration curve of nomogram predicting the early neurological recovery after IVT in verification cohort. Note: The calibration curve has been explained in Figure 2.

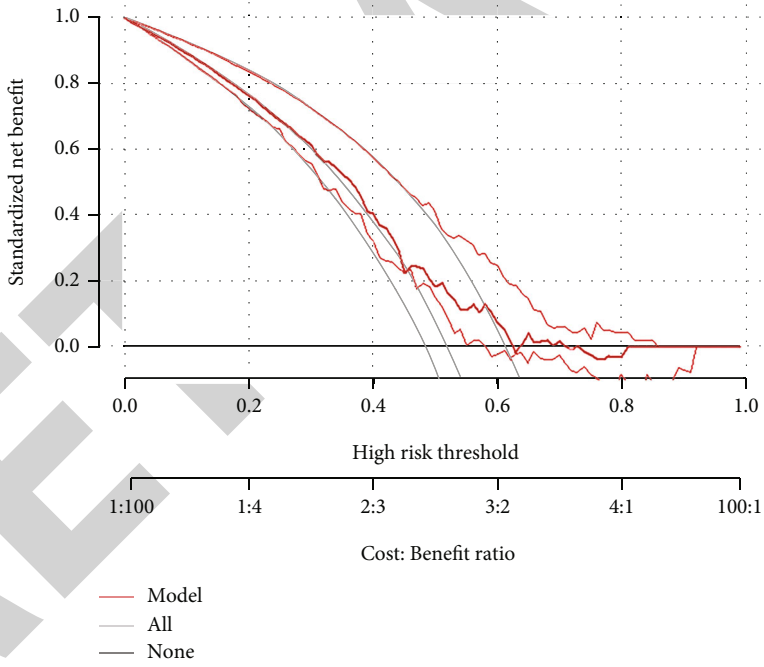
as the dependent variable. Multivariate binary logistic regression analysis was used, and the Forward: LR was used as the independent variable entry method. We analyzed the independent factors affecting the early recovery of neurological function in patients with ischemic stroke after IVT. The analysis results showed that age, NIHSS score at admission (BNIHSS), diabetes (DM), neutrophils (N), and medication

(Drugs) were independent factors affecting the prognosis of IVT patients with ischemic stroke, and a nomogram of the prognosis was constructed (Table 5).

**3.4.3. Model Verification.** The accuracy of the nomogram for early neurological function prediction was analyzed by ROC curve. The AUC (95% CI) in the training cohort was 0.641



(a)



(b)

FIGURE 5: Continued.

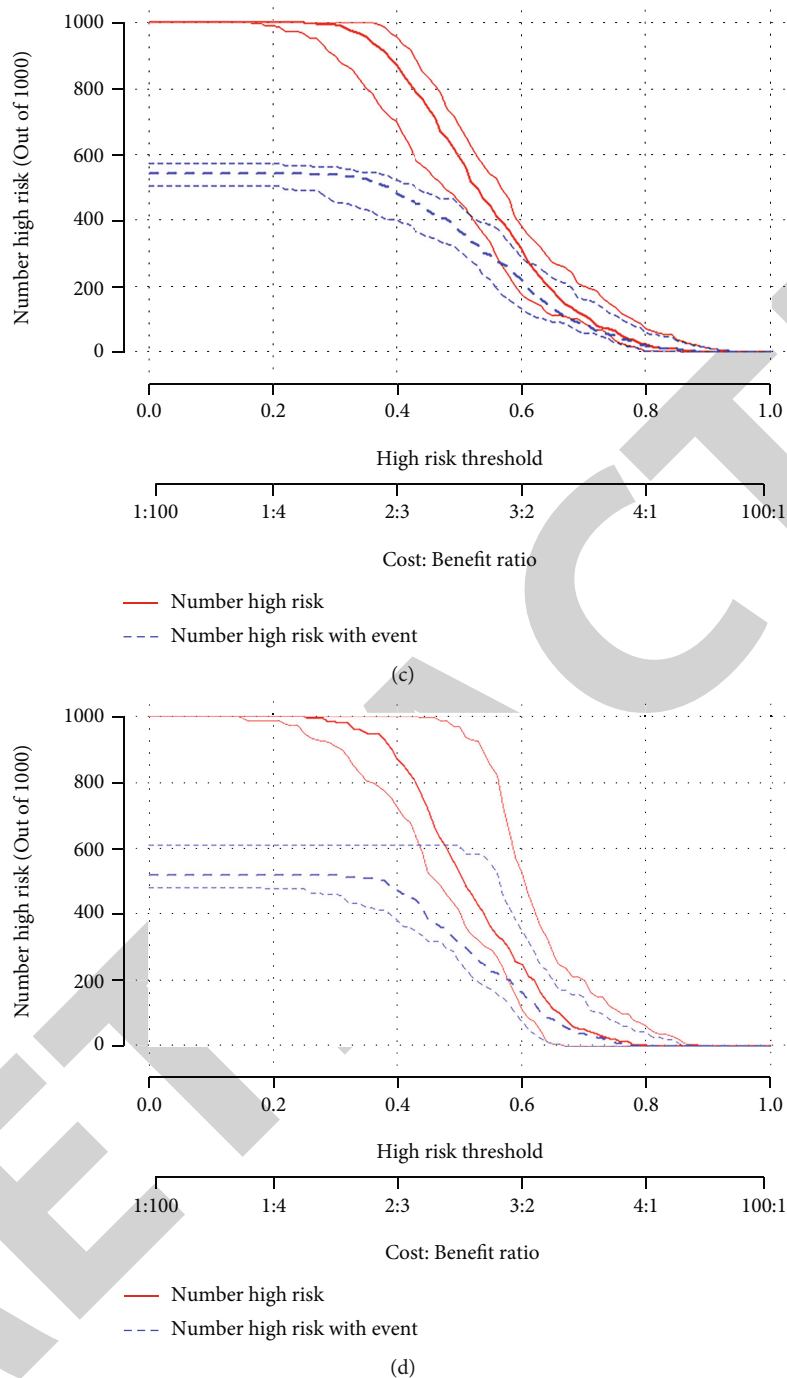


FIGURE 5: The decision curve and clinical impact curve analysis of nomogram predicting the early neurological recovery after IVT. (a) The decision curve of nomogram predicting the early neurological recovery after IVT in training cohort; (b) the decision curve of nomogram predicting the early neurological recovery after IVT in verification cohort; (c) the clinical impact curve of the nomogram predicting the early neurological recovery after IVT in training cohort; (d) the clinical impact curve of the nomogram predicting the early neurological recovery after IVT in verification cohort. Note: DCA and CICA have been explained in Figure 3.

(0.597~0.685), and the AUC (95% CI) in the verification cohort was 0.627 (0.559~0.696), which showed that the effect of distinguishing early neurological function was not ideal. The calibration curve based on the training cohort and the validation cohort showed that the predicted value of the nomogram for poor prognosis was in good accordance with the actual value (Figure 4).

Decision curve analysis (DCA) and clinical impact curve analysis (CICA) were used to evaluate the clinical applicability of the nomogram predicting early neurological recovery. Both showed that the model had a relatively narrow range of practical thresholds. CICA hypothesized that if the prognosis of 1000 people was evaluated, and we compared the model evaluation results with the actual results, when

$P_t > 0.6$ , the two curves came to be very close (that is, the number of high-risk patients predicted by the model was very close to the actual number of high-risk patients). At this time the cost/benefit = 3 : 2 (Figure 5).

#### 4. Discussions

At present, there are a variety of effective treatment for patients with acute ischemic stroke, such as IVT and intravascular interventional therapy, which can improve the neurological outcome of patients, and the two can be combined for appropriate patients [19, 20]. But still, IVT is still the first choice for a large number of patients. The China Stroke Prevention and Treatment Report 2019 shows that the number of people receiving IVT treatment in 298 advanced stroke centers in China in 2018 was 43,486 [21, 22]. Not all patients can benefit from thrombolysis. A study by Emberson et al. showed that 69% of patients still had a poor prognosis ( $mRS \geq 3$  points) at 3 months after thrombolysis [23]. Poor prognosis not only reduces the direct benefits of IVT, but also reduces the quality of life of patients and increases the medical burden on the family and society [24]. The results of the ECASS III test shows that IVT at 3.0-4.5 h still has effect [25], and the IST-3 test shows that IVT on the onset of disease within 6 hours have effect [26]. The subjects of this study were enrolled from six centers who received IVT treatment within 6 hours of acute ischemic stroke since the onset of the disease. This study discusses and analyzes the factors affecting the early neurological function recovery after IVT and the prognosis at 3 months after the surgery and establishes corresponding prediction model to form an early identification and active intervention of patients who may have a poor prognosis and improve their prognosis.

This study shows that old age, diabetes, and urokinase thrombolysis are risk factors for poor early recovery of neurological function and poor prognosis at 3 months after IVT in patients with ischemic stroke. Guidelines for the primary prevention of stroke point out that [27] old age and diabetes are not only independent risk factors for the occurrence of acute ischemic stroke, but are also considered to be important risk factors affecting the prognosis of IVT. Older age is one of the most important and independent predictors of stroke death and adverse outcomes [28, 29]. A study by Ulrich et al. [30] showed that diabetes more than doubled the risk of stroke. About 20% of diabetic patients die of stroke. The course of diabetes also increases the risk of non-hemorrhagic stroke. Morgenstern et al. [31] verified that age-specific incidence and rate showed that diabetes would increase the incidence of ischemic stroke in all age groups. The thrombolytic stroke prediction model incorporates age and diabetes history into the predictive variables. The model has an ideal effect in predicting the prognosis of thrombolytic therapy for good and severe prognosis ( $C$  values are 0.79 and 0.78, respectively) [32]. In recent years, recombinant tissue-type plasminogen activator (rt-PA) has been approved by the US Food and Drug Administration (FDA) and European Medicines Agency (EMA) as the only thrombolytic drug that can be used for ischemic stroke. However, due to the high cost, extremely short treatment

window, and increased risk of bleeding if out of the treatment window, a large number of ischemic stroke patients worldwide have not benefited from the drug. Urokinase plasminogen activator (u-PA) is usually used as an alternative [33]. As mentioned above, among the 43,486 patients in China in 2018, 7282 patients were treated with urokinase thrombolysis, accounting for 16.7%, and the rest were treated with rt-PA. A nationwide prospective Chinese registry study with a sample size of 3810 [34] compared the efficacy of rt-PA and u-PA in ischemic stroke. The results showed that the two treatments have an excellent outcome (90-day mRS; there was no significant difference between score  $< 2$ ) and symptomatic bleeding ( $P > 0.05$ ). This study showed that compared with rt-PA, u-PA can significantly increase the risk of poor early neurological function recovery and poor prognosis at 3 months after surgery.

In addition, this study shows that the NIHSS score at admission and the proportion of centrifugal cells before thrombolysis are also independent factors influencing the poor early of neurological function recovery after IVT. Perez-de-Puig et al. [35] showed through animal experiments that the accumulation of neutrophils can cause the destruction of the blood-brain barrier, thereby increasing the risk of hemorrhagic transformation and the incidence of poor prognosis after IVT. The clinical study of Liu et al. [36] showed that the increase in neutrophil count and neutrophil percentage before thrombolysis is associated with an increased risk of poor prognosis in patients with ischemic stroke after IVT. The NIHSS score at admission is used as a scale for the severity of stroke, and the severity of the disease is positively correlated with its score. Therefore, a large number of predictive models for the prognosis of thrombolysis included NIHSS score at admission as a variable [37].

At the same time, the NIHSS score 24 hours after thrombolysis and APTT before thrombolysis are also independent factors influencing the prognosis at 3 months after IVT. This study showed that the NIHSS score 24 hours after IVT is an independent influencing factor of the prognosis at 3 months after surgery rather than the NIHSS score at admission. This shows that the severity of the disease after IVT can better predict the prognosis at 3 months postoperatively than the severity before treatment. Rangaraju et al. [38] verified that the NIHSS score at 24 hours in the postmortem analysis of 2 randomized controlled stroke trials can better predict the long-term outcome of ischemic stroke. Yongtao et al. [39] showed that APTT level before thrombolysis is an independent risk factor that influences the early neurological improvement of acute ischemic stroke after intravenous IVT. APTT prediction of the best segmentation point of early neurological function improvement before thrombolysis is at 27.15(s). When the APTT level is  $< 27.15$ (s), the early neurological function improvement is significantly better than  $APTT > 27.15$ (s). However, the relationship with the prognosis at 3 months after IVT has not been verified.

In recent years, the relationship between smoking and adverse outcomes after IVT for ischemic stroke has not yet been confirmed. The study of Moulin et al. [40] showed that smoking does not independently affect the prognosis of patients with cerebral ischemia treated with rt-PA. The



better outcome of smokers is the result of different case combinations. This is also verified by the study of Kurmann et al. [41]. In the study of Sun et al. [42], smoking increases the risk of hemorrhagic transformation (HT) after IVT. This study shows that smoking is not an independent factor influencing the prognosis of IVT in patients with ischemic stroke. And among smoking patients, the propensity scoring method was used to match patients with high smoking age (>30 years) and patients with low smoking age ( $\leq 30$  years), and it is found that the poor prognosis of the two was also very similar (see Table S1 and Table S2).

**4.1. Limitations.** This study has certain limitations. Although the factors that affect the early recovery of neurological function after IVT have been analyzed, the accuracy of the prediction nomogram for the recovery of early neurological function established based on this needs to be improved.

## 5. Conclusions

This study uses only a small number of indicators to establish a predictive model for the early neurological recovery of patients with ischemic after IVT and the prognosis at 3 months after surgery. These predictive factors are easy to obtain in clinical practice. There is a large difference in the prediction accuracy of the two models (Delong's test  $P < 0.05$ ). The accuracy of the prediction nomogram based on the recovery of early neurological function needs to be improved. However, the nomogram for the prognosis 3 months after the operation has a very ideal prediction effect, which can well predict the poor prognosis 3 months after the operation. This is also the prognostic outcome that we are more concerned about.

## Data Availability

The data that support the findings of this study are available from the corresponding author upon reasonable request.

## Conflicts of Interest

The authors declare that the research was conducted in the absence of any commercial or financial relationships that could be construed as a potential conflict of interest.

## Authors' Contributions

WC and XT contributed to the conception or design of the work. NZ and WP contributed to the acquisition of data for the work. JH, ZF, XL, and FW contributed to the analysis of data for the work. JH, ZF, XL, XF, and GH contributed to the interpretation of data for the work. JH, ZF, and XL drafted the manuscript. WC and XT critically revised the manuscript. All gave final approval and agree to be accountable for all aspects of work ensuring integrity and accuracy. Jin Hu, Zhixian Fang, and Xia Lu contributed equally to this work.

## Acknowledgments

We would like to thank the researchers and study participants for their contributions. This work was funded by the Key Discipline of Jiaying Medicine Construction Project (No. 2019-zc-04, 2019-fc-04), the Science and Technology Project of Jiaying (2021 AD30157), and the Jiaying Key Laboratory of Precision Treatment for Lung Cancer.

## Supplementary Materials

Table S1: comparison of the above-mentioned independent influencing factors in the two groups. Table S2: analysis of multiple factors affecting the prognosis of stroke patients after IVT. (*Supplementary materials*)

## References

- [1] R. Lozano, M. Naghavi, K. Foreman et al., "Global and regional mortality from 235 causes of death for 20 age groups in 1990 and 2010: a systematic analysis for the Global Burden of Disease Study 2010," *Lancet*, vol. 380, no. 9859, pp. 2095–2128, 2012.
- [2] "Global, regional, and national burden of neurological disorders during 1990–2015: a systematic analysis for the Global Burden of Disease Study 2015," *Lancet Neurology*, vol. 16, no. 11, pp. 877–897, 2017.
- [3] C. J. Murray, T. Vos, R. Lozano et al., "Disability-adjusted life years (DALYs) for 291 diseases and injuries in 21 regions, 1990–2010: a systematic analysis for the Global Burden of Disease Study 2010," *Lancet*, vol. 380, no. 9859, pp. 2197–2223, 2012.
- [4] V. L. Feigin, G. Nguyen, K. Cercy et al., "Global, regional, and country-specific lifetime risks of stroke, 1990 and 2016," *The New England Journal of Medicine*, vol. 379, no. 25, pp. 2429–2437, 2018.
- [5] J. Bamford, P. Sandercock, M. Dennis, C. Warlow, and J. Burn, "Classification and natural history of clinically identifiable subtypes of cerebral infarction," *Lancet*, vol. 337, no. 8756, pp. 1521–1526, 1991.
- [6] E. S. Donkor, "Stroke in 21<sup>st</sup> the Century: A Snapshot of the Burden, Epidemiology, and Quality of Life," *Stroke research and treatment*, vol. 2018, Article ID 3238165, 10 pages, 2018.
- [7] Y. J. Wang, Z. X. Li, H. Q. Gu et al., "China Stroke Statistics 2019: a report from the National Center for Healthcare Quality Management in Neurological Diseases, China National Clinical Research Center for Neurological Diseases, the Chinese Stroke Association, National Center for Chronic and Non-communicable Disease Control and Prevention, Chinese Center for Disease Control and Prevention and Institute for Global Neuroscience and Stroke Collaborations," *Stroke and vascular neurology*, vol. 5, no. 3, pp. 211–239, 2020.
- [8] A. G. Thrift, T. Thayabaranathan, G. Howard et al., "Global stroke statistics," *International Journal of Stroke*, vol. 12, no. 1, pp. 13–32, 2017.
- [9] M. Katan and A. Luft, "Global burden of stroke," *Seminars in Neurology*, vol. 38, no. 2, pp. 208–211, 2018.
- [10] Y. Béjot, H. Bailly, J. Durier, and M. Giroud, "Epidemiology of stroke in Europe and trends for the 21st century," *Presse Médicale*, vol. 45, no. 12, pp. e391–e398, 2016.

- [11] A. A. Rabinstein, "Update on treatment of acute ischemic stroke," *Continuum (Minneapolis)*, vol. 26, no. 2, pp. 268–286, 2020.
- [12] J. Guéniat, C. Brenière, M. Graber et al., "Increasing burden of stroke: the Dijon stroke registry (1987-2012)," *Neuroepidemiology*, vol. 50, no. 1-2, pp. 47–56, 2018.
- [13] T. Brott, H. P. Adams Jr., C. P. Olinger et al., "Measurements of acute cerebral infarction: a clinical examination scale," *Stroke*, vol. 20, no. 7, pp. 864–870, 1989.
- [14] J. Pu, H. Wang, M. Tu et al., "Combination of 24-hour and 7-day relative neurological improvement strongly predicts 90-day functional outcome of endovascular stroke therapy," *Journal of Stroke and Cerebrovascular Diseases*, vol. 27, no. 5, pp. 1217–1225, 2018.
- [15] J. P. Desilles, E. Meseguer, J. Labreuche et al., "Diabetes mellitus, admission glucose, and outcomes after stroke thrombolysis: a registry and systematic review," *Stroke*, vol. 44, no. 7, pp. 1915–1923, 2013.
- [16] S. J. Kang, Y. R. Cho, G. M. Park et al., "Predictors for functionally significant in-stent restenosis: an integrated analysis using coronary angiography, IVUS, and myocardial perfusion imaging," *JACC: Cardiovascular Imaging*, vol. 6, no. 11, pp. 1183–1190, 2013.
- [17] A. J. Vickers and E. B. Elkin, "Decision curve analysis: a novel method for evaluating prediction models," *Medical Decision Making*, vol. 26, no. 6, pp. 565–574, 2006.
- [18] V. Rousson and T. Zumbo, "Decision curve analysis revisited: overall net benefit, relationships to ROC curve analysis, and application to case-control studies," *BMC Medical Informatics and Decision Making*, vol. 11, no. 1, p. 45, 2011.
- [19] B. C. Campbell, P. J. Mitchell, T. J. Kleinig et al., "Endovascular therapy for ischemic stroke with perfusion-imaging selection," *The New England Journal of Medicine*, vol. 372, no. 11, pp. 1009–1018, 2015.
- [20] M. Goyal, A. M. Demchuk, B. K. Menon et al., "Randomized assessment of rapid endovascular treatment of ischemic stroke," *The New England Journal of Medicine*, vol. 372, no. 11, pp. 1019–1030, 2015.
- [21] L. D. Wang, J. H. Wang, B. Peng, and Y. M. Xu, "Brief report on stroke prevention and treatment in China, 2019," *Chinese Journal of Cerebrovascular Disease*, vol. 17, no. 5, pp. 272–281, 2020.
- [22] Society, EMBoCG, SGoCSo E Medicine, and CSoEMo stroke, "Consensus of Chinese experts on emergency and first aid for acute ischemic stroke, 2018," *Chinese Journal of Stroke*, vol. 13, no. 9, pp. 956–967, 2018.
- [23] J. Emberson, K. R. Lees, P. Lyden et al., "Effect of treatment delay, age, and stroke severity on the effects of intravenous thrombolysis with alteplase for acute ischaemic stroke: a meta-analysis of individual patient data from randomised trials," *Lancet*, vol. 384, no. 9958, pp. 1929–1935, 2014.
- [24] M. Ali, R. Fulton, T. Quinn et al., "How well do standard stroke outcome measures reflect quality of life? A retrospective analysis of clinical trial data," *Stroke*, vol. 44, no. 11, pp. 3161–3165, 2013.
- [25] D. C. Morris, "Thrombolysis 3 to 4.5 hours after acute ischemic stroke," *The New England Journal of Medicine*, vol. 359, no. 26, p. 2841; author reply 2841, 2008, author reply 2841.
- [26] P. Sandercock, J. M. Wardlaw, R. I. Lindley, and IST-3 Collaborative Group, "The benefits and harms of intravenous thrombolysis with recombinant tissue plasminogen activator within 6 h of acute ischaemic stroke (the third international stroke trial [IST-3]): a randomised controlled trial," *Lancet*, vol. 379, no. 9834, pp. 2352–2363, 2012.
- [27] J. F. Meschia, C. Bushnell, B. Boden-Albala et al., "Guidelines for the primary prevention of stroke: a statement for healthcare professionals from the American Heart Association/American Stroke Association," *Stroke*, vol. 45, no. 12, pp. 3754–3832, 2014.
- [28] K. D. Palnum, P. Petersen, H. T. Sørensen et al., "Older patients with acute stroke in Denmark: quality of care and short-term mortality. A nationwide follow-up study," *A nationwide follow-up study. Age Ageing*, vol. 37, no. 1, pp. 90–95, 2008.
- [29] E. E. Smith, N. Shobha, D. Dai et al., "Risk score for in-hospital ischemic stroke mortality derived and validated within the Get With the Guidelines-Stroke Program," *Circulation*, vol. 122, no. 15, pp. 1496–1504, 2010.
- [30] E. L. Ulrich, J. L. Markley, and Y. Kyogoku, "Creation of a nuclear magnetic resonance data repository and literature database," *Protein Sequences & Data Analysis*, vol. 2, no. 1, pp. 23–37, 1989.
- [31] L. B. Morgenstern, M. A. Smith, L. D. Lisabeth et al., "Excess stroke in Mexican Americans compared with non-Hispanic whites: the brain attack surveillance in Corpus Christi project," *American Journal of Epidemiology*, vol. 160, no. 4, pp. 376–383, 2004.
- [32] D. M. Kent, H. P. Selker, R. Ruthazer, E. Bluhmki, and W. Hacke, "The stroke-thrombolytic predictive instrument: a predictive instrument for intravenous thrombolysis in acute ischemic stroke," *Stroke*, vol. 37, no. 12, pp. 2957–2962, 2006.
- [33] R. R. A. Kadir and U. Bayraktutan, "Urokinase plasminogen activator: a potential thrombolytic agent for ischaemic stroke," *Cellular and Molecular Neurobiology*, vol. 40, no. 3, pp. 347–355, 2020.
- [34] X. Wang, X. Li, Y. Xu et al., "Effectiveness of intravenous r-tPA versus UK for acute ischaemic stroke: a nationwide prospective Chinese registry study," *Stroke and vascular neurology*, vol. 6, no. 4, pp. 603–609, 2021.
- [35] I. Perez-de-Puig, F. Miró-Mur, M. Ferrer-Ferrer et al., "Neutrophil recruitment to the brain in mouse and human ischemic stroke," *Acta Neuropathologica*, vol. 129, no. 2, pp. 239–257, 2015.
- [36] H. Liu, R. Wang, J. Shi et al., "Baseline neutrophil counts and neutrophil ratio may predict a poor clinical outcome in minor stroke patients with intravenous thrombolysis," *Journal of Stroke and Cerebrovascular Diseases*, vol. 28, no. 11, article 104340, 2019.
- [37] L. Huang and G. Liu, "A review on risk factors associated with poor prognosis after intravenous thrombolysis in ischemic stroke patients," *Chinese Journal of Stroke*, vol. 15, no. 12, pp. 1352–1359, 2020.
- [38] S. Rangaraju, M. Frankel, and T. G. Jovin, "Prognostic value of the 24-hour neurological examination in anterior circulation ischemic stroke: a post hoc analysis of two randomized controlled stroke trials," *Interventional neurology*, vol. 4, no. 3-4, pp. 120–129, 2016.
- [39] Y. Yongtao, J. Ge, L. Xin, C. Liang, L. Xinggui, and Z. Qunling, "Improvement of neurological function after intravenous thrombolysis in patients with acute cerebral infarction," *China Pharmaceuticals*, vol. 29, no. 1, pp. 76–79, 2020.

## *Retraction*

# **Retracted: Clinical Effect of Digital Subtraction Angiography Combined with Neurointerventional Thrombolysis for Acute Ischemic Cerebrovascular Disease and Its Influence on Vascular Endothelial Function and Oxidative Stress**

### **Oxidative Medicine and Cellular Longevity**

Received 8 January 2024; Accepted 8 January 2024; Published 9 January 2024

Copyright © 2024 Oxidative Medicine and Cellular Longevity. This is an open access article distributed under the Creative Commons Attribution License, which permits unrestricted use, distribution, and reproduction in any medium, provided the original work is properly cited.

This article has been retracted by Hindawi, as publisher, following an investigation undertaken by the publisher [1]. This investigation has uncovered evidence of systematic manipulation of the publication and peer-review process. We cannot, therefore, vouch for the reliability or integrity of this article.

Please note that this notice is intended solely to alert readers that the peer-review process of this article has been compromised.

Wiley and Hindawi regret that the usual quality checks did not identify these issues before publication and have since put additional measures in place to safeguard research integrity.

We wish to credit our Research Integrity and Research Publishing teams and anonymous and named external researchers and research integrity experts for contributing to this investigation.

The corresponding author, as the representative of all authors, has been given the opportunity to register their agreement or disagreement to this retraction. We have kept a record of any response received.

## **References**

- [1] X. Wang, X. Zhang, Q. Guan, and K. Wang, "Clinical Effect of Digital Subtraction Angiography Combined with Neurointerventional Thrombolysis for Acute Ischemic Cerebrovascular Disease and Its Influence on Vascular Endothelial Function and Oxidative Stress," *Oxidative Medicine and Cellular Longevity*, vol. 2022, Article ID 2777865, 8 pages, 2022.

## Research Article

# Clinical Effect of Digital Subtraction Angiography Combined with Neurointerventional Thrombolysis for Acute Ischemic Cerebrovascular Disease and Its Influence on Vascular Endothelial Function and Oxidative Stress

Xuna Wang,<sup>1</sup> Xuesong Zhang,<sup>2</sup> Qingbo Guan,<sup>2</sup> and Kuiyang Wang<sup>1,2</sup> 

<sup>1</sup>Department of Radiology, The Second Hospital of Dalian Medical University, Dalian City, 116023 Liaoning Province, China

<sup>2</sup>Department of Invasive Technology, The Second Hospital of Dalian Medical University, Dalian City, 116023 Liaoning Province, China

Correspondence should be addressed to Kuiyang Wang; wky409@163.com

Received 10 June 2022; Revised 12 July 2022; Accepted 21 July 2022; Published 9 August 2022

Academic Editor: Anwen Shao

Copyright © 2022 Xuna Wang et al. This is an open access article distributed under the Creative Commons Attribution License, which permits unrestricted use, distribution, and reproduction in any medium, provided the original work is properly cited.

**Objective.** Ischemic cerebrovascular disease is a commonly seen vascular disorder in clinical practice. Given the difficulty of drug therapy to achieve ideal curative effects, interventional therapy has gradually become the preferred treatment for the disease. This research primarily discusses the short-term efficacy of digital subtraction angiography- (DSA-) guided neurointerventional thrombolysis for acute ischemic cerebrovascular disease (AICVD) and its influence on vascular endothelial function (VEF) and oxidative stress (OS). **Methods.** All the clinical data of 162 patients diagnosed with AICVD and treated between June 2019 and December 2021 were collected and analyzed retrospectively. They were assigned to two cohorts according to the difference in interventional methods: a conventional group (CG) given recombinant tissue plasminogen activator (rt-PA) therapy and an observation group (OG) intervened by DSA-guided neurointerventional thrombolysis. The two groups were compared with respect to short-term treatment efficacy, the National Institutes of Health Stroke Scale (NIHSS) score, cerebral hemodynamics, and VEF and OS indexes. **Results.** The short-term efficacy was better in OG (93.98%) than in CG (82.28%). After treatment, the NIHSS score decreased in both cohorts with obvious differences within the group at different time points, and the posttreatment NIHSS score was lower in OG as compared to CG. OG had higher  $Q_m$  and  $V_m$  while lower  $W_v$ ,  $Z_{cv}$ , and  $R_v$  than CG. Higher endothelial-dependent flow-mediated dilatation (FMD) was observed in OG, as well as lower ankle-brachial index (ABI) and pulse wave velocity (PWV). And the posttreatment MDA was lower while SOD, GSH-Px, and TAC were higher in OG compared with those on CG. All the above differences were of statistical significance ( $P < 0.05$ ). **Conclusions.** DSA-guided neurointerventional thrombolysis is highly effective in the treatment of AICVD, which can not only effectively improve patients' neurological function and cerebral hemodynamics but also mitigate VEF injury and help to alleviate patients' OS.

## 1. Introduction

As a common critical and severe condition worldwide, ischemic cerebrovascular disease (ICVD) refers to transient or persistent and local or diffuse brain tissue damage caused by ischemia and hypoxia of the corresponding brain tissue, resulting in a series of neurological dysfunction symptoms

or signs [1, 2], with high disability rate and fatality rate [3, 4]. As the diet structure of people changes and the aging of the population accelerates, the prevalence of ICVD, most of which occurs on the basis of hemodynamic disturbance or cerebrovascular diseases, has increased rapidly, posing a serious threat to patients' life safety and quality [5, 6]. ICVD includes transient ischemic attacks (TIA) [7] and acute

cerebral infarction (ACI) [8]. Regardless of the type, artery stenosis or occlusion caused by atherosclerosis is a very important reason [9].

Literature has revealed a close association between ICVD and atherosclerosis [10]. Ischemic cerebral vessels can cause temporary blood supply disturbance, resulting in neurological deficits, which have a serious impact on patients. Its onset is often accompanied by neurological dysfunction, and untimely treatment of the sudden attack of ICVD will seriously affect the life of patients. Thrombolysis is a commonly used clinical method to treat cerebral vascular occlusion and an important way to restore the patency of the occluded cerebral vessels [11]. The prominent feature of clinical treatment is intravenous (IV) thrombolysis (IVT). In thrombolytic drugs, plasminogen activators can dissolve fibrin in thrombi and promote the recanalization of blocked vessels, thus saving patients' lives in a timely manner [12–14]. However, IVT still has limitations. It only works within 4 hours after onset, with some certain contraindications for some patients [15]. Therefore, IVT, with limited therapeutic effectiveness, is not suitable for all cases. Interventional therapy, thanks to the progress of clinical medicine, has also been extensively applied, providing a new approach for cerebrovascular occlusion [16]. Interventional therapy is a minimally invasive method to determine the location of artery stenosis and treat cerebrovascular diseases through intubation based on computer. During interventional therapy, IVT can be used to dredge blood vessels and eliminate infarction [17], which has been confirmed by Liu et al. [18] and Lei et al. [19]. But the demerits of interventional therapy have also been gradually unveiled with its widespread application. The wrong choice of puncture site, for instance, can result in ineffective treatment while aggravating the patient's condition [20]. Due to the complexity of cerebrovascular structure, correct selection of the puncture site is critical. Hence, relevant auxiliary examination is the key to enhancing the treatment outcome of interventional therapy.

Digital subtraction angiography- (DSA-) guided neurointerventional thrombolysis is an operation assisted by imaging means, which can recanalize the lumen of the refractory occlusion or severe stenosis of cerebral blood supply artery through guidewires and catheters, and is widely used in clinic because of its advantages of small trauma, definite curative effect, and high safety [21, 22]. Besides, endothelial dysfunction (ED) in the cerebral circulation is shown to be linked to a range of vascular-related disorders, as well as a higher possibility of experiencing acute clinical events that may lead to cognitive decline [23–25]. Meanwhile, there is compelling evidence that oxidative stress (OS) is a major inducement of cerebral ED in multiple disorders [26]. Thus, this experiment primarily analyzes the therapeutic effect of DSA combined with neurointerventional thrombolysis on acute ischemic cerebrovascular disease (AICVD) patients and studies its effects on cerebral hemodynamics, vascular endothelial function (VEF), and OS, with the novelty and motivation lying in providing a scientific theoretical basis and laying a sound theoretical basis for further treatment.

## 2. Materials and Methods

**2.1. General Data.** We retrospectively analyzed the clinical data of 162 AICVD patients diagnosed and treated in the Second Hospital of Dalian Medical University between June 2019 and December 2021. Inclusive criteria: (1) all patients were confirmed by CT, MRI, and other imaging examinations and met the diagnostic criteria of AICVD [27]; (2) onset of illness  $\leq 4.5$  hours; (3) no previous interventional therapy; and (4) intact case data. Exclusion criteria: (1) presence of intracranial space-occupying lesions such as brain abscess and brain tumor, (2) severe organ dysfunction or diseases, (3) history of acute cerebral infarction or myocardial infarction within 3 months, (4) mental illness or cognitive impairment, (5) contraindications associated with other thrombolytic therapy and DSA antiplatelet drugs, and (6) incomplete case data. Patients were assigned to either the conventional group (CG;  $n = 79$ ) or the observation group (OG;  $n = 83$ ) based on the interventional methods. The comparison of baseline data (sex, age, etc.) showed no statistical difference between groups, suggesting clinical comparability ( $P > 0.05$ , Table 1). This study has obtained approval from the Medical Ethics Committee of the Second Hospital of Dalian Medical University. As this study was retrospective, the need for subjects' informed consent was waived.

**2.2. Treatment Methods.** All patients were monitored for vital signs after admission, and intracranial CT perfusion imaging and other auxiliary examinations were performed to determine the lesion site and the presence of cerebral hemorrhage. Among them, cases in OG were treated with DSA combined with neurointerventional thrombolysis. Recombinant tissue plasminogen activator (rt-PA) (alteplase for injection, specification 50 mg, Registration No. S20160055, Boehringer Ingelheim Pharma GmbH & Co. KG, Germany) was administered at 0.6 mg/kg intravenously, with the maximum dose controlled within 60 mg; 10% of the total dosage was first given via an IV bolus injection within 1 min, and the rest was pumped continuously within 1 h through the infusion pump. The Seldinger puncture technique was used to perform puncture, intubation, and arterial sheathing in the femoral artery of the patient, and a whole-brain DSA was performed to evaluate the vascular occlusion. The microguidewire was inserted, under whose guidance, the catheter was placed to the position near the diseased vessel. Then, a mixed solution of 200,000 U urease and 20 mL normal saline (0.9%) was quickly injected with a syringe, followed by pumping of 200,000 to 500,000 U urokinase and 50 mL normal saline (0.9%) with a microautolysis catheter at 1.0 mL/min. Patients in CG received conventional IV thrombolytic therapy with 0.9 mg/kg recombinant human tissue fibrinogen activator; 10% of the total dosage was first administered via an IV push within 1 min, and the rest was pumped continuously within 1 h through the infusion pump.

### 2.3. Endpoints

- (1) National Institutes of Health Stroke Scale (NIHSS) [28]; patients were assessed by the NIHSS score

TABLE 1: Comparison of general data.

	Conventional group ( $n = 79$ )	Observation group ( $n = 83$ )	$\chi^2/t$	$P$
Gender ( $n$ )			1.2481	0.2639
Male	45 (57.0)	40 (48.2)		
Female	34 (43.0)	43 (51.8)		
Age (years old)	50.52 $\pm$ 10.14	50.76 $\pm$ 10.23	0.1499	0.8810
Body mass (kg)	61.60 $\pm$ 7.32	62.87 $\pm$ 8.10	1.0453	0.2975
Primary disease ( $n$ )				
Diabetes mellitus	19 (24.1)	24 (28.9)	0.4913	0.4833
Hypertension	37 (46.8)	40 (48.2)	0.0299	0.8627
Hyperlipidemia	35 (44.3)	38 (45.8)	0.0358	0.8500
History of smoking ( $n$ )	39 (49.4)	39 (47.0)	0.0918	0.7619
History of drinking ( $n$ )	23 (29.1)	28 (33.7)	0.4007	0.5267

(score range: 0-45) before as well as 1 day, 7 days, and 3 months after treatment for neurological deficits, mainly from the dimensions of level of consciousness, response to commands, gaze, facial paralysis, motor function (leg), sensory, and dyskinesia. Higher scores were associated with more serious neurological deficits

- (2) Short-term efficacy: after 3 months of treatment, two physicians with deputy senior titles or above in the neurology department conducted efficacy assessment through the NIHSS score, with an inverse connection between the score and efficacy. Cure: NIHSS score lowered by >90%, with no disability. Marked response: NIHSS score lowered by 46%-90%, with basically independent living. Response: NIHSS score decreased by 18%-45%, with partial independent living ability. Nonresponse: NIHSS score decreased by less than 18%, with grade 3 or higher disability. Overall response rate (ORR) = (cure + marked response + response) cases/total cases  $\times$  100%
- (3) Cerebral hemodynamics: the cerebral blood flow of patients was measured using a CV-300 cerebrovascular hemodynamic analyzer (MEDENG Electronic Equipment Co., Shanghai, China). According to the empirical formula such as the basic equation of non-linear elastic cavity model, several characteristic parameters reflecting cerebrovascular function were calculated by the computer system. The indexes measured before and after treatment included the mean blood flow ( $Q_m$ ), mean blood flow velocity ( $V_m$ ), wave velocity ( $W_v$ ), vascular characteristic impedance ( $Z_{cv}$ ), and peripheral resistance ( $R_v$ )
- (4) VEF: the VEF of patients was measured with the use of an UNEXEF38g automated diagnostic ultrasound system (UNEX corporation, Sakae Naka-ku, Nagoya, Japan). The parameters detected before and after treatment included flow-mediated vasodilation (FMD), as well as bilateral ankle-brachial index (ABI) and brachial-ankle pulse wave velocity

(ba-PWV) measured by a VBP-9 arteriosclerosis tester, and the average values of ABI and ba-PWV were calculated

- (5) OS: before and after treatment, fasting venous blood samples (4 mL) were obtained from each participant during morning hours, which were then treated with centrifugation (3000 r/min, 10 min) for serum collection. The enzyme-linked immunosorbent assay (ELISA) quantified serum total antioxidant capacity (TAC), and the xanthine oxidase method, thiobarbital colorimetry, and colorimetry determined malondialdehyde (MDA), superoxide dismutase (SOD), and glutathione peroxidase (GSH-Px), respectively

**2.4. Statistical Processing.** The sample size of this study was calculated using PASS 15.0 (NCSS, Kaysville, Utah). The data from a preliminary study indicated that for a study power of 80% ( $\alpha = 0.05$ ,  $\beta = 0.2$ ), assuming an effective rate of 93% and 75% in OG and CG, respectively, the sample size required for each group was 62, with a total of 124 cases allowed for adequate data acquisition. Meanwhile, with the dropout rate of 20%, a total of 156 patients were needed (78 in each group).

All data were processed with SPSS 25.0 (SPSS, Inc., Chicago). The mean  $\pm$  standard deviation was utilized to indicate the normal distributed quantitative data, and the intergroup and multigroup comparison methods were independent sample  $t$ -test and one-way analysis of variance plus Bonferroni post hoc analysis, respectively. Counting data were expressed by the case number (percentage), and the comparison adopted the chi-square test. Statistically significant differences were present when  $P < 0.05$ .

### 3. Results

**3.1. NIHSS Scores of Two Groups.** No statistical difference was found between OG and CG in pretreatment NIHSS scores. After treatment, decreased NIHSS scores were observed in both cohorts, with a statistical difference at each time point within the group ( $P < 0.05$ ). And the NIHSS

TABLE 2: Comparison of NIHSS scores.

	Before treatment	1 d after treatment	7 d after treatment	3 months after treatment	F	P
Conventional group ( $n = 79$ )	21.05 ± 4.31	13.59 ± 2.62	8.00 ± 1.64	6.29 ± 1.27	470.4000	<0.0001
Observation group ( $n = 83$ )	21.39 ± 3.94	10.66 ± 2.68	6.23 ± 1.26	4.42 ± 0.91	765.2000	<0.0001
$t$	0.5244	7.0318	7.2515	10.8124	—	—
$P$	0.60007	<0.0001	<0.0001	<0.0001	—	—

TABLE 3: Comparison of clinical efficacy.

	Cure	Marked response	Response	Nonresponse	Overall response rate
Conventional group ( $n = 79$ )	13 (16.46)	28 (35.44)	24 (30.38)	14 (17.72)	65 (82.28)
Observation group ( $n = 83$ )	21 (25.31)	38 (45.78)	19 (22.89)	5 (6.02)	78 (93.98)
$\chi^2$					4.5871
$P$					0.0322

scores of OG were lower at 1 d, 7 d, and 3 months after treatment versus CG ( $P < 0.05$ ), as exhibited in Table 2.

**3.2. Clinical Efficacy of Two Groups.** In CG, cure, marked response, response, and nonresponse were found in 13, 28, 24, and 14 cases, respectively, with an ORR of 82.28%. In OG, cure, marked response, response, and nonresponse were identified in 21, 38, 19, and 5 cases, respectively, with an ORR of 93.98%. The above data revealed a higher ORR in OG as compared to CG ( $P < 0.05$ ), as can be found in Table 3.

**3.3. Cerebral Hemodynamics in Two Groups.** The intergroup comparison of pre- and posttreatment cerebral hemodynamics showed a statistically significant difference ( $P < 0.05$ ). The posttreatment  $Q_m$ ,  $V_m$ ,  $W_v$ ,  $Z_{cv}$ , and  $R_v$  in OG were  $4.67 \pm 1.10$  mL/s,  $12.77 \pm 2.83$  cm/s,  $18.26 \pm 4.26$  m/s, and  $82.12 \pm 14.16$  kPa·s/ms, and  $53.60 \pm 11.23$  kPa·s/m, respectively; in CG, the corresponding indexes were  $4.01 \pm 0.65$  mL/s,  $10.78 \pm 2.49$  cm/s,  $21.44 \pm 4.81$  m/s,  $90.57 \pm 17.47$  kPa·s/m, and  $59.56 \pm 11.77$  kPa·s/m, respectively. The results showed better recovery of cerebral hemodynamic indexes in OG compared with CG. See Table 4 for details.

**3.4. VEF in Two Groups.** Similarly, VEF differed significantly between groups before and after treatment ( $P < 0.05$ ). The FMD, ABI, and PWV in OG were  $5.88 \pm 1.35\%$ ,  $0.91 \pm 0.10$ , and  $1212.00 \pm 50.82$  cm/s/s after treatment, while those in CG were  $5.16 \pm 1.19\%$ ,  $1.10 \pm 0.11$ , and  $1344.06 \pm 68.82$  cm/s, respectively, suggesting better recovery of VEF indexes in OG as compared to CG ( $P < 0.05$ ). See Figure 1 for details.

**3.5. OS Response in Two Groups.** Serum SOD, MDA, GSH-Px, and TAC levels differed insignificantly between groups prior to treatment ( $P > 0.05$ ). After treatment, serum SOD, GSH-Px, and TAC in the two groups all increased, while the content of MDA decreased, with statistically significant

differences ( $P < 0.05$ ); OG showed better improvement in each index than CG after treatment, as shown in Figure 2.

## 4. Discussion

In patients with ICVD, the atherosclerotic plaque shedding in the cerebral artery or neck artery leads to reduced blood supply to the brain, which causes local cerebral blood circulation disorders [29], eventually resulting in transient damage of varying degrees. During the clinical treatment of such patients, promoting blood supply restoration in the brain tissue and clearing blocked blood vessels is most frequently needed. Among them, thrombolytic therapy is a very common treatment, which is to dredge the blocked blood vessels, so that the blood and oxygen supply to the patient's brain tissues can be restored as soon as possible [30]. Among all kinds of thrombolytic therapy, neurointerventional therapy is minimally invasive, which uses guidewires, balloon dilatation, and other related materials to explore and treat the diseased blood vessels through intravascular catheters [31], while DSA can obtain clear and pure vascular images through subtraction, enhancement, and reimaging to achieve vascular visualization. The application of DSA in the process of implementing neurointerventional thrombolytic therapy can better relieve the stenosis and obstruction of diseased blood vessels, restore the blood perfusion of brain tissue, control the development of patients' condition, and effectively improve patient prognosis [32].

This study compared the short-term therapeutic efficacy, cerebral hemodynamics, VEF, and OS indexes of ICVD patients treated with conventional IVT and those with DSA-guided neurointerventional thrombolysis. The results showed a significantly higher ORR in patients receiving DSA combined with neurointerventional thrombolysis compared those with conventional IVT alone, similar to the research of Li et al. [33]. Besides, we found decreased NIHSS scores in both cohorts after treatment, especially in OG. Thrombolytic therapy can promote cerebral vascular

TABLE 4: Comparison of cerebral hemodynamic indexes.

Time point	Groups	$Q_m$ (mL/s)	$V_m$ (cm/s)	$W_v$ (m/s)	$Z_{cv}$ (kPa·s/m)	$R_v$ (kPa·s/m)
Before treatment	Conventional group ( $n = 79$ )	$3.36 \pm 0.77$	$8.13 \pm 2.26$	$25.10 \pm 4.72$	$146.82 \pm 20.38$	$84.17 \pm 13.85$
	Observation group ( $n = 83$ )	$3.20 \pm 0.80$	$8.26 \pm 2.24$	$25.96 \pm 4.46$	$146.34 \pm 24.32$	$83.20 \pm 15.97$
$t$		1.2959	0.3676	1.1924	0.1358	0.4121
$P$		0.1969	0.7136	0.2349	0.8921	0.6808
After treatment	Conventional group ( $n = 79$ )	$4.01 \pm 0.65^*$	$10.78 \pm 2.49^*$	$21.44 \pm 4.81^*$	$90.57 \pm 17.47^*$	$59.56 \pm 11.77^*$
	Observation group ( $n = 83$ )	$4.67 \pm 1.10^\#$	$12.77 \pm 2.83^\#$	$18.26 \pm 4.26^\#$	$82.12 \pm 14.16^\#$	$53.60 \pm 11.23^\#$
$t$		4.6198	4.7423	4.4597	3.3896	3.2982
$P$		<0.0001	<0.0001	<0.0001	0.0008	0.0011

Notes: \* $P < 0.05$  vs. the conventional group before treatment;  $^\#P < 0.05$  vs. the observational group before treatment.

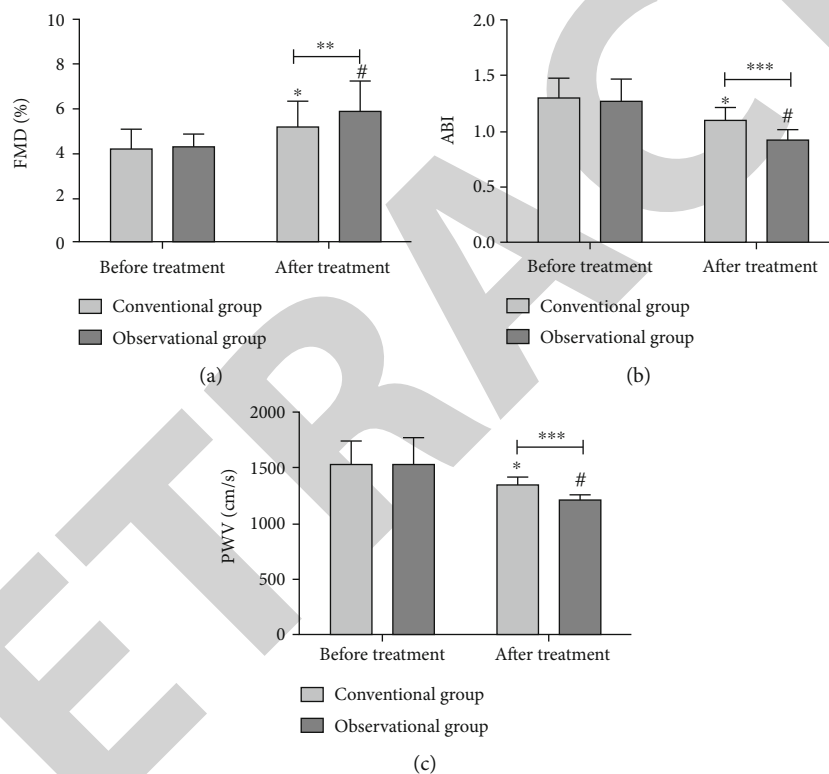


FIGURE 1: Comparison of vascular endothelial function. (a) Comparison of FMD; (b) comparison of ABI; (c) comparison of PWV; \* $P < 0.05$  vs. the conventional group before treatment;  $^\#P < 0.05$  vs. the observational group before treatment; \*\* $P < 0.01$  and \*\*\* $P < 0.001$ .

recanalization and restore cerebral blood perfusion, which is conducive to relieving symptoms of neurological deficits and promoting patients' rehabilitation. As a targeted administration through guidewires and catheters under the support of DSA and other imaging means, neurointerventional thrombolysis can directly act on the diseased blood vessels and increase the contact area between thrombolytic drugs and thrombus, playing a positive role in promoting the recovery from neurological deficits. Further, we analyzed cerebral hemodynamics and found improvements in related indexes in both groups after treatment, suggesting improved blood supply of arterial vascular bed and significantly increased

cerebral blood flow after thrombolytic therapy. Moreover, the improvement was more significant in OG, which indicates that neurointerventional thrombolysis on the basis of IVT is beneficial to improve cerebral hemodynamics, promote cerebral circulation recovery, and relieve the symptoms of ischemia, hypoxia, and neurological function damage. In the research of Yang et al. [34], insufficient blood supply to the brain would cause excessive lactic acid production and accumulation, resulting in acidosis, a process that is an important mechanism of neuronal damage. DSA-guided neurointerventional thrombolysis can effectively improve cerebral hemodynamics and blood circulation, which is



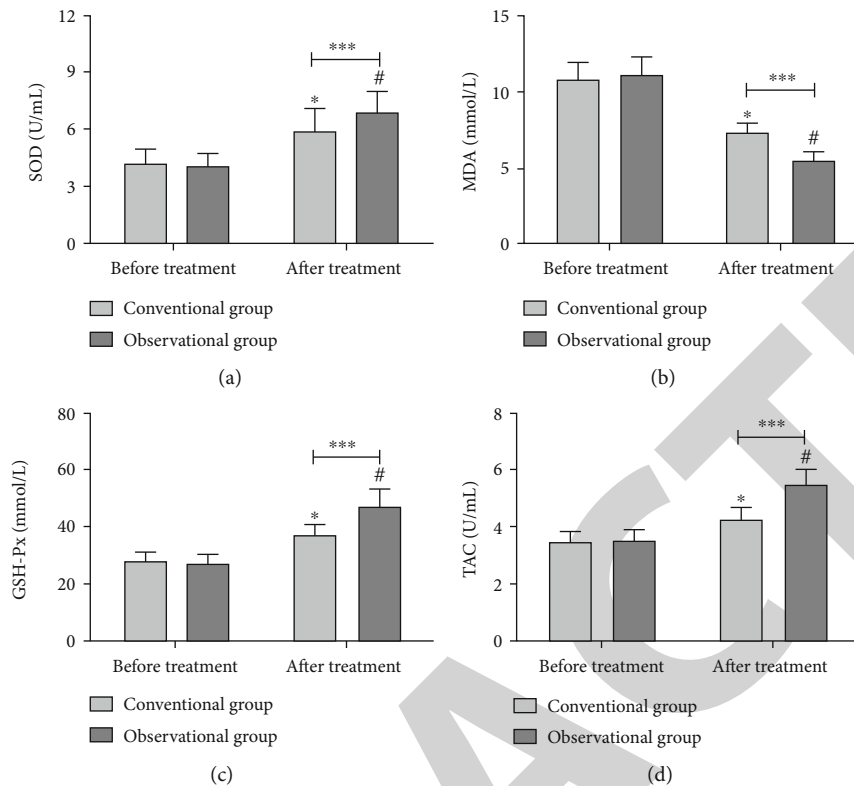


FIGURE 2: Comparison of oxidative stress indexes. (a) Comparison of SOD; (b) comparison of MDA; (c) comparison of GSH-Px; (d) comparison of TAC; \* $P < 0.05$  vs. the conventional group before treatment; # $P < 0.05$  vs. the observational group before treatment; \*\*\* $P < 0.001$ .

conductive to early and adequate blood perfusion of reversible injured neurons and alleviation of ischemia and hypoxia, thus improving neurological function.

ED is the earliest event of inflammatory injury and vascular damage after ischemia reperfusion [35]. Following ischemia, endothelial cells and astrocytes produce numerous chemokines and cytokines that induce the expression of adhesion molecules on endothelial cells, causing leukocyte adhesion and degrading endothelial tight junction proteins and extracellular matrix [36]. Therefore, inhibiting this inflammatory reaction can reduce ischemic infarct size and alleviate neurological deficits. In this study, FMD increased statistically while ABI and PWV decreased obviously after treatment in the two groups, with more significant changes in OG. FMD is an effective index to reflect the structural and functional integrity of vascular endothelial cells [37]; ABI and PWV can be used to predict the risk of atherosclerosis. The higher the ABI and PWV, the worse the vascular elasticity, and the greater the probability of developing atherosclerosis and cerebrovascular events [38]. In addition, OS is the main factor causing nerve injury after cerebral infarction [39], which is mainly manifested by increased lipid peroxidation products like MDA and reduced antioxidant enzymes like SOD, GSH-Px, and TAC, leading to increased blood vessel and cell permeability, inducing OS reaction and causing serious impact on nerve cell function. OS plays an important part in acute ischemic stroke pathogenesis [40]. In acute cerebral infarction, oxygen uptake in

brain tissue is insufficient to maintain cellular oxidative metabolism, causing metabolic changes and cell death. The brain, for many reasons, is particularly vulnerable to free radical injury. The brain is rich in polyunsaturated fatty acids, which are particularly susceptible to free radical-induced peroxidation that alters the content of antioxidant enzymes [41]. This research identified lower MDA and higher SOD, GSH-Px, and TAC in OG compared with CG. It suggests that DSA-guided neurointerventional thrombolysis has obvious advantages in improving VEF, which is conducive to restoring vascular endothelial cell structure and function, promoting vasodilation, and increasing cerebral blood supply and flow. At the same time, it downregulates lipid peroxide expression, promotes oxygen free radical scavenging, and relieves oxidative damage to brain tissue, contributing to reduced OS and accelerated neurological recovery.

## 5. Conclusion

To sum up, for the treatment of AICVD, DSA combined with neurointerventional thrombolysis can effectively improve cerebral hemodynamics, reduce VEF damage, alleviate the body's OS response, and promote the recovery of nerve function, which has high clinical popularization value. However, further in-depth research is needed to explore the interaction between DSA and neurointerventional thrombolysis. Besides, the key action sites of the treatment are still

being explored. There is still a long way to go for the wide clinical application of adverse reactions after treatment, and the benefits and risks of treatment should be effectively weighed to ensure the clinical treatment effect.

## Data Availability

The labeled dataset used to support the findings of this study is available from the corresponding author upon request.

## Conflicts of Interest

The authors declare no competing interests.

## References

- [1] G. Lanzino and R. D. Brown, "Introduction: management of ischemic cerebrovascular disease," *Neurosurgical focus*, vol. 36, no. 1, 2014.
- [2] V. J. Del Brutto, S. Chaturvedi, H.-C. Diener, J. G. Romano, and R. L. Sacco, "Antithrombotic therapy to prevent recurrent strokes in ischemic cerebrovascular disease: Jacc scientific expert panel," *Journal of the American College of Cardiology*, vol. 74, no. 6, pp. 786–803, 2019.
- [3] P. Chen, P. Lou, P. Zhang, C. Qiao, T. Li, and Z. Dong, "Trend analysis on the death rate of ischemic heart disease and cerebrovascular disease among Xuzhou residents from 2011 to 2015," *Zhonghua Xin Xue Guan Bing Za Zhi*, vol. 45, pp. 597–607, 2017.
- [4] N. Horie, Y. Tateishi, M. Morikawa et al., "Acute stroke with major intracranial vessel occlusion: characteristics of cardioembolism and atherosclerosis-related in situ stenosis/occlusion," *Journal of Clinical Neuroscience*, vol. 32, pp. 24–29, 2016.
- [5] J. E. Magalhães and P. A. Sampaio Rocha-Filho, "Migraine and cerebrovascular diseases: epidemiology, pathophysiological, and clinical considerations," *Headache: The Journal of Head and Face Pain*, vol. 58, pp. 1277–1286, 2018.
- [6] S. L. Pires, R. J. Gagliardi, and M. L. Gorzoni, "Study of the main risk factors frequencies for ischemic cerebrovascular disease in elderly patients," *Arquivos de Neuro-Psiquiatria*, vol. 62, no. 3B, pp. 844–851, 2004.
- [7] A. Duca and A. Jagoda, "Transient ischemic attacks," *Emergency Medicine Clinics*, vol. 34, no. 4, pp. 811–835, 2016.
- [8] A. Arboix and J. Alió, "Acute cardioembolic cerebral infarction: answers to clinical questions," *Current Cardiology Reviews*, vol. 8, no. 1, pp. 54–67, 2012.
- [9] J. K. Min and Y. Chandrashekar, *Atherosclerosis, stenosis, and ischemia: one primary, one secondary, and one tertiary*, American College of Cardiology Foundation Washington, DC, 11 edition, 2018.
- [10] S. Surma and M. Banach, "Fibrinogen and atherosclerotic cardiovascular diseases—review of the literature and clinical studies," *International Journal of Molecular Sciences*, vol. 23, p. 193, 2022.
- [11] S. Vedantham, G. Piazza, A. K. Sista, and N. A. Goldenberg, "Guidance for the use of thrombolytic therapy for the treatment of venous thromboembolism," *Journal of Thrombosis and Thrombolysis*, vol. 41, no. 1, pp. 68–80, 2016.
- [12] Z. Zivanovic, M. Gubi, D. Vlahovic et al., "Patients with acute lacunar infarction have benefit from intravenous thrombolysis," *Journal of Stroke and Cerebrovascular Diseases*, vol. 28, no. 2, pp. 435–440, 2019.
- [13] C. Wu, D. Wu, J. Chen, C. Li, and X. Ji, "Why not intravenous thrombolysis in patients with recurrent stroke within 3 months?," *Aging and Disease*, vol. 9, no. 2, pp. 309–316, 2018.
- [14] Y. Fan, X. Liao, Y. Pan et al., "Intravenous thrombolysis is safe and effective for the cryptogenic stroke in China: data from the thrombolysis implementation and monitor of acute ischemic stroke in China (tims-China)," *Journal of Stroke and Cerebrovascular Diseases*, vol. 28, no. 1, pp. 220–226, 2019.
- [15] M. D. Wang, X. X. Yin, T. T. Yang et al., "Chinese neurologists' perspective on intravenous thrombolysis for acute ischemic stroke," *Brain and behavior*, vol. 8, article e00882, 2018.
- [16] S. Feng, Q. Yang, M. Liu et al., "Edaravone for acute ischaemic stroke," *Cochrane Database of Systematic Reviews*, vol. 12, 2011.
- [17] K. Blackham, P. Meyers, T. Abruzzo et al., "Endovascular therapy of acute ischemic stroke: report of the standards of practice committee of the society of neurointerventional surgery," *Journal of neurointerventional surgery*, vol. 4, no. 2, pp. 87–93, 2012.
- [18] C. Liu, F. Guo, J. He et al., "Clinical efficacy of neurointerventional arterial catheter thrombolysis in the treatment of cerebral infarction," *Minerva Surgery*, 2021.
- [19] X. Lei, H. Zheng, Y. Wang, and C. Liu, "Observation of the clinical effect of interventional therapy of acute cerebral infarction with digital subtraction angiography," *Chinese Journal of Primary Medicine and Pharmacy*, pp. 3152–3155, 2017.
- [20] B. Taslakian, M. G. Sebaaly, and A. Al-Kutoubi, "Patient evaluation and preparation in vascular and interventional radiology: what every interventional radiologist should know (part 2: patient preparation and medications)," *Cardiovascular and Interventional Radiology*, vol. 39, no. 4, pp. 489–499, 2016.
- [21] S. Jiao, L. Gong, Z. Wu et al., "Assessment of the value of 3d-dsa combined with neurointerventional thrombolysis in the treatment of senile cerebrovascular occlusion," *Experimental and Therapeutic Medicine*, vol. 19, no. 2, pp. 891–896, 2020.
- [22] P. Rajbhandari, P. Gurung, S. Rajbhandari et al., "Digital subtraction angiography a door opener for neurosurgical residents who want to perform neurointerventional procedures," *Kathmandu University Medical Journal*, vol. 73, pp. 118–122, 2021.
- [23] J. Roquer, T. Segura, J. Serena, and J. Castillo, "Endothelial dysfunction, vascular disease and stroke: the artico study," *Cerebrovascular Diseases*, vol. 27, Supplement 1, pp. 25–37, 2009.
- [24] C. Zimmermann, M. Wimmer, and R. L. Haberl, "L-arginine-mediated vasoreactivity in patients with a risk of stroke," *Cerebrovascular Diseases*, vol. 17, no. 2-3, pp. 128–133, 2004.
- [25] L. Park, P. Zhou, R. Pitstick et al., "Nox2-derived radicals contribute to neurovascular and behavioral dysfunction in mice overexpressing the amyloid precursor protein," *Proceedings of the National Academy of Sciences*, vol. 105, no. 4, pp. 1347–1352, 2008.
- [26] S. Chrissobolis, A. A. Miller, G. R. Drummond, B. K. Kemp-Harper, and C. G. Sobey, "Oxidative stress and endothelial dysfunction in cerebrovascular disease," *Frontiers in Bioscience-Landmark*, vol. 16, no. 1, pp. 1733–1745, 2011.
- [27] G. Wang, X. Cheng, and X. Zhang, "Use of various ct imaging methods for diagnosis of acute ischemic cerebrovascular disease," *Neural Regeneration Research*, vol. 8, pp. 655–661, 2013.

## *Retraction*

# **Retracted: Microglia Involves in the Immune Inflammatory Response of Poststroke Depression: A Review of Evidence**

### **Oxidative Medicine and Cellular Longevity**

Received 8 January 2024; Accepted 8 January 2024; Published 9 January 2024

Copyright © 2024 Oxidative Medicine and Cellular Longevity. This is an open access article distributed under the Creative Commons Attribution License, which permits unrestricted use, distribution, and reproduction in any medium, provided the original work is properly cited.

This article has been retracted by Hindawi, as publisher, following an investigation undertaken by the publisher [1]. This investigation has uncovered evidence of systematic manipulation of the publication and peer-review process. We cannot, therefore, vouch for the reliability or integrity of this article.

Please note that this notice is intended solely to alert readers that the peer-review process of this article has been compromised.

Wiley and Hindawi regret that the usual quality checks did not identify these issues before publication and have since put additional measures in place to safeguard research integrity.

We wish to credit our Research Integrity and Research Publishing teams and anonymous and named external researchers and research integrity experts for contributing to this investigation.

The corresponding author, as the representative of all authors, has been given the opportunity to register their agreement or disagreement to this retraction. We have kept a record of any response received.

### **References**

- [1] W. Xia, Y. Xu, Y. Gong, X. Cheng, T. Yu, and G. Yu, "Microglia Involves in the Immune Inflammatory Response of Poststroke Depression: A Review of Evidence," *Oxidative Medicine and Cellular Longevity*, vol. 2022, Article ID 2049371, 11 pages, 2022.

## Review Article

# Microglia Involves in the Immune Inflammatory Response of Poststroke Depression: A Review of Evidence

Weili Xia,<sup>1</sup> Yong Xu,<sup>1</sup> Yuandong Gong,<sup>1</sup> Xiaojing Cheng,<sup>1</sup> Tiangui Yu <sup>1</sup>,  
and Gongchang Yu <sup>1,2</sup>

<sup>1</sup>Shandong Mental Health Center, Shandong University, Jinan, Shandong 250014, China

<sup>2</sup>Neck-Shoulder and Lumbocrural Pain Hospital of Shandong First Medical University, Shandong First Medical University and Shandong Academy of Medical Sciences, Jinan, Shandong 250062, China

Correspondence should be addressed to Tiangui Yu; [sdyutg@163.com](mailto:sdyutg@163.com) and Gongchang Yu; [yugongchang@sdfmu.edu.cn](mailto:yugongchang@sdfmu.edu.cn)

Received 5 May 2022; Revised 14 July 2022; Accepted 16 July 2022; Published 2 August 2022

Academic Editor: Anwen Shao

Copyright © 2022 Weili Xia et al. This is an open access article distributed under the Creative Commons Attribution License, which permits unrestricted use, distribution, and reproduction in any medium, provided the original work is properly cited.

Poststroke depression (PSD) does not exist before and occurs after the stroke. PSD can appear shortly after the onset of stroke or be observed in the weeks and months after the acute or subacute phase of stroke. The pathogenesis of PSD is unclear, resulting in poor treatment effects. With research advancement, immunoactive cells in the central nervous system, particularly microglia, play a role in the occurrence and development of PSD. Microglia affects the homeostasis of the central nervous system through various factors, leading to the occurrence of depression. The research progress of microglia in PSD has been summarized to review the evidence regarding the pathogenesis and treatment target of PSD in the future.

## 1. Microglia

Microglia can be transformed into activated microglia post-brain trauma, infection, or other central nervous system diseases. Rapid proliferation and activation of microglia can have various forms and move to the lesion area. Its activation process includes proliferation, chemotaxis, and cytokine secretion. Microglia can secrete many inflammatory cytokines and molecules, inducing immune-inflammatory reactions and increasing the blood-brain barrier (BBB) permeability. On the other hand, activated microglia promote the regeneration of the nerve cells, facilitating nerve repair after acute cerebral stroke [1–3]. When the external stimulus is eliminated, activated microglia gradually return to the resting state. Microglia can be divided into two polarized phenotypes based on their secreted cytokines, namely, M1 and M2 types [4]. M1 microglia account for most activated microglia, mainly expressing surface antigens such as CD16, CD32, and CD86 [5]. M1-type microglia can exert a phagocytic effect through contact with nerve cells or activating the colony-stimulating factor (CSF) and tumor necrosis factor- $\alpha$  (TNF- $\alpha$ ). Moreover, it promotes the synthesis and

secretion of interleukin-1 (IL-1), IL-4, and other inflammatory factors, thereby triggering the immune-inflammatory cascade reaction [6–8]. M2 microglia can be divided into M2a, M2b, and M2c subtypes based on different stimuli. M2a microglia can be generated by IL-4, IL-13, and other stimuli and release IL-10 and other anti-inflammatory factors, thus achieving inflammatory response inhibition and neuroprotection [9–11]. In general, cytokines secreted by activated M1-type microglia have proinflammatory effects, while activated M2-type microglia are essential in nerve repair and plasticity.

## 2. Microglia and Stroke

Different stimuli and pathological environments determine the phenotypes of microglia. Several studies have demonstrated that nerve cells can release cytokines to promote the transformation of M2 to M1. When a stroke occurs, microglia exhibits the characteristics of dynamic change. The early stage of stroke is dominated by the M2 type, which appears 1–3 days after stroke, peaking at 3–5 days, and is sustainable for 14 days. M1-type microglia appeared on

day three and peaked on day 14, revealing the dynamic process of microglia from neuronal protection to nerve injury after stroke [12]. Based on physiological conditions, M1 and M2 microglia maintain a dynamic balance. However, this balance will be disrupted when stimulated with stroke, trauma, inflammation, and other stimuli. Ultimately, the different substances induced by stimulation directly affect whether microglia could protect or damage the nervous system [13].

Microglia can exert a neuroprotective effect by releasing factors such as glial cell-derived neurotrophic factor (GDNF), transforming growth factor- $\beta$  (TGF- $\beta$ ), and P2X7 receptor, involved in  $\text{Ca}^{2+}$  overload inhibition, angiogenesis, and remodeling of the cytoskeleton. On the other hand, microglia can promote the induction of matrix metalloproteinases (MMPs), nitric oxides (NOS), TNF- $\alpha$ , and other inflammatory factors involved in BBB disruption, vasospasm, cellular death, and thrombosis, aggravating the brain injury poststroke [14, 15].

The activation of microglia in the inflammatory response is a “double-edged sword” which plays a dual role in the occurrence and development of ischemic stroke as the first line of defense for central nervous system injury [16, 17]. M1-type microglia mainly produces proinflammatory mediators and additionally plays a cytotoxic role in damaging the nervous system. In contrast, M2-type microglia has protective factors supporting neuronal repair and regeneration. Due to the pleiotropy of microglia during ischemic stroke, its clinical significance deserves further study. Therefore, regulating the activation of microglia and exploring the dynamic changes of microglia after stroke is crucial in the prognosis of ischemic stroke. Future studies will continue to explore how to promote the M2-type polarization of microglia, thus enabling brain injury repair. Moreover, methods to inhibit the M1-type differentiation of microglia need to be explored to reduce the secretion of inflammatory factors, attenuate the brain damage, and ultimately reduce the degree of cerebral ischemia injury and promote functional recovery of the brain tissue [18].

### 3. Ischemic Stroke and Depression

Stroke is the leading cause of death, disability, and reduced life span worldwide, and its incidence and prevalence are increasing with age [19, 20]. According to the World Health Organization (WHO) report, 15 million people suffer from stroke yearly, which significantly burdens society [20, 21]. Poststroke depression (PSD) is the most common noncognitive neuropsychiatric complication, and about 30% of patients after stroke have depression [22]. The major clinical manifestations are depressed mood, significant changes in appetite or body mass, low self-worth, sleep disorders, fatigue, inattention, and suicidal tendencies [23]. PSD harms physical, cognitive, and functional rehabilitation, reduces the survival rate, and delays the recovery among stroke patients, thereby becoming a severe social and public health problem [24–27].

The prevalence of PSD is associated with the time point of stroke onset, and about 30% of stroke survivors are affected within five years after stroke [28]. Previous studies have shown that the cumulative incidence of depression

after stroke is 39%–52%, usually occurring in the first month after stroke, then gradually increasing and reaching its peak around six months [29]. Another study assessed the occurrence of PSD at three and 12 months after stroke, with a rate of 27.6% at three months and 24.8% at 12 months [30]. Based on the severity of PSD, it is divided into mild, moderate, and severe types. A previous study revealed that 57% of patients after stroke have PSD, 33% with mild depression, 20% with moderate depression, and 4% with severe depression [31]. The prevalence of PSD varies among different studies. In the investigation of outpatients after stroke, it was observed that the prevalence of mild PSD was about 23.9%, and that of severe PSD was approximately 24.0%. Community patients had the lowest prevalence, 14% with severe depression and 9% with low depression. In hospitals, including emergency and convalescent patients, the prevalence of major depression was 21.6%. However, among the discharged patients after stroke, the prevalence rate of major depression was 24.0% [32].

The etiology of PSD includes psychosocial and biological factors. In the first year after stroke, patients with PSD depicted more neurological dysfunction, poorer recovery outcomes, and higher morbidity and mortality. Therefore, it is vital to identify the risk factors for PSD at an early stage. PSD risk factors include smoking, mild global cognitive impairment, female gender, less education, exposure to stressful life events in the months leading up to stroke, and comorbidities like diabetes and hypertension [33, 34]. Gender is the most frequently studied risk factor in PSD with controversial results [35, 36]. Other risk factors of PSD include stroke severity and lesion location [37–41].

The pathogenesis of PSD is complex, with many processes. The widely studied mechanism is the neurotransmitter imbalance, a popular theory for the pathogenesis of PSD [42–45]. Neurons can secrete a variety of monoamine neurotransmitters, such as 5-hydroxytryptamine (5-HT) and norepinephrine (NE). 5-HT exists in mammalian brain tissues, especially in the cortex and synapses. 5-HT is catalyzed by monoamine oxidase into 5-hydroxytryptophan and 5-hydroxyindoleacetic acid, excreted through the urine. Decreasing 5-HT concentration can lead to depressive symptoms, including low mood and lack of confidence. In contrast, the reduction of NE concentration causes the decline of emotion, cognitive function, and activity regulation ability [46–48]. A decrease in monoamine transmitters is inversely related to the severity of depression. The possible explanation for this may be because, among the brain regions involved in emotion regulation, the amygdala, prefrontal lobe, and hypothalamus are dominant, which play a transmitter regulation role by influencing the release of NE and 5-HT [49–51]. Stroke lesions interrupt the neural pathways of NE and 5-HT release, reducing monoamine neurotransmitters in the brain, which contribute to depression [52–54]. Previous studies depicted that the increased activity of monoamine oxidase in PSD patients increases 5-HT catabolism and decreases its function, causing neurological dysfunction of the limbic system, reticulate structure, and midline region of the brain stem, thereby aggravating depressive symptoms [55–57].

In addition, PSD is associated with dysregulation of BDNF, an essential neurotrophic factor in the hippocampus, cerebral cortex, and cerebellum. It binds to tyrosine kinase receptor B (TrkB) and plays a crucial neurotrophic role [58–61]. Its functions include nourishing damaged neurons, regulating neural plasticity, depicting a vital role in the survival, differentiation, growth, and postinjury repair of neurons, and participating in the initiation and development of depression, regarded as a landmark indicator for the diagnosis of depression [62, 63]. Many studies have revealed that the expression of BDNF and its high-affinity receptor TrkB protein in the thalamus decrease after PSD, indicating PSD occurrence is tightly associated with BDNF level, and the lesser the production of BDNF, the more likely PSD will occur [64, 65]. Infantino et al. found that the MED1/BDNF/TrkB pathway is involved in thalamic hemorrhage-induced pain and depression by regulating the activation of microglia [66]. A recently published prospective multicenter cohort study that enrolled 530 patients with minor stroke indicates that the important markers affecting PSD at three months are BDNF in females [67].

Moreover, inflammation is also involved in PSD development [68, 69]. Considerable evidence indicates that inflammation is involved in the occurrence and development of PSD through related inflammatory pathways by producing inflammatory mediators [70, 71]. Studies have suggested that brain injury during stroke stimulates the body to produce a rapid immune regulatory response. The peripheral immune system recruits inflammation-related cells and develops inflammation-related factors, which migrate to the brain injury area through the damaged blood-brain barrier for immune regulation [72–75]. The imbalance of homeostasis in the inflammatory state alters the endocrine function of nerve cells. It influences the balance of neurotransmitter secretion in the brain, reducing the synthesis and secretion of monoamine neurotransmitters, causing PSD [76–78]. P2X4 receptors on the immune cells modulate the inflammatory response, and receptor deletion protects against stroke acutely. However, it predisposes depression-like behavior chronically after stroke, associated with the P2X4 receptors-induced regulation of BDNF release [79]. Kozak et al. reported no significant relationship between major depression and basal proinflammatory cytokines such as TNF- $\alpha$ , IL-1  $\beta$ , IL-18, and BDNF expression in patients who have experienced an acute ischemic stroke [80]. Other researchers have proposed that stroke causes neurological deficits and loss of daily living and social functions, putting patients in a slow and long-term stress response that activates the hypothalamic-pituitary-adrenal (HPA) axis. Moreover, it causes excessive corticosteroid releasing hormone and sympathetic nerve activity [81–83]. Excessive hormones have toxic effects on nerve cells and affect the production of neurotransmitters; overactivated sympathetic nerve activity causes mood changes in patients leading to corresponding mood and behavior changes. In addition, the activation of the HPA axis can stimulate the upregulation of the expression of inflammatory factors, further promoting the activity of the HPA axis and forming a vicious cycle leading to the onset and persistence of PSD [84]. Presently, there are vari-

ous studies on inflammatory factors involved in PSD occurrence. Studies have shown that elevated levels of cytokines such as IL-1 $\beta$ , IL-6, and TNF- $\alpha$  in serum are related to the incidence of depression [85, 86]. Effective antidepressant therapy reduces serum levels of inflammatory cytokines, including IL-1 $\beta$ , TNF- $\alpha$ , and IL-6, in depressed patients [87]. Neutrophil-to-lymphocyte (NLRs) and platelet-to-lymphocyte ratios (PLRs) are also associated with depression. Higher NLRs and PLRs are associated with depression six months after stroke, and the combined index is more meaningful than being alone in the early clinical detection of PSD [88]. A clinical study that enrolled 299 ischemic stroke patients showed that increased NLRs at admission are associated with PSD and could add prognostic information for the early discovery of PSD [89].

There is no clear consensus on the pathogenesis of PSD. Both depression and stroke should be considered to study the pathogenesis of PSD comprehensively. The biological abnormalities and the interrelation between neurotransmitters involve multiple systems and signaling pathways. One single pathogenesis of a specific system or a particular aspect cannot provide a perfect explanation. Although detailed research progress has been made in the neurobiology of PSD, its pathogenesis's etiology has not been fully clarified. Fragmented studies are not linked together. Therefore, exploring the influence of neural cellular signaling pathways on the regulation of neurotransmitters and then revealing their role in the pathogenesis of PSD could become a hotspot of future research.

#### 4. Microglia and PSD

The imbalance of the neuroimmune system could be an essential factor in the pathophysiology of depression [90]. Compared with the control group, mice exposed to chronic unpredicted stress depict significant depressed-like behaviors and increased corticosterone levels. Moreover, the number of microglia in the hippocampus of stressed mice decreases, while certain microglia present malnutrition forms [91, 92]. Chronic stress may contribute to differences in the clinical presentation of stress-induced depression under the control of sex-specific mechanisms by differentially affecting neurons and microglia [93]. A systematic review and meta-analysis, including 69 studies, examined the cerebrospinal fluid, positron emission tomography, and postmortem brain tissue and observed that increased microglia activity and reduction of astrocytes were associated with major depressive disorder [94]. Another systematic review analyzed 51 articles evaluating inflammatory markers in postmortem bipolar disorder brain samples. Fifteen studies evaluated microglial cell markers, indicating a potential link between microglia activation and the occurrence and outcome of bipolar disorder [95]. Animal experiments and autopsy results suggested that microglia could be involved in the onset and progression of depression (Table 1). Activation of microglia has a vital role in the pathogenesis of major psychiatric disorders associated with hippocampal atrophy and disconnection of cognitive structures [96, 97].

TABLE 1: Summary of researches regarding the effect of microglia in poststroke depression.

Ref	Model	Animals	Main findings
92	MCAO/R+CUMS	Sprague-Dawley rats	Foraging exercise improves the behavioral scores, reduces the number of microglia in the frontal lobe and striatum, and downregulates serum levels of IL-6 and the IL-6/IL-10 ratio.
90	MCAO/R+CUMS	Wistar rats	LCN2 may affect PSD by regulating microglial activation in the hippocampus, with the involvement of the P38 MAPK pathway.
134	tMCAO+CUMS	Sprague-Dawley rats	Morinda officinalis oligosaccharides attenuate depressive-like behaviors after stroke by inhibiting hippocampal inflammation through modulating microglial NLRP3 inflammasome.
11	MCAO/R+CUMS	Wistar rats	The mRNA expression of proinflammatory markers (IL-1, TNF- $\alpha$ , iNOS, and IL-1 $\beta$ ), anti-inflammatory markers (CD206), and the M2 microglia marker Arg1 upregulate in the hippocampal region in the PSD group.
61	MCAO+CUMS	Sprague-Dawley rats	Amygdala microglia contribute to PSD pathogenesis and depression-like behaviors by reducing the level of BDNF and TrkB.
25	BCCAO	ICR mice	Inhibition of the fractalkine/CX3CR1 signaling pathway improves depression and cognition via inhibiting microglia activation, promoting OPC maturation and remyelination after cerebral ischemia.
13	MCAO/O+SIR	ICR mice	Neurons and microglia-released IN-18 contribute to depression-like behavior poststroke through activating the IL-18 receptor/NKCC1 signaling pathway.
18	MCAO/R+CUMS	Sprague-Dawley rats	Xingnao Jieyu alleviates PSD by attenuating neuroinflammation, including reduction of Iba1-positive cells, and downregulation of the TNF- $\alpha$ , IL-6, and IL-1 $\beta$ expressions.
129	MCAO/R+CUMS	Sprague-Dawley rats	Curcumin improves PSD by inhibiting neuroinflammation via diminishing the P2X7R-mediated Ca <sup>2+</sup> accumulation in microglia.
96	BCCAO	C57BL/6 mice	Minocycline administration exerts antidepressant and anxiolytic effects by inhibiting microglial activation.
97	BCCAO	ICR mice	Minocycline exerts an antidepressant effect by inhibiting microglia activation, promoting OPC maturation and remyelination.
45	MCAO/R+SIR	C57BL/6 mice	Microglia function-induced IDO1-dependent neurotoxic kynurenine metabolism contributes to the PSD pathogenesis. Aripiprazole reduces depressive-like behavior and cognitive impairment by inhibiting IDO1, HAAO, QUIN, and ROS.
79	MCAO/R	Global or myeloid-specific P2X4R KO and wild-type mice	Global and myeloid-specific P2X4R KO mice show intermediate microglia activation after stroke, with shorter processes, less arborization, and larger soma. Myeloid-specific P2X4R KO mice show increased mRNA levels of proinflammatory cytokines, decreased depression-related gene expression, and reduced proinflammatory cytokine IL-1 $\beta$ in plasma after stroke.
68	Social defeat+4-VO	Sprague-Dawley rats	Progesterone attenuates stress-induced microglia activation by regulating polarized microglia and the inflammatory environment in the hippocampus after ischemic injury.
69	Transient BCCAO	Gerbils	DXT is widely used for the treatment of major depressive disorders. Pretreated DXT exerts neuroprotective effect by attenuating microglia and astrocyte activation and decreasing oxidative stress.
26	MCAO/R	Young and aged Sprague-Dawley rats	HTR2B expression in the infarcted territory may render degenerating neurons susceptible to attack by activated microglia and thus aggravate the consequences of stroke, including anhedonic behavior.
27	Microsphere embolism model	Wistar rats	Anxiety-like behavior is increased in males despite a significant increase in microglial activation following microembolic stroke in both males and females.
14	MCAO/R	C57Bl/6 male	Pair housing enhances sociability and reduces avolitional and anhedonic behavior, which is associated with reducing serum IL-6 and enhancing peri-infarct microglia arginase-1 expression. Social interaction reduces PSD and improves functional recovery.

TABLE 1: Continued.

Ref	Model	Animals	Main findings
15	Microembolism model	Wistar rats	Microembolism infarcts are sufficient to lead to an increase in anxiety- and depressive-like behaviors followed by spatial memory impairment, with no trigger response of microglia, macrophages, or astrocyte. Fluoxetine is a selective serotonin reuptake inhibitor that is widely used in the treatment of major depression including after stroke. Fluoxetine exerts neuroprotective effects associated with marked repressions of microglia activation, neutrophil infiltration, and proinflammatory marker expressions.
135	MCAO/R	Sprague-Dawley rats	

CUMS: chronic unpredictable mild stress; BCCAO: bilateral common carotid artery occlusion; SIR: spatial restraint stress; 4-VO: four-vessel occlusion; PSD: poststroke depression; DXT: duloxetine; LCN2: lipocalin-2; IDO-1: indoleamine 2,3-dioxygenase 1; HAAO: hydroxyanthranilate 3,4-dioxygenase; QUIN: quinolinic acid (QUIN); ROS: reactive oxygen species; KO: knock-out; HTR2B: serotonin receptor 2B.

Various bacterial and viral infections could induce depression [98–101]. These infectious pathogens have a particular affinity for the brain and can induce microglial activation [102, 103]. These pathogens can also induce microglia to secrete proinflammatory cytokines, whose concentration levels have been associated with depression-like symptoms [104–106]. Lipopolysaccharide (LPS) can activate microglia to cause depressive symptoms, whose severity is connected with the level of inflammatory cytokines [107, 108]. LPS also induces depression by activating microglia, and many drugs have exerted an antidepressant effect by inhibiting the activation of LPS-induced microglia [109–111]. O'Connor et al. revealed a pivotal role for interferon- $\gamma$  and tumor necrosis factor- $\alpha$  in inducing indoleamine 2,3-dioxygenase and depressive-like symptoms in response to bacillus Calmette-Guerin [112]. A previous study showed that activation of peripheral blood mononuclear cells correlated with depression in patients with chronic hepatitis C. This suggests a pivotal role of immune cell activation in depression and neurocognitive dysfunction among chronic hepatitis C patients [113]. In addition, the injection of interferon- $\gamma$  and poly(I:C), a Toll-like receptor-3 (TLR3) agonist mimicking the effect of HCV double-strand RNA, caused depression-like symptoms, and the proinflammatory genes were synergistically induced in the hippocampus and prefrontal cortex [105]. The tight association between HCV infection and depression suggests that optimal care for the overall well-being of patients with HCV infection needs adequate knowledge of their psychological status [114]. Infection with human immunodeficiency virus (HIV) has been associated with an increase in the prevalence of depression [115, 116]. HIV infection is associated with neuroinflammation and more significant psychopathological symptoms, which imbalances may mediate in the kynurenic pathway [117]. As the critical kynurenic pathway enzymes that catabolize kynurenine, kynurenine-3-monooxygenase produces neurotoxic metabolites in microglia [118], while kynurenine-aminotransferase II synthesizes kynurenine acid in astrocytes [119]. Targeted intervention that reduces neuroinflammation and increases kynurenine acid in at-risk kynurenine-aminotransferase II-TT-carriers may lessen the depressive symptoms of HIV [120].

The inflammasome is a cytoplasmic protein complex, an essential immune system component [121–123]. Microglia play an important role in activating inflammasome as they carry pattern recognition receptors (PRR) such as the Toll-like receptor, triggering receptor expressed in myeloid cells 2 (TREM2). It recognizes pathogen-associated molecular patterns (PAMP) and damage-associated molecular patterns (DAMP) [124–126]. The microglia membrane is rich in P2X7, activating the NLRP3 inflammasome in the microglia under chronic stress, thus mediating depression-like behavior [127–129]. Therapy such as electroacupuncture, curcumin, and simvastatin exhibit the antidepressant effect and alleviate neuroinflammation by inhibiting the NLRP3 inflammasome and inflammatory mediators [130–135]. Selective serotonin reuptake inhibitors (SSRI) are the first-line treatment for depression. Its representative drug fluoxetine significantly inhibits the NLRP3 inflammasome activation in microglia and relieves depression-like behavior by downregulating NLRP3 [136]. In addition, fluoxetine prevents the exacerbation of cardiovascular dysfunction due to socially isolated depression by activating Nrf2/HO-1 and inhibiting the TLR4/NLRP3 inflammasome signaling pathway [137]. Moreover, clomipramine, perilla aldehyde, cholecalciferol, geraniol, and silymarin also attenuate depressive symptoms by the NLRP3-relative inflammatory response [138–142].

## 5. Conclusion

PSD is common among stroke patients and has a high recurrence rate. Its risk factors and pathophysiological mechanism are still unclear, so it is significant for preventing and treating PSD. Microglia are a vital part of maintaining mental health and a key mediator in managing stress and lifestyle. In the pathophysiological mechanism of depression, microglia could be involved in many processes and play a regulatory role in neuroinflammation, nerve growth, and neuroplasticity. The function of microglia in depression and the sequence of various mechanisms and their interrelation are not clarified. Therefore, understanding the role of microglia in the pathogenesis of depression is of great significance for developing treatment strategies against depression.



## Data Availability

The availability of data and materials is not applicable.

## Conflicts of Interest

The authors declare that they have no competing interests.

## Authors' Contributions

GCY and TGY conceptualized the research project. WLX, YX, and YDG drafted the manuscript. GCY, TGY, and XJC reviewed and modified the manuscript. GCY and TGY supervised the research and led the discussion. All authors approved the final version of the manuscript.

## Acknowledgments

This work was supported by the Major Science and Technology Innovation Project of Shandong Province (2021SFGC0504), the Shandong Provincial Medical and Health Science and Technology Development Plan (202003091037), the Shandong Traditional Chinese Medicine Science and Technology Project (2021Q123 and 2020Z15), and the Natural Science Foundation of Shandong Province (ZR2019MH102).

## References

- [1] X. Hu, R. K. Leak, Y. Shi et al., "Microglial and macrophage polarization—new prospects for brain repair," *Nature Reviews Neurology*, vol. 11, no. 1, pp. 56–64, 2015.
- [2] C. Rawlinson, S. Jenkins, L. Thei, M. L. Dallas, and R. Chen, "Post-ischaemic immunological response in the brain: targeting microglia in ischaemic stroke therapy," *Brain Sciences*, vol. 10, no. 3, p. 159, 2020.
- [3] F. Yu, T. Huang, Y. Ran et al., "New insights into the roles of microglial regulation in brain plasticity-dependent stroke recovery," *Frontiers in Cellular Neuroscience*, vol. 15, article 727899, 2021.
- [4] R. Zhao, M. Ying, S. Gu et al., "Cysteinyl leukotriene receptor 2 is involved in inflammation and neuronal damage by mediating microglia M1/M2 polarization through NF- $\kappa$ B pathway," *Neuroscience*, vol. 422, pp. 99–118, 2019.
- [5] S. Monga, N. Denora, V. Laquintana et al., "The protective effect of the TSPO ligands 2,4-Di-Cl-MGV-1, CB86, and CB204 against LPS-induced M1 pro-inflammatory activation of microglia," *Brain, Behavior, & Immunity-Health*, vol. 5, article 100083, 2020.
- [6] S. Kim and Y. Son, "Astrocytes stimulate microglial proliferation and M2 polarization in vitro through crosstalk between astrocytes and microglia," *International Journal of Molecular Sciences*, vol. 22, no. 16, p. 8800, 2021.
- [7] A. Suzumura, T. Tamaru, M. Yoshikawa, and T. Takayanagi, "Multinucleated giant cell formation by microglia: induction by interleukin (IL)-4 and IL-13," *Brain Research*, vol. 849, no. 1-2, pp. 239–243, 1999.
- [8] A. Quarta, Z. Berneman, and P. Ponsaerts, "Neuroprotective modulation of microglia effector functions following priming with interleukin 4 and 13: current limitations in understanding their mode-of-action," *Brain, Behavior, and Immunity*, vol. 88, pp. 856–866, 2020.
- [9] L. Wei, J. Guo, X. Yu et al., "Role and characteristics of hippocampal region microglial activation in poststroke depression," *Journal of Affective Disorders*, vol. 291, pp. 270–278, 2021.
- [10] X. Hu, P. Li, Y. Guo et al., "Microglia/macrophage polarization dynamics reveal novel mechanism of injury expansion after focal cerebral ischemia," *Stroke*, vol. 43, no. 11, pp. 3063–3070, 2012.
- [11] D. Wu, G. Zhang, C. Zhao, Y. Yang, Z. Miao, and X. Xu, "Interleukin-18 from neurons and microglia mediates depressive behaviors in mice with post-stroke depression," *Brain, Behavior, and Immunity*, vol. 88, pp. 411–420, 2020.
- [12] R. Verma, B. D. Friedler, N. M. Harris, and L. D. McCullough, "Pair housing reverses post-stroke depressive behavior in mice," *Behavioural Brain Research*, vol. 269, pp. 155–163, 2014.
- [13] C. L. Nemeth, M. S. Shurte, D. M. McTigue, C. B. Nemeroff, and G. N. Neigh, "Microembolism infarcts lead to delayed changes in affective-like behaviors followed by spatial memory impairment," *Behavioural Brain Research*, vol. 234, no. 2, pp. 259–266, 2012.
- [14] N. Dudvarski Stankovic, M. Teodorczyk, R. Ploen, F. Zipp, and M. H. H. Schmidt, "Microglia-blood vessel interactions: a double-edged sword in brain pathologies," *Acta Neuropathologica*, vol. 131, no. 3, pp. 347–363, 2016.
- [15] H. Takeda, T. Yamaguchi, H. Yano, and J. Tanaka, "Microglial metabolic disturbances and neuroinflammation in cerebral infarction," *Journal of Pharmacological Sciences*, vol. 145, no. 1, pp. 130–139, 2021.
- [16] Y. Yan, T. Li, D. Wang, B. Zhao, and Q. Zhou, "Antidepressant effect of Xingnao Jieyu decoction mediated by alleviating neuroinflammation in a rat model of post-stroke depression," *Journal of Traditional Chinese Medicine*, vol. 39, no. 5, pp. 658–666, 2019.
- [17] I. Turnbull, R. Clarke, N. Wright et al., "Diagnostic accuracy of major stroke types in Chinese adults: a clinical adjudication study involving 40,000 stroke cases," *The Lancet Regional Health-Western Pacific*, vol. 21, article 100415, 2022.
- [18] Q. Ma, R. Li, L. Wang et al., "Temporal trend and attributable risk factors of stroke burden in China, 1990-2019: an analysis for the Global Burden of Disease Study 2019," *The Lancet Public Health*, vol. 6, no. 12, pp. e897–e906, 2021.
- [19] T. Cumming and A. Brodtmann, "Dementia and stroke: the present and future epidemic," *International Journal of Stroke*, vol. 5, no. 6, pp. 453–454, 2010.
- [20] J. Das and G. K. Rajanikant, "Post stroke depression: the sequelae of cerebral stroke," *Neuroscience and Biobehavioral Reviews*, vol. 90, pp. 104–114, 2018.
- [21] G. L. Lenzi, M. Altieri, and I. Maestrini, "Post-stroke depression," *Revue Neurologique (Paris)*, vol. 164, no. 10, pp. 837–840, 2008.
- [22] L. Gabaldón, B. Fuentes, A. Frank-García, and E. Díez-Tejedor, "Poststroke depression: importance of its detection and treatment," *Cerebrovascular Diseases*, vol. 24, pp. 181–188, 2007.
- [23] B. Du, M. Liang, H. Zheng et al., "Anti-mouse CX3CR1 antibody alleviates cognitive impairment, neuronal loss and myelin deficits in an animal model of brain ischemia," *Neuroscience*, vol. 438, pp. 169–181, 2020.
- [24] A. M. Buga, O. Ciobanu, G. M. Bădescu et al., "Up-regulation of serotonin receptor 2B mRNA and protein in the peri-

- infarcted area of aged rats and stroke patients,” *Oncotarget*, vol. 7, no. 14, pp. 17415–17430, 2016.
- [25] C. L. Nemeth, R. Reddy, M. Bekhbat, J. Bailey, and G. N. Neigh, “Microglial activation occurs in the absence of anxiety-like behavior following microembolic stroke in female, but not male, rats,” *Journal of Neuroinflammation*, vol. 11, no. 1, p. 174, 2014.
- [26] J. M. Gaete and J. Bogousslavsky, “Post-stroke depression,” *Expert Review of Neurotherapeutics*, vol. 8, no. 1, pp. 75–92, 2008.
- [27] M. Volz, S. Ladwig, and K. Werheid, “Gender differences in post-stroke depression: a longitudinal analysis of prevalence, persistence and predictive value of known risk factors,” *Neuropsychological Rehabilitation*, vol. 31, no. 1, pp. 1–17, 2021.
- [28] B. Grabowska-Fudala, K. Jaracz, K. Górna et al., “Depressive symptoms in stroke patients treated and non-treated with intravenous thrombolytic therapy: a 1-year follow-up study,” *Journal of Neurology*, vol. 265, no. 8, pp. 1891–1899, 2018.
- [29] A. Saxena and A. Suman, “Magnitude and determinants of depression in acute stroke patients admitted in a rural tertiary care hospital,” *Journal of Neurosciences in Rural Practice*, vol. 6, no. 2, pp. 202–207, 2015.
- [30] J. P. Chau, D. R. Thompson, A. M. Chang et al., “Depression among Chinese stroke survivors six months after discharge from a rehabilitation hospital,” *Journal of Clinical Nursing*, vol. 19, no. 21–22, pp. 3042–3050, 2010.
- [31] M. Altieri, I. Maestrini, A. Mercurio et al., “Depression after minor stroke: prevalence and predictors,” *European Journal of Neurology*, vol. 19, no. 3, pp. 517–521, 2012.
- [32] Y. Shi, Y. Xiang, Y. Yang et al., “Depression after minor stroke: prevalence and predictors,” *Journal of Psychosomatic Research*, vol. 79, no. 2, pp. 143–147, 2015.
- [33] F. Acciai and M. Hardy, “Depression in later life: a closer look at the gender gap,” *Social Science Research*, vol. 68, pp. 163–175, 2017.
- [34] S. E. Kim, H. N. Kim, J. Cho et al., “Direct and indirect effects of five factor personality and gender on depressive symptoms mediated by perceived stress,” *PLoS One*, vol. 11, no. 4, article e0154140, 2016.
- [35] J. Guo, J. Wang, W. Sun, and X. Liu, “The advances of post-stroke depression: 2021 update,” *Journal of Neurology*, vol. 269, no. 3, pp. 1236–1249, 2022.
- [36] C. Wei, F. Zhang, L. Chen, X. Ma, N. Zhang, and J. Hao, “Retraction note to: factors associated with post-stroke depression and fatigue: lesion location and coping styles,” *Journal of Neurology*, vol. 265, no. 2, p. 451, 2018.
- [37] R. Perrain, D. Calvet, V. Guiraud, L. Mekaoui, J. L. Mas, and P. Gorwood, “Depressive-, cognitive- or stroke-related risk factors of post-stroke depression: which one could better help clinicians and patients?,” *Neuropsychiatric Disease and Treatment*, vol. Volume 17, pp. 1243–1251, 2021.
- [38] Y. Shi, D. Yang, Y. Zeng, and W. Wu, “Risk factors for post-stroke depression: a meta-analysis,” *Frontiers in Aging Neuroscience*, vol. 9, p. 218, 2017.
- [39] E. Zhang and P. Liao, “Brain-derived neurotrophic factor and post-stroke depression,” *Journal of Neuroscience Research*, vol. 98, no. 3, pp. 537–548, 2020.
- [40] X. E. Zhao, Y. He, S. Zhu et al., “Stable isotope labeling derivatization and magnetic dispersive solid phase extraction coupled with UHPLC-MS/MS for the measurement of brain neurotransmitters in post-stroke depression rats administered with gastrodin,” *Analytica Chimica Acta*, vol. 1051, pp. 73–81, 2019.
- [41] S. F. Nabavi, O. M. Dean, A. Turner, A. Sureda, M. Daglia, and S. M. Nabavi, “Oxidative stress and post-stroke depression: possible therapeutic role of polyphenols?,” *Current Medicinal Chemistry*, vol. 22, no. 3, pp. 343–351, 2015.
- [42] X. W. Ji, C. L. Wu, X. C. Wang, J. Liu, J. Z. Bi, and D. Y. Wang, “Monoamine neurotransmitters and fibroblast growth factor-2 in the brains of rats with post-stroke depression,” *Experimental and Therapeutic Medicine*, vol. 8, no. 1, pp. 159–164, 2014.
- [43] Y. S. Koo, H. Kim, J. H. Park et al., “Indoleamine 2,3-dioxygenase-dependent neurotoxic kynurenine metabolism contributes to poststroke depression induced in mice by ischemic stroke along with spatial restraint stress,” *Oxidative Medicine and Cellular Longevity*, vol. 2018, Article ID 2413841, 15 pages, 2018.
- [44] D. Grinchii and E. Dremencov, “Mechanism of action of atypical antipsychotic drugs in mood disorders,” *International Journal of Molecular Sciences*, vol. 21, no. 24, p. 9532, 2020.
- [45] I. O. Blokhin, O. Khorkova, R. V. Saveanu, and C. Wahlestedt, “Molecular mechanisms of psychiatric diseases,” *Neurobiology of Disease*, vol. 146, article 105136, 2020.
- [46] K. Seki, S. Yoshida, and M. K. Jaiswal, “Molecular mechanism of noradrenaline during the stress-induced major depressive disorder,” *Neural Regeneration Research*, vol. 13, no. 7, pp. 1159–1169, 2018.
- [47] P. Licznanski and R. S. Duman, “Remodeling of axo-spinous synapses in the pathophysiology and treatment of depression,” *Neuroscience*, vol. 251, pp. 33–50, 2013.
- [48] M. R. Bennett, “The prefrontal-limbic network in depression: modulation by hypothalamus, basal ganglia and midbrain,” *Progress in Neurobiology*, vol. 93, no. 4, pp. 468–487, 2011.
- [49] A. T. Beck, “The evolution of the cognitive model of depression and its neurobiological correlates,” *The American Journal of Psychiatry*, vol. 165, no. 8, pp. 969–977, 2008.
- [50] A. Zahrai, F. Vahid-Ansari, M. Daigle, and P. R. Albert, “Fluoxetine-induced recovery of serotonin and norepinephrine projections in a mouse model of post-stroke depression,” *Translational Psychiatry*, vol. 10, no. 1, p. 334, 2020.
- [51] I. Loubinoux, G. Kronenberg, M. Endres et al., “Post-stroke depression: mechanisms, translation and therapy,” *Journal of Cellular and Molecular Medicine*, vol. 16, no. 9, pp. 1961–1969, 2012.
- [52] J. Weinberger, G. Cohen, and J. Nieves-Rosa, “Nerve terminal damage in cerebral ischemia: greater susceptibility of catecholamine nerve terminals relative to serotonin nerve terminals,” *Stroke*, vol. 14, no. 6, pp. 986–989, 1983.
- [53] L. Turner-Stokes and N. Hassan, “Depression after stroke: a review of the evidence base to inform the development of an integrated care pathway. Part 2: treatment alternatives,” *Clinical Rehabilitation*, vol. 16, no. 3, pp. 248–260, 2002.
- [54] G. Li, Y. Ma, J. Ji, X. Si, and Q. Fan, “Effects of gastrodin on 5-HT and neurotrophic factor in the treatment of patients with post-stroke depression,” *Experimental and Therapeutic Medicine*, vol. 16, no. 6, pp. 4493–4498, 2018.
- [55] C. Wang, C. Wu, Z. Yan, and X. Cheng, “Ameliorative effect of Xiaoyao-jieyu-san on post-stroke depression and its potential mechanisms,” *Journal of Natural Medicines*, vol. 73, no. 1, pp. 76–84, 2019.

- [56] N. Prowse and S. Hayley, "Microglia and BDNF at the crossroads of stressor related disorders: towards a unique trophic phenotype," *Neuroscience and Biobehavioral Reviews*, vol. 131, pp. 135–163, 2021.
- [57] B. Podyma, K. Parekh, A. D. Güler, and C. D. Deppmann, "Metabolic homeostasis via BDNF and its receptors," *Trends in Endocrinology and Metabolism*, vol. 32, no. 7, pp. 488–499, 2021.
- [58] A. Berretta, Y. C. Tzeng, and A. N. Clarkson, "Post-stroke recovery: the role of activity-dependent release of brain-derived neurotrophic factor," *Expert Review of Neurotherapeutics*, vol. 14, no. 11, pp. 1335–1344, 2014.
- [59] H. X. Zhu, L. J. Cheng, R. W. Ou Yang et al., "Reduced amygdala microglial expression of brain-derived neurotrophic factor and tyrosine kinase receptor B (TrkB) in a rat model of poststroke depression," *Medical Science Monitor*, vol. 26, article e926323, 2020.
- [60] E. Castrén and L. M. Monteggia, "Brain-derived neurotrophic factor signaling in depression and antidepressant action," *Biological Psychiatry*, vol. 90, no. 2, pp. 128–136, 2021.
- [61] E. Castrén and M. Kojima, "Brain-derived neurotrophic factor in mood disorders and antidepressant treatments," *Neurobiology of Disease*, vol. 97, pp. 119–126, 2017.
- [62] D. Shan, Y. Zheng, and K. Froud, "Brain-derived neurotrophic factor as a clinical biomarker in predicting the development of post-stroke depression: a review of evidence," *Cureus*, vol. 13, no. 6, article e15662, 2021.
- [63] D. Kotłęga, B. Peda, A. Zembroń-Łacny, M. Gołąb-Janowska, and P. Nowacki, "The role of brain-derived neurotrophic factor and its single nucleotide polymorphisms in stroke patients," *Neurologia i Neurochirurgia Polska*, vol. 51, no. 3, pp. 240–246, 2017.
- [64] R. Infantino, C. Schiano, L. Luongo et al., "MED1/BDNF/TrkB pathway is involved in thalamic hemorrhage-induced pain and depression by regulating microglia," *Neurobiology of Disease*, vol. 164, p. 105611, 2022.
- [65] X. Qiu, H. Wang, Y. Lan et al., "Blood biomarkers of post-stroke depression after minor stroke at three months in males and females," *BMC Psychiatry*, vol. 22, no. 1, p. 162, 2022.
- [66] C. Espinosa-Garcia, I. Sayeed, S. Yousuf et al., "Stress primes microglial polarization during global ischemia: therapeutic potential of progesterone," *Brain, Behavior, and Immunity*, vol. 66, pp. 177–192, 2017.
- [67] T. K. Lee, J. H. Park, J. H. Ahn et al., "Pretreated duloxetine protects hippocampal CA1 pyramidal neurons from ischemia-reperfusion injury through decreases of glial activation and oxidative stress," *Journal of the Neurological Sciences*, vol. 370, pp. 229–236, 2016.
- [68] J. Hu, L. Wang, K. Fan et al., "The association between systemic inflammatory markers and post-stroke depression: a prospective stroke cohort," *Clinical Interventions in Aging*, vol. Volume 16, pp. 1231–1239, 2021.
- [69] L. Zhang, L. Zhang, and R. Sui, "Ganoderic acid A-mediated modulation of microglial polarization is involved in depressive-like behaviors and neuroinflammation in a rat model of post-stroke depression," *Neuropsychiatric Disease and Treatment*, vol. 17, pp. 2671–2681, 2021.
- [70] Y. Wang, J. H. Zhang, J. Sheng, and A. Shao, "Immunoreactive cells after cerebral ischemia," *Frontiers in Immunology*, vol. 10, p. 2781, 2019.
- [71] D. Zhang, J. Ren, Y. Luo et al., "T cell response in ischemic stroke: from mechanisms to translational insights," *Frontiers in Immunology*, vol. 12, p. 707972, 2021.
- [72] C. Couch, K. Mallah, D. M. Borucki, H. S. Bonilha, and S. Tomlinson, "State of the science in inflammation and stroke recovery: a systematic review," *Annals of Physical and Rehabilitation Medicine*, vol. 65, no. 2, article 101546, 2022.
- [73] A. Shao, Z. Zhu, L. Li, S. Zhang, and J. Zhang, "Emerging therapeutic targets associated with the immune system in patients with intracerebral haemorrhage (ICH): from mechanisms to translation," *eBioMedicine*, vol. 45, pp. 615–623, 2019.
- [74] M. S. Abdallah, A. N. Ramadan, H. Omara-Reda et al., "Double-blind, randomized, placebo-controlled pilot study of the phosphodiesterase-3 inhibitor cilostazol as an adjunctive to antidepressants in patients with major depressive disorder," *CNS Neuroscience & Therapeutics*, vol. 27, no. 12, pp. 1540–1548, 2021.
- [75] O. A. Levada and A. S. Troyan, "Poststroke depression biomarkers: a narrative review," *Frontiers in Neurology*, vol. 9, p. 577, 2018.
- [76] R. F. Villa, F. Ferrari, and A. Moretti, "Post-stroke depression: mechanisms and pharmacological treatment," *Pharmacology & Therapeutics*, vol. 184, pp. 131–144, 2018.
- [77] R. Verma, C. G. Cronin, J. Hudobenko, V. R. Venna, L. D. McCullough, and B. T. Liang, "Deletion of the P2X4 receptor is neuroprotective acutely, but induces a depressive phenotype during recovery from ischemic stroke," *Brain, Behavior, and Immunity*, vol. 66, pp. 302–312, 2017.
- [78] H. H. Kozak, F. Uğuz, İ. Kılınc et al., "A cross-sectional study to assess the association between major depression and inflammatory markers in patients with acute ischemic stroke," *Indian Journal of Psychiatry*, vol. 61, no. 3, pp. 283–289, 2019.
- [79] P. B. de la Tremblaye and H. Plamondon, "Alterations in the corticotropin-releasing hormone (CRH) neurocircuitry: insights into post stroke functional impairments," *Frontiers in Neuroendocrinology*, vol. 42, pp. 53–75, 2016.
- [80] D. Radak, I. Resanovic, and E. R. Isenovic, "Changes in hypothalamus-pituitary-adrenal axis following transient ischemic attack," *Angiology*, vol. 65, no. 8, pp. 723–732, 2014.
- [81] T. K. Craft and A. C. Devries, "Vulnerability to stroke: implications of perinatal programming of the hypothalamic-pituitary-adrenal axis," *Frontiers in Behavioral Neuroscience*, vol. 3, p. 54, 2009.
- [82] G. C. Medeiros, D. Roy, N. Kontos, and S. R. Beach, "Post-stroke depression: a 2020 updated review," *General Hospital Psychiatry*, vol. 66, pp. 70–80, 2020.
- [83] S. Kitaoka, "Inflammation in the brain and periphery found in animal models of depression and its behavioral relevance," *Journal of Pharmacological Sciences*, vol. 148, no. 2, pp. 262–266, 2022.
- [84] M. Gałecka, K. Bliźniewska-Kowalska, M. Maes, K. P. Su, and P. Galecki, "Update on the neurodevelopmental theory of depression: is there any 'unconscious code'?", *Pharmacological Reports*, vol. 73, no. 2, pp. 346–356, 2021.
- [85] P. Kopschina Feltes, J. Doorduyn, H. C. Klein et al., "Anti-inflammatory treatment for major depressive disorder: implications for patients with an elevated immune profile and non-responders to standard antidepressant therapy," *Journal of Psychopharmacology*, vol. 31, no. 9, pp. 1149–1165, 2017.

- [86] J. Hu, W. Zhou, Z. Zhou, J. Han, and W. Dong, "Elevated neutrophil-to-lymphocyte and platelet-to-lymphocyte ratios predict post-stroke depression with acute ischemic stroke," *Experimental and Therapeutic Medicine*, vol. 19, no. 4, pp. 2497–2504, 2020.
- [87] H. Chen, X. Luan, K. Zhao et al., "The association between neutrophil-to-lymphocyte ratio and post-stroke depression," *Clinica Chimica Acta*, vol. 486, pp. 298–302, 2018.
- [88] L. Wei, Y. Du, Y. Xie, X. Yu, H. Chen, and Y. Qiu, "Lipocalin-2 regulates hippocampal microglial activation in poststroke depression," *Frontiers in Aging Neuroscience*, vol. 13, article 798335, 2021.
- [89] T. Kreisel, M. G. Frank, T. Licht et al., "Dynamic microglial alterations underlie stress-induced depressive-like behavior and suppressed neurogenesis," *Molecular Psychiatry*, vol. 19, no. 6, pp. 699–709, 2014.
- [90] X. Tao, S. Wu, W. Tang et al., "Alleviative effects of foraging exercise on depressive-like behaviors in chronic mild stress-induced ischemic rat model," *Brain Injury*, vol. 36, no. 1, pp. 127–136, 2022.
- [91] R. Gaspar, C. Soares-Cunha, A. V. Domingues et al., "The duration of stress determines sex specificities in the vulnerability to depression and in the morphologic remodeling of neurons and microglia," *Frontiers in Behavioral Neuroscience*, vol. 16, article 834821, 2022.
- [92] D. Enache, C. M. Pariante, and V. Mondelli, "Markers of central inflammation in major depressive disorder: a systematic review and meta-analysis of studies examining cerebrospinal fluid, positron emission tomography and post-mortem brain tissue," *Brain, Behavior, and Immunity*, vol. 81, pp. 24–40, 2019.
- [93] V. V. Giridharan, P. Sayana, O. F. Pinjari et al., "Postmortem evidence of brain inflammatory markers in bipolar disorder: a systematic review," *Molecular Psychiatry*, vol. 25, no. 1, pp. 94–113, 2020.
- [94] Q. Camargos, B. C. Silva, D. G. Silva et al., "Minocycline treatment prevents depression and anxiety-like behaviors and promotes neuroprotection after experimental ischemic stroke," *Brain Research Bulletin*, vol. 155, pp. 1–10, 2020.
- [95] B. Du, H. Li, H. Zheng et al., "Minocycline ameliorates depressive-like behavior and demyelination induced by transient global cerebral ischemia by inhibiting microglial activation," *Frontiers in Pharmacology*, vol. 10, p. 1247, 2019.
- [96] Z. Karimi, M. Chenari, F. Rezaie, S. Karimi, N. Parhizgari, and T. Mokhtari-Azad, "Proposed pathway linking respiratory infections with depression," *Clinical Psychopharmacology and Neuroscience*, vol. 20, no. 2, pp. 199–210, 2022.
- [97] S. El-Halabi, D. H. Cooper, D. S. Cha et al., "The effects of antidepressant medications on antiretroviral treatment adherence in HIV-positive individuals with depression," *Journal of Affective Disorders*, vol. 300, pp. 219–225, 2022.
- [98] A. Mohammadkhanizadeh and F. Nikbakht, "Investigating the potential mechanisms of depression induced-by COVID-19 infection in patients," *Journal of Clinical Neuroscience*, vol. 91, pp. 283–287, 2021.
- [99] K. Zhang, X. Wang, J. Tu, H. Rong, O. Werz, and X. Chen, "The interplay between depression and tuberculosis," *Journal of Leukocyte Biology*, vol. 106, no. 3, pp. 749–757, 2019.
- [100] N. Cattane, A. C. Vernon, A. Borsini et al., "Preclinical animal models of mental illnesses to translate findings from the bench to the bedside: molecular brain mechanisms and peripheral biomarkers associated to early life stress or immune challenges," *European Neuropsychopharmacology*, vol. 58, pp. 55–79, 2022.
- [101] F. B. Del Guerra, J. L. Fonseca, V. M. Figueiredo, E. B. Ziff, and E. C. Konkiewitz, "Human immunodeficiency virus-associated depression: contributions of immuno-inflammatory, monoaminergic, neurodegenerative, and neurotrophic pathways," *Journal of Neurovirology*, vol. 19, no. 4, pp. 314–327, 2013.
- [102] L. Yarlott, E. Heald, and D. Forton, "Hepatitis C virus infection, and neurological and psychiatric disorders - a review," *Journal of Advanced Research*, vol. 8, no. 2, pp. 139–148, 2017.
- [103] C. Hoyo-Becerra, Z. Liu, J. Yao et al., "Rapid regulation of depression-associated genes in a new mouse model mimicking interferon- $\alpha$ -related depression in hepatitis C virus infection," *Molecular Neurobiology*, vol. 52, no. 1, pp. 318–329, 2015.
- [104] M. G. Frank, K. H. Nguyen, J. B. Ball et al., "SARS-CoV-2 spike S1 subunit induces neuroinflammatory, microglial and behavioral sickness responses: evidence of PAMP-like properties," *Brain, Behavior, and Immunity*, vol. 100, pp. 267–277, 2022.
- [105] C. J. Henry, Y. Huang, A. M. Wynne, and J. P. Godbout, "Peripheral lipopolysaccharide (LPS) challenge promotes microglial hyperactivity in aged mice that is associated with exaggerated induction of both pro-inflammatory IL-1 $\beta$  and anti-inflammatory IL-10 cytokines," *Brain, Behavior, and Immunity*, vol. 23, no. 3, pp. 309–317, 2009.
- [106] T. E. Nicholson and K. W. Renton, "Role of cytokines in the lipopolysaccharide-evoked depression of cytochrome P450 in the brain and liver," *Biochemical Pharmacology*, vol. 62, no. 12, pp. 1709–1717, 2001.
- [107] B. Tastan, B. I. Ario, K. U. Tufekci et al., "Dimethyl fumarate alleviates NLRP3 inflammasome activation in microglia and sickness behavior in LPS-challenged mice," *Frontiers in Immunology*, vol. 12, p. 737065, 2021.
- [108] H. T. Bian, L. Xiao, L. Liang, Y. P. Xie, H. L. Wang, and G. H. Wang, "RGFP966 is protective against lipopolysaccharide-induced depressive-like behaviors in mice by inhibiting neuroinflammation and microglial activation," *International Immunopharmacology*, vol. 101, article 108259, 2021.
- [109] W. Li, Y. Xu, Z. Liu et al., "TRPV4 inhibitor HC067047 produces antidepressant-like effect in LPS-induced depression mouse model," *Neuropharmacology*, vol. 201, p. 108834, 2021.
- [110] J. C. O'Connor, C. André, Y. Wang et al., "Interferon-gamma and tumor necrosis factor-alpha mediate the upregulation of indoleamine 2,3-dioxygenase and the induction of depressive-like behavior in mice in response to bacillus Calmette-Guerin," *The Journal of Neuroscience*, vol. 29, no. 13, pp. 4200–4209, 2009.
- [111] T. Pawlowski, M. Radkowski, K. Małyszczak et al., "Depression and neuroticism in patients with chronic hepatitis C: correlation with peripheral blood mononuclear cells activation," *Journal of Clinical Virology*, vol. 60, no. 2, pp. 105–111, 2014.
- [112] P. Amodio, L. Salari, S. Montagnese et al., "Hepatitis C virus infection and health-related quality of life," *World Journal of Gastroenterology*, vol. 18, no. 19, pp. 2295–2299, 2012.
- [113] L. M. Filiatreau, P. V. Ebasone, A. Dzudie et al., "Prevalence of stressful life events and associations with symptoms of

- depression, anxiety, and post-traumatic stress disorder among people entering care for HIV in Cameroon,” *Journal of Affective Disorders*, vol. 308, pp. 421–431, 2022.
- [114] V. Hémar, M. Hessamfar, D. Neau et al., “A comprehensive analysis of excess depressive disorder in women and men living with HIV in France compared to the general population,” *Scientific Reports*, vol. 12, no. 1, p. 6364, 2022.
- [115] N. Drivsholm, A. D. Knudsen, M. Faurholt-Jepsen et al., “Alterations in the kynurenine pathway of tryptophan metabolism are associated with depression in people living with HIV,” *Journal of Acquired Immune Deficiency Syndromes*, vol. 87, no. 2, pp. e177–e181, 2021.
- [116] S. L. Rodriguez-Zas, C. Wu, B. R. Southey et al., “Disruption of microglia histone acetylation and protein pathways in mice exhibiting inflammation-associated depression-like symptoms,” *Psychoneuroendocrinology*, vol. 97, pp. 47–58, 2018.
- [117] P. Guidetti, G. E. Hoffman, M. Melendez-Ferro, E. X. Albuquerque, and R. Schwarcz, “Astrocytic localization of kynurenine aminotransferase II in the rat brain visualized by immunocytochemistry,” *Glia*, vol. 55, no. 1, pp. 78–92, 2007.
- [118] V. Douet, N. Tanizaki, A. Franke, X. Li, and L. Chang, “Polymorphism of kynurenine pathway-related genes, kynurenic acid, and psychopathological symptoms in HIV,” *Journal of Neuroimmune Pharmacology*, vol. 11, no. 3, pp. 549–561, 2016.
- [119] W. Xu, T. Li, L. Gao et al., “Apelin-13/APJ system attenuates early brain injury via suppression of endoplasmic reticulum stress-associated TXNIP/NLRP3 inflammasome activation and oxidative stress in a AMPK-dependent manner after subarachnoid hemorrhage in rats,” *Journal of Neuroinflammation*, vol. 16, no. 1, p. 247, 2019.
- [120] S. M. Man, R. Karki, and T. D. Kanneganti, “Molecular mechanisms and functions of pyroptosis, inflammatory caspases and inflammasomes in infectious diseases,” *Immunological Reviews*, vol. 277, no. 1, pp. 61–75, 2017.
- [121] A. Thapa, M. Adamiak, K. Bujko et al., “Danger-associated molecular pattern molecules take unexpectedly a central stage in Nlrp3 inflammasome-caspase-1-mediated trafficking of hematopoietic stem/progenitor cells,” *Leukemia*, vol. 35, no. 9, pp. 2658–2671, 2021.
- [122] H. Scheiblich, L. Bousset, S. Schwartz et al., “Microglial NLRP3 inflammasome activation upon TLR2 and TLR5 ligation by distinct  $\alpha$ -synuclein assemblies,” *Journal of Immunology*, vol. 207, no. 8, pp. 2143–2154, 2021.
- [123] X. Fu, H. Zeng, J. Zhao et al., “Inhibition of dectin-1 ameliorates neuroinflammation by regulating microglia/macrophage phenotype after intracerebral hemorrhage in mice,” *Translational Stroke Research*, vol. 12, no. 6, pp. 1018–1034, 2021.
- [124] M. Gallizioli, F. Miró-Mur, A. Otxoa-de-Amezaga et al., “Dendritic cells and microglia have non-redundant functions in the inflamed brain with protective effects of type 1 cDCs,” *Cell Reports*, vol. 33, no. 3, p. 108291, 2020.
- [125] I. A. von Muecke-Heim, C. Ries, L. Urbina, and J. M. Deussing, “P2X7R antagonists in chronic stress-based depression models: a review,” *European Archives of Psychiatry and Clinical Neuroscience*, vol. 271, no. 7, pp. 1343–1358, 2021.
- [126] C. Ren, L. X. Li, A. Q. Dong et al., “Depression induced by chronic unpredictable mild stress increases susceptibility to Parkinson’s disease in mice via neuroinflammation mediated by P2X7 receptor,” *ACS Chemical Neuroscience*, vol. 12, no. 7, pp. 1262–1272, 2021.
- [127] Z. Wang, W. Ren, F. Zhao, Y. Han, C. Liu, and K. Jia, “Curcumin amends Ca(2+) dysregulation in microglia by suppressing the activation of P2X7 receptor,” *Molecular and Cellular Biochemistry*, vol. 465, no. 1–2, pp. 65–73, 2020.
- [128] W. Y. Zhang, Y. J. Guo, W. X. Han et al., “Curcumin relieves depressive-like behaviors via inhibition of the NLRP3 inflammasome and kynurenine pathway in rats suffering from chronic unpredictable mild stress,” *International Immunopharmacology*, vol. 67, pp. 138–144, 2019.
- [129] N. Yue, H. Huang, X. Zhu et al., “Activation of P2X7 receptor and NLRP3 inflammasome assembly in hippocampal glial cells mediates chronic stress-induced depressive-like behaviors,” *Journal of Neuroinflammation*, vol. 14, no. 1, p. 102, 2017.
- [130] E. T. Menze, H. Ezzat, S. Shawky et al., “Simvastatin mitigates depressive-like behavior in ovariectomized rats: possible role of NLRP3 inflammasome and estrogen receptors’ modulation,” *International Immunopharmacology*, vol. 95, p. 107582, 2021.
- [131] N. Yue, B. Li, L. Yang et al., “Electro-acupuncture alleviates chronic unpredictable stress-induced depressive- and anxiety-like behavior and hippocampal neuroinflammation in rat model of depression,” *Frontiers in Molecular Neuroscience*, vol. 11, p. 149, 2018.
- [132] Z. Li, H. Xu, Y. Xu et al., “Morinda officinalis oligosaccharides alleviate depressive-like behaviors in post-stroke rats via suppressing NLRP3 inflammasome to inhibit hippocampal inflammation,” *CNS Neuroscience & Therapeutics*, vol. 27, no. 12, pp. 1570–1586, 2021.
- [133] C. M. Lim, S. W. Kim, J. Y. Park, C. Kim, S. H. Yoon, and J. K. Lee, “Fluoxetine affords robust neuroprotection in the postischemic brain via its anti-inflammatory effect,” *Journal of Neuroscience Research*, vol. 87, no. 4, pp. 1037–1045, 2009.
- [134] R. H. Du, J. Tan, X. Y. Sun, M. Lu, J. H. Ding, and G. Hu, “Fluoxetine inhibits NLRP3 inflammasome activation: implication in depression,” *Neuropsychopharmacology*, vol. 19, no. 9, article pyw037, 2016.
- [135] K. Abu-Elfotuh, A. H. Al-Najjar, A. A. Mohammed, A. S. Aboutaleb, and G. A. Badawi, “Fluoxetine ameliorates Alzheimer’s disease progression and prevents the exacerbation of cardiovascular dysfunction of socially isolated depressed rats through activation of Nrf2/HO-1 and hindering TLR4/NLRP3 inflammasome signaling pathway,” *International Immunopharmacology*, vol. 104, p. 108488, 2022.
- [136] W. Gong, S. Zhang, Y. Zong et al., “Involvement of the microglial NLRP3 inflammasome in the anti-inflammatory effect of the antidepressant clomipramine,” *Journal of Affective Disorders*, vol. 254, pp. 15–25, 2019.
- [137] A. Camargo, A. P. Dalmagro, N. Platt et al., “Cholecalciferol abolishes depressive-like behavior and hippocampal glucocorticoid receptor impairment induced by chronic corticosterone administration in mice,” *Pharmacology, Biochemistry, and Behavior*, vol. 196, article 172971, 2020.
- [138] A. Ashraf, P. A. Mahmoud, H. Reda et al., “Silymarin and silymarin nanoparticles guard against chronic unpredictable mild stress induced depressive-like behavior in mice: involvement of neurogenesis and NLRP3 inflammasome,” *Journal of Psychopharmacology*, vol. 33, no. 5, pp. 615–631, 2019.
- [139] X. Y. Deng, J. S. Xue, H. Y. Li et al., “Geraniol produces antidepressant-like effects in a chronic unpredictable mild stress mice model,” *Physiology & Behavior*, vol. 152, pp. 264–271, 2015.

## Retraction

# Retracted: Delivery of miR-654-5p via SonoVue Microbubble Ultrasound Inhibits Proliferation, Migration, and Invasion of Vascular Smooth Muscle Cells and Arterial Thrombosis and Stenosis through Targeting TCF21

### Oxidative Medicine and Cellular Longevity

Received 8 January 2024; Accepted 8 January 2024; Published 9 January 2024

Copyright © 2024 Oxidative Medicine and Cellular Longevity. This is an open access article distributed under the Creative Commons Attribution License, which permits unrestricted use, distribution, and reproduction in any medium, provided the original work is properly cited.

This article has been retracted by Hindawi following an investigation undertaken by the publisher [1]. This investigation has uncovered evidence of one or more of the following indicators of systematic manipulation of the publication process:

- (1) Discrepancies in scope
- (2) Discrepancies in the description of the research reported
- (3) Discrepancies between the availability of data and the research described
- (4) Inappropriate citations
- (5) Incoherent, meaningless and/or irrelevant content included in the article
- (6) Manipulated or compromised peer review

The presence of these indicators undermines our confidence in the integrity of the article's content and we cannot, therefore, vouch for its reliability. Please note that this notice is intended solely to alert readers that the content of this article is unreliable. We have not investigated whether authors were aware of or involved in the systematic manipulation of the publication process.

Wiley and Hindawi regrets that the usual quality checks did not identify these issues before publication and have since put additional measures in place to safeguard research integrity.

We wish to credit our own Research Integrity and Research Publishing teams and anonymous and named external researchers and research integrity experts for contributing to this investigation.

The corresponding author, as the representative of all authors, has been given the opportunity to register their

agreement or disagreement to this retraction. We have kept a record of any response received.

### References

- [1] T. Wang, X. Tang, Y. Zhang et al., "Delivery of miR-654-5p via SonoVue Microbubble Ultrasound Inhibits Proliferation, Migration, and Invasion of Vascular Smooth Muscle Cells and Arterial Thrombosis and Stenosis through Targeting TCF21," *Oxidative Medicine and Cellular Longevity*, vol. 2022, Article ID 4757081, 24 pages, 2022.

## Research Article

# Delivery of miR-654-5p via SonoVue Microbubble Ultrasound Inhibits Proliferation, Migration, and Invasion of Vascular Smooth Muscle Cells and Arterial Thrombosis and Stenosis through Targeting TCF21

Tao Wang, Xiaoqiang Tang, Yong Zhang, Xiaoqin Wang, Haifeng Shi, Ruohan Yin, and Changjie Pan 

The Department of Radiology, The Affiliated Changzhou No. 2 People's Hospital of Nanjing Medical University, China

Correspondence should be addressed to Changjie Pan; [panchangjie@njmu.edu.cn](mailto:panchangjie@njmu.edu.cn)

Received 28 April 2022; Revised 11 June 2022; Accepted 21 June 2022; Published 19 July 2022

Academic Editor: Anwen Shao

Copyright © 2022 Tao Wang et al. This is an open access article distributed under the Creative Commons Attribution License, which permits unrestricted use, distribution, and reproduction in any medium, provided the original work is properly cited.

**Background.** Abnormal proliferation of vascular smooth muscle cells (VSMCs) is an important cause of vascular stenosis. The study explored the mechanism of inhibition of vascular stenosis through the molecular mechanism of smooth muscle cell phenotype transformation. **Methods.** Coronary heart disease-related genes were screened by bioinformatics, and the target genes of miR-654-5p were predicted by dual-luciferase method and immunofluorescence method. miR-654-5p mimic stimulation and transfection of TCF21 and MTAP into cells. SonoVue microbubble sonication was used to deliver miR-654-5p into cells. Cell proliferation, migration, and invasion were detected by CCK-8, wound scratch, and Transwell. HE and IHC staining were performed to study the effect of miR-654-5p delivery via SonoVue microbubble ultrasound on vessel stenosis in a model of arterial injury. Gene expression was determined by qRT-PCR and WB. **Results.** TCF21 and MTAP were predicted as the target genes of miR-654-5p. Cytokines induced smooth muscle cell proliferation, migration, and invasion and promoted miR-654-5p downregulation; noticeably, downregulated miR-654-5p was positively associated with the cell proliferation and migration. Overexpression of TCF21 promoted proliferation, invasion, and migration, and mimic reversed such effects. miR-654-5p overexpression delivered by SonoVue microbubble ultrasound inhibited proliferation, migration, and invasion of cells. Moreover, in arterial injury model, we found that SonoVue microbubble ultrasound transmitted miR-654-5p into the arterial wall to inhibit arterial thrombosis and stenosis, while TCF21 was inhibited. **Conclusion.** Ultrasound delivery of miR-654-5p via SonoVue microbubbles was able to inhibit arterial thrombosis and stenosis by targeting TCF21.

## 1. Introduction

Atherosclerosis is a systematic and progressive pathological process that can occur in any part of blood vessels in the human body and is the most frequently seen in arteries [1]. Atherosclerosis causes noninflammatory, degenerative, and proliferative lesions of blood vessels, increasing the incidence of cardiovascular and cerebrovascular diseases [2–4]. Pathological diagnosis showed that intravascular thrombosis and stenosis are the main characteristics of atherosclerosis [5]. In recent years, percutaneous coronary intervention (PCI) is often applied to treat patients with coronary artery

stenosis caused by atherosclerosis [6]. However, some patients have vascular stenosis recurrence in the lesions, which not only reduces the therapeutic effect of PCI but also increases the possibility of atherosclerosis and recurrence [7].

At present, it is believed that the abnormal proliferation of the neointimal membrane is the pathophysiological basis of restenosis after PCI during the process of injured vascular repair [8]. The enhancement of proliferation and migration of vascular smooth muscle cells (VSMCs) is an important cause of neointimal hyperplasia after vascular injury [9, 10]. The high elasticity of VSMCs enables them to rapidly

adapt to changes in the surrounding environment, especially when stimulated by extracellular matrix components, cytokines, shear stress, and other factors. VSMCs significantly reduce the expression of their differentiation markers, thereby increasing proliferation, the ability to migrate and synthesize the extracellular matrix involved in neointima formation [11, 12]. Accordingly, the expression of VSMC phenotype plays an important role in vascular diseases. Therefore, understanding the molecular mechanism of VSMC phenotype transformation possibly provides a regulatory target for the prevention and treatment of restenosis after PCI.

In recent years, data indicated that microRNAs (miRNAs) play an important regulatory role in a variety of cardiovascular and cerebrovascular diseases induced by atherosclerotic plaques [13, 14]. Our results indicated that miR-654-5p was expressed in patients with coronary heart disease through bioinformatics analysis, but whether miR-654-5p was involved in the formation of atherosclerotic plaques has not been reported yet. Therefore, this study further explored miR-654-5p, whether 654-5p is involved in the phenotypic transformation process of VSMCs and the degree of vascular stenosis, so as to determine the biological significance of miR-654-5p in regulating atherosclerotic plaques.

TCF21 was predicted as a target gene of miR-654-5p by TargetScan and miRWalk. A study found that TCF21 plays an important role in the activation of proinflammatory gene expression in coronary artery smooth muscle cells [15]. However, to the best of our knowledge, there is currently no research conducted on the molecular mechanism of the regulation of miR-654-5p targeting TCF21 in smooth muscle cell phenotype transformation. Thus, the current study used ultrasound microbubble contrast agent to deliver miR-654-5p into inflammatory-stimulated smooth muscle cells and carotid injury model in rats and explored the impact of the regulation of miR-654-5p in atherosclerotic plaque through targeting TCF21.

## 2. Methods

**2.1. Data Extraction from the GEO Database.** Terms “coronary artery disease” and “miRNAs” were retrieved in the GEO datasets (<https://www.ncbi.nlm.nih.gov/gds>) to obtain the datasets of differentially expressed miRNAs. We obtained the dataset GSE59421 as the basis for differentially expressed miRNA in patients with vascular embolism in the current study. Next, the differentially expressed genes in patients with coronary artery disease and healthy controls were selected to further determine differentially expressed genes, and the intersection of multiple gene sets was shown by Venny 2.1.0 software (<http://bioinfogp.cnb.csic.es/tools/venny/index.html>).

**2.2. Biological Information Analysis.** TargetScan 7.2 ([http://www.targetscan.org/vert\\_72/](http://www.targetscan.org/vert_72/)) and miRWalk (<http://mirwalk.umm.uni-heidelberg.de/>) were used to predict the target gene(s) of miR-654-5p.

**2.3. Cell Culture.** The T/G HA-VSMC cell lines were purchased from American Type Culture Collection (ATCC® CRL-1999™, Manassas, USA). The cells were cultured in Roswell Park Memorial Institute (RPMI) medium 1640 containing 10% fetal bovine serum (FBS, Gibco, USA) at 37°C in a 5% CO<sub>2</sub> atmosphere. VSMCs were treated with interleukin-1 $\beta$  (IL-1 $\beta$ , 40 ng/mL, MBF18, Sigma-Aldrich, USA), tumor necrosis factor- $\alpha$  (TNF- $\alpha$ , 25 ng/mL, T0157, Sigma-Aldrich, USA), platelet-derived growth factor BB (PDGF-BB, 20 ng/mL, P6101, Sigma-Aldrich, USA), and transforming growth factor- $\beta$  (TGF- $\beta$ , 10 ng/mL, T1940, Sigma-Aldrich, USA) for 24 h. After the treatment, CCK-8, wound scratch, Transwell, and qRT-PCR were performed to detect the proliferation, migration, invasion, apoptosis, and miR-654-5p levels, respectively. In addition, VSMCs were treated by different concentrations of PDGF-BB (0 ng/mL, 1 ng/mL, 5 ng/mL, 10 ng/mL, 20 ng/mL, and 40 ng/mL) for 48 h.

**2.4. Transfection.** Cells were seeded into 6-well plates at  $1 \times 10^6$ /mL. The next day, cells were 80-90% confluent and transfected. 20 pmol of scramble, mimics, inhibitor, NC, TCF21, MTAP, and mimics+MTAP (Shanghai Gene Pharmaceutical Co., Ltd., China) were dissolved in 50  $\mu$ L DMEM (Hyclone, USA) and 1  $\mu$ L Lipofectamine 2000 (Invitrogen, USA), respectively. Add it to 50  $\mu$ L DMEM, let stand for 5 min at room temperature, and mix the two. Next, the mixture was added to a 6-well plate and placed in a cell incubator at 37°C with 5% CO<sub>2</sub> for continued cultivation. The medium was changed 24 h after transfection, and the cells were harvested after 72 h of culture.

**2.5. Construction of miR-654-5p Lentiviral Expression Vector.** miR-654-5p primer was designed based on the characteristics of the pLVX-shRNA2 plasmid vector (VT1457, Clontech, USA). miR-654-5p was subjected to PCR amplification, and fragments were separated and purified by 1% agarose gel electrophoresis (T2036, Sigma-Aldrich, USA) and then double-digested by restriction endonucleases BamH I (IVGN0058, Thermo Fisher Scientific, USA) and EcoR I (IVGN0118, Thermo Fisher Scientific, USA) to obtain purified miR-654-5p fragments. The pLVX-shRNA2 plasmid vector was double-digested by BamH I and EcoR I, and as a linearized empty lipid vector, the vector was ligated by purified PCR product under T4 DNA ligase at 16°C overnight. After PCR amplification, positive clones of the PCR product were cultured, and plasmids were extracted using a plasmid extraction kit (K211004A, Thermo Fisher Scientific, USA).

**2.6. Luciferase Activity Assay.** For dual-luciferase reporter assays, 3'UTR of TCF21 sequence containing miR-654-5p binding sites was inserted into a pmirGLO dual-luciferase vector (Promega, USA) to generate wild-type (WT) pmirGLO-TCF21. The mutant (MUT) of TCF21 sequence in miR-654-5p binding sites was synthesized using a Site-Directed Mutagenesis Kit (F542, Thermo Fisher Scientific, USA) and inserted into a pmirGLO dual-luciferase vector to generate MUT pmirGLO-TCF21. Similarly, 3'UTR of DDR1 or MTAP containing the predicted miR-654-5p-



TABLE 1: Primers used in real-time PCR analysis.

Gene	Primer sequence	Species
miR-1	Forward: 5'-TAAAGTGGGGACAGCAAAATGC-3' Reverse: 5'-AGCACAAGGTAGAGAAGGTAGAG-3'	Human
miR-133b	Forward: 5'-CCCCTTCAACCAGCTAGTCG-3' Reverse: 5'-GTGTCGTGGAGTCGGCAATT-3'	Human
miR-431	Forward: 5'-CCGTCATGCAGTCGTATCCA-3' Reverse: 5'-GTATCCAGTGC GTGTCGTGG-3'	Human
miR-654-5p	Forward: 5'-TGC GTCGTATCCAGTGCAAT-3' Reverse: 5'-GTCGTATCCAGTGC GTGTCG-3'	Human
miR-376c	Forward: 5'-TTGTCGTATCCAGTGCAATTGC-3' Reverse: 5'-GTCGTATCCAGTGC GTGTCG-3'	Human
miR-136	Forward: 5'-TGGAGTCGTATCCAGTGCAA-3' Reverse: 5'-GTCGTATCCAGTGC GTGTCG-3'	Human
miR-411	Forward: 5'-ACGGTCGTATCCAGTGCAAT-3' Reverse: 5'-GTCGTATCCAGTGC GTGTCG-3'	Human
miR-299-3p	Forward: 5'-TGGGATGGTAAACCGCTTGT-3' Reverse: 5'-TGTCGTGGAGTCGGCAATTG-3'	Human
miR-337-5p	Forward: 5'-ACGGCTTCATACAGGAGTTGT-3' Reverse: 5'-TGTCGTGGAGTCGGCAATTG-3'	Human
miR-323-3p	Forward: 5'-TTACACGGTTCGACCTCTGTC-3' Reverse: 5'-TGTCGTGGAGTCGGCAATTG-3'	Human
miR-539	Forward: 5'-CCTGGTGTGTGTCGTATCCA-3' Reverse: 5'-GTATCCAGTGC GTGTCG-3'	Human
miR-376a	Forward: 5'-GTAGTCGTATCCAGTGCAATTGC-3' Reverse: 5'-GTCGTATCCAGTGC GTGTCG-3'	Human
miR-410	Forward: 5'-TTCGGTCGTATCCAGTGCAA-3' Reverse: 5'-GTCGTATCCAGTGC GTGTCG-3'	Human
miR-329	Forward: 5'-TCTGGGTTTCTGTTTCGTGTCG-3' Reverse: 5'-GTGTCGTGGAGTCGGCAATT-3'	Human
TCF21	Forward: 5'-TCCTGGCTAACGACAAATACGA-3' Reverse: 5'-TTTCCCGGCCACCATAAAGG-3'	Human
MTAP	Forward: 5'-CAGGCGAACATCTGGGCTTT-3' Reverse: 5'-GGACTGAGGTCTCATAGTGGT-3'	Human
GAPDH	Forward: 5'-GGTGAAGGTCGGAGTCAACG-3' Reverse: 5'-CAAAG TTGTCATGGATGTACC-3'	Human
U6	Forward: 5'-TCGCTTTGGCAGCACCTAT-3' Reverse: 5'-AATATGGAACGCTTCGCAAA-3'	Human

binding sites or MUT sites was, respectively, inserted into pmirGLO dual-luciferase vector, named accordingly as pmirGLO-DDR1-3'UTR-WT, pmirGLO-DDR1-3'UTR-MUT, pmirGLO-MTAP-3'UTR-WT, and pmirGLO-MTAP-3'UTR-MUT. After that, the pmirGLO vector containing WT or MT TCF21, DDR1, or MTAP sequence was, respectively, cotransfected with miR-654-5p mimic into T/G HA-VSMC cells by Lipofectamine 2000 (Invitrogen, USA). After incubation for 48 h, the relative luciferase activ-

ity in the cells was measured using Dual-Luciferase Reporter Assay protocol (Promega, Madison, WI).

*2.7. Construction of Ultrasound Microbubbles and Transfection of Smooth Muscle Cells.* SonoVue ultrasound microbubble contrast agent (Bracco, USA) was dissolved in 5 mL physiological saline to form a microbubble suspension. T/G HA-VSMC cells in logarithmic growth phase were selected and divided into blank group (cells without any

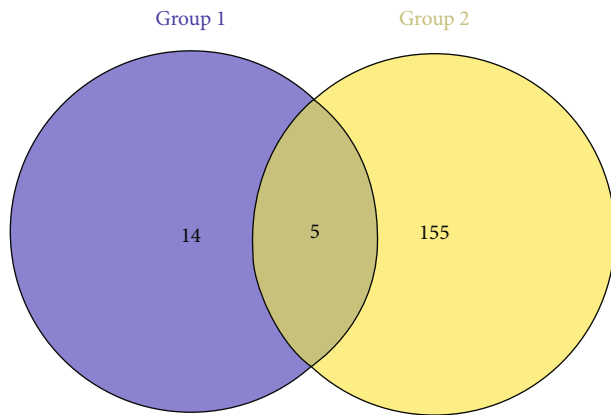


FIGURE 1: Differentially expressed genes for early-onset coronary heart disease. Venny map was drawn to find the differentially expressed miRNA of early onset in the coronary heart disease group and the healthy control group.

TABLE 2: Differentially expressed miRNAs in platelets between patients with premature coronary artery disease and healthy controls.

ID	P value	t	B	logFC
hsa-miR-1	0.03	-2.28	-3.64	-0.49
hsa-miR-133b	0.04	-2.05	-4.10	-0.45
hsa-miR-431	0.01	-2.78	-2.54	-0.37
hsa-miR-654-5p	0.01	-2.65	-2.84	-0.36
hsa-miR-376c	0.02	-2.49	-3.21	-0.35
hsa-miR-136	0.03	-2.19	-3.82	-0.33
hsa-miR-411	0.01	-2.56	-3.05	-0.33
hsa-miR-299-3p	0.01	-2.74	-2.64	-0.32
hsa-miR-337-5p	0.02	-2.41	-3.38	-0.31
hsa-miR-323-3p	0.04	-2.07	-4.06	-0.30
hsa-miR-539	0.01	-2.55	-3.07	-0.30
hsa-miR-376a	0.04	-2.07	-4.05	-0.27
hsa-miR-410	0.06	-1.93	-4.31	-0.25
hsa-miR-329	0.05	-2.02	-4.14	-0.25

treatment), control group (cells cocultured with the plasmid of miR-654-5p), liposome group (cells cocultured with liposomes carrying the miR-654-5p plasmid), SonoVue group (the microbubble contrast agent and the plasmid were immediately added to the cell suspension seeded in a 6-well culture plate, and the suspension was then irradiated by a UVX radiometer (UV Products, Upland, CA)), microbubble group (microbubble contrast agent and the plasmid were immediately added into cell suspension seeded in a 6-well culture plate), ultrasound group (the plasmid was immediately added into cell suspension seeded in a 6-well culture plate, and the suspension was then irradiated by a UVX radiometer), and microbubble ultrasound group (microbubble contrast agent was immediately added into cell suspension seeded in a 6-well culture plate, and then, the suspension was irradiated by a UVX radiometer).

**2.8. Cell Viability.** Cells at logarithmic growth phase were selected, and the cell density was adjusted to  $1 \times 10^5$ /mL in Dulbecco's modified Eagle's medium (DMEM; C11995500BT, Gibco, MA, USA) medium containing 10% FBS. Next, the cells were inoculated into a 96-well plate, and  $10 \mu\text{L}$  cell counting kit-8 (CCK-8, 96992, Sigma-Aldrich, USA) solution was added into each well and incubated for 4 h. Absorbance at 450 nm was determined by enzyme microscopy (Multiskan GO, Shanghai Baji Industrial Co., Ltd., Shanghai, China).

**2.9. Cell Apoptosis.** Cells at logarithmic growth phase were selected, the cell density was adjusted to  $1 \times 10^5$ /mL, and the cells were then washed for four times by PBS and digested by trypsin for 2 min. Next, trypsin was discarded, and 1 mL RPMI-1640 was added into cells, which were repeatedly blown into a single cell fluid. All cell suspensions were transferred into 15 mL centrifugal tube and centrifuged at  $1000 \times g$  for 5 min at  $4^\circ\text{C}$ . Subsequently, the supernatant was discarded and 1 mL RPMI-1640 was added into the centrifugal tube. The cells were resuspended in a  $1 \times$  Annexin binding buffer,  $5 \mu\text{L}$  fluorescein isothiocyanate (FITC) Annexin V, and  $1 \mu\text{L}$  of  $100 \mu\text{g}/\text{mL}$  propidium iodide (PI) (85-BMS500PI, MULTI SCIENCES, Hangzhou, China) solution, and the  $300 \mu\text{L}$   $1 \times$  Annexin binding buffer was added into the cell suspension at room temperature and held for 15 min. Finally, the stained cells were analyzed by flow cytometry.

**2.10. Wound Scratch.** Transfected cells were seeded into 6-well plates at  $5 \times 10^5$  per well. After 24 hours, scratch the cells quickly with a uniform width. After washing the suspension cells, culture the cells with a low serum concentration (1%) medium. Then, the 0 h and 48 h time points were selected to record the cell migration at the same location by photographing, and the migration distance was measured by ImageJ software version 1.8.0. Relative mobility = (0 h scratch width - 48 h scratch width)/0 h scratch width  $\times 100\%$ .

**2.11. Transwell.** After transfection for 24 h, the transfected cells were diluted into a density of  $1 \times 10^6$ /mL and pipetted into the upper chamber of the Transwell containing suspension solution with 0.2 mL FBS-free DMEM, while the complete medium was added into the lower chamber. After incubation for 48 h, the upper side of the polycarbonate membrane was wiped, leaving the underside of the membrane containing invaded cells. Finally, the cells were stained by crystal violet for 15 min at normal atmospheric temperature. Three random areas on each membrane were selected to count the number of the migrated cells under a microscope ( $\times 200$ ). ImageJ software (version 1.8.0) was used to analyze the images in this assay.

**2.12. Colony Formation Assay.** The cells were transfected and digested, counted, and cultured in 12-well plates at 100 cells per well at  $37^\circ\text{C}$  in a 5%  $\text{CO}_2$  atmosphere for 3 weeks, and the conditioned medium was changed every 3 d to observe the formation of clones. The culture was terminated when the number of cloned cells was within 50-150

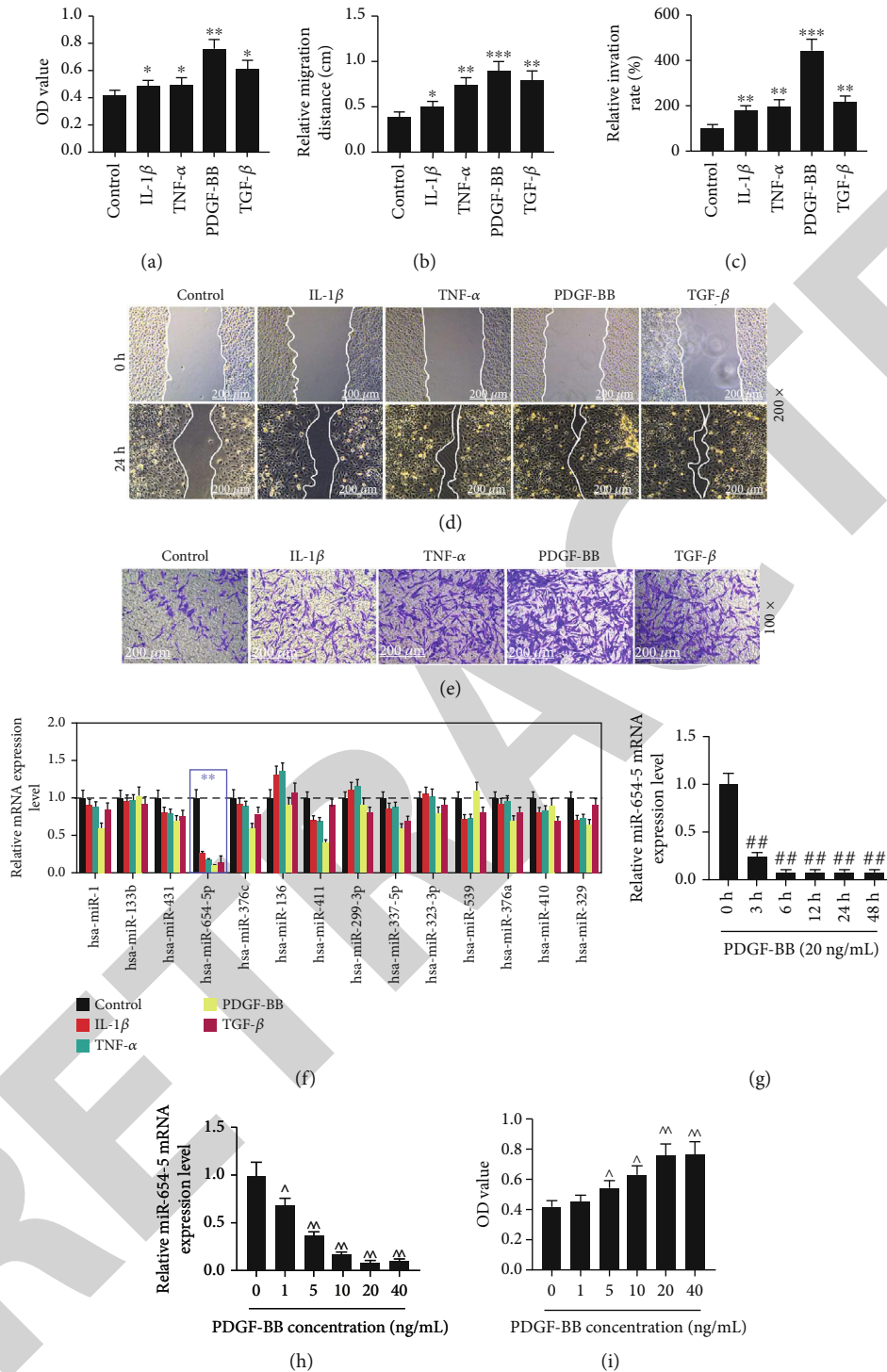


**FIGURE 2:** Effects of growth factors on the growth of VSMCs and miRNA expression. (a) CCK-8 was performed to detect viability of human aortic smooth muscle cell treated by IL-1 $\beta$  (40 ng/mL), TNF- $\alpha$  (25 ng/mL), PDGF-BB (20 ng/mL), and TGF- $\beta$  (10 ng/mL) for 24 h at 37°C in a 5% CO<sub>2</sub> atmosphere ( $n = 3$ , \* $P < 0.05$ , \*\* $P < 0.01$ , and \*\*\* $P < 0.001$  vs. control). (b, d) The migration distance of human aortic smooth muscle cell was detected by wound scratch assay ( $n = 3$ , \* $P < 0.05$ , \*\* $P < 0.01$ , and \*\*\* $P < 0.001$  vs. control). (c, e) The invasion of human aortic smooth muscle cell was detected by Transwell. (f) qRT-PCR was performed to detect the expression of miRNA in human aortic smooth muscle cell treated by IL-1 $\beta$ , TNF- $\alpha$ , PDGF-BB, and TGF- $\beta$  for 24 h at 37°C in a 5% CO<sub>2</sub> atmosphere ( $n = 3$ , \* $P < 0.05$ , \*\* $P < 0.01$ , and \*\*\* $P < 0.001$  vs. control). (g) The effect of different treatment times of PDGF-BB (20 ng/mL) on the expression of miR-654-5p in VSMCs by qRT-PCR. (h) The effect of different treatment concentrations of PDGF-BB (1 ng/mL, 5 ng/mL, 10 ng/mL, 20 ng/mL, and 40 ng/mL) on the expression of miR-654-5p in VSMCs by qRT-PCR. (i) CCK-8 was performed to detect the viability of VSMCs treated by different treatment concentrations of PDGF-BB (1 ng/mL, 5 ng/mL, 10 ng/mL, 20 ng/mL, and 40 ng/mL).

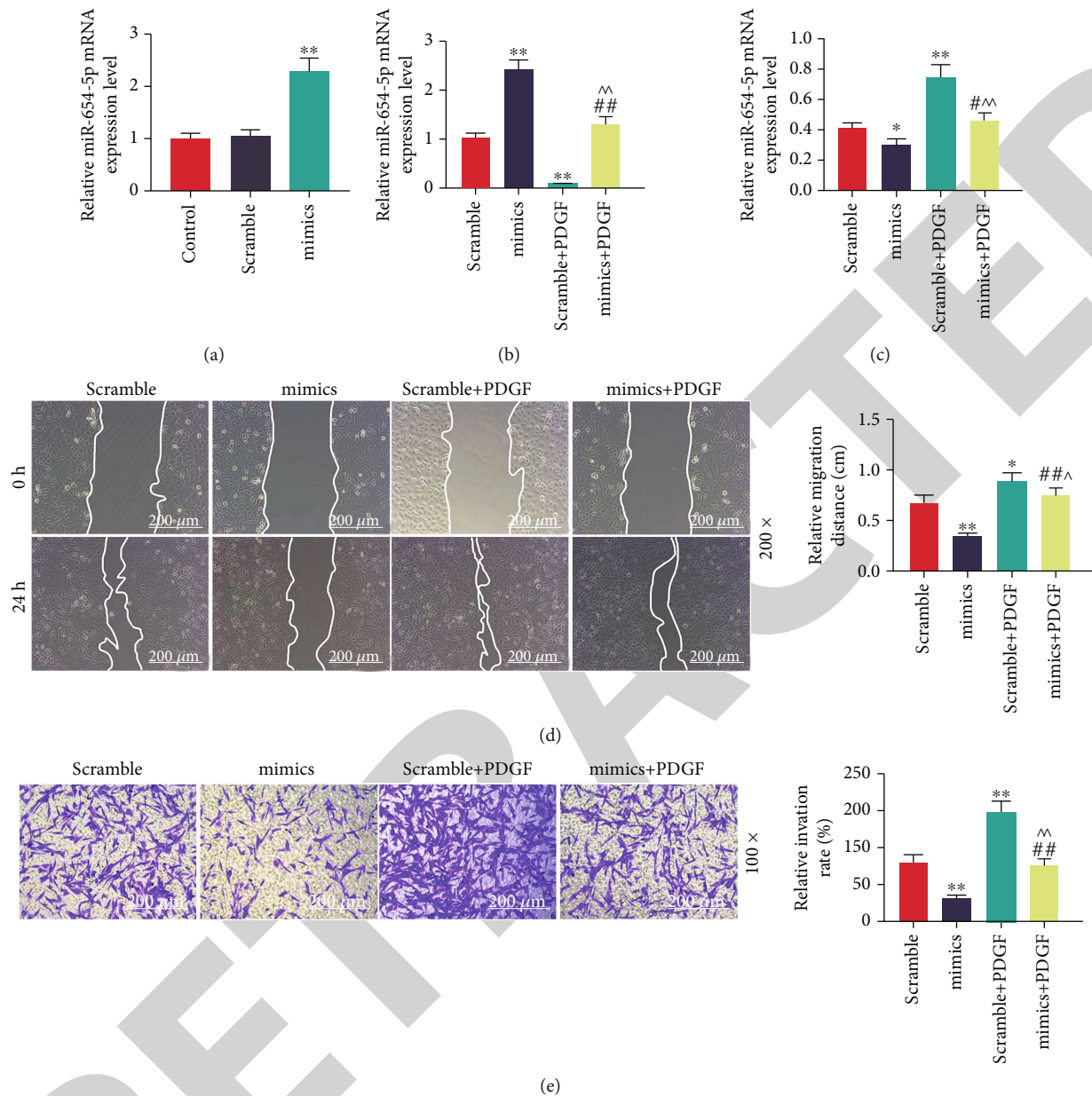
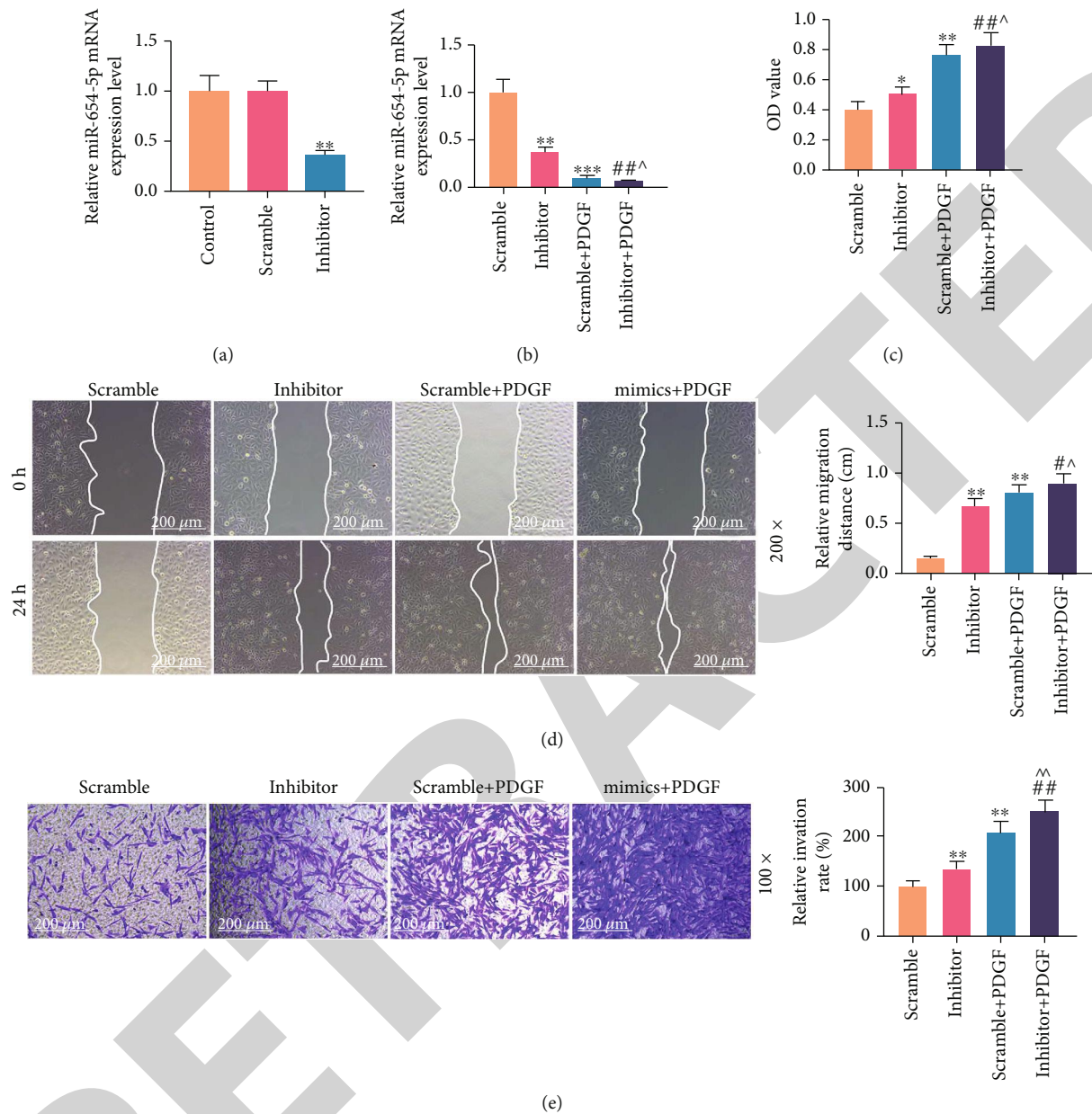


FIGURE 3: Expression of miR-654-5p in PDGF-treated VSMCs. (a) qRT-PCR was performed to detect the miR-654-5p mRNA expression in VSMCs transfected with miR-654-5p mimics. (b) qRT-PCR was performed to detect the expression of miR-654-5p in miR-654-5p mimic-transfected VSMCs treated by PDGF for 24 h. (c) The viability of miR-654-5p mimic-transfected VSMCs treated by PDGF was detected by CCK-8. (d) Wound scratch was performed to detect the migration of miR-654-5p mimic-transfected VSMCs treated by PDGF. (e) Transwell was performed to detect the invasion of miR-654-5p mimic-transfected VSMCs treated by PDGF.

fields, the medium was discarded, and the cells were rinsed twice in Dulbecco's Phosphate-Buffered Saline (DPBS, D8662, Sigma-Aldrich, USA). 1 mL methanol (34860, Sigma-Aldrich, USA) was added into the each well, and the cells were fixed for 15 min. 1 mL Giemsa (999D715, Thermo Fisher Scientific, USA) was added into each well for 30 min. Colony formation rate was calculated by colony formation rate = (number of colonies/number of seeded cells)  $\times$  100%. Each treatment was carried out in triplicate.

**2.13. Immunofluorescence.** The cells were inoculated in the petri dish at the cell density of  $1 \times 10^5$ /mL for cell crawling,

and the cells were divided into scramble-transfected cells, mimic-transfected cells, and scramble-transfected cells treated with 20 ng/mL PDGF and mimic-transfected cells treated with 20 ng/mL PDGF. After the treatment, the cells were centrifuged at  $1000 \times g$  at  $4^\circ\text{C}$  for 5 min, and immunofluorescence was performed for identifying the fluorescent of the cells. Briefly, the cell smear was washed by PBS for three times and then fixed on ice acetone (01000356-25g, Beijing Ouhe Technology Co., Ltd., <http://www.ouhechem.com/>, China) for 15 min. Next, while the cell smear was dried, PBS was used to wash the cells for three times. TCF21/Pod1 antibody (C07617Cy3, Signalway Antibody, USA)

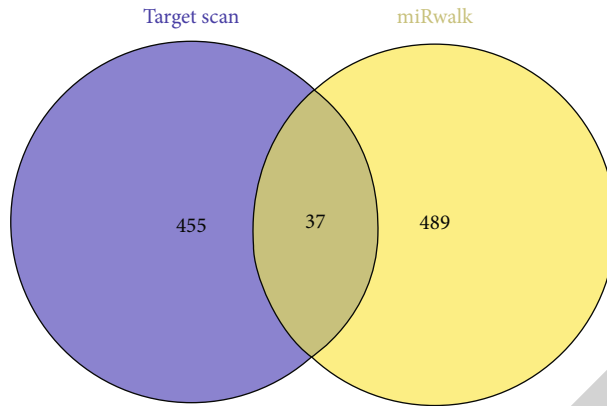


**FIGURE 4:** The effects of miR-654-5p on cell viability, migration, and invasion. (a) qRT-PCR was performed to detect the miR-654-5p mRNA expression in VSMCs transfected with miR-654-5p inhibitor. (b) qRT-PCR was performed to detect the expression of miR-654-5p in miR-654-5p inhibitor-transfected VSMCs treated by PDGF for 24 h. (c) The viability of miR-654-5p inhibitor-transfected VSMCs treated by PDGF was detected by CCK-8. (d) Wound scratch was performed to detect the migration of miR-654-5p inhibitor-transfected VSMCs treated by PDGF. (e) Transwell was performed to detect the invasion of miR-654-5p inhibitor-transfected VSMCs treated by PDGF.

and MTAP antibody (ab23393, 1:100, Abcam, USA) were added into the cells, respectively, and incubated together at 4°C in a heat preservation box incubation. Next, conjugated secondary antibody was added into the cells at 37°C for 2 h, and the cells were washed by PBS for three times and then incubated with DAPI for 3 min. Finally, fluorescence of the cells was determined under a fluorescence microscope (Delta Optical IB-100, Delta Optical, Poland).

**2.14. Source and Grouping of Rats.** The animal model was established using 8-week-old male Sprague-Dawley rats ( $n = 66$ ). Animal experiments were approved by Nanjing

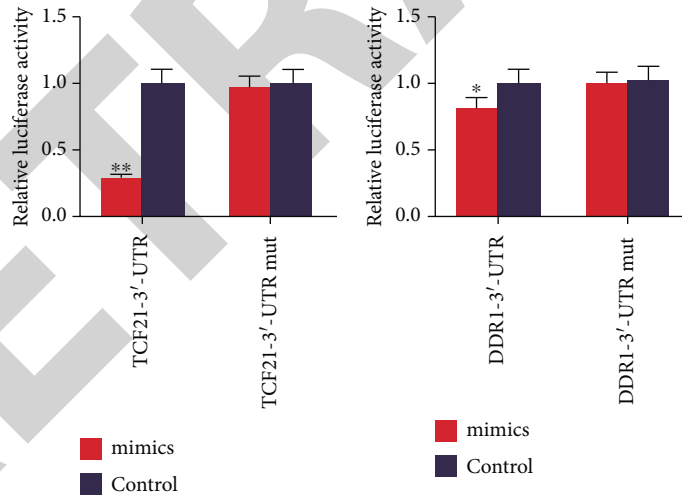
Medical University. Rats were randomly divided into control group ( $n = 6$ , rats were routinely fed), sham-operated control group ( $n = 6$ ), rat vascular injury model group ( $n = 6$ ), blank group ( $n = 6$ , sham-operated), control group ( $n = 6$ , sham-operated rats were injected with miR-654-5p cocultured plasmid in the tail vein), liposome group ( $n = 6$ , cocultured liposomes carrying miR-654-5p plasmid were injected into the tail vein of rats), vascular injury model SonoVue group ( $n = 6$ , microbubble contrast agent and plasmid were injected into rat vascular injury model via tail vein) (UVX radiometer (UV Products, Upland, CA) irradiation), microbubble group ( $n = 6$ , microbubble injury model) (bubble



(a)

Position 1649-1655 of TCF21 3' UTR	5' ...AUACCCUCCAUCACCCCACCAC...
<a href="#">hsa-miR-654-5p</a>	3' CGUGUACAAGACGCC-GGGUGGU
Position 1262-1269 of DDR1 3' UTR	5' ...GCAGGCUGCGCAGGGGCCACCA...
<a href="#">hsa-miR-654-5p</a>	3' CGUGUACAAGACGCCGGGUGGU
Position 259-265 of MTAP 3' UTR	5' ...AGGGGAAAAAAAAAACCCACCAU...
<a href="#">hsa-miR-654-5p</a>	3' CGUGUACAAGACGCCGGGUGGU

(b)



(c)

(d)

FIGURE 5: Continued.

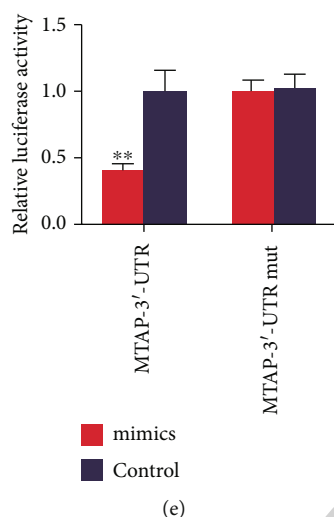


FIGURE 5: Target gene prediction of miR-654-5p. (a) The targeted gene of miR-654-5p was detected by TargetScan 7.1 and miRDB. (b) TargetScan 7.1 was used to predict the target gene of miR-654-5p. (c) Dual-luciferase reporter assay was used to analyze the fluorescence activity of TCF21 in overexpression of miR-654-5p. (d) Dual-luciferase reporter assay was used to analyze the fluorescence activity of DDR1 in overexpressed miR-654-5p. (e) Dual-luciferase reporter assay was used to analyze the fluorescence activity of MTAP in overexpression of miR-654-5p.

contrast agent and plasmid were injected into rat vascular injury model via tail vein), ultrasound group ( $n = 6$ , plasmid was injected into rat vascular injury model through tail vein and then irradiated with UVX radiometer), and microbubble ultrasound ( $n = 6$ , microbubble contrast agent was injected into the tail vein of a rat model of vascular injury and irradiated with a UVX radiometer).

**2.15. Establishment of Rat Vascular Injury Model.** Each rat was intraperitoneally injected with 30-40 mg/kg pentobarbital hydrochloride (69020181, Sinopharm Chemical Reagent Beijing Co., Ltd, (<http://www.crc-bj.com/Products.aspx/>), China). The rat was successfully anesthetized, and an incision of about 3 cm was made in the middle of the rat's neck. The left common carotid artery is found next to the left trachea, dividing the vagus and sympathetic nerves around the artery. A small opening was made at the distal end of the vessel, and a 2.0 Fogarty catheter microembolization ball (Edwards Lifesciences, Irvine, California) was injected into the vessel along the incision. When the rats could breathe stably, endotracheal intubation was removed, and 1000,000 units of penicillin sodium (SP303201, Sinopharm Chemical Reagent Beijing Co., Ltd, (<http://www.crc-bj.com/Products.aspx?/>), China) were injected into the rats after the operation. The rats were then fed by general feeding. Similarly, 0.1 mL normal saline was injected into the rats in the sham operation control group. Blood flow velocity in rat vascular injury model was measured by intelligent analysis. Vascular diameter in rat vascular injury model was measured by straightedge.

**2.16. Hematoxylin and Eosin (HE) Staining.** The sections with rat aortic tissue were stained by HE staining. The tissues were fixed by formaldehyde (SF877503, Sinopharm Chemical Reagent Beijing Co., Ltd., (<http://www.crc-bj.com/Products.aspx?/>), China), dehydrated by gradient alcohol (80%, 90%, 95%, 100%), made transparent by xylene (10023418, Sinopharm Chemical Reagent Beijing Co. Ltd., <http://www.crc-bj.com/default.aspx>, China), immersed and embedded in wax, and finally made into tissue slices ( $4 \mu\text{m}$ ). Slides containing tissue were deparaffinized in xylene, dephenylated with 100%, 95%, 80%, and 70% ethanol for 2 min, and then rinsed twice with distilled water to rehydrate. The slides were stained by hematoxylin for 20 min and then washed under running water to remove the blue. The slides were placed in acidification solution (hydrochloric acid (10011008, Sinopharm Chemical Reagent Beijing Co., Ltd., <http://www.crc-bj.com/default.aspx>, China):75% ethanol=1:99) for 1 min to remove cytoplasm blue. The slides were washed under tap water for 10 min, then stained by eosin (Beijing Zhongshan Jinqiao Biotechnology Co., Ltd., <http://med9519.yixie8.com/>, China) for 15 min, and then dehydrated in 100% ethanol for 15 min. Xylene was made transparent in 15 min; finally, neutral gum was used to seal the film, and an optical microscope (CKX31, Olympus, Japan) was used to observe the pathological changes of rat aortic tissues.

**2.17. Immunohistochemical Staining (IHC).** After dewaxing and hydrating rat aortic tissue sections, the sections were soaked in citrate buffer (pH 6.0) and heated in a microwave oven for 10 minutes for antigen retrieval. After rinsing with distilled water for 2 min, the sections were soaked in 3%  $\text{H}_2\text{O}_2$  for 10 min at room temperature to eliminate endogenous peroxidase activity. Anti-TCF21 antibody (ab32981, 1:100, Abcam, USA) and anti-MTAP antibody (ab126770, 1:100, Abcam, USA) were added to the sections and incubated overnight at  $4^\circ\text{C}$ . Sections were then incubated with goat anti-rabbit IgG H&L (HRP) (1:1000; ab205718, Abcam, USA) for 30 minutes at  $37^\circ\text{C}$ . Sections were stained

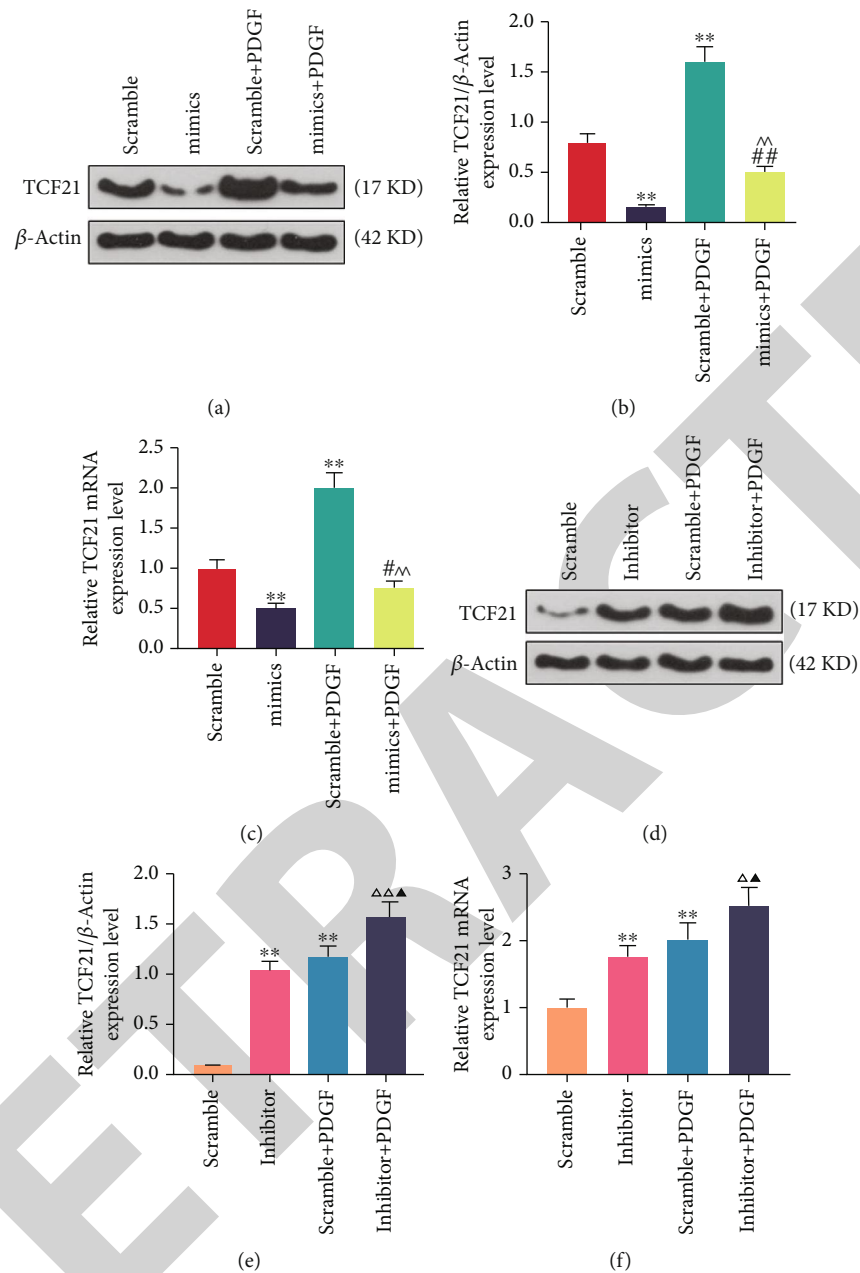


FIGURE 6: Effects of miR-654-5p on TCF21 expression in VSMCs. (a, b) Western blotting was performed to determine the expression level of TCF21 in miR-654-5p mimic-transfected VSMCs treated by PDGF. (c) qRT-PCR was used to detect the TCF21 mRNA expression level in miR-654-5p mimic-transfected VSMCs treated by PDGF. (d, e) Western blotting was used to determine the expression level of TCF21 in miR-654-5p inhibitor-transfected VSMCs treated by PDGF. (f) qRT-PCR was used to detect the TCF21 mRNA expression level in miR-654-5p inhibitor-transfected VSMCs treated by PDGF.

with DAB Horseradish Peroxidase Chromogenic Kit (Beyotime, Shanghai, China) and observed under a light microscope (CKX31, Olympus, Japan).

**2.18. Quantitative Reverse Transcription-Polymerase Chain Reaction (RT-PCR).** Total RNAs in cells and tissues were extracted using Trizol reagent (15596018, Thermo Fisher Scientific, USA), and NanoDrop (FSC-6539918, (<http://eGeneralMedical.com/>), USA) was used to determine RNA concentration and purity. Total RNA (1 μg) was converted into cDNA using a SuperScript II first-strand cDNA synthe-

sis system (Invitrogen, USA). The mRNA expression levels were determined by SYBR-Green PCR Master Mix (Thermo Fisher Scientific, USA) in the 7500 Real-Time PCR System (Thermo Fisher Scientific, USA). The PCR program was set as follows: pretreatment at 95°C for 30 s, at 60°C for 30 s, at 60°C for 30 s for 45 cycles. The  $2^{-\Delta\Delta CT}$  method was used to determine the expression levels of RT-PCR products [16]. Primers are summarized in Table 1.

**2.19. Western Blot.** The total protein of cells and tissues was extracted using RIPA Lysis and Extraction Buffer (89901,



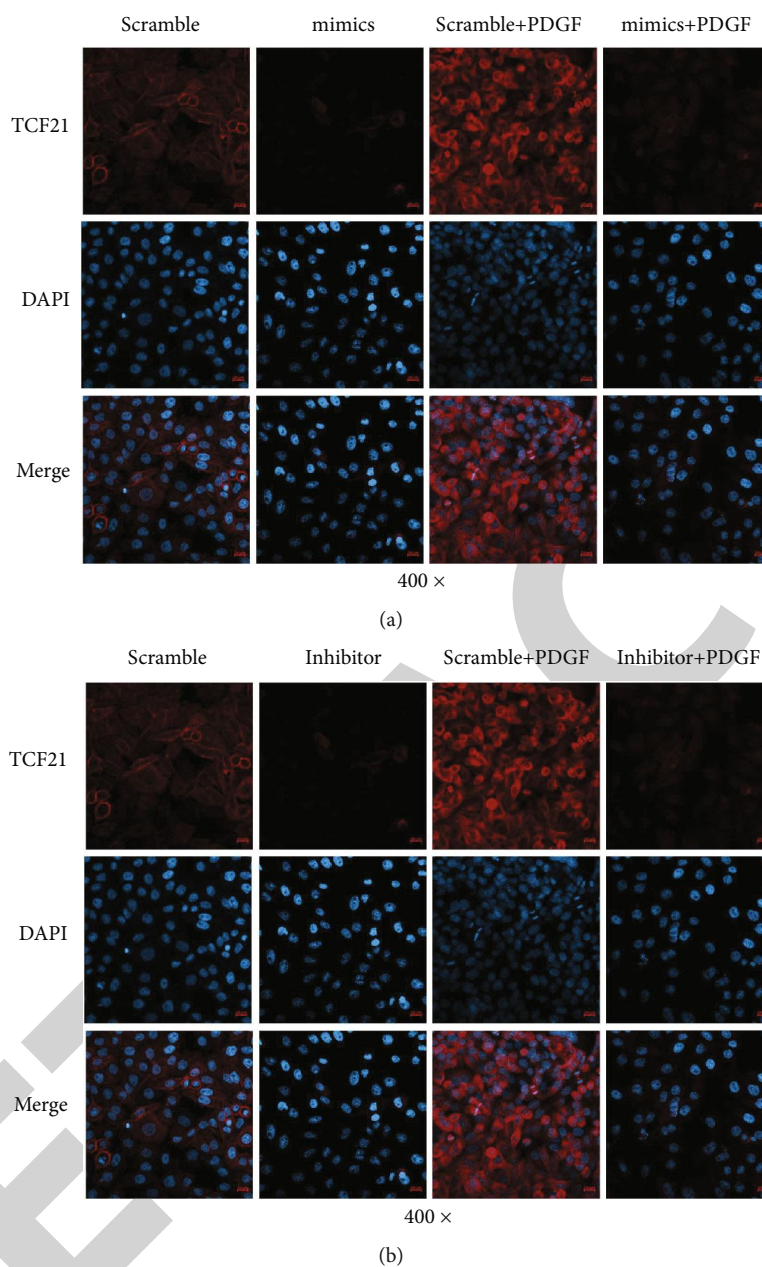


FIGURE 7: Immunofluorescence detects TCF21 expression. (a) Immunofluorescence detection of TCF21 in miR-654-5p mimic-transfected VSMCs treated by PDGF. (b) Immunofluorescence detection of TCF21 in miR-654-5p inhibitor-transfected VSMCs treated by PDGF.

Thermo Fisher Scientific, USA). Extracted protein mixture was centrifuged at  $1000 \times g$  for 5 min at  $4^{\circ}\text{C}$ . BCA protein kit (QPBCA, Sigma-Aldrich, USA) was used to determine the protein concentration. The proteins were separated by SDS-PAGE and transferred onto polyvinylidene fluoride (PVDF) membranes (EMD Millipore, USA). The membrane was blocked by 5% nonfat milk at room temperature for 1 h. The membrane was incubated with anti-TCF21 antibody (ab32981, 1:100, Abcam, USA), anti-MTAP antibody (ab126770, 1:100, Abcam, USA), and  $\beta$ -actin (mouse, 1:1000, ab8226, Abcam) at  $4^{\circ}\text{C}$  overnight. After washing, the membrane was incubated with goat anti-mouse or goat anti-rabbit IgG (H+L) (Proteintech, USA) for 2 h and then

washed by PBST for three times. The bands were detected by using an ECL kit (MAB5350, Sigma-Aldrich, USA) and scanned by a supersensitive multifunctional imager (ImageJ, version 4.7, AMERSHAM IMAGER 600, GE).

**2.20. Statistical Analysis.** The statistical analysis was performed using SPSS 17.0 software (SPSS, Inc., Chicago, IL, USA). The results were expressed as mean  $\pm$  standard deviation (SD). One-way analysis of variance (ANOVA) was used for analyzing the differences between multiple groups, and *t*-test was used for comparing the differences in the mean between the continuous variables. The

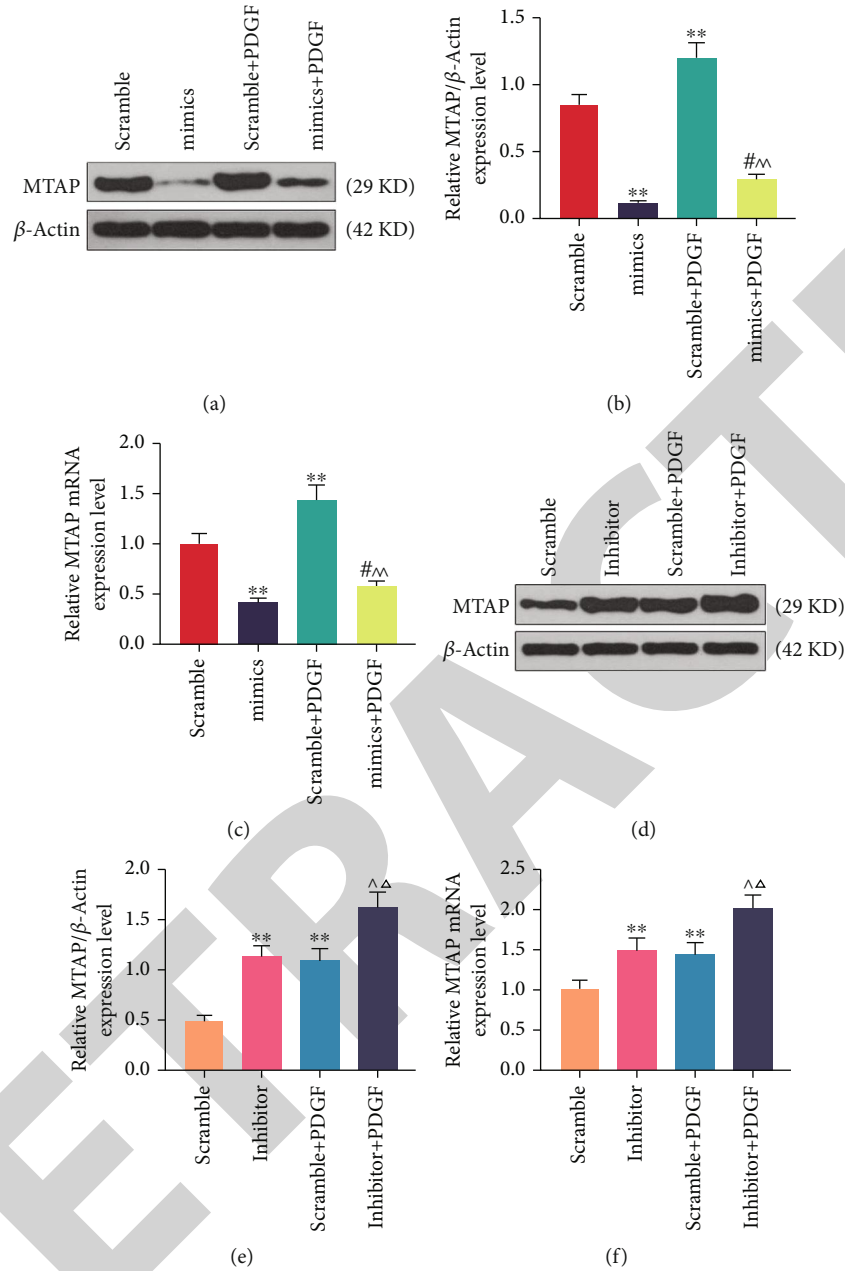


FIGURE 8: Effects of miR-654-5p on MTAP expression in VSMCs. (a, b) Western blotting was performed to determine the expression level of MTAP in miR-654-5p mimic-transfected VSMCs treated by PDGF. (c) qRT-PCR was performed to detect the MTAP mRNA expression level in miR-654-5p mimic-transfected VSMCs treated by PDGF. (d, e) Western blotting was used to determine the expression level of MTAP in miR-654-5p inhibitor-transfected VSMCs treated by PDGF. (f) qRT-PCR was used to detect the AEMA3A mRNA expression level in miR-654-5p inhibitor-transfected VSMCs treated by PDGF.

experiment was conducted in triplicate.  $P$  less than 0.05 was considered as statistically significant.

### 3. Results

**3.1. Differentially Expressed Genes for Early-Onset Coronary Heart Disease.** Bioinformatics analysis was conducted to obtain miRNAs with different platelet expressions in patients with early coronary heart disease and healthy controls. According to Figure 1, bioinformatics analysis identi-

fied 14 miRNAs differentially expressed in platelets in patients with early-onset coronary heart disease and healthy controls (group 1), and a total of 155 miRNAs were differentially expressed in platelets of healthy controls after the drug administration (group 2). Through R software, 5 differentially expressed genes, which were obtained through Venny analysis, may be confounding factors; thus, the 5 genes were removed, leaving miR-1, miR-133b, miR-431, miR-654-5p, miR-376c, miR-136, miR-411, miR-299-3p, miR-337-5p, miR-323-3p, miR-539, miR-376a, miR-410, and miR-329 (Table 2).

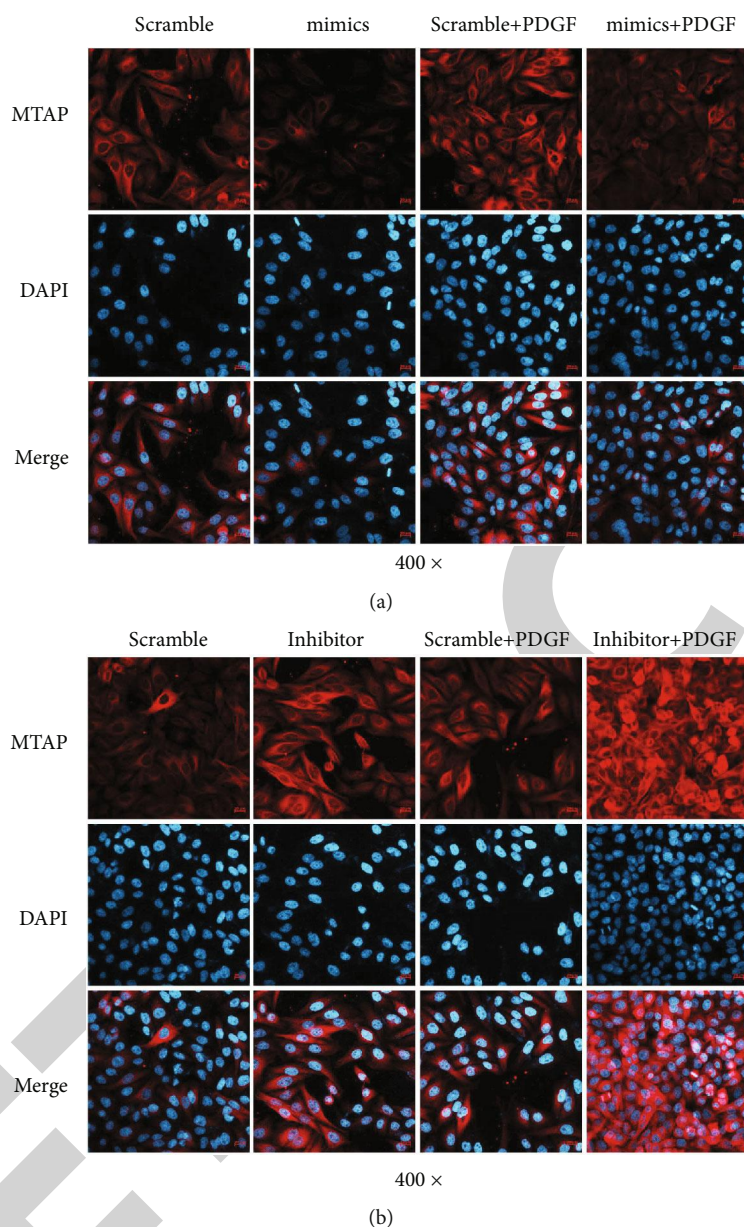


FIGURE 9: Immunofluorescence detects MTAP expression. (a) Immunofluorescence detection of MTAP in miR-654-5p mimic-transfected VSMCs treated by PDGF. (b) Immunofluorescence detection of MTAP in miR-654-5p inhibitor-transfected VSMCs treated by PDGF.

**3.2. Effects of Growth Factors on the Growth of VSMCs and miRNA Expression.** IL-1 $\beta$ , TNF- $\alpha$ , platelet-derived growth factor BB (PDGF-BB), and transforming growth factor- $\beta$  (TGF- $\beta$ ) were used to stimulate VSMCs and expressions of genes related to VSMC proliferation, migration, invasion, and apoptosis. As shown in Figure 2, the result showed that the viability of VSMCs stimulated by growth factors increased compared to the control group ( $P < 0.5$  and  $P < 0.01$ , Figure 2(a)); moreover, the migration distance (Figures 2(b) and 2(d)) and invasion (Figures 2(c) and 2(e)) of the cells increased significantly ( $P < 0.5$ ,  $P < 0.01$ ). QRT-PCR was performed to detect the expression of miRNA (Figure 2(f)), and the results showed that the expression of miR-654-5p was significantly downregulated in cells of each treatment group (IL-1 $\beta$ -treated group,

TNF- $\alpha$ -treated group, PDGF-BB-treated group, and TGF- $\beta$ -treated group). Since the expression of miR-654-5p was significantly decreased after PDGF-BB treatment, the cells were treated by PDGF-BB to explore the effects of PDGF-BB (20 ng/mL) for different treatment times (0, 3 h, 6 h, 12 h, 24 h, and 48 h) on miRNA expressions in VSMCs, and the results showed that the expression of miR-654-5p decreased in the cells treated by PDGF-BB for 3 h, 6 h, 12 h, 24 h, and 48 h ( $P < 0.01$ , Figure 2(g)). In addition, the miR-654-5p expression decreased in VSMCs treated by different concentrations (0, 1, 5, 10, 20, and 40 ng/mL) of PDGF-BB ( $P < 0.05$  and  $P < 0.01$ , Figure 2(h)), indicating that the viability of VSMCs treated by different concentrations of PDGF-BB increased in a dose-dependent manner ( $P < 0.05$  and  $P < 0.01$ , Figure 2(i)).

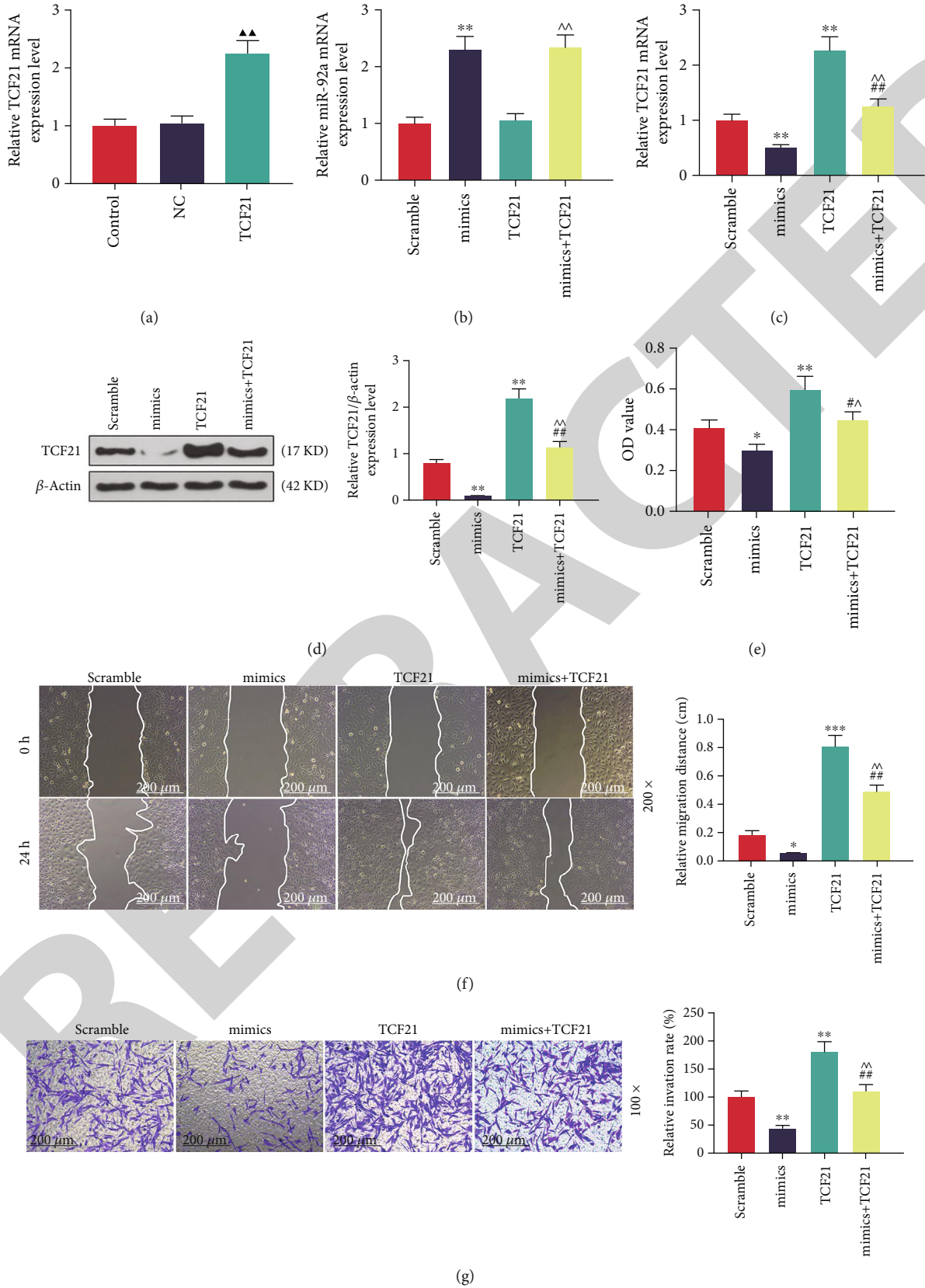


FIGURE 10: Continued.

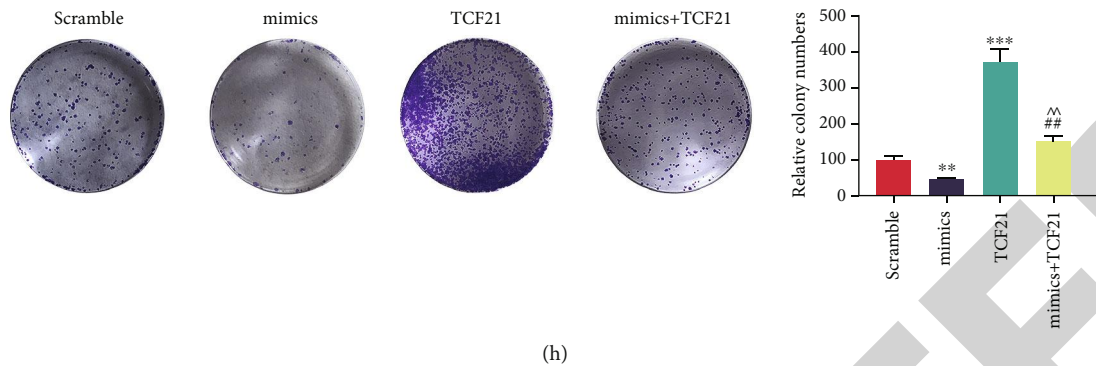


FIGURE 10: Effects of miR-654-5p on VSMC viability, migration, and invasion by targeting TCF21. (a) The expression of TCF21 in TCF21-transfected VSMCs was detected by qRT-PCR. (b) The expression of miR-654-5p in mimic- or TCF21-transfected VSMCs was detected by qRT-PCR. (c) The expression of TCF21 in mimic- or TCF21-transfected VSMCs was detected by qRT-PCR. (d) Western blotting was used to determine the expression level of TCF21 in mimic- or TCF21-transfected VSMCs. (e) The viability of mimic- or TCF21-transfected VSMCs was detected by CCK-8. (f) Wound scratch was used to detect the migration of mimic- or TCF21-transfected VSMCs. (g) Transwell was used to detect the invasions of mimic- or TCF21-transfected VSMCs. (h) Cloning formation experiment was used to detect the proliferation of mimic- or TCF21-transfected VSMCs.

**3.3. Expression of miR-654-5p in PDGF-Treated VSMCs and the Effects of miR-654-5p on Cell Viability, Migration, and Invasion.** miR-654-5p mimics were transfected into VSMCs, and we found that the expression level of miR-654-5p was increased significantly in the cells ( $P < 0.01$ , Figure 3(a)), whereas the expression of miR-654-5p was significantly inhibited when the cells were transfected with mimics treated by PDGF ( $P < 0.01$ , Figure 3(b)). Moreover, the viability decreased in VSMCs transfected by miR-654-5p mimics but increased in miR-654-5p mimic-transfected VSMCs treated by PDGF ( $P < 0.05$  and  $P < 0.01$ , Figure 3(c)). Wound scratch was performed to determine the effect of overexpressed miR-654-5p on the migration of PDGF-treated cells, and the result showed that overexpression of miR-654-5p could decrease the migration of VSMCs; however, when the cells were treated by PDGF, the migration of the cells was significantly promoted ( $P < 0.05$  and  $P < 0.01$ , Figure 3(d)). Transwell was performed to detect the effect of overexpression of miR-654-5p on the migration of PDGF-treated cells, and we found that overexpression of miR-654-5p inhibited the invasion of VSMCs, while cell invasion was significantly promoted when the cells were treated by PDGF ( $P < 0.05$  and  $P < 0.01$ , Figure 3(e)). Moreover, inhibitor was transfected into the cell to investigate the effects of low expression of miR-654-5p on cell viability, migration, and invasion. Firstly, we confirmed that the expression of miR-654-5p was inhibited in inhibitor-transfected VSMCs ( $P < 0.01$ , Figure 4(a)), and the expression level was significantly inhibited when the inhibitor-transfected cells were treated by PDGF ( $P < 0.05$  and  $P < 0.01$ , Figure 4(b)). Next, the results of CCK-8 showed that the viability was increased in VSMCs transfected by inhibitor as compared with scramble-transfected cells, and it was significantly increased in inhibitor-transfected VSMCs treated by PDGF ( $P < 0.05$  and  $P < 0.01$ , Figure 4(c)). Wound scratch data demonstrated that low-expressed miR-654-5p increased the migrations of VSMCs and inhibitor-transfected VSMCs treated by PDGF as compared with the inhibitor-transfected VSMCs ( $P < 0.05$  and  $P < 0.01$

, Figure 4(d)). Transwell results indicated that low-expressed miR-654-5p promoted the invasions of VSMCs and inhibitor-transfected VSMCs treated by PDGF as compared with the inhibitor-transfected VSMCs ( $P < 0.05$  and  $P < 0.01$ , Figure 4(e)).

**3.4. Target Gene Prediction of miR-654-5p and Its Effect on Target Gene Expression in VSMCs.** We used TargetScan and miRWalk to predict 42 genes that have a targeting relationship with miR-654-5p (Figure 5(a)); in addition, previous studies have shown that TCF21, DDR1, and MTAP are associated with coronary heart disease and blood vessels and vascular smooth muscle damage [17–19]. TargetScan 7.2 predictions revealed that miR-654-5p has reciprocal binding sites with TCF21, DDR1, and MTAP (Figure 5(b)). In addition, we constructed pmirGLO dual-luciferase reporter vectors, namely, TCF21-WT and TCF21-MUT, and cotransfected pmirGLO-TCF21 with miR-654-5p mimics into VSMCs and found that TCF21-WT luciferase vitality significantly improved inhibition ( $P < 0.01$ , Figure 5(c)). DDR1-WT and DDR1-MUT were constructed and cotransfected with miR-654-5p mimic into VSMCs; the luciferase activity of DDR1-WT ( $P < 0.05$ , Figure 5(d)) and MTAP-WT was significantly inhibited ( $P < 0.01$ , Figure 5(e)). The significant decrease in luciferase activity following TCF21 and MTAP binding to the mimic indicated that miR-654-5p binds more strongly to TCF21 and MTAP in cells. Therefore, we further explored the effect of different expression of miR-654-5p on TCF21 and MTAP, and the results of western blot (Figures 6(a) and 6(b)) and qRT-PCR (Figure 6(c)) showed that miR-654-5p mimics significantly inhibited. The expression of TCF21 was increased in VSMCs, whereas it was increased in miR-654-5p mimic-PDGF-treated transfected cells ( $P < 0.01$ ). However, PDGF significantly promoted the expression level of TCF21 in VSMCs transfected with miR-654-5p inhibitor ( $P < 0.05$  and  $P < 0.01$ , Figures 6(d)–6(f)). Furthermore, immunofluorescence staining with TCF21 antibody showed that the fluorescence of TCF21 was significantly increased in PDGF-

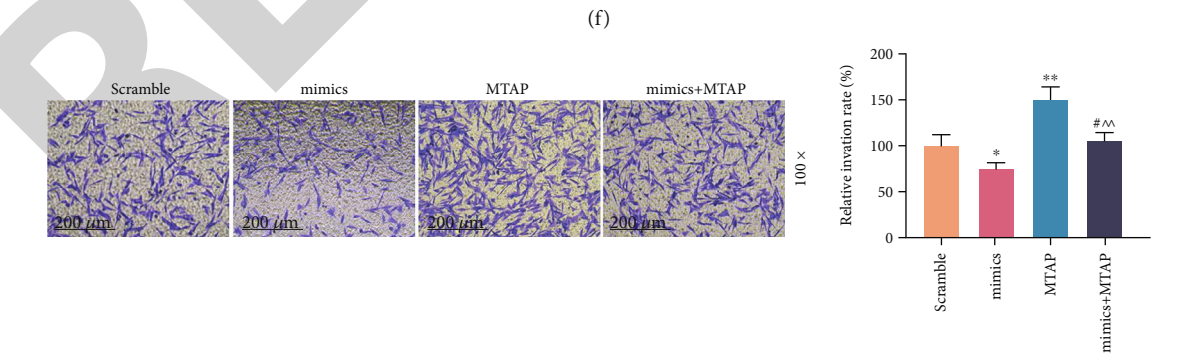
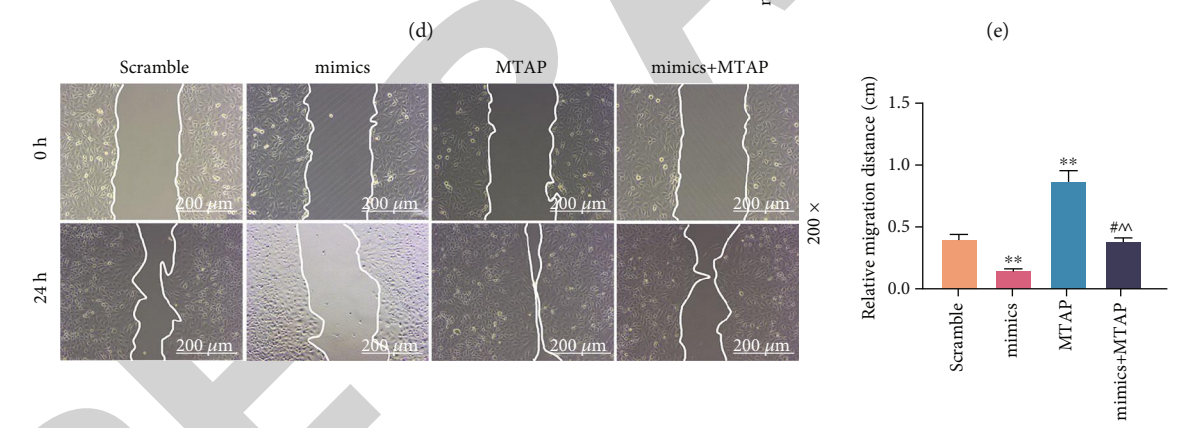
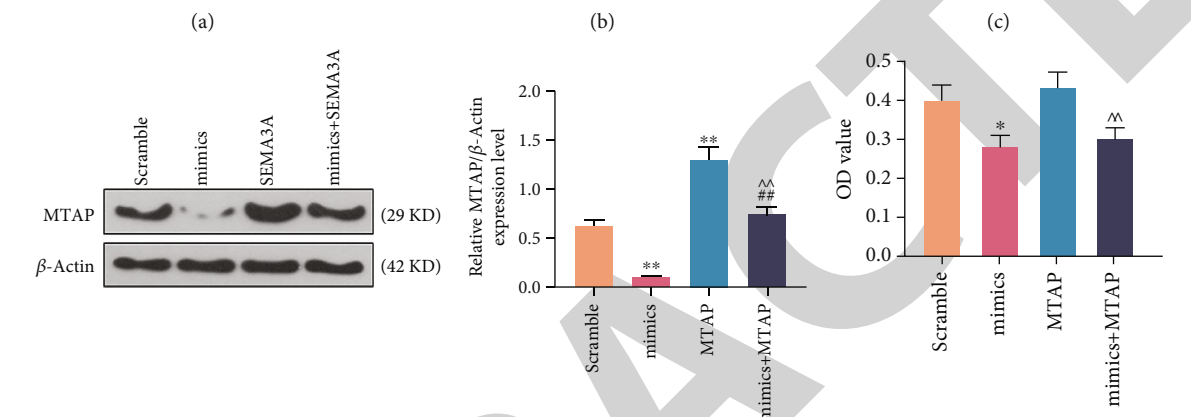
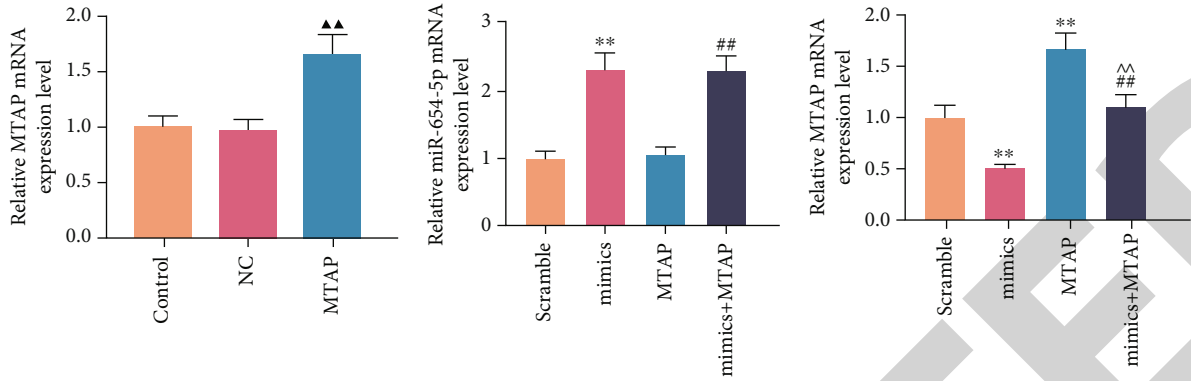


FIGURE 11: Continued.

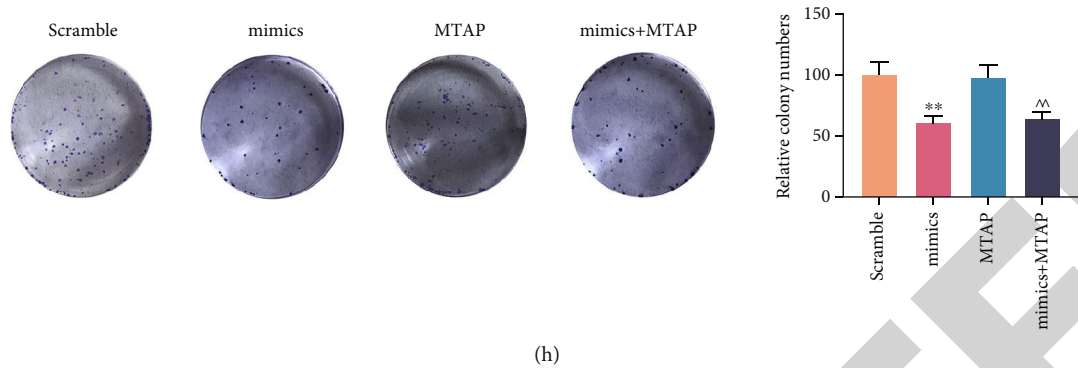


FIGURE 11: Effects of miR-654-5p on VSMC viability, migration, and invasion by targeting MTAP. (a) The expression of MTAP in MTAP-transfected VSMCs was detected by qRT-PCR. (b) The expression of miR-654-5p in mimic- or MTAP-transfected VSMCs was detected by qRT-PCR. (c) The expression of MTAP in mimic- or MTAP-transfected VSMCs was detected by qRT-PCR. (d) Western blotting was used to determine the expression level of MTAP in mimic- or MTAP-transfected VSMCs. (e) The viability of mimic- or MTAP-transfected VSMCs was detected by CCK-8. (f) Wound scratch was used to detect the migration of mimic- or MTAP-transfected VSMCs. (g) Transwell was used to detect the invasions of mimic- or MTAP-transfected VSMCs. (h) Cloning formation experiment was used to detect the proliferation of mimic- or MTAP-transfected VSMCs.

treated VSMCs, but was suppressed in PDGF-treated VSMCs transfected with mocks (Figure 7(a)). Notably, the fluorescence of TCF21 was in the VSMCs transfected with inhibitors significantly increased in PDGF treatment (Figure 7(b)).

In addition, the results of western blotting (Figures 8(a) and 8(b)) and qRT-PCR (Figure 8(c)) demonstrated that the expression of MTAP was significantly inhibited by miR-654-5p mimics in VSMCs, but was elevated in miR-654-5p mimic-transfected cells treated by PDGF ( $P < 0.01$ ). However, PDGF greatly upregulated the expression level of MTAP in VSMCs transfected with miR-654-5p inhibitor ( $P < 0.05$  and  $P < 0.01$ , Figures 8(d)–8(f)). Furthermore, immunofluorescence staining on MTAP antibody showed that the fluorescence MTAP increased significantly in VSMCs treated by PDGF, but was inhibited in PDGF-treated VSMCs transfected with mimics (Figure 9(a)). However, the fluorescence amount of MTAP was significantly increased in PDGF-treated VSMCs transfected with inhibitor (Figure 9(b)).

**3.5. Effects of miR-654-5p on VSMC Viability, Migration, and Invasion through Targeting TCF21.** We transfected TCF21 overexpression vector and mimics into the cells to further investigate the effects of miR-654-5p on cell viability, migration, and invasion through targeting TCF21. The expression of TCF21 was significantly increased in VSMCs transfected with TCF21 overexpression vector ( $P < 0.01$ , Figure 10(a)); however, the expression of miR-654-5p was greatly inhibited in cells transfected with TCF21 overexpression vector ( $P < 0.01$ , Figure 10(b)), and overexpressed miR-654-5p could inhibit the TCF21 expression ( $P < 0.01$ , Figures 10(c) and 10(d)). The viability was inhibited in VSMCs transfected with mimics, whereas overexpression of TCF21 reversed the effect of mimics on cell viability ( $P < 0.01$ , Figure 10(e)). Wound scratch data showed that the migration of VSMCs increased significantly in the cells transfected with TCF21, but mimics inhibited the effect of TCF21 overexpression vector on the migration of VSMCs ( $P < 0.01$  and  $P < 0.001$ ,

Figure 10(f)). Moreover, Transwell results demonstrated that the invasion of VSMCs increased greatly in the cells transfected with TCF21, but mimics inhibited the effect of TCF21 overexpression vector on invasion of VSMCs ( $P < 0.01$ , Figure 10(g)). Colony formation assay data showed that the proliferation of VSMCs was significantly increased in the cells transfected with TCF21, but mimics inhibited the effect of TCF21 overexpression vector on the proliferation of VSMCs ( $P < 0.01$  and  $P < 0.001$ , Figure 10(h)).

**3.6. Effects of miR-654-5p on VSMC Viability, Migration, and Invasion through Targeting MTAP.** MTAP overexpression vector and mimics were transfected into the cells to further investigate the effect of miR-654-5p on cell viability, migration, and invasion through targeting MTAP. We observed that the expression of MTAP was significantly increased in VSMCs transfected with MTAP overexpression vector ( $P < 0.01$ , Figure 11(a)); however, when the cells transfected were with MTAP overexpression vector, the expression of miR-654-5p was significantly inhibited ( $P < 0.01$ , Figure 11(b)), and overexpressed miR-654-5p could inhibit the MTAP expression ( $P < 0.01$ , Figures 11(c) and 11(d)). The viability was inhibited in VSMCs transfected with mimics, whereas overexpression of MTAP reverses the effect of mimics on cell viability ( $P < 0.05$  and  $P < 0.01$ , Figure 11(e)). Wound scratch showed that the migration of VSMCs was significantly increased in the cells transfected with MTAP, but mimics inhibited the effect of MTAP overexpression vector on migration of VSMCs ( $P < 0.05$  and  $P < 0.01$ , Figure 11(f)). Transwell data showed that the invasion of VSMCs was significantly increased in the cells transfected with MTAP, but mimics inhibited the effect of MTAP overexpression vector on invasion of VSMCs ( $P < 0.05$  and  $P < 0.01$ , Figure 11(g)). Colony formation assay showed that the proliferation of VSMCs increased significantly in the cells transfected with MTAP, but mimics inhibited the effect of MTAP overexpression vector on proliferation of VSMCs ( $P < 0.01$ , Figure 11(h)).

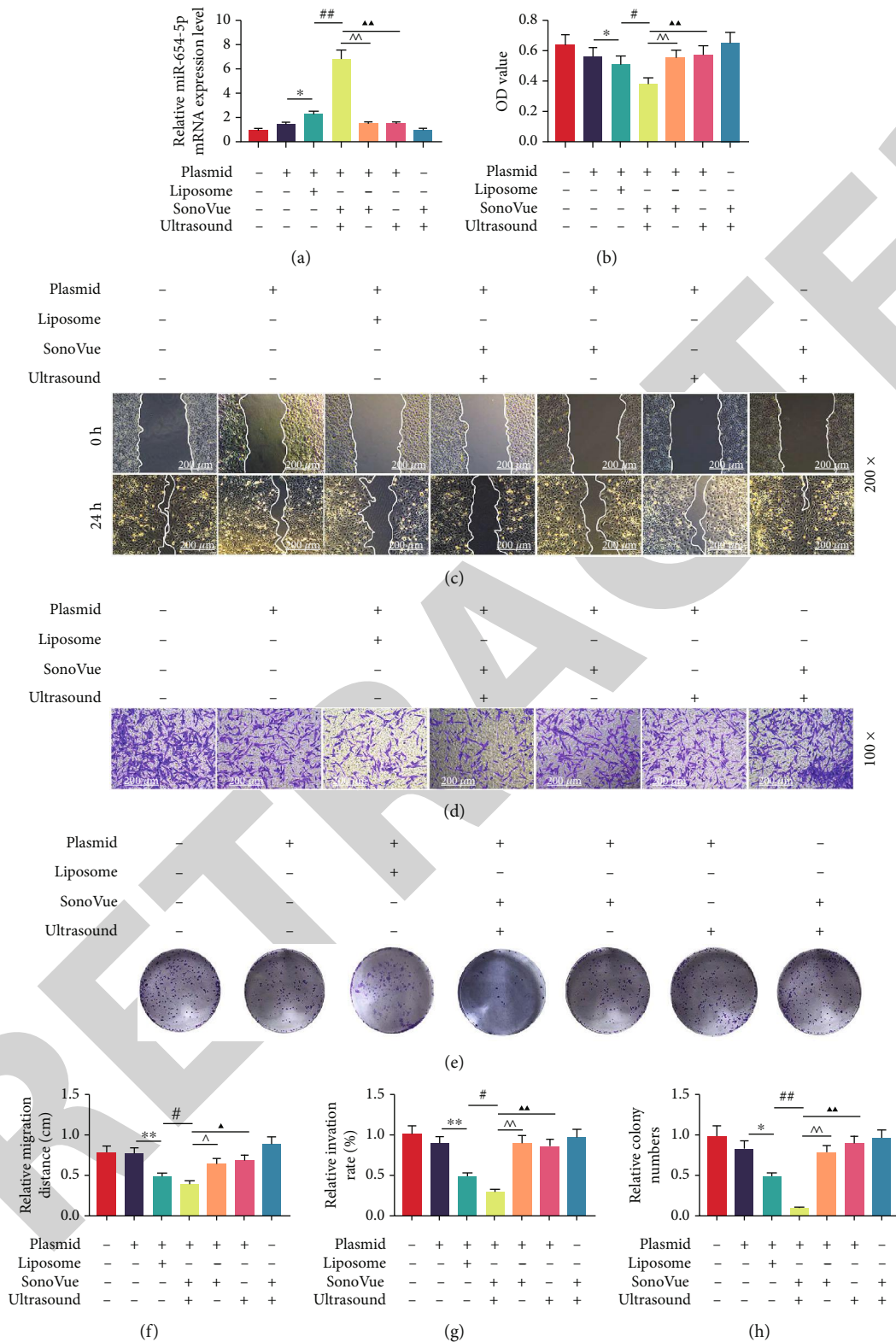


FIGURE 12: Transfection efficiency of miR-654-5p and effects of ultrasound-mediated SonoVue-miR-654-5p microbubble on VSMC viability, migration, and invasion. (a) The expression of miR-654-5p in VSMCs transfected with SonoVue-microRNA and adenovirus was detected by qRT-PCR. (b) The viability of VSMCs transfected with SonoVue-microRNA and adenovirus was detected by CCK-8. (c, f) Wound scratch detection of the effect of SonoVue-microRNA overexpression on VSMC migration. (d, g) Transwell was used to detect the invasion of VSMCs with overexpressed SonoVue-microRNA. (e, h) Cloning formation experiment was used to detect the proliferation of VSMCs with overexpressed SonoVue. Abbreviations: qRT-PCR: quantitative real-time polymerase chain reaction.



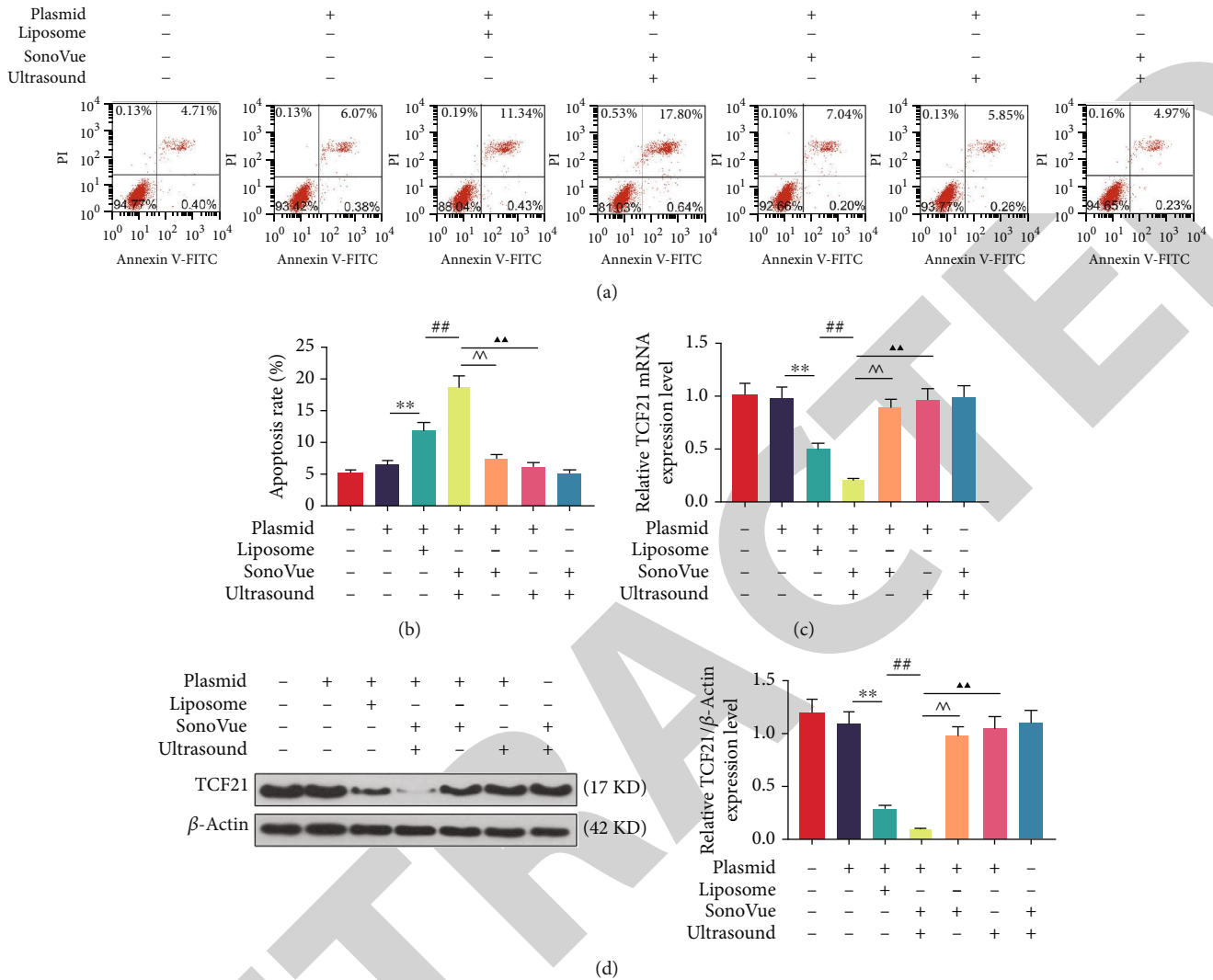


FIGURE 13: Transfection efficiency of TCF21 and effects of ultrasound-mediated SonoVue-miR-654-5p microbubble on VSMC apoptosis. (a) Flow cytometry was used to detect the effect of SonoVue-microRNA overexpression on VSMC apoptosis. (c) The expression of TCF21 in SonoVue-microRNA overexpressed with VSMCs was detected by qRT-PCR. (d) Western blotting was used to determine the expression level of TCF21 in VSMCs overexpressed with SonoVue-miRNA.

**3.7. Transfection Efficiency of miR-654-5p and TCF21 and Effects of Ultrasound-Mediated SonoVue-miR-654-5p Microbubble on VSMC Viability, Migration, Invasion, and Apoptosis.** miR-654-5p expression in cells was significantly promoted by SonoVue-miR-654-5p overexpression ( $P < 0.01$ , Figure 12(a)). The viability was significantly inhibited by SonoVue-miR-654-5p overexpression liposome transfected into VSMCs ( $P < 0.01$ , Figure 12(b)). SonoVue-miR-654-5p overexpression inhibited the migration of VSMCs ( $P < 0.01$ , Figures 12(c) and 12(f)), and cell invasion was inhibited in VSMCs transfected with SonoVue-miR-654-5p overexpression liposome ( $P < 0.01$ , Figures 12(d) and 12(g)). Moreover, colony formation assay showed that the proliferation of VSMCs decreased significantly in the cells transfected with SonoVue-miR-654-5p overexpression liposome ( $P < 0.01$ , Figures 12(e) and 12(h)). In addition, apoptosis of VSMCs was significantly promoted when SonoVue-miR-654-5p overexpression liposome was transfected

into the cells ( $P < 0.01$ , Figures 13(a) and 13(b)). The results of qRT-PCR (Figure 13(c)) and western blotting (Figure 13(d)) showed that the TCF21 expression was significantly inhibited in VSMCs transfected with SonoVue-miR-654-5p overexpression liposome ( $P < 0.01$ ).

**3.8. Effects of Ultrasound-Mediated SonoVue-miR-654-5p Microbubble Contrast Agent on Vascular Injury Model.** Injury in rat carotid artery was created by 2.0 Fogarty catheter balloon to establish carotid artery injury model as a positive group. After the establishment of the rat vascular injury model, pathological examination showed a significant increase in the degree of stenosis of the vascular vessels in the model group as compared with the control group and the sham group (Figure 14(a)); meanwhile, in rat vascular injury model, blood flow velocity increased significantly ( $P < 0.01$ , Figure 14(b)), and vascular diameter decreased significantly greatly ( $P < 0.01$ , Figure 14(c)). The result of

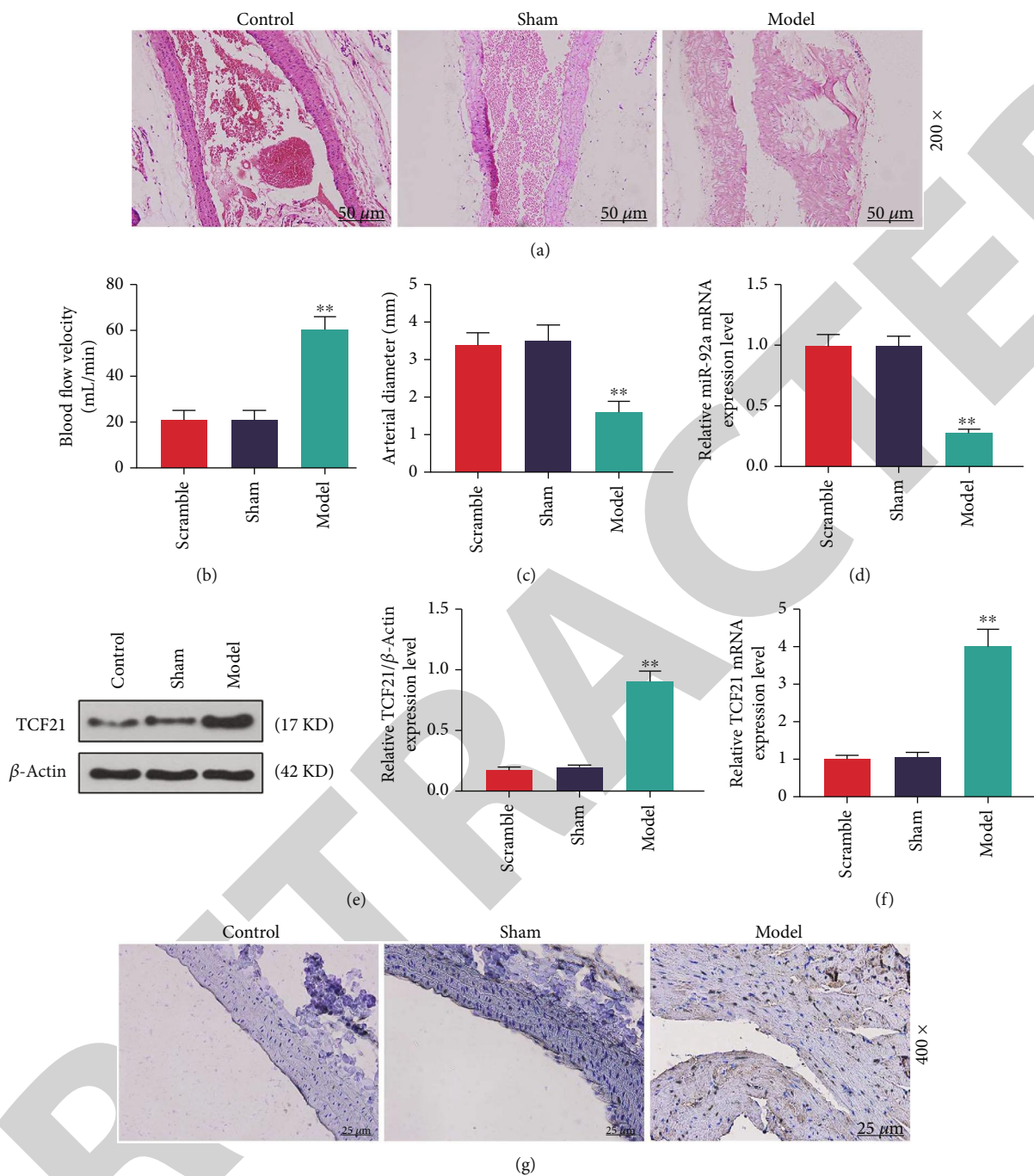


FIGURE 14: Histopathological changes and gene expression in vascular injury model. (a) Pathological examination of vascular injury of rat vascular injury model. (b) Blood flow velocity in rat vascular injury model was measured by intelligent analysis. (c) Vascular diameter in rat vascular injury model was measured by straightedge. (d) The expression of miR-654-5p was detected in blood vessel of rat vascular injury model by qRT-PCR. (e) Western blotting was used to determine the expression level of TCF21 in blood vessel of rat vascular injury model. (f) qRT-PCR was used to detect the TCF21 expression in blood vessel of rat vascular injury model. (g) Immunohistochemical assay was used to observe the damage of tissue of rat vascular injury model.

qRT-PCR showed that the miR-654-5p expression level was significantly downregulated in the model group ( $P < 0.01$ , Figure 14(d)), and from Figures 14(e) and 14(f), it was found that TCF21 expression increased noticeably in the model group ( $P < 0.01$ ). Moreover, histopathologic staining showed that the degree of vascular stenosis was highly obvious in the model group (Figure 14(g)). Furthermore, ultrasound-

mediated SonoVue-miR-654-5p microbubble was used to treat the rat model of vascular injury, and the results showed that the degree of vascular stenosis was significantly improved in the model treated by SonoVue-miR-654-5p (Figure 15(a)), and in the rat vascular injury model, blood flow velocity decreased ( $P < 0.05$ , Figure 15(b)), and vascular diameter increased as compared with untreated rats

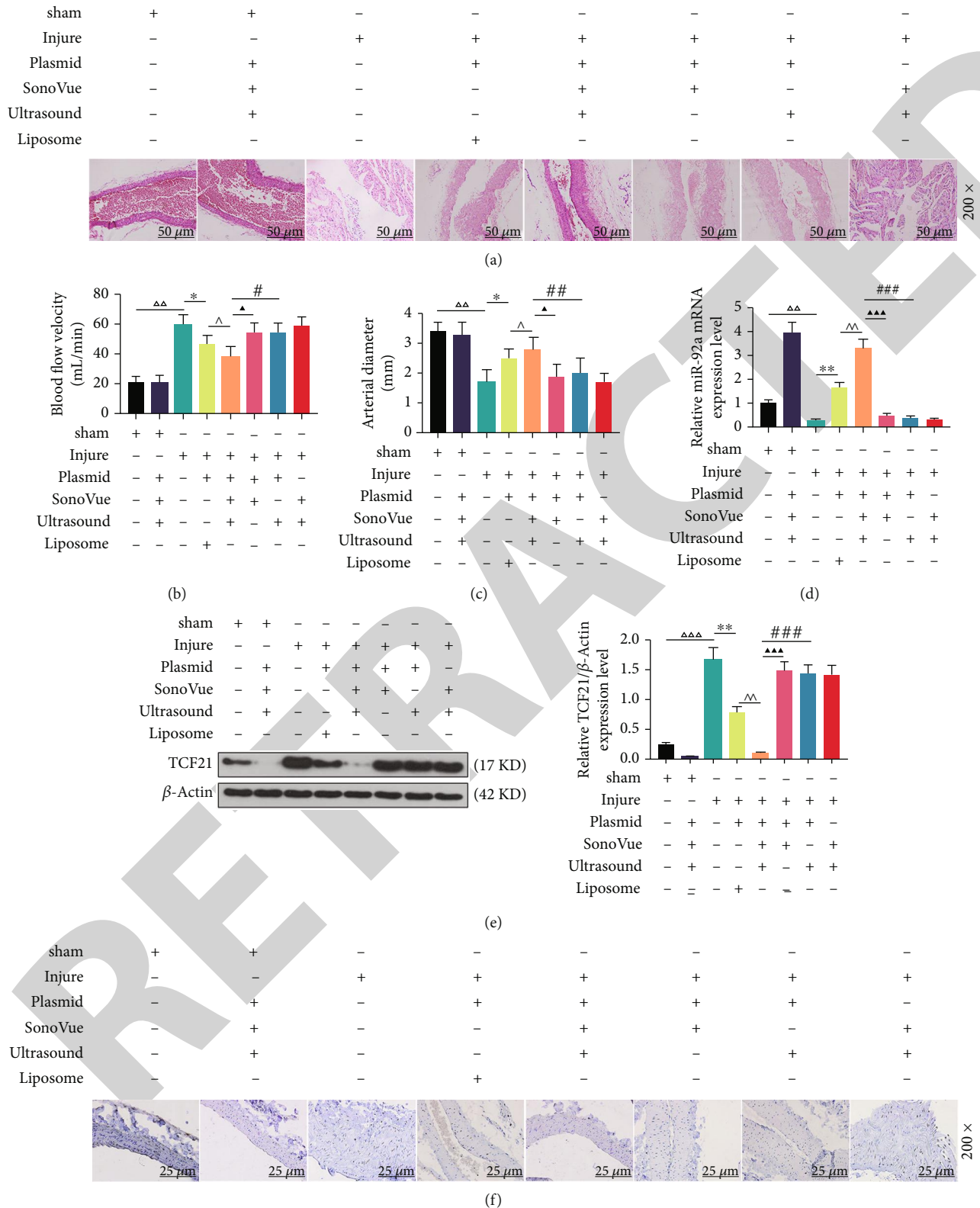


FIGURE 15: Effects of ultrasound-mediated SonoVue-miR-654-5p microbubble contrast agent on vascular injury model. (a) SonoVue delivers microRNA into the vascular wall, and the pathological degree of vascular stenosis in the model was examined. (b) Blood flow velocity in rat vascular injury model was measured by intelligent analysis. (c) Vascular diameter in rat vascular injury model was measured by straightedge. (d) qRT-PCR was used to detect the expression of miR-654-5p in rat vascular injury model treated by SonoVue-microRNA. (e) Western blotting was used to determine the expression level of TCF21 in a rat vascular injury model treated by SonoVue-microRNA. (f) Immunohistochemical assay was used to observe the damage of tissue of rat vascular injury model treated by SonoVue-microRNA.

( $P < 0.05$ , Figure 15(c)). The result of qRT-PCR showed that the miR-654-5p expression level was significantly upregulated in the model group treated by SonoVue-miR-654-5p ( $P < 0.01$ , Figure 15(d)); moreover, from Figures 15(e) and 15(f), it could be found that the TCF21 expression decreased significantly in the model group treated by SonoVue-miR-654-5p ( $P < 0.01$ ). Histopathologic staining showed that vascular stenosis was inhibited in the model group treated by SonoVue-miR-654-5p (Figure 15(g)).

#### 4. Discussion

Phenotypic transformation of VSMCs is an important cause of vascular stenosis [9]. At present, there are mainly several molecular biological mechanisms involved in the phenotypic transformation of VSMCs. Inhibition of miR-145 expression leads to airway smooth muscle cell proliferation and migration and downregulates the expression of airway type I collagen and contractile protein MHC in smooth muscle cells [20]; moreover, Wang showed that miRNA-195 can reduce proliferation and migration of VSMCs and inhibit the synthesis of IL-1 $\beta$  and IL-6 in VSMCs [21]. In this study, through bioinformatics analysis, we found that miR-654-5p is a differentially expressed gene in patients with coronary heart disease and healthy subjects. The current study explored the effects of miR-654-5p on phenotypic transformation of VSMCs, as there is currently a lack of research on such an aspect. We found that inflammatory factors play a key role in the phenotypic transformation of VSMCs; moreover, a study found that IL-1 $\beta$  can stimulate the proliferation and migration of VSMCs through P2Y2 receptor [22] and that inhibiting TNF- $\alpha$ , TGF- $\beta$ , and PDGF-BB production could inhibit proliferation and invasion of VSMCs [23, 24]. In the study, VSMCs was stimulated by IL-1 $\beta$ , TNF- $\alpha$ , TGF- $\beta$ , and PDGF-BB, and the results showed that the viability, migration, and invasion of VSMCs were promoted, which was consistent with previous studies [23, 24]. The study found that miR-638 was highly expressed in human VSMCs. When PDGF-BB was used to treat the cells, the expression of miR-638 was downregulated in dose- and time-dependent manners [25]. Subsequently, we observed that the expression of miR-654-5p decreased by PDGF-BB treatment in dose- and time-dependent manners, while overexpression of miR-654-5p inhibited the proliferation, invasion, and migration of smooth muscle cells by PDGF-BB. At the same time, inhibition of miR-654-5p enhanced the effect of PDGF-BB on the cells.

Previous study confirmed that miR-328 inhibited PDGF-BB-induced pulmonary artery smooth muscle cell proliferation and migration by binding to PIM-1 [26]. miR-638 inhibits the proliferation and migration of smooth muscle cell induced by PDGF-BB through Nor1 [25]. It was also reported that miR-654-5p can bind to genes to regulate the proliferation and metastasis of various tumors [27, 28]. In this study, we further investigated the effects of miR-654-5p on the biological characteristics of VSMCs induced by PDGF-BB through binding the cells to target genes. TCF21 and MTAP were predicted and confirmed as the target genes of miR-654-5p using the bioinformatics website, dual-

luciferase assay, and immunofluorescence. Studies showed that aryl hydrocarbon receptor protein is localized in human carotid atherosclerotic lesions [29] and that TCF21 can promote the expression of aryl hydrocarbon receptor and activate the inflammatory gene expression program, thereby increasing the risk of developing coronary artery diseases [15]. In addition, studies demonstrated that MTAP is highly expressed in atherosclerotic lesions, and that downregulation of MTAP in macrophages may be achieved by a pathway, which could inhibit TNF- $\alpha$  expression [19]. In this study, we found by *in vitro* cell experiments that overexpression of TCF21 promoted the proliferation, migration, and invasion of VSMCs. Overexpression of MTAP also promoted the migration and invasion of VSMCs but did not have much effect on cell proliferation. Furthermore, by transfecting miR-654-5p mimic into cells, we found that overexpression of miR-654-5p could inhibit the proliferation, migration, and invasion of TCF21, so we speculated that miR-654-5p could pass the target gene, and inhibition of TCF21 expression regulates PDGF-BB-induced proliferation and migration of VSMCs.

Studies showed that inhibiting miR-146 expression in rat VSMCs significantly reduces cell proliferation and migration [30]; moreover, overexpression of miR-214 in serum-free VSMCs can greatly reduce the proliferation and migration of VSMCs, while knocking down miR-214 noticeably increases the proliferation and migration of VSMCs [31]. Studies on miR-654-5p are less conducted; however, Lu et al. found that cell proliferation and metastasis were inhibited after shRNA-654-5p was transfected into oral squamous cell carcinoma cells [32]. miR-654-5p is highly expressed in breast cancer cell, and functional analysis indicated that miR-654-5p overexpression inhibits the growth and invasion of MDA-MB-468 and BT-549 cells and induces apoptosis [27]. To further investigate the effect of miR-654-5p on the biological properties of smooth muscle cells, ultrasound microbubbles were used to deliver the miR-654-5p plasmid into smooth muscle cells, and the results showed that SonoVue microbubble ultrasound-miR-654-5p overexpression inhibited VSMC proliferation, migration, and invasion, promoted apoptosis, and inhibited TCF21 expression; thus, we hypothesized that miR-654-5p is an important gene, which affects the phenotypic transformation of smooth muscle cells. Furthermore, we performed *in vivo* studies to determine the role of miR-654-5p by establishing a rat model of carotid artery injury, and the results showed that SonoVue microbubble ultrasound transmitted miR-654-5p into the arterial wall and that arterial thrombosis and stenosis and TCF21 were inhibited.

In conclusion, our findings suggested that miR-654-5p is an important gene regulating VSMC phenotypic transformation, as it inhibits TCF21 expression and cell proliferation, invasion, and metastasis, thereby controlling arterial thrombosis and stenosis.

#### Data Availability

All data were included in the manuscript.

## Conflicts of Interest

The authors declared no conflict of interest.

## References

- [1] A. Gistera and G. K. Hansson, "The immunology of atherosclerosis," *Nature Reviews. Nephrology*, vol. 13, no. 6, pp. 368–380, 2017.
- [2] T. Miyazaki and A. Miyazaki, "Dysregulation of calpain proteolytic systems underlies degenerative vascular disorders," *Journal of Atherosclerosis and Thrombosis*, vol. 25, no. 1, pp. 1–15, 2018.
- [3] C. L. Song, J. P. Wang, X. Xue et al., "Effect of circular ANRIL on the inflammatory response of vascular endothelial cells in a rat model of coronary atherosclerosis," *Cellular Physiology and Biochemistry: International Journal of Experimental Cellular Physiology, Biochemistry, and Pharmacology*, vol. 42, no. 3, pp. 1202–1212, 2017.
- [4] Y. Xu, J. Xu, K. Ge, Q. Tian, P. Zhao, and Y. Guo, "Anti-inflammatory effect of low molecular weight fucoidan from *Saccharina japonica* on atherosclerosis in apoE-knockout mice," *International Journal of Biological Macromolecules*, vol. 118, pp. 365–374, 2018.
- [5] N. Papadopoulos, G. Menikou, M. Yiannakou, C. Yiallouras, K. Ioannides, and C. Damianou, "Evaluation of a small flat rectangular therapeutic ultrasonic transducer intended for intravascular use," *Ultrasonics*, vol. 74, pp. 196–203, 2017.
- [6] D. Giacoppo, R. Colleran, S. Cassese et al., "Percutaneous coronary intervention vs coronary artery bypass grafting in patients with left main coronary artery stenosis: a systematic review and meta-analysis," *JAMA Cardiology*, vol. 2, no. 10, pp. 1079–1088, 2017.
- [7] R. A. Montone, G. Niccoli, F. Vergni et al., "Endothelial dysfunction as predictor of angina recurrence after successful percutaneous coronary intervention using second generation drug eluting stents," *European Journal of Preventive Cardiology*, vol. 25, no. 13, pp. 1360–1370, 2018.
- [8] S. T. Haller, K. L. Evans, D. A. Folt, C. A. Drummond, and C. J. Cooper, "Mechanisms and treatments for renal artery stenosis," *Discovery Medicine*, vol. 16, no. 90, pp. 255–260, 2013.
- [9] T. Usui, T. Morita, M. Okada, and H. Yamawaki, "Histone deacetylase 4 controls neointimal hyperplasia via stimulating proliferation and migration of Vascular Smooth Muscle Cells," *Hypertension*, vol. 63, no. 2, pp. 397–403, 2014.
- [10] X. L. Xiao, N. Hu, X. Z. Zhang et al., "Niclosamide inhibits vascular smooth muscle cell proliferation and migration and attenuates neointimal hyperplasia in injured rat carotid arteries," *British Journal of Pharmacology*, vol. 175, no. 10, pp. 1707–1718, 2018.
- [11] R. M. Starke, N. Chalouhi, D. Ding et al., "Vascular smooth muscle cells in cerebral aneurysm pathogenesis," *Translational Stroke Research*, vol. 5, no. 3, pp. 338–346, 2014.
- [12] M. Lehnert, H. Dobrowinski, S. Feil, and R. Feil, "cGMP signaling and VSMCs plasticity," *Journal of Cardiovascular Development and Disease*, vol. 5, no. 2, p. 20, 2018.
- [13] E. Raitoharju, N. Oksala, and T. Lehtimäki, "MicroRNAs in the atherosclerotic plaque," *Clinical Chemistry*, vol. 59, no. 12, pp. 1708–1721, 2013.
- [14] M. Li and J. Zhang, "Circulating microRNAs: potential and emerging biomarkers for diagnosis of cardiovascular and cerebrovascular diseases," *BioMed Research International*, vol. 2015, Article ID 730535, 9 pages, 2015.
- [15] J. B. Kim, M. Pjanic, T. Nguyen et al., "TCF21 and the environmental sensor aryl-hydrocarbon receptor cooperate to activate a pro-inflammatory gene expression program in coronary artery smooth muscle cells," *PLoS Genetics*, vol. 13, no. 5, article e1006750, 2017.
- [16] K. J. Livak and T. D. Schmittgen, "Analysis of relative gene expression data using real-time quantitative PCR and the 2<sup>-ΔΔC<sub>T</sub></sup> method," *Methods (San Diego, Calif.)*, vol. 25, no. 4, pp. 402–408, 2001.
- [17] L. H. Lehmann, J. S. Rostovsky, S. J. Buss et al., "Essential role of sympathetic endothelin A receptors for adverse cardiac remodeling," *Proceedings of the National Academy of Sciences of the United States of America*, vol. 111, no. 37, pp. 13499–13504, 2014.
- [18] C. Franco, G. Hou, P. J. Ahmad et al., "Discoidin domain receptor 1 (ddr1) deletion decreases atherosclerosis by accelerating matrix accumulation and reducing inflammation in low-density lipoprotein receptor-deficient mice," *Circulation Research*, vol. 102, no. 10, pp. 1202–1211, 2008.
- [19] L. M. Holdt, K. Sass, G. Gäbel, H. Bergert, J. Thiery, and D. Teupser, "Expression of Chr9p21 genes CDKN2B (p15INK4b), CDKN2A (p16INK4a, p14ARF) and MTAP in human atherosclerotic plaque," *Atherosclerosis*, vol. 214, no. 2, pp. 264–270, 2011.
- [20] Y. Liu, X. Sun, Y. Wu et al., "Effects of miRNA-145 on airway smooth muscle cells function," *Molecular and Cellular Biochemistry*, vol. 409, no. 1–2, pp. 135–143, 2015.
- [21] Y. S. Wang, H. Y. J. Wang, Y. C. Liao et al., "MicroRNA-195 regulates vascular smooth muscle cell phenotype and prevents neointimal formation," *Cardiovascular Research*, vol. 95, no. 4, pp. 517–526, 2012.
- [22] S. Y. Eun, Y. S. Ko, S. W. Park, K. C. Chang, and H. J. Kim, "IL-1β enhances vascular smooth muscle cell proliferation and migration via P2Y<sub>2</sub> receptor-mediated RAGE expression and HMGB1 release," *Vascular Pharmacology*, vol. 72, pp. 108–117, 2015.
- [23] L. Meng, W. Xu, L. Guo, W. Ning, and X. Zeng, "Paeonol inhibits the proliferation, invasion, and inflammatory reaction induced by TNF-α in vascular smooth muscle cells," *Cell Biochemistry and Biophysics*, vol. 73, no. 2, pp. 495–503, 2015.
- [24] J. Zhao, L. Jian, L. Zhang et al., "Knockdown of SCARA5 inhibits PDGF-BB-induced vascular smooth muscle cell proliferation and migration through suppression of the PDGF signaling pathway," *Molecular Medicine Reports*, vol. 13, no. 5, pp. 4455–4460, 2016.
- [25] P. Li, Y. Liu, B. Yi et al., "MicroRNA-638 is highly expressed in human vascular smooth muscle cells and inhibits PDGF-BB-induced cell proliferation and migration through targeting orphan nuclear receptor NOR1," *Cardiovascular Research*, vol. 99, no. 1, pp. 185–193, 2013.
- [26] Z. Qian, L. Zhang, J. Chen et al., "MiR-328 targeting PIM-1 inhibits proliferation and migration of pulmonary arterial smooth muscle cells in PDGFBB signaling pathway," *Oncotarget*, vol. 7, no. 34, pp. 54998–55011, 2016.
- [27] Y. Y. Tan, X. Y. Xu, J. F. Wang, C. W. Zhang, and S. C. Zhang, "MiR-654-5p attenuates breast cancer progression by targeting EPST11," *American Journal of Cancer Research*, vol. 6, no. 2, pp. 522–532, 2016.
- [28] B. Majem, A. Parrilla, C. Jiménez et al., "MicroRNA-654-5p suppresses ovarian cancer development impacting on MYC,

## *Retraction*

# **Retracted: Molecular Evolution of the Activating Transcription Factors Shapes the Adaptive Cellular Responses to Oxidative Stress**

### **Oxidative Medicine and Cellular Longevity**

Received 8 January 2024; Accepted 8 January 2024; Published 9 January 2024

Copyright © 2024 Oxidative Medicine and Cellular Longevity. This is an open access article distributed under the Creative Commons Attribution License, which permits unrestricted use, distribution, and reproduction in any medium, provided the original work is properly cited.

This article has been retracted by Hindawi following an investigation undertaken by the publisher [1]. This investigation has uncovered evidence of one or more of the following indicators of systematic manipulation of the publication process:

- (1) Discrepancies in scope
- (2) Discrepancies in the description of the research reported
- (3) Discrepancies between the availability of data and the research described
- (4) Inappropriate citations
- (5) Incoherent, meaningless and/or irrelevant content included in the article
- (6) Manipulated or compromised peer review

The presence of these indicators undermines our confidence in the integrity of the article's content and we cannot, therefore, vouch for its reliability. Please note that this notice is intended solely to alert readers that the content of this article is unreliable. We have not investigated whether authors were aware of or involved in the systematic manipulation of the publication process.

Wiley and Hindawi regrets that the usual quality checks did not identify these issues before publication and have since put additional measures in place to safeguard research integrity.

We wish to credit our own Research Integrity and Research Publishing teams and anonymous and named external researchers and research integrity experts for contributing to this investigation.



The corresponding author, as the representative of all authors, has been given the opportunity to register their agreement or disagreement to this retraction. We have kept a record of any response received.

### **References**

- [1] H. I. Ahmad, A. Iqbal, N. Ijaz et al., "Molecular Evolution of the Activating Transcription Factors Shapes the Adaptive Cellular Responses to Oxidative Stress," *Oxidative Medicine and Cellular Longevity*, vol. 2022, Article ID 2153996, 13 pages, 2022.

## Research Article

# Molecular Evolution of the Activating Transcription Factors Shapes the Adaptive Cellular Responses to Oxidative Stress

**Hafiz Ishfaq Ahmad** <sup>1</sup>, **Asia Iqbal**,<sup>2</sup> **Nabeel Ijaz**,<sup>3</sup> **Muhammad Irfan Ullah**,<sup>4</sup> **Akhtar Rasool Asif**,<sup>5,6</sup> **Abdur Rahman**,<sup>5,7</sup> **Tahir Mehmood**,<sup>8</sup> **Ghulam Haider**,<sup>9</sup> **Shakeel Ahmed**,<sup>10</sup> **Samy F. Mahmoud**,<sup>11</sup> **Fatimah Othman Alghamdi**,<sup>12</sup> **Hala Abdulrahman Al Amari**,<sup>12</sup> **Mario Juan Simirgiotis**,<sup>10</sup> and **Jinping Chen** <sup>13</sup>

<sup>1</sup>Department of Animal Breeding and Genetics, University of Veterinary and Animal Sciences, Lahore, Pakistan

<sup>2</sup>Department of Wild Life and Ecology, University of Veterinary and Animal Sciences, Lahore, Pakistan

<sup>3</sup>Department of Clinical Science, Faculty of Veterinary Sciences, Bahauddin Zakariya University, Multan, Pakistan

<sup>4</sup>Department of Pathobiology, Faculty of Veterinary Sciences, Bahauddin Zakariya University, Multan, Pakistan

<sup>5</sup>Department of Animal Sciences, University of Veterinary and Animal Sciences, Jhang, Pakistan

<sup>6</sup>Key Laboratory of Animal Genetics, Breeding and Reproduction, Huazhong Agricultural University, Wuhan, China

<sup>7</sup>Department of Animal Nutrition, Afyon Kocatepe University, Turkey

<sup>8</sup>Centre for Applied Molecular Biology (CAMB), University of the Punjab, Lahore 53700, Punjab, Pakistan

<sup>9</sup>Department of Biological Sciences, University of Veterinary and Animal Sciences, Ravi Campus, Pattoki, Pakistan

<sup>10</sup>Instituto de Farmacia, Facultad de Ciencias, Universidad Austral de Chile, Campus Isla Teja, 5090000 Valdivia, Chile

<sup>11</sup>Department of Biotechnology, College of Science, Taif University, P.O. Box 11099, Taif 21944, Saudi Arabia

<sup>12</sup>National Center for Biotechnology King Abdulaziz City for Science and Technology Riyadh, Saudi Arabia

<sup>13</sup>Guangdong Key Laboratory of Animal Conservation and Resource Utilization, Guangdong, Public Laboratory of Wild Animal Conservation and Utilization, Institute of Zoology, Guangdong Academy of Sciences, Guangzhou, Guangdong, China

Correspondence should be addressed to Hafiz Ishfaq Ahmad; [ishfaq.ahmad@uvas.edu.pk](mailto:ishfaq.ahmad@uvas.edu.pk) and Jinping Chen; [chenjp@giz.gd.cn](mailto:chenjp@giz.gd.cn)

Received 11 March 2022; Accepted 20 June 2022; Published 13 July 2022

Academic Editor: Yujie Chen

Copyright © 2022 Hafiz Ishfaq Ahmad et al. This is an open access article distributed under the Creative Commons Attribution License, which permits unrestricted use, distribution, and reproduction in any medium, provided the original work is properly cited.

Reactive oxygen species (ROS) play an essential part in physiology of individual cell. ROS can cause damage to various biomolecules, including DNA. The systems that have developed to harness the impacts of ROS are antique evolutionary adaptations that are intricately linked to almost every aspect of cellular function. This research reveals the idea that during evolution, rather than being largely conserved, the molecular pathways reacting to oxidative stress have intrinsic flexibility. The coding sequences of the ATF2, ATF3, ATF4, and ATF6 genes were aligned to examine selection pressure on the genes, which were shown to be very highly conserved among vertebrate species. A total of 33 branches were explicitly evaluated for their capacity to diversify selection. After accounting for multiple testing, significance was determined using the likelihood ratio test with a threshold of  $p \leq 0.05$ . Positive selection signs in these genes were detected across vertebrate lineages. In the selected test branches of our phylogeny, the synonymous rate variation revealed evidence (LRT,  $p$  value =  $0.011 \leq 0.05$ ) of gene-wide episodic diversifying selection. As a result, there is evidence that diversifying selection occurred at least once on at least one test branch. These findings indicate that the activities of ROS-responsive systems are also theoretically flexible and may be altered by environmental selection pressure. By determining where the genes encoding these processes are “targeted” during evolution, we may better understand the mechanism of adaptation to oxidative stress during evolution.

## 1. Introduction

Since the beginning of life on Earth, oxidative stress has been a main burden on biological systems. Since the advent of plants and the initiation of photosynthesis, living systems have had to deal with the challenge of higher oxygen levels. This has continued with the development of aerobic oxidative respiration. Reactive oxygen species include peroxides (for example,  $H_2O_2$ ), hydroxyl radicals (OH), superoxide ( $O_2^-$ ), and oxygen, to name a few (ROS) [1]. During the day and night cycle, oxidative stress varies. In more recent evolutionary times, the harmful effects of various manmade substances have resulted in oxidative stress due to human actions on the environment [2]. A balance of antioxidant and prooxidant components regulates ROS levels. An oxidative stress condition occurs when rising amounts of ROS are not responded by increased reducing or antioxidant activity. Higher levels of ROS are a possible source of injury for many macromolecules due to the production of single and double-stranded DNA breaks and irreversible denaturation of proteins produced by the oxidation and carbonylation of arginine, proline, lysine, and threonine residues (Figure 1) [3]. Many cellular systems, both enzymatic and nonenzymatic, have developed to resist these effects. Gene expression control systems that allow animals to withstand or harness the consequences of increased ROS levels are usually old evolutionary adaptations intricately linked to most levels of cellular function [4]. These routes have recognized a lot of interest in studies using genetically available model species. It is unclear how these systems originated or adapted to different environmental conditions during evolution although [5]. Researchers have found evidence of species-specific distinctions among animals when exploiting the ROS effects. During fertilization, the plasma membrane NADPH-oxidase produces an extracellular burst of  $H_2O_2$  production and the enzyme ovoperoxidase [6]. External chemical and physical stressors are imposed on cells by foreign molecules that disrupt metabolic or signaling systems and changes in temperature or pH. Internal molecular stressors, such as creating reactive metabolic products, can affect cells [7]. The ability of cells and tissues to modify molecular processes in response to such stimuli is crucial for maintaining tissue homeostasis [8].

The gene expression regulatory systems that allow organisms to endure increased ROS levels or control their effects are intricately intertwined with most aspects of cellular function. Most elements of cellular physiology are intricately intertwined with these gene expression regulatory systems, which are usually old evolutionary adaptations [1]. These processes have garnered much interest in research that has used a small number of genetically reachable model organisms [10]. However, relatively less is recognized about how these systems have evolved and how they have adapted to varied environmental situations throughout evolutionary history. This study is aimed at examining the ATF gene family's evolutionary links, physiochemical characteristics, comparative genomics, and analysis of ATF genes in vertebrate species. We conducted thorough comparative investigations of the activat-

ing transcription factor genes coding proteins directing the DNA repair process in over 164 of vertebrate species. In this study, the gene and protein sequences of vertebrate activating transcription factors were evaluated to identify the selection pressure on these genes. This selective pressure may play a major role in adaptive evolution. In this work, we investigate the evolution of these genes in diverse vertebrates and how natural selection and genetic variation have impacted the evolution of this gene family through time.

## 2. Materials and Methods

**2.1. Data Curation and Sequence Analysis.** The orthologous coding sequences of ATF genes from 164 vertebrate genomes, including the human genome, were taken using the biomart programme [11]. As a result, we got all gene sequences from Ensembl [12] and the NCBI GenBank [13]. The Ensembl database was used to find the protein sequences (Tables S1-S4). InterPro [14] domain annotation was used to identify protein domains of ATF proteins. The genome-wide domain prediction selected Activating Transcription Factor's Basic leucine zipper (bZIP) domain [15]. The sequences of all nonhuman orthologous transcript isoforms, as well as the human MANE transcript isoform, were included in a dataset [16]. The orthologous sequences were then aggregated using the MMseqs2 programme [17], with at least 80% sequence similarity within each cluster, and a cluster including the human sequence was chosen for further investigation.

**2.2. Adaptive Selection in the ATF Genes.** We evaluated the sequences to clearly identify the variations that may define adaptive phenotypes, genetic variation, and demographic statistics in order to fully comprehend the adaptiveness of positively selected sites. The abovementioned positively selected gene candidates were carefully explored by quarrying various protein databanks. We used maximum likelihood parameters to evaluate the coding sequences of ATF2, ATF3, ATF4, and ATF6 genes to discover adaptive selection [18]. The branch-site model and two alternative maximum likelihood approaches were used to find branches under positive selection employed in PAML package [19] and the HyPhy package in the Datamonkey Web Server (<http://www.datamonkey.org>) [20]. In a similar fashion, we utilised MEME derived from HyPhy v2.5 in order to identify positively chosen locations for genes that were shown to be positively selected by aBSREL. In our subsequent studies, we concentrated on potential genes and codons, for which there was evidence of positive selection based on both sets of data [19]. Positive selection was validated using the selecton server, which avoids false-positive PAML results by using the mechanistic empirical combination (MEC) model to estimate selection pressure for individual codons [21]. Within the context of a multiple sequence alignment, selecton enables the ratio to fluctuate between distinct codons. In addition to this, the results of the selecton tool were graphically displayed



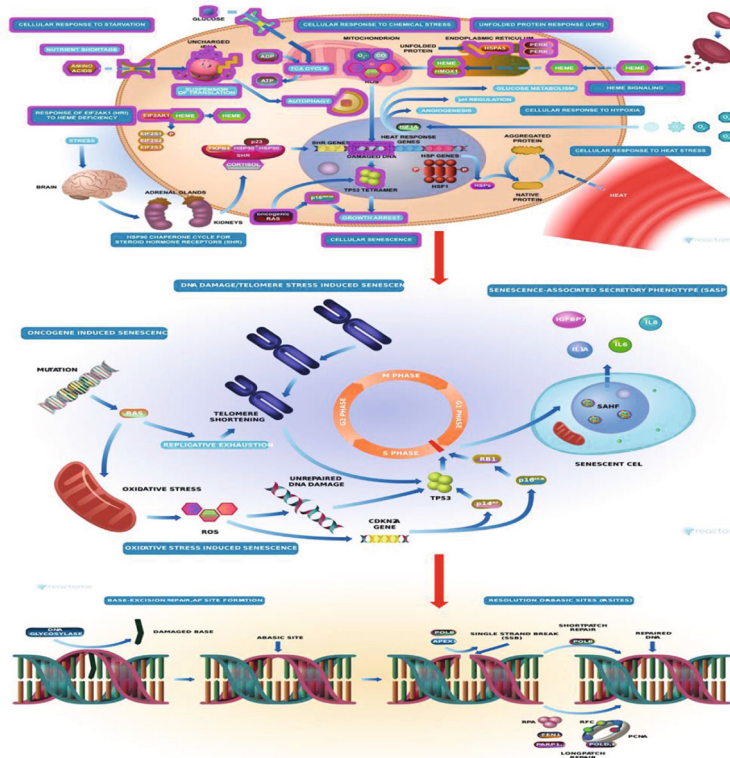


FIGURE 1: Base excision repair (BER) pathways are involved in cellular responses to stress and the repair of nucleotide damage in DNA. It is the pathway showing the number of unique enzyme activities [9].

using color scales that show the varied types of selections that were carried out [22].

**2.3. Conservation Analysis and Protein Network Analysis.** Using an intuitive user interface, the web-based application ConSurf (<http://consurf.tau.ac.il/>) calculated the evolutionary conservation scores in the human ATF2, ATF3, ATF4, and ATF6 proteins and mapped them onto protein structures. Structurally and functionally significant areas of the protein generally evolutionarily conserved residues that are geographically near to one other [23]. Due to their role in protein networks or their proximity to enzymes, these proteins have a higher level of amino acid conservation than other proteins. As a result, changes to conserved amino acids have a greater impact on protein structure and function than polymorphisms in flexible protein regions [23]. The degree of conservation is greatly dependent on the function of the protein domain and can range from being extremely conserved in position and amino acid to being quite varied. This range is due to the fact that different protein domains have different functions. When differentiated by their respective binding partners, ion-binding sites are found to have a greater tendency toward conservation than functional sites that bind peptides or nucleotides [23, 24]. We performed a protein-protein interaction study on ATF proteins to determine the functional networks between ATF genes and the other genes involved in base excision repair in oxidative stress. STRING software [25] was used to conduct the interaction analysis, and commercial Cytoscape software [26] was

used to show the results. STRING not only integrates well-known classification systems like Gene Ontology and KEGG but also provides innovative classification methods based on high-throughput text mining and clustering of the interaction network itself [27].

**2.4. Transcriptomic Analysis.** We combined the results of these large-scale transcriptome studies and shed light on ATF gene biology using the Genotype-Tissue Expression (GTEx) database Release V8 (dbGaP Accession phs000424.v8.p2) [28], which provides gene-level association data describing the testing and mediating effects of gene expression levels on phenotypes. We searched with the term activating transcription factor with the gene information (ATF2: ENSG00000115966.16, ATF3: ENSG00000162772.16, ATF4: ENSG00000128272.14, and ATF6: ENSG00000118217.5) using bulk tissue expression panel. The project's goal is to generate a complete open resource for understanding tissue-specific expression and regulation. Nearly 1000 persons had tissue samples obtained from 54 nondiseased areas for molecular tests [29].

### 3. Results

The goal of this work was to assess the gene sequences of activating transcription factor genes in various vertebrate species in order to quantify the vigour of selection in these genes, which may be implicated in adaptive evolution. We looked for three genes involved in mending DNA bases damaged by reactive oxygen species, which are triggered by

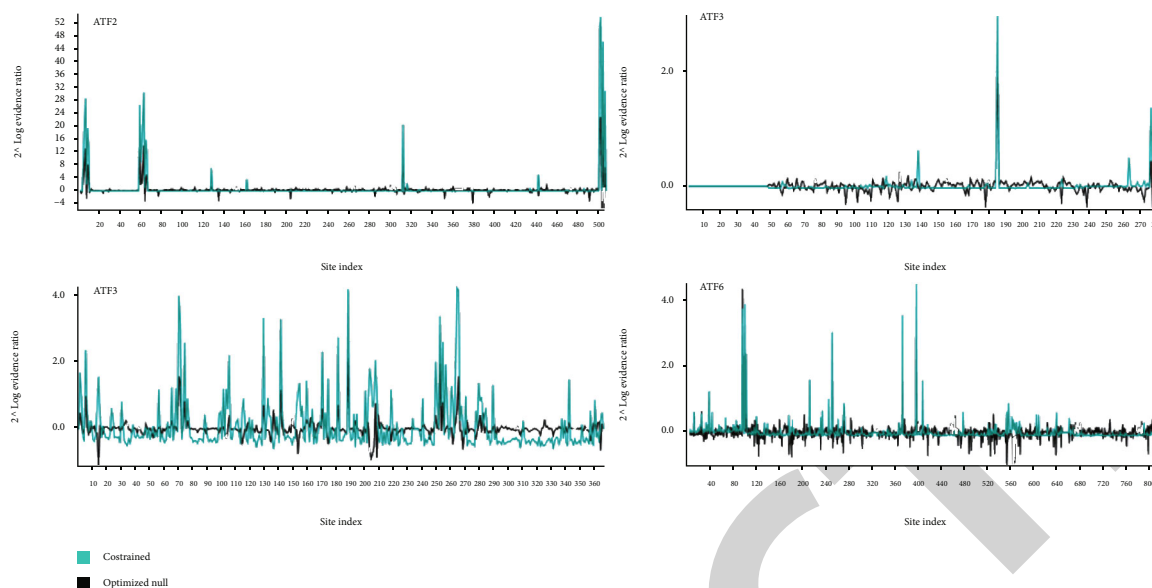


FIGURE 2: ATF gene phylogeny test branches with episodic diversifying selection over the whole genome. The BUSTED null model is the selection model for the unconstrained model, whereas the selection model for the constrained model is the BUSTED alternative model.

a sequence of DNA glycosylases such ATF2, ATF3, ATF4, and ATF6. We discovered that these genes have a signal of adaptive evolution in that they repair DNA bases that have been damaged by reactive oxygen species.

**3.1. Adaptations in the ATF Genes across Mammalian Phylogeny.** In this study, we examined ATF2, ATF3, ATF4, and ATF6 genes for evidence of adaptation ranging from modest (BUSTED ( $p < 0.01$ )) to progressively strong (BUSTED ( $p < 0.05$ )). We calculated the average fraction of codons subjected to adaptive evolution in ATF genes. We extracted the proportion of favourably chosen codons for each coding sequence and averaged this proportion across branches. In the selected test branches of ATF2 phylogeny, BUSTED with synonymous rate variation discovered evidence ( $p < 0.05$ ) of gene-wide episodic diversifying selection ( $p < 0.05$ ). As a result, there is evidence that diversifying selection occurred at least once on three test branches. Using synonymous rate variation, we found no evidence of gene-wide episodic diversifying selection ( $p > 0.05$ ) in the selected test branches of ATF2 phylogeny. In this case, there is no evidence to support the hypothesis that any sites along the test branch have experienced diversifying selection throughout this investigation (Figure 2). A gene-wide episodic diversifying selection in the test branches of ATF4 phylogeny detected diversifying selection ( $p < 0.05$ ) in the selected test branches of ATF4 phylogeny using synonymous rate variation (LRT). Diversifying selection has taken place at two test branches inferring that the site has undergone diversifying selection (Figure 2). While investigating the selected test branches of the phylogeny of ATF6 gene, BUSTED found no evidence ( $p > 0.05$ ) of gene-wide episodic diversifying selection throughout the genome (Figure 2).

**3.2. Positive Selection of Activating Transcription Factors.** The coding sequences of 164 species were aligned and compared with the reference sequence that best explain evolution in nature in order to find evidence of positive selection. Three types of tests may be used to detect and quantify adaptation in a multispecies coding sequence alignment: branch tests, site tests, and branch-site tests. Branch tests are the most popular type of test. A lineage-specific selection technique was used to identify distinct lineages under selection pressure throughout the evolution of vertebrate species. Both of these tests focused on the branch that includes humans and great apes. Our approach incorporates stringent measures for reducing the amount of false positives, such as removing orthologs that were only distantly comparable, manually correcting alignments, and only evaluating genes and sites that were found by both tests for positive selection. In addition, we investigated the potential locations for selection to see how they varied among human and nonhuman great ape population statistics. This helped us validate the candidate sites. We conducted research on archaic human genomes in order to provide a rough estimate for the date at which favourably selected sites in the human lineage occurred. An adaptive branch-site random effects likelihood (aBSREL) model was utilised by us in order to quantify selection probability and discover lineage-specific selection for each phylogenetic grouping. This was done so that lineage-specific selection could be uncovered. After that, the aBSREL approach was used to evaluate each gene in order to identify lineages that had been subjected to adaptive selection when the species were undergoing evolutionary adaptations. The aBSREL model revealed that the genes identified by BUSTED as being subject to positive selection in mammalian lineages were likewise subject to selection pressure in mammalian lineages (Table 1). The

TABLE 1: The adaptive branch-site random effects likelihood (aBSREL) test provides evidence of episodic diversifying selection on branches of the ATF gene phylogeny. In the detailed results table, significance and the number of rate categories inferred at each branch are presented.

Gene	Branch in selection	B	LRT	Test $p \leq 0.05$	Uncorrected $p \leq 0.05$	$\omega$ distribution over sites
ATF2	CHIMPANZEE	0.000	77.0226	0.000	0.001	$\omega_1 = 1.000$ (98%) $\omega_2 = 1000$ (1.8%)
	SHEEP	0.000	49.4928	0.001	0.001	$\omega_1 = 0.0460$ (99%) $\omega_2 = 1460$ (0.90%)
ATF3	CATTLE	0.000	16.0401	0.0038	0.0001	$\omega_1 = 0.000$ (100%) $\omega_2 = 1560$ (0.22%)
	MANDARIN_FISH	0.000	13.5521	0.0124	0.0004	$\omega_1 = 0.1150$ (93%) $\omega_2 = 84.80$ (7.3%)
ATF4	CATTLE	0.0296	15.6649	0.0044	0.0001	$\omega_1 = 1.0000$ (99%) $\omega_2 = 1000$ (0.93%)
	AFER_AFER	0.1048	11.0642	0.0436	0.0014	$\omega_1 = 0.2420$ (96%) $\omega_2 = 14.00$ (3.8%)
ATF6	KANGAROO_RAT	0.0816	39.5383	0.001	0.001	$\omega_1 = 0.1020$ (95%) $\omega_2 = 38500$ (5.2%)
	RED_DEER	0.0647	31.6534	0.001	0.001	$\omega_1 = 0.1810$ (96%) $\omega_2 = 38500$ (3.6%)
	PIKA	0.0909	23.7437	0.0001	0.001	$\omega_1 = 0.1460$ (96%) $\omega_2 = 21300$ (4.4%)

B: optimized branch length; LRT: likelihood ratio test statistics for selection; Test- $p$  value:  $p$  value corrected for multiple testing; Uncorrected  $p$  value: raw  $p$  value without correction for multiple testing;  $\omega$  distribution over sites: inferred  $\omega$  estimates and respective proportion of sites.

aBSREL revealed the evidence of episodic diversifying selection on 5 of the 38 branches in the phylogeny of ATF2 gene, which is a significant finding. A total of 38 branches of ATF2 gene were subjected to formal testing for the purpose of diversifying selection. After accounting for multiple testing, the significance of the results was determined using the likelihood ratio test ( $p < 0.05$ ) (Figure 3). It was discovered that episodic diversifying selection occurred on one out of every 32 branches in the phylogeny of ATF3 by aBSREL. A total of 32 branches of ATF3 gene were subjected to formal testing for the purpose of diversifying selection. After accounting for multiple testing, the significance of the results was determined using the likelihood ratio test ( $p < 0.05$ ) (Figure 3). A total of 33 branches of ATF4 were subjected to formal testing for the purpose of diversifying selection. After accounting for multiple testing, the significance of the results was determined using the likelihood ratio test ( $p < 0.05$ ) (Figure 3). A total of 33 branches were subjected to formal testing for the purpose of diversifying selection. After accounting for multiple testing, the significance of the results was determined using the likelihood ratio test ( $p < 0.05$ ) (Figure 3).

We found that these ATF genes have been under adaptive selection across vertebrate species, including chimpanzee, sheep, cattle, mandarin fish, afer afer, kangaroo rat, red deer, and pika in ATF2, ATF3, ATF4, and ATF6, respectively (Table 1). We carried out probability analysis to examine a number of different ratio-based models in order to find codons in ATF genes that are prone to positive selection.

The factors associated with gene selection in 164 species were determined with the help of the codeml programme, and positive selection was examined with the help of various models. According to the findings of the likelihood ratio test (LRT), which was 0, the ATF2 gene test in M7-M8 did not provide significant results ( $p > 0.05$ ). On the other hand, scores of 16.97, 12.19, and 190.62 on the likelihood ratio test (LRT) indicated that the ATF2, AT4, and AT6 genes had gained selection signals. According to the findings of the test for the selection model M8, which indicated that M8 was accepted and M7 was rejected ( $p > 0.05$ ), the ATF3 gene had signs of purifying selection, which indicates that M8 was chosen above M7. According to the findings of both the NEB and the BEB studies, the genes ATF2 and ATF4 exhibited evidence of positive selection at probabilities of 95 and 99 percent, respectively.

We subsequently analysed the probability values using FEL, MEME, and SLAC, analyses to reveal positive selection signals during the evolutionary process (Figure 4). Positive evolutionary selection was detected in the ATF2, ATF3, ATF4, and ATF6 genes of vertebrates (Table 2). With a posterior probability of 95 percent, we found several sites under positive selection in the basic leucine zipper (bZIP) domain of the Activating Transcription Factor protein using BEB analysis. By merging the findings of PAML with the data set in the selecton server, which recognizes adaptive selection at specified sites in the protein, we were able to confirm positive selection. The substitution rates were found using the MEC model (Figures S1-S4).

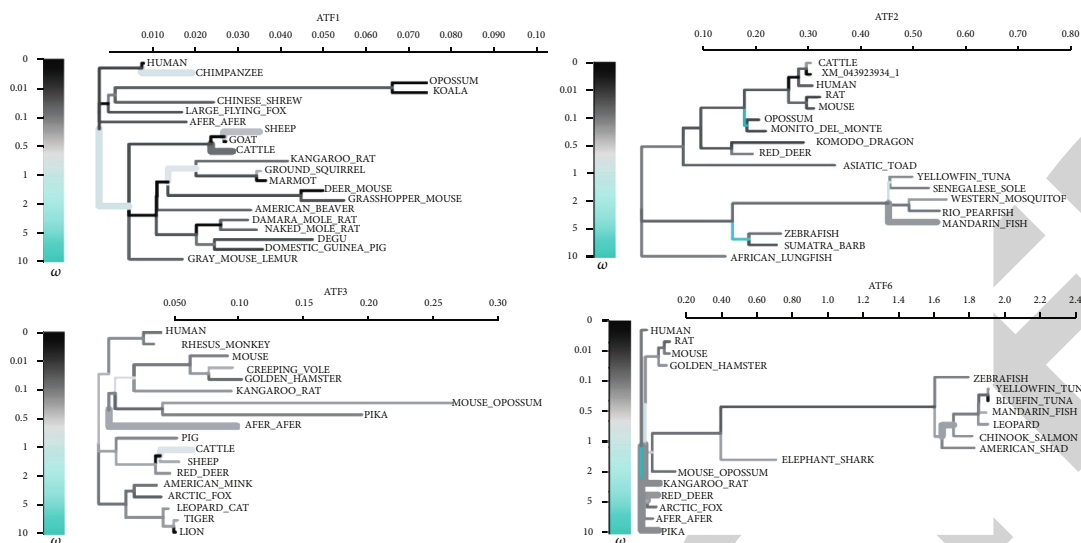


FIGURE 3: Selective assessments of vertebrate activating transcription factor genes performed with the aBSREL models are presented. It is possible to classify the sites in a branch according to the inferred beta distribution; the branch's length is divided into segments based on the proportion of sites in each class, and the color of the segment shows the magnitude of the related values. In the case of thicker branches, those with a  $p < 0.05$  (corrected for multiple testing) for rejecting the null hypothesis have undergone diversifying positive selection. In contrast, those with a  $p$  value greater than 1 are identified as having undergone diversifying negative selection.

**3.3. Conservation and Protein Network Analysis.** Using the ConSurf server, we examined at how duplicates have evolved in various animals both horizontally and vertically. Analyzing conserved residues revealed a network of interdependent connections in the structural and functional topographies of places that had been chosen with care. Protein amino acid positions may have coevolved because of structural or functional relationships. We used ATF2, ATF3, ATF4, and ATF6 homologs as inputs to a conservation analysis in order to find various conserved residues that were thought to be under positive selection. Conservation values that vary from 1 to 9 were employed to anticipate conserved amino acids. Variable conservation values range from 1–4, moderate conservation values range from 5–6, and extremely high conservation values range from 7–9 (Figures S5–S8). Between the number of amino acid residues and the strength of their coevolutionary ties, a connection has been found. Subnetworks of amino acid residues discovered in the protein's domains have favourably chosen nodes. Research shows that these ATF protein portions are physically and functionally unique from one other.

The interactive network is justified by the nodes, lines, and colors (Figure 5). In various investigations, it has been discovered that the genes for certain proteins are associated in their expression. After creating a coexpression analysis database based on RNA expression patterns and protein coregulation data supplied by ProteomeHD, the STRING calculated coexpression scores based on the data. For cytochrome proteins, the signaling intensities of the proteins were investigated in detail. When comparing the number of protein residues engaged in signal receiving and communicating, the researchers discovered that more protein residues are involved in signal receiving. Colors characterize the outcomes, which are represented on the anticipated structures (Figure 6).

**3.4. Transcriptomic Signatures of the Activating Transcription Factors.** An expression quantitative trait locus (eQTL) browser is a primary resource in the GTEx database that maintains and displays the results of a national research initiative to discover the relationship between genetic variants and high-throughput molecular-level expression phenotypes. Several tissues show considerable associations between the majority of genes. There were strong connections between oxidative stress and ATF2 and ATF6, whereas ATF3 and ATF4 were substantially expressed in the artery, adipose, colon, and skin tissues (Figures 6 and 7). However, when we looked at the average across all (significant) genes using multiple enrichment metrics, tissues predicted to be more enriched for illnesses and presently known biology did not consistently do so. Multiple tissues are implicated in several noteworthy correlations. Context specificity and a shared regulation mechanism may be to blame for this.

## 4. Discussion

Recent developments in molecular biology, including use of Microarray technology for gene expression profiling, have revealed new information on the animal stress response, notably the impact of stress on gene regulation [12, 13]. It has been determined that the ability to target ROS-induced covalent alterations of bases is a key adaptation for surviving the damaging impacts of the surrounding environment. For organisms to withstand high amounts of ROS or harness their effects, most of their physiological processes are intricately linked to gene expression regulatory systems [30]. These gene expression regulation systems are usually old evolutionary adaptations intricately intertwined with most elements of cellular physiology and function [31]. Oxidative stress activates numerous regulatory mechanisms, including cell cycle regulation

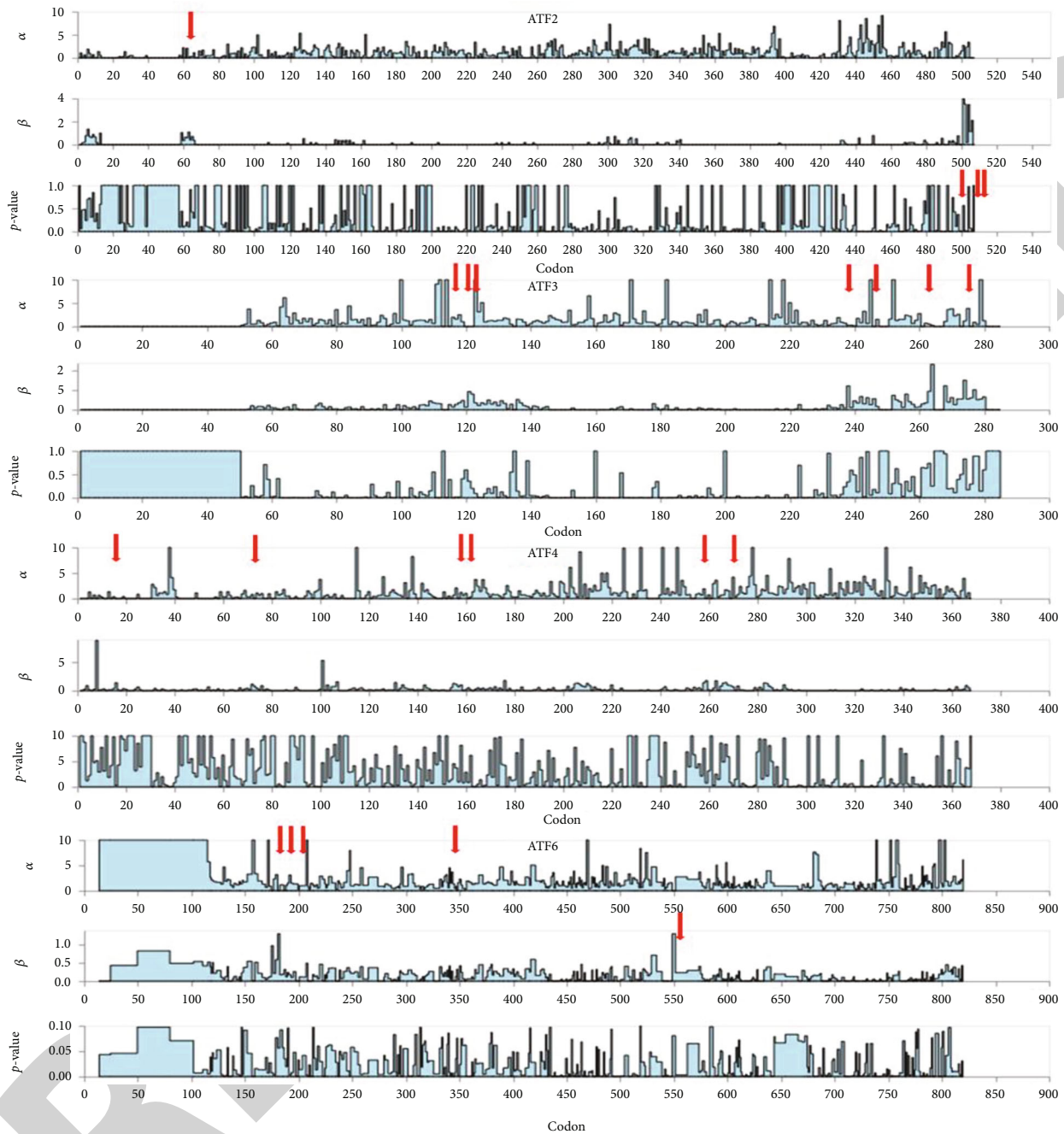


FIGURE 4: Maximum probability dN/dS estimates for each ATF site, together with predicted profile confidence intervals. A horizontal grey line represents dN/dS = 1 (neutrality). Vertical dashed lines represent division boundaries (if any exist). The asymptotic 2 distribution is used to determine statistical significance. Site-to-site synonymous rate variation is included in this research.

and apoptosis, which help shield organisms against ROS. ROS-induced cellular responses include cell cycle arrest and apoptosis, which are critical in determining a cell's destiny [32]. At lower concentrations, ROS can reversibly inactivate cysteine and methionine residues that are sensitive to redox and operate as an alternative system through the inactivation of enzymes with cysteine active site residues, such as phosphotyrosine-phosphatases [33]. We identified the adaptive selection in ATF4 and ATF6 genes in the basic leucine zipper (bZIP) domain of ATF and related proteins is a DNA-binding and dimerization

domain; ATF is a basic leucine zipper (bZIP) transcription factor that is induced by a variety of stress signals including cytokines, genotoxic agents, and physiological stresses. It is involved in cancer development and the host's defense against infections. It acts as a negative regulator of proinflammatory cytokine production and is crucial in avoiding acute inflammatory disorders. Animals lacking ATF are more susceptible to endotoxic shock-induced mortality [34]. ATF3 dimerizes with Jun and other ATF proteins; heterodimers operate as activators or repressors, depending on the promoter environment. bZIP factors

TABLE 2: The FEL study' detailed site-by-site results. The asymptotic 2 distribution is used to determine statistical significance. Site-to-site synonymous rate variation is included in this research. For site-level dN/dS ratios, approximate confidence ranges have been calculated.

Gene	Codons	$\alpha$	$\beta$	$\alpha = \beta$	LRT	$p$ value	TBL	Selection type
ATF2	63	0	1.097	0.685	2.724	0.0988	1.779	Diversifying
	502	0	3.515	2.592	5.507	0.0189	6.737	Diversifying
	505	0	1.128	0.859	3.272	0.0705	2.233	Diversifying
	506	0	2.092	1.663	5.251	0.0219	4.323	Diversifying
	115	0	0.273	0.188	0.743	0.3888	1.799	Diversifying
	121	0	0.934	0.525	0.855	0.3553	5.029	Diversifying
ATF3	122	0	0.808	0.521	1.64	0.2004	4.989	Diversifying
	238	0.259	1.224	0.861	0.916	0.3386	8.247	Diversifying
	246	0	0.567	0.423	1.8	0.1797	4.049	Diversifying
	264	0.25	2.333	0.771	1.331	0.2487	7.391	Diversifying
	276	0	0.61	0.504	1.103	0.2937	4.83	Diversifying
	16	0	1.408	0.992	4.671	0.0307	3.04	Diversifying
ATF4	73	0	0.756	0.488	3.35	0.0672	1.495	Diversifying
	157	0	0.696	0.487	2.752	0.0971	1.493	Diversifying
	161	0	0.532	0.317	2.975	0.0846	0.971	Diversifying
	259	0	1.782	1.465	3.138	0.0765	4.489	Diversifying
	269	0	0.897	0.652	3.015	0.0825	1.998	Diversifying
	176	0	0.978	0.593	7.165	0.0074	5.141	Diversifying
ATF6	181	0	1.306	0.906	3.646	0.0562	7.854	Diversifying
	187	0	0.321	0.183	4.438	0.0351	1.586	Diversifying
	348	0	0.325	0.215	3.149	0.076	1.862	Diversifying
	551	0	1.307	0.808	3.056	0.0805	7.000	Diversifying

$\alpha$ : the rate of synonymous substitution at a given location.  $\beta$ : the rate of non-synonymous substitution at a given location.  $\alpha = \beta$ : under the neutral model, the rate estimate. LRT: beta = alpha vs. beta  $\neq$  alpha  $p$  value likelihood ratio test statistic:  $p$  value: evidence of selection asymptotic  $p$  value. TBL: total branch length.

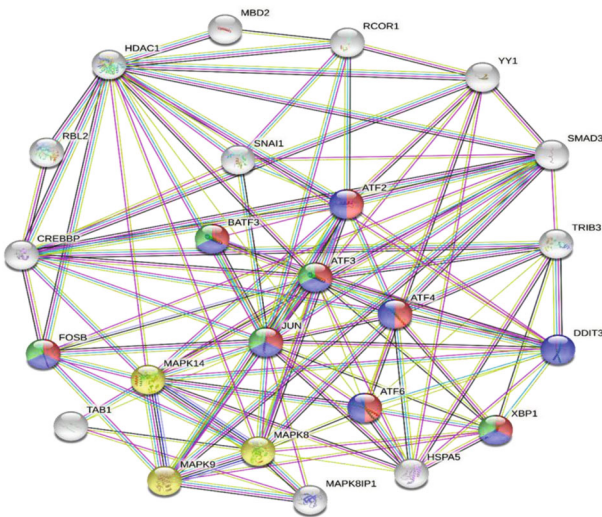


FIGURE 5: The activating transcription factors are expressed in human tissues. The expression data of the indicated genes across different human tissues from the GTEx consortium [28].

regulate a vast array of cellular functions via homo- and heterodimers networks [35].

The branch-site random effect likelihood test (BSREL test) [36] and the BUSTED test [37], both included in the HYPHY package [38], are used to evaluate this hypothesis (materials and methods). In an adaptive evolution study, the BSREL and BUSTED tests are used to determine the percentage of codons in which the rate of nonsynonymous changes is higher than the synonymous rate ( $dN/dS > 1$ ) for a certain coding sequence [38]. We used the BUSTED test to estimate the ratio of codons throughout the whole tree and the BSREL test to compute the ratios of selected codons for each branch [20]. Both of these tests were further evaluated two alternate evolutionary simulations, one with adaptive replacements and the other without, to comprehend if the adaptive model fits the data significantly better [39].

The results of this phylogenetic analysis are used to deduce the evolutionary history of repair pathways and the proteins that comprise them, as well as to predict the repair phenotypes of species with sequenced genomes [40, 41]. The ATF genes of vertebrates have been found to be under positive selection. Residues that had been positively selected were found in a wide range of amounts and locations. We uncovered two codons that were positively

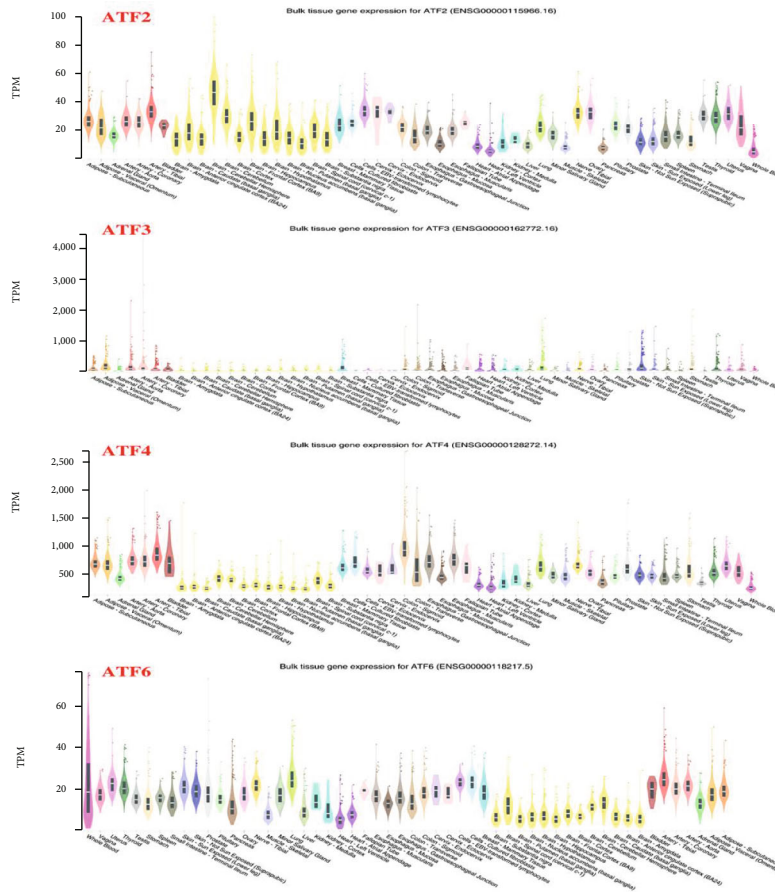


FIGURE 6: Protein-protein interaction analysis of activating transcription factor proteins. The length of a connection specifies the distance and function of interacting proteins. Unknown proteins are shown by red nodes, whereas known proteins are represented by full nodes. Protein-protein interactions are shown by black lines.

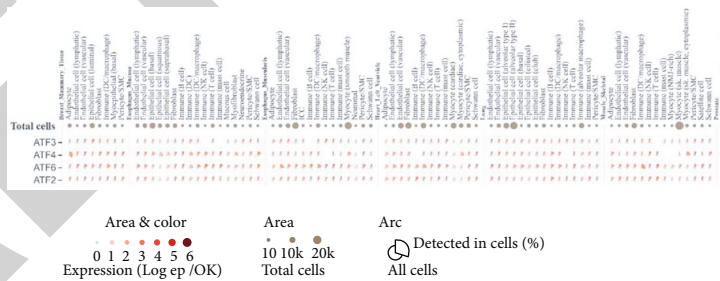


FIGURE 7: ATF differ across human tissue types but are correlated among tissues types. (a) Distribution of activating transcription factors (ATF) across 24 GTEx tissue types [28].

selected in the functional domains of the human ATF2, ATF3, ATF4, and ATF6 proteins (Figure 2). BER in vertebrate genomes relies heavily on molecules known as activating transcription factors (ATFs) [42]. Thus, the paralogues undergo relaxed purifying selection immediately after duplication. Orthologous repeats have been shown to develop under selection that is least strong. We further demonstrate that this selection affects each copy, suggesting that selection maintains the specific functional-

ity of particular repetitions throughout the genome [43]. There are strong connections between oxidative pressure and the body’s internal clock. Several researchers have hypothesized that the massive oxidation reaction resulting from the emergence of plants and photosynthesis was one of the earliest stirring forces for forming an interior time system during the genesis of life on Earth [25]. The synthesis and scavenging of hydrogen peroxide are highly dependent on the time of day; as a result, the emergence

of an endogenous 24h clock system was a crucial step in the development of a temporally synchronized homeostatic reaction to reactive oxygen species. All four ATF2, ATF3, ATF4, and ATF6 gene sequences have been analysed by MAFFT and shown to have a common protein domain (Figures 2). These genes have LRT values of 0 for the M2 and M1 evolutionary models, and LRT values of 1.48 for the M1 model for ATF2. In purifying selection zones, protein mutations undergo deleterious nonidentical changes, making it unlikely that they would remain fixed throughout time [25, 44]. The next step was to find amino acid residues with  $\omega > 1$  value. ATF2, ATF3, ATF4, and ATF6 genes have undergone positive selection with LRT values of 6.54, 9.16, and 0.48, respectively, using the M8 evolutionary model (Table 1). Some regions of other proteins that have undergone substantial positive selection have evolved more quickly than the mature protein, according to our findings [26, 27]. In the case of the ATF proteins, dynamic selection has led to a change intended to increase protein secretion efficiency [45]. Since branch-site analysis might result in unclear selection due to multinucleotide alterations, we utilised the aBSREL model to corroborate our findings. Both the aBSREL and site models demonstrated comparable selection patterns. The results demonstrate that the observed overall selection patterns are accurate [27, 46]. The cellular stress response is ubiquitous with enormous physiological and pathological implications. It is a cell defense mechanism against the harm that external factors impose on macromolecules [32]. Cellular processes triggered by DNA and protein damage are inextricably linked and have comparable components [47]. Other stressor-specific cellular responses to reestablish homeostasis are frequently engaged concurrently with the cellular stress response [39, 48]. Additionally, cells may assess stress and initiate a death mechanism (apoptosis) when tolerance limits are surpassed. Genotype-Tissue Expression (GTEx) database is maintained by the National Center for Biotechnology Information (NCBI) to investigate the link between genetic diversity and gene expression in normal human tissues [49]. The GTEx database comprises an expression quantitative trait locus (eQTL) browser, a central resource for storing and displaying results of a national research initiative to establish the genetic variation-phenotype connection. This information can help interpret results from genome-wide association studies [28]. We utilised this database to investigate the relationship between the five SNP loci found in this study and the levels of ATF expression in diverse human tissues [50]. The process of duplicating genes is an evolutionary approach that helps genomes evolve in a variety of different directions. In the case of other proteins, a process known as positive selection takes place after a duplication event. This indicates the selective pressure that maintains genetic diversity [51]. The relaxed selection was lacking during the evolution of ATF genes in avian and vertebrate lineages, adding credence to Bayesian phylogenetic approaches [52]. Further, we demonstrated that interactions, such as physical interactions, may have a part to play in the coadaptation of proteins to their environment.

We observed that amino acids that are highly diverse across geographic regions in protein-coding genes tend to be adaptable, which may contribute to the long-term evolution that has occurred [53, 54]. The aerobic range is defined by systemic limits in the oxygen supply capacity of breathing and circulation. Systemic hypoxemia results from conditions that exceed the range in which oxidative metabolism may be sustained, resulting in diminished individual development and population abundance. These systemic reactions usually precede the initiation of an organismal or cellular stress response. Due to the fact that the onset of stress and the loss of performance define the limits of normal physiological function, researching them can give crucial information about the capacity and limitations of organismal acclimation and adaptive evolution.

The structure must be extremely strong in order to support a wide range of activities that are dependent on the recognition of molecules by other molecules. Some examples of these activities include the interaction of substrates to enzymes, the assembly of proteins into transcription factors, and the linkages between transcription factors proteins and their DNA targets. However, recognition events are often simply the initial step in a process that takes place on a molecular level. A change in the conformation of the macromolecule in question must be reversible for it to be possible to carry out the aforementioned function. Because of this need, the structure of the molecule must possess the required amount of flexibility.

Given the significance of these genes, two important questions that have been raised concern the regulation of heat shock gene expression and the operation of heat shock proteins. We now understand that the alleged “heat shock response” is actually a smaller subset of a larger cellular stress response. When exposed to UV radiation, oxidative damage, DNA damage, or carbohydrate deprivation, certain reactions take place. Some of these reactions resemble the heat shock response, while others seem to be distinct.

## 5. Conclusion

Current knowledge of the molecular processes reacting to oxidative stress suggests that many major regulatory pathways are highly conserved across a wide range of species, including humans, yeast, and *Drosophila*. However, these processes have undergone significant alterations throughout time. ATF2, ATF3, ATF4, and ATF6 were found to be the strongest candidate genes associated with tree lifespan, internal, and external stress conditions that cause bulky lesions and DNA single-strand breaks and play an important role in DNA repair. As a result, our findings may provide a framework to conduct further research to explore the relationships between the DNA damage and repair pathways among vertebrate species. Our research on the molecular evolution of DNA regulatory genes revealed that transacting factors frequently contributed to an increase in the rates of nonsynonymous substitutions when compared with structural genes. These findings were based on the findings of a study that was conducted by our group. The evolution of gene families is sped up by the processes of gene



duplication, gene transfer, and gene loss, all of which play significant roles in the process. This speeds up the turnover of genes, which results in the birth of new family members and the death of others. This is apparent when seen through the lens of evolutionary theory.

## Abbreviations

ROS:	Reactive oxygen species
ATF:	Activating transcription factor
BER:	Base excision repair
MANE:	Matched annotation between NCBI and EBI
NCBI:	National Center for Biotechnology Information
EBI:	European Bioinformatics Institute
bZIP:	Basic leucine zipper
BEB:	Bayes empirical Bayes
SLAC:	Single-likelihood ancestor counting
FEL:	Fixed effects likelihood
REL:	Random effects likelihood
WGS:	Whole genome sequencing
WES:	Whole exome sequencing
LRT:	Likelihood ratio test
eQTL:	Expression quantitative trait locus
GTE <sub>x</sub> :	Genotype-tissue expression.

## Data Availability

The data used to support the findings of this study may be released upon application to Jinping Chen.

## Conflicts of Interest

There is no conflict of interest in the conduction of this study.

## Authors' Contributions

Data curation was done by HIA, GH AI, NI, IU, and TM. Formal analysis was done by HIA, AI, SFM, SOA, and TM. Funding acquisition was done by CJ. Investigation was done by CJ. Methodology was done by HIA, AI, ARA, AR, HAA, and GH. Project administration was done by CJ. Resources were done by HIA and CJ. Software was done by HIA, GH, NI, ARA, SFM, SOA, and AI. Supervision was done by CJ. Validation was done by HIA and CJ. Visualization was done by GH, AI, IU, AR, HAA, and TM. Writing—original draft was done by HIA, GA, AI, and TM. Writing—review and editing was done by GH, AI, TM, and CJ.

## Acknowledgments

This work was supported by the GDAS project of Science and Technology Development (2019-GDASYL-0103059) and Taif University Researchers Supporting Project number (TURSP-2020/138), Taif University, Taif, Saudi Arabia.

## Supplementary Materials

Supplementary material showing the list of vertebrate species and NCBI Genbank accession numbers for sequences used to build datasets for hypothesis testing of the ATF genes. Table S1: list of vertebrate species and NCBI Genbank accession numbers for sequences used to build datasets for hypothesis testing of the ATF2 gene. Table S2: list of vertebrate species and NCBI Genbank accession numbers for sequences used to build datasets for hypothesis testing of the ATF3 gene. Table S3: list of vertebrate species and NCBI Genbank accession numbers for sequences used to build datasets for hypothesis testing of the ATF4 gene. Table S4: list of vertebrate species and NCBI Genbank accession numbers for sequences used to build datasets for hypothesis testing of the ATF6 gene. Figure S1: selecton analyses of human ATF2 protein are color-coded and compared to sequences from aligned nucleotide coding sequences. Yellow and brown highlights represent positive selection, neutral selection is represented by grey and white highlights, and purple highlights on codons represent purifying selection. Figure S2: selecton analyses of human ATF3 protein are color-coded and compared to sequences from aligned nucleotide coding sequences. Yellow and brown highlights represent positive selection, neutral selection is represented by grey and white highlights, and purple highlights on codons represent purifying selection. Figure S3: selecton analyses of human ATF4 protein are color-coded and compared to sequences from aligned nucleotide coding sequences. Yellow and brown highlights represent positive selection, neutral selection is represented by grey and white highlights, and purple highlights on codons represent purifying selection. Figure S4: selecton analyses of human ATF6 protein are color-coded and compared to sequences from aligned nucleotide coding sequences. Yellow and brown highlights represent positive selection, neutral selection is represented by grey and white highlights, and purple highlights on codons represent purifying selection. Figure S5: conservation analyses of human ATF2 protein. The conservation values ranging from 1-9 were used to predict conserved amino acids; conservation values between 1 and 4 are considered variable, 5-6 indicate moderate conservation, and 7-9 indicate very high conservation. Figure S6: conservation analyses of human ATF3 protein. The conservation values ranging from 1-9 were used to predict conserved amino acids; conservation values between 1 and 4 are considered variable, 5-6 indicate moderate conservation, and 7-9 indicate very high conservation. Figure S7: conservation analyses of human ATF4 protein. The conservation values ranging from 1-9 were used to predict conserved amino acids; conservation values between 1 and 4 are considered variable, 5-6 indicate moderate conservation, and 7-9 indicate very high conservation. Figure S8: conservation analyses of human ATF6 protein. The conservation values ranging from 1-9 were used to predict conserved amino acids; conservation values between 1 and 4 are considered variable, 5-6 indicate moderate conservation, and 7-9 indicate very high conservation. (*Supplementary Materials*)

## References

- [1] R. Siauicunaite, N. S. Foulkes, V. Calabrò, and D. Vallone, "Evolution shapes the gene expression response to oxidative stress," *International Journal of Molecular Sciences*, vol. 20, no. 12, p. 3040, 2019.
- [2] M. Hayyan, M. A. Hashim, and I. M. AlNashef, "Superoxide ion: generation and chemical implications," *Chemical Reviews*, vol. 116, no. 5, pp. 3029–3085, 2016.
- [3] C. Nathan and A. Ding, "SnapShot: reactive oxygen intermediates (ROI)," *Cell*, vol. 140, no. 6, pp. 951–951, 2010.
- [4] Y. J. Taverne, D. Merkus, A. J. Bogers, B. Halliwell, D. J. Duncker, and T. W. Lyons, "Reactive oxygen species: radical factors in the evolution of animal life," *BioEssays*, vol. 40, no. 3, p. 1700158, 2018.
- [5] J. Checa and J. M. Aran, "Reactive oxygen species: drivers of physiological and pathological processes," *Journal of Inflammation Research*, vol. Volume 13, pp. 1057–1073, 2020.
- [6] E. Shekhova, "Mitochondrial reactive oxygen species as major effectors of antimicrobial immunity," *PLoS Pathogens*, vol. 16, no. 5, article e1008470, 2020.
- [7] R. Schreck, K. Albermann, and P. A. Baeuerle, "Nuclear factor  $\kappa$ B: an oxidative stress-responsive transcription factor of eukaryotic cells (a review)," *Free Radical Research Communications*, vol. 17, no. 4, pp. 221–237, 1992.
- [8] K. Ameri and A. L. Harris, "Activating transcription factor 4," *The International Journal of Biochemistry & Cell Biology*, vol. 40, no. 1, pp. 14–21, 2008.
- [9] A. Fabregat, K. Sidiropoulos, G. Viteri et al., "Reactome pathway analysis: a high-performance in-memory approach," *BMC Bioinformatics*, vol. 18, no. 1, pp. 1–9, 2017.
- [10] S. Di Meo, G. Napolitano, and P. Venditti, "Physiological and pathological role of ROS: Benefits and limitations of antioxidant treatment," *International Journal of Molecular Sciences*, vol. 20, no. 19, p. 4810, 2019.
- [11] S. Durinck, Y. Moreau, A. Kasprzyk et al., "BioMart and bioconductor: a powerful link between biological databases and microarray data analysis," *Bioinformatics*, vol. 21, no. 16, pp. 3439–3440, 2005.
- [12] A. D. Yates, P. Achuthan, W. Akanni et al., "Ensembl 2020," *Nucleic Acids Research*, vol. 48, no. D1, pp. D682–D688, 2020.
- [13] C. L. Schoch, S. Ciufò, M. Domrachev et al., "NCBI taxonomy: a comprehensive update on curation, resources and tools," *Database*, vol. 2020, 2020.
- [14] M. Blum, H.-Y. Chang, S. Chuguransky et al., "The InterPro protein families and domains database: 20 years on," *Nucleic Acids Research*, vol. 49, no. D1, pp. D344–D354, 2021.
- [15] T. Alber, "Structure of the leucine zipper," *Current Opinion in Genetics & Development*, vol. 2, no. 2, pp. 205–210, 1992.
- [16] J. Navarro Gonzalez, A. S. Zweig, M. L. Speir et al., "The UCSC genome browser database: 2021 update," *Nucleic Acids Research*, vol. 49, no. D1, pp. D1046–D1057, 2021.
- [17] M. Steinegger and J. Söding, "MMseqs2 enables sensitive protein sequence searching for the analysis of massive data sets," *Nature Biotechnology*, vol. 35, no. 11, pp. 1026–1028, 2017.
- [18] H. I. Ahmad, G. Liu, X. Jiang et al., "Maximum-likelihood approaches reveal signatures of positive selection in BMP15 and GDF9 genes modulating ovarian function in mammalian female fertility," *Ecology and Evolution*, vol. 7, no. 21, pp. 8895–8902, 2017.
- [19] Z. Yang, "PAML 4: phylogenetic analysis by maximum likelihood," *Molecular Biology and Evolution*, vol. 24, no. 8, pp. 1586–1591, 2007.
- [20] S. Weaver, S. D. Shank, S. J. Spielman, M. Li, S. V. Muse, and S. L. Kosakovsky Pond, "Datamonkey 2.0: a modern web application for characterizing selective and other evolutionary processes," *Molecular Biology and Evolution*, vol. 35, no. 3, pp. 773–777, 2018.
- [21] A. Stern, A. Doron-Faigenboim, E. Erez, E. Martz, E. Bacharach, and T. Pupko, "Selecton 2007: advanced models for detecting positive and purifying selection using a Bayesian inference approach," *Nucleic acids research*, vol. 35, suppl 2, pp. W506–W511, 2007.
- [22] M. A. Raheem, M. Xue, H. I. Ahmad et al., "Adaptation to host-specific bacterial pathogens drive rapid evolution of novel PhoP/PhoQ regulation pathway modulating the virulence," *Microbial Pathogenesis*, vol. 141, p. 103997, 2020.
- [23] H. Ashkenazy, E. Erez, E. Martz, T. Pupko, and N. Ben-Tal, "ConSurf 2010: calculating evolutionary conservation in sequence and structure of proteins and nucleic acids," *Nucleic Acids Research*, vol. 38, no. Web Server, pp. W529–W533, 2010.
- [24] G. Celniker, G. Nimrod, H. Ashkenazy et al., "ConSurf: using evolutionary data to raise testable hypotheses about protein function," *Israel Journal of Chemistry*, vol. 53, no. 3–4, pp. 199–206, 2013.
- [25] M. J. Ahmad, H. I. Ahmad, M. M. Adeel et al., "Evolutionary analysis of makorin ring finger protein 3 reveals positive selection in mammals," *Evolutionary Bioinformatics*, vol. 15, p. 1176934319834612, 2019.
- [26] H. I. Ahmad, G. Liu, X. Jiang et al., "Adaptive selection at agouti gene inferred breed specific selection signature within the indigenous goat populations," *Asian-Australasian journal of animal sciences*, 2017.
- [27] H. I. Ahmad, J. Zhou, M. J. Ahmad et al., "Adaptive selection in the evolution of programmed cell death-1 and its ligands in vertebrates," *Aging (Albany NY)*, vol. 12, no. 4, pp. 3516–3557, 2020.
- [28] G Consortium, "The GTEx consortium atlas of genetic regulatory effects across human tissues," *Science*, vol. 369, no. 6509, pp. 1318–1330, 2020.
- [29] L. J. Carithers and H. M. Moore, "The genotype-tissue expression (GTEx) project," in *Mary Ann Liebert, Inc. 140 Huguenot Street*, vol. 13, no. 5pp. 307–308, 3rd Floor New Rochelle, NY 10801 USA, 2015.
- [30] P. M. Conn, *The Unfolded Protein Response and Cellular Stress*, Academic Press, Part C, 2011.
- [31] S. A. Lambert, A. Jolma, L. F. Campitelli et al., "The human transcription factors," *Cell*, vol. 172, no. 4, pp. 650–665, 2018.
- [32] K. S. Kassahn, R. H. Crozier, H. O. Pörtner, and M. J. Caley, "Animal performance and stress: responses and tolerance limits at different levels of biological organisation," *Biological Reviews*, vol. 84, no. 2, pp. 277–292, 2009.
- [33] A. Robertson, A. Klungland, T. Rognes, and I. Leiros, "DNA repair in mammalian cells," *Cellular and Molecular Life Sciences*, vol. 66, no. 6, pp. 981–993, 2009.
- [34] C. K. Sen and L. Packer, *Redox Cell Biology and Genetics*, Elsevier, Part B, 2002.
- [35] D. S. Latchman, "Transcription factors: an overview," *The International Journal of Biochemistry & Cell Biology*, vol. 29, no. 12, pp. 1305–1312, 1997.

## Retraction

# Retracted: Asymmetric Dimethylarginine Protects Neurons from Oxygen Glucose Deprivation Insult by Modulating Connexin-36 Expression

### Oxidative Medicine and Cellular Longevity

Received 8 January 2024; Accepted 8 January 2024; Published 9 January 2024

Copyright © 2024 Oxidative Medicine and Cellular Longevity. This is an open access article distributed under the Creative Commons Attribution License, which permits unrestricted use, distribution, and reproduction in any medium, provided the original work is properly cited.

This article has been retracted by Hindawi following an investigation undertaken by the publisher [1]. This investigation has uncovered evidence of one or more of the following indicators of systematic manipulation of the publication process:

- (1) Discrepancies in scope
- (2) Discrepancies in the description of the research reported
- (3) Discrepancies between the availability of data and the research described
- (4) Inappropriate citations
- (5) Incoherent, meaningless and/or irrelevant content included in the article
- (6) Manipulated or compromised peer review

The presence of these indicators undermines our confidence in the integrity of the article's content and we cannot, therefore, vouch for its reliability. Please note that this notice is intended solely to alert readers that the content of this article is unreliable. We have not investigated whether authors were aware of or involved in the systematic manipulation of the publication process.

Wiley and Hindawi regrets that the usual quality checks did not identify these issues before publication and have since put additional measures in place to safeguard research integrity.

We wish to credit our own Research Integrity and Research Publishing teams and anonymous and named external researchers and research integrity experts for contributing to this investigation.

The corresponding author, as the representative of all authors, has been given the opportunity to register their agreement or disagreement to this retraction. We have kept a record of any response received.

### References

- [1] K. Fang, S. Chen, Y. Wang, F. Chen, M. Cui, and Q. Dong, "Asymmetric Dimethylarginine Protects Neurons from Oxygen Glucose Deprivation Insult by Modulating Connexin-36 Expression," *Oxidative Medicine and Cellular Longevity*, vol. 2022, Article ID 5339361, 8 pages, 2022.

## Research Article

# Asymmetric Dimethylarginine Protects Neurons from Oxygen Glucose Deprivation Insult by Modulating Connexin-36 Expression

Kun Fang , Shufen Chen , Yi Wang , Fangzhe Chen , Mei Cui , and Qiang Dong 

Department of Neurology, Huashan Hospital, Fudan University, Shanghai 200040, China

Correspondence should be addressed to Qiang Dong; [dong\\_qiang@fudan.edu.cn](mailto:dong_qiang@fudan.edu.cn)

Received 1 May 2022; Revised 30 May 2022; Accepted 6 June 2022; Published 6 July 2022

Academic Editor: Anwen Shao

Copyright © 2022 Kun Fang et al. This is an open access article distributed under the Creative Commons Attribution License, which permits unrestricted use, distribution, and reproduction in any medium, provided the original work is properly cited.

**Background.** Asymmetric dimethylarginine (ADMA) is a nonselective nitric oxide synthase inhibitor. ADMA is thought to inhibit the production of nitric oxide (NO) by neurons after oxygen-glucose deprivation (OGD). The gap junction protein Connexin-36 (cx-36) is involved in the pathophysiology of stroke. We investigated whether ADMA could protect neurons from OGD insults by regulating the expression of cx-36. **Methods.** Cultured rat cortical neuronal cells were used. Neurons were treated with OGD with or without ADMA pretreatment. The lactate dehydrogenase (LDH) release rate was used to assess neuronal injury. Intracellular NO levels were determined using 4-amino-5-methylamino-2',7'-difluorofluorescein diacetate. Western blotting was performed to detect cx-36 expression. **Results.** The LDH release rate increased in the supernatant of neurons after the OGD insult, whereas ADMA treatment reduced the LDH release rate. Intracellular NO levels increased following OGD treatment, and this increase was not inhibited by ADMA treatment. Expression of cx-36 was upregulated in neurons under OGD conditions, and treatment with ADMA downregulated the expression of cx-36. **Conclusions.** ADMA protects neurons from OGD insult, and cx-36 downregulation may be a possible pathway involved in ADMA-mediated neuronal protection.

## 1. Introduction

Asymmetric dimethylarginine (ADMA), an endogenous analog of arginine, was found to inhibit nitric oxide (NO) production by competing for the binding site of arginine in nitric oxide synthase (NOS). It nonselectively inhibits NOS, including endothelial NOS (eNOS), inducible NOS (iNOS), and neuronal NOS (nNOS) [1].

ADMA is used as a biomarker to identify endothelial dysfunction owing to its effect on eNOS. Increased ADMA levels have been observed in patients with hypertension, hyperlipidemia, diabetes, atrial fibrillation, old age, and atherosclerotic burden [2–4], as well as in patients with acute stroke [5, 6] and chronic stroke [7, 8]. In addition to inhibition of eNOS, ADMA can also inhibit the activity of iNOS and nNOS. NO produced by iNOS and nNOS may induce oxidative stress in neurons. It is well known that NO production significantly increases after acute ischemic stroke, thereby inducing oxidative stress, which contributes to sec-

ondary neuronal injury after stroke [9]. As a nonselective inhibitor of nNOS and iNOS, ADMA could potentially protect neurons during stroke in a very early phase; however, the literature is sparse in this area.

Gap junctions are important signal transduction pathways that allow small molecules (up to 1,000 daltons) and ions to diffuse from one cell to a neighboring cell [10, 11]. Gap junctions open when two hemichannels in adjacent plasma membranes dock with each other. Each hemichannel consists of six connexin subunits. One of these subunits, Connexin-36 (cx-36), is expressed mainly in neurons and retinal cells [12–14]. In the physiological state, there is little expression of cx-36 in the mature central nervous system. However, in the context of stroke, inflammation, epilepsy, and trauma, cx-36 expression is increased [15–19]. Amounts of opened gap junctions increase rapidly in oxygen-glucose-deprived neurons, causing ionic dysregulation and possibly contributing to neuronal death [20]. Cx-36 has been proven to play a critical role in the pathophysiology of N-methyl-D-

aspartate- (NMDA-) mediated neuronal death, with both cx-36 gene knockout and cx-36-specific inhibition showing a protective effect on neurons from NMDA toxicity [21]. However, the role of cx-36 in neuronal death when neurons undergo oxygen-glucose deprivation (OGD) is unknown, not to mention its role in the neuronal protective effect of ADMA. Although ADMA has been shown to modulate the expression of other connexins, such as cx-43, cx-37, and cx-40 [22], the effect of ADMA on cx-36 is still unknown.

Our study aimed to investigate the protective effect of ADMA on neurons in an OGD model and explore the effect of ADMA on cx-36 in neurons after OGD insult.

## 2. Methods

**2.1. Reagents.** ADMA was obtained from Sigma-Aldrich (St. Louis, MO, USA). Neurobasal A medium, B27 supplement, and no glucose DMEM were purchased from Invitrogen (Grand Island, NY, USA), and mouse anti-connexin 36 antibody was obtained from Invitrogen (Carlsbad, CA, USA). Mouse anti- $\beta$ -tubulin III (neuronal) antibody was purchased from Sigma-Aldrich (St. Louis, MO, USA). Peroxidase-conjugated AffiniPure goat anti-mouse IgG (H +L) was purchased from Jackson ImmunoResearch (West Grove, PA, USA). A cytotoxicity detection kit based on lactate dehydrogenase (LDH) was obtained from Roche Diagnostic GmbH (Mannheim, Germany). 7-Nitroindazole (7-NI), 1400w, BCA Protein Assay Kit, and fluorescent probe 3-amino, 4-aminomethyl-2',7'-difluorescein, diacetate (DAF-FM DA), and phenylmethanesulfonyl fluoride (PMSF) were purchased from Beyotime (Jiangsu, China). Other reagents were obtained from Sigma-Aldrich.

**2.2. Primary Cortical Neuronal Cultures.** Adult pregnant Wistar rats were purchased from Shanghai SLAC Laboratory Animal Company, China. Primary cortical neuronal cultures were obtained from fetal Wistar rat at embryonic day 14 (E14). Rats were placed in a 12 h light-dark cycle, under environmentally controlled conditions (ambient temperature,  $22 \pm 2^\circ\text{C}$ ; humidity, 40%) and with free access to food and water. All experimental processes were implemented according to experimental standards of Fudan University, as well as international ethical guidelines for experimentation on animals. Primary cortical neuronal cultures were prepared as previously described, with slight modification [23]. Briefly, the cerebral cortex was removed; after that, meninges were removed from the cortex. The cerebral cortex tissues were dissociated using 0.25% trypsin for 20 min at room temperature ( $24 \pm 2^\circ\text{C}$ ). After titration and resuspension in neurobasal A medium supplemented with B27, the cells were plated on poly L-lysine-coated glass coverslips, 96-well plates, or 100 mm dishes. The culture medium was changed by half every 3 days. Cultured neurons were used to investigate in vitro day 7–10 (DIV 7–10).

**2.3. Oxygen and Glucose Deprivation/Reoxygenation.** Primary neurons (DIV 7–10) were subjected to OGD/reoxygenation (OGD/R) as previously described, with minor modifications [24]. Briefly, the cells were washed three times

with Hank's balanced salt solution (HBSS), incubated in deoxygenated glucose-free DMEM in an anaerobic chamber (Forma anaerobic system, Thermo) with an atmosphere ( $<0.1\% \text{O}_2$ ) containing 85%  $\text{N}_2$ , 10%  $\text{H}_2$ , and 5%  $\text{CO}_2$  at  $37^\circ\text{C}$ , and terminated after 45 min by replacing deoxygenated glucose-free DMEM with original medium in normal incubator for the subsequent 0–24 h reoxygenation (R). Control cells were obtained normally.

**2.4. Cytotoxicity Assessment.** Neuronal cytotoxicity was assessed using a cytotoxicity detection kit ground on the LDH activity released from the cytosol of damaged cells into the supernatant [25]. The experiments were performed according to the manufacturer's protocol. Total LDH activity was measured in the supernatant of cells that had been repeatedly frozen and thawed thrice. The relative LDH release rate is represented as the ratio of extracellular LDH activity to total LDH activity.

**2.5. Intracellular NO Assay.** Intracellular NO was detected using the fluorescent probe DAF-FM DA [26]. DAF-FM DA penetrates the cell membrane and is converted to DAF-FM by intracellular esterases, which cannot penetrate the cell membrane. The fluorescence emitted by the DAF-FM was very weak; however, the signal became much stronger coexisting together with NO. Neuronal cells were cultured in 96-well plates. The cells on DIV 7–10 after OGD/R treatment were incubated with DAF-FM DA ( $5 \mu\text{M}$ ) in an incubator (at  $37^\circ\text{C}$  with dark) for 20 min and then rinsed with PBS (pH 7.8) for three times. The DAF-FM fluorescence intensity was detected by a fluorescence microplate reader (SpectraMax M5, Molecular Devices, USA) with an excitation wavelength of 495 nm and an emission wavelength of 515 nm. Intracellular NO production was reflected by the relative ratio to the control cells. The experiments were repeated thrice with eight readings for every group. To differentiate the effect of NOS subtypes, we used nNOS-specific inhibitor 7-NI (with final concentration  $50 \mu\text{M}$ ) and iNOS-specific inhibitor 1400w (with final concentration  $10 \mu\text{M}$ ).

**2.6. Neuronal Cell Pretreatment.** ADMA was added to the supernatant of cultured cells in 24 h before OGD/R treatment, and the final concentration was  $30 \mu\text{M}$ . The ADMA concentration remained unchanged throughout the experiment. 7-NI or 1400w was added to the supernatant of cultured cells immediately after OGD treatment.

**2.7. Western Blot.** Western blotting was used to assay the expression of cx-36. The cells were planted on 100 mm dishes. After diverse treatments, the cells were collected by scraping in ice-cold radioimmunoprecipitation lysis buffer containing 1% Triton, 1% deoxycholate, 0.1% SDS, 1 mmol/l EDTA, 50 mmol/l Tris (pH 7.4), and 150 mmol/l NaCl, supplemented with PMSF, and then centrifuged at  $18,000 \times g$  for 20 min. The supernatant was collected. Using the BCA kit, the quantity of the total protein was determined in every supernatant. 10% SDS-PAGE was used to separate the protein electrophoretically. Separated protein was transferred onto PVDF membranes (Millipore). Then, the

membranes were immersed in blocking buffer (1× Tris-buffered saline (TBS, pH 7.6) containing 5% BSA) for 2 h at room temperature. The membranes were then incubated overnight with primary cx-36 (diluted 1:1000) antibodies at 4°C. After rinsing three times with TBS-Tween (0.1% Tween 20), the membranes were dug into solution of goat anti-mouse secondary HRP-conjugated IgG antibodies (diluted 1:1000) for 1 h at room temperature (24 ± 2°C). Equal loading was ensured by detecting the membranes with an anti-mouse β-tubulin (neuronal) antibody (1:5,000 dilution). Detection was performed using an enhanced chemiluminescence assay kit (Millipore). The western blots were captured using a Molecular Imager (ChemIDoc™ XRS+, Bio-Rad, USA), and the intensities were quantified using Image Lab software (Bio-Rad, USA).

**2.8. Statistical Analysis.** Data are presented as mean ± SEM based on three separate experiments. One-way ANOVA analysis was used to analyze the difference between different groups, followed by LSD post hoc tests for multiple comparisons tests or Kruskal–Wallis nonparametric ANOVA with adjustment for multiple comparisons. Paired Student's *t*-tests were used for comparisons between two groups only. Differences were considered statistically significant at  $P < 0.05$ .

### 3. Results

**3.1. ADMA Protects Neurons from OGD/R Injury.** We measured the relative LDH release rate to assess neuronal injury resulting from OGD/R. Compared with those in the control, neurons undergoing OGD injury showed a time-dependent increase in LDH release rate during the time course of reperfusion (Figure 1). The relative LDH release rate was 46.82% ± 0.72% of maximal LDH release 24 h after reperfusion. We selected a reperfusion time point of 2 h for further analysis. We found that neurons pretreated with ADMA (0 μM, 3 μM, 10 μM, 30 μM, and 100 μM) showed a decreased LDH release rate after OGD/R. However, we did not observe any concentration-dependent decreases. When pretreated with a high dose of ADMA (300 μM), the LDH release rate remained slightly elevated, although without significance (Figure 2).

**3.2. ADMA Did Not Inhibit the NO Production of Neurons after OGD/R Insult.** The NO production in neurons after OGD/R showed a time-dependent profile (Figure 3(a)). Using the nNOS-specific inhibitor 7-NI and the iNOS-specific inhibitor 1400w, we could easily identify the type of NOS that was the primary source of NO production at different time points after OGD/R. Immediately after OGD/R, NO production markedly increased, which was catalyzed by nNOS (Figure 3(c)). After that, NO production started to decrease until 4 h after OGD/R then started to rise again reaching a peak at 6 h after OGD/R. iNOS was responsible for the second peak in NO production (Figure 3(b)). Surprisingly, as a nonselective NOS inhibitor, ADMA at 30 μM did not suppress NO production in the pretreated neurons. In contrast, the ADMA 30 μM group produced

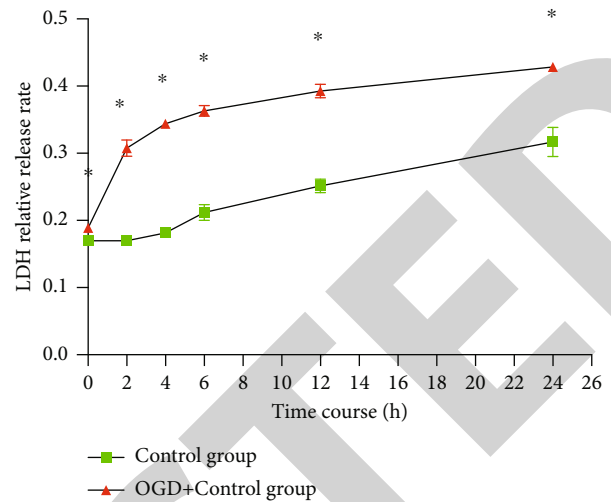


FIGURE 1: The relative LDH release rate of neurons in control and OGD groups. \*Compared with control in indicated time points,  $p < 0.05$ . Red: OGD group, neurons were subjected to OGD for 45 min and reperused for 0–24 h. Green: control group, neurons were obtained in normal conditions.  $n = 3$ .

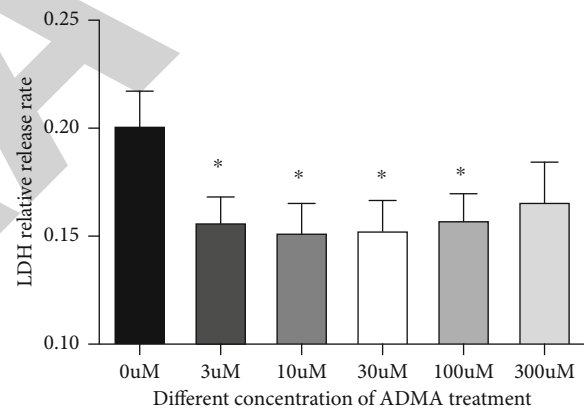


FIGURE 2: The LDH release rate of neurons after OGD/R pretreated with different ADMA concentrations. \*Compared with ADMA blank control, LDH release rate decreased significantly in neurons with different ADMA concentration pretreatment,  $p < 0.01$ ,  $n = 3$ .

more NO than that by the baseline OGD/R group at 12 h after OGD/R (Figure 3(d)).

**3.3. ADMA Attenuated the Expression of cx-36 in Neurons after OGD/R.** Since the protective effect of ADMA on neurons after OGD/R was not due to its inhibitory effect on NOS, there must be other mechanisms. Previous studies showed that cx-36 expression increased after ischemic stroke [27] and was accompanied by the transfer of electrolytes from one cell to another, which might lead to the dysfunction and eventual death of cells [20]. Further studies were conducted to explore the effect of ADMA on cx-36 expression after OGD/R. Cortical neurons plated in 10 cm dishes were used in this experiment. The neurons underwent OGD treatment for 45 min and reperfusion under normal condition for 0–24 h. During the time course of reperfusion,

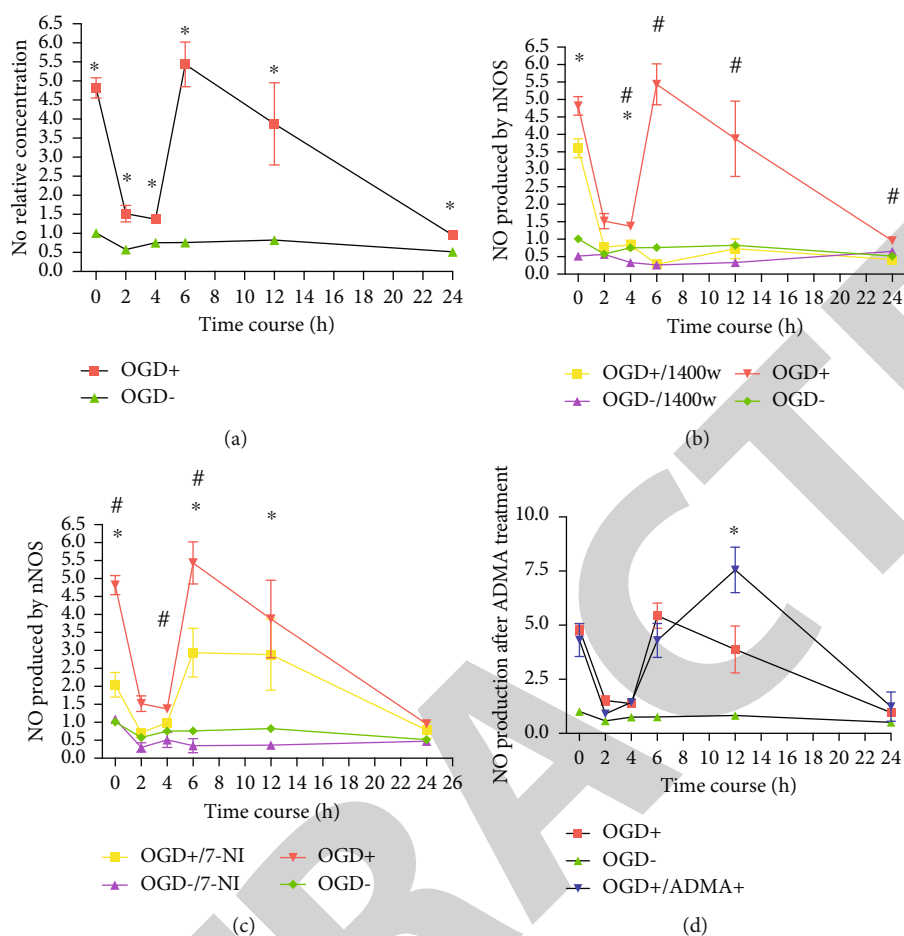


FIGURE 3: Time profile of NO production after OGD/R with different NOS inhibitors. (a) NO production in different time points was higher in neurons after OGD/R than in neurons in normal conditions. (b) NO production in the late stage after OGD/R was inhibited by iNOS-specific inhibitor 1400w, which indicated NO produced in the late stage was mainly produced by iNOS. (c) NO production in the early stage after OGD/R was inhibited by nNOS-specific inhibitor 7-NI, which indicated NO produced in the early stage was mainly produced by nNOS. (d) ADMA  $30 \mu\text{M}$  could not inhibit NO production after OGD/R ( $n = 3$ ) and \*compared with normal condition group,  $p < 0.05$ . #Compared with OGD/R group,  $p < 0.05$ .

the expression of cx-36 increased, which was higher than that of the control and higher than that at 0 h after OGD treatment (Figure 4). We considered 4 h as the time point for further investigation. Neurons were pretreated with ADMA at  $30 \mu\text{M}$  for 24 h before OGD treatment, as designed previously. The duration of OGD was 45 min. Subsequently, neurons were returned to normal conditions for another 4 h. Our results showed that pretreatment with ADMA at  $30 \mu\text{M}$  attenuated the increased expression of cx-36 4 h after OGD/R (Figure 5).

#### 4. Discussion

To the best of our knowledge, this is the first study to focus on the protective effect of ADMA on neurons undergoing an OGD/R insult. Our results showed that ADMA may protect neurons from OGD/R insults. However, intracellular NO level in neurons was not, as we supposed, affected by ADMA following OGD/R insult. Protection might be mediated via the suppression of cx-36 expression.

As mentioned above, ADMA can inhibit nNOS and iNOS, reducing the production of neurotoxic NO, thereby demonstrating its potential neuroprotective ability. Several studies have already proven this hypothesis using different models [28, 29]. Cardounel and Zweier showed that ADMA protected neurons from NMDA-induced neurotoxicity [28]. Tang et al. demonstrated that ADMA attenuated ROS accumulation in MPP<sup>+</sup>-treated PC12 cells and protected neurons from MPP<sup>+</sup>-triggered cell death [29, 30]. However, Wang et al. reported that exogenous ADMA may induce apoptosis in PC12 cells in a concentration- and time-dependent manner [31]. The different effects of ADMA in PC12 cells may be due to differences in the treatment protocols and assessment assays. Zhao et al. found that dimethylarginine dimethylamino hydrolase-1- (DDAH-1-) knockout rats demonstrated aggravated neurological damage after MCAO/R in an in vivo study [32]. This result seems contradictory to that of the present study. As reported previously, DDAH-1 is distributed in multiple cell types, including neurons, astrocyte cells, and vascular structures, while DDAH-2 is distributed exclusively in neurons [33]. As a result, DDAH-1 knockout might affect

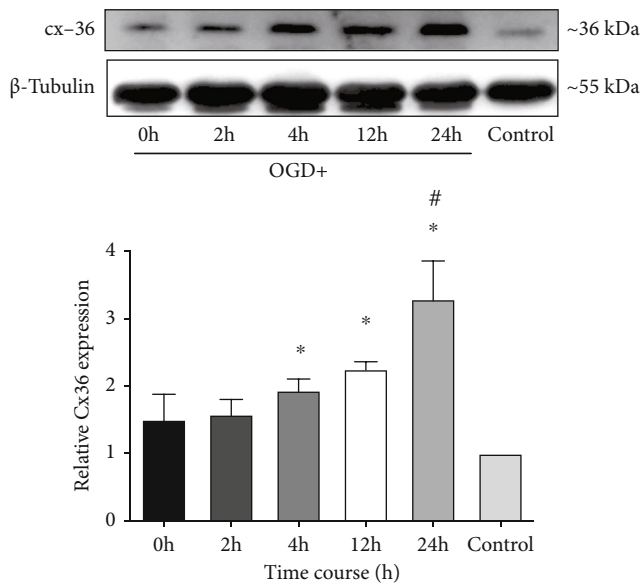


FIGURE 4: Neurons expressed more connexin-36 underwent OGD/R in a time dependent profile. Data were presented as means  $\pm$  SEM ( $n = 3$ ). \*Compared with normal condition group,  $p < 0.05$ . #Compared with OGD 0h,  $p < 0.05$ .

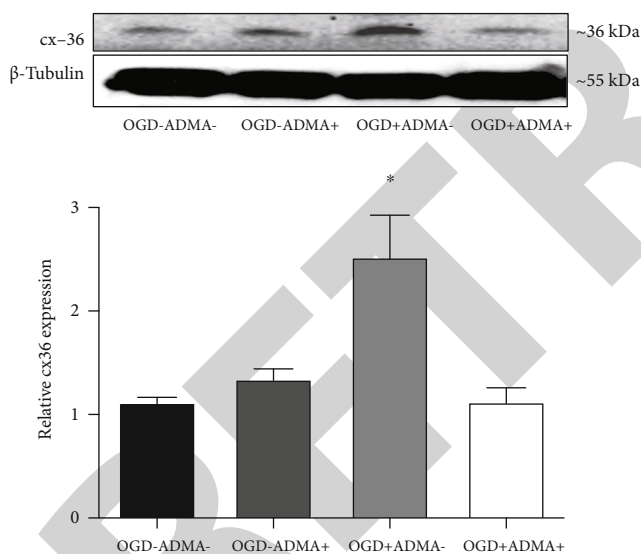


FIGURE 5: ADMA attenuated the expression of connexin-36 in neurons after OGD/R. Data were presented as means  $\pm$  SEM ( $n = 3$ ). \*Compared with the other three groups,  $p < 0.05$ .

various cell types of animals and is not limited to neurons, which could not explain the effect of DDAH-1 knockout in neurons. Our study focused on cortical neurons and provided evidence of the neuroprotective effect of ADMA in cortical neurons undergoing OGD treatment. The different results might lie in different models.

It is well known that ADMA is a competitive inhibitor of NOS, where iNOS and nNOS are involved in the pathophysiology of stroke. We hypothesized that ADMA protected neurons from OGD/R treatment by attenuating NO levels

in neurons. However, we could not prove our hypothesis in this study. We found that the NO levels burst with two peaks in the context of OGD/R (Figure 3(a)). However, exogenous ADMA treatment did not suppress NO (Figure 3(d)). Furthermore, 12h after OGD/R, NO production increased to a peak level in the OGD/R group with ADMA pretreatment, higher than that in the OGD/R group without ADMA pretreatment. Previous data showed that the nNOS inhibitory effect of ADMA was concentration-dependent. An ADMA concentration of  $30 \mu\text{M}$  might inhibit 23% of NO production by nNOS, while an ADMA concentration of  $100 \mu\text{M}$  could inhibit nNOS activity by 100% [28]. In our study, we used  $30 \mu\text{M}$  as the pretreatment dosage. However, inhibition of nNOS by ADMA was not observed. The possible reasons might be as follows: first, the insult procedures were different in the two studies. In the study by Cardounel and Zweier, neurons were treated with NMDA; as in our study, neurons were treated with OGD/R. The mechanisms underlying the neurotoxic effects of OGD/R are more complex than those of NMDA. Second, the sensitivities of the NO detection assays were different. Third, compared with the specific nNOS inhibitor 7-NI, the nNOS inhibitory effect of ADMA is very weak, and the dosage of ADMA used in our study was not powerful enough to inhibit nNOS. Klein et al. showed that ADMA upregulated iNOS expression in airway epithelial cells in vivo and in vitro [34]; however, the inhibition of iNOS was quite weak as well [35]. ADMA pretreatment might also increase expression of iNOS in neurons. As a result, when the neurons underwent OGD/R, the NO production might appear higher than that without ADMA pretreatment, which might partly explain our data where NO production was higher in group with ADMA pretreatment than those without ADMA treatment at 12h after OGD/R (Figure 3(d)).

Nevertheless, despite the level of NO in neurons, ADMA still protected neurons from OGD/R (Figure 2). This is consistent with previous data [28]. Therefore, there may be other mechanisms that enable ADMA-mediated neuronal protection. In the subarachnoid hemorrhage rat model, ADMA was positively correlated with cx-43, indicating that ADMA might regulate the expression of connexins [36].

cx-36 is an electrical synapse that allows the transmission of ions and electricity between neighboring neurons, and cx-36 plaques were found to strengthen gap-junctional conductance rapidly and profoundly [37]. It has been previously shown that cx-36 promotes cortical spreading depolarization and induces ischemic brain damage [38]. Cx-36 may also upregulate the expression of inflammatory cytokines in a depressive-like behavior animal model [39]. As a result, the downregulation or inhibition of cx-36 may have a neuroprotective effect. A transient increase in cx-36 expression was observed in ischemic cortex neurons in vivo and in vitro, and using the cx-36 gene elimination technique and a cx-36 inhibitor, cx-36 was proven to be toxic in stroke [40]. In the case of OGD/R, cx-36 expression in neurons increased. This is consistent with previous in vitro studies that were not limited to cortical neurons [41, 42]. According to a study performed by Li et al., leonurine decreased the expression of cx-36 in OGD PC12 cells, indicating that cx-



36 might be the target protein for the protective effect of leonurine in OGD PC12 cells [43]. Moreover, cx-36 inhibition might reduce the level of phosphorylated calmodulin-dependent protein kinase II (pCaMKII) and the ratio of pCaMKII/CaMKII, thus protecting PC-12 cells from OGD insult [43]. Similar results were observed in the present study. When pretreated with ADMA, the increased expression of cx-36 was attenuated in OGD/R neurons, indicating that ADMA might protect neurons from OGD/R by modulating the cx-36 expression.

The limitation of our study was that we did not use a cx-36 specific inhibitor. It has been shown that cx-36 inhibition is neuroprotective [40, 44]. We did not know the mechanism underlying the effect of ADMA on cx-36 expression in this work. According to previous studies, the potential regulator of cx-36 expression or function included CaMKII pathway [45], group II metabotropic glutamate receptors (mGluRs) pathway, and cAMP-dependent protein kinase-dependent signaling pathway [40]. However, we have no idea whether these pathways are also involved in the regulation of ADMA on cx-36, and we also do not know if there is any other pathway. To make the mechanism clear, further investigation is needed.

In our work, we proposed a possibility of ADMA to be a neuroprotective agent in the early stage of stroke. Pretreatment in the study did restrict the clinical application in the current situation. However, situation in human body is quite different from animals, let alone cultured cells. To achieve the goal of translation from bench to bed, lots of work need to be done in the future.

In conclusion, ADMA may protect neurons from OGD/R insult by attenuating the cx-36 expression. Therefore, ADMA might be a potential agent to protect neurons from death in the early stages of stroke, which requires further experimental and clinical investigation.

## Data Availability

The data used to support the findings of this study are available from the corresponding author upon request.

## Conflicts of Interest

The authors declare that they have no conflicts of interest.

## Authors' Contributions

Kun Fang and Shufen Chen contributed equally to this work.

## Acknowledgments

This work was supported by the National Natural Science Foundation of China (Nos. 81300997 and 82001259) and the Ministry of Science and Technology of China (No. 2021YFC2500100).

## References

- [1] S. Chen, N. Li, M. Deb-Chatterji et al., "Asymmetric dimethylarginine as marker and mediator in ischemic stroke," *International Journal of Molecular Sciences*, vol. 13, no. 12, pp. 15983–16004, 2012.
- [2] J. D. Horowitz, R. De Caterina, T. Heresztyn et al., "Asymmetric and symmetric dimethylarginine predict outcomes in patients with atrial fibrillation: an ARISTOTLE substudy," *Journal of the American College of Cardiology*, vol. 72, no. 7, pp. 721–733, 2018.
- [3] L. Dowsett, E. Higgins, S. Alanazi, N. A. Alshuwayer, F. C. Leiper, and J. Leiper, "ADMA: a key player in the relationship between vascular dysfunction and inflammation in atherosclerosis," *Journal of Clinical Medicine*, vol. 9, no. 9, article 3026, 2020.
- [4] A. M. Youssef, H. A. Elghoneimy, M. W. Helmy, A. M. Abdelazeem, and N. M. El-Khodary, "Effect of amlodipine versus bisoprolol in hypertensive patients on maintenance hemodialysis: a randomized controlled trial," *Medicine (Baltimore)*, vol. 100, no. 51, article e28322, 2021.
- [5] H. Worthmann, S. Chen, J. Martens-Lobenhoffer et al., "High plasma dimethylarginine levels are associated with adverse clinical outcome after stroke," *Journal of Atherosclerosis and Thrombosis*, vol. 18, no. 9, pp. 753–761, 2011.
- [6] Z. Qin, L. Tang, Q. Huang, Y. Chen, W. Zhong, and X. Tang, "A systematic review of the correlation between serum asymmetric dimethylarginine, carotid atherosclerosis and ischaemic stroke," *European Journal Of Clinical Investigation*, vol. 51, no. 8, article e13558, 2021.
- [7] J. H. Yoo and S. C. Lee, "Elevated levels of plasma homocyst(e)ine and asymmetric dimethylarginine in elderly patients with stroke," *Atherosclerosis*, vol. 158, no. 2, pp. 425–430, 2001.
- [8] A. Rufa, P. Bardi, A. De Lalla et al., "Plasma levels of asymmetric dimethylarginine in cerebral autosomal dominant arteriopathy with subcortical infarct and leukoencephalopathy," *Cerebrovascular Diseases*, vol. 26, no. 6, pp. 636–640, 2008.
- [9] C. Forster, H. Clark, M. Ross, and C. Iadecola, "Inducible nitric oxide synthase expression in human cerebral infarcts," *Acta Neuropathologica*, vol. 97, no. 3, pp. 215–220, 1999.
- [10] J. Neijssen, C. Herberts, J. Drijfhout, E. Reits, L. Janssen, and J. Neefjes, "Cross-presentation by intercellular peptide transfer through gap junctions," *Nature*, vol. 434, no. 7029, pp. 83–88, 2005.
- [11] E. C. Beyer and V. M. Berthoud, "Gap junction gene and protein families: Connexins, innexins, and pannexins," *Biochimica et Biophysica Acta - Biomembranes*, vol. 1860, no. 1, pp. 5–8, 2018.
- [12] D. F. Condorelli, R. Parenti, F. Spinella et al., "Cloning of a new gap junction gene (Cx36) highly expressed in mammalian brain neurons," *The European Journal of Neuroscience*, vol. 10, no. 3, pp. 1202–1208, 1998.
- [13] G. Söhl, J. Degen, B. Teubner, and K. Willecke, "The murine gap junction gene connexin36 is highly expressed in mouse retina and regulated during brain development," *FEBS Letters*, vol. 428, no. 1-2, pp. 27–31, 1998.
- [14] K. Fusz, T. Kovács-Öller, P. Kóbor et al., "Regional variation of gap junctional connections in the mammalian inner retina," *Cell*, vol. 10, no. 9, p. 2396, 2021.

- [15] S. Thalakoti, V. Patil, S. Damodaram et al., "Neuron-glia signaling in trigeminal ganglion: implications for migraine pathology," *Headache*, vol. 47, no. 7, pp. 1008–1023, 2007.
- [16] K. Oguro, T. Jover, H. Tanaka et al., "Global ischemia-induced increases in the gap junctional proteins connexin 32 (Cx32) and Cx36 in hippocampus and enhanced vulnerability of Cx32 knock-out mice," *Journal of Neuroscience*, vol. 21, no. 19, pp. 7534–7542, 2001.
- [17] A. Belousov, J. Fontes, M. Freitas-Andrade, and C. Naus, "Gap junctions and hemichannels: communicating cell death in neurodevelopment and disease," *BMC Cell Biology*, vol. 18, pp. 1–11, 2017.
- [18] X. L. Wu, D. M. Ma, W. Zhang, Y. W. Huo, M. Lu, and F. R. Tang, "Cx36 in the mouse hippocampus during and after pilocarpine-induced status epilepticus," *Epilepsy Research*, vol. 141, pp. 64–72, 2018.
- [19] A. B. Belousov and J. D. Fontes, "Neuronal gap junctions: making and breaking connections during development and injury," *Trends in Neurosciences*, vol. 36, no. 4, pp. 227–236, 2013.
- [20] R. J. Thompson, N. Zhou, and B. A. Mac Vicar, "Ischemia opens neuronal gap junction hemichannels," *Science*, vol. 312, no. 5775, pp. 924–927, 2006.
- [21] Y. Wang, J. V. Denisova, K. S. Kang, J. D. Fontes, B. T. Zhu, and A. B. Belousov, "Neuronal gap junctions are required for NMDA receptor-mediated excitotoxicity: implications in ischemic stroke," *Journal of Neurophysiology*, vol. 104, pp. 3551–3556, 2010.
- [22] C. Y. Huang, T. Zhou, G. Li et al., "Asymmetric dimethylarginine aggravates blood-retinal barrier breakdown of diabetic retinopathy via inhibition of intercellular communication in retinal pericytes," *Amino Acids*, vol. 51, no. 10–12, pp. 1515–1526, 2019.
- [23] F. Boato, S. Hendrix, S. C. Huelsenbeck et al., "C3 peptide enhances recovery from spinal cord injury by improved regenerative growth of descending fiber tracts," *Journal of Cell Science*, vol. 123, no. 10, pp. 1652–1662, 2010.
- [24] L. Liu, R. Zhang, K. Liu et al., "Tissue kallikrein protects cortical neurons against in vitro ischemia-acidosis/reperfusion-induced injury through the ERK1/2 pathway," *Experimental Neurology*, vol. 219, no. 2, pp. 453–465, 2009.
- [25] F. Wang, J. Liu, D. Wang, Y. Yao, and X. Jiao, "Knockdown of circ\_0007290 alleviates oxygen-glucose deprivation-induced neuronal injury by regulating miR-496/PDCD4 axis," *Metabolic Brain Disease*, vol. 37, no. 3, pp. 807–818, 2022.
- [26] J. Liu, M. Fu, J. Miao et al., "The toxicity of cooking oil fumes on human bronchial epithelial cells through ROS-mediated MAPK, NF- $\kappa$ B signaling pathways and NLRP3 inflammasome," *Environmental Toxicology*, vol. 37, no. 5, pp. 1071–1080, 2022.
- [27] E. M. Hartfield, F. Rinaldi, C. P. Glover, L. F. Wong, M. A. Caldwell, and J. B. Uney, "Connexin 36 expression regulates neuronal differentiation from neural progenitor cells," *PLoS One*, vol. 6, no. 3, article e14746, 2011.
- [28] A. J. Cardounel and J. L. Zweier, "Endogenous methylarginines regulate neuronal nitric-oxide synthase and prevent excitotoxic injury," *The Journal of Biological Chemistry*, vol. 277, no. 37, pp. 33995–34002, 2002.
- [29] X. Q. Tang, Y. J. Li, J. Zhao et al., "Neuroprotective effect of asymmetric dimethylarginine against 1-methyl-4-phenylpyridinium ion-induced damage in PC12 cells," *Clinical and Experimental Pharmacology & Physiology*, vol. 37, no. 5–6, pp. 530–535, 2010.
- [30] X. Q. Tang, H. R. Fang, Y. J. Li et al., "Endogenous hydrogen sulfide is involved in asymmetric dimethylarginine-induced protection against neurotoxicity of 1-methyl-4-phenylpyridinium ion," *Neurochemical Research*, vol. 36, no. 11, pp. 2176–2185, 2011.
- [31] S. Wang, C. P. Hu, D. J. Jiang et al., "All-trans retinoic acid inhibits cobalt chloride-induced apoptosis in PC12 cells: role of the dimethylarginine dimethylaminohydrolase/asymmetric dimethylarginine pathway," *Journal of Neuroscience Research*, vol. 87, no. 8, pp. 1938–1946, 2009.
- [32] Y. Zhao, X. Ma, Y. Zhou, J. Xie, X. Liu, and Y. Zhao, "DDAH-1, via regulation of ADMA levels, protects against ischemia-induced blood-brain barrier leakage," *Laboratory Investigation*, vol. 101, no. 7, pp. 808–823, 2021.
- [33] A. A. Kozlova, V. N. Ragavan, N. Jarzebska et al., "Divergent dimethylarginine dimethylaminohydrolase isoenzyme expression in the central nervous system," *Cellular and Molecular Neurobiology*, 2021.
- [34] E. Klein, J. Weigel, M. C. Buford, A. Holian, and S. M. Wells, "Asymmetric dimethylarginine potentiates lung inflammation in a mouse model of allergic asthma," *American Journal of Physiology. Lung Cellular and Molecular Physiology*, vol. 299, no. 6, pp. L816–L825, 2010.
- [35] S. M. Wells and A. Holian, "Asymmetric dimethylarginine induces oxidative and nitrosative stress in murine lung epithelial cells," *American Journal of Respiratory Cell and Molecular Biology*, vol. 36, no. 5, pp. 520–528, 2007.
- [36] D. Zhao, Q. Liu, Y. Ji et al., "Effect of 18 $\beta$ -glycyrrhetic acid on cerebral vasospasm caused by asymmetric dimethylarginine after experimental subarachnoid hemorrhage in rats," *Neurological Research*, vol. 37, no. 6, pp. 476–483, 2015.
- [37] C. A. Brown, C. Del Corso, C. Zoidl, L. W. Donaldson, D. C. Spray, and G. Zoidl, "Tubulin-dependent transport of connexin-36 potentiates the size and strength of electrical synapses," *Cell*, vol. 8, no. 10, article 1146, 2019.
- [38] P. Bargiotas, S. Muhammad, M. Rahman et al., "Connexin 36 promotes cortical spreading depolarization and ischemic brain damage," *Brain Research*, vol. 1479, pp. 80–85, 2012.
- [39] Q. Jiang, C. R. Li, W. F. Zeng et al., "Inhibition of connexin 36 attenuates HMGB1-mediated depressive-like behaviors induced by chronic unpredictable mild stress," *Brain and Behavior: A Cognitive Neuroscience Perspective*, vol. 12, no. 2, article e2470, 2022.
- [40] Y. Wang, J. Song, J. Denisova, W. Park, J. Fontes, and A. Belousov, "Neuronal gap junction coupling is regulated by glutamate and plays critical role in cell death during neuronal injury," *Journal of Neuroscience*, vol. 32, no. 2, pp. 713–725, 2012.
- [41] Q. Chang, A. Pereda, M. Pinter, and R. Balice-Gordon, "Nerve injury induces gap junctional coupling among axotomized adult motor neurons," *Journal of Neuroscience*, vol. 20, no. 2, pp. 674–684, 2000.
- [42] A. Belousov, H. Nishimune, J. Denisova, and J. Fontes, "A potential role for neuronal connexin 36 in the pathogenesis of amyotrophic lateral sclerosis," *Neuroscience Letters*, vol. 666, pp. 1–4, 2018.
- [43] J. Li, S. Zhang, X. Liu, D. Han, J. Xu, and Y. Ma, "Neuroprotective effects of leonurine against oxygen-glucose deprivation by

## Retraction

# Retracted: Aquaporin 4 Depolarization-Enhanced Transferrin Infiltration Leads to Neuronal Ferroptosis after Subarachnoid Hemorrhage in Mice

### Oxidative Medicine and Cellular Longevity

Received 8 January 2024; Accepted 8 January 2024; Published 9 January 2024

Copyright © 2024 Oxidative Medicine and Cellular Longevity. This is an open access article distributed under the Creative Commons Attribution License, which permits unrestricted use, distribution, and reproduction in any medium, provided the original work is properly cited.

This article has been retracted by Hindawi, as publisher, following an investigation undertaken by the publisher [1]. This investigation has uncovered evidence of systematic manipulation of the publication and peer-review process. We cannot, therefore, vouch for the reliability or integrity of this article.

Please note that this notice is intended solely to alert readers that the peer-review process of this article has been compromised.

Wiley and Hindawi regret that the usual quality checks did not identify these issues before publication and have since put additional measures in place to safeguard research integrity.

We wish to credit our Research Integrity and Research Publishing teams and anonymous and named external researchers and research integrity experts for contributing to this investigation.

The corresponding author, as the representative of all authors, has been given the opportunity to register their agreement or disagreement to this retraction. We have kept a record of any response received.

### References

- [1] Y. Liu, Z. Wang, C. Cao et al., “Aquaporin 4 Depolarization-Enhanced Transferrin Infiltration Leads to Neuronal Ferroptosis after Subarachnoid Hemorrhage in Mice,” *Oxidative Medicine and Cellular Longevity*, vol. 2022, Article ID 8808677, 14 pages, 2022.

## Research Article

# Aquaporin 4 Depolarization-Enhanced Transferrin Infiltration Leads to Neuronal Ferroptosis after Subarachnoid Hemorrhage in Mice

Yuan Liu <sup>1,2</sup>, Zongqi Wang <sup>1,2</sup>, Chang Cao <sup>1,2</sup>, Zhongmou Xu <sup>1,2</sup>, Jinxin Lu <sup>1,2</sup>,  
Haitao Shen <sup>1,2</sup>, Xiang Li <sup>1,2</sup>, Haiying Li <sup>1,2</sup>, Jiang Wu <sup>1,2</sup> and Gang Chen <sup>1,2</sup>

<sup>1</sup>Department of Neurosurgery & Brain and Nerve Research Laboratory, The First Affiliated Hospital of Soochow University, 188 Shizi Street Suzhou Jiangsu Province 215006, China

<sup>2</sup>Institute of Stroke Research, Soochow University, China

Correspondence should be addressed to Haiying Li; [lhy1015@suda.edu.cn](mailto:lhy1015@suda.edu.cn) and Jiang Wu; [jiangwu@suda.edu.cn](mailto:jiangwu@suda.edu.cn)

Received 4 May 2022; Revised 30 May 2022; Accepted 3 June 2022; Published 17 June 2022

Academic Editor: Anwen Shao

Copyright © 2022 Yuan Liu et al. This is an open access article distributed under the Creative Commons Attribution License, which permits unrestricted use, distribution, and reproduction in any medium, provided the original work is properly cited.

The infiltration of blood components into the brain parenchyma through the lymphoid system is an important cause of subarachnoid hemorrhage injury. AQP4, a water channel protein located at the astrocyte foot, has been reported to regulate blood–brain barrier integrity, and its polarization is disrupted after SAH. Neuronal ferroptosis is involved in subarachnoid hemorrhage- (SAH-) induced brain injury, but the inducing factors are not completely clear. Transferrin is one of the inducing factors of ferroptosis. This study is aimed at researching the role and mechanism of AQP4 in brain injury after subarachnoid hemorrhage in mice. An experimental mouse SAH model was established by endovascular perforation. An AAV vector encoding AQP4 with a GFAP-specific promoter was administered to mice to achieve specific overexpression of AQP4 in astrocytes. PI staining, Fer-1 intervention, and transmission electron microscopy were used to detect neuronal ferroptosis, and dextran (40 kD) leakage was used to detect BBB integrity. Western blot analysis of perfused brain tissue protein samples was used to detect transferrin infiltration. First, neuronal ferroptosis 24 h after SAH was observed by PI staining and Fer-1 intervention. Second, a significant increase in transferrin infiltration was found in the brain parenchyma 24 h after SAH modeling, while transferrin content was positively correlated with neuronal ferroptosis. Then, we observed that AQP4 overexpression effectively improved AQP depolarization and BBB injury induced by SAH and significantly reduced transferrin infiltration and neuronal ferroptosis after SAH. Finally, we found that AQP4 overexpression could effectively improve the neurobehavioral ability of SAH mice, and the neurobehavioral ability was negatively correlated with transferrin brain content. Taken together, these data indicate that overexpression of AQP4 in the mouse brain can effectively improve post-SAH neuronal ferroptosis and brain injury, at least partly by inhibiting transferrin infiltration into the brain parenchyma in the lymphatic system.

## 1. Introduction

Stroke is divided into ischemic stroke and hemorrhagic stroke, and hemorrhagic stroke accounts for 20%~30% of all strokes [1]. Although the incidence of hemorrhagic stroke is lower than that of ischemic stroke, its prognosis is worse, and its mortality and disability rates are higher than those of ischemic stroke [2]. Subarachnoid hemorrhage caused by ruptured intracranial aneurysm is one of the main forms of

hemorrhagic stroke, with an annual incidence of approximately 10.5/100,000 people in China [3]. At present, there have been a large number of experimental studies on the intervention of brain injury after stroke, but the results of experimental studies have little effect in clinical application [4]. The scientific prevention and treatment of brain injury after SAH is an urgent problem in today's society [1].

Neuronal death is an important component of brain injury after SAH [5]. An increasing number of studies

suggest that SAH triggers neuronal ferroptosis [6–8], and intervention with ferroptosis inhibitors is beneficial for improving early brain injury (EBI) after SAH [9, 10]. Mature neurons have a high level of polyunsaturated ether phospholipids (PUFA-EPLS), which makes them sensitive to ferroptosis [11, 12]. Glutamine (0.1 mM) and recombinant transferrin (0.25–5  $\mu\text{g}/\text{mL}$ ) caused ferroptosis in mouse embryonic fibroblasts (MEFs) deprived of amino acids [13]. The normal medium of primary cortical neurons contained 0.5–2 mM glutamine, suggesting that the environment of neurons was rich in glutamine. Transferrin is not typically expressed by neurons, but it is absorbed by neurons through TFR1-mediated endocytosis, which is the primary source of iron in neurons [14]. Blood is known to be rich in transferrin [15]. Therefore, it is worth considering whether transferrin enters the glymphoid system after SAH infiltrates the brain parenchyma and participates in neuronal ferroptosis.

The glymphoid system is a channel for the exchange of cerebrovascular cerebrospinal fluid and interstitial fluid, distributed in the Virchow-Robin space and perivascular space (PVS) [16]. Previous research has stated “Bathing the brain” to describe the role of the glymphoid system under physiological conditions [17]. PVS includes the spaces around small cerebral arteries, capillaries, and venules, which constitute channels that allow a range of substances to move [18]. Within a few minutes of the occurrence of SAH, blood components rapidly diffuse into the subarachnoid space and PVS [19]. Loss of astrocyte foot process anchoring to the basement membrane accompanied by the loss of polarized localization of AQP4 to astrocytic endfeet has been shown to be associated with vasogenic/extracellular edema in neuroinflammation [20]. In addition, it has been shown that SAH impairs the polarization of astrocyte AQP4 [21], while AQP4 knockout aggravates SAH-induced brain injury through impairment of the glymphoid system [22]. In addition, literature studies have shown that upregulation of AQP4 improves blood–brain barrier integrity and perihematomal edema following intracerebral hemorrhage [23].

Here, we investigated the occurrence and possible initiator of neuronal ferroptosis after SAH in mice. By using propidium iodide (PI) staining, we provided a description of the correlation between brain cell ferroptosis and transferrin content, alluding to the critical role of transferrin in SAH-induced brain cell ferroptosis. We assessed the effect of AQP4 overexpression on transferrin content as well as brain cell ferroptosis. Finally, we demonstrated that AQP4 overexpression effectively improved the neurobehavioral ability of SAH mice. In this study, we provide the first demonstration of transferrin function in an animal model of SAH and establish the essential role of AQP4 in regulating transferrin infiltration into the brain parenchyma.

## 2. Materials and Methods

**2.1. Animals.** Five to 8-week-old C57BL/6J male mice weighing 25–30 g were purchased from Zhaoyan Research Center (Suzhou, China) Co., Ltd. Standard feed and drinking water were provided. This study was approved by the Ethics Committee of the First Affiliated Hospital of Soochow University.

Detailed animal usage information is provided in the supplementary material 1 (Supplementary Table S1).

**2.2. Mouse SAH Model.** The endovascular perforation method was used to establish the mouse SAH model as previously reported [24, 25]. Mice were anesthetized with 3% isoflurane using a small animal gas anesthesia machine (R500IP; RWD Life Technology Co., Shenzhen, China), and anesthesia was maintained with 1.5% isoflurane [26]. Then, they were placed in a stereotaxic apparatus (Anhui Zhenghua Biological Equipment Co., Ltd., Anhui, China). The mice were placed in a supine position, and a midline incision was made in the neck. After exposing the right common carotid artery (CCA), external carotid artery (ECA), and internal carotid artery ICA, the ECA was ligated and fashioned into a stump. The suture (L2000, Guangzhou Jialing) was advanced into the ICA from the ECA stump through the common carotid bifurcation. The suture was further advanced into the intracranial ICA until resistance was felt. Before the suture was withdrawn from the ICA, it was pushed an additional 1 mm further. After ensuring hemostasis, the wound was adapted and sutured. For the sham-operated animals, all procedures were the same as those for the SAH mice, except for artery puncture. Then, all the mice were returned to their cages after injecting 1 ml 0.9% saline. All mice had free access to food and water. The grade of SAH was evaluated with a score of 0–18 to measure the degree of bleeding and was carried out by two researchers who were unaware of the experiment. Images of the bottom of the brain were taken, and the 6 segments at the bottom of the basal cistern were evaluated on a scale from 0 to 3 (0, no SAH; 1, very little subarachnoid blood; 2, moderate blood with visible arteries; and 3, blood clot obliterating all arteries within the segment). Finally, the scores of each part are summed. Mice with SAH classification scores < 8 were excluded and replaced. In sham-operated mice, the score is always 0.

**2.3. Ferrostatin-1 Treatment.** For in vivo experiments, we injected 1 pmol ferrostatin-1 (1  $\mu\text{l}$  of 25 mg Fer-1 dissolved in 0.01% DMSO saline, Sigma Aldrich, SML0583) into the lateral ventricle immediately after 0.5 h of SAH modeling and simultaneously injected 1  $\mu\text{l}$  solvent into the control group in the same way [27]. The coordinates of intraventricular injection were 1.0 mm in the lateral direction relative to the bregma, 0.5 mm in the posterior direction, and 2.5 mm in depth. After 24 hours, the head was decapitated, and the brain tissue was harvested. PI dye (Sigma–Aldrich, St. Louis, MO, USA) (1  $\mu\text{g}/\text{g}$ ) was injected intraperitoneally 2 hours before the head was decapitated.

**2.4. Immunofluorescence Staining.** As previously reported, brain tissue was cut into 7  $\mu\text{m}$  paraffin sections [28]. Briefly, the antigens were retrieved using freshly prepared 1% sodium citrate antigen retrieval solution for 20 min. The paraffin sections were boiled in antigen retrieval solution for 5 min and then soaked in cooled antigen retrieval solution for 5 min. The above operation was repeated twice. Next, 0.1% Triton was added for 10 min. After that, we used 5%

BSA to block these sections for 1 h at room temperature. The target protein primary antibody was added according to the manual, and the solution was incubated overnight at 4°C. The primary antibodies were as follows: AQP4 rabbit mAb (1:300, Cell Signaling Technology, #59678, USA) and goat CD31 antibody (1:300, R&D systems, AF3628, USA). Then, the corresponding fluorescent secondary antibody was added. The secondary antibodies were as follows: donkey anti-rabbit IgG Alexa Fluor 488 (1:300, Thermo Fisher Scientific, A-21206, USA) and donkey anti-goat IgG Alexa Fluor 555 (Thermo Fisher Scientific, A-21432, USA). The solution was incubated at 37°C for 1.5 h [26]. Brain sections were sealed with DAPI and observed under a fluorescence microscope. Coronal brain sections containing the basal temporal lobe were analyzed (Fig. S2).

**2.5. Propidium Iodide (PI) Staining.** As previously reported, twenty-two hours after the establishment of the SAH model, mice were injected with PI (Sigma-Aldrich, St. Louis, MO, USA) (1 µg/g) intraperitoneally [29]. After 2 hours, they were perfused with PBS, the heads were decapitated, and the materials were removed. After being fixed with paraformaldehyde for 24 hours, they were dehydrated with 30% sucrose. Then, brain tissue was cut into 8 µm sections in the dark and under freezing conditions. Quick Antigen Retrieval Solution for Frozen Sections (Beyotime, P0090) was added for 10 min. Next, 0.1% Triton was added for 10 min, and 5% BSA was used to block these sections for 1 h at room temperature. The target protein primary antibody was added, and the solution was incubated overnight at 4°C. The primary antibody was mouse anti-NeuN (1:300, Abcam, ab279296, USA). Then, the corresponding fluorescent secondary antibody was added, and the solution was incubated at 37°C for 1.5 h. The secondary antibodies were as follows: donkey anti-mouse IgG Alexa Fluor 488 (1:300, Thermo Fisher Scientific, A-21202, USA). Brain sections were sealed with DAPI and observed under a fluorescence microscope (OLYMPUS BX50/BX-FLA/DP70; Olympus Co.). Coronal brain sections containing the basal temporal lobe were analyzed (Fig. S2). In short, PI+/NeuN+ cells were counted by observers who were blinded to the experimental groups. We inspected and photographed six microscopic fields of each sample and calculated the average.

**2.6. Western Blot Analysis.** The brain tissues were collected from the base of the temporal lobe and stored immediately at -80°C. As previously reported, the temporal base brain tissues of C57 mice were collected and homogenized in cell lysate buffer for Western blotting and IP (P0013, Beyotime Institute of Biotechnology, China) and allowed to stand for 30 minutes. The tissue homogenate was collected into a centrifuge tube and centrifuged at 12,000 rpm/min for 10 minutes at 4°C. The supernatant was taken, and the protein concentration was measured by the bicinchoninic acid assay (BCA, Beyotime Institute of Biotechnology) [30]. Then, each protein sample (10~60 µg/lane) was loaded on a 10% SDS-PAGE gel, separated by electrophoresis, and transferred to a polyvinylidene fluoride membrane by electrophoresis (Millipore Corporation, Billerica, MA, USA), followed by

blocking with 5% BSA at room temperature for 60 minutes and then incubating with primary antibody overnight at 4°C. The primary antibodies were as follows: rabbit anti-transferrin antibody (1:1000, Abcam, ab278498, USA) and β-tubulin (9F3) rabbit mAb (1:1000, Cell Signaling Technology, #2128, USA). The diluted horseradish peroxidase-labeled secondary antibody was incubated at room temperature for approximately 1 hour and then washed with PBST (PBS +0.05% Tween 20) 3 times for 5 minutes each. The secondary antibodies were as follows: anti-rabbit IgG and HRP-linked antibody (1:2000, Cell Signaling Technology, #7074, USA). After the Ponceau was stained and washed off, the enhanced chemiluminescence kit was used for band visualization, and then, the protein relative quantitative normalization analysis was performed by the ImageJ software. Detailed antibody information is provided in the supplementary material 1 (Supplementary Tables S3, S4 and S5). Full Western blot lane is presented in supplementary material 2.

**2.7. Stereotaxic Adenoassociated Virus Injection.** AAV9-AQP4 containing adenoassociated virus GFAP-MCS-EGFP was used for overexpression of AQP4 protein (NM\_009700.3→NP\_033830.2 aquaporin-4 isoform M1) in mouse astrocytes and its negative control (Jike gene; GenBank: NM-009700) and stored at -80°C. According to the manufacturer's instructions, 1 µl adenoassociated virus (1.1E+13 v.g/ml) was injected into the lateral ventricle. The coordinates from bregma were 1.0 mm posterior, 1.8 mm lateral, and 2.4 mm deep [21]. Leave the needle for 5 minutes after the AAV injection and then pull it out slowly. We established an SAH model three weeks after AAV9-AQP4 injection. Detailed AAV information is provided in the supplementary material 1 (Supplementary Table S2).

**2.8. Quantification of AQP4 Polarization.** Perivascular polarization of AQP4 was measured as previously described [31]. DAPI images were used to identify blood vessels. Blood vessels have flattened nuclei and clusters or lines of nuclei out of focus compared to the surrounding tissue. CD31 images were used to identify the astrocytes around the blood vessels [32]. Briefly, the median immunofluorescence intensity of perivascular regions was measured. A threshold analysis was then used to measure the percentage of the region exhibiting AQP4 immunofluorescence greater than or equal to perivascular AQP4 immunofluorescence (AQP4% area). Polarization was expressed as the percentage of the region that exhibited lower AQP4 immunoreactivity than the perivascular endfeet ("polarization" = 100 - AQP4%area). AQP4 vessel coverage was measured by first delineating the area of the vessel from the CD31 channel image. This region of interest was then placed on the AQP4 channel image thresholded for immunoreactivity for extraction of the percentage vessel coverage (% immunoreactivity of AQP4 of whole delineated vessel).

**2.9. FITC-Dextran (40 kD) Injection.** Briefly, FITC-dextran (40 kD, Thermo Fisher, D3328) was injected intravenously 21 hours post-SAH [33]. The mice were sacrificed 3 hours following tracer infusions, perfused, and fixed with

paraformaldehyde. Brains were removed and cut into 10  $\mu\text{m}$  slices. Cerebrovascular permeability was evaluated by fluorescence imaging.

**2.10. Electron Microscopy.** Briefly, the brain tissue sections were postfixed with 4% paraformaldehyde +2.5% glutaraldehyde in 0.1 M PB for 14 hours at 4°C. Then, they were washed and stored in 0.1 M PB [34]. The coverslips were processed for electron microscopy as previously described with modifications [35]. Ultrathin sections at 70-80 nm were cut on an ultramicrotome and collected on Formvar-coated single slot grids (Electron Microscopy Sciences). Grids were stained with uranyl acetate and lead citrate solutions, dried, and stored in a grid box for EM imaging. Micrographs were taken on a Tecnai Biotwin transmission electron microscope (FEI, Hillsboro, Oregon, USA). We measured mitochondrial size as the percentage area of the total area of the cytoplasm [36] (comprising >1800 mitochondria in total) using ImageJ v.1.49 (<http://imagej.nih.gov/ij/>). Analysis was performed by an investigator blinded to treatment group assignment.

**2.11. Foot Fault Test.** As previously reported, the mouse was placed on an elevated steel grid (30 cm (*L*)  $\times$  35 cm (*W*)  $\times$  3 cm (*H*)) with a grid opening of 2.25 cm  $\times$  2 (1.5 cm  $\times$  1.5 cm square) [37, 38]. The mice received 5 days of pretraining before the operation. The data in the last training session were recorded as baseline. The total number of steps was counted for a videotaped 1-minute observation period. The number of forelimb and posterior limb foot faults (when the forelimb or posterior limb fell through the grid) was recorded. The data were collected by unwitting staff. The data are expressed as the percentage of errors with damage to the forelimb and posterior limb. This test will be repeated three times at the indicated times after the operation, recorded separately, and averaged.

**2.12. Adhesive Removal Test.** As previously reported, the sticker (0.2  $\times$  0.2 cm<sup>2</sup>) was placed on the paw on the inner radius of each animal's upper limb with equal pressure [37]. The stickers were placed on the left forelimbs of each animal. Then, the mouse was gently placed into the plexiglass box, and the number of seconds to touch and remove each tape was recorded. The mice were trained 3 times a day before surgery for 5 consecutive days and were tested regularly (3 times, 15 minutes apart for each mouse) at the indicated times after SAH [26]. The average time of the three trials of touching and removing the sticker will be calculated.

**2.13. Rotarod Test.** As previously reported, low speed: the instrument is set to accelerate from 0 rpm to 10 rpm within 30 s and maintained to 300 s; high speed: the instrument is set to accelerate from 4 rpm to 40 rpm and maintained to 300 s within 120 s [39, 40]. The mice will be placed on a rotating rod apparatus, and preoperative training will continue for 5 days. On the first and second days, the mice will be trained on a low-speed rotating rod once a day. On the third day, low-speed and high-speed training will be carried out successively. Then, on the fourth day, the mice were trained twice at high speed at the test speed. High-speed training was performed three times on the fifth day. The last three test data recorded the day before the operation were

taken as the baseline. The mice were subjected to three tests at the indicated times after the SAH operation, with an interval of 15 minutes, and the average value was taken [26].

**2.14. Garcia Neuroscore.** The sensorimotor Garcia test was performed on mice at the indicated times after SAH [41]. In short, the modified Garcia score is a complete sensorimotor evaluation system. We scored each test from 0 to 3 (full score = 18 points): (A) body proprioception, (B) forelimb walking, (C) limb symmetry, (D) roll over, and (E) climb. Autonomous movement: in a quiet environment, place the mouse in a new squirrel cage, observe its activity within 5 minutes, and score according to the number of touches on the four sides of the cage wall; autonomous movement of the limbs: move the mouse and lift the tail end to observe the free movement and symmetry of its limbs; forelimb extension exercise: lift the tail end of the mouse so that its forelimbs are close to the edge of the table, and observe the extension of its forelimbs; metal net climbing: place the mouse on the tilted metal cage cover and observe its climbing situation. Normal mice will climb up with their limbs. Lift the tail of the mouse and drag it away from the cage cover to observe the grasping power of its limbs; body tactile response: in a quiet environment, from back to front, avoiding the sight of the mouse, touch the body of the mouse with a blunt-headed wooden stick to observe its response; whisker response: in a quiet environment, use a blunt-headed wooden stick to touch the rat from the back side; response to vibrissae touch: in a quiet environment, a blunt stick was brushed against the vibrissae on each side; the stick was moved toward the whiskers from the rear of the animal to avoid entering the visual fields. The reaction of mice was observed.

**2.15. qPCR.** The mRNA expression of AQP4 (NM\_009700.3) was measured as previously described [42]. Briefly, total RNA was isolated from the brain tissues of mice using the TRIzol kit (15596018, Thermo Fisher, US) and reverse transcribed into cDNA (2  $\mu\text{g}$  total RNA per sample) using the High-Capacity cDNA Reverse Transcription Kit (4368814, Thermo Fisher, USA) according to the manufacturer's instructions. The primer sequences used for the reaction were AGATCAGCATCGCTAAGTCCGT TCCCAATCCTC CAACCACAC (Ribobio, China). qPCR was performed using the PowerUp™ SYBR™ Green Master Mix, and mRNA expression levels were quantified using the 2<sup>- $\Delta\Delta\text{Ct}$</sup>  method.

**2.16. Statistical Analysis.** All data are expressed as the mean  $\pm$  standard deviation (SD). The GraphPad Prism 9.0 software (GraphPad, San Diego, CA, USA) was used for statistical analysis. Post hoc power analysis was performed according to power analysis. The Kolmogorov-Smirnov test was used to test the normality of the distribution of the test data set. Data groups with normal distribution (two groups) were compared using two-sided unpaired Student's *t*-test. One-way or two-way ANOVA was used for multiple comparisons, and Tukey's post hoc test was used for comparisons between two pairs of multiple groups.  $P < 0.05$  indicates a statistically significant difference. The correlation between transferrin and PI staining was analyzed with Spearman's rank correlation coefficient for the neuroscore

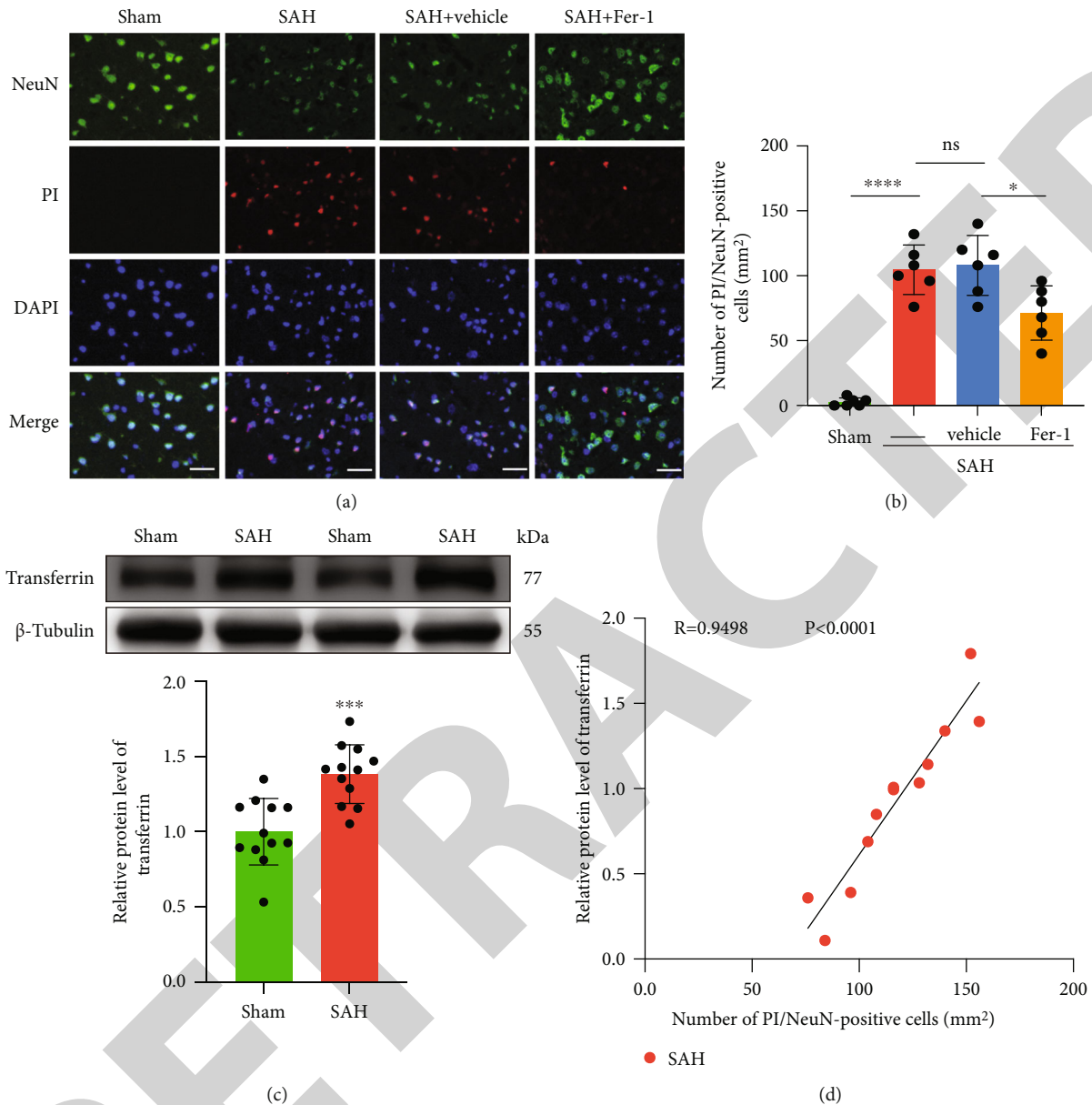


FIGURE 1: SAH triggers brain cell ferroptosis and transferrin infiltration. (a, b) Representative photomicrographs and quantification of PI-positive nerve cells in the ipsilateral cortex after Fer-1 was used.  $n = 6$  per group. Fluorescence colors: DAPI: blue; PI: red; NeuN: green. Scale bar = 40  $\mu\text{m}$ . The quantification of PI-positive and NeuN-positive cells is expressed as positive cells per square millimeter. Data are the mean  $\pm$  standard deviation (SD) (ANOVA  $F(3, 20) = 42.78$ ,  $P < 0.0001$ ;  $***P < 0.001$ ,  $*P = 0.0119$ , post hoc Tukey's test). (c) Western blot analysis shows the level of transferrin protein in the ipsilateral cortex after SAH.  $n = 12$  per group. Data are the mean  $\pm$  standard deviation (SD) ( $t$ -test  $t_{(11)} = 4.511$ ;  $***P < 0.001$ ). (d) Spearman correlation analysis between transferrin- and PI-positive cells in mouse brain tissue 24 h after SAH.

and beam walking score. For the Garcia neuroscore, adhesive removal, foot fault tests, and rotarod test, the correlation between neurobehavior and transferrin was analyzed with Pearson's product-moment correlation coefficient. The best-fit linear regressions are shown. A  $P$  value of 0.05 was considered statistically significant.

### 3. Results

#### 3.1. SAH Triggers Brain Cell Ferroptosis and Transferrin Infiltration.

Ferostatin-1 is a recognized ferroptosis inhibitor [27]. To verify the existence of ferroptosis of nerve cells after SAH in mice, we used Fer-1 intraventricular injection after surgery. The results showed that compared with the vehicle group, the Fer-1 group had significantly reduced neuronal death (sham vs. SAH,  $P < 0.0001$ ; SAH vs. SAH+vehicle,  $P = 0.9888$ ; and SAH+vehicle vs. SAH+Fer-1,  $P = 0.0119$ ; Figures 1(a) and 1(b)). This phenomenon indicates ferroptosis in mouse brain cells after SAH. Transferrin is an important factor in ferroptosis in cells [13]. Twenty-four hours after puncture-induced SAH in mice, brain tissues from the base of the temporal lobe were collected for



western blot analysis. Our results showed that compared with that in the sham group, the expression of transferrin in the SAH group was increased (sham vs. SAH,  $P = 0.0002$ ; Figure 1(c)). Next, we measured the correlation between the expression of transferrin and PI<sup>+</sup> nerve cells. The results showed that there was a significant positive correlation between the number of PI<sup>+</sup> cells and the expression of transferrin (Figure 1(d)). The above results show that SAH triggers brain cell ferroptosis and transferrin infiltration.

**3.2. AQP4 Overexpression Improves SAH-Induced AQP4 Depolarization.** qPCR was used to detect the expression level of AQP4 mRNA in brain tissue after AAV-AQP4 overexpression. Our results showed that the expression level of AQP4 mRNA in the AAV-AQP4 group was approximately 2-fold that in the vector group ( $P = 0.0427$ , Fig. S1). To further explore this possibility, we assessed the level of AQP4 using immunofluorescence staining. Twenty-four hours after SAH, the AQP4 level in astrocytes was significantly decreased compared with that in the sham group, and compared with that in the SAH+vector group, AAV-AQP4 significantly increased the expression of AQP4 (sham vs. SAH,  $P < 0.0001$ ; SAH vs. SAH+vector,  $P = 0.9945$ ; and SAH+vector vs. SAH+AAV-AQP4,  $P < 0.0001$ ; Figures 2(a), 2(g), and 2(e)). Vascular cross-sectional analysis of the temporal cortex from mice revealed impaired perivascular AQP4 expression after SAH (Figures 2(b), 2(c), 2(h), and 2(i)). Perivascular localization of AQP4 was reduced, and polarization was reduced. SAH+AAV-AQP4 reversed this change compared to the SAH+vector group. 89.01% ( $\pm 2.74\%$ ), 72.34% ( $\pm 2.90\%$ ), 72.90% ( $\pm 2.11\%$ ), and 80.23% ( $\pm 2.32\%$ ) are in the cortex of mice (sham vs. SAH,  $P < 0.0001$ ; SAH vs. SAH+vector,  $P = 0.9809$ ; and SAH+vector vs. SAH+AAV-AQP4,  $P = 0.0004$ ; Figure 2(g)). Together, these data provide evidence that astrocytic AQP4 expression and its polarized localization are similarly perturbed in a region of the SAH mouse brain.

**3.3. AQP4 Overexpression Reduces Transferrin Content and Neuronal Ferroptosis in the Brain Parenchyma of SAH Mice.** The effects of AAV-AQP4 on BBB integrity in SAH model mice were assessed by a FITC-dextran permeability assay [33]. At 24h after SAH, 40 kD dextran extravasation was detected in the mouse brain parenchyma, which was improved to some extent by AAV-AQP4 treatment (Figure 3(a)). We evaluated the expression of transferrin using Western blotting. Compared with the vector treatment group, the transferrin expression level in the AQP4 overexpression group was significantly decreased (SAH vs. SAH+vector,  $P = 0.9146$  and SAH+vector vs. SAH+AAV-AQP4,  $P = 0.0053$ ; Figures 3(b) and 3(c)). We used PI staining to evaluate the death of neurons after SAH. Our results showed that the number of neurons containing PI in the SAH+vector group was significantly higher than that in the SAH+AAV-AQP4 group, and there were no significant changes in the SAH+AAV-AQP4+vehicle group compared with the SAH+AAV-AQP4 group (SAH+vector vs. SAH+AAV-AQP4,  $P < 0.0001$  and SAH+AAV-AQP4 vs. SAH+AAV-AQP4+vehicle,  $P = 0.9943$ ; Figures 3(d) and 3(e)). There were no significant changes in the SAH+AAV-AQP4+veh-

icle group compared with the SAH+AAV-AQP4+Fer-1 group ( $P = 0.9992$ ). The results showed that overexpression of AQP4 reduced ferroptosis in neurons after SAH in mice. In ferroptosis, shrunken mitochondria have been observed, while the formation of apoptotic bodies was absent, and the plasma membrane remained intact [43]. As the sole positive morphologic criterion for ferroptosis is shrunken mitochondria, we quantified mitochondrial size following AAV-AQP4 treatment. AAV-AQP4 treatment increased the mean percentage area of cytoplasm covered by mitochondria (SAH+vector vs. SAH+AAV-AQP4,  $P = 0.0186$ ; Figures 3(f) and 3(g)). These results indicate that overexpression of AQP4 can reduce transferrin and neuronal ferroptosis in brain tissue after SAH.

**3.4. AQP4 Overexpression Improves Neurobehavioral Dysfunction in SAH Mice.** Mice developed sensorimotor impairment after stroke, which was manifested by a decrease in Garcia neuroscore, an increase in the number of foot faults, an increase in the time of the adhesive removal test, and a decrease in the time of the rotarod test (Figures 4(a)–4(f)). To evaluate the neurological damage after SAH in mice, the evaluation was carried out by researchers who did not know the group. The results showed that compared with the baseline, the Garcia score of the mice decreased significantly one, two, three, and seven days after SAH. Compared with the vehicle group, the Garcia score of the AAV-AQP4 group was significantly improved on day 3 (SAH+vector vs. SAH+AAV-AQP4,  $P = 0.0296$ ; Figure 4(a)). Compared with the baseline, the proportion of the number of wrong steps in the contralateral forelimbs and hindlimbs of mice after SAH was significantly increased. AQP4 treatment significantly reduced the percentage of incorrect steps three days after SAH (SAH+vector vs. SAH+AAV-AQP4, day 1,  $P = 0.0079$ ; day 2,  $P = 0.0133$ ; and day 3,  $P = 0.0008$ ; Figure 4(b)). SAH+vector vs. SAH+AAV-AQP4, day 1,  $P = 0.0002$ ; day 2,  $P = 0.0207$ ; and day 3,  $P = 0.0038$ ; Figure 4(c)). At the same time, we found that compared with the vehicle treatment group, the waiting time for SAH mice in the AQP4 treatment group to touch and remove the tape from the paw was significantly reduced at 1, 2, 3, and 5 days after SAH (SAH+vector vs. SAH+AAV-AQP4, day 1,  $P = 0.0066$ ; day 2,  $P = 0.0019$ ; day 3,  $P = 0.0004$ ; and day 5,  $P = 0.0002$ ; Figure 4(d)). SAH+vector vs. SAH+AAV-AQP4, day 1,  $P = 0.0174$ ; day 2,  $P = 0.002$ ; day 3,  $P = 0.0154$ ; and day 5,  $P = 0.0002$ ; Figure 4(e)). In addition, in the mice in the AQP4 treatment group, on days 1, 2, 3, and 5 after SAH, compared with the vehicle treatment group, the rod time in the rod rotation experiment was slightly increased (SAH+vector vs. SAH+AAV-AQP4, day 1,  $P < 0.0001$ ; day 2,  $P < 0.0001$ ; day 3,  $P < 0.0001$ ; and day 5,  $P = 0.0197$ ; Figure 4(f)). Overall, AQP4 treatment significantly improved the early sensory and dyskinesias of SAH in mice.

**3.5. Neurobehavioral Ability Was Negatively Correlated with Transferrin Brain Content in SAH Mice.** The results of Pearson correlation analysis showed that there was a significant negative correlation between the Garcia score ( $R = -0.8746$ ,  $P < 0.0001$ ), the residence time of the rod ( $R = -0.7088$ ,

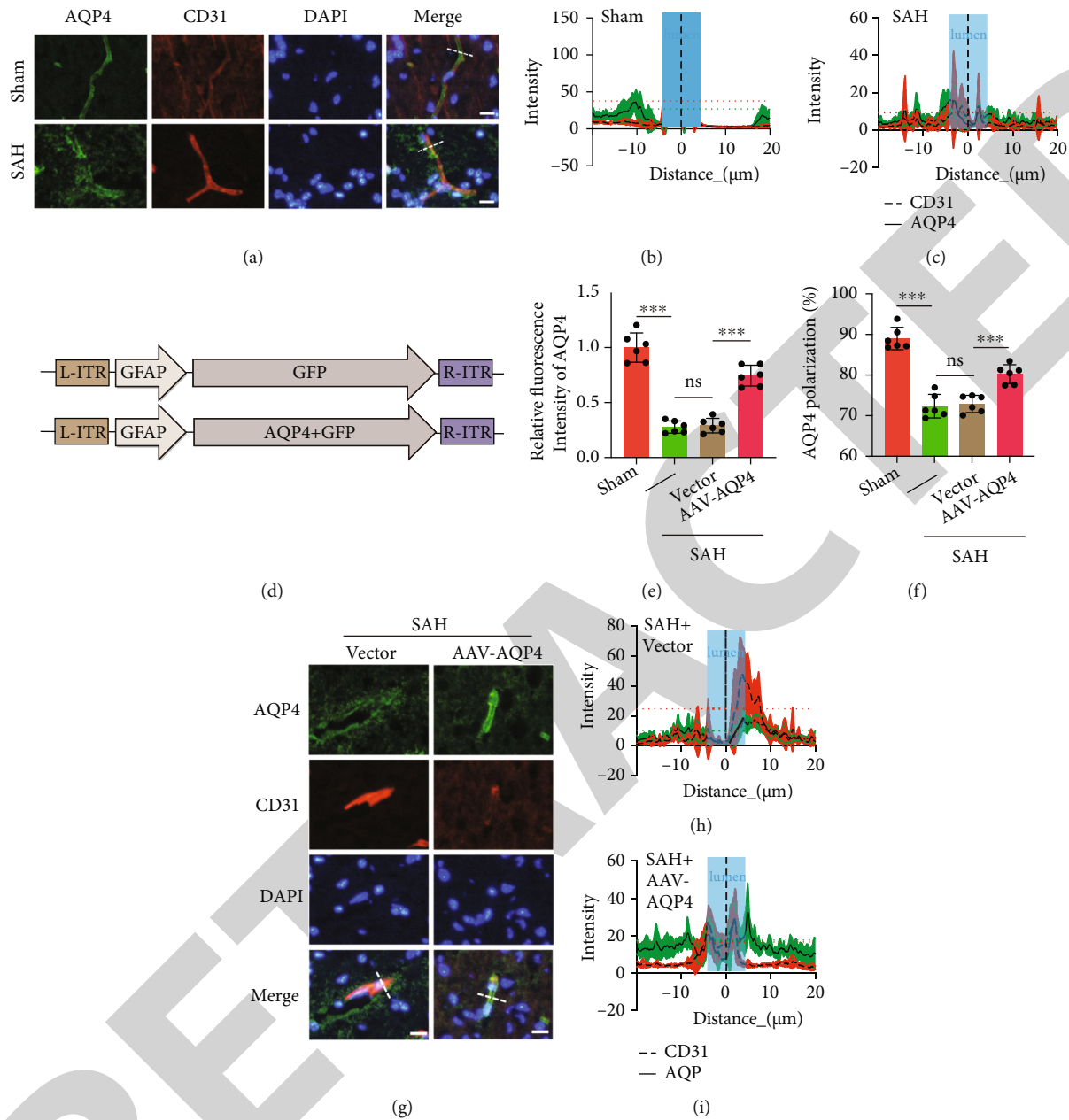


**FIGURE 2: AQP4 overexpression improves SAH-induced AQP4 depolarization.** (a, g) Immunofluorescence staining analysis of perivascular AQP4 expression changes in mouse temporal cortex large vessels 24 h after SAH.  $n = 6$  per group. CD31: red, AQP4: green; DAPI: blue. Scale bar =  $20 \mu\text{m}$ . Data are the mean  $\pm$  standard deviation (SD). (b, c, h, i) Representative immunofluorescence images of blood vessels in the cortex of (b) sham, (c) SAH, (h) SAH+vector, and (i) SAH+AAV-AQP4 group mice stained for AQP4 and CD31, illustrating placement of the  $40 \mu\text{m}$  axis perpendicular to blood vessels for quantification of expression across vessel cross-sections, illustrating AQP4 expression surrounding blood vessels in the cortex. Ten cross-sections of one blood vessel from one mouse were selected. (d) Viral vector pattern diagram. (e) Immunofluorescence intensity statistics for AQP4. Data are the mean  $\pm$  standard deviation (SD) (ANOVA  $F(3, 20) = 88.80P < 0.0001$ ;  $***P < 0.001$ , post hoc Tukey's test). (f) Quantification of AQP4 polarization.  $n = 6$  per group (ANOVA  $F(3, 20) = 56.75P < 0.0001$ ;  $***P < 0.001$ ; post hoc Tukey's test).

$P < 0.0001$ ), and the expression of transferrin after 24 h of SAH (Figures 5(a) and 5(f)). At the same time, there was a significant positive correlation between the foot fault rate ( $R = 0.7481$ ,  $R < 0.0001$ ;  $R = 0.7368$ ,  $R < 0.0001$ ) as well as the adhesive removal test time ( $R = 0.7485$ ,  $P < 0.0001$ ;  $R = 0.7368$ ,  $P < 0.0001$ ) and the expression level of transferrin (Figures 5(b)–5(e)). Overall, neurobehav-

ioral ability was negatively correlated with transferrin brain content in SAH mice.

#### 4. Discussion

Ferroptosis has drawn wide attention since the term was put forward in 2012 [43]. This unique cell death program is

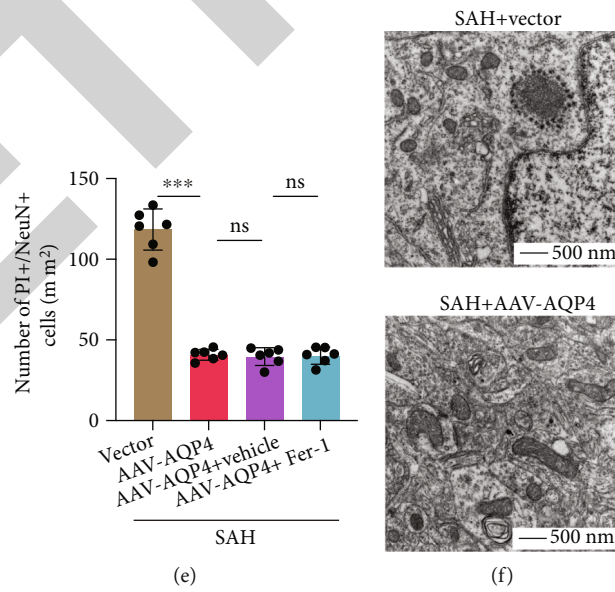
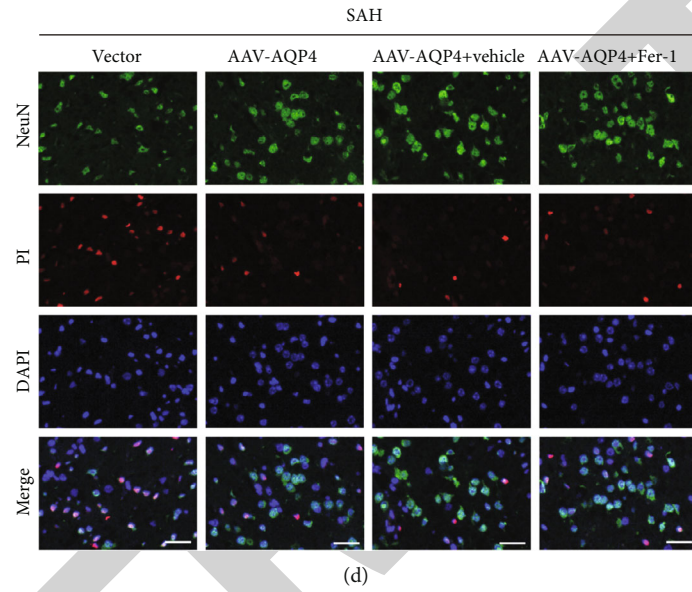
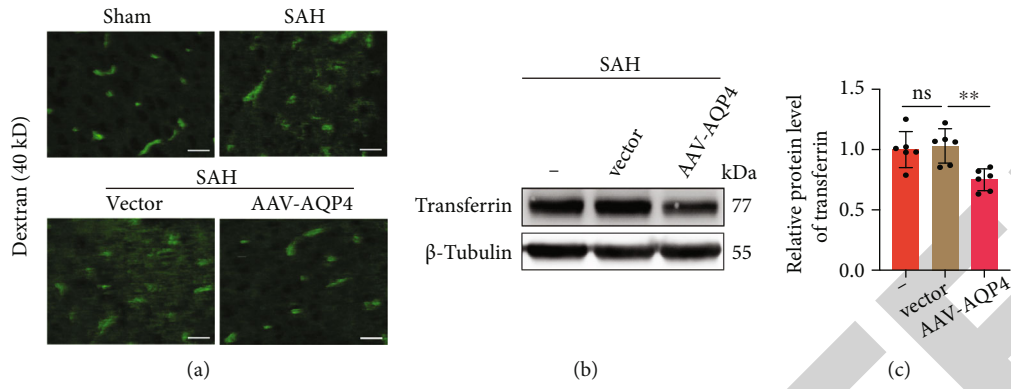


FIGURE 3: Continued.

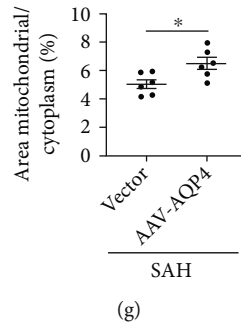


FIGURE 3: AQP4 overexpression reduces transferrin content and neuronal ferroptosis in the brain parenchyma of SAH mice. (a) Representative images of FITC-dextran (40 kD) after post-SAH intravenous injections at 24 hours after SAH (scale bar = 50  $\mu$ m). (b, c) Western blot analysis showed the levels of transferrin in the cortex after AAV overexpression of AQP4.  $n = 6$  per group. Data are the mean  $\pm$  SD (ANOVA  $F(2, 15) = 8.3P = 0.0036$ ;  $**P = 0.0053$ , post hoc Tukey's test). (d, e) Representative fluorescence micrographs and quantification of PI-positive and neuron-positive cells in the cortex after AAV overexpression of AQP4,  $n = 6$  per group. Fluorescence colors: NeuN: green; PI: red; DAPI: blue. Scale bar = 20  $\mu$ m. The quantification of PI-positive and NeuN-positive neurons is expressed as positive cells per square millimeter. Data are the mean  $\pm$  SD (ANOVA  $F(3, 20) = 157.2P < 0.0001$ ;  $***P < 0.001$ , post hoc Tukey's test). (f) Electron microscopic images of the SAH+vector group and SAH+AAV-AQP4 group. (g) AAV-AQP4 treatment reduced the mean percentage area of cytoplasm covered by mitochondria. Data are the mean  $\pm$  SEM (as this is the convention in the electron microscopy field) ( $*P = 0.0186$ ,  $t$ -test).

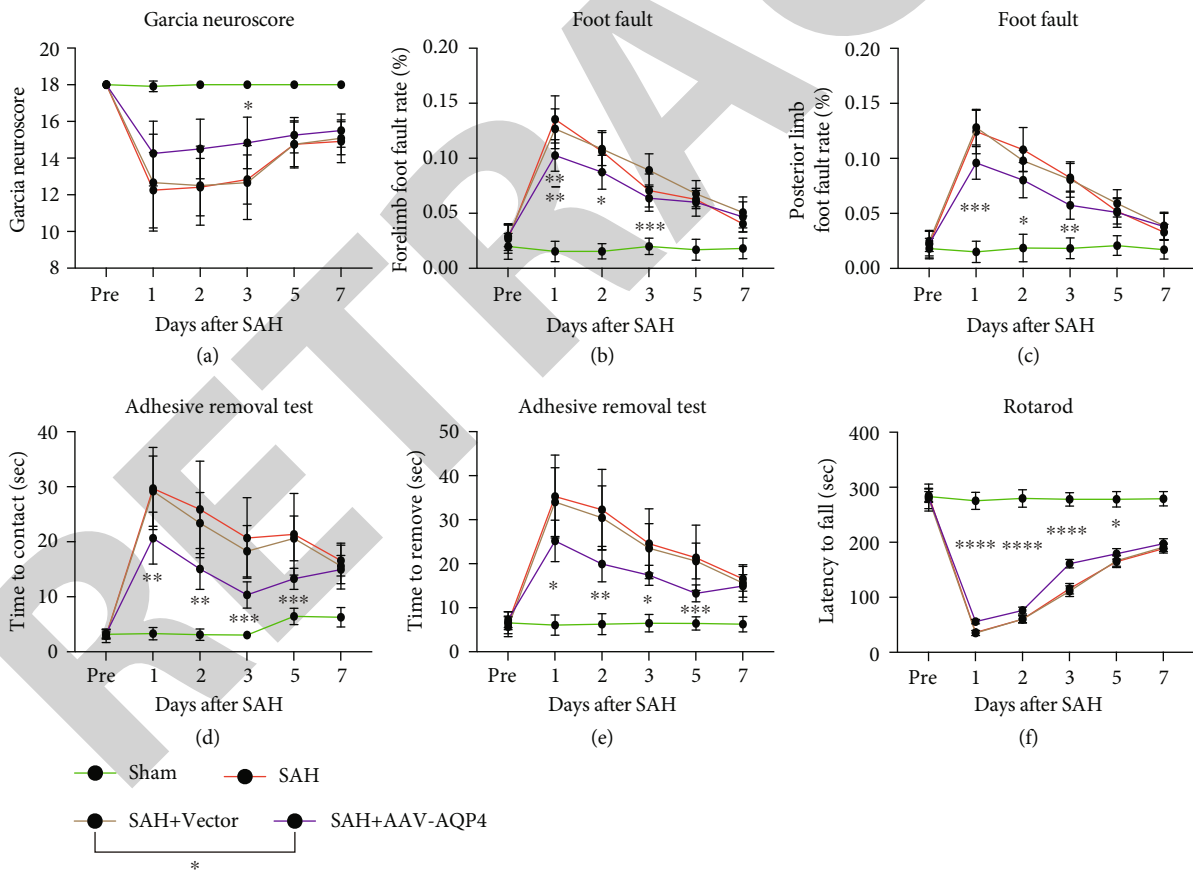


FIGURE 4: AQP4 overexpression improves neurobehavioral dysfunction in SAH mice. AAV-specific overexpression of AQP4 is beneficial to the early recovery of neurological function after SAH. (a) Garcia neuroscore.  $n = 12$  per group (ANOVA  $F(15,220) = 16.37P < 0.0001$ ;  $*P = 0.0296$ , post hoc Tukey's test). (b, c) Foot fault test of the left forelimb and left hind limb.  $n = 12$  per group (ANOVA  $F(15,220) = 28.88P < 0.0001$ ;  $**P = 0.0079$ ,  $*P = 0.0133$ ,  $***P < 0.001$ ; post hoc Tukey's test. ANOVA  $F(15,220) = 29.60P < 0.0001$ ;  $***P \leq 0.001$ ,  $*P = 0.0207$ ,  $**P = 0.0038$ ; post hoc Tukey's test). (d, e) Adhesive removal test.  $n = 12$  per group (ANOVA  $F(15,220) = 28.24P < 0.0001$ ;  $**P = 0.0066$ ,  $**P = 0.0019$ ,  $***P < 0.001$ ; post hoc Tukey's test. ANOVA  $F(15,220) = 21.80P < 0.0001$ ;  $*P = 0.0174$ ,  $**P = 0.002$ ,  $*P = 0.0154$ ,  $***P < 0.001$ , post hoc Tukey's test). (f) Rotarod test.  $n = 12$  per group (ANOVA  $F(15,220) = 188.2P < 0.0001$ ;  $***P < 0.001$ ,  $*P = 0.0197$ ; post hoc Tukey's test). Data are the mean  $\pm$  SD, SAH+AAV-AQP4 group vs. SAH+vector group.

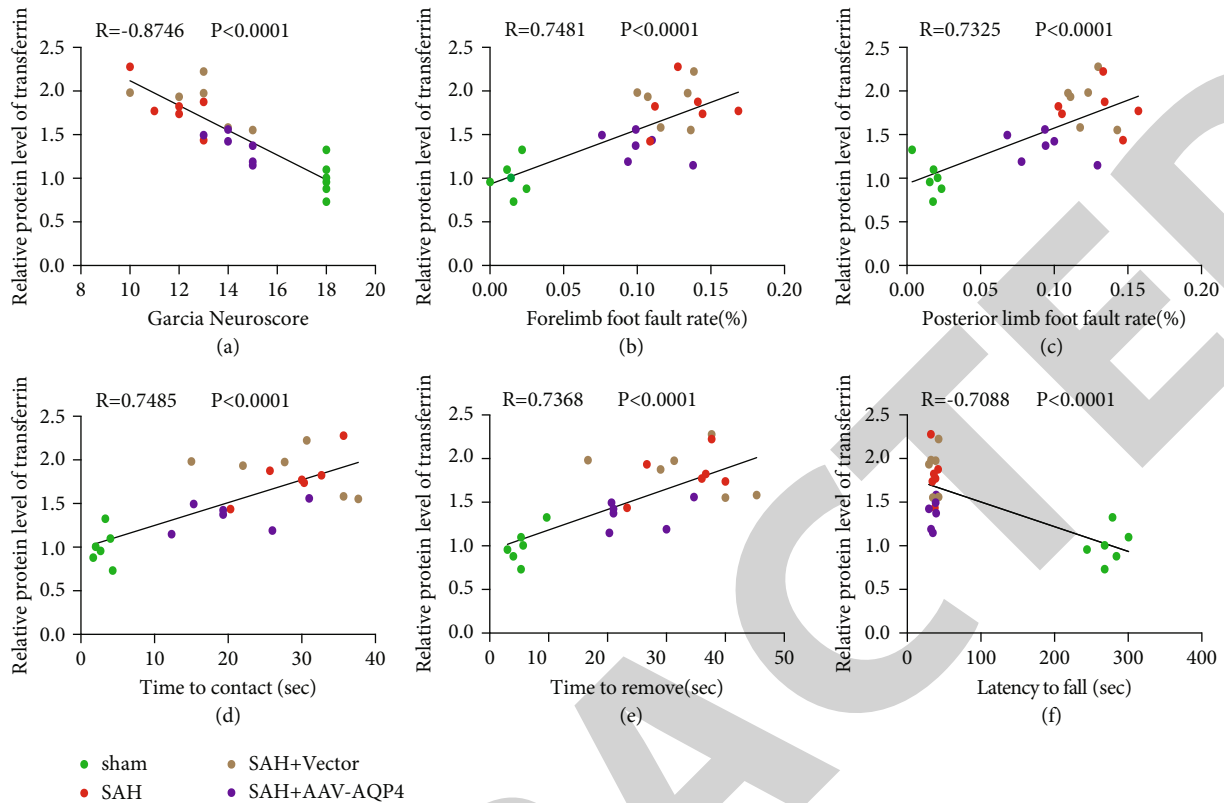


FIGURE 5: Neurobehavioral ability was negatively correlated with transferrin brain content in SAH mice. Correlation analysis between the expression of transferrin in brain tissue and behavior at 24 hours after SAH. (a) Correlation analysis between the expression of transferrin in brain tissue and the modified Garcia neuroscore 24 hours after SAH.  $n = 6$  per group. (b, c) Correlation analysis between the expression of transferrin in brain tissue and the stumping rate of the contralateral forelimb and hindlimb 24 hours after SAH.  $n = 6$  per group. (d, e) Correlation analysis between the expression of transferrin in brain tissue and the time of sticker touch and avulsion 24 h after SAH.  $n = 6$  per group. (f) Correlation analysis between the expression of transferrin in brain tissue and the stick time 24 h after SAH.  $n = 6$  per group.

driven by iron-dependent phospholipid peroxidation and is modulated by multiple cellular metabolic pathways, including redox homeostasis, iron metabolism, and mitochondrial activity [44]. Neuronal death after SAH is an important factor affecting prognosis [45]. Previous studies have shown that neuronal ferroptosis occurs after SAH, but the mechanism is unclear [46]. In addition, neurons have high levels of PUFA-EPLS and live in an environment rich in glutamine, which makes mature neurons sensitive to ferroptosis [12]. Studies have shown that 1 minute after the modeling of the intravascular puncture SAH model in mice, the erythrocyte flow rate and blood flow in the anterior capillary arteriole decreased to 20% of those before modeling [47]. Subsequently, the arterioles dilated or contracted inconsistently for 60 minutes, and the red blood cell flow and blood flow in the arterioles continued to decrease, suggesting neurovascular dysfunction [47]. The results obtained in these studies indicate that the transient disturbance of microcirculation after SAH in the acute phase may lead to oxidative stress, which in turn mediates ferroptosis. Therefore, ferroptosis may play a more important role in brain injury than the current understanding. The focus of this study was to clarify

the factors that induce neuronal ferroptosis after SAH and the role of AQP4 in this process.

AQP4 is not just involved in ferroptosis; previous studies have shown that AQP4 knockout aggravates brain edema, blood-brain barrier disruption, and neuronal apoptosis after subarachnoid hemorrhage [22, 48]. Consistent with our study, it has been reported that the perivascular polarity of AQP4 is reduced after SAH in rats, leading to dysfunction of the glymphatic system and neuronal apoptosis and neurological deficits after SAH [21]. In addition, in a mouse model of intracerebral hemorrhage, AQP4 reduction increases neuronal apoptosis and astrocyte apoptosis after intracerebral hemorrhage, and the underlying mechanism may be through cytokines, especially  $TNF-\alpha$  and  $IL-1\beta$  initiate the apoptotic cascade and activate caspase-3 and caspase-8 [49]. In addition, in a rat model of ischemia-reperfusion, induction of pyroptosis leads to loss of AQP4 polarization, which can be ameliorated by inhibition of pyroptosis [50]. The process and mechanism of AQP4 involvement in various forms of programmed cell death deserve further study.

Previous studies have focused on the neurotoxicity of erythrocyte lysis products such as iron, hemoglobin, and

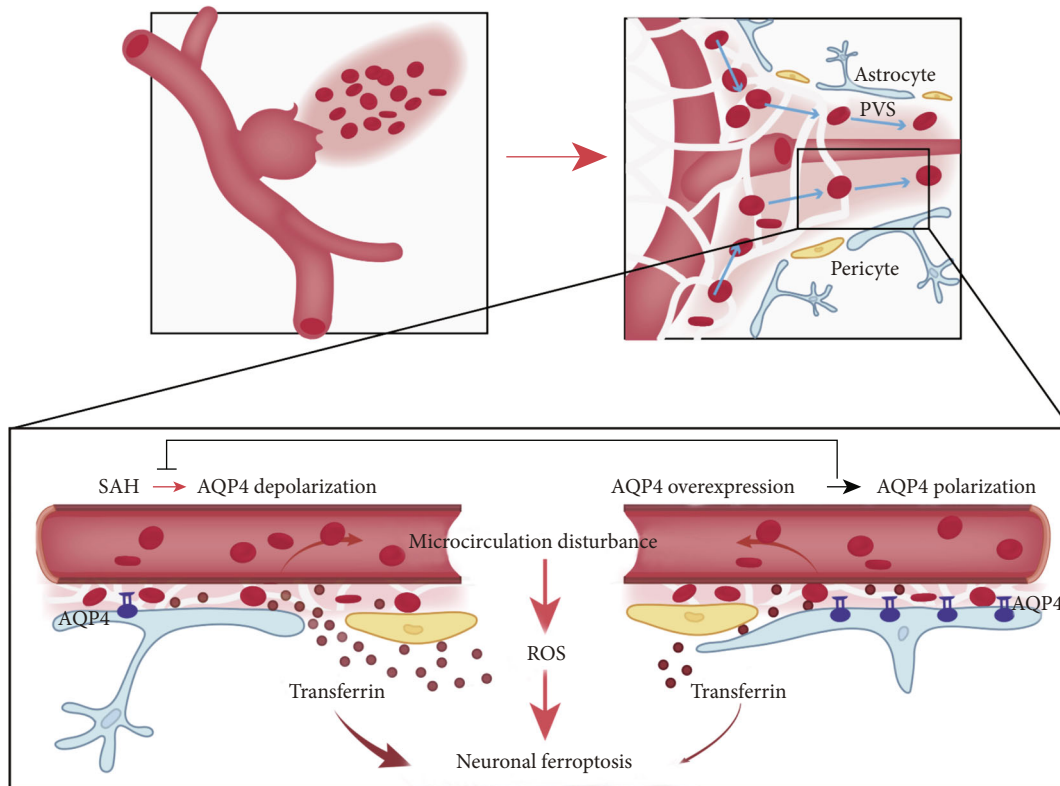


FIGURE 6: The mechanism of AQP4 involvement in early brain injury after SAH. In the early stage of SAH, transient disturbance of microcirculation and transferrin induced neuronal oxidative stress and iron uptake, leading to neuronal ferroptosis. Overexpression of AQP4 can improve SAH-induced AQP4 depolarization and transferrin infiltration and thus improve neuronal ferroptosis and neurological dysfunction.

heme for neuronal death after SAH [27, 35]. However, less attention has been given to transient microcirculation disorders and the blood component transferrin in the early stages of SAH. Our work suggests that the infiltration of transferrin into the brain parenchyma at the early stage of SAH may be one of the causes of neuronal ferroptosis.

Aquaporin (AQP) is abundant in the brain and spinal cord, and AQP1 and AQP4 are believed to play an important role in water metabolism and osmotic regulation [51]. In the early stage of SAH, blood components rapidly diffuse into the subarachnoid space and the glymphoid system in the PVS [19]. After SAH, microglia/macrophages can remove blood components in the glymphoid system [52]. Enhanced PVS barrier action can make time for blood component clearance [53]. PVS permeability has been reported to have a circadian rhythm and is closely related to AQP4 polarization [20]. It has been reported that the increased expression of AQP4 in rats after subarachnoid hemorrhage will aggravate the occurrence of cerebral edema [54], and the inhibition of AQP4 can inhibit cerebral edema [55, 56]. In addition, studies have shown that the nervous system function of *AQP4<sup>-/-</sup>* mice was improved in a model of cytotoxic edema simulated by intraventricular injection of *Streptococcus* [57]. However, brain swelling and clinical outcomes are worse in *AQP4<sup>-/-</sup>* mice in models of vasogenic

(fluid leak) edema, probably due to impaired AQP4-dependent brain water clearance [57]. AQP4 mediates bidirectional water flux as well as water inflow and outflow during the evolution of edema [58, 59]. AQP4 dysfunction in mouse brain tissue leads to impaired water and solute processing and may lead to brain edema or abnormal protein accumulation [60, 61]. Although some studies have shown that AQP4 is involved in brain edema after SAH [62], in recent years, AQP4 knockout has been found to aggravate brain injury after SAH [23], suggesting the functional diversity and potential neuroprotective effect of AQP4. Our work is the first to show that AQP4 overexpression can reduce SAH-induced AQP4 depolarization, brain parenchymal ferritin content, and neuronal ferroptosis to a certain extent.

Stroke affects both men and women, and studies revealed that estrogen has a protective effect after subarachnoid hemorrhage [63]. Our study just used male animals. We will consider gender factors in our subsequent studies to explain the role of AQP4 in animals of different genders after subarachnoid hemorrhage.

In conclusion, in the early stage of SAH, transient disturbance of microcirculation and transferrin induced neuronal oxidative stress and iron uptake, leading to neuronal ferroptosis. Overexpression of AQP4 can improve SAH-induced

AQP4 depolarization and transferrin infiltration and thus improve neuronal ferroptosis and neurological dysfunction (Figure 6).

## Abbreviations

AQP4: Aquaporin 4  
EBI: Early brain injury  
PVS: Perivascular space  
SAH: Subarachnoid hemorrhage.

## Data Availability

The data presented in this study are available on request from the corresponding author.

## Ethical Approval

All animal experiments were performed strictly in accordance with the guidelines of the Soochow University Institutional Animal Care and Use Committee.

## Conflicts of Interest

The authors declare that they have no competing interests.

## Authors' Contributions

Conceptualization was contributed by Haiying Li, Jiang Wu, and Gang Chen. Data curation was done by Zhongmou Xu and Jinxin Lu. Formal analysis was contributed by Zhongmou Xu and Jinxin Lu. Methodology was carried out by Haitao Shen. Project administration was contributed by Yuan Liu, Zongqi Wang, and Chang Cao. Supervision was contributed by Haiying Li, Jiang Wu, and Gang Chen. Writing—original draft was completed by Yuan Liu and Zongqi Wang. Writing—review and editing was completed by Xiang Li. All authors approved the final version of the paper.

## Acknowledgments

This work was supported by the National Natural Science Foundation of China under Grant (82071307, 82002643, 82071297, and 82171294), China Postdoctoral Science Foundation under Grant (2019M651954), Natural Science Foundation of Jiangsu Province under Grant (BK20211552), Gusu Health Personnel Training Project (GSWS2019030), and Grants from Suzhou Government (SYS2019045).

## Supplementary Materials

*Supplementary 1.* Table S1: total mortality and exclusion rates of experimental mice. Table S2: detailed AQP4 overexpression adenoassociated virus information. Table S3, S4, and S5; resource identifiers for antibodies. Figure S1: qPCR revealed that AQP4 mRNA expression in AAV-APQ4 group was higher compared with the vector group. The expression level of AQP4-mRNA (NM\_009700.3) after AAV-AQP4 treatment was detected by qPCR analyses.  $n = 6$  per group. Data are the mean  $\pm$  standard deviation (SD) ( $t$ -test  $t =$

2.320,  $*P = 0.0427$ ). Figure S2: schematic diagram of whole brain pictures and sampling sites of sham group and SAH group. The brain tissues were collected from the base of the temporal lobe and stored immediately  $-80^{\circ}\text{C}$  for Western blot. Coronal brain sections containing the basal temporal lobe were used for PI staining.

*Supplementary 2.* Full western blot lane.

## References

- [1] W. Wang, B. Jiang, H. Sun et al., "Prevalence, incidence, and mortality of stroke in China: results from a nationwide population-based survey of 480 687 adults," *Circulation*, vol. 135, no. 8, pp. 759–771, 2017.
- [2] S. D'Souza, "Aneurysmal subarachnoid hemorrhage," *Journal of Neurosurgical Anesthesiology*, vol. 27, no. 3, pp. 222–240, 2015.
- [3] C. Ji and G. Chen, "Signaling pathway in early brain injury after subarachnoid hemorrhage: news update," *Acta Neurochirurgica. Supplement*, vol. 121, pp. 123–126, 2016.
- [4] H. Li, J. Wu, H. Shen et al., "Autophagy in hemorrhagic stroke: mechanisms and clinical implications," *Progress in Neurobiology*, vol. 163–164, pp. 79–97, 2018.
- [5] J. Mo, B. Enkhjargal, Z. D. Travis et al., "AVE 0991 attenuates oxidative stress and neuronal apoptosis via Mas/PKA/CREB/UCP-2 pathway after subarachnoid hemorrhage in rats," *Redox Biology*, vol. 20, pp. 75–86, 2019.
- [6] X. F. Qu, T. Y. Liang, D. G. Wu et al., "Acyl-CoA synthetase long chain family member 4 plays detrimental role in early brain injury after subarachnoid hemorrhage in rats by inducing ferroptosis," *CNS Neuroscience & Therapeutics*, vol. 27, no. 4, pp. 449–463, 2021.
- [7] Y. Liang, Y. Deng, J. Zhao et al., "Ferritinophagy is involved in experimental subarachnoid hemorrhage-induced neuronal ferroptosis," *Neurochemical Research*, vol. 47, no. 3, pp. 692–700, 2022.
- [8] H. Kuang, T. Wang, L. Liu et al., "Treatment of early brain injury after subarachnoid hemorrhage in the rat model by inhibiting p 53-induced ferroptosis," *Neuroscience Letters*, vol. 762, article 136134, 2021.
- [9] Y. Li, Y. Liu, P. Wu et al., "Inhibition of ferroptosis alleviates early brain injury after subarachnoid hemorrhage in vitro and in vivo via reduction of lipid peroxidation," *Cellular and Molecular Neurobiology*, vol. 41, no. 2, pp. 263–278, 2021.
- [10] Y. Cao, Y. Li, C. He et al., "Selective ferroptosis inhibitor liproxstatin-1 attenuates neurological deficits and neuroinflammation after subarachnoid hemorrhage," *Neuroscience Bulletin*, vol. 37, no. 4, pp. 535–549, 2021.
- [11] C. Iadecola and J. Anrather, "Stroke research at a crossroad: asking the brain for directions," *Nature Neuroscience*, vol. 14, no. 11, pp. 1363–1368, 2011.
- [12] Y. Zou, W. S. Henry, E. L. Ricq et al., "Plasticity of ether lipids promotes ferroptosis susceptibility and evasion," *Nature*, vol. 585, no. 7826, pp. 603–608, 2020.
- [13] M. Gao, P. Monian, N. Quadri, R. Ramasamy, and X. Jiang, "Glutaminolysis and transferrin regulate ferroptosis," *Molecular Cell*, vol. 59, no. 2, pp. 298–308, 2015.
- [14] D. F. Leitner and J. R. Connor, "Functional roles of transferrin in the brain," *Biochimica et Biophysica Acta*, vol. 1820, no. 3, pp. 393–402, 2012.

- [15] A. H. Schmaier, "Transferrin: a blood coagulation modifier," *Cell Research*, vol. 30, no. 2, pp. 101–102, 2020.
- [16] J. J. Iliff, H. Lee, M. Yu et al., "Brain-wide pathway for waste clearance captured by contrast-enhanced MRI," *The Journal of Clinical Investigation*, vol. 123, no. 3, pp. 1299–1309, 2013.
- [17] W. J. Strittmatter, "Bathing the brain," *The Journal of Clinical Investigation*, vol. 123, no. 3, pp. 1013–1015, 2013.
- [18] J. M. Wardlaw, H. Benveniste, M. Nedergaard et al., "Perivascular spaces in the brain: anatomy, physiology and pathology," *Nature Reviews. Neurology*, vol. 16, no. 3, pp. 137–153, 2020.
- [19] C. Luo, X. Yao, J. Li et al., "Paravascular pathways contribute to vasculitis and neuroinflammation after subarachnoid hemorrhage independently of glymphatic control," *Cell Death & Disease*, vol. 7, no. 3, article e2160, 2016.
- [20] E. Steiner, G. U. Enzmann, S. Lin et al., "Loss of astrocyte polarization upon transient focal brain ischemia as a possible mechanism to counteract early edema formation," *Glia*, vol. 60, no. 11, pp. 1646–1659, 2012.
- [21] T. Pu, W. Zou, W. Feng et al., "Persistent malfunction of glymphatic and meningeal lymphatic drainage in a mouse model of subarachnoid hemorrhage," *Experimental Neurobiology*, vol. 28, no. 1, pp. 104–118, 2019.
- [22] E. Liu, L. Sun, Y. Zhang, A. Wang, and J. Yan, "Aquaporin4 knockout aggravates early brain injury following subarachnoid hemorrhage through impairment of the glymphatic system in rat brain," *Acta Neurochirurgica. Supplement*, vol. 127, pp. 59–64, 2020.
- [23] H. Jeon, M. Kim, W. Park et al., "Upregulation of aqp4 improves blood-brain barrier integrity and perihematomal edema following intracerebral hemorrhage," *Neurotherapeutics*, vol. 18, no. 4, pp. 2692–2706, 2021.
- [24] Y. Dong, C. Fan, W. Hu et al., "Melatonin attenuated early brain injury induced by subarachnoid hemorrhage via regulating NLRP3 inflammasome and apoptosis signaling," *Journal of Pineal Research*, vol. 60, no. 3, pp. 253–262, 2016.
- [25] T. Sugawara, R. Ayer, V. Jadhav, and J. H. Zhang, "A new grading system evaluating bleeding scale in filament perforation subarachnoid hemorrhage rat model," *Journal of Neuroscience Methods*, vol. 167, no. 2, pp. 327–334, 2008.
- [26] X. Li, H. Li, Z. Xu et al., "Ischemia-induced cleavage of OPA1 at S1 site aggravates mitochondrial fragmentation and reperfusion injury in neurons," *Cell Death & Disease*, vol. 13, no. 4, p. 321, 2022.
- [27] Q. Li, X. Han, X. Lan et al., "Inhibition of neuronal ferroptosis protects hemorrhagic brain," *JCI Insight*, vol. 2, no. 7, article e90777, 2017.
- [28] M. Ma, H. Li, J. Wu et al., "Roles of prokineticin 2 in subarachnoid hemorrhage-induced early brain injury via regulation of phenotype polarization in astrocytes," *Molecular Neurobiology*, vol. 57, no. 9, pp. 3744–3758, 2020.
- [29] J. R. Li, H. Z. Xu, S. Nie et al., "Fluoxetine-enhanced autophagy ameliorates early brain injury via inhibition of NLRP3 inflammasome activation following subarachnoid hemorrhage in rats," *Journal of Neuroinflammation*, vol. 14, no. 1, p. 186, 2017.
- [30] L. Zhang, Z. Li, D. Feng et al., "Involvement of Nox 2 and nox4 NADPH oxidases in early brain injury after subarachnoid hemorrhage," *Free Radical Research*, vol. 51, no. 3, pp. 316–328, 2017.
- [31] I. F. Harrison, O. Ismail, A. Machhada et al., "Impaired glymphatic function and clearance of tau in an Alzheimer's disease model," *Brain*, vol. 143, no. 8, pp. 2576–2593, 2020.
- [32] B. T. Kress, J. J. Iliff, M. Xia et al., "Impairment of paravascular clearance pathways in the aging brain," *Annals of Neurology*, vol. 76, no. 6, pp. 845–861, 2014.
- [33] L. Kang, H. Yu, X. Yang et al., "Neutrophil extracellular traps released by neutrophils impair revascularization and vascular remodeling after stroke," *Nature Communications*, vol. 11, no. 1, p. 2488, 2020.
- [34] X. B. Liu and C. M. Schumann, "Optimization of electron microscopy for human brains with long-term fixation and fixed-frozen sections," *Acta Neuropathologica Communications*, vol. 2, no. 1, p. 42, 2014.
- [35] M. Zille, S. S. Karuppagounder, Y. Chen et al., "Neuronal death after hemorrhagic stroke in vitro and in vivo shares features of ferroptosis and necroptosis," *Stroke*, vol. 48, no. 4, pp. 1033–1043, 2017.
- [36] S. B. Berman, Y. B. Chen, B. Qi et al., "Bcl-x l increases mitochondrial fission, fusion, and biomass in neurons," *The Journal of Cell Biology*, vol. 184, no. 5, pp. 707–719, 2009.
- [37] X. C. Ye, Q. Hao, W. J. Ma et al., "Dectin-1/Syk signaling triggers neuroinflammation after ischemic stroke in mice," *Journal of Neuroinflammation*, vol. 17, no. 1, p. 17, 2020.
- [38] M. E. Lie, E. K. Gowing, N. B. Johansen et al., "GAT3 selective substrate l-isoserine upregulates GAT 3 expression and increases functional recovery after a focal ischemic stroke in mice," *Journal of Cerebral Blood Flow and Metabolism*, vol. 39, no. 1, pp. 74–88, 2019.
- [39] S. Kim, S. H. Kwon, T. I. Kam et al., "Transneuronal propagation of pathologic alpha-synuclein from the gut to the brain models Parkinson's disease," *Neuron*, vol. 103, no. 4, article e627, pp. 627–641.e7, 2019.
- [40] D. R. Scoles, P. Meera, M. D. Schneider et al., "Antisense oligonucleotide therapy for spinocerebellar ataxia type 2," *Nature*, vol. 544, no. 7650, pp. 362–366, 2017.
- [41] K. Matsumura, T. P. Kumar, T. Guddanti, Y. Yan, S. L. Blackburn, and D. W. McBride, "Neurobehavioral deficits after subarachnoid hemorrhage in mice: sensitivity analysis and development of a new composite score," *Journal of the American Heart Association*, vol. 8, no. 8, article e011699, 2019.
- [42] H. Yao, J. Liu, C. Zhang et al., "Apatinib inhibits glioma cell malignancy in patient-derived orthotopic xenograft mouse model by targeting thrombospondin 1/myosin heavy chain 9 axis," *Cell Death & Disease*, vol. 12, no. 10, p. 927, 2021.
- [43] S. J. Dixon, K. M. Lemberg, M. R. Lamprecht et al., "Ferroptosis: an iron-dependent form of nonapoptotic cell death," *Cell*, vol. 149, no. 5, pp. 1060–1072, 2012.
- [44] T. Hirschhorn and B. R. Stockwell, "The development of the concept of ferroptosis," *Free Radical Biology & Medicine*, vol. 133, pp. 130–143, 2019.
- [45] Z. P. Xiao, T. Lv, P. P. Hou et al., "Sirtuin 5-mediated lysine desuccinylation protects mitochondrial metabolism following subarachnoid hemorrhage in mice," *Stroke*, vol. 52, no. 12, pp. 4043–4053, 2021.
- [46] Y. Fang, S. Gao, X. Wang et al., "Programmed cell deaths and potential crosstalk with blood-brain barrier dysfunction after hemorrhagic stroke," *Frontiers in Cellular Neuroscience*, vol. 14, p. 68, 2020.



## Research Article

# Inhibiting Microglia-Derived NLRP3 Alleviates Subependymal Edema and Cognitive Dysfunction in Posthemorrhagic Hydrocephalus after Intracerebral Hemorrhage via AMPK/Beclin-1 Pathway

Zhaoqi Zhang <sup>1,2,3</sup>, Peiwen Guo,<sup>1,2,3</sup> Suna Huang,<sup>1,2,3</sup> Zhengcai Jia,<sup>1,2,3</sup> Tunan Chen,<sup>1,2,3</sup> Xin Liu,<sup>1,2,3</sup> Hua Feng <sup>1,2,3</sup> and Yujie Chen <sup>1,2,3,4</sup>

<sup>1</sup>Department of Neurosurgery and State Key Laboratory of Trauma, Burn and Combined Injury, Southwest Hospital, Third Military Medical University (Army Medical University), Chongqing 400038, China

<sup>2</sup>Chongqing Key Laboratory of Precision Neuromedicine and Neuroregeneration, Southwest Hospital, Third Military Medical University (Army Medical University), Chongqing 400038, China

<sup>3</sup>Chongqing Clinical Research Center for Neurosurgery, Southwest Hospital, Third Military Medical University (Army Medical University), Chongqing 400038, China

<sup>4</sup>CAS Key Laboratory of Separation Science for Analytical Chemistry, Dalian Institute of Chemical Physics, Chinese Academy of Sciences, Dalian 116023, China

Correspondence should be addressed to Hua Feng; [fenghua8888@vip.163.com](mailto:fenghua8888@vip.163.com) and Yujie Chen; [yujiechen6886@foxmail.com](mailto:yujiechen6886@foxmail.com)

Received 14 November 2021; Accepted 29 April 2022; Published 17 May 2022

Academic Editor: Alessandra Durazzo

Copyright © 2022 Zhaoqi Zhang et al. This is an open access article distributed under the Creative Commons Attribution License, which permits unrestricted use, distribution, and reproduction in any medium, provided the original work is properly cited.

For posthemorrhagic hydrocephalus (PHH) patients, whether occur subependymal edema indicates poor outcomes, partially manifested as cognitive impairment. In the brain, NLRP3 inflammasome mainly derived from microglia/macrophages is involved in proinflammatory and neurodeficits after hemorrhage, and autophagy is vital for neuronal homeostasis and functions. Accumulating evidence suggest that NLRP3 inflammasome and autophagy played an essential role after intracerebral hemorrhage (ICH). We aimed to dissect the mechanisms underlying subependymal edema formation and cognitive dysfunction. Here, based on the hydrocephalus secondary to ICH break into ventricular (ICH-IVH) in rats, this study investigated whether microglia/macrophage-derived NLRP3 induced subependymal edema formation and neuron apoptosis in subventricular zones (SVZ). In the acute phase of ICH-IVH, both the expression of NLRP3 inflammasome of microglia/macrophages and the autophagy of neurons were upregulated. The activated NLRP3 in microglia/macrophages promoted the release of IL-1 $\beta$  to extracellular, which contributed to excessive autophagy, leading to neurons apoptosis both in vivo and in vitro through the AMPK/Beclin-1 pathway combined with transcriptomics. Administration of MCC950 (NLRP3 inflammasome specific inhibitor) after ICH-IVH significantly reduced edema formation and improved cognitive dysfunction. Thus, inhibiting NLRP3 activation in SVZ may be a promising therapeutic strategy for PHH patients that warrants further investigation.

## 1. Introduction

Intracerebral hemorrhage (ICH) has high morbidity and mortality and is associated with severe long-term disability [1, 2]; however, there is still no effective treatment so far [3]. About 40% of ICH break into the ventricle (ICH-

IVH), and more than half of these patients will develop into varying degrees of hydrocephalus, which makes the unfavorable outcome even worse [2, 4, 5]. Although there are many hypotheses about the pathogenesis of hydrocephalus after ICH-IVH, such as blood-clot blockage, barrier impairment, inflammation, and blood components [6],

due to the rare experimental verification, the exact pathogenesis remains unclear.

Clinically, the subependymal edema of imaging results is associated strongly with poor outcomes in PHH patients. Clinical treatments of reducing hydrocephalus by shunting operation or dehydrating agents have not demonstrated therapeutic efficacy in reducing subependymal edema [4, 5]. ICH-IVH causes primary brain injury through direct mechanical effects of the hematoma and leads to the development of subependymal edema as ICP increases or inflammation activation, which induces secondary brain injury manifested by loss of neurons [7, 8]. However, how the subependymal edema occurred remains unclear, especially the source of water that contributed to edema formation. As such, PHH remains the worse compliant of hemorrhage. Considering the contribution of subependymal edema to secondary clinical deterioration, subependymal edema may represent an attractive therapeutic target in PHH.

Once ICH-IVH occurred, the robust cellular immune response rapidly activated, especially the resident neuroglia (microglia/macrophages) and recruited peripheral leukocytes were soon activated to release proinflammation cytokines, causing neuroinflammation and brain injury at acute phase [9–11]. Evidence indicates that focal inflammation contributes significantly to BBB disruption and brain edema. The NLRP3 inflammasome, highly expressed in microglia/macrophages, has been proved to participate in a variety of pathological processes such as psychiatric and neurodegenerative disorders [12, 13]. Activating NLRP3 inflammasome can induce cytokines, such as IL-1 $\beta$ , a new cardiovascular risk biomarker [14]. Accumulating evidence that NLRP3 inflammasome inhibition could relieve neuroinflammation, disrepute BBB intensity, and reduce cell death in early brain injury [15, 16] make the NLRP3 inflammasome-induced anti-inflammatory treatment be a potential strategy to reduce brain edema.

Autophagy is an evolutionarily conserved intracellular process to maintain cellular homeostasis by the phagosome and lysosomal pathways [17]. Abnormal autophagy has been found to play an important role in the pathogenic process of a variety of neurodegenerative diseases [18–20], such as Parkinson disease (PD) and Alzheimer disease (AD) [21, 22]. What is more, recent studies have revealed that autophagy is upregulated under some restrest conditions in neurons [23], and excessive autophagy can lead to neurons apoptosis after ischemia [24]. However, there are few reports about autophagy dysfunction in the acute phase of ICH.

Herein, we explored the mechanism of subependymal edema formation-related cognitive dysfunction after ICH-IVH. Since inflammation and autophagy were closely related, we further studied the relationship between NLRP3 inflammasome (a crucial molecular regulator in inflammation) activation in microglia/macrophages and autophagy in neurons after ICH-IVH. A rat model of ICH with ventricular extension and PC12 cells were performed to address this proposal.

## 2. Materials and Methods

**2.1. Animals.** All experimental procedures were approved by the Laboratory Animal Welfare and Ethics Committee of

Third Military Medical University (AMUWEC2020762) and were performed according to the guide for the care and use of laboratory animals of the national institutes of health and reported in compliance with the ARRIVE (animal research: reporting of in vivo experiments) guidelines. A total of 261 male rats (weight 220–250 g) were housed in a temperature and humidity-controlled room under a standard 12 h light/dark cycle for a minimum of 3 days before ICH-IVH induction and were provided free access to food and water.

**2.2. ICH-IVH Model and Groups.** ICH-IVH was induced by autologous arterial blood injection into the right perilateral ventricles as previously described [25]. Briefly, rats were anesthetized with pentobarbital (40 mg/kg, IP). The right femoral artery was catheterized as a source of the blood sample. A cranial burr hole (1 mm) was drilled after rats were positioned in a stereotaxic frame. Aliquots of 200  $\mu$ l nonheparinized arterial blood were infused into the right caudate nucleus (coordinates: 0.2 mm posterior, 2.2 mm lateral, and 5.0 mm ventral to the bregma) at a rate of 14  $\mu$ l/min using a microinfusion pump. The burr hole was sealed with bone wax, and skin incision was closed with sutures after the needle was removed.

Rats were randomly divided into the following 3 groups: sham, ICH-IVH, and MCC950. The sham group had only a needle insertion. MCC950 group received MCC950 (10 mg/kg, IP; MCE, USA) which was dissolved in saline at 1 hour after ICH-IVH model. ICH-IVH group was given an equal volume of saline at the same time.

**2.3. Cell Culture and Treatment.** PC12 neurons cells of rats (ScienCell, USA) were used for in vitro study. PC12 cells were cultured in Dulbecco's Modified Eagle Medium (DMEM) supplemented with 10% (v/v) fetal bovine serum (FBS) and 1% penicillin/streptomycin at 37°C in a humidified atmosphere of 5% CO<sub>2</sub>. After the completion of cell processing, IL-1 $\beta$  (Novoprotein, China) was added to DMEM and diluted at a dosage of concentrations (10  $\mu$ g/l). PC12 cells were then treated with L-1 $\beta$  or Compound C for 24 h before use.

**2.4. Apoptosis Assay.** Apoptosis was detected using ANNEXIN V-FITC/PI cell apoptosis detection kit (CST, USA). PC12 cells from different groups were digested with trypsin but without EDTA, resuspended in the blinding buffer, and stained with Annexin V-FITC for 15 min and PI for 5 min. The results were analyzed by flow cytometry (Canto2, BD, USA).

**2.5. Immunofluorescence Staining.** Under deep anesthesia, rats were sacrificed by transcardial perfusion with 100 ml normal saline followed by 50 ml 4% neutral buffered paraformaldehyde. Brains were fixed in 4% neutral buffered paraformaldehyde for 24 h at 4°C followed by 25% and 30% sucrose solution until brains were dehydrated fully. Then, brains were cut into 10  $\mu$ m thick coronal sections using a cryostat (LM3050S, Leica, Germany) after being frozen at -80°C. Slides were washed with 0.01 M of PBS 3 times for 10 min and then incubated in 0.3% Triton X-100 for

30 min at room temperature. After being blocked with 5% BSA for 1 h at room temperature, the sections were incubated with primary antibody at 4°C overnight as follows: anti-CD31 (1:200; Abcam, USA), anti-ZO-1 (1:200; Abcam, USA), anti-Caspase1 (1:200; NOVUS; USA), anti-IL1beta (1:400; GeneTex, USA), anti-Iba1 (1:200; Genetex, USA), anti-CD68 (1:200; Abcam, USA), anti-NLRP3 (1:200; Abcam, USA), anti-Atg5 (1:100; ZEN-BIO; China), anti-p62 (1:100; ZEN-BIO; China), and anti-NeuN (1:200; Abcam, USA). Then, the sections were washed with 0.01 M PBS and incubated with appropriate fluorescence-conjugated secondary antibodies (1:400; Invitrogen, USA) for 2 h at room temperature. The slides were observed and photographed under a fluorescence microscope (LSM880; ZEISS, Germany).

**2.6. Western Blotting.** The subventricular zone (SVZ) tissue was separated and homogenized to collect the protein samples at 3 days after hemorrhage. Equal amounts of protein samples (20 µg) were loaded on SDS-PAGE gels, electrophoresed, and transferred onto a polyvinylidene difluoride membrane. The membrane was blocked and incubated overnight at 4°C with the following primary antibodies: anti-ZO-1 (1:1000; Abcam, USA), anti-NLRP3 (1:1000; Abcam, USA), anti-Caspase1 (1:1000; NOVUS, USA), anti-IL1beta (1:1000; GeneTex, USA), anti-Atg5 (1:1000; ZEN-BIO, China), anti-LC3B (1:1000; ZEN-BIO, China), anti-p62 (1:1000; ZEN-BIO, China), anti-pAMPK (1:1000; CST, USA), anti-AMPK (1:1000; CST, USA), anti-ULK1 (1:1000; CST, USA), anti-Beclin-1 (1:1000; CST, USA), and anti-β-actin (1:1000; CST, USA). Appropriate secondary antibodies (1:3000, CST; 1:5000, abcam) were selected to incubate with the membrane for 1 h at room temperature. The bands were probed with an ECL Plus chemiluminescence reagent kit (ThermoFisher, USA) and visualized with the image system (Bio-Rad, USA). Relative density of the protein immunoblot images was analyzed by Image J software (NIH, USA).

**2.7. Transmission Electron Microscope.** Electron microscopy was performed as previously described [26]. Rats were anaesthetised and subjected to intracardiac perfusion with 4% paraformaldehyde and 2.5% glutaraldehyde in 0.1 mol/l Sorensen's buffer (pH 7.4). The subventricular zones were removed from the brain, and a 1 mm thick coronal tissue slice was cut with a blade 4 mm overnight at 4°C. Samples were then postfixed with 1.0% OsO<sub>4</sub> and dehydrated in graded ethyl alcohol. After dehydration was complete, the samples were infiltrated with propylene oxide, embedded in Epon resin and sectioned. Ultrathin sections were then stained with uranyl acetate and Reynold's lead citrate. Sections were evaluated using a Philips CM 100 transmission electron microscope (Hillsboro, OR, USA) and were digitally acquired using a Hamamatsu ORCA-HR camera (Hamamatsu City, Shizuoka, Japan).

**2.8. MRI and Edema Volume Analysis.** Rats were anesthesia with 2% isoflurane/air mixture throughout MRI examination. The MRI scans were performed using a 7.0-T Varian

MR scanner (Bruker, USA) with a T2\*gradient-echo sequence and a T2 fasts spin-echo sequence using a view field of 35 mm \* 35 mm with 20 coronal slices (1.0 mm thickness). Volumes were calculated as previously described. The edema areas were outlined, and the areas of all slices were multiplied by the section thickness [27]. All image analyses were performed using Image J (National Institutes of Health, Bethesda, Maryland, USA) by two observers in a blinded manner.

**2.9. Brain Water Content Assessment.** Brain water content was measured on day 3 after ICH-IVH, as previously described [28]. Briefly, without perfusion, the subventricular zones on both sides and cerebellum were removed. Brain tissues were weighted to measure wet weights and then dried for 24 h at 100°C to obtain dry weights. The following formula was used to calculate brain water content: (wet weight – dry weight)/wet weight × 100%.

**2.10. TUNEL Staining.** On day 3 after ICH-IVH, the brains were sampled for TUNEL staining using Apoptosis Detection Kit (Roche, USA) according to the manufacturer's instructions. The number of TUNEL-positive cells in the SVZ was counted using Image J software (NIH, USA). Six sections per brain were used for counting. Data were expressed as the number of TUNEL-positive neurons cells/mm<sup>2</sup> in SVZ.

**2.11. Fluoro-Jade C Staining.** Neuronal degeneration was evaluated by Fluoro-Jade C (FJC) staining as previously reported [29]. The FJC Ready-to-Dilute Staining Kit (Biosensis Inc., Thebarton, SA, Australia) was used. Six continuous pictures of SVZ were photographed under a fluorescence microscope, and the average number of FJC-positive cells was calculated as cells/mm<sup>2</sup> by Image J software.

**2.12. Cell Counting.** Cell counting was performed on brain coronal sections. Three high-power images (×40 magnification) were taken in SVZ using a digital camera. Interested positive cells were counted from 4 areas in each brain section by two researchers in a blinded manner.

### 2.13. Neurofunction Assessment

**2.13.1. Corner Test.** On days 3, 7, and 14 after ICH-IVH, the corner turn was used to evaluate the motor and balance functions of animals as previously described [30]. In the corner turn test, each rat was allowed to proceed into a corner (the angle of 30°) for 10 times with at least 30 s intervals between every trial. The rats need to turn to right or left, and the percentage of right turns was calculated to assess the neurofunction.

**2.13.2. Open Field Test.** Anxiety, exploratory activity, and motor function were examined in the open field test. The testing apparatus was a 100 × 100 cm square with lateral walls. A video camera suspended above recorded spontaneous motor activity over 5 min trials. Rats ( $n = 8$  per group) were placed in the center of the area, and both total distances travelled and time spent in the center were recorded.

**2.13.3. Morris Water Maze Task.** Water maze tasks were performed as described previously [31]. Briefly, rats ( $n = 8$  per group) received four trials on five consecutive training days and then received a single 60 s probe trial on day 6. The latency to reach the platform during training days, the times crossing the target area (former platform position), and the time spent in the target quadrant during the probe trial were recorded.

**2.14. H&E Staining.** Rats were transcardially perfused with 0.9% sodium chloride and 4% paraformaldehyde at 3 days after ICH-IVH. The brain was dissected out after perfusion and paraffin-embedded followed by sectioning. H&E staining was performed as previously described [32].

**2.15. Quantitative RNA Sequencing.** Rats were euthanized on day 3 after ICH-IVH. RNA-Seq experiments were performed according to manufacturer's protocol, and data were analyzed by LC Biotech. Briefly, total RNA was extracted from the SVZ tissue using TRIzol reagent, and the quantified and purified total RNA were used to reverse-transcribed to generate cDNAs, which were used to synthesize U-labeled second-stranded DNAs. The ligated products were amplified with PCR, and the average inset size for the final cDNA library was 300 bp (50 bp). The expression levels of all transcripts were evaluated by calculating the fragments per kilobase per million reads. The threshold of significantly differential expression was set to  $P < 0.05$  and  $|\log_2(\text{fold change})| \geq 1$ . The Gene Orthology (GO) and Kyoto Encyclopedia of Genes and Genomes (KEGG) databases were used to explore the biological pathways.

**2.16. Statistical Analysis.** All data were presented as mean  $\pm$  SD. Data were analyzed by investigators blinded to experimental treatments. All analyses were performed using GraphPad Prism 8 (GraphPad software). We determined each sample size by power analysis using a significance level of  $\alpha = 0.05$  with 80% power to detect statistical differences. Statistical evaluation of the data was performed by analysis of variance (ANOVA), followed by Tukey multiple-comparison post hoc analysis. Statistical significance was defined as  $P < 0.05$ .

### 3. Results

**3.1. NLRP3 Inhibition Attenuates Neurofunction Deficits, Especially Cognitive Dysfunction after ICH-IVH.** According to previous studies, based on autologous blood ICH-IVH rats, we had found ICH-IVH rats showed severe motor function disorder [25]. Here, we aimed to assess cognitive dysfunction in ICH-IVH rats. To determine whether the NLRP3 inflammasome inhibitor, MCC950, affects cognitive function in ICH-IVH rats receiving MCC950 or not, we hypothesized that NLRP3 inhibition after ICH-IVH would improve cognitive function. Cognitive function was evaluated by the open-field test and the Morris test at day 3 after ICH-IVH. Compared with the sham group, we found the ICH-IVH rats had significant cognitive dysfunction and decreased exercise activity according to the open-field test results, and MCC950 treatment reduced cognitive and

motor dysfunction after hemorrhage (Figure 1(b)). As for the motor dysfunction, the corner test results showed that inhibition NLRP3 improved motor deficits after ICH-IVH (Figure 1(g)). Next, the water maze test was used to evaluate cognitive function furthermore, a classical method to assess cognitive function showed the same results as the open-field test (Figure 1(c)). There were no group differences during the training phase to find a hidden platform (Figure 1(e)). However, in the probe trial for spatial memory in which the hidden platform was removed, administration of MCC950 significantly increased the number of former platform crossings among ICH-IVH rats, and the number of former platform crossing was significantly greater among the sham group than the ICH-IVH group (Figure 1(d)). Similarly, the ICH-IVH rats with MCC950 treatment increased target quadrant time compared with the ICH-IVH group (Figure 1(f)). Collectively, these findings suggest that MCC950 administration could improve NLRP3 inflammasome-dependent neurodysfunction after ICH-IVH, especially spatial memory deficit.

**3.2. Inhibiting NLRP3 Inflammasome Decreased Subependymal Edema after ICH-IVH.** Hydrocephalus patients which had subependymal edema indicate a lousy outcome. We detected edema in subventricular zones at 3 days after ICH-IVH and MCC950 administration. According to T2 magnetic resonance imaging scans (MRIs) and pseudocolor images depending on grayscale value, we found the ICH-IVH group occurred prominent edema in SVZ. Interesting, MCC950 treatment reduced SVZ edema after ICH-IVH (Figure 2(a)). Combined with the MRIs images, we measured the edema volumes and found that inhibition NLRP3 with MCC950 decreased edema volumes after ICH-IVH at 3 days (Figure 2(c)). We also measured brain water content in different brain zones, and we found the MCC950 treatment group had lower edema than the ICH-IVH group of the subventricular zones (Figure 2(b)). Although the subventricular zones effusion had been found in many aspects, where is the source of additional water still not been explained clearly. The classical explanation of edema contained vasogenic, cellular, and osmotic brain edema [7]. Combined with HE-staining results, we found obviously interstitial edema and cellular edema after ICH-IVH. MCC950 administration reduced both two kinds of brain edema. Interestingly, the edema around capillaries was observed, and a mass of capillaries closed after ICH-IVH in SVZ. The capillaries reopened and the around edema reduced after inhibiting NLRP3 inflammasome (Figure 2(d) upper). Furthermore, observing capillaries using TEM in SVZ, we found the changes of edema around capillaries and the openness of capillaries are the same as the HE-staining results (Figure 2(d) lower). According to HE-staining and TEM results, we speculated that the edema belongs to nonangiogenic edema. To further prove this conclusion, we assessed tight junction-related protein ZO-1 of capillaries (CD31) in SVZ and found there is no difference of ZO-1 expression level among the sham group, the ICH-IVH group, and the ICH-IVH + MCC950 group (Figures 2(e) and 2

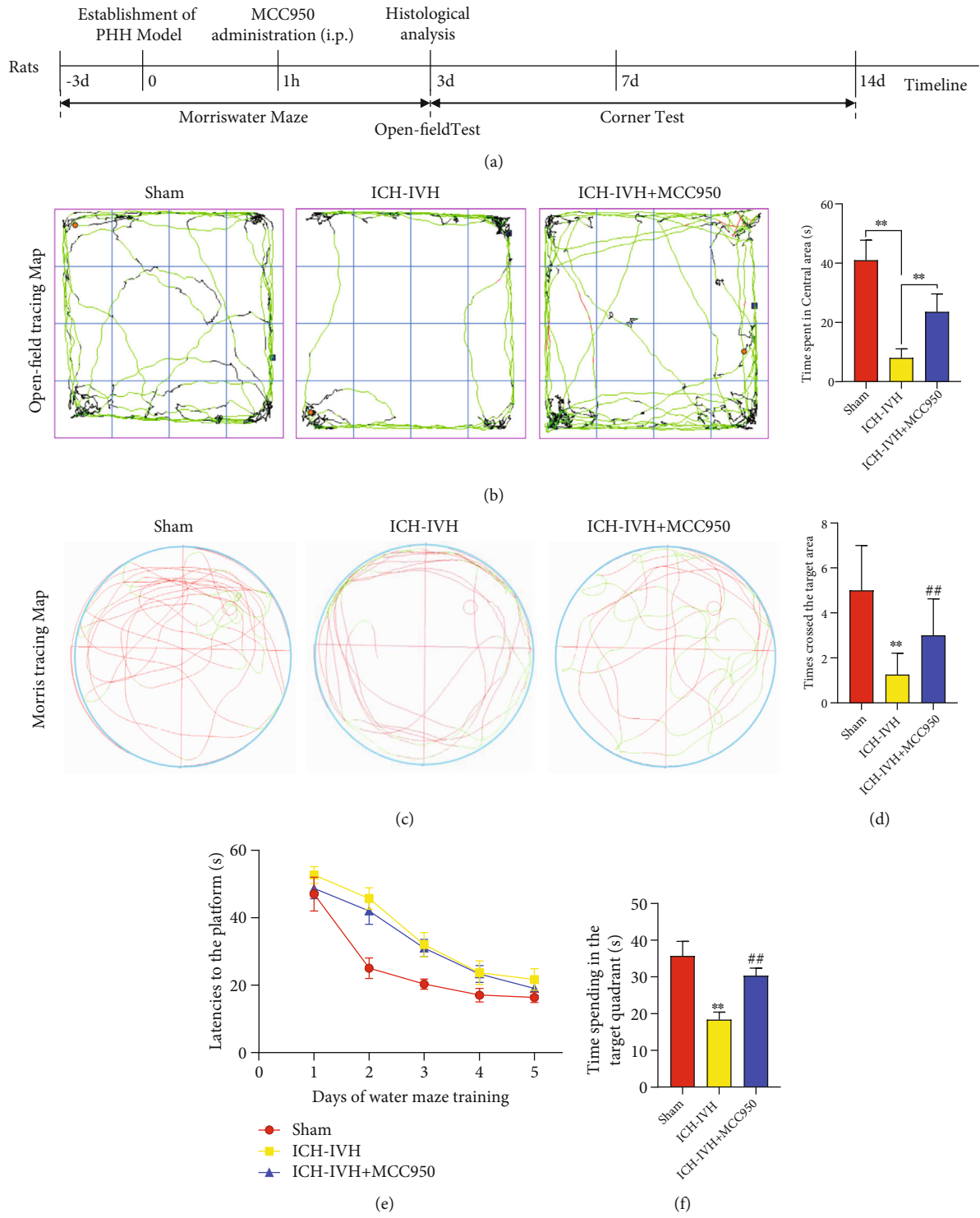


FIGURE 1: Continued.

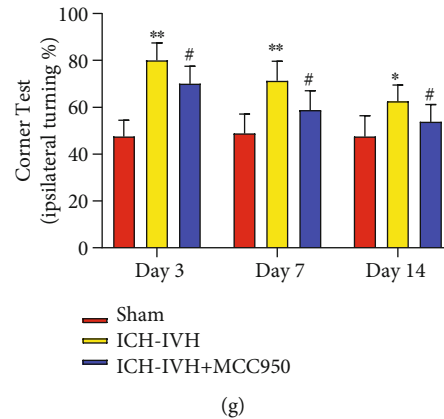


FIGURE 1: Spatial and recognition memory and spontaneous motor behavior assessment after ICH-IVH and inhibiting NLRP3 inflammasome with MCC950. (a) Schematic diagram of the experimental design. (b) Representative movement tracks and recognition memory in the sham and MCC950 treatment or not groups at 3 days after ICH-IVH. (c) Representative swim paths during the probe trial for spatial memory showing that ICH-IVH rats with MCC950 treatment made more crossings over the former platform location and spent more swim time in the target quadrant than ICH-IVH rats, indicating spatial memory impairment improved. (d) Comparison of times crossing the former target area of different groups. (e) Comparison of latency to the platform during the 5 days of Morris water maze training. (f) Comparison of time spent in the target quadrant in the probe trial. (g) Corner tests aimed at the motor function after ICH-IVH and MCC950 treatment. ( $n = 8/\text{group}$ ). Results are presented as mean  $\pm$  SD, \*\* $P < 0.01$  and \* $P < 0.05$  versus sham group, \*\* $P < 0.01$  and # $P < 0.05$  ICH-IVH group versus MCC950 group.

(f). Totally, the edema that occurred after hydrocephalus was nonangiogenic edema, and inhibition of NLRP3 reduced edema in SVZ.

**3.3. MCC950 Inhibits Microglia/Macrophage-Derived NLRP3 Inflammasome Activation in SVZ.** Inflammation response was activated in many kinds of diseases, leading to tissue damage and edema, especially in the acute phase. Combined with previous parts results that inhibition of NLRP3 could reduce interstitial and cellular edema, next we investigated the specific mechanism of NLRP3 inflammasome-mediated edema in SVZ. Microglia/macrophages are the main immunity and inflammation cells that react to injury or infection in the brain. The effect of MCC950 on NLRP3 inflammasome activation and IL-1 $\beta$  production was examined in subventricular zones tissues of ICH-IVH rats (Figure 3(a)). At 3 days after ICH-IVH, we found IL-1 $\beta$  and Caspase-1 positive cells increased in SVZ, and MCC950 treated decreased the number of IL-1 $\beta$ (+) and Caspase-1(+) cells (Figure 3(b)). These indicated NLRP3-related inflammation activated in SVZ after ICH-IVH. Next, we examined the NLRP3 inflammasome expressed in which kind of cells and found NLRP3 located in microglia/macrophages after ICH-IVH. Compared with the ICH-IVH group, MCC950 treatment obviously decreased NLRP3 positive microglia/macrophages in SVZ (Figures 3(c) and 3(d)). To quantitative analysis of the expression of NLRP3 and related cytokines: IL-1 $\beta$ , Caspase-1, and Western blots results showed that MCC950 treatment decreased NLRP3 inflammasome and related cytokines expression after ICH-IVH in SVZ (Figure 3(e)). We indicated that NLRP3 inflammasome activated in microglia/macrophages and released cytokines might be a reason that resulted in brain edema after ICH-IVH in SVZ.

**3.4. NLRP3 Inhibition Prevents Neurons Excessive Autophagy-Mediated Apoptosis after ICH-IVH in SVZ.** Subependymal edema could be improved by inhibiting NLRP3 activated in microglia/macrophages. But how the microglia/macrophage-derived edema contributed to cognitive dysfunction after ICH-IVH still needs investigation. Hence, we assessed the status of neurons in SVZ. Under normal physiological conditions, autophagy was activated at a low level to regulate cell homeostasis. After the external stimulus, autophagy is upregulated or downregulated to defence against avoiding self-injury. However, excessive autophagy out-balance led to neurons injury. We examined neurons autophagy level in SVZ and found autophagy upregulated after ICH-IVH, and administration of MCC950 reduced autophagy level in neurons. The autophagy-related proteins LC3B, Atg5 (LC3B and Atg5 indicate autophagosome formation), and p62 (p62 indicates autophagosome degradation) were detected. The images of Atg5(+) and p62(+) neurons demonstrated autophagy upregulated in neurons after ICH-IVH, and inhibited NLRP3 downregulated autophagy level of neurons (Figure 4(a)). The Western blot results examined Atg5 LC3B, and p62 expression showed the same conclusion (Figure 4(b)). Then, we evaluated the relationship between autophagy level and neuron states after ICH-IVH and MCC950 treatment; the FJC-staining and TUNEL-staining of neurons were used in this process. According to images and positive cell counting results, we found a mass of neurons dysfunction after ICH-IVH and inhibition of NLRP3 reduced FJC(+) cells and TUNEL(+) neurons in SVZ (Figures 4(c) and 4(d)). Then, we used TEM to observe neuron structure in SVZ and found neurons edema and apoptosis after ICH-IVH. After MCC950 administration, the neurons state ameliorated, and the edema also reduced (Figure 4(e)). Based on these results, we proved that

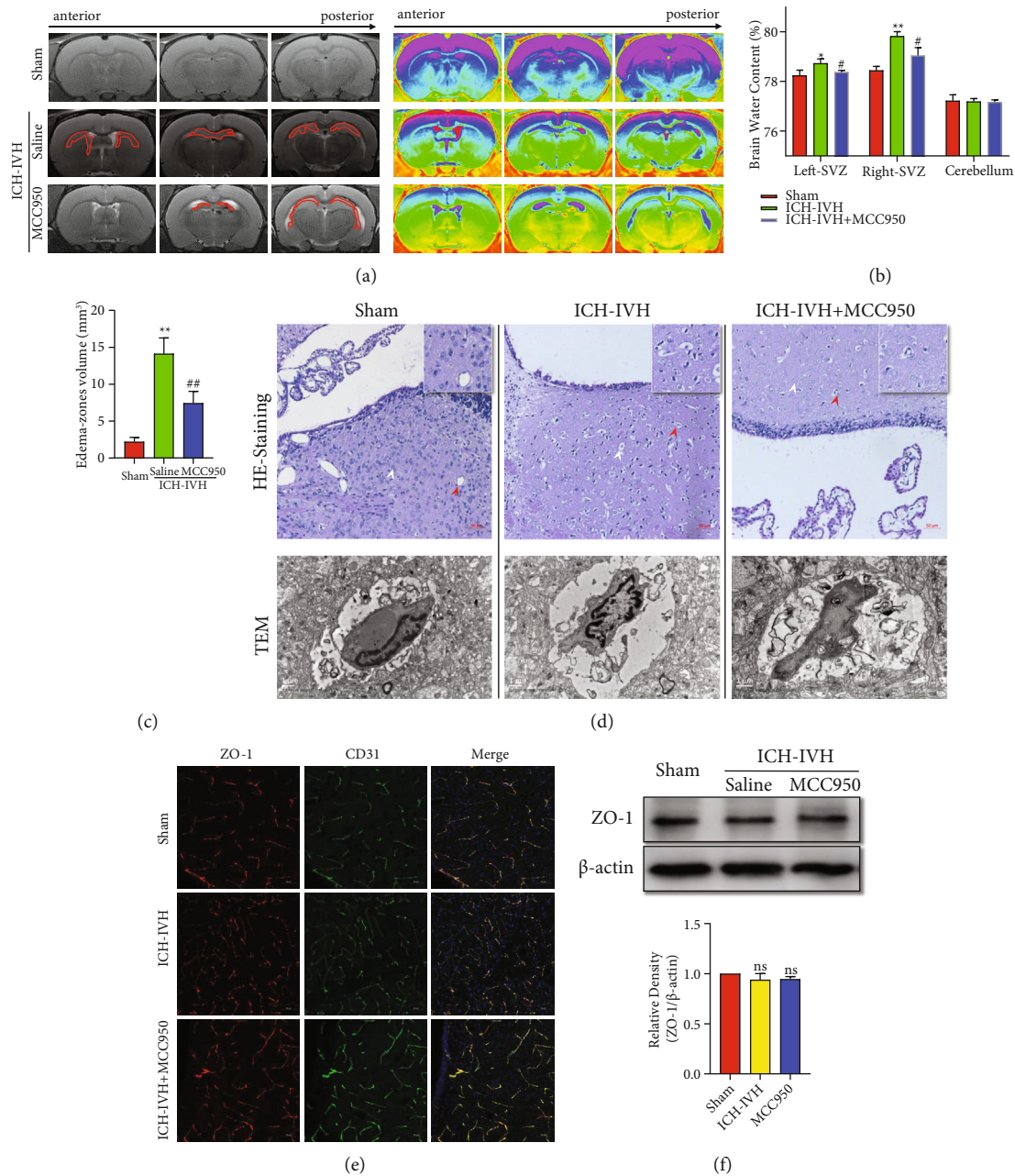
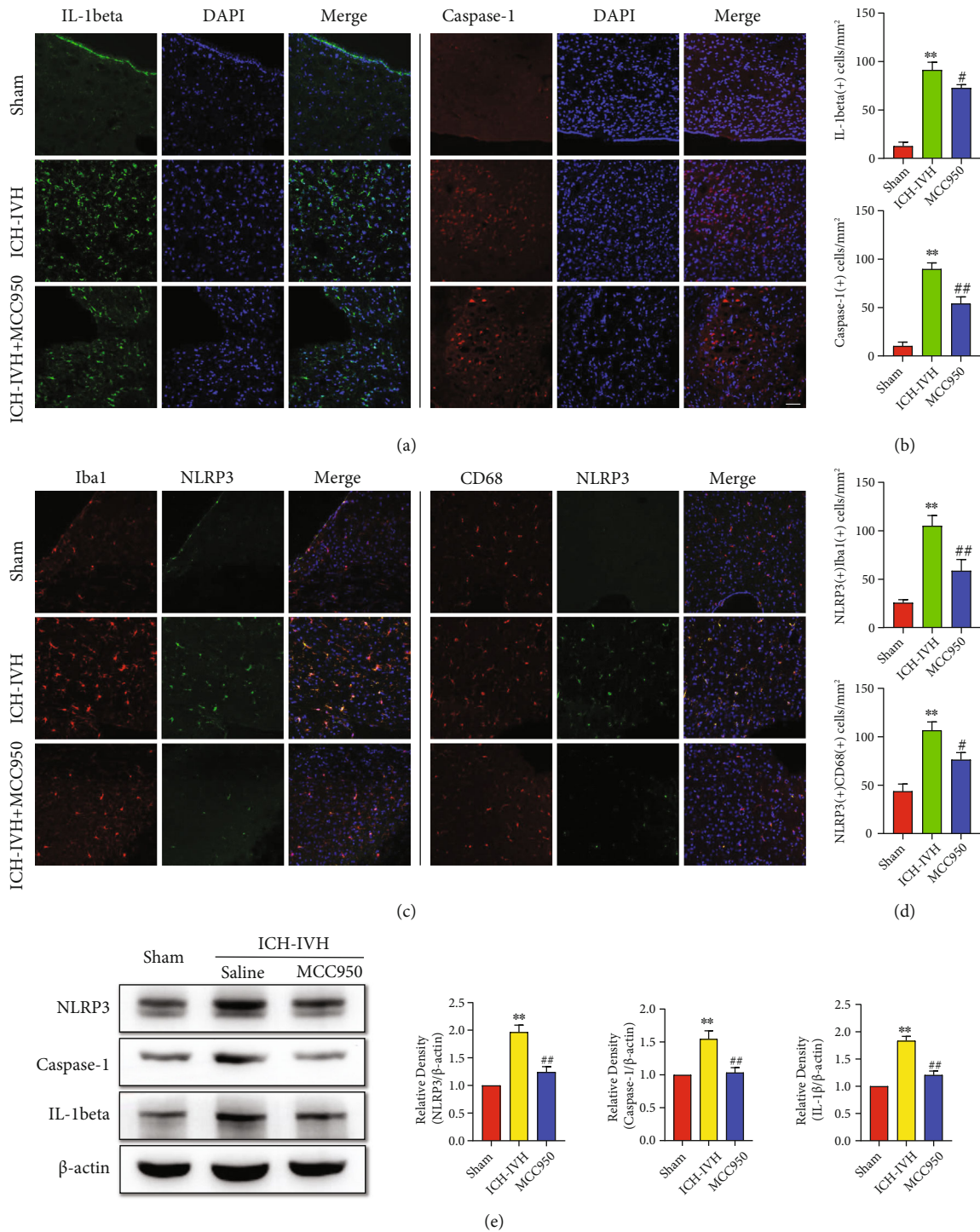


FIGURE 2: Subependymal edema assessment after ICH-IVH mediated hydrocephalus and MCC950 treatment. (a) Representative images of T2-weighted and pseudocolor showed subependymal edema at 3 days in different groups. (b) The brain water content of different parts of brain after various treatments. (c) Quantification analysis of volumes of brain edema of subventricular zones according to MRI images. (d) HE-staining images of subventricular zones tissues showed edema and capillaries conditions (upper). Bar = 50 μm. TEM images of capillaries of all 3 groups (lower). Bar = 1 μm. (e) Representative images of ZO-1 expressed in capillaries (CD31). Bar = 50 μm. (f) Western blots images and analysis results showed the ZO-1 expression of different groups in SVZ. Results are presented as mean ± SD, ns  $P > 0.05$ , \*\* $P < 0.01$  and \* $P < 0.05$  versus sham group, ## $P < 0.01$  and # $P < 0.05$  ICH-IVH group versus MCC950 group.

inhibiting NLRP3 inflammasome expression in microglia/macrophages could reduce brain edema and downregulate neurons autophagy to protect neurological function in SVZ.

**3.5. NLRP3 Upregulated Neuron Autophagy through the AMPK/Beclin-1 Pathway Combined with Transcriptomics.** To explore the molecular mechanism between NLRP3 inflammasome and neurons autophagy, subventricular zone tissues from the sham group, the ICH-IVH group, and the

ICH-IVH + MCC950 group were obtained for transcriptomics. Compared with the sham group, 565 gene expression obviously changed after ICH-IVH (518 genes upregulated, 47 genes downregulated) (Figure 5(a)). Heatmap of different expression genes after ICH-IVH contained NLRP3, autophagy, and apoptosis-related genes (Figure 5(b)). According to GO enrichment, we found the inflammatory response and innate immune response had noticeable changes (Figure S1A). Focusing on KEGG pathway enrichment, the



**FIGURE 3:** NLRP3 inflammasome and related cytokine expression of microglia/macrophages after ICH-IVH and MCC950 treatment in SVZ. (a) Representative images of IL-1beta and Caspase-1 positive cells in SVZ. Bar = 50  $\mu$ m. (b) Statistical results of IL-1beta and Caspase-1 positive cells in SVZ. (c) Photos of double immunofluorescence staining of NLRP3 expressed at Iba1 and CD68 positive cells in SVZ. Bar = 50  $\mu$ m. (d) Counting results of NLRP3-positive microglia/macrophages in SVZ. (e) Western blots images and analysis results showed the expression of NLRP3, Caspase-1, and IL-1beta with MCC950 treatment or not at 3 days after ICH-IVH. Results are presented as mean  $\pm$  SD, \*\* $P < 0.01$  versus sham group, ## $P < 0.01$  and # $P < 0.05$  ICH-IVH group versus MCC950 group.

phagosome pathway changed drastically (36 genes expression changed in this pathway) (Figure S1B). Compared with the ICH-IVH group, the MCC950 treatment group had 167 gene expression changed

(Figure 5(a)). The heatmap of different expression genes after MCC950 treatment was used to select obviously related genes, which contained possible pathways that NLRP3 inflammasome mediated neuron autophagy



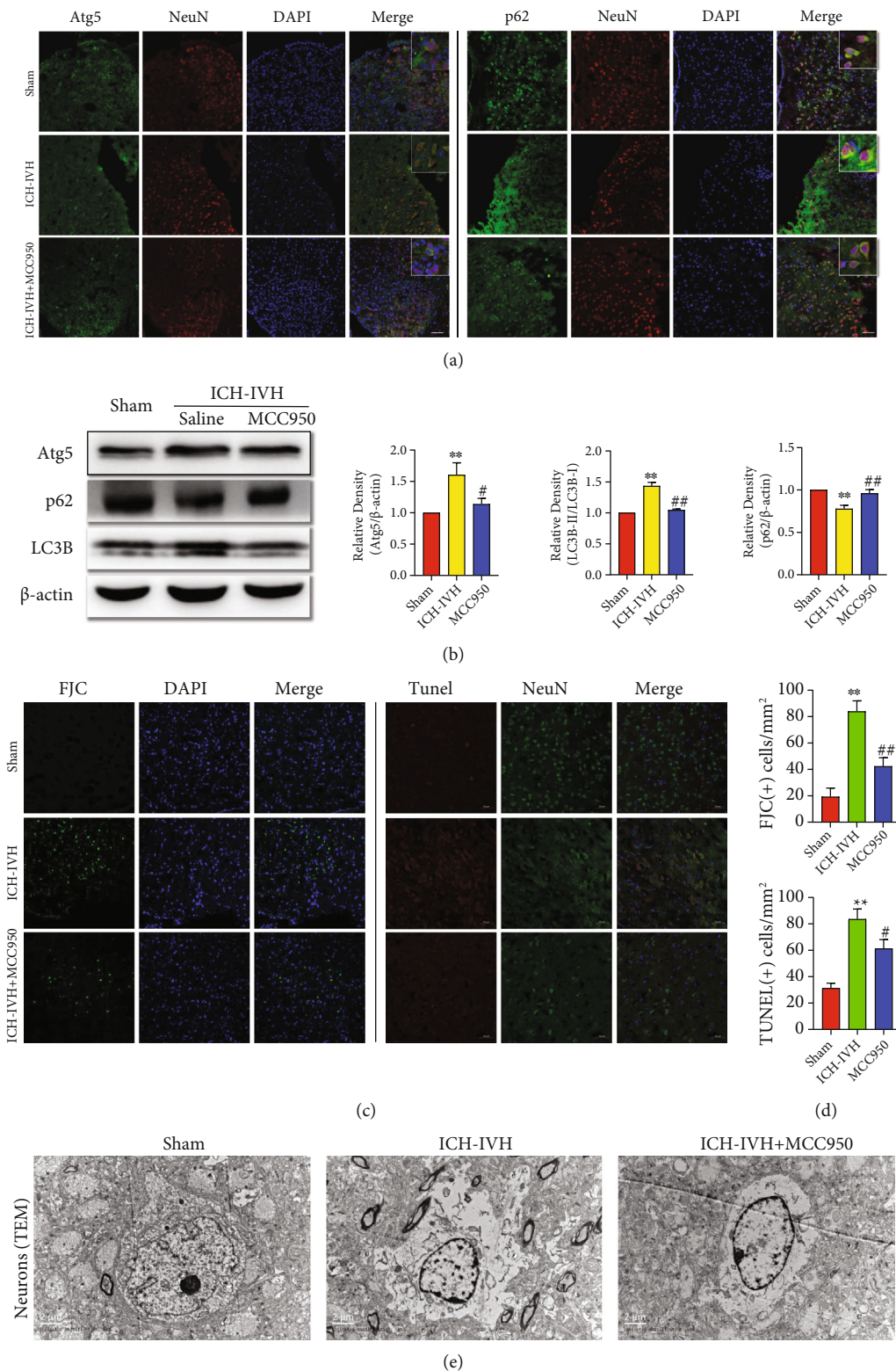


FIGURE 4: Autophagy flux changes mediated neurons degenerated and apoptosis after ICH-IVH and MCC950 treatment in SVZ. (a) Representative immunofluorescence staining images of Atg5 and p62 positive neurons in SVZ. Bar = 50  $\mu$ m. (b) Western blots images and analysis results showed the expression of autophagy proteins, Atg5, LC3B, and p62, in the SVZ of ICH-IVH rats receiving MCC950 or saline. (c, d) Images of FJC-staining and TUNEL-staining of neurons in SVZ after ICH-IVH and MCC950 treatment (c), analysis results of FJC(+) and TUNEL(+) neurons (d). Bar = 50  $\mu$ m. (e) TEM images of neurons located in SVZ showed microstructure and edema. Bar = 2  $\mu$ m. Results are presented as mean  $\pm$  SD, \*\* $P$  < 0.01 versus sham group, ## $P$  < 0.01 and # $P$  < 0.05 ICH-IVH group versus MCC950 group.

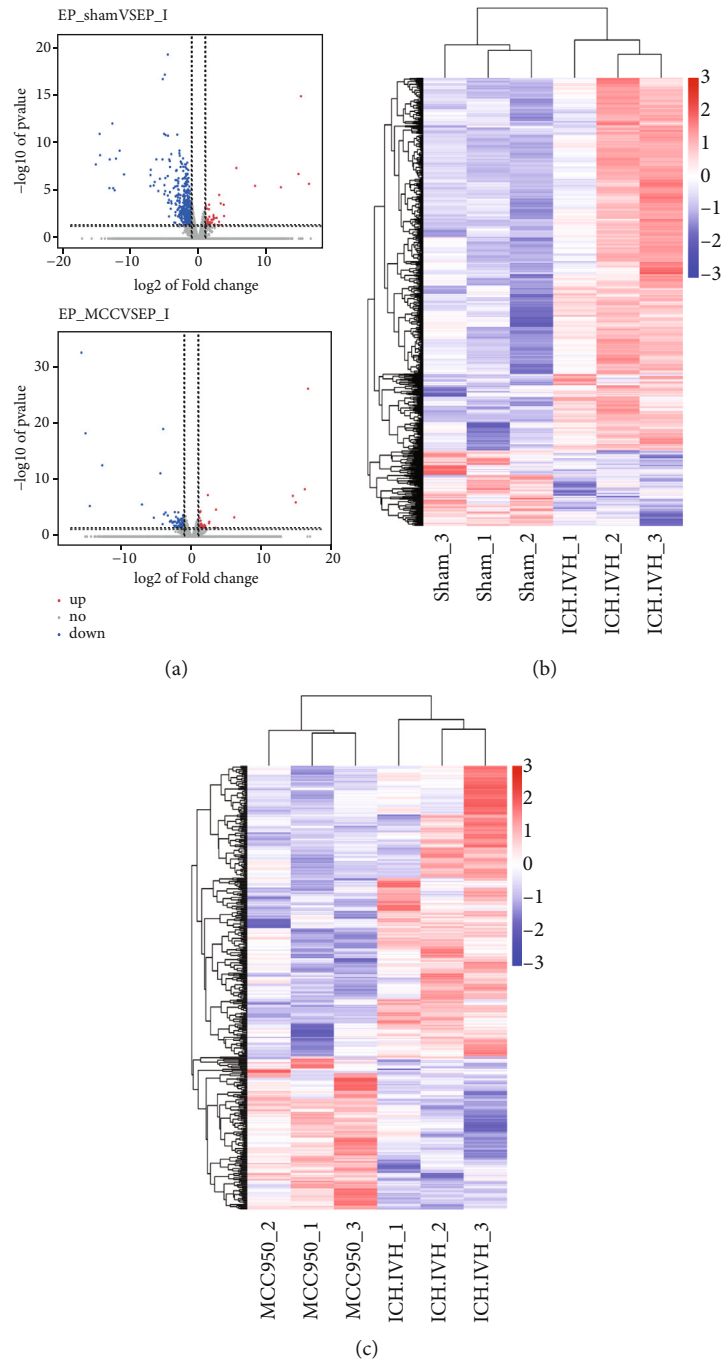


FIGURE 5: Continued.

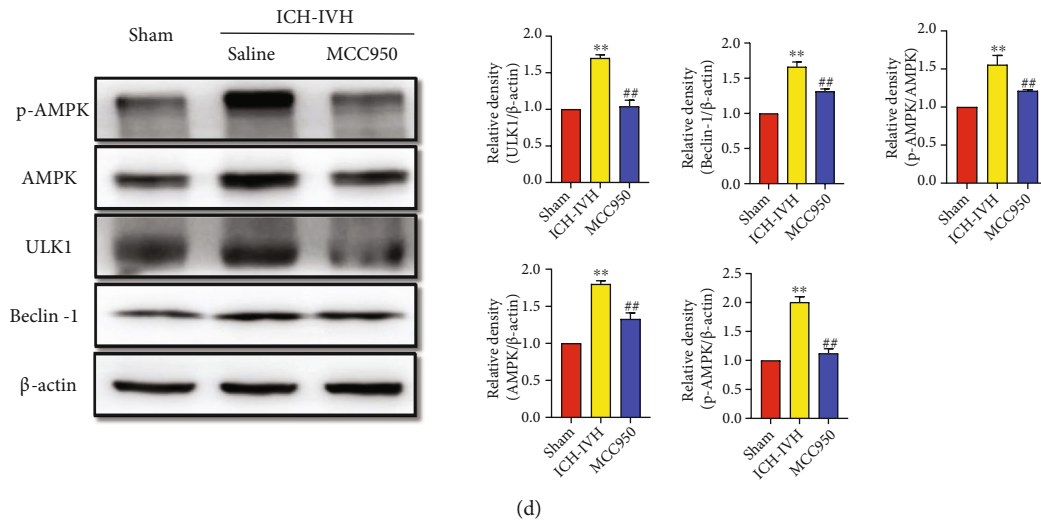


FIGURE 5: Transcriptional analysis of SVZ tissues identified AMPK/ULK1/Beclin-1 as a potential pathway of the microglia/macrophage-derived NLRP3 inflammasome and neuron excessive autophagy-mediated apoptosis after ICH-IVH. (a) Volcano plot showed differentially expressed genes in SVZ on day 3 after ICH-IVH and MCC950 treatment. (b) Heatmap of the significantly different expression genes identified by PCA for each sample between the sham group and the ICH-IVH group. (c) Heatmap showed obviously different expression genes with MCC950 treatment or not after ICH-IVH. Data were clustered hierarchically in GENE-E and colored according to row minimum and maximum. (d) Representative Western blots images of AMPK/ULK1/Beclin-1 pathway and quantitative analyses results. Data were represented as mean  $\pm$  SD, \*\* $P < 0.01$  versus sham group, ## $P < 0.01$  ICH-IVH group versus MCC950 group.

through (Figure 5(c)). Combined with the GO enrichment pathway and KEGG enrichment pathway, the AMPK/Beclin-1 pathway was selected to explore further (Figure S1C and Figure S1D). In order to verify the transcriptomics results, Western blots were used to quantitatively analyze the expression of AMPK/Beclin-1 pathway-related protein. After ICH-IVH, the expression of AMPK, p-AMPK, ULK1, and Beclin-1 was increased. What is more, p-AMPK/AMPK was also increased. Inhibiting NLRP3 inflammasome by MCC950 downregulated the expression of essential proteins in the AMPK/Beclin-1 pathway (Figure 5(d)). Based on the above results, we speculated that the NLRP3 inflammasome might mediate neuron apoptosis through the AMPK/Beclin-1 pathway, and the AMPK/Beclin-1 pathway also could regulate autophagy. In addition, the transcriptome sequencing results also supported our previous conclusion.

**3.6. IL-1beta Accelerated to Neurons Excessive Autophagy and Apoptosis in PC12 Cells.** As reported that IL-1beta which could be secreted to extracellular from microglia/macrophages was the major cytokine after NLRP3 was activated [33]. PC12 cell was a kind of neuron line which was widely used in vitro experiments. Here, IL-1beta was used to stimulate PC12 cells to investigate our previously proved conclusion in vivo. Compound C is a kind of autophagy inhibitor that plays function by the AMPK/Beclin-1 pathway. First, IL-1beta with a dosage of  $10 \mu\text{g/l}$  was used to stimulate PC12 cells, and we found more Atg5 and fewer p62 positive neurons compared with the PBS-treated group. Next, Atg5 and p62 positive neurons showed an opposite change trend after compound C was added to inhibit autophagy (Figure 6(a)). In addition, the expression of LC3B and p62 which indicated the different processes of autophagy were

measured with Western blots. The quantitative of autophagy proteins showed the same results as before (Figure 6(c)). Whether as the vivo experiment results that excessive autophagy-mediated neurons apoptosis, we used different ways to assess neurons function after different treatments. IL-1beta treatment mediated more neurons apoptosis compared with the PBS treated group both in TUNEL-staining and flow cytometry. When inhibiting autophagy with compound C, the percentage of apoptosis neurons decreased after IL-1beta treatment (Figures 6(b) and 6(d)). The vitro experiment results also supported our vivo experiment with that excessive autophagy-mediated neurons apoptosis.

#### 4. Discussion

In this study, we found that activation of NLRP3 in microglia/macrophages contributes to subependymal edema formation and cognitive dysfunction after ICH-IVH, and the edema was nonvascular origin. NLRP3 inflammasome aggravated neuron apoptosis by upregulating autophagy through the AMPK/Beclin-1 pathway in SVZ after ICH-IVH (Figure 7; this image is plotted by Biorender). Besides, IL-1beta whose secretion was mainly promoted by NLRP3 activation mediated autophagy-induced PC12 cells apoptosis. This study provides compelling evidence that NLRP3 activation mediated edema formation and neuron apoptosis in SVZ played a pivotal role in the pathogenesis of PHH.

After ICH, resident glial cells were activated and circulating immune cells were recruited to participate in the occurrence and development of neuroinflammation [34–36]. Microglia was the resident immune cell distributed in brain that could be rapidly activated to mediate neuroinflammation in response to pathological conditions, including hypoxia, infection, and brain tissue injury [37]. Besides

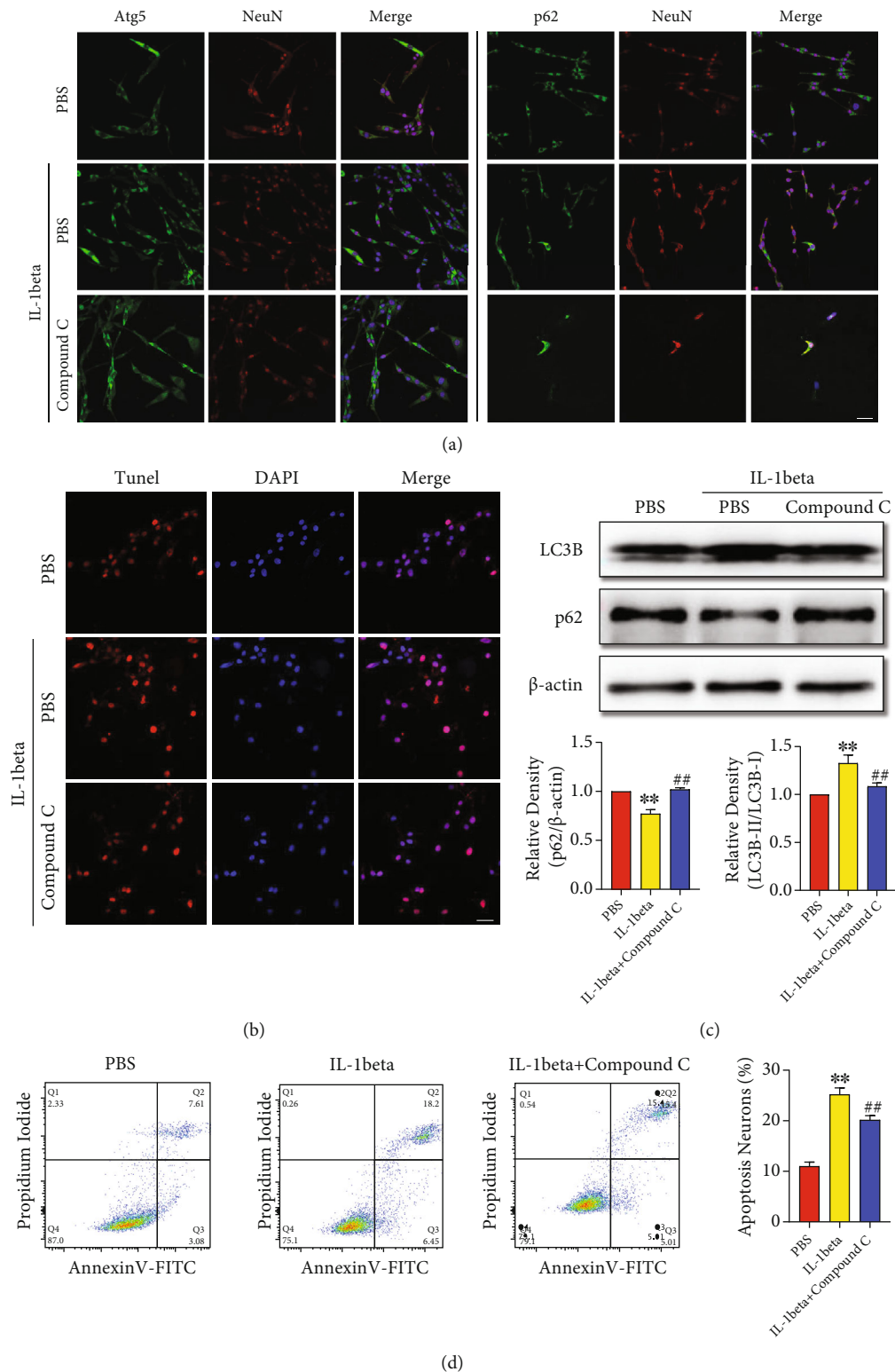


FIGURE 6: IL-1 $\beta$  upregulated neurons autophagy and apoptosis, and inhibiting autophagy could reduce neurons apoptosis mediated by IL-1 $\beta$  which was released after NLRP3 activated. (a) Representative immunofluorescence staining images of Atg5- and p62-positive PC12 cells. Bar = 50  $\mu$ m. (b) Immunofluorescence TUNEL-staining images of PC12 cells, and statistic result of TUNEL(+) cells after different treatments. Bar = 50  $\mu$ m. (c) Representative Western blot images of LC3B and p62 expressions in PC12 cells, and statistic results of LC3B-II:LC3B-I ratio and p62 after IL-1 $\beta$  and compound C treated. (d) Representative images and statistic results of flow cytometry showed early/late apoptotic cells after IL-1 $\beta$  and compound C treated. \*\* $P < 0.01$  versus sham group, ## $P < 0.01$  IL-1 $\beta$  group versus IL-1 $\beta$  + compound C group.

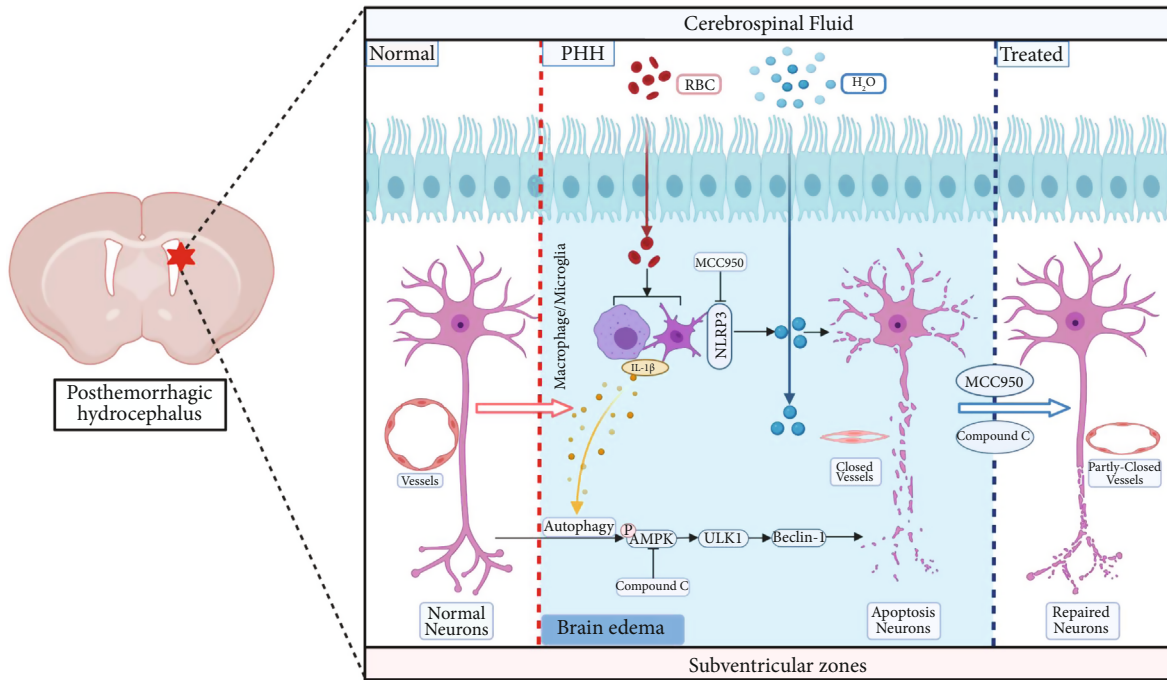


FIGURE 7: Schematic mechanism of NLRP3 activation in microglia/macrophages contributes to subependymal edema and neurons apoptosis by upregulating autophagy through AMPK/ULK1/Beclin-1 pathway. After ICH-IVH, rats occurred subependymal edema which contributes to cognitive dysfunction. Next, we found NLRP3 inflammasome activation in microglia/macrophage-mediated neurons excessive autophagy, and excessive autophagy caused neuron damage through the AMPK/Beclin-1 pathway. Administration NLRP3 specific inhibitor MCC950 could reduce edema in SVZ and improve neurofunction after hydrocephalus.

directly attacking neurons, the polarized microglia could also indirectly damage the neurons by changing the micro-environment via releasing neurotoxicity factors such as IL-1beta or recruiting other neurotoxicity cells such as macrophages to amplify inflammatory response [38]. Inflammation cytokines (IL-1beta, IL-6, IL-27, and TNF- $\alpha$ ) mainly released from microglia/macrophages and neutrophils during neuroinflammation aggravated secondary injury to neurons [16, 39, 40]. Thus, inhibiting neuroinflammation might play a protective role in hydrocephalus after hemorrhage.

Nucleotide-binding oligomerization domain-like receptor containing pyrin domain 3 (NLRP3) inflammasome, the apoptosis-associated speck-like protein, has been proposed as a crucial mediator in innate immunity [41]. The activated NLRP3 could cleave pro-IL-1beta and pro-IL-18 into their mature and functional form, resulting in the activation of a subsequent inflammatory response [41, 42]. Recent studies indicated NLRP3 inflammasome could also polarize microglia and exacerbate ischemia/hemorrhage-induced brain injury [33, 43]. NLRP3 activation aggravates neuronal cell death and behavioral deficits, knockdown or downregulating NLRP3 could improve neurological functions of ICH animals [44]. In addition, cell swelling, edema and inflammation are closely related. It has been proved that edema could cause neuron dysfunction, and most of studies considered that BBB dysfunction is the main reason for brain edema [45, 46]. In this study, we found that rats showed obvious subependymal edema which was nonvascular origin, while NLRP3 was widely activated in microglia/macrophages on day 3 after ICH-IVH. In addition, we found

that using NLRP3 inhibitor MCC950 could reduce subependymal edema and improve the cognitive function of ICH-IVH rats. Therefore, we aim at neurons to explore how the NLRP3 activation in microglia/macrophages influences cognitive and motor function after hemorrhage.

As the terminally differentiated cells, neurons did not divide and replicate themselves, which was the main reason a severe brain injury was often difficult to recover [47]. Autophagy was a conserved intracellular process to degrade dysfunctional organelles and protein aggregates and played an essential role in maintaining neuronal homeostasis [47]. Much of the evidence to support this derives from studies adjusting autophagy in neurons and observing neurodegeneration, especially in AD and PD [48–50]. Normal autophagy was considered as a protective factor against neurodegeneration, infection, and brain injury disease [51]; however, autophagy dysfunction was associated with increased susceptibility of neurons to ischemic injury. It was reported that the activation of autophagy was coincide with axonal swelling of PC12 cells when nerve growth factor was deprived or cells were in excitotoxicity, suggesting a close relationship between autophagic process and neurite degeneration [52]. In addition, neurotoxin exposure induced apoptosis with a concomitant increase of autophagy flux in primary cortical neurons [53]. All evidence indicated that autophagy flux participated in neuronal injury in many kinds of CNS diseases. However, the role of autophagy after ICH remained controversial. Studies found that autophagy-related disorders promoted the occurrence of stroke in some cases [54], and autophagy exacerbated brain injury after

ICH. Autophagic cell death of neurons after ICH was confirmed by using conditional knockout *Atg7* mice [55]. Although autophagy was involved in promoting brain injury during the acute phase of ICH, studies showed that autophagy had a neuroprotective function via clearing up the accumulation of cell rubbish [56], and the antineuronal apoptosis effects were related to the enhancement of autophagy [57]. Several studies showed that ICH induced autophagy of immune cells, especially microglia/macrophages, contributing to the improvement of outcomes by regulating inflammation [58–60]. Hence, we aimed to explore the relationship between neuronal apoptosis and NLRP3-mediated autophagy in the acute phase of ICH-IVH and to prove that excessive neuronal autophagy aggravated neuronal apoptosis, which contributed to cognitive dysfunction after ICH-IVH.

NLRP3 activation in microglia/macrophages was the critical process to adjust neuronal autophagy, and according to the RNA sequencing results, we found that NLRP3 mediated neuronal autophagy through the AMPK/Beclin-1 pathway. Since NLRP3 activation could promote the release of cytokines, among which IL-1beta played the most important role among these factors [61, 62], we further explored the role of IL-1beta and found that IL-1beta was the key factor mediating excessive autophagy and neuronal apoptosis after NLRP3 activation by using PC12 cells in vitro.

Several limitations need to be mentioned in this study. First, NLRP3 plays multifunctional roles in inflammation response, and NLRP3 inflammasome is activated in many kinds of neural cells. Further research is needed to investigate the other mechanisms underlying the neuroprotective effects of NLRP3 inhibition in secondary brain injury after ICH-IVH. In addition, since NLRP3 is not only expressed on microglia/macrophages as our immunofluorescence staining showed, further study about the roles of NLRP3 on other CNS cells, such as astrocytes, is necessary. Second, we found that NLRP3 activation could adjust subependymal edema formation, but the specific mechanism NLRP3 mediated cellular, and nonangiogenic interstitial edema still needs investigation. Third, how the neuron autophagy affects neuronal function after hemorrhage and the related mechanism associated with NLRP3 should be more deeply evaluated. Recent studies and our present study have demonstrated the effectiveness of inhibiting NLRP3 expression by using MCC950 [63, 64]. However, the time window and stability of MCC950 are very limited. This study only focused on the early pathophysiological changes (3 days) in SVZ after ICH-IVH, the longer time research is needed in the further study. At the same time, the effects of NLRP3 on specific cell types require more precise gene-editing techniques, such as the use of *cre/loxP* rat to edit NLRP3 genes in specific cells.

## 5. Conclusion

An earlier version of this work has been present as preprint in Research Square [65]. The present study demonstrated that NLRP3 inflammasome activation in microglia/macrophages aggravated edema formation and neuronal apoptosis after ICH-IVH in SVZ, and neuron apoptosis was mediated

by upregulating autophagy through AMPK/Beclin-1 signaling pathway. At least in part, NLRP3-related extracellular cytokine IL-1beta contributed to this process. Therefore, inhibition NLRP3 activation may be a potential therapeutic strategy which could reduce subependymal edema to improve cognitive function in the management of hydrocephalus patients after hemorrhage.

## Abbreviations

AD:	Alzheimer disease
Atg5:	Autophagy related 5 homolog
AMPK:	Adenosine 5'-monophosphate- (AMP-) activated protein kinase
FJC:	Fluoro-jade C
Iba1:	Ionized calcium-binding adaptor molecule 1
ICH:	Intracerebral hemorrhage
ICH-IVH:	Intracerebral hemorrhage with ventricle extension
IL-1beta:	Interleukin-1beta
IL-18:	Interleukin-18
IL-6:	Interleukin-6
IL-27:	Interleukin-27
LC3B:	Microtubule-associated proteins 1A/1B light chain 3B
NLRP3:	NACHT, LRR and PYD domains-containing protein 3
p-AMPK:	Phospho-adenosine 5'-monophosphate- (AMP-) activated protein kinase
PBS:	Phosphate-buffered saline
PD:	Parkinson disease
PHH:	Posthemorrhagic hydrocephalus
p62:	Sequestosome-1
SVZ:	Subventricular zone
TNF- $\alpha$ :	Tumor necrosis factor- $\alpha$
TUNEL:	Terminal deoxynucleotidyl transferase dUTP nick end labeling
ULK1:	Serine/threonine-protein kinase ULK1
ZO-1:	Zonula occludens 1.

## Data Availability

All data generated or analyzed during this study are included in this published article. The datasets used and/or analyzed during the current study are available from the corresponding author on reasonable request.

## Conflicts of Interest

The authors declare that they have no competing interests.

## Authors' Contributions

YC and HF conceived and designed the study. ZZ, PG, SH, ZJ, TC, and XL acquired and analyzed the data. ZZ and YC drafted a substantial portion of the manuscript. All authors read and approved the present version of the manuscript to be published.

## Acknowledgments

This work was supported by the State Key Laboratory of Trauma, Burn and Combined Injury (SKLYQ202002 to Yujie Chen), National Natural Science Foundation of China (82030036 to Hua Feng), Chongqing Talent Program (4139Z2391 to Hua Feng), and Southwest Hospital (SWH2018BJKJ-05 to Yujie Chen).

## Supplementary Materials

Figure S1: GO and KEGG enrichment results according to transcriptional analysis. (a, c) GO enrichment showed different expression genes clustered into cellular function after ICH-IVH and MCC950 treatment in SVZ. (b, d) KEGG enrichment clustered different expression genes into respective pathways. (*Supplementary Materials*)

## References

- W. C. Ziai and J. R. Carhuapoma, "Intracerebral hemorrhage," *Continuum (Minneapolis, Minn)*, vol. 24, no. 6, pp. 1603–1622, 2018.
- D. F. Hanley, "Intraventricular hemorrhage: severity factor and treatment target in spontaneous intracerebral hemorrhage," *Stroke*, vol. 40, no. 4, pp. 1533–1538, 2009.
- S. A. Mayer and F. Rincon, "Treatment of intracerebral haemorrhage," *The Lancet Neurology*, vol. 4, no. 10, pp. 662–672, 2005.
- M. Stein, M. Luecke, M. Preuss, D. K. Boeker, A. Joedicke, and M. F. Oertel, "Spontaneous intracerebral hemorrhage with ventricular extension and the grading of obstructive hydrocephalus: the prediction of outcome of a special life-threatening entity," *Neurosurgery*, vol. 67, no. 5, pp. 1243–1252, 2010, discussion 1252.
- A. Pappas, I. Adams-Chapman, S. Shankaran et al., "Neurodevelopmental and behavioral outcomes in extremely premature neonates with ventriculomegaly in the absence of periventricular-intraventricular hemorrhage," *JAMA Pediatrics*, vol. 172, no. 1, pp. 32–42, 2018.
- Y. Bu, M. Chen, T. Gao, X. Wang, X. Li, and F. Gao, "Mechanisms of hydrocephalus after intraventricular haemorrhage in adults," *Stroke and Vascular Neurology*, vol. 1, no. 1, pp. 23–27, 2016.
- R. Thiex and S. E. Tsirka, "Brain edema after intracerebral hemorrhage: mechanisms, treatment options, management strategies, and operative indications," *Neurosurgical Focus*, vol. 22, no. 5, article E6, pp. 1–7, 2007.
- S. Urday, W. T. Kimberly, L. A. Beslow et al., "Targeting secondary injury in intracerebral haemorrhage–perihematomal oedema," *Nature Reviews. Neurology*, vol. 11, no. 2, pp. 111–122, 2015.
- W. C. Ziai, "Hematology and inflammatory signaling of intracerebral hemorrhage," *Stroke*, vol. 44, 6, Supplement 1, pp. S74–S78, 2013.
- T. Wang, D. Nowrangi, L. Yu et al., "Activation of dopamine D1 receptor decreased NLRP3-mediated inflammation in intracerebral hemorrhage mice," *Journal of Neuroinflammation*, vol. 15, no. 1, p. 2, 2018.
- Y. Zhou, Y. Wang, J. Wang, R. Anne Stetler, and Q. W. Yang, "Inflammation in intracerebral hemorrhage: from mechanisms to clinical translation," *Progress in Neurobiology*, vol. 115, pp. 25–44, 2014.
- Y. Pan, X. Y. Chen, Q. Y. Zhang, and L. D. Kong, "Microglial NLRP3 inflammasome activation mediates IL-1 $\beta$ -related inflammation in prefrontal cortex of depressive rats," *Brain, Behavior, and Immunity*, vol. 41, pp. 90–100, 2014.
- H. Scheiblich, A. Schlutter, D. T. Golenbock, E. Latz, P. Martinez-Martinez, and M. T. Heneka, "Activation of the NLRP3 inflammasome in microglia: the role of ceramide," *Journal of Neurochemistry*, vol. 143, no. 5, pp. 534–550, 2017.
- M. D. Cordero, M. R. Williams, and B. Ryffel, "AMP-activated protein kinase regulation of the NLRP3 inflammasome during aging," *Trends in Endocrinology and Metabolism*, vol. 29, no. 1, pp. 8–17, 2018.
- J. Li, J. Chen, H. Mo et al., "Minocycline protects against NLRP3 inflammasome-induced inflammation and P53-associated apoptosis in early brain injury after subarachnoid hemorrhage," *Molecular Neurobiology*, vol. 53, no. 4, pp. 2668–2678, 2016.
- H. Ren, Y. Kong, Z. Liu et al., "Selective NLRP3 (pyrin domain-containing protein 3) inflammasome inhibitor reduces brain injury after intracerebral hemorrhage," *Stroke*, vol. 49, no. 1, pp. 184–192, 2018.
- L. Galluzzi, J. M. Bravo-San Pedro, K. Blomgren, and G. Kroemer, "Autophagy in acute brain injury," *Nature Reviews. Neuroscience*, vol. 17, no. 8, pp. 467–484, 2016.
- M. H. Cho, K. Cho, H. J. Kang et al., "Autophagy in microglia degrades extracellular  $\beta$ -amyloid fibrils and regulates the NLRP3 inflammasome," *Autophagy*, vol. 10, no. 10, pp. 1761–1775, 2014.
- J. Houtman, K. Freitag, N. Gimber, J. Schmoranzner, F. L. Heppner, and M. Jendrach, "Beclin1-driven autophagy modulates the inflammatory response of microglia via NLRP3," *The EMBO Journal*, vol. 38, no. 4, 2019.
- T. You, Y. Cheng, J. Zhong et al., "Roflupram, a phosphodiesterase 4 inhibitor, suppresses inflammasome activation through autophagy in microglial cells," *ACS Chemical Neuroscience*, vol. 8, no. 11, pp. 2381–2392, 2017.
- Y. Qin, J. Qiu, P. Wang et al., "Impaired autophagy in microglia aggravates dopaminergic neurodegeneration by regulating NLRP3 inflammasome activation in experimental models of Parkinson's disease," *Brain, Behavior, and Immunity*, vol. 91, pp. 324–338, 2021.
- M. S. Uddin, A. Stachowiak, A. A. Mamun et al., "Autophagy and Alzheimer's disease: from molecular mechanisms to therapeutic implications," *Frontiers in Aging Neuroscience*, vol. 10, p. 04, 2018.
- N. Mizushima, B. Levine, A. M. Cuervo, and D. J. Klionsky, "Autophagy fights disease through cellular self-digestion," *Nature*, vol. 451, no. 7182, pp. 1069–1075, 2008.
- X. Zhang, M. Wei, J. Fan et al., "Ischemia-induced upregulation of autophagy precludes dysfunctional lysosomal storage and associated synaptic impairments in neurons," *Autophagy*, vol. 17, no. 6, pp. 1519–1542, 2021.
- Q. Chen, J. Zhang, J. Guo et al., "Chronic hydrocephalus and perihematomal tissue injury developed in a rat model of intracerebral hemorrhage with ventricular extension," *Translational Stroke Research*, vol. 6, no. 2, pp. 125–132, 2015.
- S. Hu, G. Xi, H. Jin, Y. He, R. F. Keep, and Y. Hua, "Thrombin-induced autophagy: a potential role in intracerebral hemorrhage," *Brain Research*, vol. 1424, pp. 60–66, 2011.

- [27] M. Okauchi, Y. Hua, R. F. Keep, L. B. Morgenstern, and G. Xi, "Effects of deferoxamine on intracerebral hemorrhage-induced brain injury in aged rats," *Stroke*, vol. 40, no. 5, pp. 1858–1863, 2009.
- [28] M. Li, Z. Li, H. Ren et al., "Colony stimulating factor 1 receptor inhibition eliminates microglia and attenuates brain injury after intracerebral hemorrhage," *Journal of Cerebral Blood Flow and Metabolism*, vol. 37, no. 7, pp. 2383–2395, 2017.
- [29] J. Mo, B. Enkhjargal, Z. D. Travis et al., "AVE 0991 attenuates oxidative stress and neuronal apoptosis via Mas/PKA/CREB/UCP-2 pathway after subarachnoid hemorrhage in rats," *Redox Biology*, vol. 20, pp. 75–86, 2019.
- [30] J. Chen, P. R. Sanberg, Y. Li et al., "Intravenous administration of human umbilical cord blood reduces behavioral deficits after stroke in rats," *Stroke*, vol. 32, no. 11, pp. 2682–2688, 2001.
- [31] R. D. Topuz, O. Gunduz, E. Tastekin, and C. H. Karadag, "Effects of hippocampal histone acetylation and HDAC inhibition on spatial learning and memory in the Morris water maze in rats," *Fundamental & Clinical Pharmacology*, vol. 34, no. 2, pp. 222–228, 2020.
- [32] J. Ning, T. Junyi, M. Chang et al., "TOM7 silencing exacerbates focal cerebral ischemia injury in rat by targeting PINK1/Beclin1-mediated autophagy," *Behavioural Brain Research*, vol. 360, pp. 113–119, 2019.
- [33] Q. Ma, S. Chen, Q. Hu, H. Feng, J. H. Zhang, and J. Tang, "NLRP3 inflammasome contributes to inflammation after intracerebral hemorrhage," *Annals of Neurology*, vol. 75, no. 2, pp. 209–219, 2014.
- [34] Y. Dong, C. Fan, W. Hu et al., "Melatonin attenuated early brain injury induced by subarachnoid hemorrhage via regulating NLRP3 inflammasome and apoptosis signaling," *Journal of Pineal Research*, vol. 60, no. 3, pp. 253–262, 2016.
- [35] K. M. W. Khey, A. Huard, and S. H. Mahmoud, "Inflammatory pathways following subarachnoid hemorrhage," *Cellular and Molecular Neurobiology*, vol. 40, no. 5, pp. 675–693, 2020.
- [36] W. Xu, T. Li, L. Gao et al., "Apelin-13/APJ system attenuates early brain injury via suppression of endoplasmic reticulum stress-associated TXNIP/NLRP3 inflammasome activation and oxidative stress in an AMPK-dependent manner after subarachnoid hemorrhage in rats," *Journal of Neuroinflammation*, vol. 16, no. 1, p. 247, 2019.
- [37] T. Gris, P. Laplante, P. Thebault et al., "Innate immunity activation in the early brain injury period following subarachnoid hemorrhage," *Journal of Neuroinflammation*, vol. 16, no. 1, p. 253, 2019.
- [38] X. Wang, G. Sun, T. Feng et al., "Sodium oligomannate therapeutically remodels gut microbiota and suppresses gut bacterial amino acids-shaped neuroinflammation to inhibit Alzheimer's disease progression," *Cell Research*, vol. 29, no. 10, pp. 787–803, 2019.
- [39] M. Wang, X. Ye, J. Hu et al., "NOD1/RIP2 signalling enhances the microglia-driven inflammatory response and undergoes crosstalk with inflammatory cytokines to exacerbate brain damage following intracerebral haemorrhage in mice," *Journal of Neuroinflammation*, vol. 17, no. 1, p. 364, 2020.
- [40] X. Zhao, S. M. Ting, C. H. Liu et al., "Neutrophil polarization by IL-27 as a therapeutic target for intracerebral hemorrhage," *Nature Communications*, vol. 8, no. 1, p. 602, 2017.
- [41] N. A. Bracey, H. J. Duff, and D. A. Muruve, "Hierarchical regulation of wound healing by NOD-like receptors in cardiovascular disease," *Antioxidants & Redox Signaling*, vol. 22, no. 13, pp. 1176–1187, 2015.
- [42] G. J. Martinez, S. Robertson, J. Barraclough et al., "Colchicine acutely suppresses local cardiac production of inflammatory cytokines in patients with an acute coronary syndrome," *Journal of the American Heart Association*, vol. 4, no. 8, article e002128, 2015.
- [43] Z. Yang, L. Zhong, R. Xian, and B. Yuan, "MicroRNA-223 regulates inflammation and brain injury via feedback to NLRP3 inflammasome after intracerebral hemorrhage," *Molecular Immunology*, vol. 65, no. 2, pp. 267–276, 2015.
- [44] L. Xiao, H. Zheng, J. Li, Q. Wang, and H. Sun, "Neuroinflammation mediated by NLRP3 inflammasome after intracerebral hemorrhage and potential therapeutic targets," *Molecular Neurobiology*, vol. 57, no. 12, pp. 5130–5149, 2020.
- [45] T. Iannitti, V. Rottigni, and B. Palmieri, "Corticosteroid transdermal delivery to target swelling, edema and inflammation following facial rejuvenation procedures," *Drug Design, Development and Therapy*, vol. 7, pp. 1035–1041, 2013.
- [46] N. J. Yang, D. V. Neel, L. Deng et al., "Nociceptive sensory neurons mediate inflammation induced by bacillus anthracis edema toxin," *Frontiers in Immunology*, vol. 12, p. 642373, 2021.
- [47] A. K. H. Stavoe and E. L. F. Holzbaur, "Autophagy in neurons," *Annual Review of Cell and Developmental Biology*, vol. 35, no. 1, pp. 477–500, 2019.
- [48] I. Ahmed, Y. Liang, S. Schools, V. L. Dawson, T. M. Dawson, and J. M. Savitt, "Development and characterization of a new Parkinson's disease model resulting from impaired autophagy," *The Journal of Neuroscience*, vol. 32, no. 46, pp. 16503–16509, 2012.
- [49] T. Hara, K. Nakamura, M. Matsui et al., "Suppression of basal autophagy in neural cells causes neurodegenerative disease in mice," *Nature*, vol. 441, no. 7095, pp. 885–889, 2006.
- [50] S. Sato, T. Uchihara, T. Fukuda et al., "Loss of autophagy in dopaminergic neurons causes Lewy pathology and motor dysfunction in aged mice," *Scientific Reports*, vol. 8, no. 1, p. 2813, 2018.
- [51] F. M. Menzies, A. Fleming, A. Caricasole et al., "Autophagy and neurodegeneration: pathogenic mechanisms and therapeutic opportunities," *Neuron*, vol. 93, no. 5, pp. 1015–1034, 2017.
- [52] Y. Yang, K. Xu, T. Koike, and X. Zheng, "Transport of autophagosomes in neurites of PC12 cells during serum deprivation," *Autophagy*, vol. 4, no. 2, pp. 243–245, 2008.
- [53] S. Li, Z. Jiang, W. Chai, Y. Xu, and Y. Wang, "Autophagy activation alleviates nonylphenol-induced apoptosis in cultured cortical neurons," *Neurochemistry International*, vol. 122, pp. 73–84, 2019.
- [54] U. Feldt-Rasmussen, "Fabry disease and early stroke," *Stroke Research and Treatment*, vol. 2011, Article ID 615218, 7 pages, 2011.
- [55] C. W. Chen, T. Y. Chen, K. L. Tsai et al., "Inhibition of autophagy as a therapeutic strategy of iron-induced brain injury after hemorrhage," *Autophagy*, vol. 8, no. 10, pp. 1510–1520, 2012.
- [56] X. C. Duan, W. Wang, D. X. Feng et al., "Roles of autophagy and endoplasmic reticulum stress in intracerebral hemorrhage-induced secondary brain injury in rats," *CNS Neuroscience & Therapeutics*, vol. 23, no. 7, pp. 554–566, 2017.
- [57] J. Chen, L. Wang, C. Wu et al., "Melatonin-enhanced autophagy protects against neural apoptosis via a mitochondrial



- pathway in early brain injury following a subarachnoid hemorrhage,” *Journal of Pineal Research*, vol. 56, no. 1, pp. 12–19, 2014.
- [58] H. Shi, J. Wang, J. Wang, Z. Huang, and Z. Yang, “IL-17A induces autophagy and promotes microglial neuroinflammation through ATG5 and ATG7 in intracerebral hemorrhage,” *Journal of Neuroimmunology*, vol. 323, pp. 143–151, 2018.
- [59] Z. Yang, B. Liu, L. Zhong et al., “Toll-like receptor-4-mediated autophagy contributes to microglial activation and inflammatory injury in mouse models of intracerebral haemorrhage,” *Neuropathology and Applied Neurobiology*, vol. 41, no. 4, pp. e95–106, 2015.
- [60] A. Yu, T. Zhang, W. Zhong et al., “miRNA-144 induces microglial autophagy and inflammation following intracerebral hemorrhage,” *Immunology Letters*, vol. 182, pp. 18–23, 2017.
- [61] M. S. J. Mangan, E. J. Olhava, W. R. Roush, H. M. Seidel, G. D. Glick, and E. Latz, “Targeting the NLRP3 inflammasome in inflammatory diseases,” *Nature Reviews. Drug Discovery*, vol. 17, no. 8, pp. 588–606, 2018.
- [62] K. V. Swanson, M. Deng, and J. P. Ting, “The NLRP3 inflammasome: molecular activation and regulation to therapeutics,” *Nature Reviews. Immunology*, vol. 19, no. 8, pp. 477–489, 2019.
- [63] D. Wu, Y. Chen, Y. Sun et al., “Target of MCC950 in inhibition of NLRP3 inflammasome activation: a literature review,” *Inflammation*, vol. 43, no. 1, pp. 17–23, 2020.
- [64] Y. Yang, H. Wang, M. Kouadir, H. Song, and F. Shi, “Recent advances in the mechanisms of NLRP3 inflammasome activation and its inhibitors,” *Cell Death & Disease*, vol. 10, no. 2, p. 128, 2019.
- [65] Z. Zhang, P. Guo, Z. Jia, T. Chen, and H. Feng, *NLRP3 inflammasome activation attenuates neuronal apoptosis by upregulating autophagy through AMPK/Beclin-1 pathway after intracerebral hemorrhage with ventricular extension in rats*, Research Square, 2021.

## Retraction

# Retracted: Automatic Detection of Epilepsy Based on Entropy Feature Fusion and Convolutional Neural Network

### Oxidative Medicine and Cellular Longevity

Received 8 January 2024; Accepted 8 January 2024; Published 9 January 2024

Copyright © 2024 Oxidative Medicine and Cellular Longevity. This is an open access article distributed under the Creative Commons Attribution License, which permits unrestricted use, distribution, and reproduction in any medium, provided the original work is properly cited.

This article has been retracted by Hindawi following an investigation undertaken by the publisher [1]. This investigation has uncovered evidence of one or more of the following indicators of systematic manipulation of the publication process:

- (1) Discrepancies in scope
- (2) Discrepancies in the description of the research reported
- (3) Discrepancies between the availability of data and the research described
- (4) Inappropriate citations
- (5) Incoherent, meaningless and/or irrelevant content included in the article
- (6) Manipulated or compromised peer review

The presence of these indicators undermines our confidence in the integrity of the article's content and we cannot, therefore, vouch for its reliability. Please note that this notice is intended solely to alert readers that the content of this article is unreliable. We have not investigated whether authors were aware of or involved in the systematic manipulation of the publication process.

In addition, our investigation has also shown that one or more of the following human-subject reporting requirements has not been met in this article: ethical approval by an Institutional Review Board (IRB) committee or equivalent, patient/participant consent to participate, and/or agreement to publish patient/participant details (where relevant).

Wiley and Hindawi regrets that the usual quality checks did not identify these issues before publication and have since put additional measures in place to safeguard research integrity.

We wish to credit our own Research Integrity and Research Publishing teams and anonymous and named external researchers and research integrity experts for contributing to this investigation.

The corresponding author, as the representative of all authors, has been given the opportunity to register their agreement or disagreement to this retraction. We have kept a record of any response received.

### References

- [1] Y. Sun and X. Chen, "Automatic Detection of Epilepsy Based on Entropy Feature Fusion and Convolutional Neural Network," *Oxidative Medicine and Cellular Longevity*, vol. 2022, Article ID 1322826, 13 pages, 2022.

## Research Article

# Automatic Detection of Epilepsy Based on Entropy Feature Fusion and Convolutional Neural Network

Yongxin Sun <sup>1,2</sup> and Xiaojuan Chen <sup>1</sup>

<sup>1</sup>College of Electronic Information Engineering, Changchun University of Science and Technology, Changchun, Jilin 130000, China

<sup>2</sup>College of Physics and Electronic Information, Baicheng Normal University, Baicheng, Jilin 137000, China

Correspondence should be addressed to Xiaojuan Chen; [cxj001@cust.edu.cn](mailto:cxj001@cust.edu.cn)

Received 1 February 2022; Revised 4 April 2022; Accepted 12 April 2022; Published 11 May 2022

Academic Editor: Anwen Shao

Copyright © 2022 Yongxin Sun and Xiaojuan Chen. This is an open access article distributed under the Creative Commons Attribution License, which permits unrestricted use, distribution, and reproduction in any medium, provided the original work is properly cited.

Epilepsy is a neurological disorder, caused by various genetic and acquired factors. Electroencephalogram (EEG) is an important means of diagnosis for epilepsy. Aiming at the low efficiency of clinical artificial diagnosis of epilepsy signals, this paper proposes an automatic detection algorithm for epilepsy based on multifeature fusion and convolutional neural network. Firstly, in order to retain the spatial information between multiple adjacent channels, a two-dimensional Eigen matrix is constructed from one-dimensional eigenvectors according to the electrode distribution diagram. According to the feature matrix, sample entropy SE, permutation entropy PE, and fuzzy entropy FE were used for feature extraction. The combined entropy feature is taken as the input information of three-dimensional convolutional neural network, and the automatic detection of epilepsy is realized by convolutional neural network algorithm. Epilepsy detection experiments were performed in CHB-MIT and TUH datasets, respectively. Experimental results show that the performance of the algorithm based on spatial multifeature fusion and convolutional neural network achieves excellent results.

## 1. Introduction

Epilepsy is a common brain disease, and more and more people suffer from it for a long time [1–3]. There are around 65 million people in the world have epilepsy, and the number will reach almost 1 billion by 2030 [4]. The older population aged more than 65 years have higher incidence as one quarter of the new-onsets are diagnosed after this time-point [5]. The individuals with dementias such as Alzheimer's disease have higher risk of developing epilepsy [6–9]. Oxidative stress is an important intrinsic mechanism involved in the development of epilepsy causing brain damage. The imbalance between the antioxidant system and increased oxygen radicals in epilepsy accelerates the process of apoptosis [10]. During seizures, the patient suffers great physical and mental pain. Therefore, automatic detection of epilepsy by techniques such as EEG signals is of great importance.

The seizure of epilepsy has suddenness and repeatability. It causes intense mental pain to patients and their families and reduces their quality of life [11]. When the brain activity

of epileptic patients is abnormal, abnormal epileptic discharge often occurs in the EEG signal [12]. The signal includes spike wave, spike slow wave, sharp wave, sharp slow wave, sharp slow complex wave, and sharp slow complex wave. Spikes have sharp waveforms, most of which occur in grand or localized seizures. Spike wave and sharp wave have the same mechanism, longer time than spike wave, reflecting the synchronization degree of discharge. The occurrence of sharp slow complex wave and spinous slow complex wave at different locations or times indicates that there may be multiple abnormal electrical activity regions. At present, the diagnosis of these abnormal signals is still done by doctors through visual observation, based on long-term work experience. This work not only consumes a lot of time and energy of doctors but also has low accuracy. It is difficult for different doctors to reach a common judgment standard, which is highly subjective. Therefore, automatic recognition of epileptic EEG signals can help doctors reduce their workload and assist clinical treatment. It has important practical significance and economic value [13].

In recent years, researches on the recognition of EEG signal mostly reflect the change process of brain transition from one state to another state by extracting the characteristics of time domain, frequency domain [14], time frequency domain [15], linear [16], and nonlinear [17]. The literature [18] shows that in the process of the interaction of multiple brain regions in the brain, the synchronous phenomenon leads to seizures. When a seizure is imminent, seizure-like discharges begin to spread through various pathways in the patient's brain to surrounding brain areas. It then passes through some neural circuits to return to the place where the discharge began, forming a closed circuit. This happens in an endless cycle, transforming the brain's normal, random discharges into a steady, rhythmic discharge. Such an attack mechanism shows that there is a certain correlation between brain regions in the course of the disease. The above characteristics do not fully consider this correlation. Therefore, through the synchronous analysis of the whole brain, it can more truly reflect the changes in the interaction between brain areas during clinical seizures.

With the development of machine learning, more and more intelligent algorithms are applied to EEG signal epilepsy detection. It contains classification methods such as support vector [19], naive Bayes [20], neural network [21], and fuzzy logic system [22]. It also includes principal component analysis (PCA) [23], wavelet packet decomposition (WPD) [24], and the higher order crossings (HOC) [25]. These methods first feature extraction from the original features. Then, a classification model is trained using the new features obtained. Finally, the trained model is used for prediction, so as to achieve the function of epilepsy detection. Although many feature extraction and classification methods have been used in EEG epilepsy detection, it is still an important challenge to extract effective features with rich identification information for subsequent effective detection.

In recent years, as a machine learning method, deep learning has attracted extensive attention in feature learning and other aspects [11]. Deep learning learns the weight of each layer through the desired output. Each layer of the hierarchy adjusts the features to get the features that are more likely to yield the desired output. Each layer optimizes the learning of the input features to obtain more and more discriminating features. In recent years, deep learning technology has been effectively applied in EEG signal processing. Some studies [26–28] have used different feature extraction methods to obtain the characteristics of EEG signals. Then, a convolutional neural network is used to detect epilepsy.

At present, there are only a few literatures that use combined features as the input data of classifier to detect epilepsy. In addition, few literatures have considered the spatial information between electrodes while adopting the combined feature. Therefore, in order to use EEG signals to construct effective features for epilepsy detection, this paper proposes an automatic detection algorithm. The innovations and contributions of this paper are listed below. (1) Single entropy (sample entropy (SE), fuzzy entropy (FE), and permutation entropy (PE)) and different combinations of entropy were input as features to the three-dimensional convolutional neural network for epilepsy detection. (2)

Three-dimensional input can not only retain spatial information between electrodes but also integrate various eigenvalues extracted from EEG. The experimental results show that compared with single entropy feature, combined entropy feature can effectively improve the accuracy of epilepsy detection.

The structure of this paper is listed as follows. A related work is described in the next section. The proposed method is expressed in Section 3. Section 4 focuses on the experiment and analysis. Section 5 is the conclusion.

## 2. Related Work

**2.1. Epilepsy Detection.** Bioinformatics, medical image processing, and biological signal processing are all applications of intelligent technologies in biomedicine. Bioinformatics studies protein and genetic information. Medical image processing mainly includes analysis of CT and NMR. Biological signal processing is the study of electrical signals such as EEG and ECG. EEG signal is the expression of brain neuron activity and contains a lot of information about human physiological activity. EEG signals have been widely used in the field of epilepsy detection. Epilepsy detection usually involves the use of automated algorithms to analyze a patient's biological signals to determine whether an epileptic is having a seizure or has had one. An important goal of epilepsy detection is to perform this transformation as quickly and efficiently as possible. In recent years, a variety of algorithms for epilepsy detection have been proposed and achieved certain results [13, 14, 29, 30].

There are three kinds of characteristic states of data distribution in EEG signal, which can be roughly distributed as follows: (1) EEG signals of healthy subjects under normal conditions. (2) EEG signals of epileptic patients during the onset, and (3) epileptic intermittent signals. These three signals all contain their own independent data distribution characteristics, and there are certain differences among them [31]. In previous studies, researchers mostly used signal data under state (1) and state (2) with a large amount of known category information to construct classifiers. According to the study, the performance of the classifier will decline if the above classifiers are used to classify and recognize the signal data in state (3), which is different from the data distribution in state (1) and state (2). At the same time, the existing traditional intelligent modeling technology will no longer be applicable. The transfer learning strategies were introduced to cope with the above challenges and achieved satisfactory results.

EEG signals can be divided into the following five categories [12, 31]: (1) EEG signals measured when the healthy volunteers kept their eyes open, (2) EEG signals measured when eyes were closed in healthy subjects, (3) EEG signals of hippocampal structures in patients with epilepsy during interseizure period, (4) EEG signals in epileptic regions of the brain during interseizure period in epileptic patients, and (5) EEG signals measured during seizures in patients with epilepsy, where type (1) and type (2) belong to the signals under state (1). Signals of type (3) and type (4) belong to state (3). Type (5) corresponds to the EEG signal in state (2).

The classifier with transfer learning ability constructed in Reference [15] can classify and recognize signal data in states (1) and (3) with large distribution differences based on EEG signals in states (1) and (2). However, the signals of state (1) in the source domain and target domain EEG signals come from the same subclass. However, when the source domain EEG signals come from type (1) and type (5), and the target domain signals come from type (2) and type (5), the classification recognition effect will be significantly reduced. This is because although both types (1) and (2) are EEG signals measured by healthy people under normal conditions, they still have different distribution characteristics and belong to different classes.

In practical application, the data obtained is incomplete, and the loss of a small type of data often occurs. In this case, simply introducing transfer learning strategy into the classification model construction can not effectively solve this problem. Because these methods only consider the distribution difference between the source domain and the target domain when building the classification model. In feature extraction, the dimension of source and target EEG signals is reduced separately, just like the traditional EEG intelligent recognition method, and the difference of source and target distribution is ignored. Features that contribute greatly to the establishment of classification models in the source domain may not contribute greatly to the recognition of the target domain. However, the features of the source domain which can help the target domain classification and recognition are not selected, which leads to the reduction of the classifier recognition effect.

The recognition of epileptic EEG signal is generally divided into the following steps. Firstly, an appropriate feature extraction method is selected for feature extraction of EEG epileptic signals, and the feature vector set composed of relevant and useful feature information is obtained. Secondly, the training samples are used to model the specific classification methods to get the relevant classifier. Then, the trained classifier is used to classify and recognize other EEG epileptic signals.

**2.2. Classification and Identification Technology.** Since 1990, many intelligent classification methods have been applied to the recognition of EEG signals. The following is a brief description of some common methods.

- (1) Decision tree algorithm: DT uses induction to generate decision tree and rules in its process and then classifies test data with the obtained decision tree and rules. The decision tree classifier proposed in reference [32] based on fast Fourier transform to extract EEG signal features has achieved better classification accuracy.
- (2) Naive Bayes algorithm: NB is derived from Bayes' theorem in probability theory, with solid theoretical foundation and high efficiency. The literature [33] proposed a data mining model based on the NB algorithm to realize automatic detection of epilepsy.

- (3) *K*-nearest neighbor algorithm: KNN helps to determine the class standard of a sample according to the categories of most samples in *K*-nearest neighbors of the sample in its feature space. The KNN classification algorithm based on nonlinear discrete wavelet transform to extract EEG signal features described in literature achieves high classification accuracy.
- (4) Support vector machine: SVM is considered to be an effective tool to solve the problem of pattern recognition and function estimation [34]. The classification of small samples and high dimensional datasets is particularly effective and has been widely used in EEG intelligent detection.
- (5) Deep learning algorithm: in recent years, some people have tried to use convolutional neural network to process EEG signals and achieved good results. In the literature [19], the original EEG signals were convolved with convolutional neural network in one dimension to predict epileptic seizures. In [35, 36], the original signal is transformed into the frequency domain through the Fourier transform, and then the convolutional neural network is used for classification.

### 3. The Proposed Method

#### 3.1. The Feature of Entropy

**3.1.1. Sample Entropy SE.** Sample entropy SE represents the rate at which a nonlinear dynamical system generates new modes. The higher the sample entropy, the more complex the sequence. The SE algorithm is as follows:

- (1) The original sequence phase space  $i = \{i_1, i_2, \dots, i_T\}$  is reconstructed to obtain the  $w$ -dimension vector, as shown follows:

$$I(x) = [i(x) \ i(x+1) \ \dots \ i(x+w-1)] \quad (1)$$

- (2) Calculate the distance between vectors  $I(x)$  and  $I(y)$ , and the distance between vectors  $I(y)$  and  $I(y)$  is the one with the largest absolute value of difference between the corresponding elements

$$d[I(x), I(y)] = \max \{|i(x+z) - i(y+z)|\}, \quad (2)$$

where  $z = 1, 2, \dots, w-1, x, y = 1, 2, \dots, w-1$

- (3) For each  $x$  value, use  $t$  to represent the number of  $d[I(x), I(y)]$  less than  $r$ . Calculate the ratio of this number to the total distance  $T - w - 1$ , and call it  $H_x^w(r)$

$$H_x^w(r) = \frac{t}{T-w-1}. \quad (3)$$

The average of all its  $x$  values is calculated as follows:

$$H^w(r) = \frac{1}{T-w} \sum_{x=1}^{T-w} H_x^w(r) \quad (4)$$

- (4) Increase the dimension by 1, and the dimension becomes  $w+1$ . Repeat steps (1) to (3) to obtain  $H_x^{w+1}(r), H^{w+1}(r)$
- (5) When the sequence length  $t$  is finite, the estimated value of sample entropy can be obtained, which can be expressed as

$$SE = \lim_{T \rightarrow \infty} \left\{ -lt \left[ \frac{H^{w+1}(r)}{H^w(r)} \right] \right\} \quad (5)$$

**3.1.2. Permutation Entropy PE.** Permutation entropy PE can measure the randomness of one-dimensional time series. The algorithm has the advantages of simplicity, fast calculation speed, and strong antinoise ability. The basic process is as follows:

- (1) For sequence  $i = \{i_1, i_2, \dots, i_T\}$  phase space reconstruction, the following equation is obtained:

$$i_s(n) = \{i_s(n), i_s(n+\tau), \dots, i_s(n+(w-1)\tau)\}, \quad (6)$$

where  $w$  is the embedding dimension and  $\tau$  is the delay time

- (2) The reconstructed components in  $i_s(n)$  are arranged in ascending order of numerical size as follows:

$$i_s[(n+(y_1-1)\tau) \leq \dots \leq (n+(y_w-1)\tau)], \quad (7)$$

where  $y_1, y_2, \dots, y_w$  represents the sequence number of each element in the reconstructed sequence, so the sequence number  $\pi = \{y_1, y_2, \dots, y_w\}$  has  $w!$  different situations

- (3)  $f(\pi)$  is used to represent the frequency of occurrence of each sort mode, then the probability of occurrence of its corresponding sort mode is

$$u_x(\pi) = \frac{f(\pi)}{(T/S) - w + 1}, \quad (8)$$

where  $1 \leq x \leq w!$ . According to Shannon entropy definition, the permutation entropy is

$$B_u(w) = - \sum_{x=1}^{w!} u_x(\pi) \ln u_x(\pi), \quad (9)$$

when  $u_x(\pi) = 1/w!$  and  $B_u(w)$  reaches its maximum  $\ln(w!)$

- (4) Normalize the entropy value, and obtain

$$PE = \frac{B_u(w)}{\ln(w!)} \quad (10)$$

**3.1.3. Fuzzy Entropy FE.** Fuzzy entropy (FE) is an improvement of sample entropy SE, which uses exponential function as fuzzy function to measure the similarity of sample entropy. The fuzzy entropy is smoothed by the continuity of exponential function. The specific steps of the algorithm are as follows:

- (1) Reconstruct the phase space of the original sequence  $i = \{i_1, i_2, \dots, i_T\}$  to obtain the  $M$ -dimension vector, as shown in the following equation:

$$I(x) = [i(x) \ i(x+1) \ \dots \ i(x+w-1)] \quad (11)$$

- (2) Calculate the distance between vector  $I(x)$  and  $I(y)$ , and the distance between vector  $I(x)$  and  $I(y)$  is the one with the largest absolute value of difference between the corresponding elements, namely,

$$d[I(x), I(y)] = wgi\{|i(x+z) - i(y+z)|\}, \quad (12)$$

where  $z = 1, 2, \dots, w-1, x, y = 1, 2, \dots, w-1$

- (3) Define the similarity  $D_{xy}^w$  between vector  $I(x)$  and  $I(y)$  by fuzzy function  $\mu(d_{xy}^w, t, r)$ , namely,

$$D_{xy}^w = \mu(d_{xy}^w, t, r) = e^{-(d_{xy}^w/r)^t}, \quad (13)$$

where  $t$  and  $r$  are the boundary gradient and width of the fuzzy function, respectively

- (4) Define the function as follows:

$$\phi^w(t, r) = \frac{1}{T-w} \sum_{x=1}^{T-w} \left( \frac{1}{T-W-1} \sum_{y=1, y \neq x}^{T-w} D_{xy}^w \right) \quad (14)$$

- (5) Increase the dimension by 1, and the dimension becomes  $w+1$ . Repeat steps (2) to (4) to get  $\phi^{w+1}$
- (6) The fuzzy entropy is defined as follows:

$$FE = \ln \phi^w(t, r) - \ln \phi^{w+1}(t, r) \quad (15)$$

**3.2. Data Preprocessing.** The open source datasets CHB-MIT and TUH were used in this experiment. In order to increase the number of samples, the experimental data were segmented. The EEG data for each epileptic seizure and epileptic-free period is of 2s, and there are 100 instances on average for each class for each patient. In this paper, sample entropy, permutation entropy, and fuzzy entropy are used for feature extraction of EEG signals, respectively. The main method is to extract three kinds of entropy of each EEG channel and get one-dimensional eigenvectors, respectively.

In general, EEG datasets are acquired according to the standard international 10-20 system of electrode distribution of EEG signals. Figure 1(a) is a plan of the International 10-20 system, where the electrodes used in the actual EEG signal are marked in yellow. In the EEG electrode diagram, you can see that each electrode is adjacent to multiple electrodes. These electrodes record EEG signals in specific areas of the brain. In order to retain the spatial information between multiple adjacent channels, a two-dimensional eigenmatrix ( $H \times W$ ) was constructed based on the one-dimensional eigenvector according to the electrode distribution diagram in the manner shown in Figure 1, where  $H$  and  $W$  of the matrix are the maximum values of the channel in the vertical and horizontal directions, respectively. In this case, both  $H$  and  $W$  are equal to 7. In addition, empty channels are filled with zero. In this experiment, three different eigenvalues of EEG signals were extracted from each EEG signal, and the obtained one-dimensional vectors were converted into two-dimensional matrices according to the method shown in Figure 2, and then three two-dimensional matrices were obtained. Then, these three two-dimensional matrices are superimposed into a three-dimensional matrix as the input of CNN. The specific transformation process is shown in Figure 2.

**3.3. Neural Network Structure.** A convolutional neural network is a kind of deep feedforward neural network, which has been widely used in many fields such as image recognition. The CNN has the advantages of good fault tolerance and strong self-learning ability. At the same time, it has the advantages of automatic feature extraction and weight sharing. Through many experiments, the convolutional neural network model is finally constructed by four convolutional layers, a full connection layer, and a softmax layer.

The input of CNN network is a three-dimensional feature matrix composed of two-dimensional feature matrices obtained by three different feature extraction methods. The main function of the pooling layer is to reduce the data dimension. But it comes at the cost of lost information. Due to the small amount of data input from the network in this paper, a pooling layer is not added to the CNN network in this paper in order to retain useful information as much as possible. The specific CNN network model structure is shown in Figure 3. The first convolution layer has 32 feature graphs. The feature graph of the later convolution layer is twice that of the previous one, which is 64, 128, and 256, respectively. The convolution kernel is  $3 \times 3$ , and the

step is 1. After the convolution operation, SELU activation function is added to make the model have nonlinear feature transformation capability. Then, a full connection layer is connected to map  $7 \times 7 \times 256$  feature graphs to feature vector  $F \in R^{1024}$ . The last part of the network is a softmax classifier, which outputs the result value of epilepsy classification and recognition. In this paper, truncated normal distribution function is used to initialize weights and Adam optimizer is used to minimize cross entropy loss function. The initial learning rate is set to 0.0001. Use Dropout to output with 50% probability to avoid overfitting. In addition, L2 regularization is used to avoid overfitting and improve generalization ability, and the weight of regularization term is set to 0.5.

## 4. Experiment

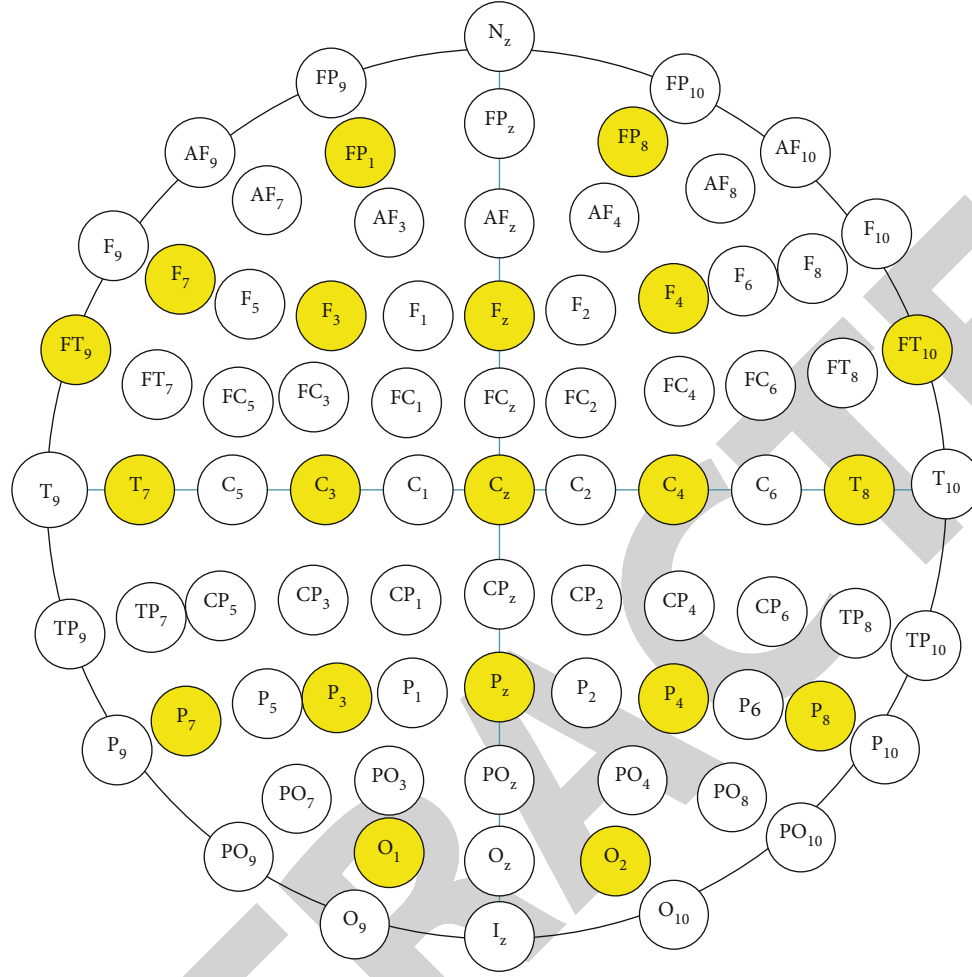
**4.1. Experimental Dataset.** The hardware devices used in this experiment are Intel I7-11700 CPU and NVIDIA GTX 960 GPU. The experimental software is Python 3.10. At the same time, Google open-source deep learning system TensorFlow is used to build the neural network.

EEG data from Boston Children's Hospital is found in the CHB-MIT dataset [30]. It includes EEG recordings of pediatric patients with refractory epileptic seizures. It collected EEG data from 23 of the 22 subjects. Here, data case CHB21 was obtained from the same female subject 1.5 years after data case CHB01. Each case contains between 9 and 42 consecutive.edf files from a single topic. In most cases, the .edf file contains only one hour of digitized EEG signals. All signals were sampled at a rate of 256 samples per second with 16-bit resolution. Most files contain 23 EEG signals (24 or 26 in some cases). These records were recorded using an international 10-20 EEG electrode location and naming system. In some recordings, other signals were also recorded.

Temple University Hospital (TUH) EEG dataset is the largest EEG dataset available [37]. It included 25,000 EEG recordings and 14,000 cases. It is the total dataset of Temple University Hospital since 2002. EEG signals in this dataset were recorded using Natus Medical Incorporated's Nicolet™ EEG recording technology. The original signal consists of 20 to 128 channel records sampled at the lowest frequency of 250 Hz using a 16-bit A/D converter. Eight types of seizures were recorded, among which focal nonspecific epilepsy, generalized nonspecific epilepsy, and complex partial epilepsy were more common. In the subsequent experiments in this paper, only this three common epilepsy information was detected in the TUH dataset.

**4.2. Validation of the Algorithm.** In this section, the CHB-MIT dataset is used to verify the validity of the algorithm. The experimental results in this section are the results of CHB-MIT dataset sent into the network. Accuracy rate (ACC) and recall rate (REC) are introduced in this paper to measure the performance of classifier comprehensively. Its definition is shown below.

$$ACC = \frac{TP + TN}{TP + TN + FN + FP}, \quad (16)$$



(a) EEG signal distribution

$$\begin{bmatrix} 0 & 0 & 0 & 0 & 0 & 0 & 0 \\ 0 & FP_1 - F_7 & FP_1 - F_3 & 0 & FP_2 - F_4 & FP_2 - F_8 & 0 \\ T_7 - FT_9 & 0 & 0 & 0 & 0 & 0 & FT_{10} - T_8 \\ 0 & F_7 - T_7 & F_3 - C_3 & F_z - C_z & F_4 - C_4 & F_8 - TC_8 & 0 \\ 0 & T_7 - P_7 & C_3 - P_3 & C_z - P_z & C_4 - P_4 & T_8 - P_8 & 0 \\ 0 & P_7 - O_1 & P_3 - O_1 & 0 & P_4 - O_2 & P_8 - O_2 & 0 \\ 0 & 0 & 0 & 0 & 0 & 0 & 0 \end{bmatrix}$$

(b) Space matrix

FIGURE 1: The transformation of space matrix.

$$REC = \frac{TP}{TP + FN}, \quad (17)$$

where TP and TN are positive and negative samples correctly classified and FP and FN are positive and negative samples incorrectly classified. In this paper, the positive samples are the EEG signals of the “reverse” response, and the negative samples are the EEG signals of the “forward” response.

The selection of feature directly determines the performance of classifier. Classifiers based on different feature combinations have different performance. There are seven input features in this experiment. It includes single entropy feature and combined entropy feature, respectively (SE, PE,

FE, SE + PE, SE + FE, PE + FE, and SE + PE + FE). Among them, the sequence of entropy combination has little influence on the recognition accuracy after several comparative experiments. The three-dimensional characteristic matrix is constructed by referring to the above experimental pretreatment methods and steps. SE, PE, and FE are the Eigen matrices of  $9 \times 9 \times 1$ . SE + PE, SE + FE, and PE + FE are  $9 \times 9 \times 2$  eigenmatrices. SE + PE + FE is the Eigen matrix of  $9 \times 9 \times 3$ . The above 7 Eigen matrices were, respectively, input into the convolutional neural network shown in Figure 3 for experiment. That is, 7 groups of experiments were conducted on each dimension. In addition, this paper also carries on the comparison experiment according to the conventional



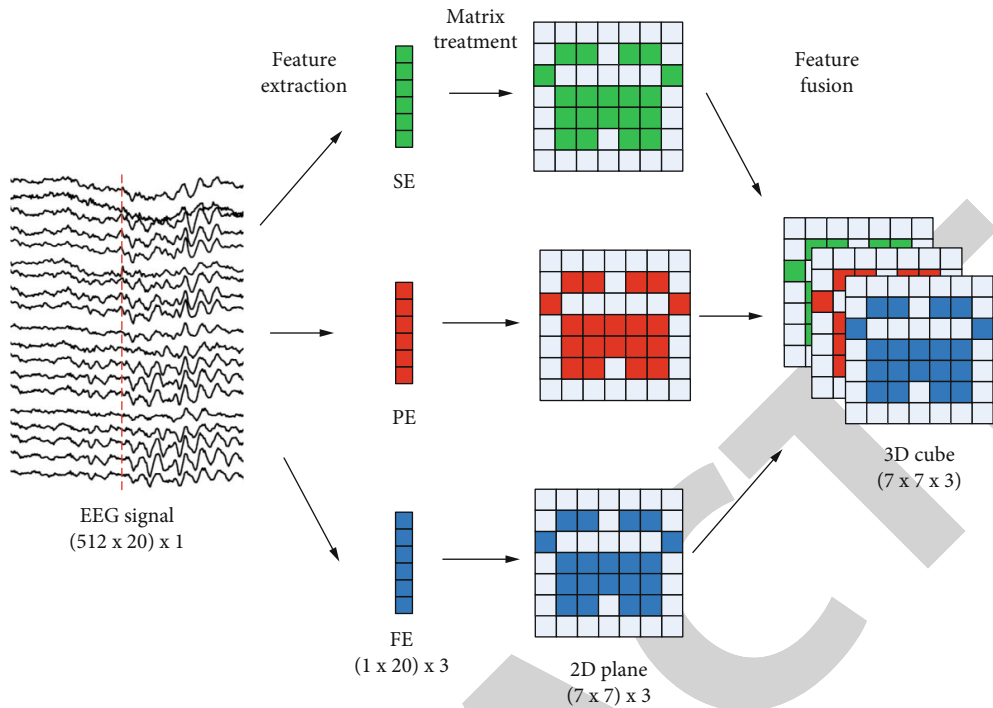


FIGURE 2: The feature extraction process of EEG signal.

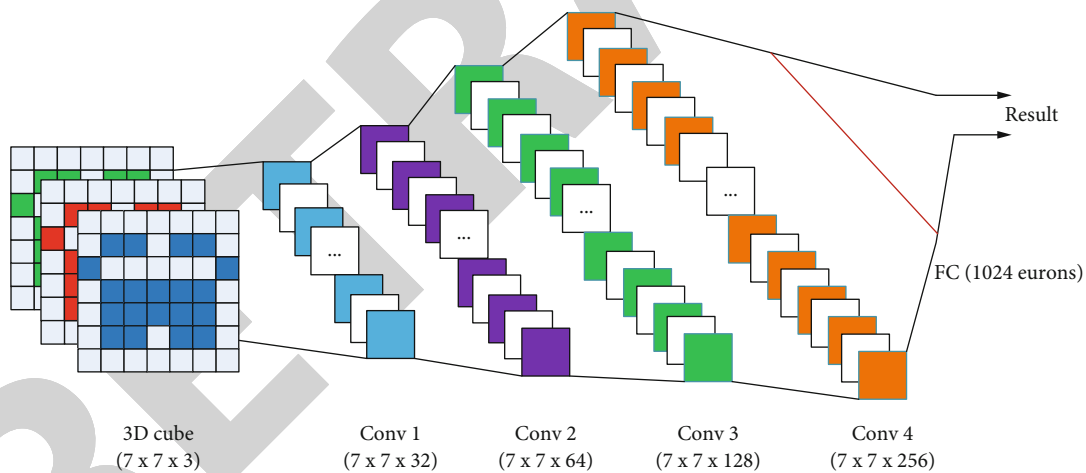
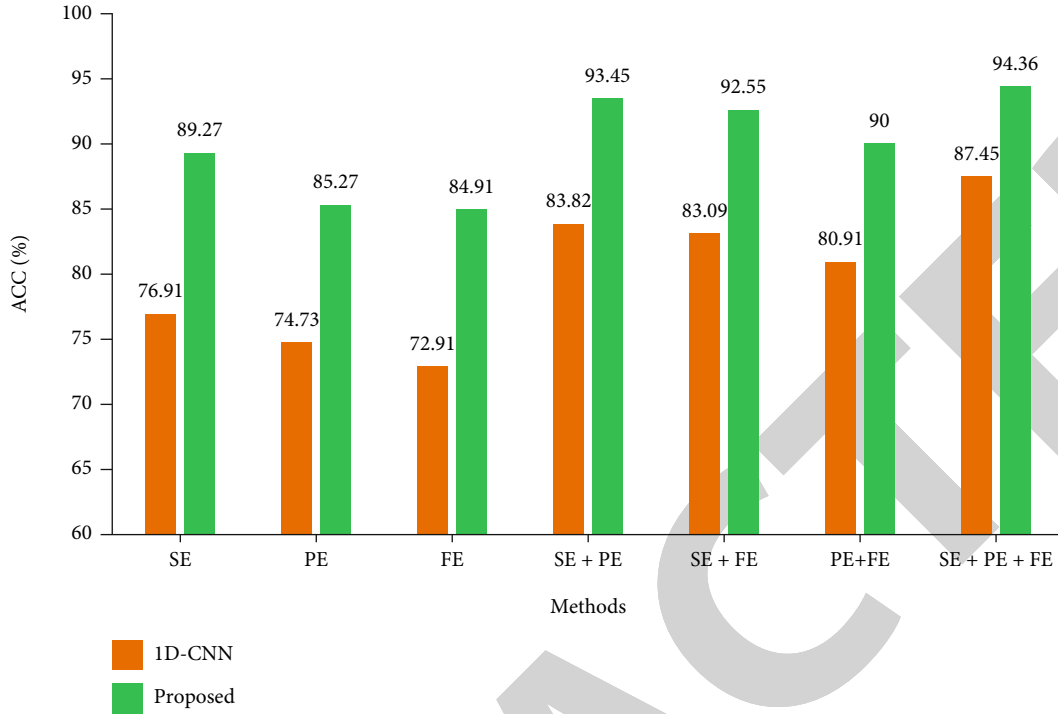


FIGURE 3: The structure of proposed neural network.

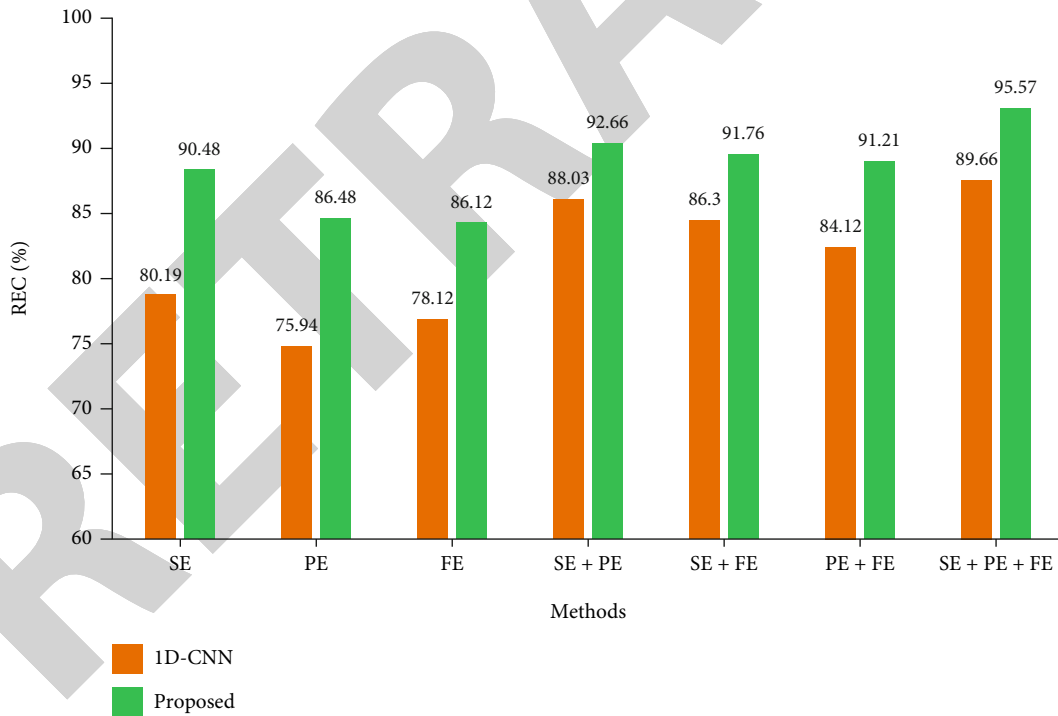
entropy combination method. In this experiment, the spatial information of EEG electrodes is not considered when constructing the input features; that is, the input features are not converted from one-dimensional feature vector to two-dimensional feature matrix according to the EEG electrode distribution. The seven features without spatial information were input to the one-dimensional convolutional neural network with the same network structure as Figure 3 for experiment, and the experimental Settings were consistent with the neural network Settings proposed in this paper.

In order to verify the influence of single entropy feature, combined entropy feature, and spatial information on epilepsy recognition, this paper conducted experiments on

single entropy feature including spatial information, single entropy feature without spatial information, and different combined entropy feature. The results are shown separately in Figure 4. The yellow bar graph in the figure represents the experimental results of the one-dimensional convolutional neural network without spatial information, and the green bar graph represents the experimental results of the neural network proposed in this paper. As can be seen from Figure 4, when comparing the three single entropy features, the classification accuracy of sample entropy as the feature is higher than that of fuzzy entropy and permutation entropy. The accuracy and recall rate of sample entropy in a one-dimensional convolutional neural network are 76.91% and



(a) Accuracy rate results of different methods

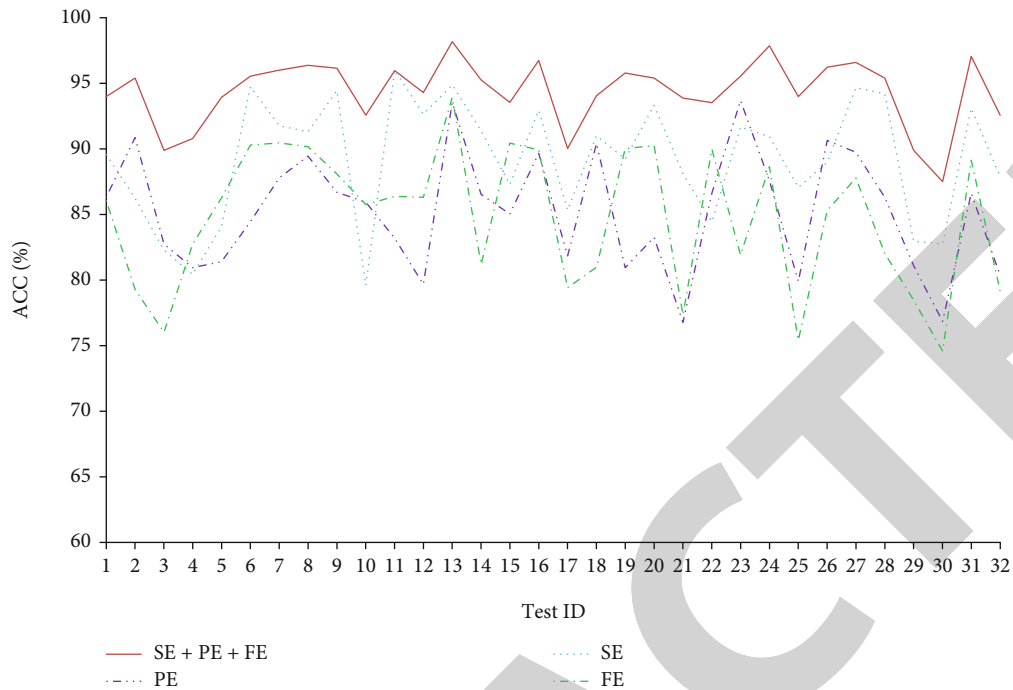


(b) Recall rate results of different methods

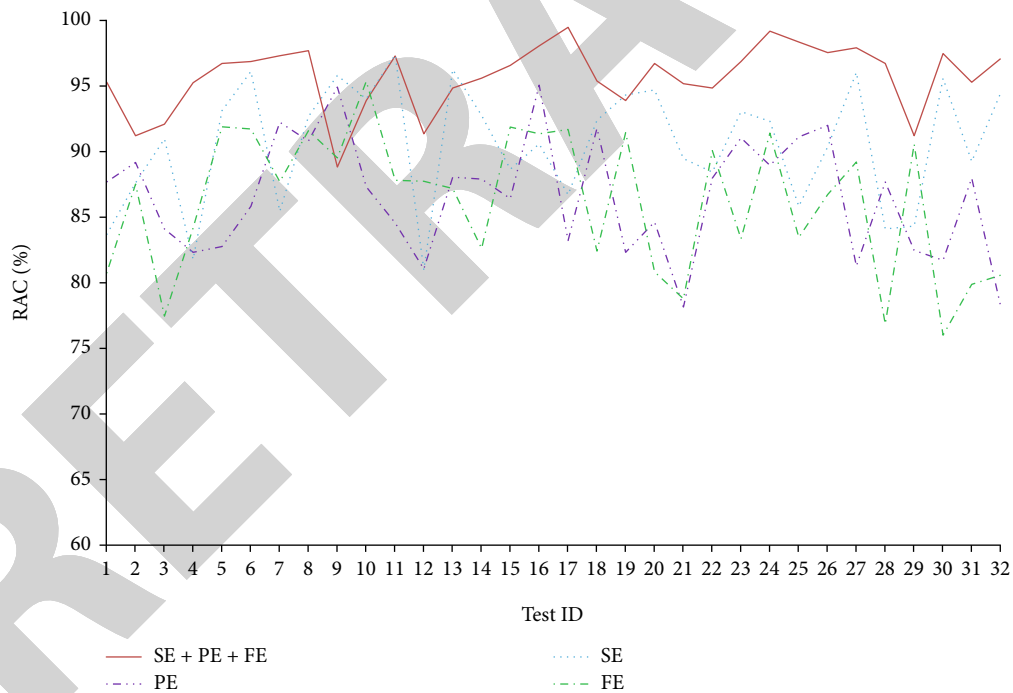
FIGURE 4: The results of accuracy rate and recall rate in different features.

80.19%, respectively. Compared with single entropy feature, the classification accuracy of combined entropy feature is improved. The average accuracy was the highest when SE + PE + FE was used as the input feature. The average accuracy and recall rate in a one-dimensional convolutional neural network are 86.97% and 87.47%, respectively. The

average accuracy and recall rate of the proposed three-dimensional convolutional neural network are 94.36% and 95.57%, respectively, which are 7.39 percentage points and 8.1 percentage points higher than the highest average accuracy of single entropy. Experimental results show that the accuracy of epilepsy detection can be improved significantly



(a) Accuracy rate results of different methods



(b) Recall rate results of different methods

FIGURE 5: The results of different features.

when combined entropy is used as the feature input. In addition, the experimental results using spatial information are compared with those using the same type of entropy feature without spatial information. The results show that the detection accuracy of all entropy features using spatial information is higher than that of entropy features without spatial information. When SE + PE + FE was used as the input feature, the average accuracy and recall rate were the highest. There-

fore, the experimental results show that the spatial information of EEG electrode distribution can effectively improve the accuracy of epilepsy detection.

In order to further analyze the experimental results of the neural network proposed in this paper, Figures 5(a) and 5(b), respectively, show the accuracy and recall rate of epilepsy detection in different features. As can be seen from the figure, when single entropy is used as the input feature,

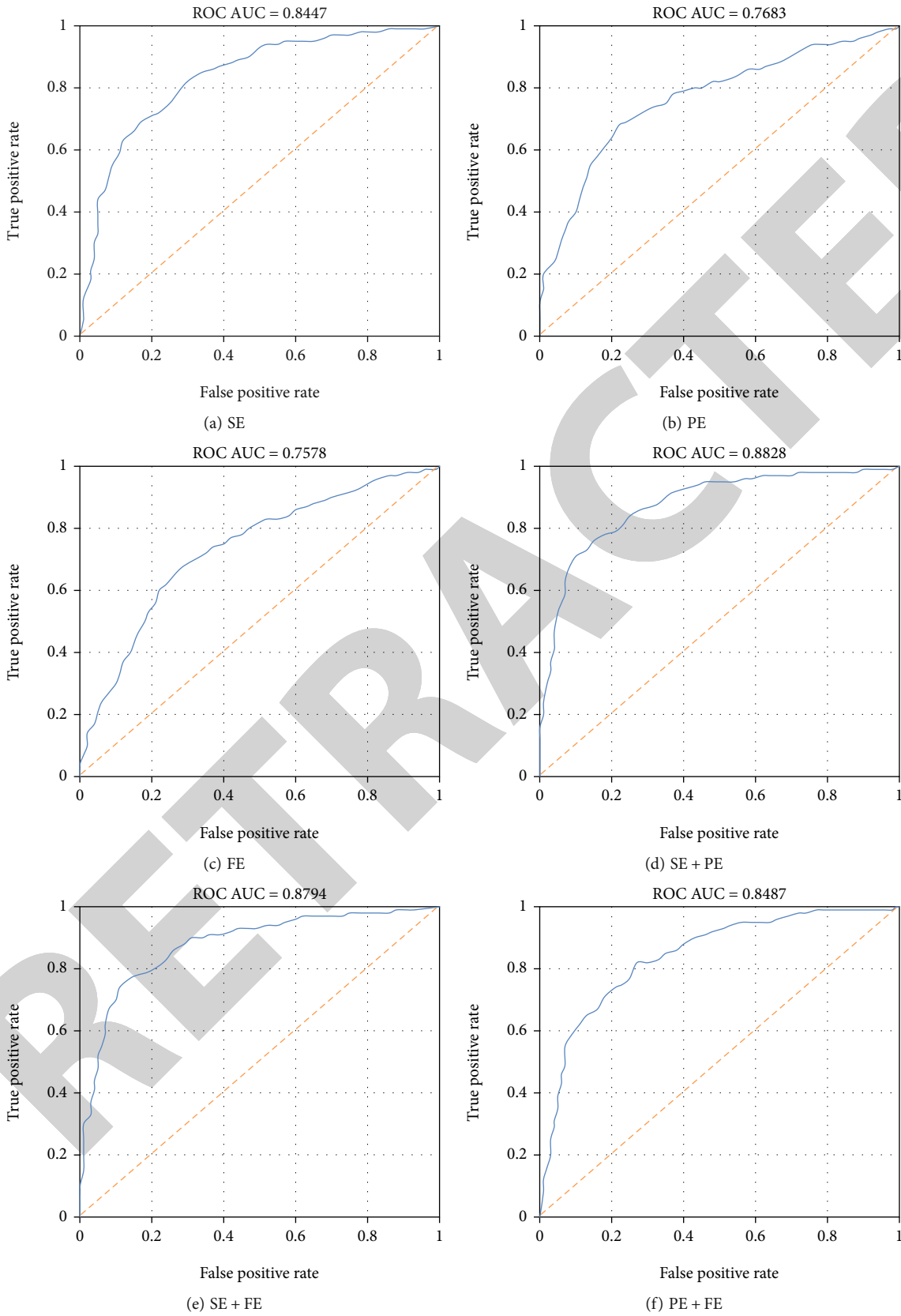


FIGURE 6: Continued.

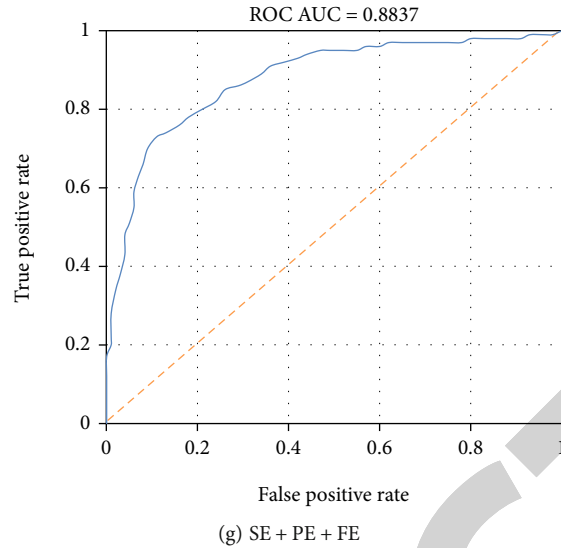


FIGURE 6: The ROC curves and AUC values in different features.

TABLE 1: The results of CHB-MIT dataset.

Methods	ACC (%)	REC (%)
Literature [2]	82.52	81.67
Literature [3]	86.15	86.59
Literature [13]	88.69	89.76
Literature [24]	91.45	92.24
Proposed	94.36	95.57

TABLE 2: The results of TUH dataset.

Methods	ACC (%)	REC (%)
Literature [2]	80.41	79.56
Literature [3]	84.04	84.48
Literature [13]	86.31	87.42
Literature [24]	89.16	90.33
Proposed	92.26	93.86

the accuracy and recall rate of epilepsy detection vary greatly among different subjects. Moreover, its overall accuracy is relatively low. When SE + PE + FE was used as the input feature, the difference of accuracy and recall rate among different subjects was small. And its accuracy rate basically maintains at about 95%. The maximum value of single subject in accuracy and recall rate was 76.91% and 80.19%, respectively. Compared with single entropy as the input feature, when the features of SE + PE + FE was used as the input feature, the classification accuracy of the other subjects improved in both dimensions except for the slight decrease of subject 11 in the arousal dimension. Therefore, the experimental results show that when extracting EEG features, different entropies can be combined to complement each other, thus effectively improving the accuracy of epilepsy detection.

In addition, Figure 6 shows the ROC curve and AUC value of the classification model based on training of differ-

ent feature combinations. The best value of single entropy is the AUC value of SE, which is only 0.8447. SE + PE + FE had the highest AUC value, which was 0.8837. The feature combination method of the proposed algorithm significantly improves the performance of epilepsy detection.

**4.3. Comparison of Relevant Algorithms.** In order to be further compared with other methods, the algorithms of literature [2], literature [3], literature [13], and literature [24] are selected here for experimental comparison. The TUH dataset is used for comparison experiments. Different from the previous CHB-MIT dataset, the TUH dataset contains three common epilepsy information: focal nonspecific epilepsy, generalized nonspecific epilepsy, and complex partial epilepsy. Therefore, the detection on the TUH dataset is difficult. If we can achieve good performance on this dataset, it will be more beneficial to prove the effectiveness of our proposed method. Finally, the accuracy and recall rate of epilepsy detection are shown in Tables 1 and 2. By observing the results in Tables 1 and 2, the average accuracy and recall rate of the algorithm presented in this paper exceed those of the other four methods.

Meanwhile, by observing the data in Table 2, the highest accuracy and recall rate of the algorithm in this paper are 92.26% and 93.86%. The result in Table 2 is significantly lower than the result in Table 1. This is because there are more types of epilepsy in the TUH dataset, which belongs to multiclassification task. However, in the CHB-MIT dataset, there are only two types of epilepsy and normal data, which belong to the dichotomous task. The multiclassification task is more difficult to detect than the two-classification task, so the performance of the TUH dataset in this paper is lower than that of the CHB-MIT dataset.

## 5. Conclusion

In this paper, the EEG data for each epileptic seizure and epileptic-free period is of 2 s and there are 100 instances on

average for each class for each patient, and the entropy value per epoch was calculated, respectively. Transform a one-dimensional vector into a two-dimensional matrix according to the method shown in Figure 1. In this paper, sample entropy, permutation entropy, and fuzzy entropy are analyzed, respectively. Three different eigenvalues of EEG signals were extracted from each EEG signal, and three two-dimensional matrices were obtained. The three two-dimensional matrices and their different combinations were input into the convolutional neural network as features, respectively, for analysis of epilepsy detection in two dimensions of accuracy and recall rate.

The experimental results show that compared with the single entropy feature, the combined entropy feature proposed in this paper can effectively improve the accuracy and recall rate of epilepsy detection. In addition, the spatial information of EEG electrode distribution can effectively improve the accuracy of epilepsy detection. The three-dimensional input convolution neural network combined with the combined entropy feature can retain the spatial information between electrodes and fully extract the EEG signal features. Compared with other relevant methods, the accuracy and recall rate of the proposed method are significantly improved.

### Data Availability

The labeled dataset used to support the findings of this study is available from the corresponding author upon request.

### Conflicts of Interest

The authors declare that they have no competing interests.

### Authors' Contributions

Yongxin Sun as the primary contributor, completed the analysis, experiments, and paper writing. Xiaojuan Chen helped perform the analysis with constructive discussions.

### Acknowledgments

This work is supported by the Changchun University of Science and Technology.

### References

- [1] G. L. Birbeck, "Epilepsy care in developing countries: part II of II," *Epilepsy Currents*, vol. 10, no. 5, pp. 105–110, 2010.
- [2] G. L. Birbeck, "Epilepsy care in developing countries: part I of II," *Epilepsy Currents*, vol. 10, no. 4, pp. 75–79, 2010.
- [3] A. K. Ngugi, C. Bottomley, I. Kleinschmidt, J. W. Sander, and C. R. Newton, "Estimation of the burden of active and life-time epilepsy: a meta-analytic approach," *Epilepsia*, vol. 51, no. 5, pp. 883–890, 2010.
- [4] J. F. Annegers, W. A. Hauser, S. P. Coan, and W. A. Rocca, "A population-based study of seizures after traumatic brain injuries," *The New England Journal of Medicine*, vol. 338, no. 1, pp. 20–24, 1998.
- [5] R. D. Verboket, N. Sohling, I. Marzi et al., "Prevalence, risk factors and therapeutic aspects of injuries and accidents in women with epilepsy," *European Journal of Trauma and Emergency Surgery*, vol. 45, no. 3, pp. 375–381, 2019.
- [6] A. Sen, V. Capelli, and M. Husain, "Cognition and dementia in older patients with epilepsy," *Brain*, vol. 141, no. 6, pp. 1592–1608, 2018.
- [7] L. Hopia, M. Andersson, E. Svenungsson, M. Khademi, F. Piehl, and T. Tomson, "Epilepsy in systemic lupus erythematosus: prevalence and risk factors," *European Journal of Neurology*, vol. 27, no. 2, pp. 297–307, 2020.
- [8] E. Beghi and G. Giussani, "Aging and the epidemiology of epilepsy," *Neuroepidemiology*, vol. 51, no. 3–4, pp. 216–223, 2018.
- [9] R. J. Kotloski, J. Dowding, B. P. Hermann, and T. P. Sutula, "Epilepsy and aging," *Handbook of Clinical Neurology*, vol. 167, pp. 455–475, 2019.
- [10] U. Geronzi, F. Lotti, and S. Grosso, "Oxidative stress in epilepsy," *Expert Review of Neurotherapeutics*, vol. 18, no. 5, pp. 427–434, 2018.
- [11] M. K. Siddiqui, R. Morales-Menendez, X. Huang, and N. Hussain, "A review of epileptic seizure detection using machine learning classifiers," *Brain Inform.*, vol. 7, no. 1, p. 5, 2020.
- [12] A. Shoeibi, M. Khodatars, N. Ghassemi et al., "Epileptic seizures detection using deep learning techniques: a review," *International Journal of Environmental Research and Public Health*, vol. 18, no. 11, 2021.
- [13] X. Wang, G. Gong, and N. Li, "Automated recognition of epileptic EEG states using a combination of symlet wavelet processing, gradient boosting machine, and grid search optimizer," *Sensors*, vol. 19, no. 2, 2019.
- [14] H. Chao, L. Dong, Y. Liu, and B. Lu, "Emotion recognition from multiband EEG signals using CapsNet," *Sensors*, vol. 19, no. 9, 2019.
- [15] R. Alazrai, R. Homoud, H. Alwanni, and M. I. Daoud, "EEG-based emotion recognition using quadratic time-frequency distribution," *Sensors*, vol. 18, no. 8, 2018.
- [16] Y. Li, W. Zheng, Z. Cui, Y. Zong, and S. Ge, "EEG emotion recognition based on graph regularized sparse linear regression," *Neural Processing Letters*, vol. 49, no. 2, pp. 555–571, 2019.
- [17] B. García-Martínez, A. Fernández-Caballero, L. Zunino, and A. Martínez-Rodrigo, "Recognition of emotional states from EEG signals with nonlinear regularity- and predictability-based entropy metrics," *Cognitive Computation*, vol. 13, no. 2, pp. 403–417, 2021.
- [18] H. Yu, L. Zhu, L. Cai et al., "Variation of functional brain connectivity in epileptic seizures: an EEG analysis with cross-frequency phase synchronization," *Cognitive Neurodynamics*, vol. 14, no. 1, pp. 35–49, 2020.
- [19] I. Santoso, Y. Adrianto, A. Sensusiati, D. Wulandari, and I. Purnama, "Epileptic EEG signal classification using convolutional neural network based on multi-segment of EEG signal," *International Journal of Intelligent Engineering and Systems*, vol. 14, no. 3, pp. 160–176, 2021.
- [20] H.-S. Chiang, M.-Y. Chen, and Y.-J. Huang, "Wavelet-based EEG processing for epilepsy detection using fuzzy entropy and associative petri net," *IEEE Access*, vol. 7, pp. 103255–103262, 2019.
- [21] O. Turk and M. S. Ozerdem, "Epilepsy detection by using scalogram based convolutional neural network from EEG signals," *Brain Sciences*, vol. 9, no. 5, p. 115, 2019.

## Retraction

# Retracted: Long Noncoding RNA TUG1 Aggravates Cerebral Ischemia/Reperfusion Injury by Acting as a ceRNA for miR-3072-3p to Target St8sia2

### Oxidative Medicine and Cellular Longevity

Received 8 January 2024; Accepted 8 January 2024; Published 9 January 2024

Copyright © 2024 Oxidative Medicine and Cellular Longevity. This is an open access article distributed under the Creative Commons Attribution License, which permits unrestricted use, distribution, and reproduction in any medium, provided the original work is properly cited.

This article has been retracted by Hindawi, as publisher, following an investigation undertaken by the publisher [1]. This investigation has uncovered evidence of systematic manipulation of the publication and peer-review process. We cannot, therefore, vouch for the reliability or integrity of this article.

Please note that this notice is intended solely to alert readers that the peer-review process of this article has been compromised.

Wiley and Hindawi regret that the usual quality checks did not identify these issues before publication and have since put additional measures in place to safeguard research integrity.

We wish to credit our Research Integrity and Research Publishing teams and anonymous and named external researchers and research integrity experts for contributing to this investigation.

The corresponding author, as the representative of all authors, has been given the opportunity to register their agreement or disagreement to this retraction. We have kept a record of any response received.

### References

- [1] M. Chen, F. Wang, L. Fan, H. Wang, and S. Gu, "Long Noncoding RNA TUG1 Aggravates Cerebral Ischemia/Reperfusion Injury by Acting as a ceRNA for miR-3072-3p to Target St8sia2," *Oxidative Medicine and Cellular Longevity*, vol. 2022, Article ID 9381203, 20 pages, 2022.

## Research Article

# Long Noncoding RNA TUG1 Aggravates Cerebral Ischemia/Reperfusion Injury by Acting as a ceRNA for miR-3072-3p to Target St8sia2

Miao Chen <sup>1</sup>, Feng Wang,<sup>2</sup> Limin Fan,<sup>3</sup> Hairong Wang <sup>4</sup>, and Shuo Gu <sup>5</sup>

<sup>1</sup>Department of Emergency, The First Affiliated Hospital of Hainan Medical University, No. 31, Longhua Road, Longhua District, Haikou City, Hainan Province 570102, China

<sup>2</sup>Neurology Department, Seventh People's Hospital of Shanghai University of Traditional Chinese Medicine, Shanghai 200137, China

<sup>3</sup>The Institute for Biomedical Engineering and Nano Science, Tongji University School of Medicine, No. 1239, Siping Road, Shanghai 200092, China

<sup>4</sup>Department of Emergency, Xinhua Hospital Affiliated to Shanghai Jiaotong University, School of Medicine, No. 1665, Kongjiang Road, Shanghai 20092, China

<sup>5</sup>Department of Pediatric Neurosurgery, The First Affiliated Hospital of Hainan Medical University, No. 31, Longhua Road, Longhua District, Haikou City, Hainan Province 570102, China

Correspondence should be addressed to Hairong Wang; wanghairong@xinhumed.com.cn and Shuo Gu; gushuo007@hainmc.edu.cn

Received 27 January 2022; Revised 22 February 2022; Accepted 7 March 2022; Published 19 April 2022

Academic Editor: Anwen Shao

Copyright © 2022 Miao Chen et al. This is an open access article distributed under the Creative Commons Attribution License, which permits unrestricted use, distribution, and reproduction in any medium, provided the original work is properly cited.

Long noncoding RNA taurine-upregulated gene 1 (TUG1) is considered to be involved in postischemic cerebral inflammation, whereas polysialic acid (polySia, PSA), the product of St8sia2, constitutes polysialylated neural adhesion cell molecule (PSA-NCAM) in both mice and humans and that cerebral PSA-NCAM level is elevated in neuronal progenitor cells in response to transient focal ischemia. Herein, we aim to identify novel miRNAs that bridge the functions of St8sia2 and TUG1 in ischemia-associated injuries. In both *in vivo* (C57BL/6J mouse ischemia/reperfusion, I/R model) and *in vitro* (mouse neuroblastoma N2A cell oxygen glucose deprivation/reoxygenation, OGD model) settings, we observed upregulated TUG1 and St8sia2 after the induction of ischemic injury, accompanied by reduced miR-3072-3p expression. We performed siRNA-induced TUG1 knockdown combined with the induction of ischemic injury; the results showed that inhibiting TUG1 expression led to the reduced infarct area and improved neurological deficit. Through bioinformatics analysis, miR-3072-3p was found to target both St8sia2 and TUG1, which was subsequently verified by the luciferase reporter system and RNA binding protein immunoprecipitation assay. Also, the addition of miR-3072-3p mimic/inhibitor resulted in reduced/elevated St8sia2 expression at the protein level. Further studies revealed that in both *in vivo* and *in vitro* settings, TUG1 bound competitively to miR-3072-3p to regulate St8sia2 expression and promote apoptosis. In summary, targeting the TUG1/miR-3072-3p/St8sia2 regulatory cascade, a novel cascade we identified in cerebral ischemia injury, may render feasible therapeutic possibilities for overcoming cerebral ischemic insults.

## 1. Introduction

Stroke is also called cerebral infarction. In the past four decades, the prevalence of stroke has declined by 42% in high-income countries and doubled in low-income coun-

tries [1]. In China, the annual new cases of stroke are up to 2 million, with an upward trend of stroke incidence among the young population [2], and more than 65% of the surviving patients have different degrees of disability [3]. The direct medical expenses for stroke care in China



TABLE 1: The primer sequences.

Subjects	The primer sequences
TUG1	Forward: 5'-TTCCTACCACCTTACTACTGACG-3' Reverse: 5'-GGAGGTAAAGGCCACATC-3'
miR-3072-3p	TGCCCC TCCAGGAAGC CTTCTT
St8sia2	Forward: 5'-GACATAACCAGACGCTCTCTCT-3' Reverse: 5'-ACGATGGCACAAGTCCCAAA-3'
U6	Forward: 5'-GACTGCGCAAGGATGACAC-3' Reverse: 5'-CAGTGCCTGTCGTGGAGTC-3'
$\beta$ -Actin	Forward: 5'-TTGCCGACAGGATGCAGAA-3' Reverse: 5'-GCCGATCCACACGGAGTACT-3'

increased rapidly at an average annual growth rate of 18.04%, reaching 37.45 billion yuan in 2003, accounting for 6.52% and 5.68% of the total medical and health expenses, respectively [4]. Therefore, stroke poses a serious threat to the health of the population and brings a heavy economic burden to the society.

Thrombolytic drugs can be used to dissolve the newly formed "blood clots" to reopen the blood vessels and restore the blood flow, which is currently recognized as the most effective way to save the uninjured ischemic brain tissue [5]. However, the thrombolysis rate of acute ischemic stroke (AIS) is only 2.4% in China [6]. Although patients generally experience improvement in symptom manifested by significantly reduced or even completed restored neurological deficit at the beginning of thrombolytic drugs application, the symptoms might be aggravated again shortly afterwards, presumably related to the ischemia-reperfusion injury [7]. Therefore, further understanding of the mechanism underlying ischemia-reperfusion is crucial for better clinical outcome of ischemia.

Noncoding RNAs (ncRNAs) have been well documented to be strongly linked to stroke and poststroke recovery of neurofunction [8]; among which long noncoding RNAs (lncRNAs) as well as microRNAs (miRNAs) are the most representative ones [9, 10]. lncRNAs are a type of RNA longer than 200 nt [11] and mainly distributed in the nucleus or cytoplasm [12], with an organ- and tissue-specific expression pattern [13]. Generally, lncRNAs are transcribed by RNA polymerase II and usually undergo a splicing process, although they possess both cap structure and a polyA tail. The lack of an open reading frame (ORF) prevents them from encoding protein [14]. In recent years, lncRNAs were found to be related to multiple biological processes such as among others, X chromosome silencing [15], chromosome modification [16], transcription activation and suppression [17], cell differentiation [18], carcinogenesis [19], and ontogeny [20]. Therefore, the identification of functional lncRNAs, especially the study of the effect mechanism, has attracted more and more attention from scholars at home and abroad [21]. Several studies have indicated that lncRNAs play role in many pathophysiological processes,

such as nervous system development [22], stroke [23], and Alzheimer's disease [24]. Taurine-upregulated gene 1 (TUG1) is a highly conserved member of the lncRNA family and widely expressed throughout the body tissues. Previous studies indicated that TUG1 was indispensable for male fertility [25] and involved in the progression of preeclampsia [26]. Importantly, TUG1 was found to be a sponge of miR-145a-5p, thus modulating microglial polarization of BV-2 microglial cells that undergo glucose deprivation [27], indicating its pivotal role in cerebral inflammation. Moreover, another study on myocardial infarction revealed a potential TUG1-miR-9a-5p axis that mediates apoptosis of cardiomyocyte [27]. Hence, we hypothesized that TUG1 might also be involved in the ischemia stroke.

Sialyltransferase 2 (St8sia2) is a polysialyltransferase [28]. A recent research has found that St8sia2 is related to the remodeling of nerve cells and the interaction between neurons [29]. It is also closely related to Alzheimer's disease [30], anxiety [31], and manic depression [32]. Of note, a previous study on human brain ischemia showed that the combination of polysialic acid (polySia, PSA, the main product of St8sia2) moiety and neural adhesion cell molecule (NCAM), abbreviated as PSA-NCAM, was significantly elevated in neuronal progenitor cells (NPCs) [33], implying the involvement of St8sia2 in this process. However, the direct relationship between St8sia2 and stroke has not yet been reported so far.

Considering that both TUG1 and St8sia2 are associated with ischemia stroke, this paper is aimed at elucidating the way through which they work in concert to regulate the ischemic process. In addition, there have been no reports on the correlation of TUG1 and St8sia2 in any other field; thus, the novelty and motivation of the study are to first identify the relationship between TUG1 and St8sia2 in cerebral ischemia/reperfusion injury. Besides, miRNA is an important member of the ncRNA family. Past evidence has indicated that miRNAs exert a negative regulatory function mainly by binding to their target genes' mRNA and promoting mRNA degradation/inhibiting mRNA translation [34]. Recent studies have found that miRNAs have a wide range of effects on stroke [35]. The miRNAs unique to brain tissues participate

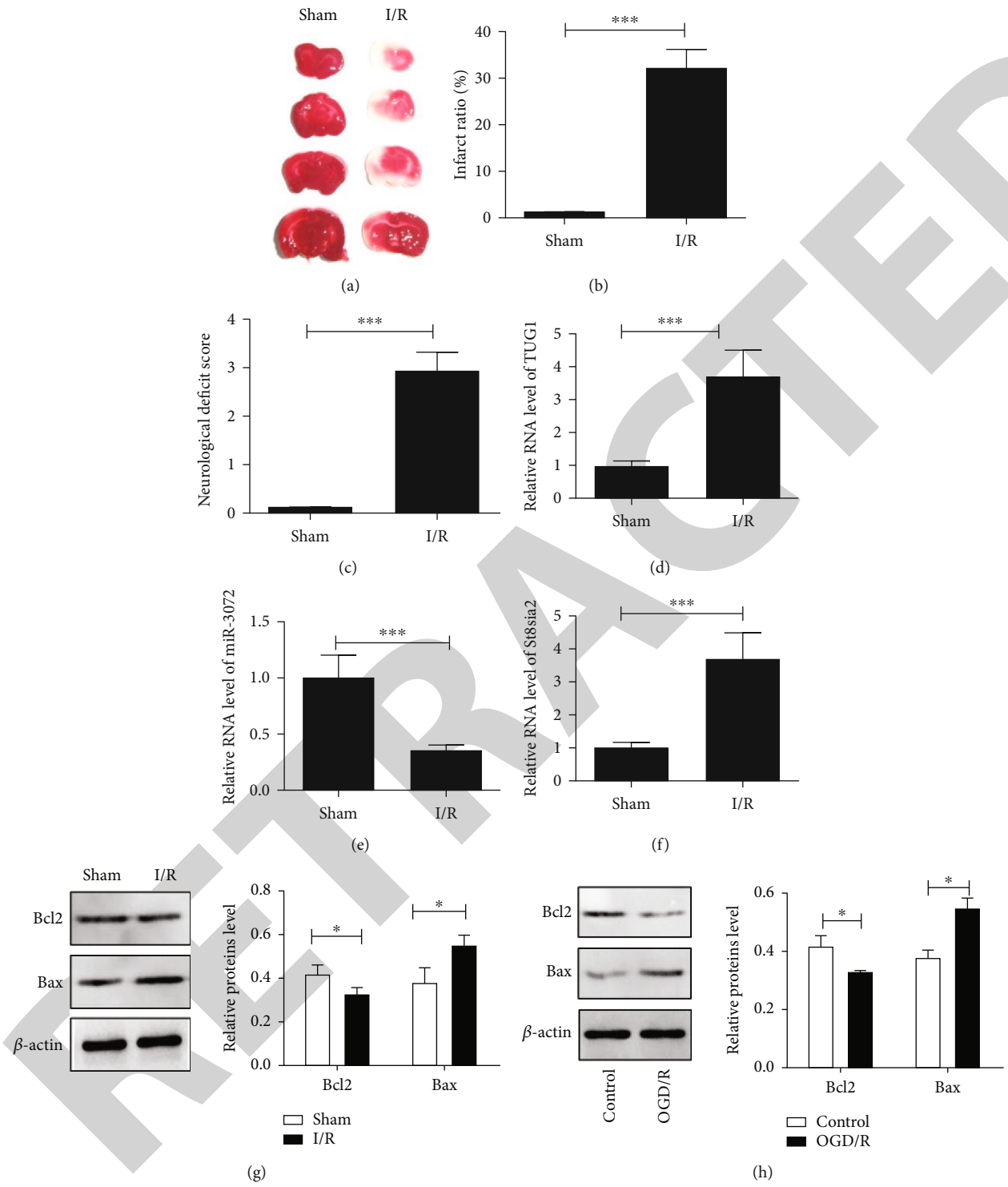


FIGURE 1: Continued.

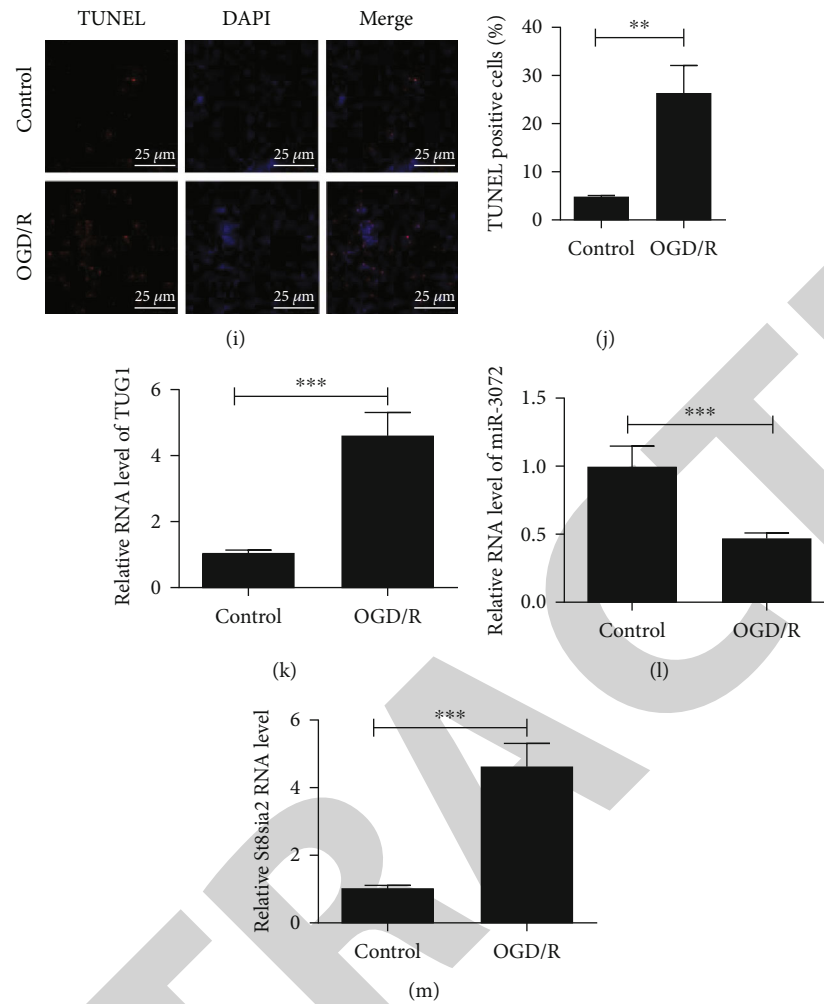


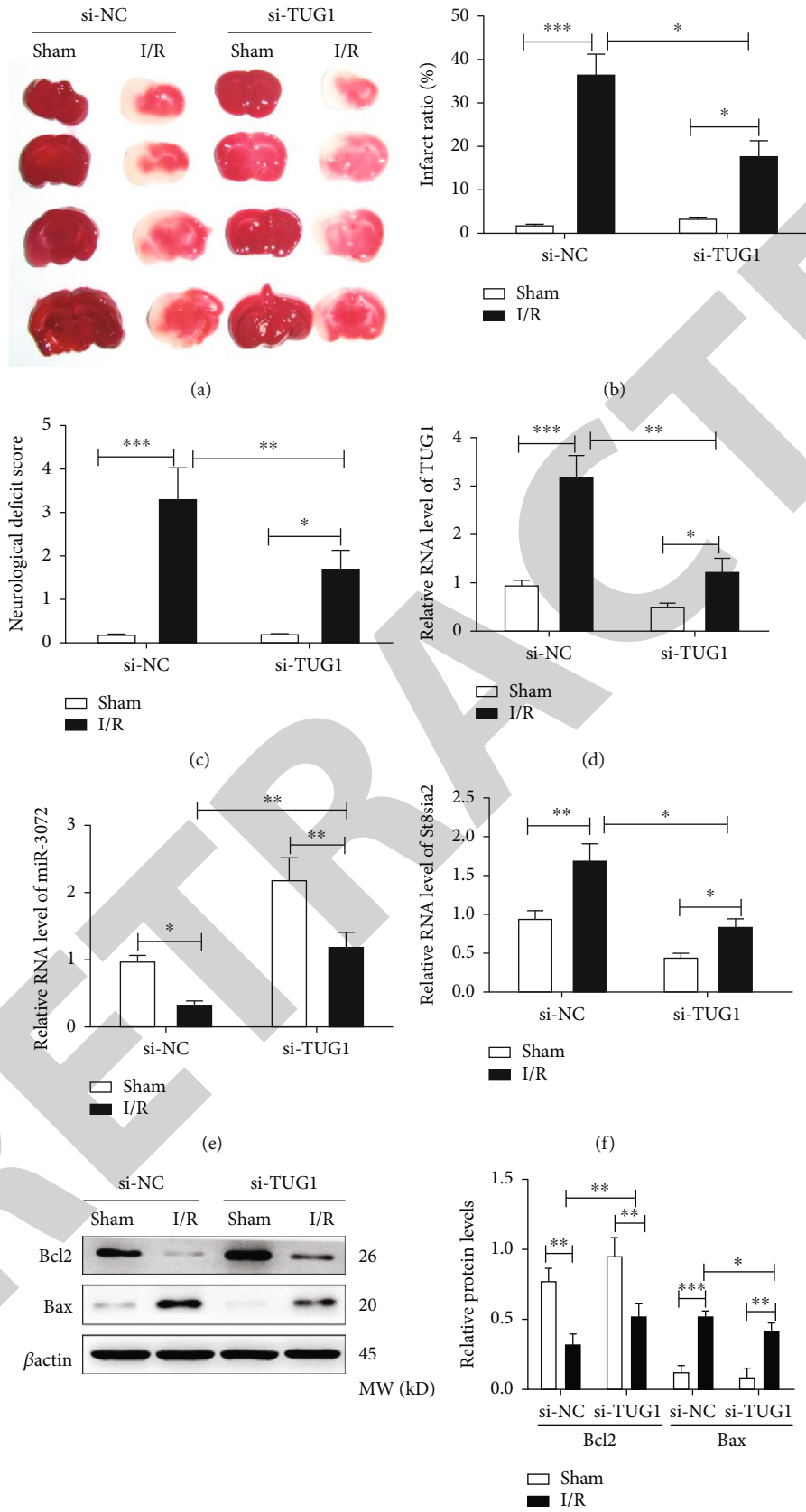
FIGURE 1: TUG1 and St8sia2 were upregulated and accompanied by reduced miR-3072-3p level following *in vitro* and *in vivo* ischemic injuries. (a–g) C57BL/6J mice were subjected to MCAO/R (1.5 h/24 h) or sham operation. (a) Images of brain sections (underwent sham operation or I/R treatment) with TTC staining, the infarction zones were stained white. (b) Cerebral infarct ratio quantified by ImageJ. (c) Neurological deficit scores; the higher score represents more severe neurological deficit. (d) Expression of cerebral TUG1 at the transcript level in response to I/R was quantitated by Q-PCR. (e) Expression of cerebral miR-3072-3p at the transcript level in response to I/R was quantitated by Q-PCR. (f) Expression of cerebral St8sia2 at the transcript level in response to I/R was quantitated by Q-PCR. (g) Cerebral Bcl-2 and Bax levels in response to I/R were measured by western blot analysis. (h–m) N2A cells were subjected to OGD/R (4 h/24 h). Untreated cells were regarded as control. (h) Cellular Bcl-2 and Bax levels in response to oxygen glucose deprivation/reoxygenation were measured by western blot analysis. (i) Representative cell images of the TUNEL staining (scale bar = 25  $\mu$ m), N2A cells with excessive DNA damage were stained with red (TUNEL), whereas the blue counterstaining (DAPI) localized the nuclei. (j) Cell apoptosis percentage was quantified based on TUNEL-positive cells. (k–m) Expression of cerebral TUG1 at the transcript level in response to oxygen glucose deprivation/reoxygenation was quantitated by Q-PCR. (l) Expression of cerebral miR-3072-3p at the transcript level in response to oxygen glucose deprivation/reoxygenation was quantitated by Q-PCR. (m) Expression of cerebral St8sia2 at the transcript level in response to oxygen glucose deprivation/reoxygenation was quantitated by Q-PCR. \* $P < 0.05$ , \*\* $P < 0.01$ , and \*\*\* $P < 0.001$ . Sham: sham-operated animals; I/R: MCAO-induced ischemia/reperfusion group; control: untreated cells; OGD/R: oxygen glucose deprivation/reoxygenation group.

in the regulation of different physiological and pathological processes of the nervous system, such as the occurrence, development, synapse formation, and neuroprotection of the nervous system [36], aside from their involvement in cerebral infarction, cerebral hemorrhage, brain trauma, Parkinson's disease, and cognitive impairment [37]. Given the foregoing, we assumed that miRNA might bring TUG1 and St8sia2 together to regulate the ischemia-associated pathological processes. To verify the joint action of TUG1, St8sia2, and miRNA in ischemia stroke, a series of experiments was

performed in the current study; the corresponding effects on ischemia-reperfusion injury were also investigated.

## 2. Material and Methods

**2.1. Rat Ischemia/Reperfusion (I/R) Model.** All animal experiments had got ethical approval from the University of Shanghai for Science and Technology and were conducted strictly following the guidelines stipulated in the Institutional Animal Care and Use. The experimental animals were



(g)

FIGURE 2: Continued.

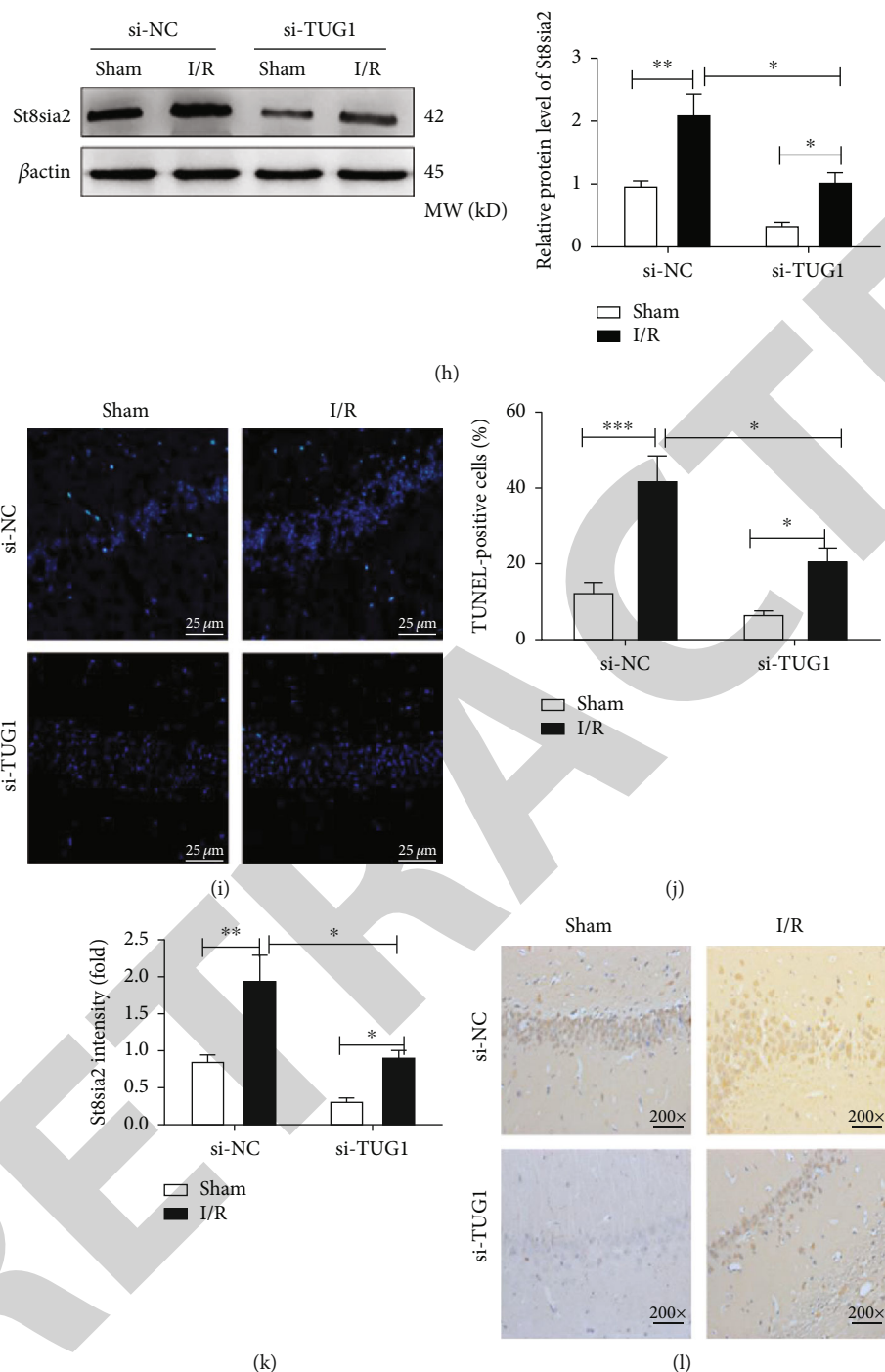


FIGURE 2: TUG1 knockdown attenuated *in vivo* ischemic injuries, accompanied by reduced St8sia2 and elevated miR-3072-3p levels. (a) Images of brain sections (underwent sham operation or I/R treatment combined with si-TUG1 or si-NC) with TTC staining, the infarction zones were stained white. (b) Cerebral infarct ratio quantified by ImageJ. (c) Neurological deficit scores; the higher score represents more severe neurological deficit. (d) Expression of cerebral TUG1, miR-3072-3p, and St8sia2 at the transcript level in response to I/R combined with si-NC or si-TUG1 was quantitated by Q-PCR. (e) Expression of cerebral miR-3072-3p at the transcript level in response to I/R combined with si-NC or si-TUG1 was quantitated by Q-PCR. (f) Expression of cerebral St8sia2 at the transcript level in response to I/R combined with si-NC or si-TUG1 was quantitated by Q-PCR. (g) Cerebral Bcl-2/Bax protein levels in response to I/R combined with si-NC or si-TUG1 were measured by western blot analysis. (h) Cerebral St8sia2 protein levels in response to I/R combined with si-NC or si-TUG1 were measured by western blot analysis. (i) Representative tissue images of the TUNEL staining (scale bar = 25  $\mu$ m), cerebral cells with excessive DNA damage were stained with green (TUNEL), whereas the blue counterstaining (DAPI) localized the nuclei. (j) Cell apoptosis percentage was quantified based on TUNEL-positive cells. (k) IHC staining intensity of St8sia2 was quantified by ImageJ. (l) Representative IHC image for St8sia2 in brain tissues that underwent I/R treatment combined with si-NC or si-TUG1. \* $P < 0.05$ , \*\* $P < 0.01$ , and \*\*\* $P < 0.001$ .

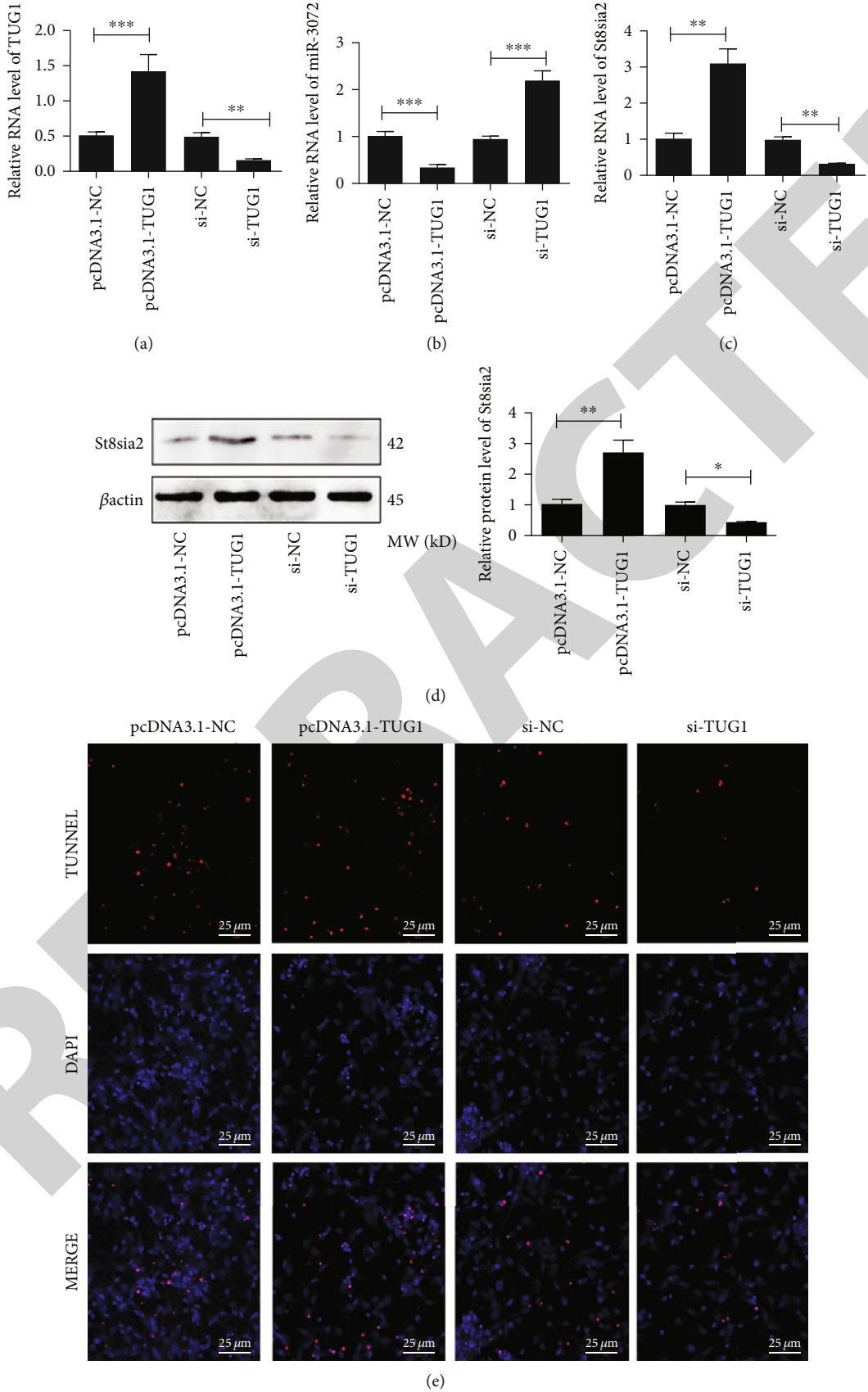


FIGURE 3: Continued.

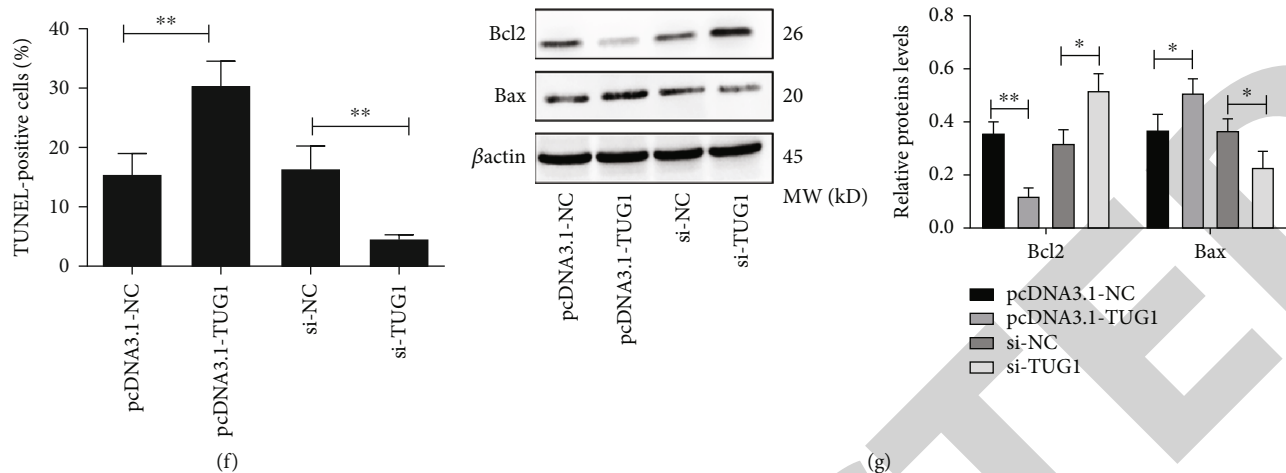


FIGURE 3: Forced overexpression of TUG1 resulted in ischemic-vulnerable phenotype of N2A cells opposite to that induced by TUG1 knockdown. (a–c) Expression of cerebral TUG1 at the transcript level in N2A cells underwent TUG1 overexpression (pc-DNA3.1-TUG1) or TUG1 knockdown (si-TUG1) was quantitated by Q-PCR. (b) Expression of cerebral miR-3072-3p at the transcript level in N2A cells (c) Expression of cerebral St8sia2 at the transcript level in N2A cells. (d, e) Bcl-2/Bax cell apoptosis percentage was quantified based on TUNEL-positive cells. (f) Representative cell images of the TUNEL staining (scale bar = 25  $\mu$ m), N2A cells with excessive DNA damage were stained with red (TUNEL), whereas the blue counterstaining (DAPI) localized the nuclei. (g) Protein levels in response to TUG1 overexpression/knockdown were measured by western blot analysis. \* $P < 0.05$ , \*\* $P < 0.01$ , and \*\*\* $P < 0.001$ .

male C57BL/6J mice (6–8 weeks of age,  $25 \pm 5$  g) supplied by the Shanghai SLAC Laboratory Animal Co., Ltd. (Shanghai, China). Following previously reported procedures, intraluminal middle cerebral artery occlusion (MCAO) [38] was performed to establish focal cerebral ischemia, followed by reperfusion 2 h later. Under isoflurane anesthetization, mice were placed on a heating panel kept at  $37.0^{\circ}\text{C} \pm 0.5^{\circ}\text{C}$  throughout the procedure. Animals after 24 h of reperfusion were reared for an additional two weeks and then euthanized. The same surgical procedure was performed on sham-operated mice in the absence of MCAO.

**2.2. Infarct Area Determination.** 2,3,5-Triphenyltetrazolium chloride monohydrate (TTC; Sigma-Aldrich) staining was performed to identify the brain infarct area 48 h post-MCAO treatment. In brief, 2 mm thick coronal brain slices were immobilized overnight in 10% formaldehyde after 15 min of soaking in 2% TTC solution. After observing the caudal and rostral surfaces of each slice, the percentage of infarct area was computed with the use of ImageJ software (NIH, USA).

**2.3. Evaluation of Neurological Deficits.** Referring to a previous neurological deficit score [39], mice were scored for neurological status 24 h postreperfusion with the criteria described as follows: 0: absence of observable deficits; 1: difficulty in fully extending the contralateral forelimb; 2: inability to extend the contralateral forelimb; 3: slight circling to the contralateral side; 4: severe circling to the unaffected side; 5: falling to the unaffected side. The evaluation and grading of the animals were made by a scientist who had no knowledge of treatments.

**2.4. Terminal Transferase Uridyl Nick End Labeling (TUNEL) Assay.** Apoptosis, as manifested by severely dam-

aged DNA, was assessed by TUNEL staining. N2A as well as mouse brain tissue staining was performed using either the ApopTag Kit S7100 (Millipore, Temecula, CA, USA) or TUNEL Apoptosis Detection Kit (Abbkine Scientific, Waltham, MA, USA) following the supplier's recommendations, whereas the cell nucleus was counterstained with DAPI. A Nikon ECLIPSE Ti confocal microscope ( $\times 200$  magnification) was utilized for the calculation of TUNEL-positive cell nuclei. The percentage of TUNEL-positive cell nuclei in 10 randomly selected fields was used to calculate the apoptosis (%) in each sample.

**2.5. Immunohistochemistry Analysis.** The brain tissues that underwent I/R or sham operation were subjected to 24 h of paraformaldehyde (4%) immobilization and paraffin embedding before being sliced into sections (5  $\mu$ m thickness). The prepared sections underwent subsequent dewaxing and antigen repair; the endogenous antigen was then inactivated by hydrogen peroxide. They were then treated with 3 PBS washes and 30 min of culture in 5% bovine serum albumen (BSA) prior to incubation ( $4^{\circ}\text{C}$ ) with St8sia2-specific polyclonal antibody (Proteintech Group, Rosemont, IL, USA). 24 h postincubation, the resultant reactions were visualized by staining with horseradish peroxidase and diaminobenzidine. St8sia2 expression was evaluated based on IHC images using ImageJ software.

**2.6. Stereotaxic Injection.** After anesthesia, the mice were fixed to a stereotaxic apparatus supplied by David Kopf Instruments, Tujunga, CA, USA. Then, a mixture prepared by si-TUG1/miR-3072-3p-mimic/si-St8sia2 (5  $\mu$ l) or corresponding scrambled controls (109 infectious units/ml; GenePharma, Shanghai, China) with *in vivo* RNAiMAX transfection reagent (Invitrogen) was administered via mouse lateral ventricle. MCAO was performed 24 h later.

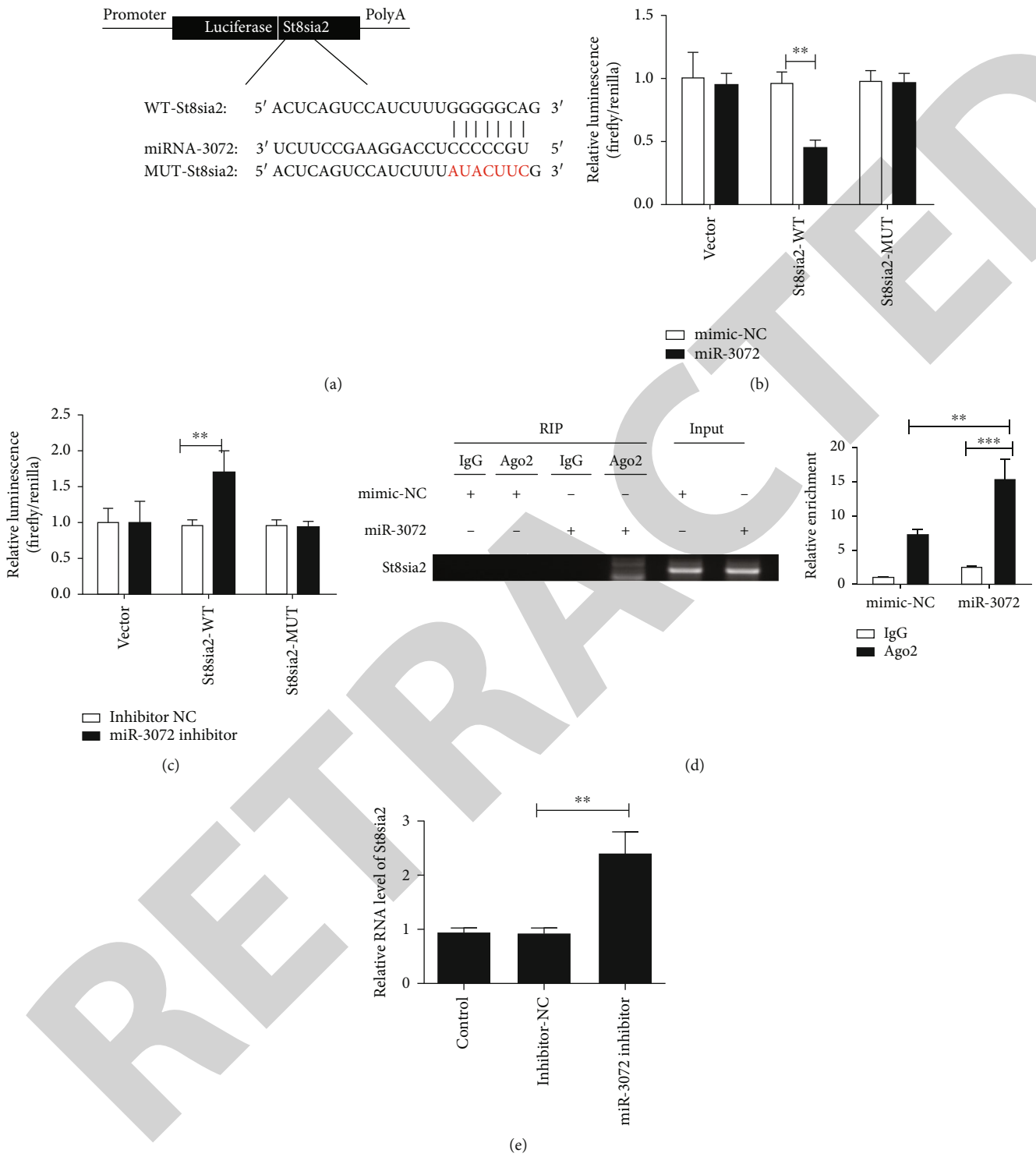


FIGURE 4: Continued.



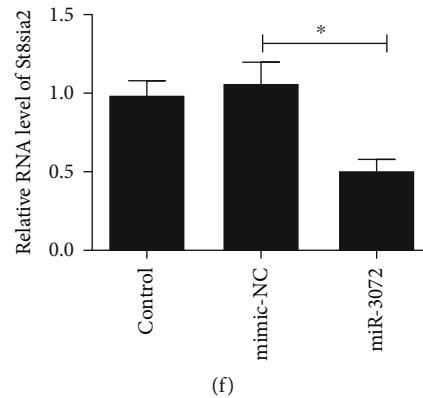


FIGURE 4: miR-3072-3p directly binds to St8sia2 and regulates St8sia2 expression. (a) The sequence of wild-type St8sia2 (St8sia2-WT) and the mutant St8sia2 with mutations at the predicted miR-3072-3p binding site (St8sia2-MUT). (b, c) The luciferase reporter vector carrying St8sia2-WT or St8sia2-MUT or the empty vector was cotransfected into N2A cells with miR-3072-3p mimic or mimic-NC, the relative luciferase activity was detected 48 h after transfection. (c) The luciferase reporter vector carrying St8sia2-WT or St8sia2-MUT or the empty vector was cotransfected into N2A cells with miR-3072-3p inhibitor or inhibitor-NC, the relative luciferase activity was detected 48 h after transfection. (d) The direct interaction between St8sia2 and miR-3072-3p was confirmed by RNA immunoprecipitation assay after being transfected with miR-3072-3p mimic or mimic-NC for 48 h. (e) Expression of St8sia2 in N2A cells at the transcript level was measured 48 h post miR-3072-3p inhibitor transfection. (f) Expression of St8sia2 in N2A cells at the transcript level was measured 48 h post miR-3072-3p mimic transfection. Untransfected cells were defined as control (control). \* $P < 0.05$ , \*\* $P < 0.01$ , and \*\*\* $P < 0.001$ .

0.2 mm posterior to bregma, 1.0 mm lateral to the midline, and 1.5 mm below the brain surface were used as stereotaxic coordinates.

**2.7. Cell Cultivation and Oxygen Glucose Deprivation/Reoxygenation (OGD/R) Model [40].** In a humidified incubator at 37°C with 5% CO<sub>2</sub> in air, mouse neuroblastoma cells (N2A; Cell Bank of Shanghai Institute of Cell Biology, Chinese Academy of Sciences, Shanghai, China) were cultivated in Dulbecco's Modified Eagle's Medium (DMEM; Invitrogen) added with 10% fetal bovine serum (FBS; Invitrogen) + 2 mM glutamine (Invitrogen) + 100 µg/ml streptomycin (Invitrogen) + 100 U/ml penicillin (Invitrogen). To investigate the impacts of ischemia *in vitro*, the cells underwent OGD treatment by 4 h of incubation (37°C) with opti-MEM (Invitrogen) in a hypoxic chamber with 5% CO<sub>2</sub> and 95% N<sub>2</sub> in air. The cells were then immersed in a normal culture medium and kept under normoxia (5% CO<sub>2</sub>, 37°C) for 24 h.

**2.8. Construction of Plasmid Cloning Vehicles and Transfection of Cells.** For TUG1 overexpression, pcDNA3.1-TUG1 plasmids were constructed via subcloning the mouse full-length TUG1 cDNA into the pcDNA3.1(+) mammalian expression vector (Invitrogen) at the KpnI and XhoI loci. DNA Midiprep kits (Qiagen, Germany) were employed for the isolation of all plasmids. N2A cells post pcDNA3.1-TUG1 transfection were collected using G418 (geneticin) to produce stable clones. Those with empty pcDNA3.1(+) vector (pcDNA3.1-NC) transfection functioned as negative control. As to miR-3072-3p overexpression and knockdown, the synthesis of miR-3072-3p mimic and inhibitor, along with two scrambled miRNAs that served as their corresponding negative controls (mimic-NC and inhibitor-NC for miR-3072-3p mimic and miR-3072-

3p inhibitor, respectively), was done at Qiagen (Germany). For all transfections, Lipofectamine 3000 reagent (Invitrogen) was used following the recommendations.

**2.9. qPCR Analysis.** The TRIzol (Invitrogen)-isolated total RNA from cell samples was quantified before being reversely transcribed. Reverse transcription reactions of RNA/miRNA were performed by PrimeScript™ RT Master Mix and SYBR® PrimeScript™ miRNA RT-PCR kit, respectively, both supplied by TaKaRa (Shiga, Japan). The primer sequences are shown in Table 1. According to the manufacturer's protocol, rapid real-time polymerase chain reaction (QPCR) and FastStart Essential DNA Green Master (Rosh, Indiana, USA) were employed for the determination of the levels of reverse-transcribed cDNA templates relative to β-actin. Each test was run in triplicate, and fold changes were computed by  $2^{-\Delta\Delta CT}$ , a relative quantification method. The device used for amplification tests was ROCHE 480II real-time PCR machine (ROCHE, USA).

**2.10. Western Blot.** Cells after cultivation were collected and lysed in RIPA lysis buffer (P0013B; Beyotime, Shanghai, China) after ice-cold PBS washing. After detecting the protein concentration using the BCA protein assay kit (P0012; Beyotime), the whole lysates were immersed in a 5x SDS loading buffer (P0015; Beyotime) at 1 : 4. Then, samples with equal amounts were subjected to isolation by sodium dodecyl sulfate (SDS) polyacrylamide gel electrophoresis (PAGE) and subsequent transfer onto PVDF membranes at 180 mA for 60 min. Blots were blocked for 2 h in TBST added with 5% skim milk and then cultivated (4°C) overnight with I antibodies. This was followed by treatment with horseradish peroxidase- (HRP-) labeled (1 : 1000, Cell Signaling Technology, USA) secondary antibodies. The I antibodies were anti-Bcl2 (1 : 1000, Cell Signaling Technology, USA), anti-Bax

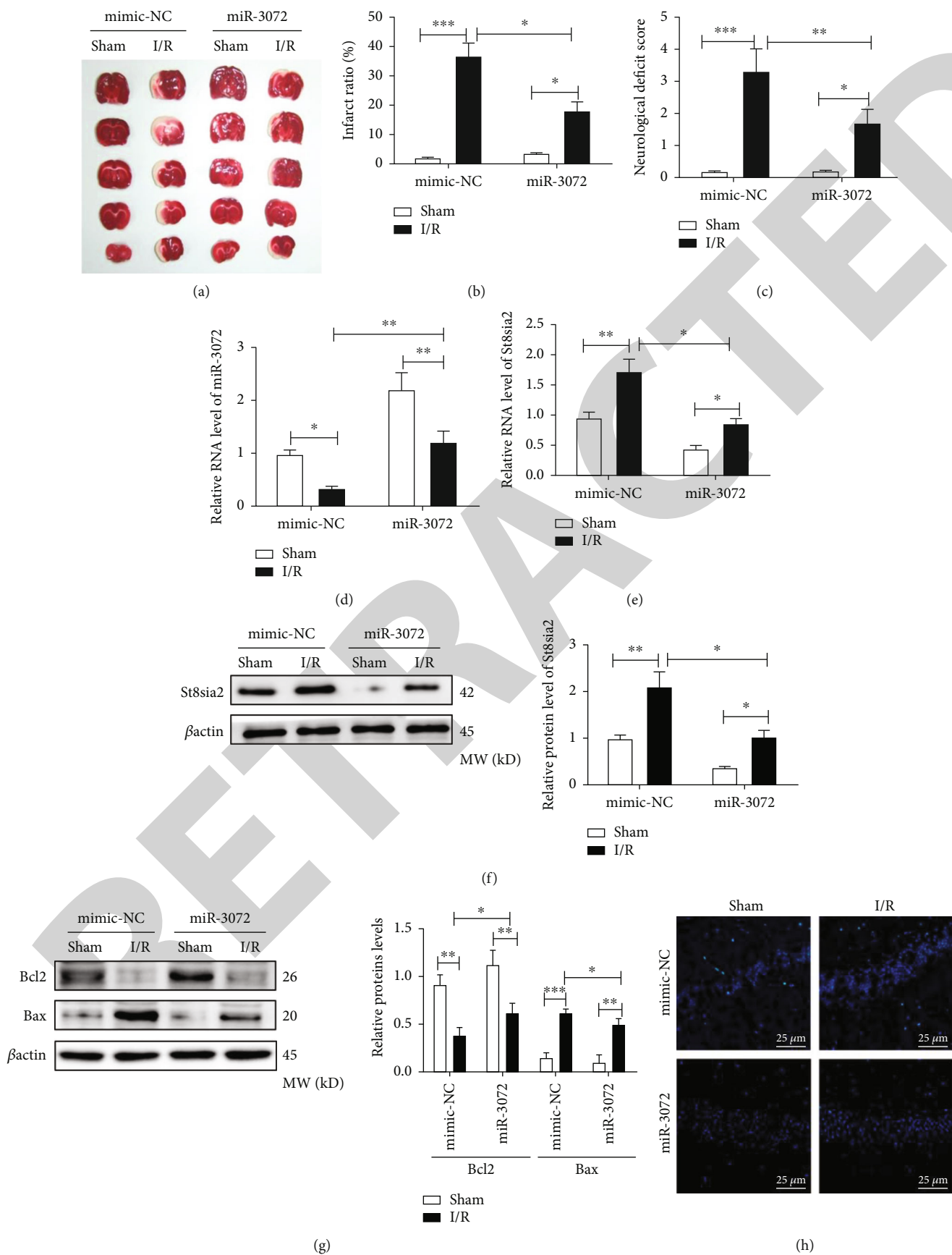


FIGURE 5: Continued.

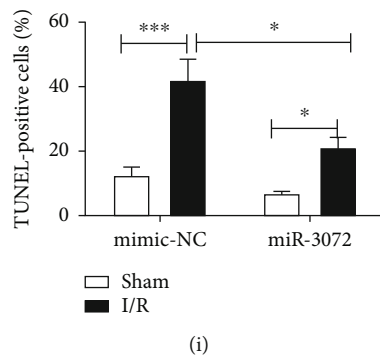


FIGURE 5: miR-3072-3p overexpression protects against I/R-induced ischemic injury in brain tissues. (a) Images of brain sections (underwent sham operation or I/R treatment combined with miR-3072 mimic or mimic-NC) with TTC staining, the infarction zones were stained white. (b) Cerebral infarct ratio quantified by ImageJ. (c) Neurological deficit scores; the higher score represents more severe neurological deficit. (d) Expression of cerebral miR-3072-3p at the transcript level in response to I/R combined with miR-3072 mimic or mimic-NC was quantitated by Q-PCR. (e) Expression of cerebral St8sia2 at the transcript level in response to I/R combined with miR-3072 mimic or mimic-NC was quantitated by Q-PCR. (f) Cerebral St8sia2 protein levels in response to I/R combined with si-NC or si-TUG1 were measured by western blot analysis. (g) Cerebral Bcl-2/Bax protein levels in response to I/R combined with si-NC or si-TUG1 were measured by western blot analysis. (h) Representative tissue images of the TUNEL staining (scale bar = 25  $\mu$ m), cerebral cells with excessive DNA damage were stained with green (TUNEL), whereas the blue counterstaining (DAPI) localized the nuclei. (i) Cell apoptosis percentage was quantified based on TUNEL-positive cells. \* $P < 0.05$ , \*\* $P < 0.01$ , and \*\*\* $P < 0.001$ .

(1 : 1000, Cell Signaling Technology, USA), and anti-St8sia2 (1 : 200, Proteintech, USA).  $\beta$ -Actin (1 : 1000, Cell Signaling Technology, USA) was the internal control. The protein expression was normalized to  $\beta$ -actin. Chemiluminescence was performed with an enhanced chemiluminescence detection kit to display protein bands according to the manufacturer's recommendations.

**2.11. Luciferase Reporter Gene Assay (LRGA).** By using StarBase and TargetScan with URLs of <http://starbase.sysu.edu.cn/mirMrna.php> and <http://www.targetscan.org>, respectively, putative miR-3072-3p binding sites in both the sequence of TUG1 and the 3'-UTR of St8sia2 were predicted. Genechem (Shanghai, China) was responsible for the synthesis of the wild-type (WT)/mutant (MUT) TUG1 sequence and the WT/MUT 3'-UTR fragment of St8sia2 containing putative miR-3072-3p binding sites and then came the cloning of the synthesized sequences into pmir-GLO dual luciferase reporter vector (Promega, Madison, WI, USA) downstream to generate TUG1-WT/MUT as well as St8sia2-WT/MUT luciferase reporter systems. Thereafter, N2A cells seeded onto 24-well plates were treated with luciferase reporter plasmids, miR-3072-3p mimic and its non-specific control mimic-NC, as well as miR-3072-3p inhibitor and its nonspecific control inhibitor-NC transfections for 48 h, either alone or in combination. The Dual LRGA system (Promega, Madison, WI, USA) was utilized for luciferase activity determination, and the data were normalized to a Renilla luciferase internal control.

**2.12. RNA Immunoprecipitation Assay.** RNA-IP was performed using a RIP Kit (Millipore, Billerica, MA, USA) following the manufacturer's protocol. After being transfected miR-3072 mimic or miR-NC, N2A cells were lysed in RNA immunoprecipitation (RIP) lysis buffer and magnetic beads conjugated to human anti-Ago2 antibody (Millipore) or

control IgG antibody. Then, the samples were digested with proteinase K, and RNA was extracted from the beads using TRIzol. Then, qRT-PCR analysis was performed to measure the enrichment of the miR-3072 and St8sia2.

**2.13. Statistical Analysis.** We used GraphPad Prism 8.0 (GraphPad Software, Inc., USA) to conduct statistical analyses. All data were exhibited as mean  $\pm$  standard error of the mean (SEM). The intergroup and multigroup comparison was made by Student's *t*-test and one-way analysis of variance (ANOVA) with Duncan's test, respectively, with the difference considered significant when  $P < 0.05$ .

### 3. Result

**3.1. In Vitro and In Vivo Ischemic Injuries Induced Upregulation of TUG1 and St8sia2 and Reduced miR-3072-3p Level.** C57BL/6J mice that underwent I/R (1.5 h/24 h) exhibited obvious nerve dysfunction and serious brain infarction (Figures 1(a)–1(c)), accompanied by elevated TUG1 and St8sia2 and reduced miR-3072-3p expression at the mRNA level (Figures 1(d)–1(f)). The ischemic injury was manifested by reduced Bax/Bcl-2 ratio in both *in vivo* and *in vitro* settings (Figures 1(g) and 1(h)). Consistent with the findings by western blot, TUNEL assay revealed an increased number of apoptotic N2A cells after OGD/R treatment (Figures 1(i) and 1(j)). The alterations of TUG1, miR-3072-3p, and St8sia2 in N2A cells undergoing OGD/R treatment were similar to those in the I/R mouse model (Figures 1(k)–1(m)). These findings suggested that TUG1, miR-3072-3p, and St8sia2 might orchestrate the ischemic process.

**3.2. TUG1 Knockdown Attenuated In Vivo Ischemic Injuries, Accompanied by Reduced St8sia2 and Elevated miR-3072-3p Levels.** Since we have confirmed that TUG1 was upregulated

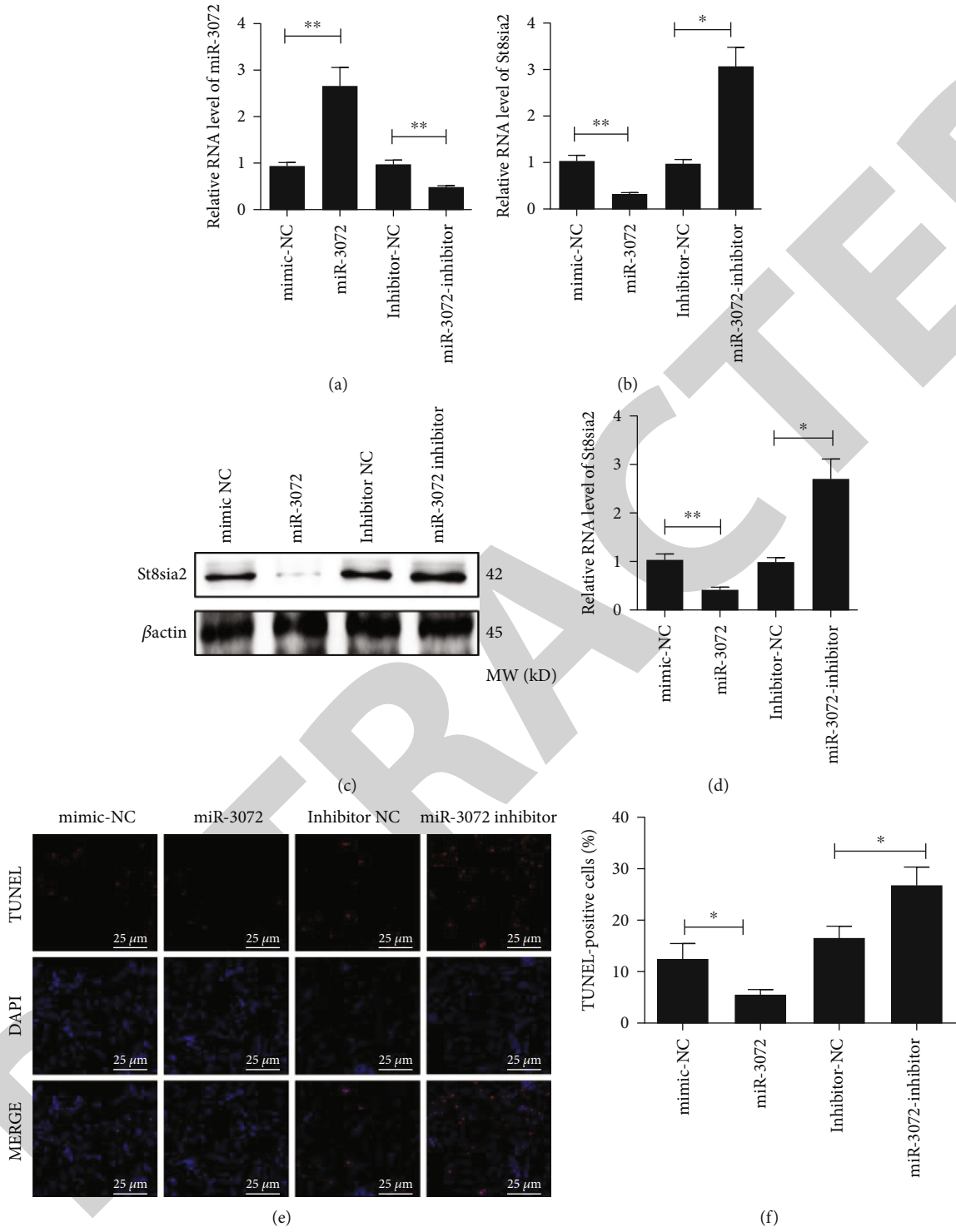


FIGURE 6: Continued.

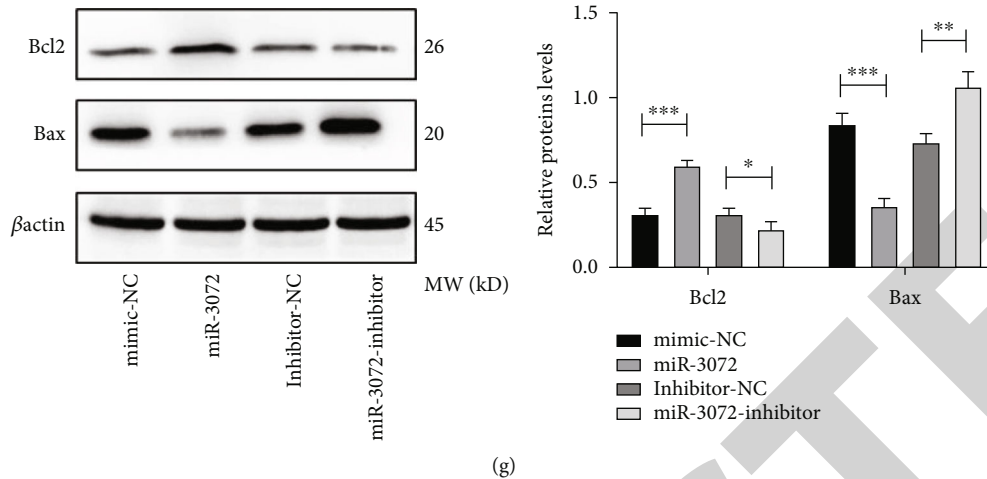


FIGURE 6: miR-3072-3p overexpression protects against OGD/R-induced ischemic injury in N2A cells. (a, b) Expression of cellular miR-3072-3p and St8sia2 at the transcript level after the treatment with miR-3072-3p mimic or inhibitor was quantitated by Q-PCR. (c) Bar plot of cellular St8sia2 at the protein level after treatment was measured by western blot. (d) Expression of cellular St8sia2 at the protein level after treatment was measured by western blot and quantified. (e) Representative cell images of the TUNEL staining (scale bar = 25  $\mu$ m), N2A cells with excessive DNA damage were stained with red (TUNEL), whereas the blue counterstaining (DAPI) localized the nuclei. (f) Cell apoptosis percentage was quantified based on TUNEL-positive cells. (g) Alteration of Bcl2/Bax expression in N2A cells at the protein level after the treatment of miR-3072-3p mimic/inhibitor. \* $P < 0.05$ , \*\* $P < 0.01$ , and \*\*\* $P < 0.001$ .

in response to ischemic injury, to further understand the regulatory role of TUG1 in this process, we performed siRNA-induced TUG1 knockdown combined with the induction of ischemic injury, as shown in (Figures 2(a)–2(d)); inhibited TUG1 expression led to the reduced infarct area and improved neurological deficit. These improvements were coincided with reduced St8sia2 and elevated miR-3072-3p expression at the mRNA level (Figures 2(e) and 2(f)). At the protein level, the reduced Bax/Bcl-2 ratio and St8sia2 expression (Figures 2(g) and 2(h)) were observed in mice undergoing TUG1 knockdown combined with I/R treatment by comparing their siNC+I/R treatment counterparts. Consistently, the TUNEL assay (Figures 2(h) and 2(i)) showed that the absence of TUG1 attenuated the apoptosis of brain tissue that underwent I/R, which coincided with reduced St8sia2 expression as revealed by IHC (Figures 2(k) and 2(l)).

**3.3. Forced Overexpression of TUG1 Resulted in an Ischemic-Vulnerable Phenotype of N2A Cells Opposite to That Induced by TUG1 Knockdown.** To further confirm the regulatory role of TUG1 in ischemic injury, we constructed a TUG1 overexpression cell model, namely, pcDNA 3.1-TUG1-N2A cells, to perform a comparison with the effect of si-TUG1 in an *in vitro* setting. As shown in (Figure 3(a)), both overexpression and knockdown of TUG1 were successful in N2A, and miR-3072-3p/St8sia2 in mRNA level was inversely/positively correlated to the modified TUG1 expression (Figures 3(b) and 3(c)). The change of St8sia2 at the protein level in response to altered TUG1 was consistent with that in the mRNA level (Figure 3(d)), while the increased/decreased Bax/Bcl ratio was induced by TUG1 overexpression/knockdown (Figure 3(g)), suggesting that TUG1 have a proapop-

totic effect, which was also verified by TUNEL assay (Figures 3(e) and 3(f)).

**3.4. miR-3072-3p Directly Binds to St8sia2 and Regulates St8sia2 Expression.** TargetScan (<http://www.targetscan.org>) website revealed a binding site between St8sia2 and miR-3072-3p (Figure 4(a)). To test this hypothesis, we first verified the interaction between St8sia2 and miR-3072-3p in the N2A cell model. As indicated by LRGAs, St8sia2-WT vector+miR-3072-3p mimic cotransfection significantly reduced the relative luminescence, whereas the addition of miR-3072-3p inhibitor induced an inverse trend and that no significant alteration regarding luminescence was observed in the St8sia2-MUT group (Figures 4(b) and 4(c)). The physical association between miR-3072 and St8sia2 was further confirmed by RIP analysis (Figure 4(d)). Moreover, as depicted in Figures 4(e) and 4(f), St8sia2 had an inverse connection with miR-3072-3p, further corroborating their interaction.

**3.5. miR-3072-3p Overexpression Protects from I/R-Induced Ischemic Injury in Brain Tissues.** As aforementioned, miR-3072-3p was downregulated in I/R-treated mouse brains; to better understand its role in ischemic injury, the reduced miR-3072-3p was reversed by the addition of exogenous miR-3072-3p mimic. As shown in Figures 5(a)–5(c), partial relief of I/R-induced ischemic injury was observed in the presence of miR-3072-3p mimic. In both I/R-treated and sham-operated groups, miR-3072-3p mimic effectively elevated miR-3072-3p expression (Figure 5(d)) and inhibited St8sia2 at both mRNA and protein (Figures 5(e) and 5(f)) levels, together with reduced Bax/Bcl ratio (Figure 5(g)) and attenuated apoptosis (Figures 5(h) and 5(i)).

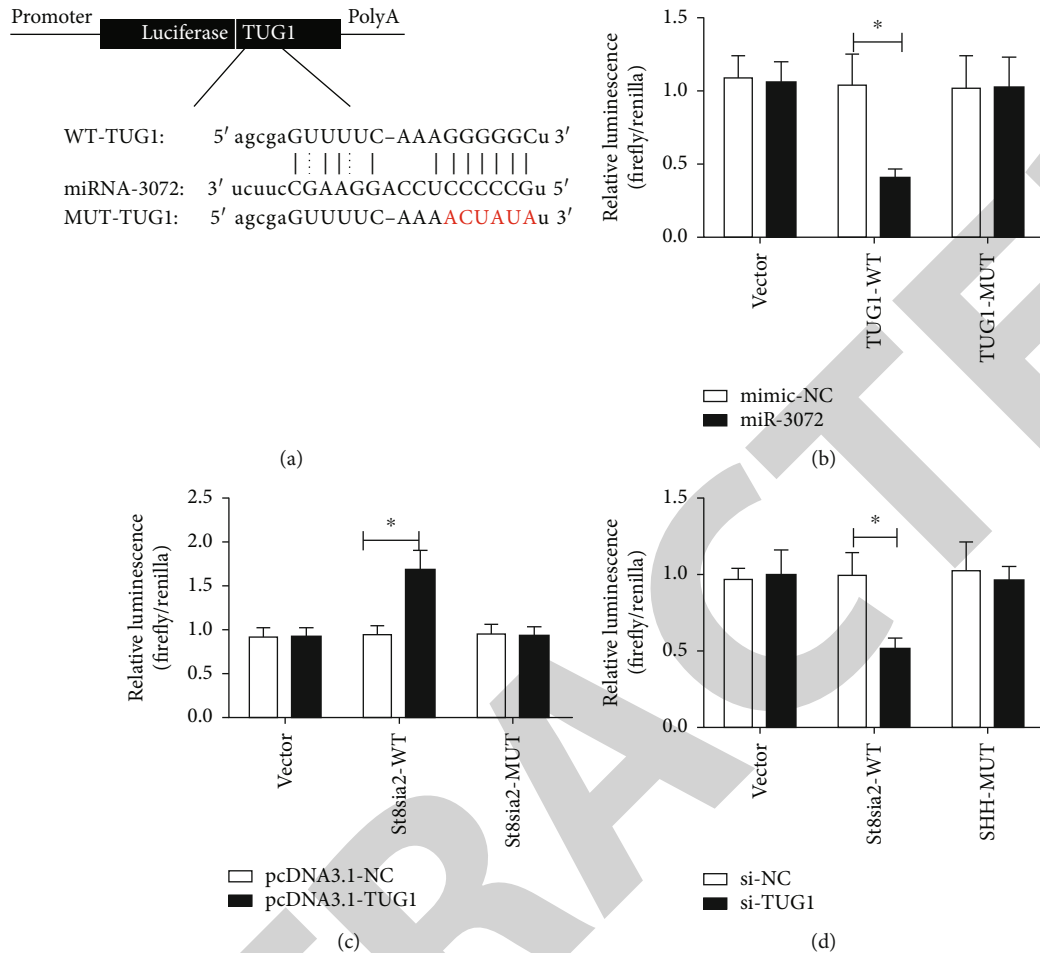


**FIGURE 7: TUG1 acts as a ceRNA for miR-3072-3p to target St8sia2.** (a) The sequence of wild-type TUG1 (TUG1-WT) and the mutant TUG1 with mutations at the predicted miR-3072-3p binding site (TUG1-MUT). (b) The luciferase reporter vector carrying TUG1-WT or TUG1-MUT or the empty vector was cotransfected into N2A cells with miR-3072-3p mimic or mimic-NC; the relative luciferase activity was detected 48 h after transfection. (c) The luciferase reporter vector carrying St8sia2-WT or St8sia2-MUT or the empty vector was cotransfected into N2A cells with pcDNA3.1-TUG1 (along with the corresponding control); the relative luciferase activity was detected 48 h after transfection. (d) The luciferase reporter vector carrying St8sia2-WT or St8sia2-MUT or the empty vector was cotransfected into N2A cells with si-TUG1 (along with the corresponding control); the relative luciferase activity was detected 48 h after transfection. \* $P < 0.05$ .

**3.6. miR-3072-3p Overexpression Protects against OGD/R-Induced Ischemic Injury in N2A Cells.** For the purpose of further validating the protective action of miR-3072-3p in an *in vitro* setting, we performed both overexpression and inhibition of miR-3072 in N2A cells; as shown in Figure 6(a), the treatments of miR-3072-3p mimic and inhibitor achieved the desired results. The addition of miR-3072-3p mimic/inhibitor resulted in reduced/elevated St8sia2 expression at the protein level (Figures 6(b)–6(d)) and was responsible for attenuated/aggravated apoptosis in N2A cells (Figures 6(e)–6(g)).

**3.7. TUG1 Acts as a ceRNA of miR-3072-3p Targeting St8sia2.** Combined with the above results, we speculate that there exists a potential TUG1/miR-3072-3p/St8sia2 axis in the regulation of ischemic stroke in the cerebral hemisphere. Recognizing that miR-3072-3p could directly bind to St8sia2, we focused on the connection between TUG1 and miR-3072-3p. After StarBase prediction of the putative bind-

ing site of miR-3072-3p in TUG1 (Figure 7(a)), LRGAs were performed for confirmation. First, the interaction between miR-3072-3p and TUG1 was confirmed in Figure 7(b), where luminescence of the TUG1-WT group cotransfected with miR-3072-3p was significantly reduced, indicating that the miR-3072-3p could directly bind to TUG1; next, the indirect interaction between TUG1 and St8sia2 was confirmed in Figures 7(c) and 7(d), where overexpressed/inhibited TUG1 significantly increased/decreased the relative luminescence of the St8sia2-WT group, indicating that TUG1 might function as a ceRNA to modulate St8sia2. Finally, a TUG1-miR-3072-3p-St8sia2 regulatory axis was confirmed.

**3.8. St8sia2 Might Account for the Regulatory Effects of the TUG1-miR-3072-3p-St8sia2 Axis in Both In Vivo and In Vitro Settings.** Since proteins were responsible for the majority of biological processes [41], we speculated that the

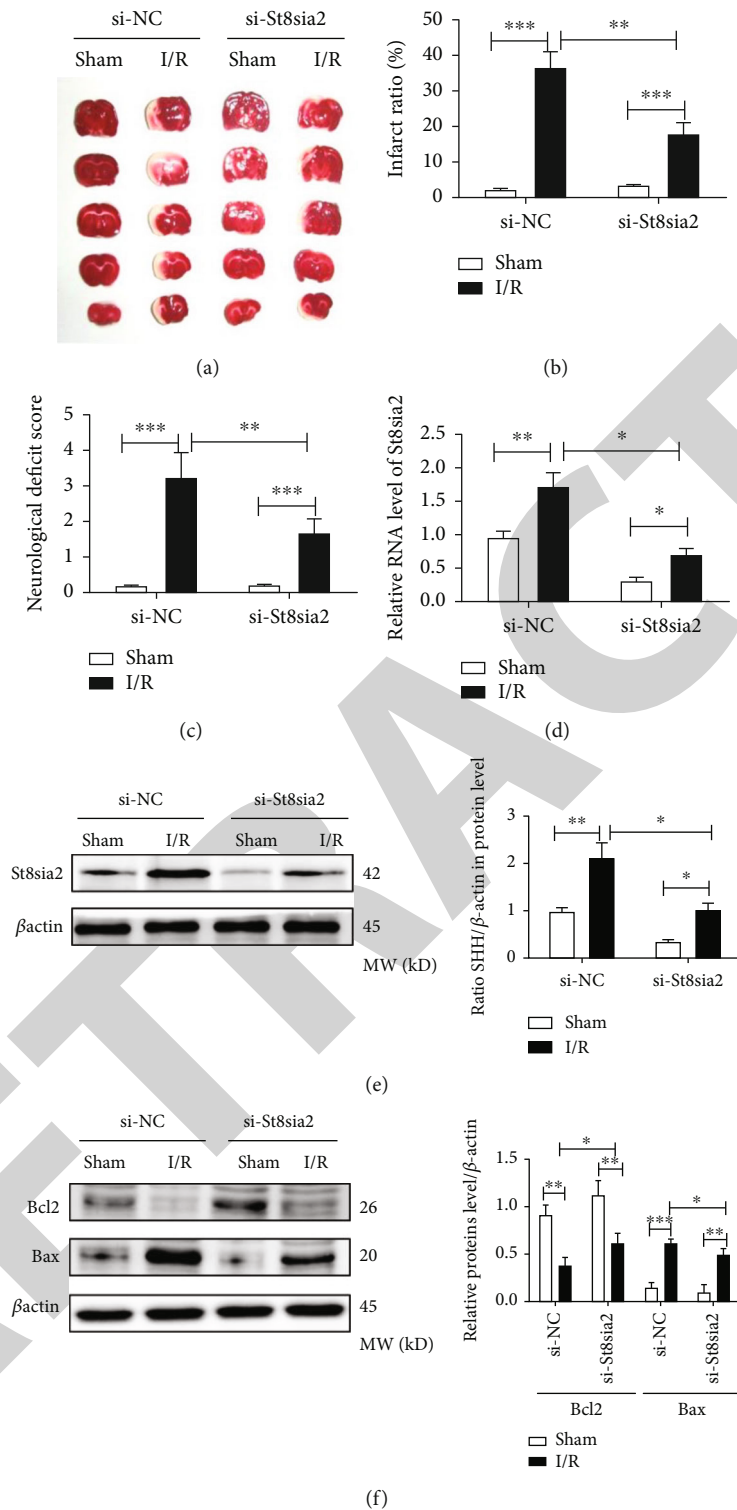
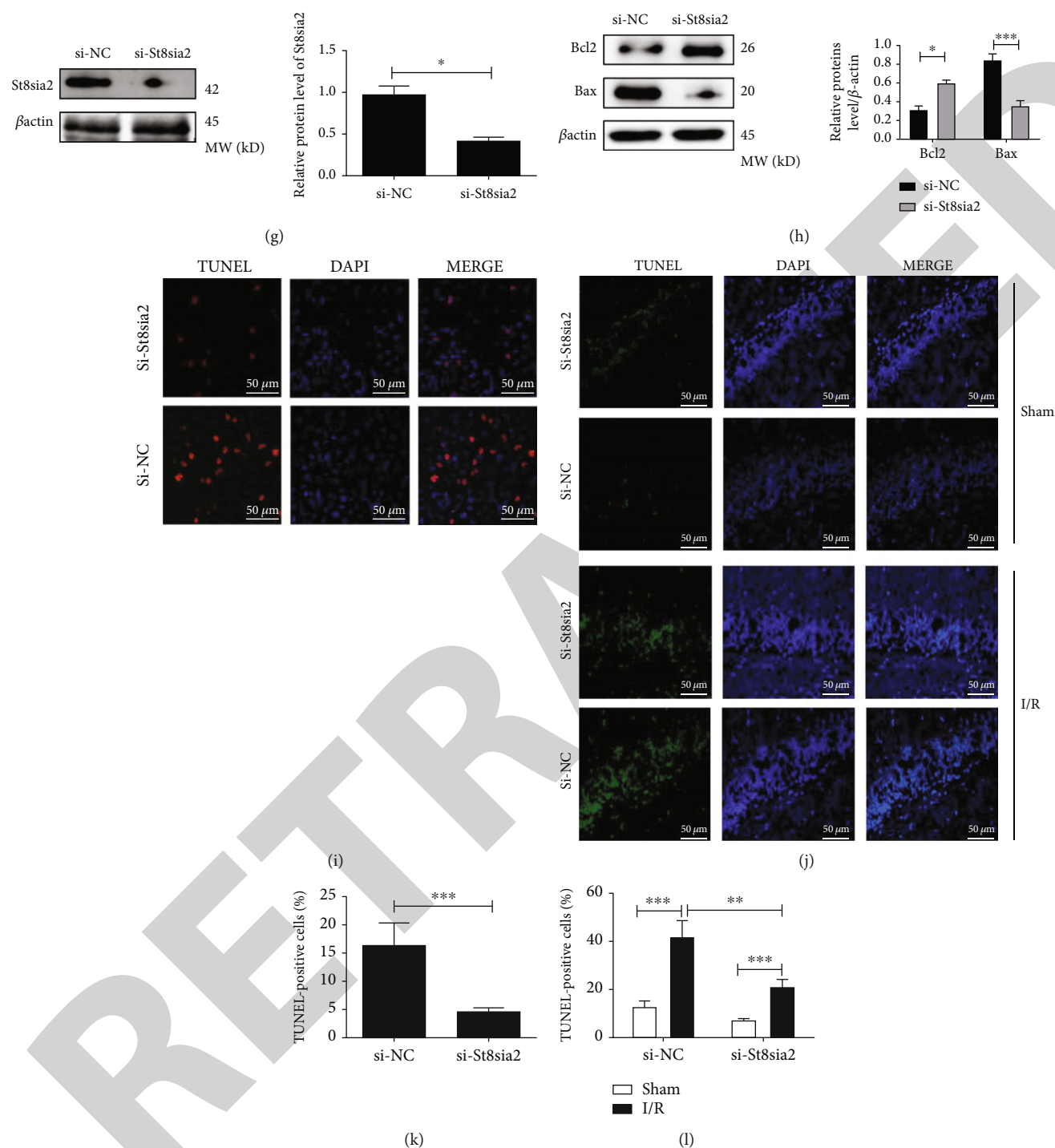


FIGURE 8: Continued.



**FIGURE 8:** St8sia2 might account for the regulatory effects of the TUG1-miR-3072-3p-St8sia2 axis in both *in vivo* and *in vitro* settings. (a) Images of brain sections (underwent sham operation or I/R treatment combined with si-St8sia2 or si-NC) with TTC staining, the infarction zones were stained white. (b) Cerebral infarct ratio quantified by ImageJ. (c) Neurological deficit scores; the higher score represents more severe neurological deficit. (d) Expression of cerebral St8sia2 at the transcript level in response to I/R combined with si-St8sia2 mimic or si-NC was quantitated by Q-PCR. (e) Cerebral St8sia2 protein levels in response to I/R combined with si-St8sia2 mimic or si-NC treatment were measured by western blot analysis. (f) Cerebral Bcl-2/Bax protein levels. (g) Alteration of St8sia2 expression in N2A at the protein level after the treatment of si-St8sia2 mimic or si-NC. (h) Alteration of Bcl-2/Bax expression in N2A at the protein level after the treatment of si-St8sia2 mimic or si-NC. (i) Representative tissue images of the TUNEL staining (scale bar = 50  $\mu$ m), N2A cells with excessive DNA damage were, respectively, stained with green/red (TUNEL), whereas the blue counterstaining (DAPI) localized the nuclei. (j) Representative tissue images of the TUNEL staining (scale bar = 50  $\mu$ m) of cerebral cells. (k) Cell apoptosis percentage of N2A cells was quantified based on TUNEL-positive cells. (l) Cell apoptosis percentage of cerebral cells was quantified based on TUNEL-positive cells. \* $P < 0.05$ , \*\* $P < 0.01$ , and \*\*\* $P < 0.001$ .



TUG1-miR-3072-3p-St8sia2 axis might converge on St8sia2. To test this hypothesis, we performed St8sia2 knockdown in both *in vivo* and *in vitro* settings. As shown in Figures 8(a)–8(c), St8sia2 knockdown significantly alleviated the I/R-induced *in vivo* ischemic injury, which might be ascribed to the high inhibitory efficiency of si-St8sia that significantly reduced the St8sia2 expression in response to I/R treatment (Figure 8(d)). Next, we detected the expression of St8sia2 and apoptosis markers in I/R-treated mouse brains; as shown in (Figure 8(e)), si-St8sia significantly reversed the I/R-induced elevation of St8sia2 level in mouse brains, accompanied by reduced Bax/Bcl2 ratio (Figure 8(f)); similar trends were observed in N2A *in vitro* cell model (Figures 8(g) and 8(h)). The si-St8sia2-mediated attenuation of apoptosis was further confirmed by TUNEL assay *in vitro* (Figures 8(i) and 8(j)) and *in vivo* (Figures 8(k) and 8(l)).

#### 4. Discussion

Aberrant lncRNA expression was observed in stroke; in a previous study, thousands of differentially expressed lncRNA in patients who underwent ischemic stroke were detected by high-throughput method based on peripheral blood [42]. Several lncRNAs were related to specific ischemic processes, including inflammation and cell death induced by ischemic injury and angiogenesis that are responsible for postischemic repair and regeneration [43]. Hence, lncRNAs might serve as diagnostic markers or therapeutic target for alleviating ischemic symptoms. Altered miRNA profile was also reported in both animal stroke models and stroke patients [10]; importantly, miRNA could directly target and regulate proteins that were involved in stroke-related processes, such as plasminogen activator inhibitor-1 and MMP-9 [44]. Several miRNA such as miR-26a and miR145 exhibited neuroprotective properties by elevating the expression of interferon- (IFN-) beta (anti-inflammatory cytokine) [45]. In addition, the therapeutic potential of antagomirs (anti-miRNAs) has been confirmed in a number of *in vivo* models [46]. Hence, miRNAs are also a promising candidate for combating stroke. The latest research found that lncRNA-miRNA-mRNA constitutes an intricate regulatory network that participates in the pathophysiology of ischemic stroke and plays an important role in neuroprotection and postischemic recovery [47]. This work identified that TUG1, as a ceRNA for miR-3072-3p to target St8sia2, was a regulator of ischemic stroke.

Although it was previously reported that the number of cells with PSA- (synthesized by St8sia2-) NCAM marker was elevated in response to ischemia [33], the exact function of St8sia2 in stroke has not yet been completely clarified. In this research, we first determined an evident increase in St8sia2 expression in mouse brains under I/R as well as in N2A cells exposed to OGD/R and that elevated St8sia2 was accompanied by increased apoptosis. Previously, the enzymatic product of St8sia2, namely, PSA, was proposed to be responsible for polysialylation [48] that exerted proapoptotic effects in granulosa cells [49], which was in line with its proapoptotic property in the present study. It should also be noted that PSA regulate brain development and neural

cell migration [50], which might be important for the repair of cerebral-ischemic injury. Hence, in the cerebral ischemia setting, St8sia2 might be a double-edged sword, and the adverse effects of St8sia2 might be ascribed to its interaction with other ischemia-promoting factors.

TUG1 was also recognized as a promoter of cardiomyocyte apoptosis through indirectly regulating proapoptotic KLF5 via miR-9a-5p [51]; in this study, we also found a positive correlation between TUG1 and ischemia-induced cerebral apoptosis. Moreover, we observed an elevated TUG1 expression that coincided with aggravated ischemic injury after I/R treatment, which was later reversed by TUG1 knockdown; these results also agreed with the observations of TUG1-promoted myocardial infarction [51]. Collectively, we discovered that TUG1 could also aggravate the cerebral ischemic injury and induce apoptosis in experimental models, in addition to its ischemia-promoting role in cardiomyocyte that was already established [51]. Li et al. [52] demonstrated that inhibiting the expression of TUG1 could protect mouse astrocyte cells and reverse the decrease in growth viability and increasing apoptosis of mouse astrocyte cells caused by OGD/R stimulation.

Intriguingly, the elevation of St8sia2 after the induction of ischemic injury coincided with increased TUG1/decreased miR-3072-3p expression. Subsequently, the binding of miR-3072-3p to both TUG1 and St8sia2 was confirmed by LRGAs. Although the exact role of miR-3072-3p was not previously reported, due to its inhibitory effect on ischemic apoptosis (confirmed by miR-3072-3p knockdown alone), we propose that miR-3072-3p not only serve as a bridge between TUG1 and St8sia2 but also alleviate the ischemic injury. In addition, previous study [53] has found that TUG1 aggravated cerebral ischemia and reperfusion injury by sponging miR-493-3p/miR-410-3p. This suggested that TUG1 might obtain the same mechanism by sponging miR-3072-3p.

Notably, inhibition of TUG1/St8sia2 or overexpression of miR-3072-3p partially antagonized the ischemic injury in several aspects including reduced infarct area, decreased neurologic deficit score, and attenuated apoptosis. Specifically, knockdown of St8sia2 alone exhibited an anti-ischemic effect similar to that induced by TUG1 inhibition/miR-3072-3p overexpression, suggesting that the effect of TUG1-miR-3072-3p/St8sia2 axis might converge on St8sia2.

However, the mechanism of the effect of the TUG1-miR-3072-3p/St8sia2 axis still needs to be further studied. There might be another signaling pathway involved with the TUG1-miR-3072-3p/St8sia2 axis to coprotect cerebral ischemia/reperfusion injury. Our prospect is to deeply investigate the TUG1-miR-3072-3p/St8sia2 axis in cerebral ischemia/reperfusion injury and apply it into clinical aspect which hopefully is a potential choice for the diagnosis/treatment of ischemic stroke.

#### 5. Conclusion

In summary, the regulatory cascade identified in the current study provides a novel perspective for understanding the molecular mechanism underlying the pathogenesis of

ischemic stroke, as well as providing a theoretical basis for the diagnosis/treatment of ischemic stroke.

### Data Availability

The labeled dataset used to support the findings of this study are available from the corresponding author upon request.

### Conflicts of Interest

The authors declare that there are no competing interests.

### Authors' Contributions

Shuo Gu and Hairong Wang contributed to the design of the study and revised the manuscript. Miao Chen, Feng Wang, and Limin Fan drafted the manuscript, performed the experiments, and analyzed the data. All the authors read and approved the final version of the manuscript. Miao Chen and Feng Wang contributed equally to this work.

### Acknowledgments

This study was supported by (1) Project Supported by Hainan Province Clinical Medical Center, (2) Finance Science and Technology Project of Hainan Province (No. ZDYF2020225), (3) General Project of Shanghai Natural Science Foundation (18ZR14307000), and (4) 2020 Health Science and Technology Project of Pudong New Area Health Commission (PW2020D-5).

### References

- [1] V. L. Feigin, M. H. Forouzanfar, R. Krishnamurthi et al., "Global and regional burden of stroke during 1990-2010: findings from the Global Burden of Disease Study 2010," *The Lancet*, vol. 383, pp. 245–255, 2014.
- [2] W. Wang, D. Wang, H. Liu et al., "Trend of declining stroke mortality in China: reasons and analysis," *Neurology*, vol. 2, pp. 132–139, 2017.
- [3] B. Dobkin, "Clinical practice. Rehabilitation after stroke," *New England Journal of Medicine*, vol. 352, pp. 1677–1684, 2005.
- [4] Y. L. Wang, D. Wu, X. Liao, W. Zhang, X. Zhao, and Y. J. Wang, "Burden of stroke in China," *International Journal of Stroke*, vol. 2, pp. 211–213, 2007.
- [5] L. B. Goldstein, "Acute ischemic stroke treatment in 2007," *Circulation*, vol. 116, pp. 1504–1514, 2007.
- [6] Q. Dong, Y. Dong, L. Liu et al., "The Chinese Stroke Association scientific statement: intravenous thrombolysis in acute ischaemic stroke. Stroke and Vascular," *Neurology*, vol. 2, 2017.
- [7] S. Maiocchi, I. Alwis, M. Wu, Y. Yuan, and S. Jackson, "Thromboinflammatory functions of platelets in ischemia-reperfusion injury and its dysregulation in diabetes," *Seminars in Thrombosis and Hemostasis*, vol. 44, pp. 102–113, 2018.
- [8] S. W. Wang, Z. Liu, and Z. S. Shi, "Non-coding rna in acute ischemic stroke: mechanisms, biomarkers and therapeutic targets," *Cell Transplantation*, vol. 27, 2018.
- [9] H. Kaur, D. Sarmah, J. Saraf et al., "Noncoding RNAs in ischemic stroke: time to translate," *Annals of the New York Academy of Sciences*, vol. 1421, no. 1, pp. 19–36, 2018.
- [10] G. Koutsis, G. Siasos, and K. Spengos, "The emerging role of microRNA in stroke," *Current Topics in Medicinal Chemistry*, vol. 13, no. 13, pp. 1573–1588, 2013.
- [11] Y. Zhang, M. Wu, Y. Cao, F. Guo, and Y. Li, "Linking lncrnas to regulation, pathogenesis, and diagnosis of pulmonary hypertension," *Critical Reviews in Clinical Laboratory Sciences*, vol. 57, pp. 1–15, 2020.
- [12] H. Miao, L. Wang, H. Zhan, J. Dai, and X. Song, "A long non-coding rna distributed in both nucleus and cytoplasm operates in the pycard-regulated apoptosis by coordinating the epigenetic and translational regulation," *PLoS Genetics*, vol. 15, article e1008144, 2019.
- [13] S. J. Liu, T. J. Nowakowski, A. A. Pollen, J. H. Lui, and D. A. Lim, "Single-cell analysis of long non-coding rnas in the developing human neocortex," *Genome Biology*, vol. 17, no. 1, p. 67, 2016.
- [14] L. Statello, C. J. Guo, L. L. Chen, and M. Huarte, "Gene regulation by long non-coding RNAs and its biological functions," *Nature Reviews Molecular Cell Biology*, vol. 22, no. 2, pp. 96–118, 2021.
- [15] J. T. Lee and M. S. Bartolomei, "X-inactivation, imprinting, and long noncoding rnas in health and disease," *Cell*, vol. 152, pp. 1308–1323, 2013.
- [16] A. Saxena and P. Carninci, "Long non-coding rna modifies chromatin: epigenetic silencing by long non-coding rnas," *BioEssays*, vol. 33, pp. 830–839, 2011.
- [17] X. Zhang, W. Wang, W. Zhu et al., "Mechanisms and functions of long non-coding rnas at multiple regulatory levels," *International Journal of Molecular Sciences*, vol. 20, 2019.
- [18] Q. Yang, Q. Wan, L. Zhang et al., "Analysis of lncrna expression in cell differentiation," *RNA Biology*, vol. 15, pp. 413–422, 2018.
- [19] M. C. Jiang, J. J. Ni, W. Y. Cui, B. Y. Wang, and W. Zhuo, "Emerging roles of lncrna in cancer and therapeutic opportunities," *American Journal of Cancer Research*, vol. 9, 2019.
- [20] J. S. Mattick, "The state of long non-coding RNA biology," *Non-coding RNA*, vol. 4, no. 3, p. 17, 2018.
- [21] M. Muers, "Genome-wide views of long non-coding RNAs," *Nature Reviews Genetics*, vol. 12, no. 11, pp. 742–743, 2011.
- [22] T. R. Mercer, I. A. Qureshi, S. Gokhan et al., "Long noncoding rnas in neuronal-glia fate specification and oligodendrocyte lineage maturation," *BMC Neuroscience*, vol. 11, no. 1, p. 14, 2010.
- [23] A. Dharap, V. P. Nakka, and R. Vemuganti, "Effect of focal ischemia on long noncoding rnas," *Stroke*, vol. 43, pp. 2800–2802, 2012.
- [24] M. Farzaneh, F. M. Ali, N. S. Patel, B. G. Sahagan, W. Claes, and M. A. Lopez-Toledano, "Knockdown of BACE1-AS nonprotein-coding transcript modulates beta-amyloid-related hippocampal neurogenesis," *International Journal of Alzheimer's Disease*, vol. 2011, article 929042, 2011.
- [25] J. P. Lewandowski, G. Dumbovi, A. R. Watson, T. Hwang, and J. L. Rinn, "The tug1 lncrna locus is essential for male fertility," *Genome Biology*, vol. 21, no. 1, p. 237, 2020.
- [26] Q. Li, J. Zhang, D. M. Su, L. N. Guan, and R. J. Yang, "Lncrna tug1 modulates proliferation, apoptosis, invasion, and angiogenesis via targeting mir-29b in trophoblast cells," *Human Genomics*, vol. 13, 2019.
- [27] H. Wang, S. Liao, H. Li, Y. Chen, and J. Yu, "Long non-coding rna tug1 sponges mir-145a-5p to regulate microglial

## Retraction

# Retracted: Radioanatomical Study of the Skull Base and Septum in Chinese: Implications for Using the HBF for Endoscopic Skull Base Reconstruction

### Oxidative Medicine and Cellular Longevity

Received 26 September 2023; Accepted 26 September 2023; Published 27 September 2023

Copyright © 2023 Oxidative Medicine and Cellular Longevity. This is an open access article distributed under the Creative Commons Attribution License, which permits unrestricted use, distribution, and reproduction in any medium, provided the original work is properly cited.

This article has been retracted by Hindawi following an investigation undertaken by the publisher [1]. This investigation has uncovered evidence of one or more of the following indicators of systematic manipulation of the publication process:

- (1) Discrepancies in scope
- (2) Discrepancies in the description of the research reported
- (3) Discrepancies between the availability of data and the research described
- (4) Inappropriate citations
- (5) Incoherent, meaningless and/or irrelevant content included in the article
- (6) Peer-review manipulation

The presence of these indicators undermines our confidence in the integrity of the article's content and we cannot, therefore, vouch for its reliability. Please note that this notice is intended solely to alert readers that the content of this article is unreliable. We have not investigated whether authors were aware of or involved in the systematic manipulation of the publication process.

In addition, our investigation has also shown that one or more of the following human-subject reporting requirements has not been met in this article: ethical approval by an Institutional Review Board (IRB) committee or equivalent, patient/participant consent to participate, and/or agreement to publish patient/participant details (where relevant).

Wiley and Hindawi regrets that the usual quality checks did not identify these issues before publication and have since put additional measures in place to safeguard research integrity.

We wish to credit our own Research Integrity and Research Publishing teams and anonymous and named external

researchers and research integrity experts for contributing to this investigation.

The corresponding author, as the representative of all authors, has been given the opportunity to register their agreement or disagreement to this retraction. We have kept a record of any response received.

### References

- [1] D. Gu, "Radioanatomical Study of the Skull Base and Septum in Chinese: Implications for Using the HBF for Endoscopic Skull Base Reconstruction," *Oxidative Medicine and Cellular Longevity*, vol. 2022, Article ID 9940239, 11 pages, 2022.

## Research Article

# Radioanatomical Study of the Skull Base and Septum in Chinese: Implications for Using the HBF for Endoscopic Skull Base Reconstruction

Dongsheng Gu <sup>1,2</sup>

<sup>1</sup>Department of Otolaryngology-Head and Neck Surgery, The Affiliated Huaian No. 1 People's Hospital of Nanjing Medical University, Huai'an City, Jiangsu Province, China

<sup>2</sup>Department of Otolaryngology-Head and Neck Surgery, ENT Hospital of Huaian, Huai'an City, Jiangsu Province, China

Correspondence should be addressed to Dongsheng Gu; [gudongsheng@139.com](mailto:gudongsheng@139.com)

Received 26 January 2022; Revised 22 February 2022; Accepted 4 March 2022; Published 29 March 2022

Academic Editor: Anwen Shao

Copyright © 2022 Dongsheng Gu. This is an open access article distributed under the Creative Commons Attribution License, which permits unrestricted use, distribution, and reproduction in any medium, provided the original work is properly cited.

**Objective.** Radioanatomy provides surgeons with different choices to prevent the failure of reconstruction caused by improper flap selection and the occurrence of CSF leakage or other severe complications. To establish a radioanatomical model, this study radioanatomically investigated the use of the Hadad-Bassagasteguy nasoseptal flap (HBF) in skull base reconstruction performed via the transthemoidal, transsphenoidal, and transclival approaches to provide preoperative guidance for the selection of approaches for skull base reconstruction and preparation of the HBF. **Methods.** The computed tomography images of 40 Chinese adults were selected for the radioanatomical measurement of data related to the HBF and skull base reconstruction via the transthemoidal, transsphenoidal, and transclival approaches. The results were analyzed using radioanatomy combined with SPSS-based analysis. **Results.** In the 40 patients, the area of the HBF exceeded that of skull base defects reconstructed via the transthemoidal approach by  $10.21 \pm 1.97 \text{ cm}^2$ , and the anterior margin width, posterior margin width, upper margin length, and lower margin lengths of the HBF all exceeded the corresponding values of skull base defects requiring reconstruction by at least 8.4 mm. The area of the HBF exceeded that of reconstructed skull base defects by an average of  $10.72 \pm 2.04 \text{ cm}^2$ . The area of the HBF exceeded that of skull base defects reconstructed via the transclival approach by  $9.01 \pm 2.87 \text{ cm}^2$ . The difference between the anterior margin width of the HBF and the middle width of skull base defects reconstructed via the transclival approach did not exceed 6 mm in only one case (5.4 mm). **Conclusion.** In Chinese adults, the HBF can cover skull base defects reconstructed via the transthemoidal, transsphenoidal, and transclival approaches, permitting its use in skull base reconstruction performed via all three approaches. Radioanatomy can be used for preoperative guidance to plan surgery via the transthemoidal, transsphenoidal, and transclival approaches.

## 1. Introduction

Endoscopic skull base surgery was initially used to treat pituitary macroadenoma and cerebrospinal rhinorrhea with endoscopic visualization. Currently, it is selectively used to treat lesions located from the frontal sinus to the clivus, including lesions in the anterior, middle, and posterior cranial fossae through the ethmoidal plate, sella turcica/sphenoid bone, and clivus [1, 2]. The development of skull base surgery has been restricted by difficulties with defect reconstruction. Reconstruction of the skull base barrier is

conducted to permanently separate the nasal cavity, nasal sinus, and cranial cavity; eliminate postoperative dead space; and protect the physiological functions of the brain as well as important nerves and blood vessels. Therefore, the main challenges of skull base surgery include reconstructing dural defects and preventing cerebrospinal fluid (CSF) leakage [3]. Similar to reconstruction techniques used in open surgery, endoscopic repair must achieve multiple goals: reestablishing the separation between the sterile cranial cavity and nasal cavity colonized by microorganisms, preventing CSF from leaking through the defects, and filling the cavity after

tumor resection [3]. The advantages of transcranial endoscopic skull base surgery include low surgical trauma, good tumor exposure, complete resection, and rapid postoperative recovery. The low success of skull base reconstruction is one of the main obstacles preventing the widespread use of transcranial endoscopic skull base surgery [4]. The application of synthetic materials, intranasal and extranasal flaps, and autogenous free tissues in reconstruction after transcranial endoscopic skull base surgery has been reported with good results [5, 6]. Clinicians must increase their mastery of transcranial endoscopic skull base reconstruction because of the high incidence of CSF leakage during and after the surgery. The selection of repair materials and technologies as well as strategies for evaluating these materials has recently become a key area of focus for transcranial endoscopic skull base surgery [7].

In 2006, Hadad et al. [8] firstly designed the Hadad-Bassagasteguy nasoseptal flap (HBF) based on the posterior septal artery, which has been widely used in endoscopic skull base reconstruction. Pinheiro-Neto et al. [9] initially measured the linear data of the anterior skull base, sellar area, and clival area via multiplanar CT image reconstruction and also examined the length, width, and area of the pedicled nasoseptal flap to evaluate whether the tissue flap could completely cover skull base defects created during surgery via different intranasal approaches. A later study by Pinheiro-Neto et al. [10] introduced more parameters in the radioanatomical measurement, improved the selection of measurement markers and methods, expanded the sample size, and increased and improved parameter measurement.

Radioanatomy provides surgeons with different choices to prevent the failure of reconstruction caused by improper flap selection and the occurrence of CSF leakage or other severe complications. To select the proper strategy for skull base reconstruction, preoperative imaging can be used to evaluate the size of tissue flaps and defects. Our study used radioanatomy to explore the clinical significance of the HBF in reconstruction performed after endoscopic skull base surgery. The purpose of this study is to establish a radioanatomical model, carry out the radioanatomical study of HBF and transcribriform, transsphenoidal, and transclival skull base reconstruction, and evaluate the significance of HBF for reconstructing transcribriform, transsphenoidal, and transclival approach skull base defect. It also provides preoperative guidance for the approach size selection for transcribriform, transsphenoidal, and transclival skull base reconstruction and the preparation of HBF.

## 2. Materials and Methods

**2.1. Clinical Data.** Thin-slice axial computed tomography (CT; thickness = 0.3 mm, tube voltage = 110 kV, exposure time = 3.6 s) data of the skull base for 40 adults were used. Inclusion criteria are as follows: in adults (>17 years); including the complete skull base and nasal sinus, which could be used for subsequent MPR using software; exclusion criteria: fractures of the skull base, nasal cavity, or nasal sinus; the presence of tumors and other space-occupying

diseases; history of surgery head and face deformities. The included subjects (including 24 women and 16 men) were 21–78 years old (median, 44.5 years). This study was performed in accordance with policies approved by the Ethics Committee of the Affiliated Huaian No. 1 People's Hospital of Nanjing Medical University.

**2.2. Variables of the Sphenopalatine Foramen (SPF).** After multiplanar reconstruction of CT images, coronal images in which the inferior orbital fissure, pterygopalatine fossa, and SPF were all visible were selected, and the projection points of the SPF in the axial and midsagittal planes were located. Six variables were measured: the distance from the projection point of the SPF to the ipsilateral sphenoidal suture through the infra-anterior sphenoid sinus in the midsagittal position (Figure 1(a)); the distance from the projection point of the SPF to the sphenoidal suture through the base and posterior wall of the ipsilateral sphenoid sinus and then the superior margin of the dorsum sellae in the midsagittal plane (Figure 1(b)); the distance from the projection point of the SPF to the posterior margin of the planum sphenoidale through the base of the sphenoid sinus in the midsagittal plane (Figure 1(b)); the distance from the projection point of the SPF to the vertex of the posterior margin of the dorsum sellae through the base of the sphenoid sinus in the midsagittal plane (Figure 1(b)); the distance from the projection point of the SPF to the vertex of the posterior margin of the clivus through the base of the sphenoid sinus in the midsagittal plane (Figure 1(a)); and the distance from the SPF to the posterior margin of the nasal septum below the anterior wall of the sphenoid sinus in the axial plane (Figure 1(c)). In Figure 1(b), the green line presented the distances from the anterior of planum sphenoidale to tuberculum sellae, the blue line presented the distances from tuberculum sellae to the base of the sphenoid sinus, the red line presented the distances from the top of dorsum sellae to the base of the sphenoid sinus, and the white line presented the distances from SPF to the base of the sphenoid sinus.

**2.3. HBF Variables.** Five HBF variables were measured. The anterior margin width of the HBF was measured as the distance between the anterior nasal spine and rhinion in the midsagittal plane (Figure 2(a)). The posterior margin width of the HBF was measured as the distance from 10 mm below the ethmoidal roof to the nasal floor in the coronal plane (Figure 2(b)). The upper margin length of the HBF was measured as the distance from the rhinion 10 mm below the ethmoidal roof to the anterior wall of the sphenoid sinus in the midsagittal plane (Figure 2(a)). The lower margin length of the HBF was measured as the distance from the lowest end of the nasal septum to the front end of the palatine process of the maxilla in the midsagittal plane (Figure 2(a)). The area of the HBF was measured from the anterior wall of the sphenoid sinus 10 mm below the ethmoidal roof horizontally forward to the posterior wall of the frontal sinus, to the nasal floor forward and downward along the skin mucous junction of the nasal septum, horizontally backward to the posterior margin of the nasal

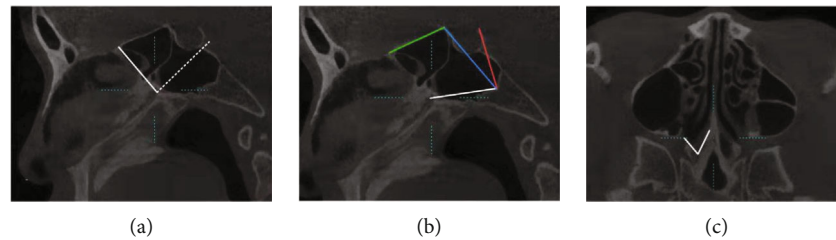


FIGURE 1: Sphenopalatine foramen (SPF) variables. (a) Distances from the SPF to the sphenothmoidal suture through the anterior sphenoid sinus (solid line) and to the clivus through the base of the sphenoid sinus in the midsagittal plane (dotted line). (b) Distances from the SPF to the sphenothmoidal suture through the sphenoid sinus (white + blue + green lines), to the posterior margin of the planum sphenoidale through the sphenoid sinus (white + blue lines), and to the upper margin of the dorsum sellae through the sphenoid sinus (white + red lines) in the midsagittal plane. (c) Distance from the SPF to the posterior margin of the nasal septum below the sphenoid sinus in the axial plane.

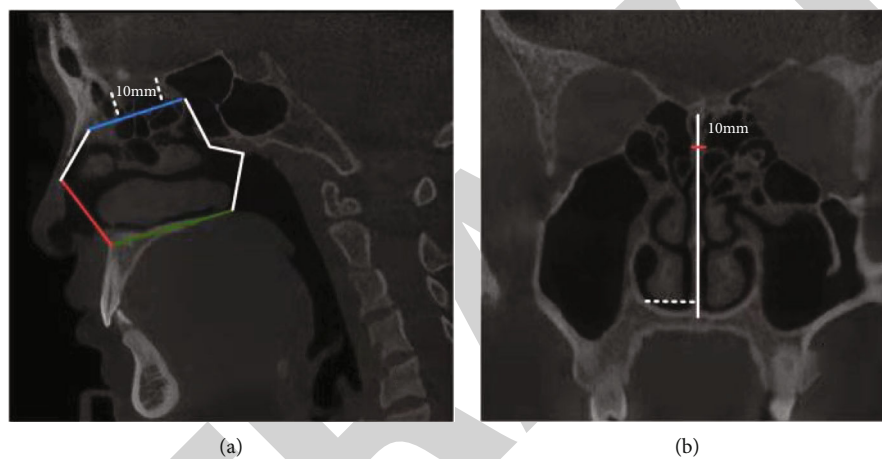


FIGURE 2: Hadad-Bassagasteguy nasoseptal flap (HBF) variables. (a) The anterior margin width (red line), upper margin length (blue line), lower margin length (white arrow), and area of the HBF (enclosed by solid lines). (b) The posterior margin width (solid line) and extended width of the HBF (dotted line).

septum, and then to the starting point upward along the anterior wall of the sphenoid sinus (Figure 2(a)). The width of the HBF could be extended to measure the distance between the lateral wall of the nasal cavity under the head end of the inferior turbinate and the nasal septum in the coronal plane (Figure 2(b)).

**2.4. Variables for Skull Base Reconstruction Performed via the Transethmoidal Approach.** Four variables were measured. The anterior margin width was measured as the horizontal distance between the orbital plates of the ethmoid bone at the bilateral anterior ethmoidal foramina in the coronal plane (Figure 3(a)). The posterior margin width was measured as the horizontal distance between the orbital plates of the ethmoid bone at the bilateral sphenothmoidal sutures in the coronal plane (Figure 3(b)). The defect length was measured as the distance between the frontoethmoidal and sphenothmoidal sutures in the midsagittal plane (Figure 3(c)). The defect area was measured as the rectangular area of the bilateral orbital plates of the ethmoid bone between the posterior wall of the frontal sinus and the anterior wall of the sphenoid sinus (Figure 3(d)).

**2.5. Variables for Skull Base Reconstruction Performed via the Transsphenoidal Approach.** Seven variables were measured. The anterior margin width was measured as the horizontal distance between the bilateral sphenothmoidal sutures in the coronal plane (Figure 3(b)). The middle width was measured as the distance between the bilateral optic struts in the coronal plane (Figure 4(a)). The posterior margin width was measured as the distance between the bilateral paraclinoid internal carotid arteries in the coronal plane (Figure 4(b)). The length of the planum sphenoidale was measured as the distance between the sphenothmoidal suture and the tuberculum sellae in the midsagittal plane (Figure 4(c)). The length of the roof of the sella turcica was measured as the distance between the tuberculum sellae and the upper end of the dorsum sellae in the midsagittal plane (Figure 4(c)). The total length was measured as the distance between the sphenothmoidal suture and the upper end of the dorsum sellae in the midsagittal plane (Figure 4(c)). The defect area was measured by locating the ethmoidal roof in the midsagittal position and measuring the area forward to the sphenothmoidal suture and backward to the upper end of the dorsum sellae and bilateral optic strut (Figure 4(d)).

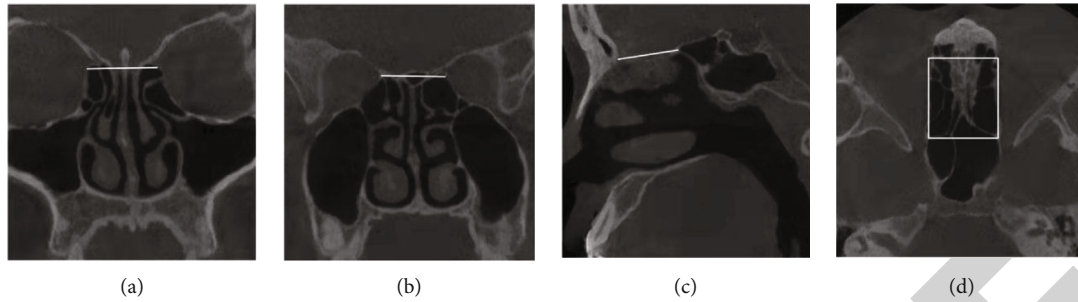


FIGURE 3: Measurements in skull base reconstruction performed via the transethmoidal approach. (a) Anterior margin width. (b) Posterior margin width. (c) Length. (d) Area.

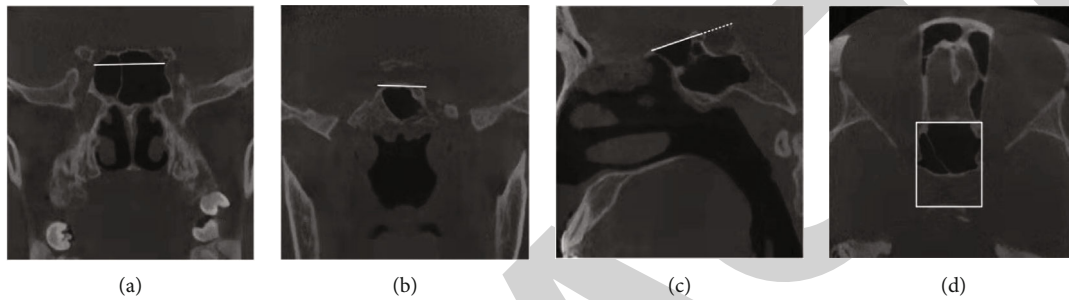


FIGURE 4: Variables for skull base reconstruction performed via the transsphenoidal approach. (a) Middle width. (b) Posterior margin width. (c) Planum sphenoidale (solid line), the length of the sella turcica (dotted line), and the total length (solid line + dotted line). (d) Area.

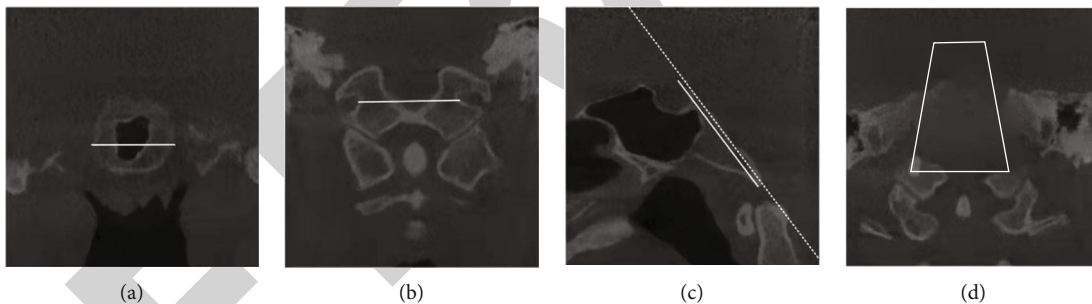


FIGURE 5: Variables for skull base reconstruction performed via the transclival approach. (a) Middle width. (b) Lower margin width. (c) Length (solid line), clivus section (dotted line). (d) Area.

**2.6. Variables for Skull Base Reconstruction Performed via the Transclival Approach.** Five variables were measured. The posterior margin width was measured as the distance between the bilateral paraclinoid internal carotid arteries in the coronal or axial plane (Figure 4(b)). The middle width was measured as the distance between the bilateral internal carotid arteries at the lacerated foramen in the coronal or axial plane (Figure 5(a)). The lower margin width was measured as the distance between the internal margins of the external orifice of the bilateral hypoglossal canals in the coronal or axial plane (Figure 5(b)). The clivus length was measured as the distance between the head end and tail end of the clivus in the midsagittal plane (Figure 5(c)). The clivus area was measured by selecting the long axis section of the clivus in the midsagittal plane in the MPR mode (Figure 5(c)) and reconstructing the

images of the clivus (Figure 5(d)). In Figure 5(c), the white dotted line denotes the tangent line of the clivus in the long axis, and the white solid line presents the range from the head end to the tail end of the clivus. Figure 5(d) is the section image of the clivus reconstructed according to the long axis tangent of the clivus, and the area enclosed within the white solid lines corresponds to that enclosed by white solid lines in Figure 5(c).

**2.7. Radioanatomical Measurement Software.** Image Viewer 3.1.14 (Start Technology Co., Ltd., China) was used for radioanatomical measurements, and the measurement results were accurate to 0.1 mm.

Data were input using WPS2019 11.1 (Kingsoft Corp., Zhuhai). Statistical analysis was conducted using SPSS 26.0 (IBM, USA). All values were expressed as the mean  $\pm$

TABLE 1: Radioanatomical measurement results (distance, mm; area, cm<sup>2</sup>).

	Overall average	Female average	Male average
Distance from the SPF to the sphenothmoidal suture through the anterior sphenoid sinus (SPF_SEJ1, mm)	23.02 ± 3.26	23.82 ± 3.27	21.83 ± 2.94
Distance from the SPF to the sphenothmoidal suture through the sphenoid sinus (SPF_SEJ2, mm)	62.54 ± 7.78	63.75 ± 7.38	60.71 ± 8.24
Distance from the SPF to the posterior margin of the planum sphenoidale through the base of the sphenoid sinus (SPF_P, mm)	47.17 ± 6.78	48.48 ± 6.61	45.20 ± 6.77
Distance from the SPF to the upper margin of the dorsum sellae through the base of the sphenoid sinus (SPF_S, mm)	44.10 ± 5.02	44.73 ± 5.24	43.16 ± 4.68
Distance from the SPF to the clivus through the base of the sphenoid sinus (SPF_C, mm)	29.68 ± 2.88	29.05 ± 2.80	30.62 ± 2.81
Distance from the SPF to the posterior margin of the nasal septum through the anterior sphenoid sinus (SPF_NS, mm)	33.99 ± 3.42	34.36 ± 3.54	33.44 ± 3.26
Anterior margin width of the HBF (HBF_AW, mm)	50.09 ± 3.53	49.57 ± 3.63	50.87 ± 3.35
Posterior margin width of the HBF (HBF_PW, mm)	47.35 ± 3.97	47.38 ± 3.95	47.29 ± 4.14
Upper margin length of the HBF (HBF_UL, mm)	50.62 ± 3.84	49.72 ± 4.15	51.96 ± 2.95
Lower margin length of the HBF (HBF_LL, mm)	46.26 ± 2.62	45.90 ± 2.39	46.78 ± 2.94
Extensible width of the HBF (HBF_W, mm)	12.80 ± 1.89	12.85 ± 1.99	12.73 ± 1.79
Length of the HBF with vascular pedicles (HBF_TL)	84.92 ± 4.79	84.53 ± 4.93	85.50 ± 4.66
HBF area (HBF_S, cm <sup>2</sup> )	19.14 ± 2.20	18.81 ± 2.02	19.65 ± 2.44
Anterior margin width of transthemoidal skull base defects (SKB_E_AW, mm)	25.33 ± 1.84	25.20 ± 1.71	25.53 ± 2.05
Posterior margin width of transthemoidal skull base defects (SKB_E_PW, mm)	26.38 ± 2.84	26.32 ± 2.24	26.46 ± 3.64
Length of transthemoidal skull base reconstruction through the anterior sphenoid sinus (SKB_E_AS, mm)	52.43 ± 5.55	53.44 ± 5.47	50.91 ± 5.50
Length of transthemoidal skull base reconstruction through the sphenoid sinus (SKB_E_PS, mm)	91.94 ± 8.64	93.37 ± 7.53	89.79 ± 9.95
Length of transthemoidal skull base reconstruction (SKB_E_L, mm)	29.40 ± 4.60	29.62 ± 3.87	29.08 ± 5.64
Area of transthemoidal skull base reconstruction (SKB_E_S, cm <sup>2</sup> )	8.93 ± 1.49	8.71 ± 1.36	9.25 ± 1.66
Anterior margin width of transsphenoidal skull base reconstruction (SKB_S_AW, mm)	26.38 ± 2.84	26.32 ± 2.24	26.46 ± 3.64
Middle width of transsphenoidal skull base reconstruction (SKB_S_MW, mm)	28.84 ± 2.37	29.12 ± 2.10	28.41 ± 2.73
Posterior margin width of transsphenoidal skull base reconstruction (SKB_S_PW, mm)	20.13 ± 1.91	19.61 ± 1.63	20.91 ± 2.09
Length of transsphenoidal defects in the planum sphenoidale reconstruction (SKB_S_PL, mm)	15.37 ± 3.36	15.27 ± 3.18	15.51 ± 3.72
Length of transsphenoidal defects in the sellar region reconstruction (SKB_S_SL, mm)	12.42 ± 2.04	11.71 ± 1.67	13.49 ± 2.12
Total length of transsphenoidal skull base reconstruction (SKB_S_TL, mm)	27.79 ± 3.80	26.98 ± 3.42	29.00 ± 4.13
Area of transsphenoidal skull base reconstruction (SKB_S_S, cm <sup>2</sup> )	8.43 ± 1.03	8.24 ± 1.06	8.70 ± 0.96
Anterior margin width of transclival skull base reconstruction (SKB_C_AW, mm)	20.13 ± 1.91	19.61 ± 1.63	20.91 ± 2.08
Middle width of transclival skull base reconstruction (SKB_C_MW, mm)	21.53 ± 2.24	22.01 ± 2.32	20.80 ± 1.96
Posterior margin width of transclival skull base reconstruction (SKB_C_PW, mm)	29.52 ± 3048	28.93 ± 3.00	30.41 ± 4.03
Length of transclival skull base reconstruction (SKB_C_L, mm)	36.78 ± 3.41	36.52 ± 3.08	37.16 ± 3.91
Area of transclival skull base reconstruction (SKB_C_S, cm <sup>2</sup> )	10.13 ± 1.83	10.28 ± 1.96	9.91 ± 1.64

standard deviation. The normal distribution of data was tested using the Kolmogorov–Smirnov test. Gender differences in data conforming to a normal distribution were analyzed using the independent-samples *t*-test; otherwise, the  $\chi^2$  test was used for analysis. Age differences were evaluated using Spearman's correlation analysis. The 95% confidence interval was selected for correlation analyses of gender and age.  $P < 0.05$  denoted statistical significance.

### 3. Results

**3.1. SPF and HBF.** The measurement results including SPF and HBF variables are presented in Table 1. Excluding the extensible width of the HBF, all variables exhibited a normal distribution without gender differences as verified using the independent-samples *t*-test ( $P > 0.05$ ). No gender difference was found for the extensible width of the HBF according



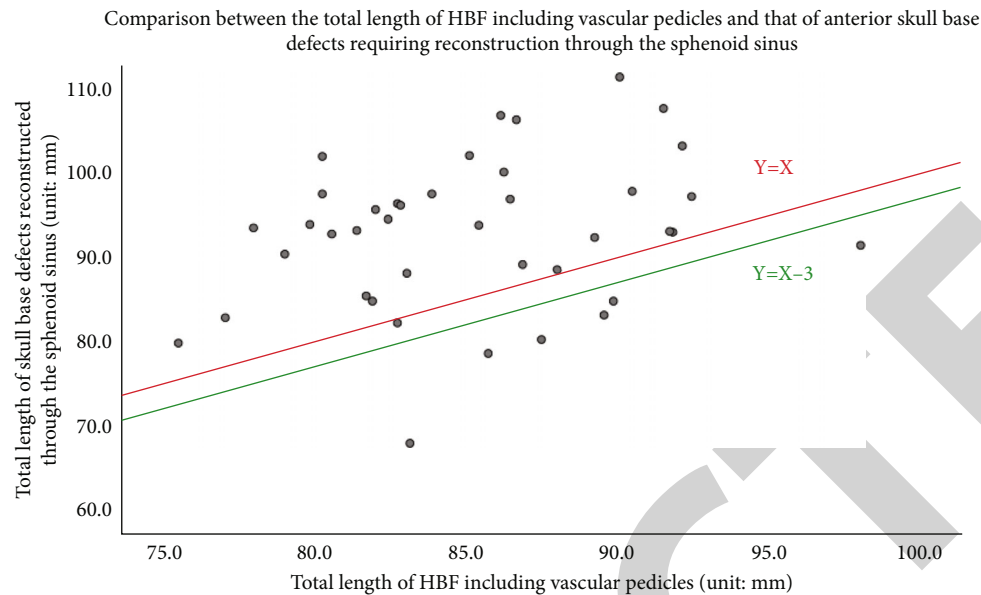


FIGURE 6: The X-axis represents the total length of the HBF including vascular pedicles, and the Y-axis represents the total length of ASB reconstruction through the sphenoid sinus. The red line ( $Y = X$ ) denotes when the total length of the HBF including vascular pedicles was equal to that of ASB reconstruction through the sphenoid sinus. The green line ( $Y = X - 3$ ) denotes when the total length of the HBF including vascular pedicles was 3 mm longer than that of ASB reconstruction through the sphenoid sinus.

to the  $\chi^2$  test ( $P > 0.05$ ). Spearman's correlation analysis revealed no age differences for any variable ( $P > 0.05$ ).

**3.2. Skull Base Defects Reconstructed via the Transethmoidal Approach.** The average anterior margin width, posterior margin width, defect length, and area of skull base defects reconstructed via the transethmoidal approach are presented in Table 1. Among them, the length of skull base defects reconstructed via the transethmoidal approach through the anterior sphenoid sinus was the sum of the length from the projection point of the SPF to the ipsilateral sphenothmoidal suture through the infra-anterior sphenoid sinus and the length of skull base defects reconstructed via the transethmoidal approach (the sum of the measured values in Figure 2(a) and Figure 6(c)). The length of skull base defects reconstructed via the transethmoidal approach through the sphenoid sinus was the sum of the length from the projection point of the SPF to the ipsilateral sphenothmoidal suture through the sphenoid sinus and the length of skull base defects reconstructed via the transethmoidal approach (the sum of the measured values in Figure 2(b) and Figure 6(c)). The mean differences of the data corresponding to HBF are shown in Table 2. All data were normally distributed. The independent-samples  $t$ -test revealed gender differences in the posterior margin width of skull base defects reconstructed via the transethmoidal approach ( $P = 0.015$ ), the lower margin length of the HBF, and the length of skull base defects reconstructed via the transethmoidal approach ( $P = 0.015$ ), but no gender differences were noted for other variables ( $P > 0.05$ ). Spearman's correlation analysis revealed no age differences for any variable ( $P > 0.05$ ). Using the measured data, we evaluated whether the HBF could completely cover skull base defects reconstructed by the transethmoidal approach. In the 40 patients,

the area of the HBF exceeded that of skull base defects reconstructed via the transethmoidal approach by  $10.21 \pm 1.97 \text{ cm}^2$ , and the anterior margin width, posterior margin width, upper margin length, and lower margin lengths of the HBF all exceeded the corresponding values of skull base defects requiring reconstruction by at least 8.4 mm. Therefore, the HBF could completely cover skull base defects reconstructed via the transethmoidal approach. The total length of the HBF including vascular pedicles was at least 17.6 mm longer than that needed for skull base defect reconstruction via the transethmoidal approach through the anterior sphenoid sinus, but the total length of the HBF including vascular pedicles was  $7.02 \pm 8.71 \text{ mm}$  shorter than that needed for skull base defect reconstruction via the transethmoidal approach through the sphenoid sinus. The HBF could not be used to reconstruct skull base defects via the transethmoidal approach through the sphenoid sinus in any patients. Additionally, the total length of the HBF including vascular pedicles when reconstruction could not be completed in this study and the total length of skull base defects reconstructed via the transethmoidal approach through the sphenoid sinus was analyzed using a scatterplot. The results illustrated that reconstruction requirements were not met in 34/40 (85.0%) cases, and in 33/40 (82.5%) cases, the total length of the HBF including vascular pedicles did not exceed that of skull base defects reconstructed via the transethmoidal approach through the sphenoid sinus (Figure 6).

**3.3. Skull Base Defects Reconstructed via the Transsphenoidal Approach.** The average anterior margin width, middle width, posterior margin width, length of the planum sphenoidale, length of the roof of the sella turcica, total length, and area of skull base defects reconstructed via the transsphenoidal

TABLE 2: Differences between HBF variables and those of transethmoidal, transsphenoidal, and transclival skull base reconstructed (distance, mm; area, cm<sup>2</sup>).

	Overall		Female		Male	
	Average	Minimum	Average	Minimum	Average	Minimum
HBF_AW – SKB_E_AW (mm)	24.76 ± 3.84	15.9	24.38 ± 4.11	15.9	25.34 ± 3.45	17.3
HBF_PW – SKB_E_PW (mm)	20.97 ± 4.30	13.7	21.06 ± 3.35	14.9	20.84 ± 5.56	13.7
HBF_UL – SKB_E_L (mm)	21.21 ± 4.70	13.7	20.10 ± 4.40	13.7	22.88 ± 4.77	17.4
HBF_LL – SKB_E_L (mm)	16.85 ± 4.92	8.4	16.29 ± 3.55	10.6	17.70 ± 6.52	8.4
HBF_TL – SKB_E_AS (mm)	32.49 ± 7.46	17.6	31.09 ± 7.92	17.6	34.59 ± 6.38	23.9
HBF_TL – SKB_E_PS (mm)	-7.02 ± 8.71	-20.7	-8.84 ± 7.98	-20.7	-4.29 ± 9.30	-20.3
HBF_S – SKB_E_S (cm <sup>2</sup> )	10.21 ± 1.97	6.3	10.09 ± 1.76	6.3	10.40 ± 2.31	6.2
HBF_AW – SKB_S_AW (mm)	10.91 ± 3.06	5.8	10.40 ± 2.78	5.8	11.69 ± 3.39	6.1
HBF_AW – SKB_S_MW (mm)	18.51 ± 4.74	10.7	18.26 ± 4.35	11.6	18.89 ± 5.39	10.7
HBF_PW – SKB_S_PW (mm)	31.46 ± 4.60	24.2	32.55 ± 4.21	24.5	29.83 ± 4.80	24.2
HBF_UL – SKB_S_TL (mm)	23.14 ± 4.88	14.7	23.19 ± 5.03	14.7	23.06 ± 4.79	14.9
HBF_TL – SKB_PS_TL (mm)	22.38 ± 8.75	7.8	20.78 ± 8.35	8.6	24.79 ± 9.03	7.8
HBF_TL – SKB_ST_TL (mm)	13.03 ± 7.14	0.7	12.82 ± 7.32	2.0	13.34 ± 7.09	0.7
HBF_S – SKB_S_S (cm <sup>2</sup> )	10.72 ± 2.04	6.9	10.56 ± 1.95	6.9	10.95 ± 2.21	7.0
HBF_PW – SKB_C_AW (mm)	31.46 ± 4.60	24.2	32.55 ± 4.21	24.5	29.83 ± 4.80	24.2
HBF_AW – SKB_C_MW (mm)	15.76 ± 3.80	5.4	14.70 ± 3.88	5.4	17.34 ± 3.15	9.8
HBF_AW – SKB_C_PW (mm)	21.21 ± 4.70	13.7	20.10 ± 4.40	13.7	22.88 ± 4.77	17.4
HBF_UL – SKB_C_L (mm)	14.15 ± 4.36	6.1	13.65 ± 4.71	6.1	14.90 ± 3.80	7.5
HBF_TL – SKB_C_TL (mm)	18.46 ± 6.19	6.4	18.95 ± 6.44	6.4	17.72 ± 5.92	9.5
HBF_S – SKB_C_S (cm <sup>2</sup> )	9.01 ± 2.87	3.94	8.53 ± 2.59	3.94	9.74 ± 3.18	5.1

approach are presented in Table 1. The mean differences of the data corresponding to the HBF are shown in Table 2. All data were normally distributed. The independent-samples *t*-test revealed gender differences only for the anterior margin width of skull base defects reconstructed via the transsphenoidal approach ( $P = 0.015$ ). Spearman's correlation analysis revealed age differences for the anterior margin width of the HBF and the anterior margin width of skull base defects reconstructed via the transsphenoidal approach ( $P = 0.040$ ). Using the study data, we evaluated whether the HBF could completely cover skull base defects reconstructed via the transsphenoidal approach. In the 40 patients, the area of the HBF exceeded that of reconstructed skull base defects by an average of  $10.72 \pm 2.04$  cm<sup>2</sup>. The anterior and posterior margin widths of the HBF both exceeded the corresponding values of skull base defects reconstructed via the transsphenoidal approach by at least 10.7 mm. The total length of the HBF including vascular pedicles was 7.8 mm longer than that needed for reconstruction of the planum sphenoidale via the transsphenoidal approach. The anterior margin width of the HBF was at least 5.8 mm wider than that of skull base defects needing reconstruction via the transsphenoidal approach. The total length of the HBF including vascular pedicles was 0.7 mm longer than that needed for reconstruction of the sella turcica via the transsphenoidal approach. The differences between the anterior margin width of the HBF and that of skull base defects requiring

reconstruction via the transsphenoidal approach were sorted from low to high using the WPS tool. The difference was 5.8 mm in one case, whereas the value exceeded 6 mm in the remaining cases. The total length of the HBF including vascular pedicles and that needed for reconstruction of the sella turcica via the transsphenoidal approach was analyzed using a scatterplot, as shown in Figure 7. The criterion of a >3 mm difference was achieved for all but three cases. The total length of the HBF including vascular pedicles exceeded that needed for reconstruction of the sella turcica via the transsphenoidal approach in all 40 cases.

**3.4. Variables of Skull Base Defects Reconstructed via the Transclival Approach.** The area of the HBF exceeded that of skull base defects reconstructed via the transclival approach by  $9.01 \pm 2.87$  cm<sup>2</sup>. The difference between the anterior margin width of the HBF and the middle width of skull base defects reconstructed via the transclival approach did not exceed 6 mm in only one case (5.4 mm). The total length of the HBF with vascular pedicles exceeded that required for reconstruction of the skull base defect via the transclival approach by at least 3 mm in all cases (Table 2).

The average upper margin width, middle width, lower margin width, length, and area of skull base defects reconstructed via the transclival approach are presented in Table 1. The mean differences with the corresponding data of the HBF are shown in Table 11. All data were normally

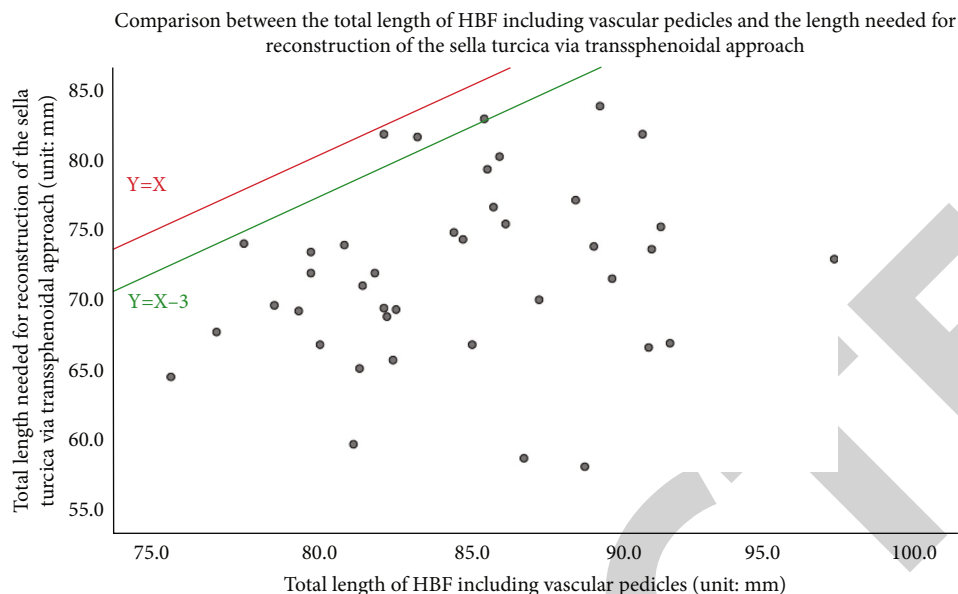


FIGURE 7: The X-axis represents the total length of the HBF including vascular pedicles, and the Y-axis represents the total length needed for reconstruction of the sella turcica via the transsphenoidal approach. The red line ( $Y = X$ ) denotes when the total length of HBF including vascular pedicles was equal to that needed for reconstruction of the sella turcica via the transsphenoidal approach. The green line ( $Y = X - 3$ ) denotes when the total length of the HBF including vascular pedicles exceeded that needed for reconstruction of the sella turcica via the transsphenoidal approach by 3 mm.

distributed. The independent-samples *t*-test revealed no gender differences for any variables ( $P > 0.05$ ). Spearman's correlation analysis revealed that the difference between the posterior margin width of the HBF and the upper margin width of skull base defects reconstructed via the transclival approach was correlated with age ( $P < 0.05$ ), whereas no other correlations with age were identified ( $P > 0.05$ ). Using these data, we evaluated whether the HBF could completely cover skull base defects reconstructed via the transclival approach. In all 40 patients, the area of the HBF exceeded that of skull base defects reconstructed via the transclival approach by  $9.01 \pm 2.87 \text{ cm}^2$ . The difference between the anterior margin width of the HBF and the middle width of skull base defects reconstructed via the transclival approach did not exceed 6 mm in only one case (5.4 mm). The total length of the HBF including vascular pedicles exceeded that needed for reconstruction of skull base defects via the transclival approach by at least 3 mm in all cases (Table 2).

#### 4. Discussion

The success of small skull base defect reconstruction is not related to the technique or tissue used, and thus, tissue flaps with vascular pedicles are not widely used for this purpose [11]. Conversely, large-scale defects require tissue flaps with vascular pedicles [12–14]. Tissue flaps with vascular pedicles provide faster, more reliable, and complete healing, thereby reducing the risk of complications associated with continued communication between the cranial and nasal cavities [15]. At present, the HBF is the most widely used flap clinically. This tissue flap has high toughness and good extendability, and its pedicles can rotate flexibly and cover a large area of skull base defects caused by endoscopic skull base surgery

[8]. Currently, the HBF is widely used in endoscopic skull base reconstruction, but little research has assessed its competence for reconstruction. Concerning radioanatomy, the Pinheiro-Neto [16] and Peris-Celda [17] models are two representative radioanatomical models with some common features. It is worth noting that, in theory, the Peris-Celda model provides a more accurate measurement, but it requires curves or polygonal lines, in addition to high requirements for CT image reconstruction in nonstandard planes (both high requirements for CT scanning and postprocessing software), which will affect the accuracy of measurement. The Pinheiro-Neto model is more reliable and permits easier measurements, but its use is limited by difficulty in setting the measuring straight line reasonably in an irregular cavity. Moreover, the possibility of eliminating the dead space using free fat or other grafts is not considered in either model. In this manner, the demand for flap size can be reduced.

At the beginning of this study, we collected a large amount of radioanatomical data to determine the optimal method to measure HBF variables via CT. We measured every variable described in the literature. Considering the repeatability of the measurement results, we used straight lines instead of curves whenever possible. After comprehensive comparison, we chose a quadrilateral area (rectangle and trapezoid) for the measurement. Although the extent to which the HBF is larger than skull base defects in radioanatomy has not been determined, we accepted the standard value of 6 mm [8] and quoted this standard in specific experiments. The model used in our study was extremely likely to underestimate the size of the HBF and overestimate that of skull base defects. First, Peris-Celda et al. [17] found that measurements using straight lines underestimated the

increased length of mucosal curves and folds. Second, we adopted a limited model in which some parts of the HBF that can be fully utilized in the clinic might not be included in the measurement. Thus, we chose to design a limited model because overestimating the size of tissue flaps is problematic in clinical application. On the contrary, it is assumed that bones in the whole approach area should be resected for each skull base defect model, whereas only partial resection is needed in the actual surgery. Such a design ensures that mismatches will not occur. Moreover, we designed measurement markers of the model based on the anatomical results and investigated the reconstruction results after changing the route of HBF application by blocking the sphenoid sinus cavity using autogenous free fat.

The vascular pedicle of the HBF is rotatable with a large rotation angle, and its usable surface area covers a wide range. Therefore, it is a commonly used intranasal flap in clinical practice, including uses in the repair and reconstruction of defects in the anterior, middle, and posterior cranial fossae in the midsagittal plane [8, 9]. This flap branches out from its vascular pedicles supplied by the posterior nasal septal artery, which serves as the terminal branch sphenopalatine artery of the maxillary artery. Considering the self-contraction of mucosal flaps, defects are considered to be completely covered when the length and width of the HBF exceeds those of the defect by more than 6 mm and the total length of the tissue flap including pedicles exceeds that of the route of tissue flap implantation for defect reconstruction by 3 mm. If one of these criteria is not met, then the tissue flap is considered to be incompetent for reconstruction [8, 9]. According to the aforementioned criteria and our research results, the length and width of the HBF exceeded those of skull base defects reconstructed via the transethmoidal approach. However, in clinical practice, the extent of opening of the sphenoid sinus during surgery performed via the transethmoidal approach is high [18]. The HBF cannot reach the defect until it passes through the base and posterior wall of the sphenoid sinus and the planum sphenoidale. The total length of the HBF including vascular pedicles cannot meet the lengthened path. The current study results illustrated that the HBF was fully competent for this task in 6/40 patients. Even if the length criterion was adjusted so that the HBF only needed to be longer than the reconstruction length, only seven cases met this standard. Moreover, this result did not differ by age or gender. However, this does not indicate that the HBF is not suitable for the reconstruction of large skull base defects caused by endoscopic skull base surgery performed via the transethmoidal approach. If proper case selection is performed before surgery and the preoperative images of the cases are fully analyzed, then the HBF can be used for skull base defect reconstruction via the transethmoidal approach in some cases [19]. At this time, radioanatomy is particularly important for preoperative surgical planning.

Considering that the anterior margin of the HBF in the horizontal direction is 3 mm wider than that of the defect in practical reconstruction, the anterior margin width of the HBF can completely cover the defect in actual reconstruction [8]. The length difference did not meet the stan-

dard requirement of 3 mm in 3/40 cases. Obviously, according to the anatomical findings in the study, this gap is caused by the fact that the HBF can only reach the defect region truly requiring reconstruction through the base and posterior wall of the sphenoid sinus during reconstruction, which can also be solved. Before the surgery, we can evaluate the defect size on CT images according to the range of lesions and surgical approach and examine the size of the required HBF on the images to guide the planning of the surgical approach and design of the HBF.

In the reconstruction of skull base defects via the transclival approach using the HBF, the posterior margin of the HBF covered the upper part of the clivus, and the anterior margin of the HBF covered the end of the clivus defect. On the one hand, the anterior margin of the HBF in the horizontal direction should be 3 mm wider than that of the defect in practical reconstruction. On the other hand, the HBF can also be moved to the tail of the clivus or pushed to the tail of the clivus by blocking the sphenoid sinus, allowing a wider mucosal flap to cover the middle part of the defect. The length and area were sufficient for covering the defects in all 40 cases. Before the surgery, we can evaluate the size of the defect on CT images according to the range of lesions and surgical approach and evaluate the size of the required HBF on the images to guide the planning of the surgical approach and design of the HBF.

According to the aforementioned model design, we conducted this research in three parts. In the first part, gender differences were found for the posterior margin width of skull base defects reconstructed via the transethmoidal approach, the upper length of the HBR, and the length of skull base defects reconstructed via the transethmoidal approach ( $P = 0.015$ ), but no age or gender differences were identified. The results indicate that sphenoid sinus blocking may be necessary, but the effect of sphenoid sinus blocking has been confirmed in clinical practice [20]. The HBF can be used to complete skull base reconstruction via the transethmoidal approach, and radioanatomy can also be used as a guide for preoperative design of the surgical scheme via the transethmoidal approach. In the second part, a gender difference was found for the anterior margin width of skull base defects reconstructed via the transsphenoidal approach ( $P = 0.015$ ), and an age difference was found for the difference between the anterior margin width of the HBF and that of skull base defects reconstructed via the transsphenoidal approach ( $P = 0.040$ ). No other age or gender differences were identified. These findings indicate that sphenoid sinus blocking may be necessary, but the effect of sphenoid sinus blocking has been confirmed in clinical practice [20]. In the third part, an age difference was noted for the difference between the posterior margin width of the HBF and the upper margin width of the defect reconstructed via the transclival approach ( $P = 0.003$ ). No other age or gender differences were observed. Thus, the HBF can be used to complete skull base reconstruction via the transclival approach, and radioanatomy can also be used as a guide for preoperative design of the surgical scheme via the transclival approach. The analysis of gender and age differences was repeated. Therefore, we believe that there are no significant

differences related to gender or age overall in the measurement of the HBF and skull base defects reconstructed via the transthemoidal, transsphenoidal, and transclival approaches.

Although the HBF has been widely used in skull base reconstruction in clinical practice and its efficacy is certain, this study also have the deficiencies that the research does not include the content of the HBF in the reconstruction of skull base defects via the transthemoidal, transsphenoidal, and transclival approaches in surgical practice, which also needs to be further developed. In addition, in our study, the HBF area was smaller than the total area of skull base defects reconstructed via the transthemoidal and transsphenoidal approaches in 5/40 cases, smaller than the total area of skull base defects reconstructed via the transsphenoidal and transclival approaches in 16/40 cases, and smaller than the total area of the three defect regions. Therefore, skull base defects caused by transregional or multiapproach surgery will increase significantly when the HBF does not meet the needs of reconstruction.

## 5. Conclusion

This study for the first time performed radioanatomical modeling and systematic radioanatomical analysis of the HBF and skull base defects reconstructed via the transthemoidal, transsphenoidal, and transclival approaches in Chinese adults. The HBF can cover skull base defects reconstructed via the transthemoidal, transsphenoidal, and transclival approaches, and they can be used for skull base reconstruction via all three approaches. Additionally, radioanatomy can be used as a guide for preoperative design of the surgical scheme via the transthemoidal, transsphenoidal, and transclival approaches.

## Data Availability

The labeled dataset used to support the findings of this study are available from the corresponding author upon request.

## Conflicts of Interest

The author declares no competing interests.

## Acknowledgments

The study was supported by Project Name: Radioanatomical Study on the Significance of Pedicled Nasoseptal Flap in Skull Base Reconstruction (Project No. HAB202136).

## References

- [1] D. H. Jho, R. "Endoscopic endonasal transsphenoidal surgery: experience with 50 patients," *Journal of Neurosurgery*, vol. 87, no. 1, pp. 44–51, 1997.
- [2] H. Maggiano, F. A. Papay, S. Dominquez, H. L. Levine, P. Lavertu, and S. J. Hassenbusch, "Rigid endoscopic repair of paranasal sinus cerebrospinal fluid fistulas," *Laryngoscope*, vol. 99, pp. 1195–1201, 2010.
- [3] C. M. Jeon, S. D. Hong, H. J. Seol et al., "Reconstructive outcome of intraoperative cerebrospinal fluid leak after endoscopic endonasal surgery for tumors involving skull base," *Journal of Clinical Neuroscience: Official Journal of the Neurosurgical Society of Australasia*, vol. 45, pp. 227–231, 2017.
- [4] C. H. Snyderman, H. Pant, R. L. Ca Rrau, D. Prevedello, P. Gardner, and A. B. Kassam, "What are the limits of endoscopic sinus surgery?: the expanded endonasal approach to the skull base," *Keio Journal of Medicine*, vol. 58, no. 3, pp. 152–160, 2009.
- [5] G. G. Kim, A. X. Hang, C. A. Mitchell, and A. M. Zanation, "Pedicled extranasal flaps in skull base reconstruction," *Advances in Oto-Rhino-Laryngology*, vol. 74, pp. 71–80, 2012.
- [6] A. M. Zanation, B. D. Thorp, P. Parmar, and R. J. Harvey, "Reconstructive options for endoscopic skull base surgery," *Otolaryngologic Clinics of North America*, vol. 44, no. 5, pp. 1201–1222, 2011.
- [7] A. Shahangian, Z. M. Soler, A. Baker, S. K. Wise, and R. J. Schlosser, "Successful repair of intraoperative cerebrospinal fluid leaks improves outcomes in endoscopic skull base surgery," *International Forum of Allergy & Rhinology*, vol. 7, pp. 80–86, 2017.
- [8] G. Hadad, L. Bassagasteguy, R. L. Carrau et al., "A novel reconstructive technique after endoscopic expanded endonasal approaches: vascular pedicle nasoseptal flap," *The Laryngoscope*, vol. 116, no. 10, pp. 1882–1886, 2006.
- [9] C. D. Pinheiro-Neto, D. M. Prevedello, R. L. Carrau et al., "Improving the design of the pedicled nasoseptal flap for skull base reconstruction: a radioanatomic study," *The Laryngoscope*, vol. 117, no. 9, pp. 1560–1569, 2007.
- [10] C. D. Pinheiro-Neto, H. F. Ramos, M. Peris-Celda et al., "Study of the nasoseptal flap for endoscopic anterior cranial base reconstruction," *The Laryngoscope*, vol. 121, no. 12, pp. 2514–2520, 2011.
- [11] H. M. Hegazy, R. L. Carrau, C. H. Snyderman, A. Kassam, and J. Zweig, "Transnasal endoscopic repair of cerebrospinal fluid rhinorrhea: a meta-analysis," *Laryngoscope*, vol. 110, pp. 1166–1172, 2000.
- [12] "Nasoseptal flap takedown and reuse in revision endoscopic skull base reconstruction," *Laryngoscope*, vol. 121, no. 1, pp. 42–46, 2011.
- [13] B. Thakur, A. R. Jesurasa, R. Ross, T. A. Carroll, S. Mirza, and S. Sinha, "Transnasal trans-sphenoidal endoscopic repair of csf leak secondary to invasive pituitary tumours using a nasoseptal flap," *Pituitary*, vol. 14, no. 2, pp. 163–167, 2011.
- [14] G. G. Nyquist, V. K. Anand, A. Singh, and T. H. Schwartz, "Janus flap: bilateral nasoseptal flaps for anterior skull base reconstruction," *Otolaryngology-Head and Neck Surgery*, vol. 142, no. 3, pp. 327–331, 2010.
- [15] Y. Nobutaka and A. L. Rhoton, "Vascular anatomy of the anteriorly based pericranial flap," *Operative Neurosurgery*, vol. 57, Supplement 1, pp. 11–16, 2005.
- [16] C. D. Pinheiro-Neto, C. H. Snyderman, J. Fernandez-Miranda, and P. A. Gardner, "Endoscopic endonasal surgery for nasal dermoids," *Otolaryngologic Clinics of North America*, vol. 44, no. 4, pp. 981–987, 2011.
- [17] M. Peris-Celda, C. D. Pinheiro-Neto, T. Funaki et al., "The extended nasoseptal flap for skull base reconstruction of the clival region: an anatomical and radiological study," *Skull Base*, vol. 74, no. 6, pp. 369–385, 2013.

## Research Article

# The Novel Nrf2 Activator Omaveloxolone Regulates Microglia Phenotype and Ameliorates Secondary Brain Injury after Intracerebral Hemorrhage in Mice

Libin Hu,<sup>1</sup> Yang Cao,<sup>1</sup> Huaijun Chen,<sup>1</sup> Lei Xu,<sup>2</sup> Qiguo Yang,<sup>2</sup> Hang Zhou,<sup>1</sup> Jianru Li,<sup>1</sup> Qian Yu,<sup>1</sup> Zhangqi Dou,<sup>1</sup> Yin Li,<sup>1</sup> Feng Yan,<sup>1</sup> Fuyi Liu <sup>1</sup>, and Gao Chen <sup>1</sup>

<sup>1</sup>Department of Neurosurgery, The Second Affiliated Hospital of Zhejiang University School of Medicine, China

<sup>2</sup>Zhejiang University School of Medicine, China

Correspondence should be addressed to Fuyi Liu; [liufuyi@zju.edu.cn](mailto:liufuyi@zju.edu.cn) and Gao Chen; [d-chengao@zju.edu.cn](mailto:d-chengao@zju.edu.cn)

Received 19 August 2021; Revised 8 December 2021; Accepted 22 February 2022; Published 11 March 2022

Academic Editor: Hansen Chen

Copyright © 2022 Libin Hu et al. This is an open access article distributed under the Creative Commons Attribution License, which permits unrestricted use, distribution, and reproduction in any medium, provided the original work is properly cited.

The polarization of microglia is recognized as a crucial factor in reducing neuroinflammation and promoting hematoma clearance after intracerebral hemorrhage (ICH). Previous studies have revealed that redox components participate in the regulation of microglial polarization. Recently, the novel Nrf2 activator omaveloxolone (Oma) has been validated to improve neurological function in patients with neurodegenerative disorders by regulating antioxidant responses. In this study, we examined the efficacy of Oma in ICH. Oma significantly promoted Nrf2 nuclear accumulation and the expression of HO-1 and NQO1 in BV2 cells. In addition, both *in vitro* and *in vivo* experiments showed that Oma treatment inhibited M1-like activation and promoted the activation of the M2-like microglial phenotype. Oma inhibited OxyHb-induced ROS generation and preserved the function of mitochondria in BV2 cells. Intraperitoneal administration of Oma improved sensorimotor function in the ICH mouse model. Importantly, these effects were blocked by pretreatment with ML385, a selective inhibitor of Nrf2. Collectively, Oma modulated microglial polarization by activating Nrf2 and inhibiting ROS generation in ICH models, suggesting that it might be a promising drug candidate for the treatment of ICH.

## 1. Introduction

Intracerebral hemorrhage (ICH), which is mainly caused by rupture of blood vessels in the brain, inflicts 10-30 per 100000 population each year [1]. In addition to surgical removal of the hematoma, limited medical treatments are effective at improving neurological functional recovery [2, 3]. Brain injury caused by ICH includes primary injury and secondary injury. Primary brain injury is mainly caused by direct mechanical effects of the hematoma, while secondary brain injury is mediated by blood components, activation of microglia/macrophages, reactive oxygen species (ROS) generation, and cytokine release. Based on accumulating evidence, secondary brain injury strongly contributes to neurological deficiency [4]. However, to date, few treatments for secondary injury have proven beneficial for improving the prognosis.

Microglia, as brain-resident macrophages of the immune system, are activated by exudative blood components to further participate in inflammation and hematoma clearance. Microglia are endowed with spectacular plasticity, which allows them to acquire different phenotypes and exert multiple effects on tissue damage and repair [5]. Typically, the activation state of microglia exhibits a spectrum of proinflammatory (M1) or alternative (M2) responses [6, 7]. M1 microglia secrete proinflammatory cytokines (IL-1 $\beta$  and TNF- $\alpha$ ) and induce the production of ROS, which subsequently amplify M1 polarization and result in neuronal injury [8]. M2 microglia, which are mainly polarized in the subacute and chronic phase, are important for resolving the hematoma and wound healing and are generally characterized by the expression of factors such as CD206, arginase (Arg-1), and chitinase-like protein 3 (known as Ym1) [6, 7, 9, 10]. Published evidence indicates that dysregulated

microglial activation leads to a deleterious and neurotoxic microglial phenotype, which is defined by prolonged inflammation and inefficient hematoma clearance [11–13]. The balance of microglia polarization is currently postulated to be beneficial for functional recovery after ICH [14, 15].

Accumulating evidence indicates a crucial role for redox components in microglial polarization [16, 17]. Nuclear factor erythroid-2 related factor 2 (Nrf2) is a key transcription factor and regulator of antioxidant responses that exerts a protective effect after ICH [17–19]. Once activated, Nrf2 translocates to the nucleus and binds to the antioxidant response element (ARE) to initiate the expression of antioxidant enzymes and proteins such as heme oxygenase-1 (HO-1), NAD(P)H: quinone oxidoreductase-1 (NQO1), and superoxide dismutase (SOD). Recent studies have reported that Nrf2 knockout (Nrf2<sup>-/-</sup>) mice presented higher ROS levels, leukocyte infiltration, and larger injury volumes that correlated with more severe neurological deficits in the post-ICH period [19]. Moreover, the upregulation of HO-1 contributes to a reduction in ROS accumulation, which was the main inducer of secondary injury after ICH [8]. Selective suppression of mitochondrial ROS production inhibits microglial M1 polarization and attenuates secondary brain injury [11]. In recent years, the Nrf2 pathway has attracted increasing attention as a potential target for oxidative stress-related CNS disease. Monascin, an Nrf2 activator, has been shown to facilitate hematoma clearance and attenuate iron overload after experimental ICH [20]. Another Nrf2 activator, RS9, exerts its neuroprotective effect on ICH by upregulating HO-1 and SOD-1 expressions [21]. Nevertheless, the safety, pharmacokinetics, and pharmacodynamics of monascin and RS9 remain unclear in both mouse models and humans.

Omaveloxolone (Omap) is a novel synthetic oleanane triterpenoid compound that is currently being evaluated in clinical trials for the therapy of Friedreich ataxia (FA). Clinical trials have shown that Omap significantly improves the neurological function of patients with FA [22, 23]. In addition, Omap exerts a pharmacological effect on the treatment of mitochondrial diseases and seizures [24, 25]. Based on these studies, Omap exerts antioxidant and anti-inflammatory effects by activating Nrf2 and inducing the transcription of cytoprotective genes. In conclusion, Omap has the potential to play an important role in the treatment of redox-related CNS diseases. Hence, this study focused on determining the effect of Omap on microglial polarization after ICH and the relationship between these effects and neurological functional recovery.

## 2. Materials and Methods

**2.1. Ethics Statement.** The animal study was reviewed and approved by the Institutional Ethics Committee of the Second Affiliated Hospital, Zhejiang University School of Medicine.

**2.2. Animals and Grouping.** All mice were obtained from SLAC Laboratory Animal Co., Ltd. (Shanghai, China) and housed in a temperature- and humidity-controlled environ-

ment on a 12-hour light/dark cycle with free access to water and food. The present study was conducted according to the National Institutes of Health Guide for the Care and Use of Laboratory Animals.

Mice were randomly assigned to the sham group, ICH+vehicle group, ICH+Omap group, and ICH+Omap+ML385 group.

**2.3. ICH Model.** The autologous blood injection model of ICH was established using the previously reported protocols with some modifications [26, 27]. Briefly, mice were anesthetized with pentobarbital sodium (25 mg/kg, intraperitoneal injection) and then fixed on a stereotaxic device. The scalp was incised along the midline, and the skull was drilled on the right side (0.2 mm anterior and 2.5 mm lateral to the bregma). The tail was sterilized with 70% ethanol and then incised with a sterilized surgical blade. Next, autologous tail arterial blood was collected in a sterilized film and transferred into a 50  $\mu$ l Hamilton syringe. The needle was inserted at a depth of 3.5 mm into the right ventral basal ganglia. Thirty microliters of autologous blood was injected at a rate of 2  $\mu$ l/min using a microinjection pump. The needle was slowly withdrawn after retention for 10 minutes. Mice in the sham group underwent identical surgical procedures without blood injection. The core body temperature was maintained at 36.0–36.5°C, as measured using a rectal thermometer, by incubating animals on a heating pad. All animals were allowed to completely recover from anesthesia in a heated chamber before being returned to their home cages.

**2.4. Cell Culture.** The murine BV2 microglial cell line was obtained from the China Center for Type Culture Collection (Wuhan, China) and cultured in Dulbecco's modified Eagle's high glucose medium supplemented with 10% FBS, 100 U/ml penicillin, and 100  $\mu$ g/ml streptomycin at 37°C and 95% O<sub>2</sub>/5% CO<sub>2</sub>. Twenty-four hours before stimulation, BV2 cells were inoculated into the cell culture plate with serum-free medium. BV2 cells were exposed to 30  $\mu$ M oxy-hemoglobin (OxyHb, Solarbio, Shanghai, China) for 24 hours to mimic ICH, according to the previous studies [15, 28], and the control group was treated with an equivalent volume of phosphate-buffered saline (PBS).

*In vitro* experimental groups were assigned as follows: control group, OxyHb+vehicle group, OxyHb+Omap group, and OxyHb+Omap+ML385 group.

**2.5. Drug Administration.** Omaveloxolone (MedChemExpress, United States) was diluted with 5% dimethyl sulfoxide (DMSO), 5% TWEEN 80, 40% PEG, and 50% sterile saline to a concentration of 1.125 mg/ml for intraperitoneal injection. Intraperitoneal administration (10 mg/kg) of Omap was performed 30 minutes following ICH and once a day over the next two days. The ICH+vehicle group and control group received an equal volume of solvent. For *in vitro* experiments, after 24 hours of culture, 10 nM Omap dissolved in 0.1% DMSO/DMEM was applied with OxyHb to BV2 microglial cells and incubated for another 24 hours.

The rational dosage of Omav was based on the previous studies [29–31].

ML385 (MedChemExpress, United States), a selective inhibitor of Nrf2, was dissolved in 5% dimethyl sulfoxide (DMSO), 5% TWEEN 80, 40% PEG, and 50% sterile saline to a concentration of 3.375 mg/ml for *in vivo* experiments. Intraperitoneal administration (10 mg/kg) of ML385 was performed 1 day before ICH modeling and 1 hour before Omav administration over the next few days. Mice in the ICH+vehicle and ICH+Omav groups received an equivalent volume of solvent instead of drug for the same duration as the vehicle control. ML385 was diluted with 0.1% DMSO/DMEM to a concentration of 5 nM for *in vitro* experiments. BV2 cells were pretreated with ML385 2 hours before OxyHb stimulation. The dosage of ML385 was based on the previous studies [32, 33].

**2.6. Behavioral Assessments.** Neurological function was assessed 1 day and 3 days after ICH modeling by investigators who were blinded to the group information. All procedures were performed as previously described [33, 34]. Briefly, for the corner turn test, mice were placed into a corner with a 30-degree angle. The mouse could turn either to the left or the right to leave of the corner, and the percentage of the right turns was calculated after 10 trials. For the forelimb placement test, mice were held by their torsos, and their left side vibrissae were gently brushed on the corner of a countertop. The percentage of trials in which the mouse placed the left forelimb on the edge of the countertop was calculated after 10 trials. For the cylinder test, mice were placed into a transparent cylinder for 5 minutes in 20 trials. The percentage of occasions when the ipsilateral or contralateral forelimb was used to fully contact the wall was recorded, and the percent difference between the ipsilateral and contralateral forelimbs was calculated.

**2.7. In Vitro Phagocytosis Assay.** BV2 cells were inoculated on coverslips and stimulated as described above. Erythrocytes were isolated from newly drawn mouse blood with Ficoll (Merck Millipore, Germany). Briefly, the same amounts of PBS and blood were mixed, gently added to Ficoll in a centrifuge tube, and centrifuged at 2000 rpm for 25 minutes with minimum acceleration and deceleration. The erythrocytes were washed twice with PBS before labeling with DiI (Beyotime, China), a fluorescence indicator for the cytomembrane. The labeled erythrocytes were added to the BV2 cells in the plate at a ratio of 10:1. After 2 hours of phagocytosis, undigested erythrocytes were dislodged with Red Blood Cell Lysis Buffer (Beyotime, China), and the BV2 cells were labeled with Actin-Tracker Green (Beyotime, China) according to the product manual. The proportion of BV2 cells containing ingested erythrocytes was quantified using fluorescence microscopy. For flow cytometry (FCM), latex beads (Merck Millipore, Germany) with red fluorescence were used for the phagocytosis assay, and the cells were harvested to quantify the phagocytic ability after 2 hours of phagocytosis. The gating strategy of phagocytosis is shown in Sup. Fig 1 B and the data were analyzed using FlowJo software.

**2.8. Western Blot Analysis.** Western blotting was performed as previously described [35]. Protein was extracted from perihematoma samples and BV2 cells with RIPA lysis buffer. Nuclear proteins were extracted according to the instructions of the nuclear and cytoplasmic protein extraction kit (Beyotime, China). Then, equivalent amounts of protein samples were loaded onto sodium dodecyl sulfate–polyacrylamide gels and electrophoresed. The protein was transferred onto PVDF membranes and blocked with 5% nonfat dry milk in buffer, followed by an incubation with primary antibodies against the following proteins overnight at 4°C:  $\beta$ -actin (cat. no. ab8226), Nrf2 (cat. no. ab137550), NQO1 (cat. no. ab80588), HO-1 (cat. no. ab52947), and H3 (cat. no. ab1791). The membranes were then washed with Tris-buffered saline containing Tween 20 (TBST) and incubated with appropriate horseradish peroxidase-conjugated secondary antibodies at room temperature for 1 hour. The protein band densities were detected using chemiluminescence with Amersham™ ImageQuant™ 800 (GE Health care, Beijing, China) and quantified using ImageJ software.

**2.9. Enzyme-Linked Immunosorbent Assay (ELISA).** After appointed treatments, the cell supernatant was harvested and centrifuged at 1,000 rpm for 5 minutes to remove floating cells. The levels of TNF- $\alpha$  (cat. no. KE10003) and IL-1 $\beta$  (cat. no. KE10003) in the supernatants of treated BV2 cells were examined using ELISA kits (Proteintech) according to the manufacturer's instructions. As for perihematoma tissues, 20 mg tissues was added into 0.2 ml extraction reagent and swayed for 30 minutes at 4°C to gain lysis. After 2 minutes of sonication on ice and 30 minutes of centrifugation at 10,000  $\times g$ , the concentration of total protein in supernatants was measured. The content of IL-1 $\beta$  and TNF- $\alpha$  in per mg total protein was quantified according to the standard curve.

**2.10. Quantitative Real-time PCR.** Total RNA was extracted from tissues and cells using TRIzol reagent (Beyotime, China). RNA (1  $\mu$ g) from each sample was reverse transcribed to cDNAs using a PrimeScript™ RT reagent kit (Takara Bio Inc., Japan) according to the product manuals. Quantitative real-time PCR was performed with SYBR Premix Ex Taq™ (Takara Bio Inc., Japan) on a 7500 Plus Real-Time PCR System. The transcript levels of target genes were normalized to  $\beta$ -actin.

**2.11. ROS Detection.** ROS generation was detected using 2',7'-dichlorodihydrofluorescein diacetate (DCFH-DA, Beyotime, China), which can cross cell membrane and be enzymatically hydrolyzed to DCFH, a fluorogenic indicator of superoxide. Intracellular reactive oxygen species can oxidize nonfluorescent DCFH to generate fluorescent DCF. Briefly, after administering the vehicle, OxyHb, Omav, and ML385 to the appropriate groups, the medium was removed, and the cells were washed with PBS and then stained with 10 nM DCFH-DA for 20 minutes at 37°C in the dark. After 3 washes with PBS and staining nuclei with Hoechst (Beyotime, China), the fluorescence intensities were detected using



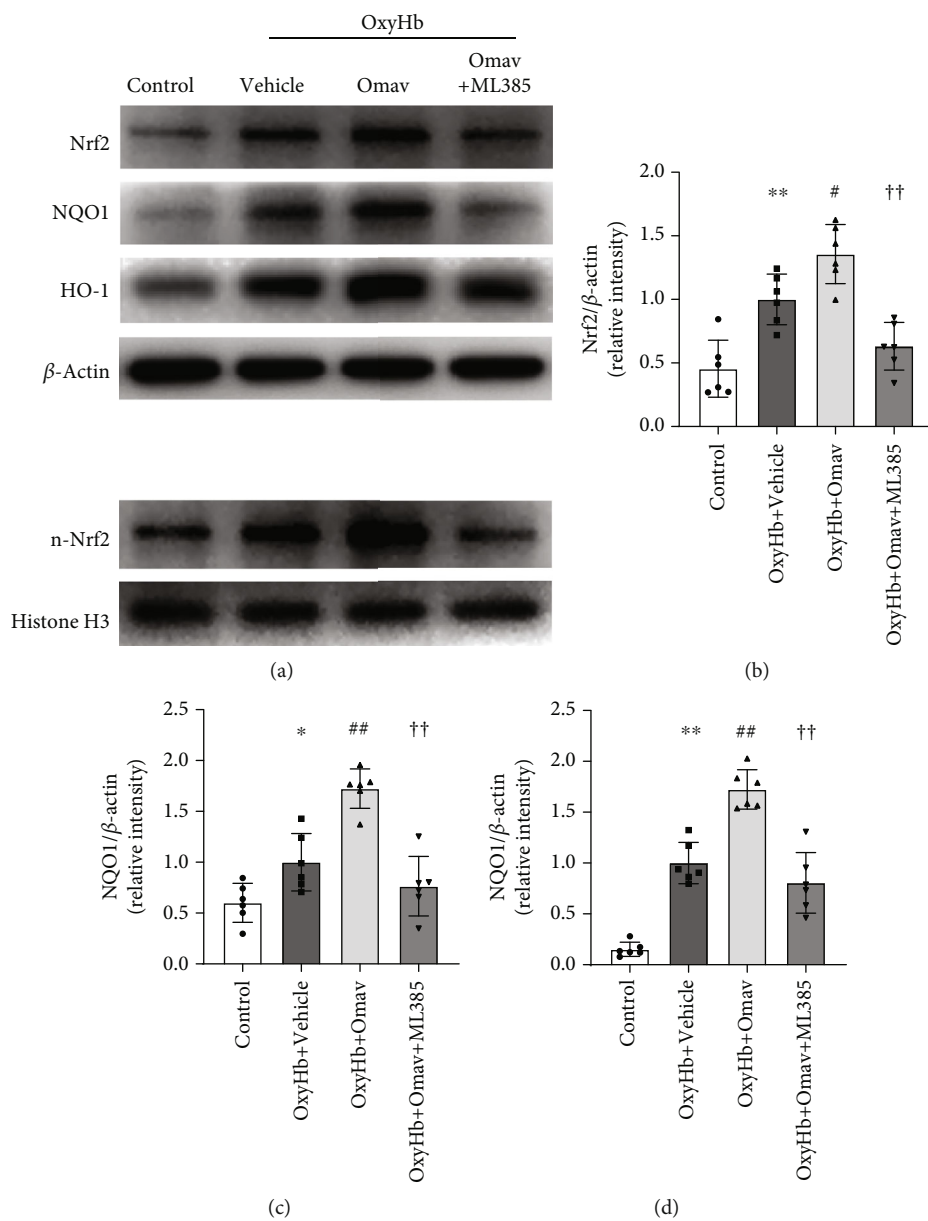


FIGURE 1: Continued.

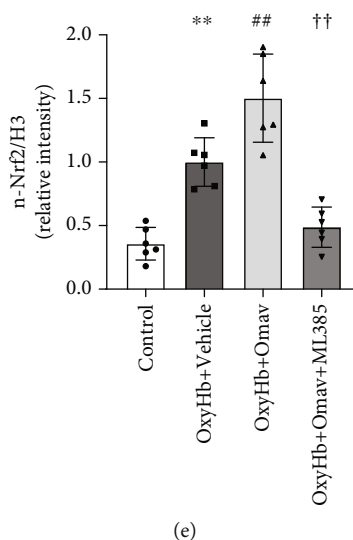


FIGURE 1: Omav increased Nrf2, NQO1, and HO-1 expressions and Nrf2 nuclear translocation *in vitro*. (a) Western blots showing the levels of Nrf2, NQO1, HO-1, and n-Nrf2 in BV2 cells treated with vehicle, OxyHb, Omav, and ML385. (b–e) Relative quantification of Nrf2, NQO1, HO-1, and n-Nrf2 expression ( $n = 6$ ). Data are presented as the means  $\pm$  SEM. \* $P < 0.05$  and \*\* $P < 0.01$  compared with the control group; # $P < 0.05$  and ## $P < 0.01$  compared with the OxyHb group; †† $P < 0.01$  compared with the OxyHb+Omav group.

a microscope (Leica DM6B, Germany) under a fixed exposure condition.

**2.12. Detection of Mitochondrial Bioactivity.** The bioactivity of mitochondria was measured using MitoTracker Red CMXRos (Beyotime, China), which specifically labels active mitochondria in cells. Briefly, CMXRos was added to the cell medium to a final concentration of 50 nM and coincubated for 30 minutes. The cells were then washed with PBS and fixed with 4% paraformaldehyde for 15 minutes. After 3 washes, the cells were harvested for FCM detection using a flow cytometer (Beckman Coulter, United States); the gating strategy of mitochondrial bioactivity detection was shown in Sup. Fig1 A.

**2.13. Residual Hematoma Volume.** The assessment of the residual hematoma volume was based on the previously described methods with some modifications [36]. Briefly, mouse brains were removed after transcardial perfusion with cold PBS and cut into 1 mm thick coronal sections. A set of digital images was acquired and analyzed with ImageJ software to quantify the residual hematoma volume. After converting the image to 8 bits and inverting it, the area of residual hematoma volume was measured, and the difference in gray value between the hematoma and contralateral regions was calculated. The total residual hematoma volume from these sections was then integrated using the following formula  $V = \sum(\text{Areas of hematoma} \times 1)$ , where  $V$  is the residual hematoma volume calculated in cubic millimeters. Similarly, the hematoma index was integrated by adding the difference in the gray value.

**2.14. Hemoglobin Index.** The concentration of hemoglobin in the residual hematoma was detected using Drabkin's reagent (Merck Millipore, Germany) according to the man-

ufacturer's instructions. Briefly, the residual hematoma samples were collected and homogenized. After centrifuging the homogenate, the supernatant was mixed with the reagent and incubated for 20 minutes. The absorbance was detected with a microplate reader, and the concentration of hemoglobin was calculated from a standard curve.

**2.15. Immunofluorescence Staining.** Immunofluorescence staining was performed as previously described [37]. Mice were sacrificed and perfused with cold PBS followed by 4% cold paraformaldehyde (PFA). The brains were removed intact, immersed in 4% PFA, and incubated at 4°C for 24 hours. After dehydration in a 30% sucrose solution, the samples were sliced into 8  $\mu\text{m}$  coronal sections for staining. Brain slices were then sequentially washed with PBS and blocked with 10% donkey serum and 0.3% Triton X-100 to prevent nonspecific binding. The primary antibodies used for immunofluorescence staining were as follows: Iba-1 (cat. no. ab5076), iNOS (cat. no. ab178945), and Arg1 (cat. no. 16001-1-AP). After an overnight incubation at 4°C and washing, slices were incubated with secondary antibodies for 2 hours at room temperature in the dark. The sections were rinsed and mounted using Antifade Mounting Medium with DAPI (cat. no. MA0222, Meilunbio). The images were captured with a fluorescence microscope.

**2.16. Statistical Analysis.** All data are presented as the means  $\pm$  standard errors. All statistical analyses were performed using SPSS 26.0 software. Comparisons between two groups were evaluated using unpaired Student's  $t$  tests. Differences between different treatment groups were analyzed using one-way ANOVA with Bonferroni's post hoc multiple comparison tests. Statistical significance was defined as  $P < 0.05$ .

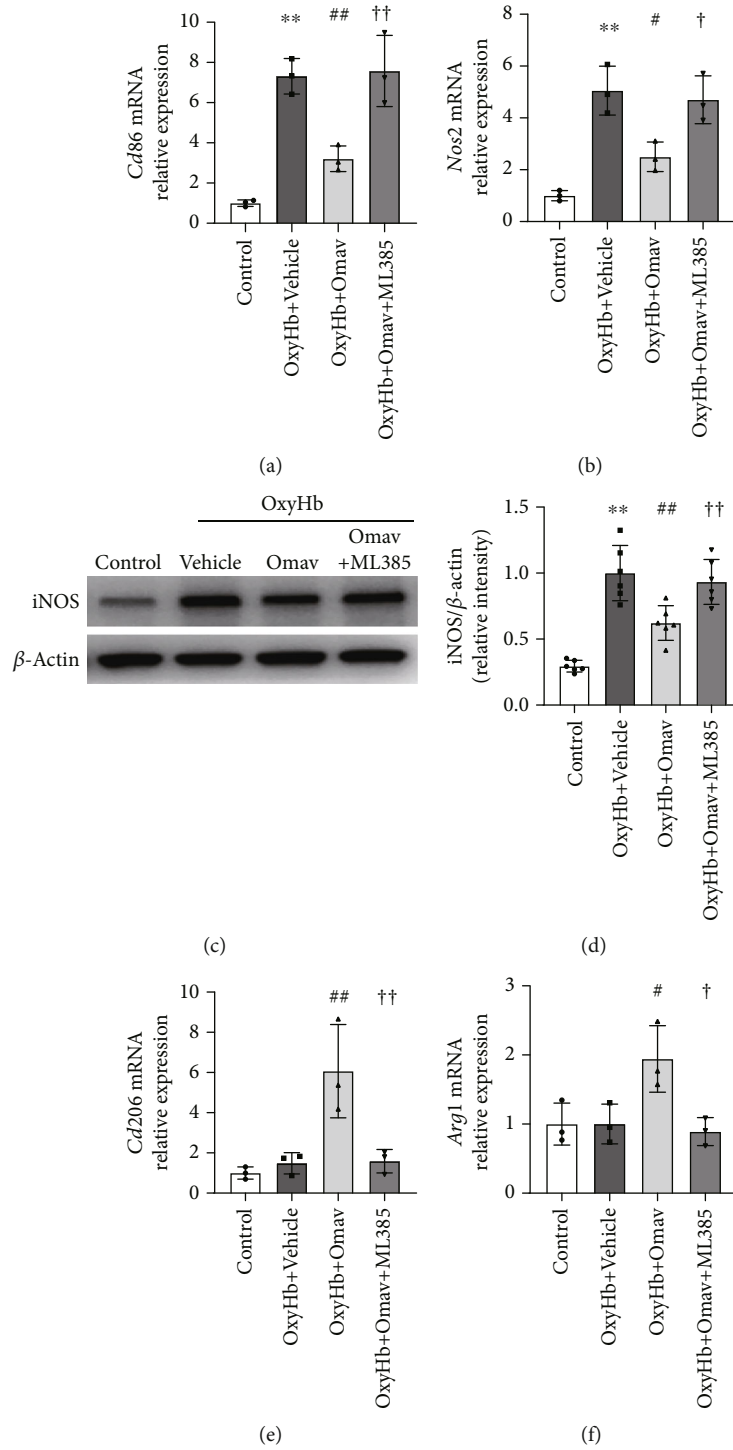


FIGURE 2: Continued.

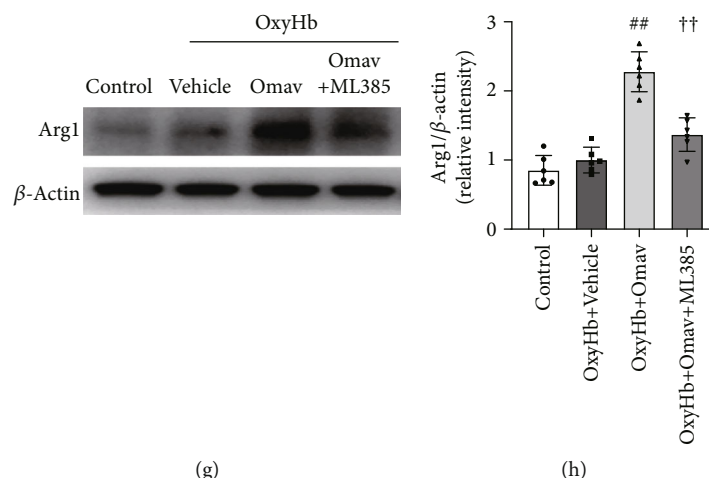


FIGURE 2: Omap reduced the expression of M1-related genes and proteins but increased the expression of M2-related genes and proteins *in vitro*. (a and b) Levels of the *Cd86* and *Nos2* mRNAs in the control group, OxyHb group, OxyHb+Omap group, and OxyHb+Omap+ML385 group ( $n = 3$ ). (c and d) Representative western blot bands and the quantification of the expression of iNOS ( $n = 6$ ). (e and f) mRNA Levels of the *Cd206* and *Arg1* assessed via qPCR ( $n = 3$ ). (g and h) Representative western blot bands and the quantification of the expression of Arg1 ( $n = 6$ ). Data are presented as the means  $\pm$  SEM. \*\* $P < 0.01$  compared with the control group; # $P < 0.05$  and ## $P < 0.01$  compared with the OxyHb group; † $P < 0.05$  and †† $P < 0.01$  compared with the OxyHb+Omap group.

### 3. Results

**3.1. Omap Increased Nrf2, NQO1, and HO-1 Expressions and Nrf2 Nuclear Translocation in OxyHb-Stimulated BV2 Microglial Cells.** First, we explored the effect of Omap on microglia *in vitro* by measuring the expression of Nrf2 and its downstream proteins in the BV2 cell line. The western blot results indicated that Omap increased Nrf2 expression in cells under OxyHb stress, and this effect was partially blocked by ML385, a selective inhibitor of Nrf2 (Figures 1(a) and 1(b) and Sup. Fig. 2 a, b). Consistent with Nrf2, the expression of HO-1 and NQO1 was increased in the OxyHb+Omap group compared to the OxyHb group, and ML385 also reversed this change (Figures 1(c) and 1(d)). Since the nuclear translocation of Nrf2 primes downstream protein expression, we additionally measured nuclear Nrf2 (n-Nrf2) and cytoplasmic Nrf2 levels in each group. As shown in Figure 1(e) and Sup. Fig. 2 c, d, Omap increased n-Nrf2 and cyto-Nrf2 levels, while ML385 treatment diminished n-Nrf2 and cyto-Nrf2 levels. Thus, Omap promotes the expression of antioxidant proteins in BV2 cells by facilitating the expression and translocation of Nrf2.

**3.2. Omap Decreased M1 Microglial-Related Gene Expression but Increased M2 Microglial-Related Gene Expression In Vitro.** According to the previous studies, OxyHb stimulation caused microglia to activate the M1 phenotype [38]. We assessed the expression of phenotype-related genes and proteins to explore the effect of Omap on microglial polarization. BV2 microglial cells were treated as described in Section 3.1 for 6 hours. qRT-PCR revealed that Omap inhibited M1-related gene (*Cd86* and *Nos2*) transcription (Figures 2(a) and 2(b)). Western blots of iNOS showed a consistent tendency (Figures 2(c) and 2(d)). Meanwhile, M2-related gene (*Cd206* and *Arg1*) transcription and Arg1 expression were promoted by Omap (Figures 2(e)–2(h)).

Pretreatment with ML385 blocked the effect of Omap. Taken together, these results indicated that Omap modulated microglial polarization toward the M2 phenotype following OxyHb stimulation.

**3.3. Omap Administration Decreased the Proinflammatory Cytokine Production but Promoted Phagocytosis after OxyHb Stimulation in BV2 Microglial Cells.** We tested the proinflammatory or prophagocytic functions of BV2 cells treated with Omap to further verify the pharmacological effects of Omap on the microglial polarization. The mRNA expression of inflammatory cytokines (*Il-1 $\beta$*  and *Tnf- $\alpha$* ) was upregulated upon stimulation with OxyHb but downregulated after treatment with Omap (Figures 3(a) and 3(b)). Regarding the M2 phenotype, Omap increased the mRNA expression of *Il-10*, an anti-inflammatory M2 signature cytokine secreted by M2 microglia (Figure 3(c)). Fluorescence imaging showed that Omap improved the phagocyte ratio of BV2 cells (Figures 3(d) and 3(e)), which was decreased by pretreatment with ML385. We further detected the secretion of IL-1 $\beta$  and TNF- $\alpha$  using ELISAs, which showed that Omap decreased the levels of these cytokines compared with the OxyHb treatment group (Figures 3(f) and 3(g)). Both transcriptional and translational changes induced by Omap were blocked by ML385 pretreatment. Furthermore, flow cytometry (FCM) revealed a parallel result of higher phagocytosis of latex beads by the OxyHb+Omap group than by the OxyHb+vehicle group and OxyHb+Omap+ML385 group (Figures 3(h) and 3(i)). Collectively, these results suggested that Omap treatment inhibited M1-like polarization but promoted M2-like phenotype activation following OxyHb challenge.

**3.4. Omap Reduced ROS Production and Increased Mitochondrial Membrane Potential after OxyHb In Vitro.** Intracellular ROS induced a self-propelling cycle to maintain

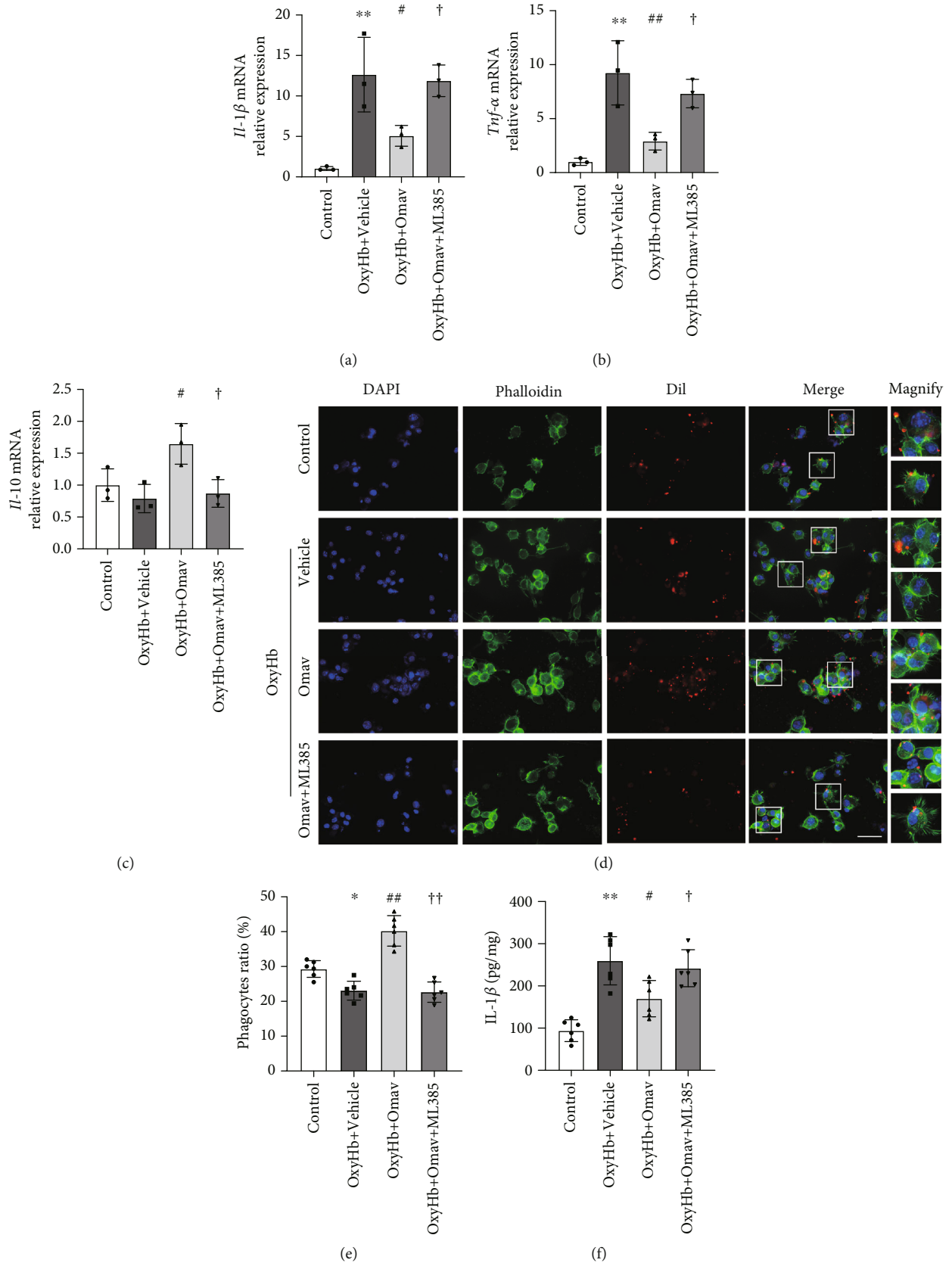


FIGURE 3: Continued.

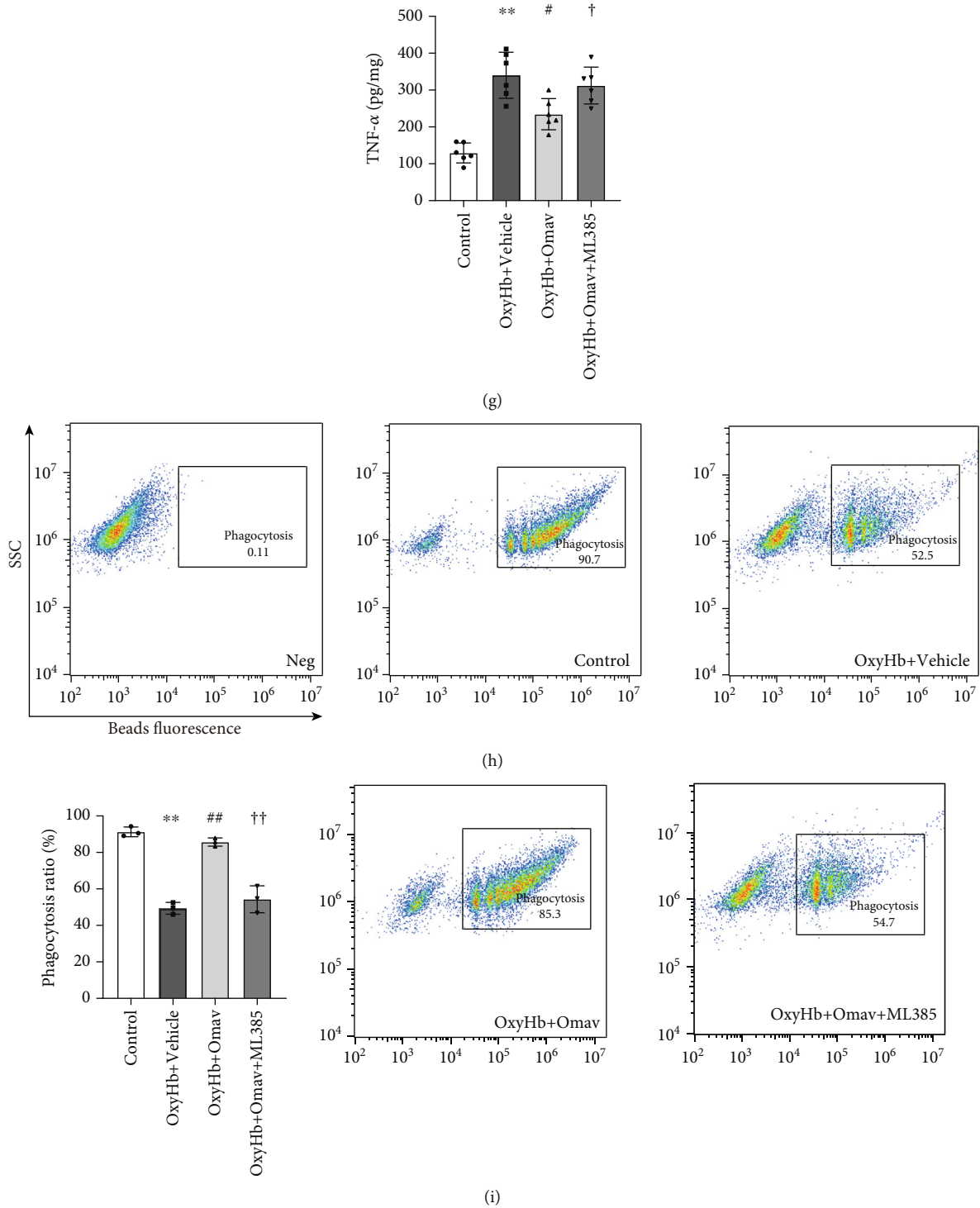
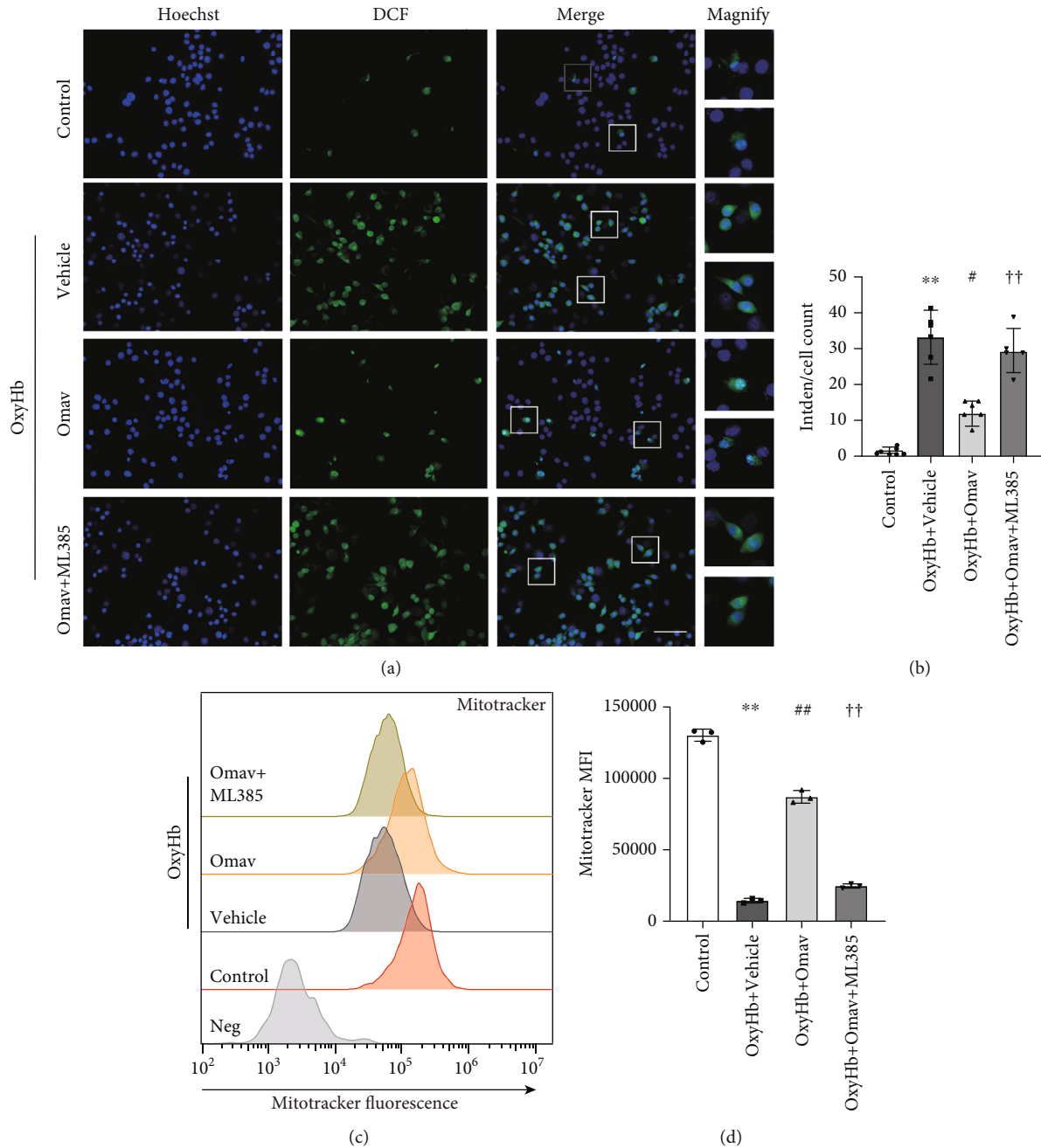


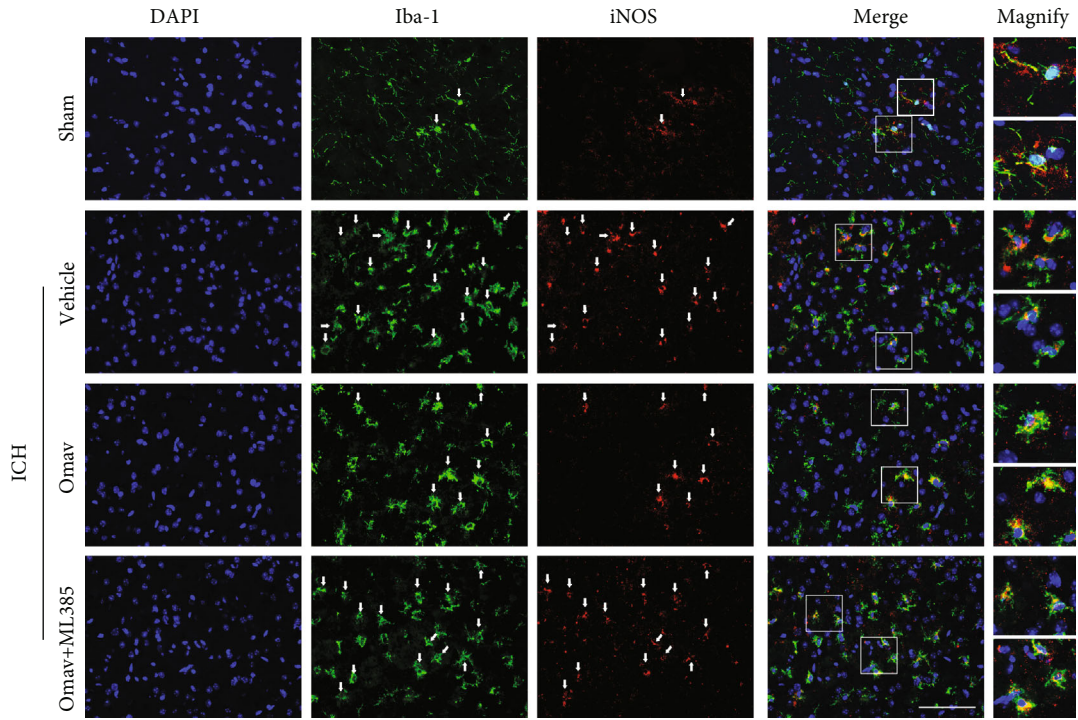
FIGURE 3: Omav reduced the expression of inflammatory cytokines but enhanced BV2 phagocytosis under the stress of OxyHb. (a–c) Levels of the *Il-1β*, *Tnf-α*, and *Il-10* mRNAs in treated BV2 cells ( $n = 3$ ). (d) Representative fluorescent images of the phagocytosis assay in BV2 cells.  $\beta$ -Actin in BV2 cells was labeled with phalloidin-FITC, and RBCs were labeled with DiI. Scale bar:  $50 \mu\text{m}$ . (e) Quantification of the phagocyte proportion according to fluorescence ( $n = 6$ ). (f and g) The concentrations of  $\text{IL-1}\beta$  and  $\text{TNF-}\alpha$  were detected using ELISAs ( $n = 6$ ). (h) Phagocytosis ratio of BV2 cells in each group detected via FCM. (i) Quantification of the ratio of BV2 cells phagocytoses labeled RBCs from each group ( $n = 3$ ). Data are presented as the means  $\pm$  SEM. \* $P < 0.05$  and \*\* $P < 0.01$  compared with the control group; # $P < 0.05$  and ## $P < 0.01$  compared with the OxyHb group; † $P < 0.05$  and †† $P < 0.01$  compared with the OxyHb+Omav group.



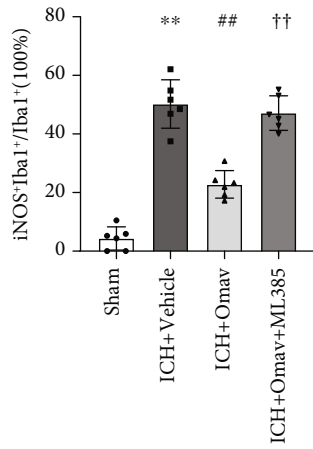
**FIGURE 4:** Omap reduced ROS generation and increased mitochondrial membrane potential of BV2 in response to OxyHb. (a) ROS levels were detected using an ROS assay kit with fluorescence microscopy after exposure to the corresponding stimulus; scale bar: 50  $\mu$ m. (b) Quantification of fluorescence intensity per cell in each group ( $n=6$ ). (c) Mitochondrial bioactivity was detected using MitoTracker Red CMXRos with FCM. (d) Quantification of the mean fluorescence intensity (MFI) assessed via FCM ( $n=3$ ). Data are presented as the means  $\pm$  SEM. \* $P < 0.05$  and \*\* $P < 0.01$  compared with the control group; # $P < 0.05$  and ## $P < 0.01$  compared with the OxyHb group; † $P < 0.05$  and †† $P < 0.01$  compared with the OxyHb+Omap group.

the continued activation of the M1-like phenotype [39]. We hypothesized that the mechanisms underlying the function of Omap in modulating microglial polarization are associated with ROS. Fluorescence imaging showed that OxyHb increased the mean ROS level, and Omap treatment significantly reduced the elevated fluorescence signal, while the ML385 pretreatment attenuated the inhibitory effect of Omap on OxyHb-induced ROS generation (Figures 4(a)

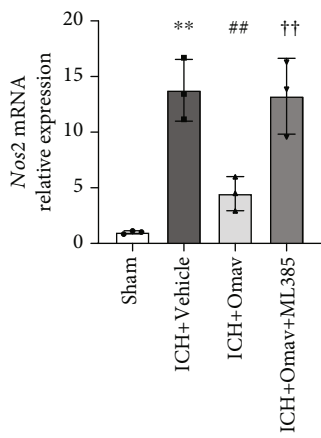
and 4(b)). We then performed FCM to detect the mitochondrial membrane potential, which indicates the bioactivity of mitochondria. Compared with the control group, OxyHb stimulation markedly decreased mitochondrial bioactivity, Omap administration attenuated the impairment caused by OxyHb, and the protective effect of Omap on mitochondrial bioactivity was blocked by the ML385 pretreatment (Figures 4(c) and 4(d)). These results indicated that the



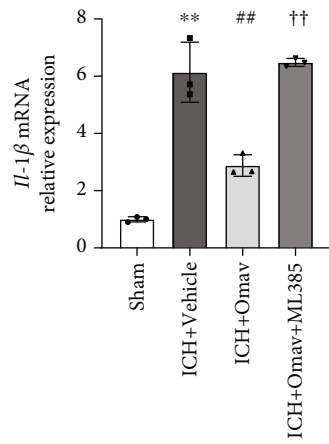
(a)



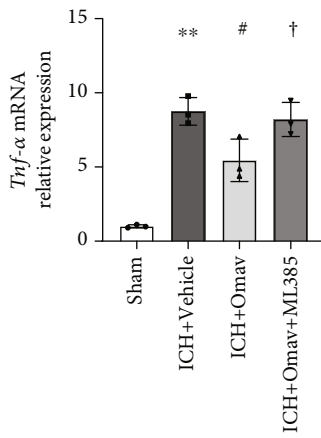
(b)



(c)



(d)



(e)

FIGURE 5: Continued.



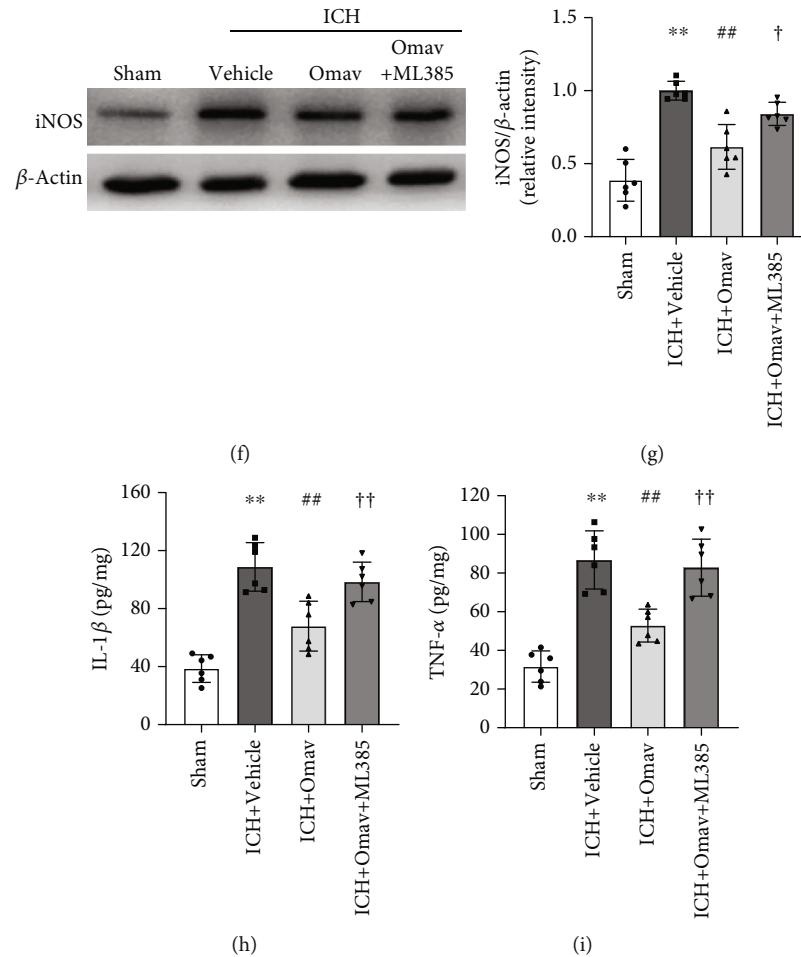


FIGURE 5: Omav reduced the expression of proinflammatory genes and proteins after ICH. (a) Immunofluorescence staining for Iba-1 (green) and iNOS (red) in the ipsilateral basal ganglia region 3 days after ICH; the nuclei were stained with DAPI (blue); scale bar: 50  $\mu\text{m}$  ( $n = 6$ ). (b) Quantification of the ratio of microglia expressing iNOS. (c–e) qRT-PCR analysis of the expression of the mRNAs encoding iNOS, IL-1 $\beta$ , and TNF- $\alpha$  ( $n = 3$ ). (f) Western blot showing iNOS levels in peripheral hematoma tissues from each group ( $n = 6$ ). (g) Quantitative analysis of the iNOS band. (h–i) The concentrations of IL-1 $\beta$  and TNF- $\alpha$  in perihematoma 3 days after ICH were detected using ELISAs ( $n = 6$ ). Data are presented as the means  $\pm$  SEM. \* $P < 0.05$  and \*\* $P < 0.01$  compared with the control group; # $P < 0.05$  and ## $P < 0.01$  compared with the OxyHb group; † $P < 0.05$  and †† $P < 0.01$  compared with the OxyHb+Omav group.

modulation of microglial polarization by Omav was associated with reducing ROS generation and mitochondrial protection.

**3.5. Omav Downregulated Proinflammatory Cytokines after ICH.** After documenting the modulatory effect of Omav on BV2 microglial polarization, we assumed that Omav exerted anti-inflammatory effects on the ICH insult. Inducible nitric oxide synthase (iNOS) is a key factor associated with microglia-mediated neuropathology [40]. Immunofluorescence staining revealed that Omav decreased the ratio of iNOS-positive microglia around the perihematoma region 1 and 3 days after ICH (Figures 5(a) and 5(b); Sup. Fig. 3A, B; and Sup. Fig. 4A, C). We also discovered diminished expression of the iNOS (*Nos2*), IL-1 $\beta$ , and TNF- $\alpha$  mRNAs (Figures 5(c), 5(d), and 5(e)) in the ICH+Omav group. Western blot showed that iNOS was expressed at lower levels in the ICH+Omav group than in the ICH+vehicle group (Figures 5(f) and 5(g)). In addition, the results of

ELISA suggested that Omav treatment significantly reduced the levels of IL-1 $\beta$  and TNF- $\alpha$  at 1 and 3 days after ICH (Figures 5(h) and 5(i) and Sup. Fig. 4E, F). Furthermore, with ML385 pretreatment, the percentage of iNOS-positive cells in brain sections was increased, and the expression levels of M1 microglial markers were increased. Together, these findings suggested that Omav exerted an anti-inflammatory effect that attenuated M1 microglial activation after ICH injury *in vivo*.

**3.6. Omav Increased the Expression of Arg1 on Microglia and Promoted Hematoma Resolution 3 Days Post-ICH.** Generally, M2 polarization follows M1 activation at later stages in ICH pathology, and Arg1 is a crucial M2 marker that downregulates iNOS activity [16]. Here, immunofluorescence staining revealed that Omav increased the percentage of Arg1+Iba1+/Iba1+ cells around the perihematoma region (Figures 6(a) and 6(b); Sup. Fig. 3c, d; and Sup. Fig. 4b, d). Western blot analysis revealed an increase in Arg1

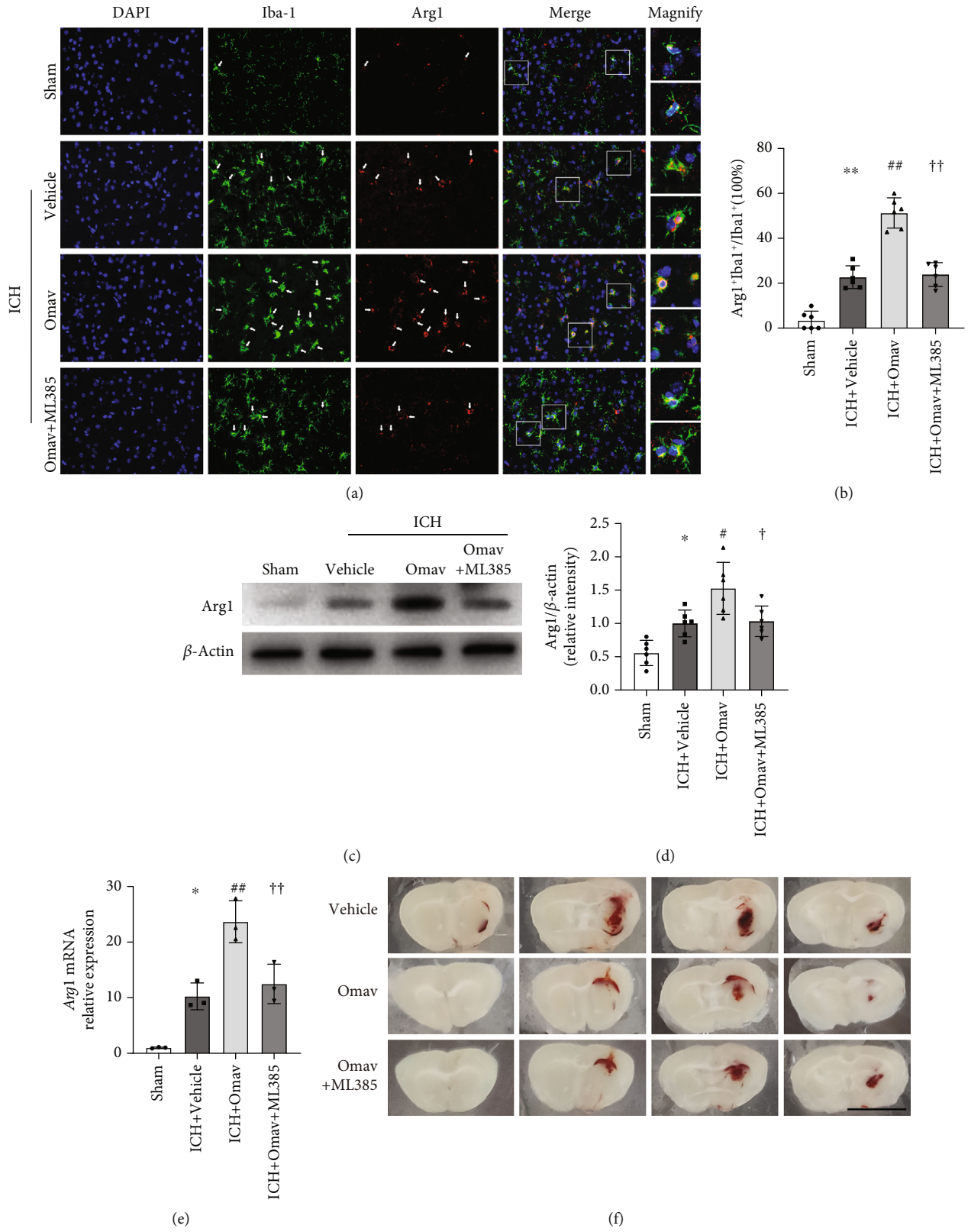


FIGURE 6: Continued.

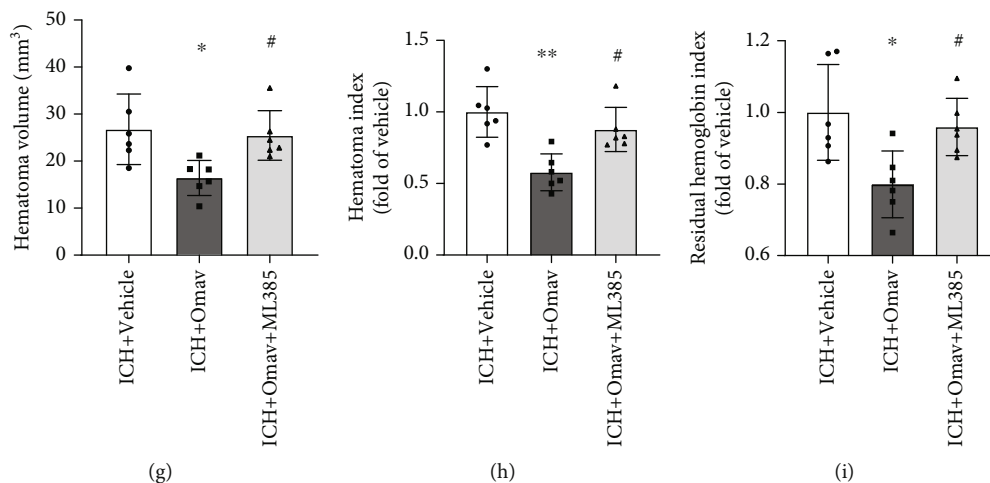


FIGURE 6: Omap promoted M2-like microglial polarization and accelerated hematoma resolution after ICH. (a) Immunofluorescence staining for Iba-1 (green) and Arg1 (red) in the ipsilateral basal ganglia region; the nuclei were stained with DAPI (blue); scale bar: 50  $\mu\text{m}$  ( $n = 6$ ). (b) Quantification of the ratio of microglia expressing Arg1. (c) Western blot showing Arg1 levels in peripheral hematoma tissues from each group ( $n = 6$ ). (d) Quantitative analysis of the Arg1 band. (e) qRT-PCR analysis of the expression of the Arg1 mRNA ( $n = 3$ ). (f) Representative images of brain slices from each group; scale bar: 5 mm. (g) Quantification of the hematoma volume in each group ( $n = 6$ ). (h) Quantification of the hematoma index (hematoma volume  $\times$  density), which considers incomplete hematoma absorption ( $n = 6$ ). (i) Quantification of the residual hemoglobin content detected using Drabkin's reagent ( $n = 6$ ). Data are presented as the means  $\pm$  SEM. \* $P < 0.05$  and \*\* $P < 0.01$  compared with the control group; # $P < 0.05$  and ## $P < 0.01$  compared with the OxyHb group; † $P < 0.05$  and †† $P < 0.01$  compared with the OxyHb+Omap group.

protein levels in the ICH+Omap group compared to the ICH+vehicle group (Figures 6(c) and 6(d)). qRT-PCR showed increased expression of the *Arg1* mRNA following Omap treatment (Figure 6(e)). Furthermore, we acquired images of 1 mm thick coronal sections to evaluate the residual hematoma volume before collecting the hematoma for hemoglobin tests and protein samples for western blotting (Figure 6(f)). Measurement of the area and gray value of these images showed a lower hematoma volume and hematoma index in the ICH+Omap group than in the other groups (Figures 6(g) and 6(h)). Consistent with the volume changes, the residual hemoglobin content was decreased by Omap treatment (Figure 6(i)). Collectively, Omap enhanced M2 microglial polarization to protect against ICH, thereby promoting hematoma absorption.

**3.7. Omap Treatment Alleviated Neurological Deficits in Mouse ICH Models.** We assessed the neurological functions of each group 3 days after ICH modeling to intuitively evaluate the neuroprotective effect of Omap. The results of the cylinder test showed that Omap decreased the ratio of using the nonimpaired forelimb for weight shifting movements after ICH (Figure 7(a)). In addition, the administration of Omap increased the forelimb placement score (Figure 7(b)). Moreover, the corner turn test showed a lower ratio of turning right in the ICH+Omap group (Figure 7(c)). Based on these results, Omap administration improved the sensorimotor/proprioceptive capacity 3 days after ICH. In contrast, inhibition of Nrf2 by ML385 blocked the amelioration of neurological deficits. Taken together, the modulation of microglial polarization by Omap might be a functional neuroprotective target after ICH.

## 4. Discussion

This study examined the effect of Omap, a potent Nrf2 activator, on ICH both *in vivo* and *in vitro*. Omap attenuated ICH-induced neuroinflammation and promoted hematoma clearance by modulating microglial M1/M2 polarization, subsequently facilitating neurological recovery after ICH. Omap promoted the nuclear translocation of Nrf2 and increased the expression of HO-1 and NQO1 to then reduce ROS accumulation and preserve mitochondrial functions in microglia. In addition, ML385-mediated inhibition of Nrf2 abolished the protective effects of Omap on ICH.

Hematoma evacuation was once the mainstay of ICH treatment, yet the improvement of functional outcome or mortality was limited, as reported in several well-known clinical trials, such as STICH and MISTIE [41, 42]. These results do not deny the role of early clearance of hematoma but rather highlight that secondary brain injury is as important as primary injury in influencing long-term neurological recovery after ICH. As key innate immune cells, microglia are the first nonneuronal cells to respond to acute brain injuries [43–45]. M1 microglia are presumed to be proinflammatory and release cytokines such as TNF- $\alpha$ , IL-1 $\beta$ , and IL-6, whereas M2 microglia are presumed to secrete anti-inflammatory cytokines such as IL-10 and contribute to the phagocytosis of hematoma [12]. Previous studies have revealed dynamic changes in the M1 to M2 phenotype over time in response to traumatic brain injury [46], ischemic brain injury [10], and ICH. In a study of ICH in mice, microglia responded to hemorrhagic attack within the first hour after surgery and presented an M1-like phenotype. Markers of M2 microglia increased later than those of M1

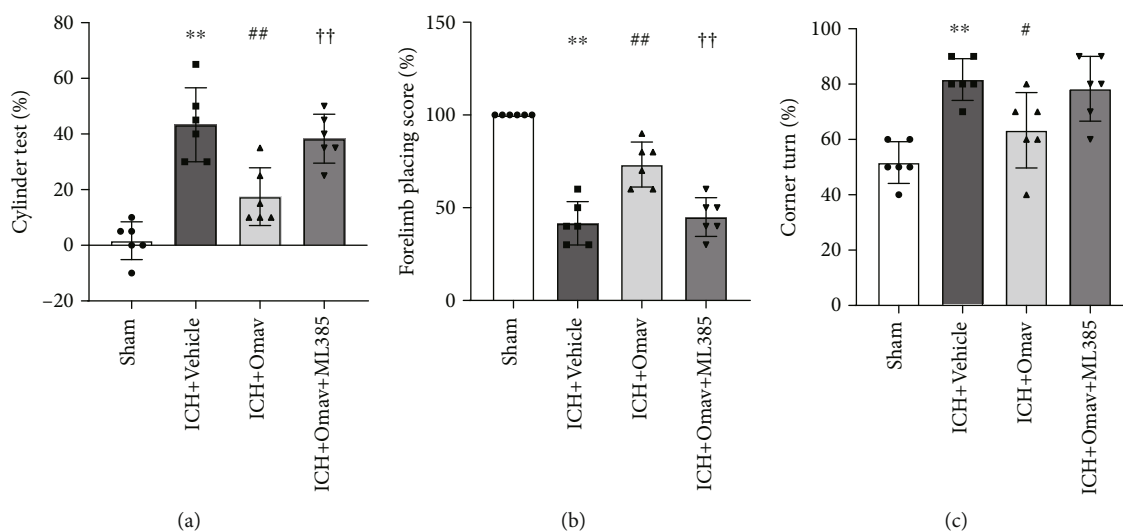


FIGURE 7: Omap alleviated neurological deficits in mice 3 days after ICH. The results of the following neurological behavior tests: the cylinder test (a), forelimb placement score (b), and corner test (c) ( $n = 6$ ). \*\* $P < 0.01$  compared with the control group; # $P < 0.05$  and ## $P < 0.01$  compared with the OxyHb group; †† $P < 0.01$  compared with the OxyHb+Omap group.

microglia, peaked from days 3 to 7 after ICH induction. In clinical studies, both M1 and M2 microglia were detected in the hematoma of patients with ICH within 30 hours after ICH onset. More importantly, higher levels of IL-10 in the hematoma and serum and lower amounts of M1 microglia were independently associated with a better recovery at 90 days after ICH. In this regard, modulating the phenotypic changes of activated microglia may provide opportunities for future therapeutic interventions. Consistent with previous studies, our study indicated that both M1 and M2 microglia existed after ICH induction in mice. The proportions of iNOS-positive and Arg-positive microglia cells in ICH groups at 3 days were higher than those in the corresponding group at 1 day post-ICH. However, the proportion of iNOS-positive microglia in the Omap treatment group was lower than that in the vehicle group, and the ratio of Arg1-positive microglia was higher than that in the vehicle group. This indicated that Omap administration may advance the polarization of microglia toward the M2 phenotype, which ultimately attenuated the neurological deficits of ICH mice. Indeed, the M1/M2 paradigm is oversimplified to describe the true nature of microglia, especially in complicated situations such as ICH. Here in this study, we tend to use the concept of M1 and M2 to represent the functional properties of microglia rather than emphasize the polarization itself. Fortunately, as the methodology advances, the identification and classification of microglia are becoming more adequate and accurate. For example, the discovery of disease-associated microglia (DAM) has vastly improved our understanding of the diversity and functional role of microglia in AD. Further investigations are urgently needed to better characterize microglia in other brain diseases, including ICH.

In microglia, the main source of ROS is the activation of NADPH oxidase (NOX) and nitric oxide synthase (NOS) enzymes [47, 48]. ROS and the subsequently formed peroxynitrite contribute to cell death by damaging mitochondria

and DNA, inhibiting the activity of mitochondrial complexes and the production of ATP, and promoting lipid peroxidation [49, 50]. In addition, ROS production and redox homeostasis have been shown to affect the phenotype of microglia. Pharmacological inhibition of NOX or knockout of its functional subunit p47phox shift LPS-challenged microglia from the M1 phenotype to the M2 phenotype [51]. A mitochondria-targeted antioxidant alleviated brain damage in an autologous blood injection-induced ICH model by polarizing microglia to the M2 phenotype [11]. According to these studies, modulating oxidative stress may be a potential therapeutic target for treating ICH in the future. Antioxidant drugs such as edaravone have been shown to scavenge ROS and modulate the phenotype of microglia either in individuals with hemorrhagic stroke or LPS-induced neuroinflammation [52, 53], yet they failed to reduce mortality and provide long-term clinical benefits in clinical studies [54, 55]. Thus, more efforts are needed to develop novel antioxidant therapies that improve the outcomes of patients with ICH.

Nrf2 regulates a variety of antioxidant genes and is tightly related to redox homeostasis [56]. Nrf2<sup>-/-</sup> mice suffered more severe brain damage and had a significantly lower survival rate than wild-type mice after ICH [19, 57]. Deletion of Nrf2 impaired hematoma clearance and enhanced neuroinflammation after ICH, while the induction of HO-1, one of the major targets of Nrf2, polarizes microglia/macrophages to the M2 phenotype [57, 58]. Omap is one of the most potent activators of Nrf2. Oral administration of Omap to monkeys is associated with dose-proportional concentrations in the brain and induces Nrf2 target gene mRNA expression [59]. More importantly, Omap is currently being investigated in clinical trials as a treatment for mitochondrial myopathies (NCT02255422), melanoma (NCT02259231), non-small-cell lung cancer (NCT02029729), and Friedreich ataxia (FA, NCT02255435). The results of FA research revealed

that Omav is safe and well tolerated, and Omav improved the neurological functions of patients with FA. In this study, we found that Omav alleviated ROS accumulation in microglia by activating Nrf2. Furthermore, Omav downregulates iNOS-positive microglia polarization but promotes Arg1-positive phenotype, which led to the attenuation of ICH-induced neuroinflammation and the acceleration of hematoma clearance. Based on these data, Omav might represent a promising candidate for treating ICH in the future.

## Abbreviations

ICH:	Intracerebral hemorrhage
Nrf2:	Nuclear factor erythroid-2 related factor 2
Omav:	Oma voxelolone
HO-1:	Heme oxygenase-1
NQO1:	NAD(P)H: quinone oxidoreductase-1
ROS:	Reactive oxygen species
DMSO:	Dimethyl sulfoxide
PBS:	Phosphate-buffered saline
qRT-PCR:	Quantitative Real-time polymerase chain reaction
OxyHb:	Oxyhemoglobin
SOD:	Superoxide dismutase
CNS:	Central nervous system
DCFH-DA:	2',7'-Dichlorodihydrofluorescein diacetate
FCM:	Flow cytometry
PFA:	Paraformaldehyde.

## Data Availability

The raw data involved in the manuscript are available on reasonable request.

## Conflicts of Interest

The authors have no conflicts of interest to declare.

## Authors' Contributions

Libin Hu, Yang Cao, and Huaijun Chen contributed equally to this work.

## Acknowledgments

This research was supported by the National Key R&D Program of China (2018YFC1312600 and 2018YFC1312603), TCM Science and Technology Plan of Zhejiang Province (2017ZZ013), TCM Key Discipline of Zhejiang Province (2017-XK-A39), Zhejiang Province Natural Science Foundation (LQ20H090015 and LY20H090016), and Zhejiang Provincial Health Innovative Talents Project (2020RC012).

## Supplementary Materials

Supplementary Figure 1: (a) gating strategy for FCM in mitochondrial bioactivity detection. (b) In vitro phagocytosis gating strategy. Supplementary Figure 2: (a) western blots showing the levels of Nrf2 in BV2 cells treated with vehicle

and ML385 under the stress of OxyHb. (b) Quantification of the Nrf2 expression ( $n = 6$ ). (c) Western blots showing the levels of cytoplasmic Nrf2 in BV2 cells treated with vehicle, OxyHb, Omav, and ML385. (d) Quantification of the cyto-Nrf2 expression ( $n = 6$ ). Data are presented as the means  $\pm$  SEM.  $*P < 0.05$  and  $**P < 0.01$  compared with the control group;  $^{\#}P < 0.05$  and  $^{\#\#}P < 0.01$  compared with the OxyHb group;  $^{\dagger\dagger}P < 0.01$  compared with the OxyHb+Omav group. Supplementary Figure 3: (A) quantification of the number of cells expressing iNOS. (b) Quantification of number of Iba1-positive cells ( $n = 6$ ). (c) Quantification of the count of cells expressing Arg1. (d) Quantification of count of Iba1+ cells ( $n = 6$ ). Data are presented as the means  $\pm$  SEM.  $*P < 0.05$  and  $**P < 0.01$  compared with the Control group;  $P < 0.05$  and  $P < 0.01$  compared with the OxyHb group;  $^{\dagger\dagger}P < 0.01$  compared with the OxyHb+Omav group. Supplementary Figure 4: (A) immunofluorescence staining for Iba-1 (green) and iNOS (red) in the ipsilateral basal ganglia region 1 day after ICH; the nuclei were stained with DAPI (blue); scale bar: 50  $\mu$ m. (B) Immunofluorescence staining for Iba-1 (green) and Arg1 (red) in the ipsilateral basal ganglia region 1 day after ICH; the nuclei were stained with DAPI (blue); scale bar: 50  $\mu$ m. (c) Quantification of the ratio of microglia expressing iNOS. (d) Quantification of the ratio of microglia expressing Arg1. (E–F) The concentrations of IL-1 $\beta$  and TNF- $\alpha$  in perihematoma 1 day after ICH were detected using ELISAs ( $n = 6$ ). Data are presented as the means  $\pm$  SEM.  $*P < 0.05$  and  $**P < 0.01$  compared with the control group;  $^{\#\#}P < 0.01$  compared with the OxyHb group;  $^{\dagger}P < 0.05$  and  $^{\dagger\dagger}P < 0.01$  compared with the OxyHb+Omav group. (Supplementary Materials)

## References

- [1] A. I. Qureshi, A. D. Mendelow, and D. F. Hanley, "Intracerebral haemorrhage," *Lancet*, vol. 373, no. 9675, pp. 1632–1644, 2009.
- [2] A. I. Qureshi, S. Tuhim, J. P. Broderick, H. H. Batjer, H. Hondo, and D. F. Hanley, "Spontaneous intracerebral hemorrhage," *The New England Journal of Medicine*, vol. 344, no. 19, pp. 1450–1460, 2001.
- [3] C. S. Anderson, E. Heeley, Y. Huang et al., "Rapid blood-pressure lowering in patients with acute intracerebral hemorrhage," *The New England Journal of Medicine*, vol. 368, no. 25, pp. 2355–2365, 2013.
- [4] R. F. Keep, Y. Hua, and G. Xi, "Intracerebral haemorrhage: mechanisms of injury and therapeutic targets," *Lancet Neurology*, vol. 11, no. 8, pp. 720–731, 2012.
- [5] V. Stratoulis, J. L. Venero, M. E. Tremblay, and B. Joseph, "Microglial subtypes: diversity within the microglial community," *The EMBO Journal*, vol. 38, no. 17, p. e101997, 2019.
- [6] D. Boche, V. H. Perry, and J. A. Nicoll, "Review: activation patterns of microglia and their identification in the human brain," *Neuropathology and Applied Neurobiology*, vol. 39, no. 1, pp. 3–18, 2013.
- [7] B. A. Durafourt, C. S. Moore, D. A. Zammit et al., "Comparison of polarization properties of human adult microglia and blood-derived macrophages," *Glia*, vol. 60, no. 5, pp. 717–727, 2012.

- [8] J. Qu, W. Chen, R. Hu, and H. Feng, "The injury and therapy of reactive oxygen species in intracerebral hemorrhage looking at mitochondria," *Oxidative Medicine and Cellular Longevity*, vol. 2016, Article ID 2592935, 9 pages, 2016.
- [9] J. Suenaga, X. Hu, H. Pu et al., "White matter injury and microglia/macrophage polarization are strongly linked with age-related long-term deficits in neurological function after stroke," *Experimental Neurology*, vol. 272, pp. 109–119, 2015.
- [10] X. Hu, P. Li, Y. Guo et al., "Microglia/macrophage polarization dynamics reveal novel mechanism of injury expansion after focal cerebral ischemia," *Stroke*, vol. 43, no. 11, pp. 3063–3070, 2012.
- [11] W. Chen, C. Guo, S. Huang et al., "MitoQ attenuates brain damage by polarizing microglia towards the M2 phenotype through inhibition of the NLRP3 inflammasome after ICH," *Pharmacological Research*, vol. 161, article 105122, 2020.
- [12] X. Lan, X. Han, Q. Li, Q. W. Yang, and J. Wang, "Modulators of microglial activation and polarization after intracerebral haemorrhage," *Nature Reviews Neurology*, vol. 13, no. 7, pp. 420–433, 2017.
- [13] C. Tschoe, C. D. Bushnell, P. W. Duncan, M. A. Alexander-Miller, and S. Q. Wolfe, "Neuroinflammation after intracerebral hemorrhage and potential therapeutic targets," *Journal of stroke*, vol. 22, no. 1, pp. 29–46, 2020.
- [14] C. F. Chang, J. Wan, Q. Li, S. C. Renfro, N. M. Heller, and J. Wang, "Alternative activation-skewed microglia/macrophages promote hematoma resolution in experimental intracerebral hemorrhage," *Neurobiology of Disease*, vol. 103, pp. 54–69, 2017.
- [15] X. Fu, H. Zeng, J. Zhao et al., "Inhibition of dectin-1 ameliorates neuroinflammation by regulating microglia/macrophage phenotype after intracerebral hemorrhage in mice," *Translational Stroke Research*, vol. 12, no. 6, pp. 1018–1034, 2021.
- [16] T. Taetsch, S. Levesque, C. McGraw et al., "Redox regulation of NF- $\kappa$ B p50 and M1 polarization in microglia," *Glia*, vol. 63, no. 3, pp. 423–440, 2015.
- [17] Y. Wang, Y. Huang, Y. Xu et al., "A dual AMPK/Nrf2 activator reduces brain inflammation after stroke by enhancing microglia M2 polarization," *Antioxidants & Redox Signaling*, vol. 28, no. 2, pp. 141–163, 2018.
- [18] M. J. Calkins, D. A. Johnson, J. A. Townsend et al., "The Nrf2/ARE pathway as a potential therapeutic target in neurodegenerative disease," *Antioxidants & Redox Signaling*, vol. 11, no. 3, pp. 497–508, 2009.
- [19] J. Wang, J. Fields, C. Zhao et al., "Role of Nrf2 in protection against intracerebral hemorrhage injury in mice," *Free Radical Biology & Medicine*, vol. 43, no. 3, pp. 408–414, 2007.
- [20] P. Fu, J. Liu, Q. Bai et al., "Long-term outcomes of monascin - a novel dual peroxisome proliferator-activated receptor  $\gamma$ /nuclear factor-erythroid 2 related factor-2 agonist in experimental intracerebral hemorrhage," *Therapeutic Advances in Neurological Disorders*, vol. 13, p. 175628642092108, 2020.
- [21] T. Sugiyama, T. Imai, S. Nakamura et al., "A novel Nrf2 activator, RS9, attenuates secondary brain injury after intracerebral hemorrhage in sub-acute phase," *Brain Research*, vol. 1701, pp. 137–145, 2018.
- [22] D. R. Lynch and J. Johnson, "Omaveloxolone: potential new agent for Friedreich ataxia," *Neurodegener Dis Manag*, vol. 11, no. 2, pp. 91–98, 2021.
- [23] D. R. Lynch, M. P. Chin, M. B. Delatycki et al., "Safety and efficacy of omaveloxolone in Friedreich ataxia (MOXIe study)," *Annals of Neurology*, vol. 89, no. 2, pp. 212–225, 2021.
- [24] A. W. El-Hattab, A. M. Zarante, M. Almannai, and F. Scaglia, "Therapies for mitochondrial diseases and current clinical trials," *Molecular Genetics and Metabolism*, vol. 122, no. 3, pp. 1–9, 2017.
- [25] T. Shekh-Ahmad, R. Eckel, S. Dayalan Naidu et al., "KEAP1 inhibition is neuroprotective and suppresses the development of epilepsy," *Brain : a journal of neurology*, vol. 141, no. 5, pp. 1390–1403, 2018.
- [26] M. A. Rynkowski, G. H. Kim, R. J. Komotar et al., "A mouse model of intracerebral hemorrhage using autologous blood infusion," *Nature Protocols*, vol. 3, no. 1, pp. 122–128, 2008.
- [27] N. H. Khatibi, Q. Ma, W. Rolland et al., "Isoflurane posttreatment reduces brain injury after an intracerebral hemorrhagic stroke in mice," *Anesthesia and Analgesia*, vol. 113, no. 2, pp. 343–348, 2011.
- [28] J. Cao, Y. Zhuang, J. Zhang et al., "Leucine-rich repeat kinase 2 aggravates secondary brain injury induced by intracerebral hemorrhage in rats by regulating the P38 MAPK/Drossha pathway," *Neurobiology of Disease*, vol. 119, pp. 53–64, 2018.
- [29] X. Sun, Z. Xie, B. Hu et al., "The Nrf2 activator RTA-408 attenuates osteoclastogenesis by inhibiting STING dependent NF- $\kappa$ B signaling," *Redox Biology*, vol. 28, article 101309, 2020.
- [30] B. C. Creelan, D. I. Gabrilovich, J. E. Gray et al., "Safety, pharmacokinetics, and pharmacodynamics of oral omaveloxolone (RTA 408), a synthetic triterpenoid, in a first-in-human trial of patients with advanced solid tumors," *Oncotargets and Therapy*, vol. 10, pp. 4239–4250, 2017.
- [31] X. Liu, K. Ward, C. Xavier et al., "The novel triterpenoid RTA 408 protects human retinal pigment epithelial cells against H<sub>2</sub>O<sub>2</sub>-induced cell injury via NF-E2-related factor 2 (Nrf2) activation," *Redox Biology*, vol. 8, pp. 98–109, 2016.
- [32] S. Deng, P. Sherchan, P. Jin et al., "Recombinant CCL17 enhances hematoma resolution and activation of CCR4/ERK/Nrf2/CD163 signaling pathway after intracerebral hemorrhage in mice," *Neurotherapeutics : the journal of the American Society for Experimental NeuroTherapeutics*, vol. 17, no. 4, pp. 1940–1953, 2020.
- [33] S. Deng, S. Liu, P. Jin et al., "Albumin reduces oxidative stress and neuronal apoptosis via the ERK/Nrf2/HO-1 pathway after intracerebral hemorrhage in rats," *Oxidative Medicine and Cellular Longevity*, vol. 2021, Article ID 8891373, 14 pages, 2021.
- [34] T. Schallert, S. M. Fleming, J. L. Leasure, J. L. Tillerson, and S. T. Bland, "CNS plasticity and assessment of forelimb sensorimotor outcome in unilateral rat models of stroke, cortical ablation, parkinsonism and spinal cord injury," *Neuropharmacology*, vol. 39, no. 5, pp. 777–787, 2000.
- [35] J. Chen, G. Chen, J. Li et al., "Melatonin attenuates inflammatory response-induced brain edema in early brain injury following a subarachnoid hemorrhage: a possible role for the regulation of pro-inflammatory cytokines," *Journal of Pineal Research*, vol. 57, no. 3, pp. 340–347, 2014.
- [36] E. J. Su, C. Cao, L. Fredriksson et al., "Microglial-mediated PDGF-CC activation increases cerebrovascular permeability during ischemic stroke," *Acta Neuropathologica*, vol. 134, no. 4, pp. 585–604, 2017.
- [37] H. Xu, J. Li, Z. Wang et al., "Methylene blue attenuates neuroinflammation after subarachnoid hemorrhage in rats through the Akt/GSK-3 $\beta$ /MEF2D signaling pathway," *Brain, Behavior, and Immunity*, vol. 65, pp. 125–139, 2017.
- [38] S. Wei, C. Luo, S. Yu et al., "Erythropoietin ameliorates early brain injury after subarachnoid haemorrhage by modulating

- microglia polarization via the EPOR/JAK2-STAT3 pathway,” *Experimental Cell Research*, vol. 361, no. 2, pp. 342–352, 2017.
- [39] Z. Lijia, S. Zhao, X. Wang, C. Wu, and J. Yang, “A self-propelling cycle mediated by reactive oxide species and nitric oxide exists in LPS-activated microglia,” *Neurochemistry International*, vol. 61, no. 7, pp. 1220–1230, 2012.
- [40] A. Bal-Price and G. C. Brown, “Inflammatory neurodegeneration mediated by nitric oxide from activated glia-inhibiting neuronal respiration, causing glutamate release and excitotoxicity,” *Journal of Neuroscience*, vol. 21, no. 17, pp. 6480–6491, 2001.
- [41] A. D. Mendelow, B. A. Gregson, E. N. Rowan et al., “Early surgery versus initial conservative treatment in patients with spontaneous supratentorial lobar intracerebral haematomas (STICH II): a randomised trial,” *Lancet*, vol. 382, no. 9890, pp. 397–408, 2013.
- [42] D. F. Hanley, R. E. Thompson, M. Rosenblum et al., “Efficacy and safety of minimally invasive surgery with thrombolysis in intracerebral haemorrhage evacuation (MISTIE III): a randomised, controlled, open-label, blinded endpoint phase 3 trial,” *Lancet*, vol. 393, no. 10175, pp. 1021–1032, 2019.
- [43] J. Wang, “Preclinical and clinical research on inflammation after intracerebral hemorrhage,” *Progress in Neurobiology*, vol. 92, no. 4, pp. 463–477, 2010.
- [44] L. Fourgeaud, P. G. Traves, Y. Tufail et al., “TAM receptors regulate multiple features of microglial physiology,” *Nature*, vol. 532, no. 7598, pp. 240–244, 2016.
- [45] D. Davalos, J. Grutzendler, G. Yang et al., “ATP mediates rapid microglial response to local brain injury in vivo,” *Nature Neuroscience*, vol. 8, no. 6, pp. 752–758, 2005.
- [46] G. Wang, J. Zhang, X. Hu et al., “Microglia/macrophage polarization dynamics in white matter after traumatic brain injury,” *Journal of Cerebral Blood Flow & Metabolism*, vol. 33, no. 12, pp. 1864–1874, 2013.
- [47] L. Qin and F. T. Crews, “NADPH oxidase and reactive oxygen species contribute to alcohol-induced microglial activation and neurodegeneration,” *Journal of Neuroinflammation*, vol. 9, no. 1, pp. 1–19, 2012.
- [48] A. I. Rojo, G. McBean, M. Cindric et al., “Redox control of microglial function: molecular mechanisms and functional significance,” *Antioxidants & Redox Signaling*, vol. 21, no. 12, pp. 1766–1801, 2014.
- [49] P. H. Willems, R. Rossignol, C. E. Dieteren, M. P. Murphy, and W. J. Koopman, “Redox Homeostasis and Mitochondrial Dynamics,” *Cell Metabolism*, vol. 22, no. 2, pp. 207–218, 2015.
- [50] J. Y. Tang, F. Ou-Yang, M. F. Hou et al., “Oxidative stress-modulating drugs have preferential anticancer effects - involving the regulation of apoptosis, DNA damage, endoplasmic reticulum stress, autophagy, metabolism, and migration,” *Seminars in Cancer Biology*, vol. 58, pp. 109–117, 2019.
- [51] S. H. Choi, S. Aid, H. W. Kim, S. H. Jackson, and F. Bosetti, “Inhibition of NADPH oxidase promotes alternative and anti-inflammatory microglial activation during neuroinflammation,” *Journal of Neurochemistry*, vol. 120, no. 2, pp. 292–301, 2012.
- [52] Z. Wang, C. Ma, C. J. Meng et al., “Melatonin activates the Nrf2-ARE pathway when it protects against early brain injury in a subarachnoid hemorrhage model,” *Journal of Pineal Research*, vol. 53, no. 2, pp. 129–137, 2012.
- [53] J. Li, X. Dai, L. Zhou, X. Li, and D. Pan, “Edaravone plays protective effects on LPS-induced microglia by switching M1/M2 phenotypes and regulating NLRP3 inflammasome activation,” *Frontiers in Pharmacology*, vol. 12, article 691773, p. 1352, 2021.
- [54] J. Yang, M. Liu, J. Zhou et al., “Edaravone for acute intracerebral haemorrhage,” *Cochrane Database of Systematic Reviews*, vol. 2, article CD007755, 2011.
- [55] X. Duan, Z. Wen, H. Shen, M. Shen, and G. Chen, “Intracerebral hemorrhage, oxidative stress, and antioxidant therapy,” *Oxidative Medicine and Cellular Longevity*, vol. 2016, Article ID 1203285, 17 pages, 2016.
- [56] D. S. A. Simpson and O. P. L. ROS, “ROS generation in Microglia: Understanding Oxidative Stress and Inflammation in Neurodegenerative Disease,” *Antioxidants*, vol. 9, no. 8, p. 743, 2020.
- [57] Y. Cheng, M. Liu, H. Tang et al., “iTRAQ-based quantitative proteomics indicated Nrf2/OPTN-mediated mitophagy inhibits NLRP3 inflammasome activation after intracerebral hemorrhage,” *Oxidative Medicine and Cellular Longevity*, vol. 2021, Article ID 6630281, 26 pages, 2021.
- [58] Y. Naito, T. Takagi, and Y. Higashimura, “Heme oxygenase-1 and anti-inflammatory M2 macrophages,” *Archives of Biochemistry and Biophysics*, vol. 564, pp. 83–88, 2014.
- [59] S. A. Reisman, S. S. Gahir, C. I. Lee, J. W. Proksch, M. Sakamoto, and K. W. Ward, “Pharmacokinetics and pharmacodynamics of the novel Nrf2 activator omaveloxolone in primates,” *Drug Design, Development and Therapy*, vol. 13, pp. 1259–1270, 2019.

## Research Article

# Luteolin Confers Cerebroprotection after Subarachnoid Hemorrhage by Suppression of NLRP3 Inflammasome Activation through Nrf2-Dependent Pathway

Zi-Huan Zhang,<sup>1</sup> Jia-Qiang Liu,<sup>1</sup> Cheng-Di Hu,<sup>2</sup> Xin-Tong Zhao,<sup>1</sup> Fei-Yun Qin,<sup>1</sup> Zong Zhuang<sup>1,3</sup> and Xiang-Sheng Zhang<sup>1,4</sup>

<sup>1</sup>Department of Neurosurgery, The First Affiliated Hospital of Wannan Medical College (Yijishan Hospital of Wannan Medical College), Wuhu 241001, China

<sup>2</sup>Department of Neurosurgery, Wuwei People's Hospital, Wuwei City, 238399, China

<sup>3</sup>Department of Neurosurgery, Nanjing Drum Tower Hospital, The Affiliated Hospital of Nanjing University Medical School, Nanjing, 210008 Jiangsu, China

<sup>4</sup>Department of Neurosurgery, Beijing Friendship Hospital, Capital Medical University, Beijing 100050, China

Correspondence should be addressed to Zong Zhuang; zongzhuang@126.com and Xiang-Sheng Zhang; zhangxssp@163.com

Received 28 August 2021; Revised 7 October 2021; Accepted 8 October 2021; Published 5 November 2021

Academic Editor: Yuanjian Fang

Copyright © 2021 Zi-Huan Zhang et al. This is an open access article distributed under the Creative Commons Attribution License, which permits unrestricted use, distribution, and reproduction in any medium, provided the original work is properly cited.

Luteolin (LUT) possesses multiple biologic functions and has beneficial effects for cardiovascular and cerebral vascular diseases. Here, we investigated the protective effects of LUT against subarachnoid hemorrhage (SAH) and the involvement of underlying molecular mechanisms. In a rat model of SAH, LUT significantly inhibited SAH-induced neuroinflammation as evidenced by reduced microglia activation, decreased neutrophil infiltration, and suppressed proinflammatory cytokine release. In addition, LUT markedly ameliorated SAH-induced oxidative damage and restored the endogenous antioxidant systems. Concomitant with the suppressed oxidative stress and neuroinflammation, LUT significantly improved neurologic function and reduced neuronal cell death after SAH. Mechanistically, LUT treatment significantly enhanced the expression of nuclear factor-erythroid 2-related factor 2 (Nrf2), while it downregulated nod-like receptor pyrin domain-containing 3 (NLRP3) inflammasome activation. Inhibition of Nrf2 by ML385 dramatically abrogated LUT-induced Nrf2 activation and NLRP3 suppression and reversed the beneficial effects of LUT against SAH. In neurons and microglia coculture system, LUT also mitigated oxidative stress, inflammatory response, and neuronal degeneration. These beneficial effects were associated with activation of the Nrf2 and inhibitory effects on NLRP3 inflammasome and were reversed by ML385 treatment. Taken together, this present study reveals that LUT confers protection against SAH by inhibiting NLRP3 inflammasome signaling pathway, which may be modulated by Nrf2 activation.

## 1. Introduction

Subarachnoid hemorrhage (SAH), a detrimental type of stroke, is considered a life-threatening disease with limited therapeutic options [1]. There are urgent unmet needs for intervention that could block progressive brain damage after SAH. Recently, numerous clinical and experimental studies have suggested that the robust reactive oxygen species (ROS) overproduction and neuroinflammation play impor-

tant roles in the secondary brain injury after SAH and contribute greatly to the neurological deficits [2–5]. Accordingly, identifying new and effective therapeutic strategies to mitigate excessive oxidative damage and neuroinflammation is a pressing need.

Luteolin (LUT) is an abundant flavonoid distributed in vegetables and fruits such as broccoli and carrots [6]. Previous reports have demonstrated that LUT is a neuroprotective flavonoid by scavenging free-radical and inhibiting



inflammation in a series of neurological disorders, including traumatic brain injury (TBI), ischemic stroke, and Alzheimer's disease [6–8]. Moreover, LUT can easily penetrate the blood-brain barrier and improve behavioral performance in acute brain injuries [8, 9]. However, whether LUT could exert cerebroprotective effects against SAH remains unknown.

There is emerging evidence indicates that nod-like receptor pyrin domain-containing 3 (NLRP3) inflammasome-mediated neuroinflammation plays a critical role in the development of secondary brain injury after SAH [10–13]. In addition, ROS generation is closely associated with oxidative damage and is one of the major signals that trigger the NLRP3 inflammasome activation. Nuclear factor-erythroid 2-related factor 2 (Nrf2) is considered as the most important endogenous factor in the maintenance of cellular homeostasis. Under the condition of oxidative stress, Nrf2 translocates into the nucleus and binds with an antioxidant response element (ARE), thereby promoting a battery of antioxidative gene expressions, such as heme oxygenase-1 (HO-1), glutathione peroxidase (GSH-Px), and superoxide dismutase (SOD) [14–16]. Accumulating studies have indicated that activating the Nrf2 signaling pathway plays a key role in attenuation of oxidative damage in a variety of oxidative disorders [8, 17]. Moreover, recent studies have suggested that NLRP3 inflammasome activation is modulated by Nrf2 signaling [18, 19]. Intriguingly, LUT is a powerful Nrf2 activator and can inhibit NLRP3 inflammasome in a series of disease models [8, 20, 21]. Thus, in this study, we investigated whether LUT had therapeutic potential in SAH and verified whether the beneficial effects of LUT were associated with the inhibition of NLRP3 inflammasome activation by Nrf2-dependent pathway.

## 2. Materials and Methods

**2.1. Animals.** All of the procedures were approved by the Institutional Animal Care and Use Committee of Wannan Medical University and met the accordance of National Institutes of Health. Health adult male Sprague Dawley rats (250–300 g) were bought from the Nanjing Biomedical Research Institute of Nanjing University. The animals had free access to food pellets and water ad libitum.

**2.2. SAH Model.** A prechiasmatic cistern injection model was used in our study. Anesthesia was induced by intraperitoneal injection avertin (200 mg/kg). After anesthetization, rats were positioned prone in a stereotactic frame. And then, a burr hole was drilled into the skull 7.5 mm anterior to the bregma. A total of 0.35 mL of nonheparinized fresh autologous arterial blood was retracted from the femoral artery and injected into the burr hole (in the course of 20 s) under aseptic conditions [22]. Bone wax was employed to block cerebrospinal fluid leakage. Sham operation animals were injected with 0.35 mL physiological saline instead of blood into prechiasmatic cistern. Consistent with previous studies [17, 23], the inferior basal temporal lobe always contained blood and differed histologically from control rat brain. Therefore, the basal temporal lobe adjacent to the clotted

blood was used for histopathologic examination in the current study.

**2.3. Study Design.** In the first set of experiments, 108 rats (127 rats were used, and 19 rats died) were divided into the following groups: sham ( $n = 14$ ), sham+vehicle ( $n = 16$ ), SAH+vehicle ( $n = 20$ , 5 rats died), SAH+10 mg/kg LUT ( $n = 20$ , 5 rats died), SAH+30 mg/kg LUT ( $n = 19$ , 3 rats died), SAH+60 mg/kg LUT ( $n = 19$ , 3 rats died), and SAH+90 mg/kg LUT ( $n = 19$ , 3 rats died) groups. Rats were killed at 24 h and 72 h after operation. Post-assessments included behavior performance, brain water content, and histopathological study.

In the second set of experiments, 48 rats (57 rats were used, and 9 rats died) were assigned into four groups: sham+vehicle ( $n = 12$ ), SAH+vehicle ( $n = 15$ , 3 rats died), SAH+60 mg/kg LUT ( $n = 14$ , 2 rats died), and SAH+60 mg/kg LUT+ML385 ( $n = 16$ , 4 rats died) groups. Rats were killed at 24 h after SAH. Post-assessments included immunofluorescence staining, biological estimation, and behavior performance.

**2.4. Primary Cell Culture and In Vitro SAH Model.** Primary cortical neurons and microglia were performed according to our previous study [24]. Rat pups were sacrificed on postnatal days 0–1. For primary neurons culture, cortical cells were cultured onto poly-D-lysine-coated plates and suspended in neurobasal media supplemented with B27, glutamate, Hepes, penicillin, and streptomycin. For primary microglia culture, cortical cells were placed in serum-free DMEM-F12 culture medium. Regarding the neurons and microglia coculture system, microglia were seeded in transwell upper chamber (Corning, pore size = 0.4  $\mu\text{m}$ ) and the neurons were cultured in the plates. Coculture medium was DMEM with 10% FBS.

To mimic SAH in vitro, the coculture system was stimulated with 10  $\mu\text{M}$  oxyhemoglobin (OxyHb) for 24 h. The dose of OxyHb was chosen according to our previous study [23]. Hemoglobin (Sigma, USA) was used to produce OxyHb as we described in detail before [25]. The neuron–microglia cocultures were partitioned into the following groups: control, oxyHb, OxyHb+5  $\mu\text{M}$  LUT, OxyHb+10  $\mu\text{M}$  LUT, OxyHb+25  $\mu\text{M}$  LUT, and OxyHb+25  $\mu\text{M}$  LUT+ML385. The coculture system was harvested 24 h after indicated intervention. The culture medium, neurons, and microglia were collected for cell viability analysis, biochemical estimation, and immunofluorescence staining.

**2.5. Drug Administration.** For in vivo experiments, LUT (Sigma-Aldrich, St. Louis, MO, USA) was dissolved in dimethylsulfoxide (DMSO) (<1%) and physiological saline at different concentrations (10, 30, 60, and 90 mg/kg). Rats were intraperitoneally administrated with LUT at different doses at 2 h after insults and then once daily until euthanasia. ML385, a selective Nrf2 inhibitor, was dissolved in DMSO and physiological saline and was administered intraperitoneally (30 mg/kg) for 2 days before SAH induction. For in vitro experiments, LUT (5  $\mu\text{M}$ , 10  $\mu\text{M}$ , and 25  $\mu\text{M}$ ) and ML385 (10  $\mu\text{M}$ ) were dissolved in 0.1% DMSO (in

physiologic saline) and then added to culture medium [8, 26]. LUT was administered for 0.5 h prior to OxyHb incubation. Cells were pretreated with ML385 24 h before OxyHb stimulation.

**2.6. Neurological Behavior.** Neurologic functions were recorded using an 18-point scoring system reported by Zhao et al. [21]. Rotarod test was used to assess motor function according to a previous study [16]. The rotating speed was gradually increased from 4 to 40 rpm over a 5 min period. The latency to fall was recorded. The mean latency was calculated based on three consecutive trials.

**2.7. Brain Water Content.** In brief, the brains were harvested immediately after sacrificing the rats and dissected into cerebrum, cerebellum, and brainstem. Each part was weighed to record the wet weight. The dry weight was recorded after the samples were being dried at 80°C for 72 h. Brain edema ratio was calculated as  $[(\text{wet weight} - \text{dry weight})/\text{wet weight}] \times 100\%$ .

**2.8. Nissl Staining.** In brief, the brain tissue was first fixed in 4% paraformaldehyde for 48 h and then performed as we described in detail before [17]. Afterward, tissue sections were stained with Nissl solution for 10 min and mounted with Permount. All the sections were photographed in the microscope.

**2.9. Immunofluorescence Staining.** Immunofluorescence staining was performed as we described in detail before [17]. In brief, the sections were first fixed by 0.1% Triton X-100 and then were blocked by 5% BSA for 2 h. After three washes with PBS, brain tissues or cultured neurons were incubated with primary antibodies against Iba-1 (1:50, Santa Cruz Biotechnology or 1:100, Abcam), myeloperoxidase (MPO, 1:50, Santa Cruz Biotechnology), 8-hydroxydeoxyguanosine (8-OHdG) (1:100, Abcam), Nrf2 (1:100, Abcam), caspase-1 p20 (1:50, Santa Cruz Biotechnology), and NeuN (1:200, EMD Millipore). Sections were then incubated with corresponding secondary antibodies (Alexa Fluor 488 and Alexa Fluor 594) overnight at 4°C. Fluorescence microscopy imaging was examined under a ZEISS HB050 inverted microscope system. The fluorescently stained cells were recorded using Image J program.

**2.10. TUNEL Staining.** TUNEL staining was detected by a terminal deoxynucleotidyl transferase-mediated dUTP nick-end labeling (TUNEL) detection kit (Roche Inc., Indianapolis, USA) in line with the manufacturer's instructions. The brain slices and coverslips were incubated with the primary antibody anti-NeuN (1:200, EMD Millipore) overnight. And then, a reaction solution and converter-AP were incubated subsequently. The fluorescently stained cells were recorded using Image J program.

**2.11. ELISA.** Brain samples and culture medium were collected. The levels of IL-1 $\beta$ , tumor necrosis factor- $\alpha$  (TNF- $\alpha$ ), and IL-6 were evaluated in line with the manufacturer instructions (Multi Sciences, China).

**2.12. Biochemical Estimation.** The contents of malondialdehyde (MDA), GSH-Px, glutathione (GSH), and SOD were evaluated by using commercially available kits in line with the manufacturer instructions (Nanjing Jiancheng Bioengineering Institute, Nanjing, China). For MDA, brain samples were mixed with thiobarbituric acid, acetic acid, and sodium dodecyl sulphate at 95°C for 30 min. And then, the sample was centrifuged at a rate of 4,000 rpm for 10 min. The MDA contents in all tubes were measured at the wavelength of 532 nm using a spectrophotometer. For H<sub>2</sub>O<sub>2</sub>, the fresh brain tissue was homogenized using the assay buffer and processed per kit instructions (Abcam). Absorbance at 590 nm was recorded. For GSH-Px, the supernatant was mixed with sodium azide, glutathione reductase enzyme, NADPH, and H<sub>2</sub>O<sub>2</sub>. The GSH-Px activity was measured at the wavelength of 340 nm using a spectrophotometer. For GSH, the supernatant was mixed with 1% trichloroacetic acid and centrifuged at 10,000  $\times$  g for 15 min. The reaction mixture consisted of lysates and 5,5'-dithiobis-(2-nitrobenzoic acid). GSH was measured at the wavelength of 405 nm. For SOD, sample was mixed with the xanthine and xanthine oxidase in potassium phosphate buffer at 37°C for 20 min. SOD was measured at the wavelength of 450 nm using a spectrophotometer.

**2.13. Western Blotting.** The brain samples and the primary microglia in transwell upper chambers and neurons in the plates were collected for Western blotting. In brief, the extracted proteins were separated by Tris-glycine SDS-PAGE and then transferred to PVDF membranes for 30 min. Primary antibodies used were Nrf2 (1:1000, cat# ab31163, Abcam), HO-1 (1:1000, cat# ab13243, Abcam), NLRP3 (1:200, cat# SC-66846, Santa Cruz Biotechnology), adaptor apoptosis-related speck-like protein (ASC) (1:200, cat# SC-22514, Santa Cruz Biotechnology), caspase-1 (1:200, cat# SC-56036, Santa Cruz Biotechnology), caspase-1 p20 (1:200, cat# SC-398715, Santa Cruz Biotechnology), Histone H3 (1:3000, cat# BS7416, Bioworld Technology), and  $\beta$ -actin (1:3000, cat# AP0060, Bioworld Technology, Minneapolis, MN, USA). Then, the membranes were incubated for 2 h at room temperature with corresponding second antibody. Detection was conducted by using chemiluminescence solution.

**2.14. Cell Viability Analysis.** Cell viability was detected by the cell counting kit- (CCK-) 8 assays or lactate dehydrogenase (LDH) activity with commercially available kits (Beyotime Biotechnology, China) in accordance with the manufacturer's instructions.

**2.15. DCFH-DA Staining and Propidium Iodide Staining.** For ROS measurements, primary cultured neurons were incubated with 2,7-dichlorodihydrofluorescein diacetate (DCFH-DA, Sigma) for 10 min at 37°C. For propidium iodide (PI) staining, the primary neurons were stained with 2  $\mu$ g/mL of PI for 10 min at 37°C. Quantifications were performed with Image Pro Plus 6.0.

**2.16. Statistical Analysis.** Statistical software GraphPad Prism 8.02 (GraphPad Software, La Jolla, CA, USA) was

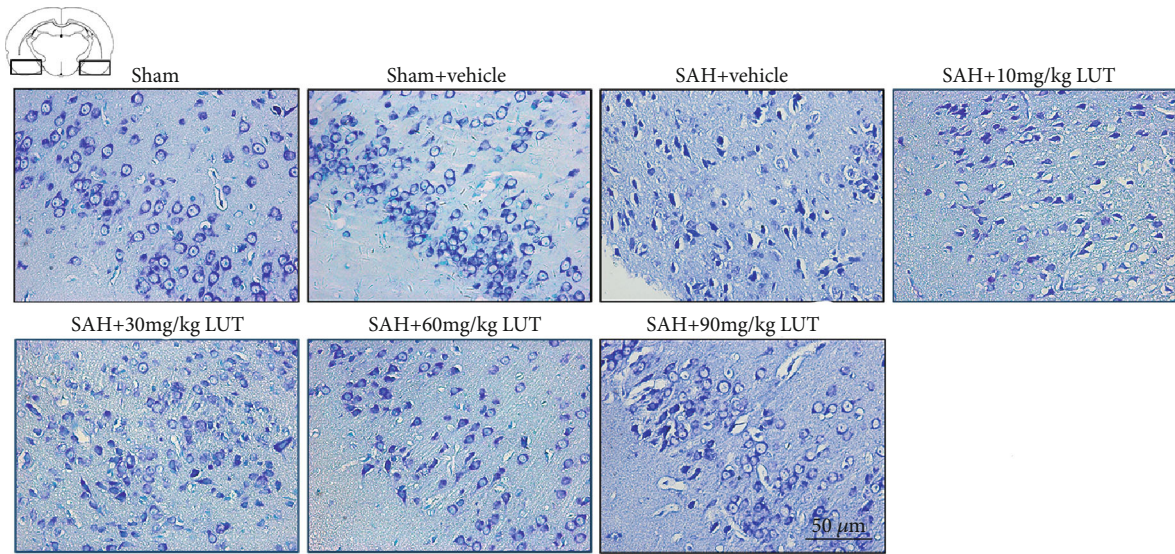
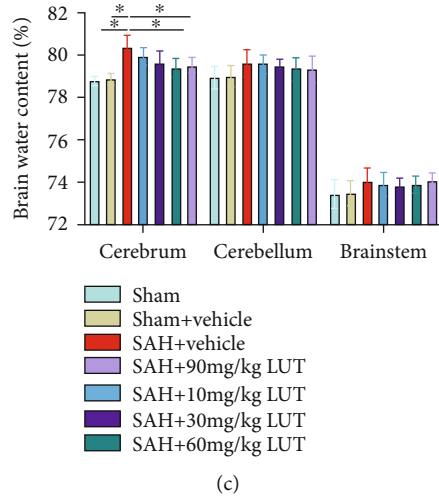
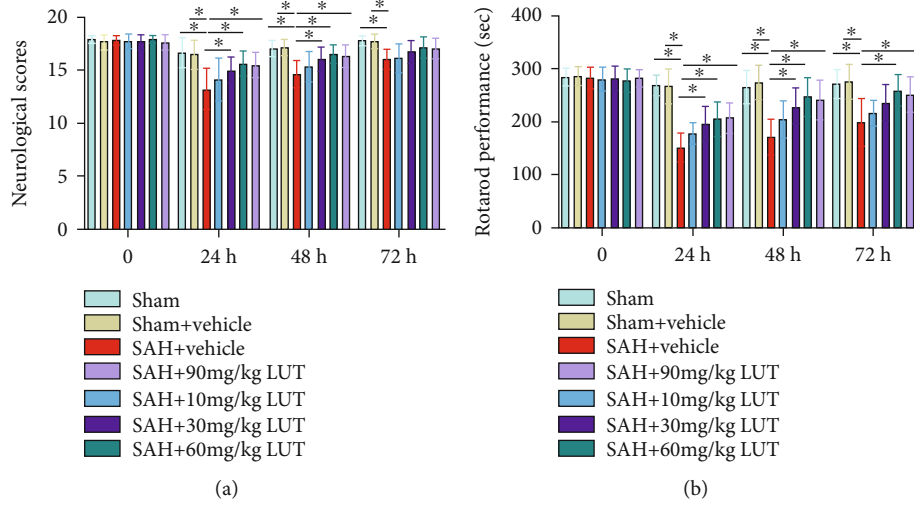


FIGURE 1: Continued.

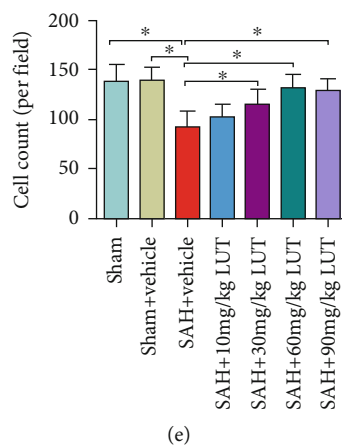


FIGURE 1: Dose-response effects of luteolin (LUT) on subarachnoid hemorrhage (SAH) in rats. Effects of three LUT doses on (a) neurologic scores ( $n = 8-10$  per group), (b) rotarod performance ( $n = 8-10$  per group), and (c) brain water content ( $n = 6$  per group). (d) Representative photomicrographs of Nissl staining at 72 h after SAH. (d) Magnification  $\times 200$ , scale bar  $50 \mu\text{m}$ . For Nissl staining, the basal temporal lobe adjacent to the clotted blood was evaluated. (e) Quantification of the proportion of surviving neurons at 72 h after SAH ( $n = 6$  per group). Bars represent the mean  $\pm$  SD. \* $P < 0.05$ .

used for statistical analysis. All data were expressed as mean  $\pm$  SD. Differences among multiple groups were compared by one-way or two-way analysis of variance with Bonferroni post hoc test. Statistical significance was inferred at  $P < 0.05$ .

### 3. Results

**3.1. Dose-Response Effects of LUT on SAH.** No animals died in the sham and sham+vehicle groups. The mortality rate of the rats was 22.9% (8 of 35) in the SAH+vehicle group, 17.6% (16 of 91) in the SAH+LUT group, and 25% (4 of 16) in the SAH+LUT+ML385 group. In a dose-response study, LUT was administered to rats after SAH at 10, 30, 60, and 90 mg/kg. Doses of 30 mg/kg, 60 mg/kg, and 90 mg/kg, but not 10 mg/kg, markedly improved neurologic scores and rotarod performance in the early period after SAH (Figures 1(a) and 1(b)). In addition, LUT treatment at 60 mg/kg and 90 mg/kg, but not 10 mg/kg and 30 mg/kg, significantly reduced brain water content in cerebrum after SAH (Figure 1(c)). Nissl staining further showed that evident damage was seen in the SAH+vehicle group, with a decrease of cell number, sparse cell arrangements, and loss of integrity. In contrast, LUT treatment at 30 mg/kg, 60 mg/kg, and 90 mg/kg, but not 10 mg/kg, significantly improved neuronal survival after SAH (Figures 1(d) and 1(e)). There were no significant differences among 30 mg/kg, 60 mg/kg, and 90 mg/kg LUT treatment in ameliorating neurological deficits, brain edema, and neuronal degeneration after SAH (Figures 1(a)–1(e)). Based on the results of these tests, we found that 60 mg/kg was the optimum dosage. Therefore, we used this dose for the remaining experiments.

**3.2. Effects of LUT on the Nrf2 Signaling Pathway and NLRP3 Inflammasome Activation after SAH.** LUT has been considered as a powerful Nrf2 activator in a variety of disorders. In addition, numerous studies have suggested that

NLRP3 inflammasome activation is modulated by Nrf2 signaling [18, 19]. Thus, we used Western blot analysis to determine whether LUT induced Nrf2 activation and inhibited NLRP3 inflammasome signaling after SAH. ML385, a selective Nrf2 inhibitor, was further employed to inhibit Nrf2 signaling in this experiment. As shown in Figure 2, nuclear and total expression levels of Nrf2 protein and HO-1 protein were significantly increased after SAH, which could be further enhanced after LUT supplementation (Figures 2(a)–2(d)). In addition, SAH significantly induced the expression of NLRP3, ASC, and cleaved caspase-1, which was effectively inhibited by LUT administration (Figures 2(e)–2(h)). In contrast, ML385 pretreatment reversed LUT-induced Nrf2 expression and further increased protein levels of NLRP3, ASC, and cleaved caspase-1 (Figures 2(a)–2(h)). Double immunofluorescent staining confirmed the Western blot results, indicating that LUT enhanced nuclear translocation of Nrf2 after SAH, which was abrogated by LUT administration (Figures 2(i) and 2(j)). These data suggested that LUT could induce Nrf2 signaling and inhibit NLRP3 inflammasome activation after SAH.

**3.3. Influence of LUT on Oxidative Damage at 24 h Post-SA H.** Nrf2 plays an important role in maintenance of redox homeostasis after SAH. We next evaluated whether LUT could ameliorate oxidative stress after SAH. As shown, SAH insults significantly induced oxidative damage, as evidenced by increases in lipid peroxidation,  $\text{H}_2\text{O}_2$  generation, and 8-OHdG immunity (Figures 3(a)–3(d)). In addition, SAH markedly decreased the endogenous antioxidant systems including SOD, GSH, and GSH-Px activities as compared with those of the sham+vehicle group (Figures 3(e)–3(g)). In contrast, LUT administration significantly decreased oxidative insults and restored the impairment antioxidant systems after SAH (Figures 3(a)–3(g)). However, the antioxidant effects of LUT against SAH were abated by ML385 administration (Figures 3(a)–3(g)).

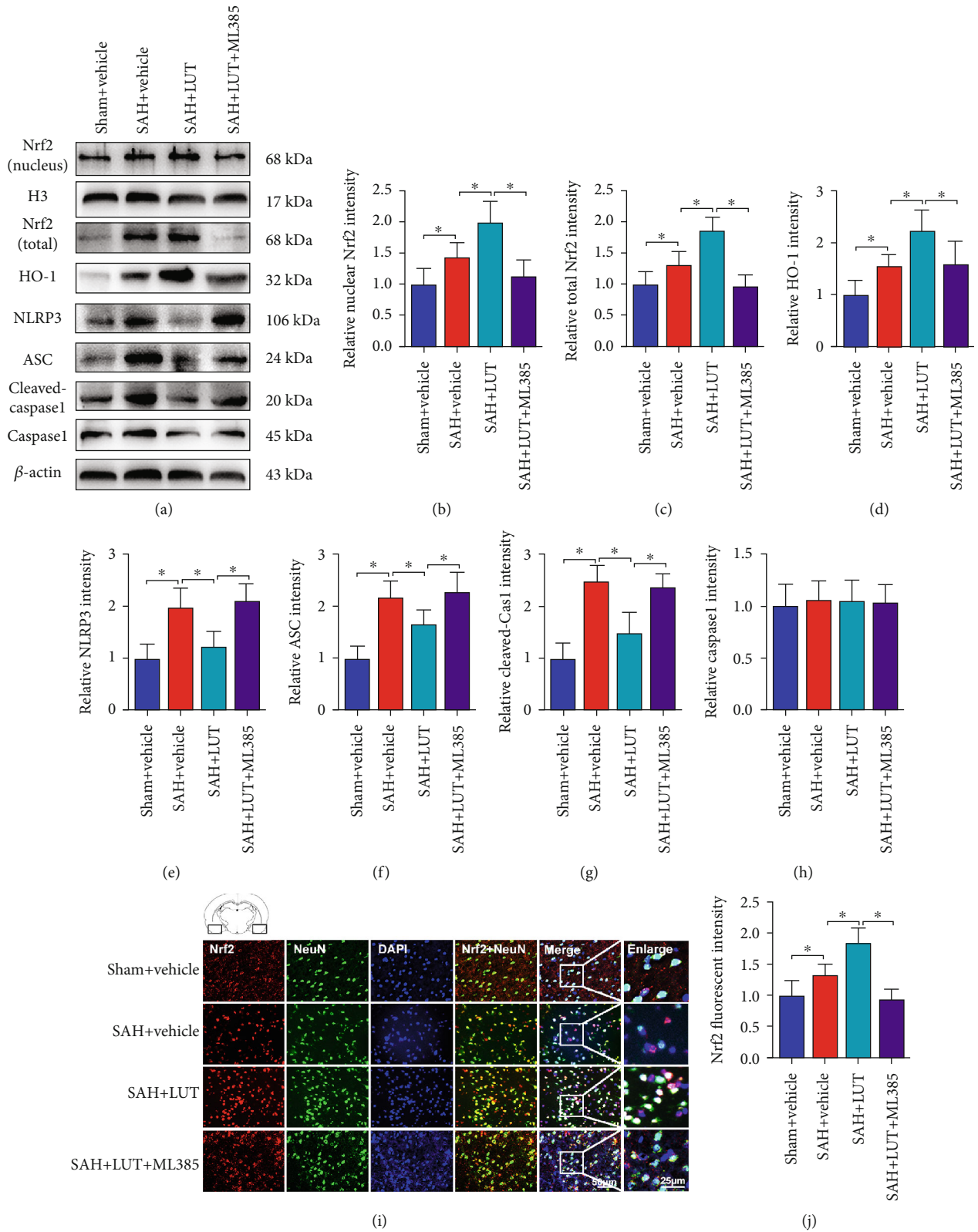


FIGURE 2: Effects of LUT treatment on Nrf2 and NLRP3 inflammasome signaling pathway after SAH. (a) Western blot assay for the expression of Nrf2, HO-1, NLRP3, ASC, cleaved caspase-1, and caspase-1 in the indicated groups. Quantitative analyses of (b) nucleus Nrf2, (c) total Nrf2, (d) HO-1, (e) NLRP3, (f) ASC, (g) cleaved caspase-1, and (h) caspase-1 expression in each group ( $n = 6$  per group). (i, j) Representative photomicrographs and quantification of Nrf2 immunofluorescence staining ( $n = 6$  per group). Magnification  $\times 200$ , scale bar  $50 \mu\text{m}$ ; (i) inset magnification  $\times 400$ , scale bar  $25 \mu\text{m}$ . For immunofluorescence staining, the basal temporal lobe adjacent to the clotted blood was evaluated. Bars represent the mean  $\pm$  SD. \* $P < 0.05$ .

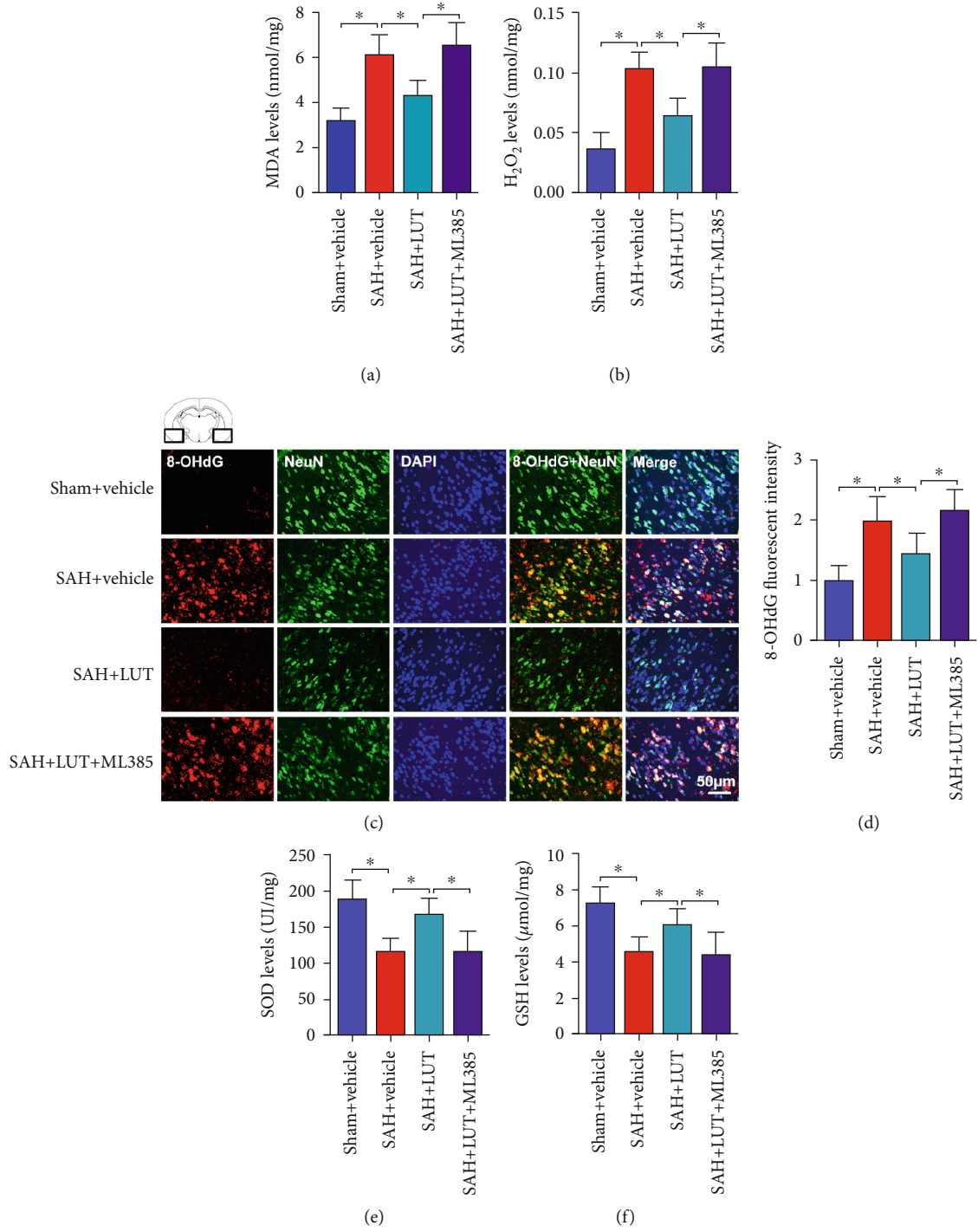


FIGURE 3: Continued.

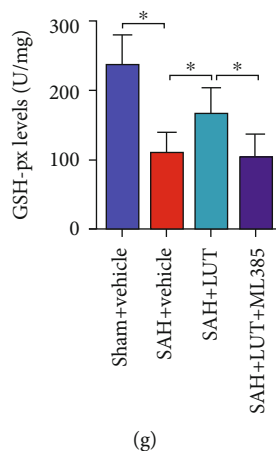


FIGURE 3: Effects of LUT on oxidative damage after SAH. Quantification of (a) MDA and (b)  $H_2O_2$  levels in all groups ( $n = 6$  per group). (c, d) Representative photomicrographs and quantification of 8-OHdG staining ( $n = 6$  per group). (c) Magnification  $\times 200$ , scale bar  $50 \mu m$ . For immunofluorescence staining, the basal temporal lobe adjacent to the clotted blood was evaluated. Quantification of (e) SOD, (f) GSH, and (g) GSH-Px in all groups ( $n = 6$  per group). Bars represent the mean  $\pm$  SD. \* $P < 0.05$ .

**3.4. Influence of LUT on Neuroinflammation at 24h Post-SAH.** NLRP3 inflammasome plays a critical role in initiating a series of immune-inflammatory reactions after SAH. We also evaluated whether LUT was able to mitigate neuroinflammation after SAH. The immunofluorescence staining showed that SAH insults significantly induced microglia activation and neutrophil infiltration when compared with those of the sham+vehicle group. LUT treatment significantly inhibited microglia activation and neutrophil infiltration after SAH, and that these effects were abolished by ML385 (Figures 4(a)–4(d)). In addition, SAH significantly induced the proinflammatory cytokine generation, which was suppressed by LUT treatment, while the decreased proinflammatory cytokine generation by LUT administration was reversed by Nrf2-specific inhibitor ML385 (Figures 4(e)–4(g)).

**3.5. Effects of LUT on Neurologic Function and Neuronal Death after SAH.** We next evaluated whether LUT could improve neurological function and ameliorate neuronal death. As shown, SAH caused significant neurologic impairment that was alleviated by LUT treatment (Figures 5(a) and 5(b)). In contrast, the beneficial effects of LUT on neurological function were reversed by ML385 pretreatment. Both neuronal apoptosis and pyroptosis contribute to the development of EBI after SAH. Cleaved caspase-1 is the canonical executor of pyroptosis. We further performed caspase-1 staining and TUNEL staining to examine neuronal pyroptosis and apoptosis, respectively. As shown, rats with SAH had greater numbers of caspase-1- and TUNEL-positive neurons when compared with sham-operated rats. LUT treatment significantly reduced the number of caspase-1- and TUNEL-positive neurons after SAH (Figures 5(c)–5(f)), while ML385 treatment reversed the LUT-induced decreases in neuronal apoptosis and pyroptosis after SAH (Figures 5(a)–5(f)).

**3.6. Effects of LUT on Cell Viability, Oxidative Stress, and Inflammatory Response In Vitro.** We further confirmed the

potential beneficial effects of LUT in vitro. As shown, our data indicated that LUT significantly improved neuronal viability, reduced oxidative damage, and decreased expression of proinflammatory cytokines including IL-1 $\beta$ , IL-6, and TNF- $\alpha$  after OxyHb stimulation (Figures 6(a)–6(g)). However, all these changes were abrogated by ML385 treatment (Figures 6(a)–6(g)).

**3.7. Effects of LUT on Nrf2 and NLRP3 Inflammasome Signaling In Vitro.** We next evaluated the effects of LUT on Nrf2 and NLRP3 inflammasome signaling in vitro. Western blot analysis showed that LUT treatment significantly increased the expression of Nrf2 and reduced expression of NLRP3, ASC, and cleaved caspase-1 in primary microglia and neurons exposed to OxyHb. These changes were abrogated by Nrf2-selective inhibitor ML385 (Figures 7(a)–7(e)). Double immunofluorescence staining further showed that LUT enhanced the expression of Nrf2 in primary cortical neurons, which was abated by ML385 treatment (Figures 7(f) and 7(g)).

**3.8. Effects of LUT on Neuronal Degeneration In Vitro.** It has demonstrated that both neuronal apoptosis and pyroptosis contribute to the development of EBI after SAH. PI cannot pass intact plasma membrane and can only be present in DNA of cells where the plasma membrane has been compromised. During pyroptosis, pores can be formed in the cell membrane and can be detected by PI staining [26]. TUNEL staining can detect the DNA breaks when DNA fragmentation occurs in the last phase of apoptosis. Therefore, in this experiment, we used PI and TUNEL staining to examine neuronal pyroptosis and apoptosis, respectively. As shown, OxyHb stimulation significantly increased the number of PI- and TUNEL-positive neurons, which were decreased by LUT treatment (Figures 8(a)–8(d)). In contrast, the improvement by LUT was reversed by ML385 administration (Figures 8(a)–8(d)). These suggested that LUT could reduce neuronal pyroptosis and apoptosis in vitro.

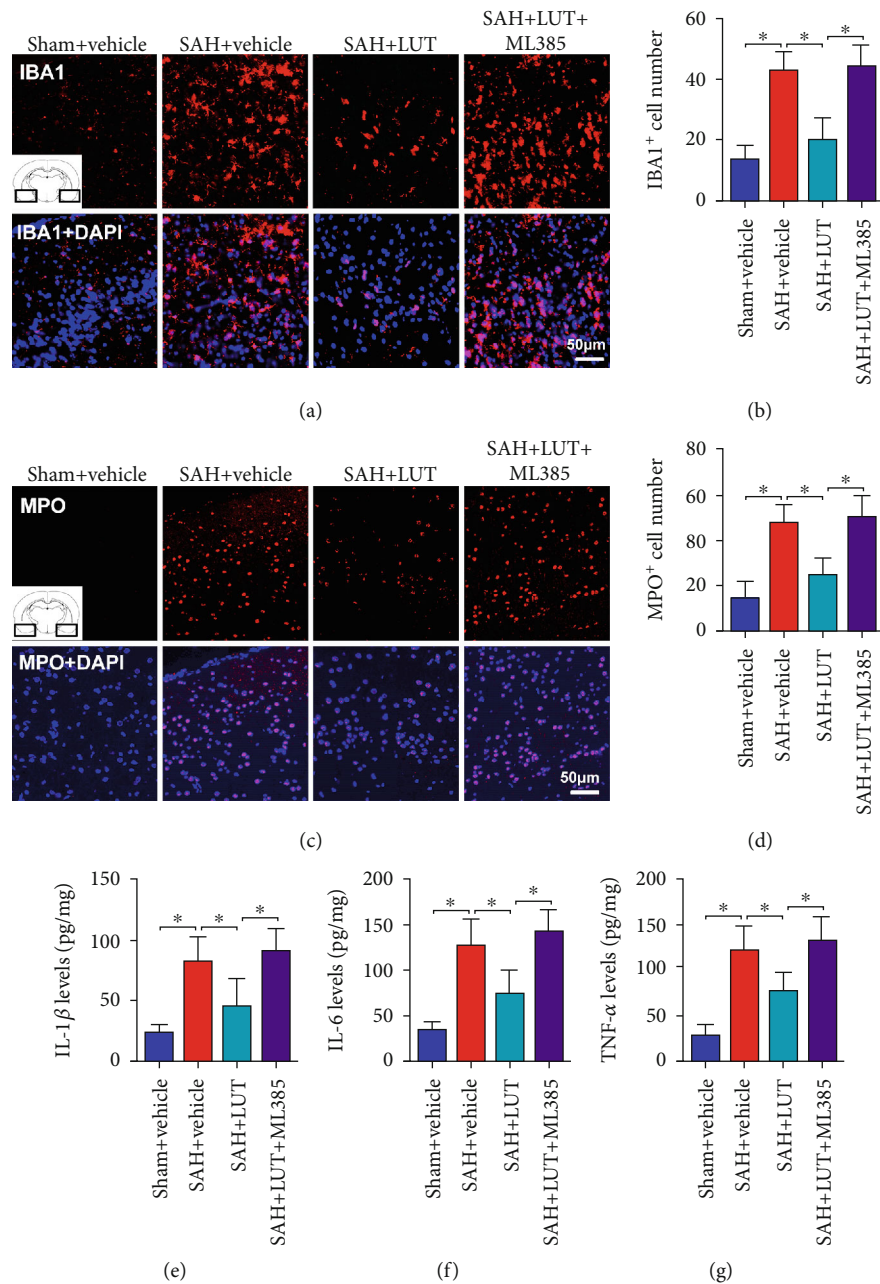


FIGURE 4: Effects of LUT on inflammatory response after SAH. Representative photomicrographs and quantification of (a, b) Iba-1 and (c, d) myeloperoxidase (MPO) staining ( $n = 6$  per group). (a, c) Magnification  $\times 200$ , scale bar  $50 \mu\text{m}$ . For immunofluorescence staining, the basal temporal lobe adjacent to the clotted blood was evaluated. Quantification of (e) IL-1 $\beta$ , (f) IL-6, and (g) TNF- $\alpha$  in all groups ( $n = 6$  per group). Bars represent the mean  $\pm$  SD. \* $P < 0.05$ .

#### 4. Discussion

Neuroinflammation and oxidative damage are two major etiological factors resulting in the secondary brain injury after SAH [27–29]. After the initial hemorrhage, blood components enter the subarachnoid space and activate innate and adaptive immune cascade responses. Microglia activation and neutrophils recruit to the damaged tissue and release a variety of inflammatory factors that exacerbate neurons [30]. Excessive ROS can elicit neuronal damage by promoting lipid peroxidation and DNA damage. Moreover,

the robust inflammatory response produces additional excess ROS, further aggravating the redox imbalance and thereby inducing neuronal cell death and neurological deficits after SAH [31–33]. Accordingly, pharmacologically reducing neuroinflammation and oxidative damage might provide a means to ameliorate SAH.

In recent years, mounting evidence has suggested that LUT is a promising neuroprotective agent in a variety of neurological disorders [6]. It has been demonstrated that LUT has a wide range of pharmacological properties including antioxidant free-radical scavenging and anti-



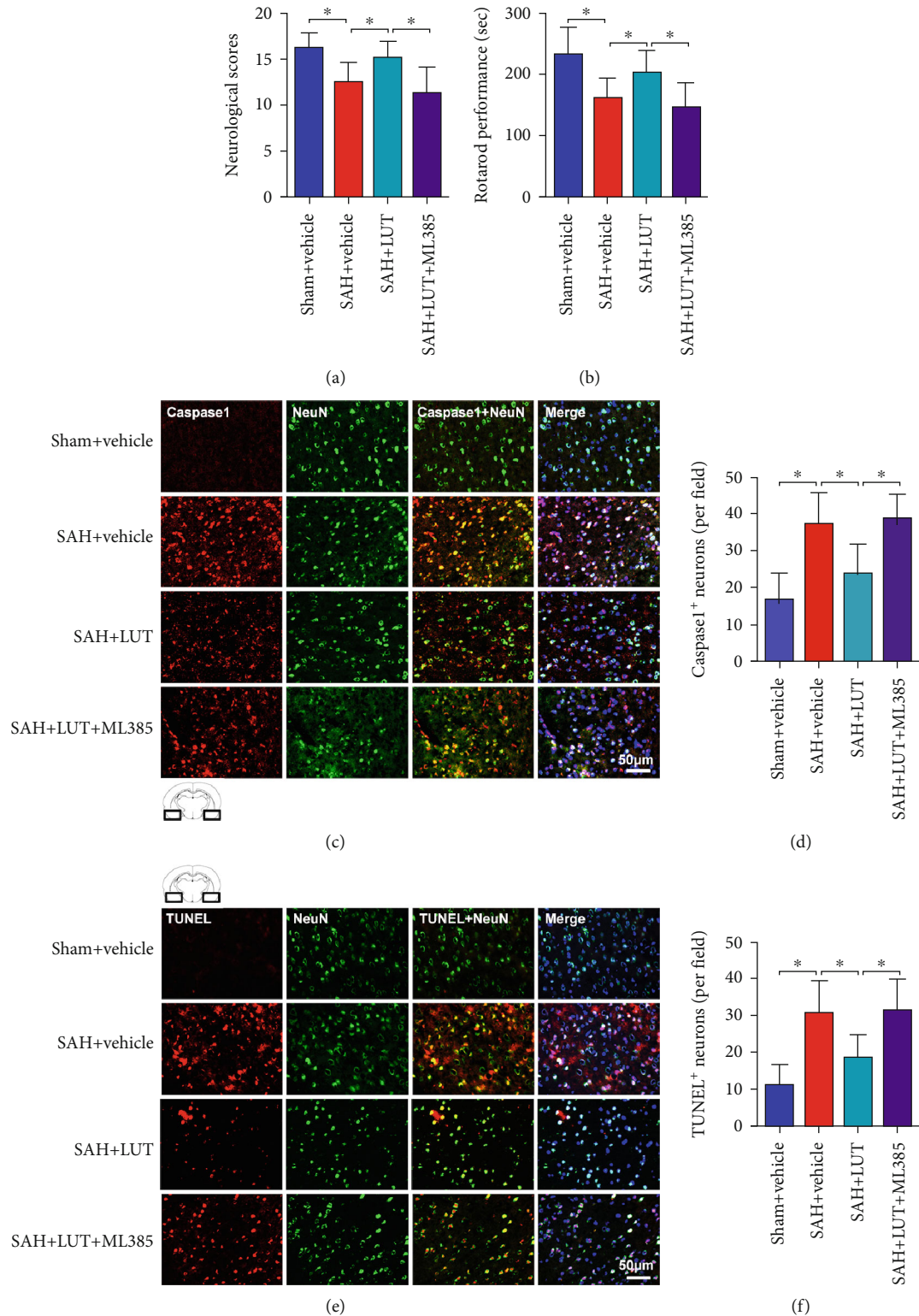


FIGURE 5: Effects of LUT on neurological function and neuronal death after SAH. Effects of LUT on (a) neurologic function and latency to fall in the (b) rotarod test after SAH ( $n = 12$  per group). Representative photomicrographs and quantification of (c, d) caspase-1 and (e, f) TUNEL staining ( $n = 6$  per group). (c, e) Magnification  $\times 200$ , scale bar  $50 \mu\text{m}$ . For immunofluorescence staining, the basal temporal lobe adjacent to the clotted blood was evaluated. Bars represent the mean  $\pm$  SD.  $*P < 0.05$ .

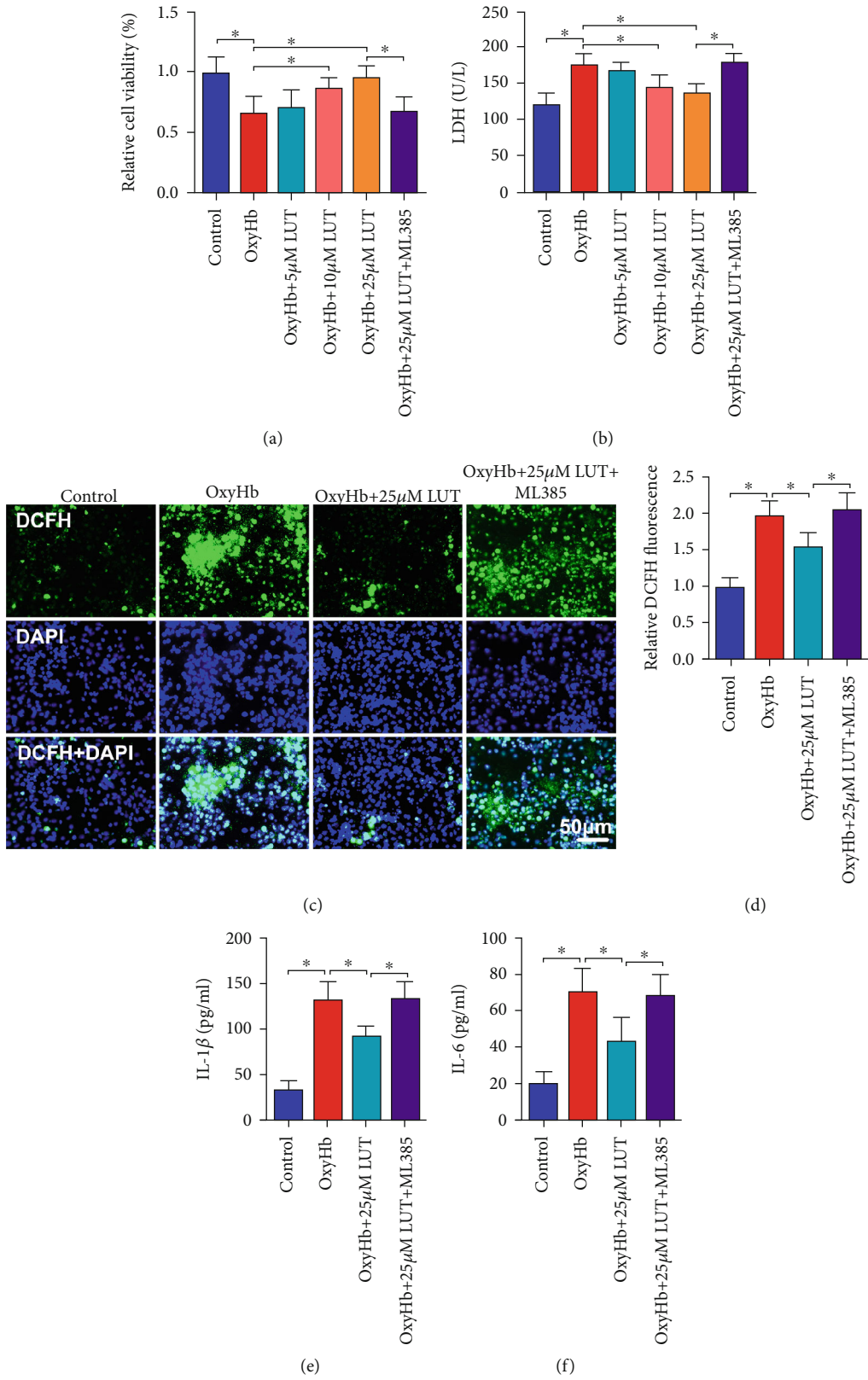


FIGURE 6: Continued.

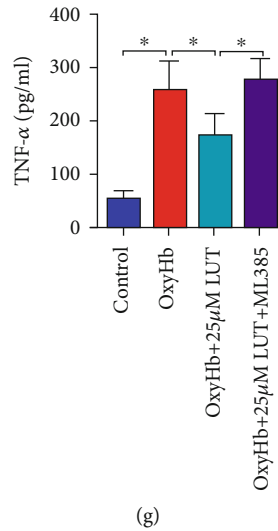


FIGURE 6: Effects of LUT treatment on oxidative stress, inflammatory response, and neuronal damage in vitro. Quantitative analysis of (a) cell viability and (b) LDH activity in the indicated groups ( $n = 6$  per group). (c) Representative photomicrographs and (d) quantification of DCFH immunofluorescence ( $n = 6$  per group). (e) Magnification  $\times 200$ , scale bar  $50 \mu\text{m}$ . Quantification of (e) IL-1 $\beta$ , (f) IL-6, and (g) TNF- $\alpha$  in culture medium ( $n = 6$  per group). Bars represent the mean  $\pm$  SD. \* $P < 0.05$ .

inflammatory effects [20, 34, 35]. For example, Kou et al. reported that LUT alleviated cognitive impairment in Alzheimer's disease mouse model via inhibiting endoplasmic reticulum stress in astrocytes and subsequent neuroinflammation [36]. Tan et al. demonstrated that LUT provided autophagy and antioxidative effects in both in vivo and in vitro models of intracerebral hemorrhage [7]. However, to our knowledge, no study has yet investigated the potential effects of LUT in experimental SAH and the underlying molecular mechanisms.

Nrf2 as a critical translocate factor in maintenance of redox homeostasis is widely studied in recent years. After stimulation by oxidative stress, Nrf2 translocates into the nucleus and binds to the ARE, subsequently inducing antioxidant enzyme expression [37, 38]. Loads of evidence have indicated that Nrf2 signaling activation could significantly ameliorate SAH-induced oxidative damage and brain injury [39, 40]. Intriguingly, LUT has been considered as a powerful Nrf2 activator in a variety of disorders [7, 8]. Xu et al. reported that LUT could provide neuroprotective effects in TBI models both in vivo and in vitro through the activation of Nrf2-ARE pathway [8]. Xiao et al. indicated that LUT attenuated cardiac ischemia/reperfusion injury in diabetic rats by activation of Nrf2 signaling [41]. Thus, it is reasonable to predict that LUT can activate Nrf2 signaling and confer cerebroprotective effects in SAH. It has been clarified that Nrf2 can transcriptionally induce numerous antioxidative genes including HO-1, GSH-Px, and SOD. HO-1 plays a prominent role in maintenance of cellular homeostasis by degrading heme [42]. SOD and GSH-Px are antioxidant enzymes which play fundamental and indispensable role in against free radical attack [43]. Consistent with these previous studies, we found that LUT also markedly enhanced the translocation of Nrf2 into the nucleus and Nrf2-involved antioxidative enzyme expression. Meanwhile, LUT significantly reduced the brain MDA and 8-OHdG

contents after SAH insults. MDA and 8-OHdG are two key biomarkers for lipid peroxidation and DNA oxidative damage caused by excessive ROS, respectively. These results indicated that LUT could protect against SAH injury through scavenging ROS and enhancing the endogenous antioxidative system by the modulation of Nrf2 signaling.

Another interesting finding in the current study was that LUT ameliorated neuroinflammation and inhibited NLRP3 inflammasome signaling activation. NLRP3 inflammasome is a cytoplasmic multiprotein complex of the innate immune system that can initiate a series of immune-inflammatory reactions [44]. It has been proved that NLRP3 inflammasome-mediated neuroinflammation plays a prominent role in the secondary brain injury after SAH [11, 12]. Once activated, NLRP3 inflammasome cleaves procaspase-1 resulting in pro-IL-1 $\beta$  and pro-IL-18 activation. The inflammatory cytokines can further activate immune-related cells, such as neutrophils, to generate the corresponding immune effects. In addition to amplify inflammation, cleaved caspase-1 is the canonical executor of pyroptosis to further exacerbate neuronal cell death after SAH [10]. According to recent studies, LUT is able to inhibit NLRP3 inflammasome activation in different research fields [20, 21]. In our current study, we also observed that LUT significantly suppressed NLRP3 inflammasome activation after SAH and the subsequent inflammatory response, including microglia activation, neutrophil infiltration, and inflammatory cytokine release. In addition, the SAH-induced neuronal apoptosis and pyroptosis were markedly reduced after LUT administration. However, the underlying mechanism that mediates the inhibition of NLRP3 inflammasome by LUT in SAH needs to be elucidated.

It is known that ROS production is one of the major signals that trigger the NLRP3 inflammasome activation [13]. Both ROS overproduction and neuroinflammation are considered crucial elements of EBI after SAH, and each of them

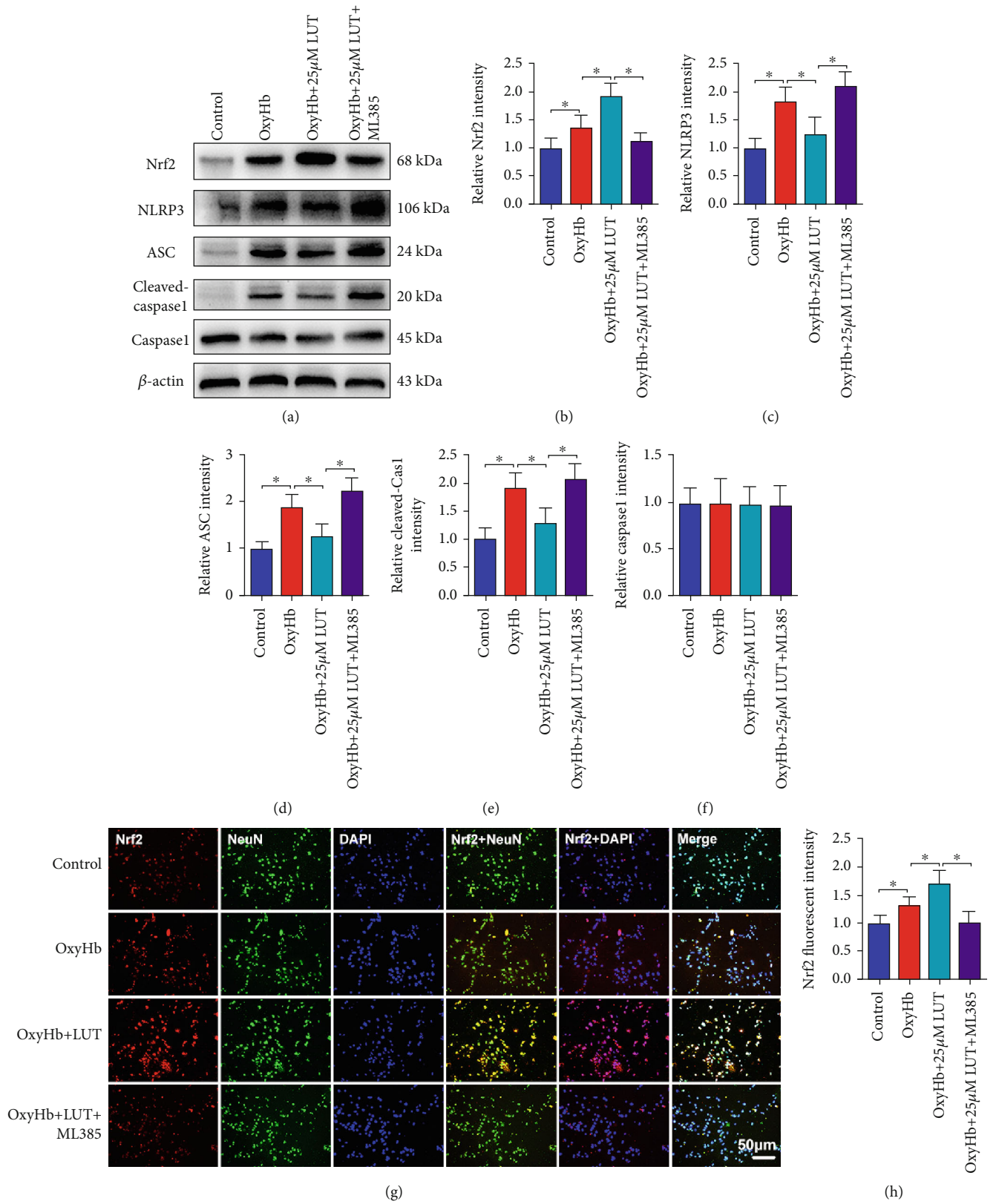


FIGURE 7: Effects of LUT treatment on Nrf2 and NLRP3 inflammasome activation in vitro. (a) Representative Western blots and quantification of expression of (b) Nrf2, (c) NLRP3, (d) ASC, (e) cleaved caspase-1, and (f) caspase-1 ( $n = 6$  per group). (g) Representative photomicrographs of Nrf2 immunofluorescence staining. (g) Magnification  $\times 200$ , scale bar  $50 \mu\text{m}$ . (h) Quantification of Nrf2 immunofluorescence staining in all experimental groups ( $n = 6$  per group). Bars represent the mean  $\pm$  SD. \*  $P < 0.05$ .

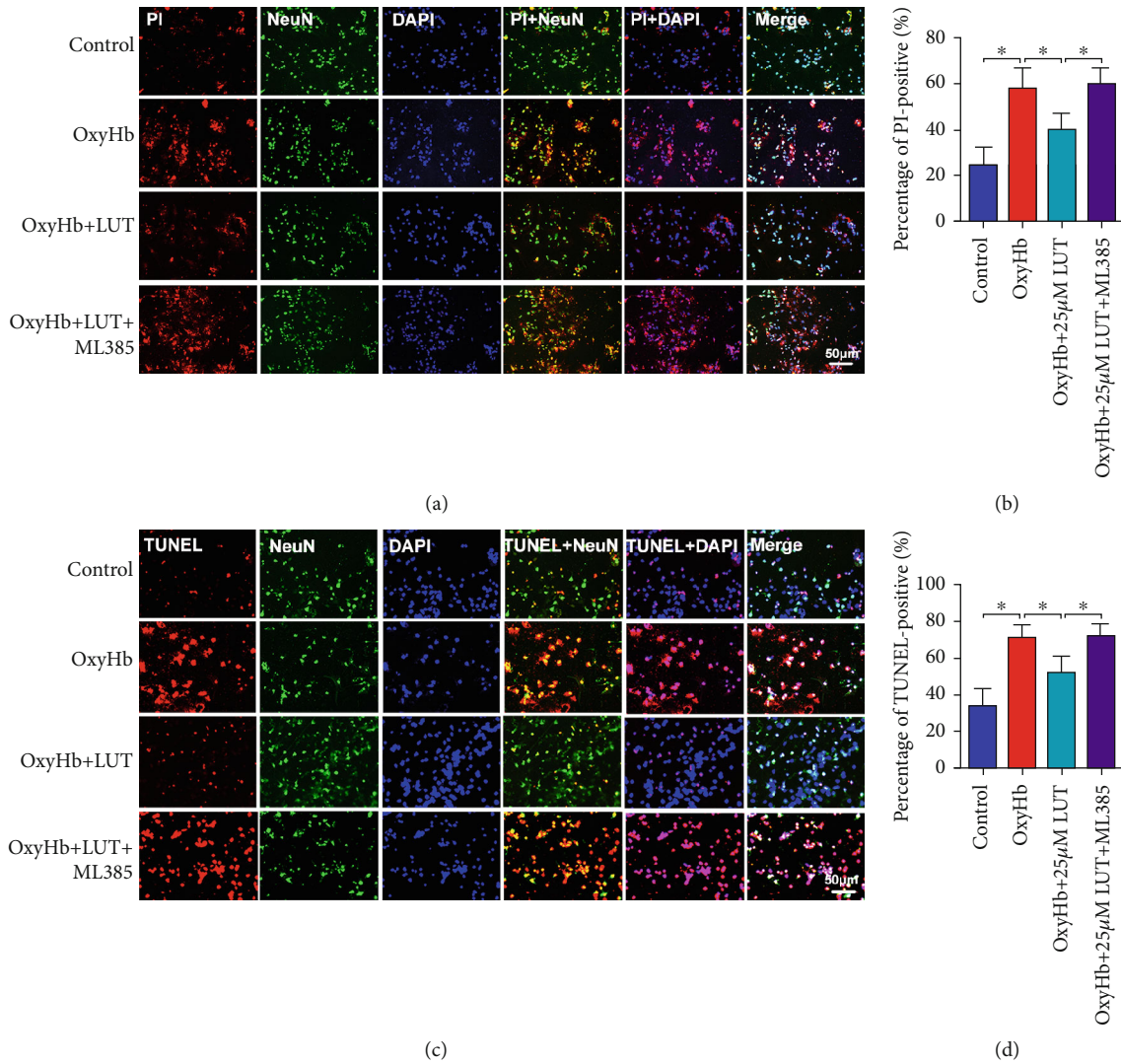


FIGURE 8: Effects of LUT treatment on PI staining and TUNEL staining in vitro. (a) Representative photomicrographs of PI immunofluorescence staining. (b) Quantification of PI staining in primary cortical neurons ( $n=6$  per group). (c) Representative photomicrographs of TUNEL immunofluorescence staining. (d) Quantification of TUNEL staining in primary cortical neurons ( $n=6$  per group). (a, c) Magnification  $\times 200$ , scale bar  $50 \mu\text{m}$ . Bars represent the mean  $\pm$  SD. \* $P < 0.05$ .

promotes and amplifies the other one [23]. Under normal conditions, the basal level of the NLRP3 inflammasome is low in immune cells. Upon stimulation by ROS, the NLRP3 inflammasome is assembled and activated to amplify the innate immune response after SAH [23]. Previous studies have proved that decreasing ROS overproduction could prevent NLRP3 inflammasome activation and mitigate the elevated levels of proinflammatory cytokine release in different neurological disorders, thereby ameliorating neuroinflammation [13, 23, 45]. As discussed above, we hypothesized that LUT might affect ROS production by modulating Nrf2 activation, thereby preventing NLRP3 inflammasome signaling after SAH. The relationship between Nrf2 signaling and NLRP3 inflammasome in other research fields has been well discussed in a variety of studies in recent years [46, 47]. Mounting evidence has demonstrated that Nrf2 activation could inhibit NLRP3 inflammasome by inducing

numerous antioxidative genes including HO-1, thereby scavenging ROS production [48, 49]. HO-1, one of the cytoprotective enzymes induced by the Nrf2-ARE pathway, has been widely regarded as a protective mechanism against oxidative stress and ROS [50, 51]. It has been proved that increased HO-1 expression could remove ROS and maintenance of the internal cellular environment. For example, Seiwert et al. reported that HO-1 protects human colonocytes against ROS formation, oxidative DNA damage, and cytotoxicity induced by heme iron [52]. Interestingly, we also observed that LUT treatment significantly increased HO-1 expression after SAH, suggesting that HO-1 might be involved in the inhibitory effects of LUT on NLRP3 inflammasome activation. To further address this hypothesis, we employed a novel and selective Nrf2 inhibitor ML385 in our study [53]. As expected, we observed that ML385 pretreatment significantly abated LUT-induced Nrf2 signaling-

mediated HO-1 expression, ROS suppression, and NLRP3 inflammasome inhibition. Additionally, ML385 treatment abrogated the neuroprotective effects of LUT against SAH-induced oxidative damage, neuroinflammation, neuronal apoptosis, and pyroptosis. These findings supported the notion that LUT inhibited NLRP3 inflammasome activation might involve Nrf2 signaling pathway. Based on these outcomes, we further evaluated the effects of LUT in an *in vitro* SAH model. In agreement with the results *in vivo*, LUT inhibited neuroinflammation, oxidative damage, and neuronal apoptosis and pyroptosis *in vitro*, which were associated with NLRP3 inflammasome inhibition and Nrf2 activation and were reversed by ML385. Taken together, our data indicated that the cerebroprotective effects of LUT might be attributed to its ability to induce Nrf2 activation and thereby inhibiting the NLRP3 inflammasome signaling.

However, there are several limitations in our study. Firstly, in the dose-response experiments, we cannot conclude that 60 mg/kg LUT is the optimum dose to provide maximal effect. Although there were no statistical differences between 30 mg/kg and 60 mg/kg LUT in ameliorating neurological deficits and neuronal degeneration, we can still see that 60 mg/kg LUT had a better act on neurological outcomes and neuronal survival after SAH. A larger sample size might decipher these discrepancies. Additionally, the toxicity studies should be further conducted to verify the optimal dose of LUT in SAH. Secondly, how LUT regulates Nrf2 activation remains unclear. Some possible mechanisms might be involved in this action, such as sirtuin 1 (SIRT1), adenosine monophosphate-activated protein kinase (AMPK), and PI3K [14–16, 54]. Yang et al. reported that dietary LUT could attenuate HgCl<sub>2</sub>-induced liver dysfunction by regulating SIRT1/Nrf2/TNF- $\alpha$  signaling pathway. Another two previous studies have indicated that LUT could significantly increase levels of PI3K and phosphorylated AMPK to activate Nrf2 pathway in different research areas [14, 55]. However, whether these molecular targets are attributable to the activation of Nrf2 signaling by LUT after SAH is needed to be clarified. Lastly, it should be noted that in addition to HO-1, Nrf2 can transcriptionally induce a variety of antioxidative genes including NAD(P) H dehydrogenase quinone 1 (NQO-1). It has been demonstrated that NQO-1 plays a critical role in monitoring cellular redox state and protects against oxidative stress induced by a variety of metabolic situations [56, 57]. Whether NQO-1 is involved in the beneficial effects of LUT against SAH remains obscure. Given that the present research is a pilot study, further experiments are still needed to validate the exact role of LUT following SAH.

## 5. Conclusion

In conclusion, we provide the first evidence that LUT exerts cerebroprotective effects against SAH by inhibiting NLRP3 inflammasome activation, which may be largely dependent on upregulation of the Nrf2 signaling pathway. LUT may serve as a promising candidate for SAH treatment.

## Abbreviations

8-OHdG:	8-Hydroxydeoxyguanosine
AMPK:	Adenosine monophosphate-activated protein kinase
ARE:	Antioxidant response element
ASC:	Adaptor apoptosis-related speck-like protein
DCFH-DA:	2,7-Dichlorodihydrofluorescein diacetate
DMSO:	Dimethylsulfoxide
GSH:	Glutathione
GSH-Px:	Glutathione peroxidase
H <sub>2</sub> O <sub>2</sub> :	Hydrogen peroxide
LDH:	Lactate dehydrogenase
LUT:	Luteolin
MDA:	Malondialdehyde
NLRP3:	Nod-like receptor pyrin domain-containing 3
NQO-1:	NAD(P)H dehydrogenase quinone 1
Nrf2:	Nuclear factor-erythroid 2-related factor 2
OxyHb:	Oxyhemoglobin
PI:	Propidium iodide
ROS:	Reactive oxygen species
SAH:	Subarachnoid hemorrhage
SIRT1:	Sirtuin 1
SOD:	Superoxide dismutase
TBI:	Traumatic brain injury
TNF- $\alpha$ :	Tumor necrosis factor- $\alpha$
TUNEL:	Terminal deoxynucleotidyl transferase-mediated dUTP nick-end labeling.

## Data Availability

All the data supporting the results were shown in the paper and can be applicable from the corresponding author upon reasonable request. Some data may not be made available because of privacy or ethical restrictions.

## Ethical Approval

All experimental procedures were approved by the Animal Care and Use Committee of Wannan Medical College and were conformed to Guide for the Care and Use of Laboratory Animals by National Institutes of Health.

## Conflicts of Interest

The authors declare no conflict of interest.

## Authors' Contributions

ZHZ performed the studies and wrote the manuscript. JQL and CDH participated in creating the experimental animal model. JQL and XTZ contributed to the Western blotting and the immunofluorescence staining. ZHZ, CDH, and FYQ performed the *in vitro* studies. ZHZ, ZZ, and XSZ contributed to the design and analysis of the study and revised the manuscript. All authors analyzed the results and approved the final version of the manuscript.

## Acknowledgments

This work was supported by grants from the National Natural Science Foundation of China (NSFC) (Nos. 81971127 for ZZ and 81501022 for XSZ), the Key project of Anhui Provincial Education Department (No. KJ2019A0423 for ZHZ), and the Science Research Project of Professional of the First Affiliated Hospital of Wannan Medical College (No. YR202004 for ZHZ).

## References

- [1] R. L. Macdonald and T. A. Schweizer, "Spontaneous subarachnoid haemorrhage," *Lancet*, vol. 389, no. 10069, pp. 655–666, 2017.
- [2] Y. Luo, Y. Fang, R. Kang et al., "Inhibition of EZH2 (enhancer of zeste homolog 2) attenuates neuroinflammation via H3k27me3/SOCS3/TRAF6/NF-kappaB (trimethylation of histone 3 lysine 27/suppressor of cytokine signaling 3/tumor necrosis factor receptor family 6/nuclear factor-kappaB) in a rat model of subarachnoid hemorrhage," *Stroke*, vol. 51, pp. 3320–3331, 2020.
- [3] R. Heinz, S. Brandenburg, M. Nieminen-Kelha et al., "Microglia as target for anti-inflammatory approaches to prevent secondary brain injury after subarachnoid hemorrhage (SAH)," *Journal of Neuroinflammation*, vol. 18, p. 36, 2021.
- [4] Y. N. Paudel, E. Angelopoulou, C. Piperi, I. Othman, and M. F. Shaikh, "HMGB1-mediated neuroinflammatory responses in brain injuries: potential mechanisms and therapeutic opportunities," *International Journal of Molecular Sciences*, vol. 21, 2020.
- [5] A. Shao, D. Lin, L. Wang, S. Tu, C. Lenahan, and J. Zhang, "Oxidative stress at the crossroads of aging, stroke and depression," *Aging and Disease*, vol. 11, no. 6, pp. 1537–1566, 2020.
- [6] A. Delgado, C. Cholevas, and T. C. Theoharides, "Neuroinflammation in Alzheimer's disease and beneficial action of luteolin," *BioFactors*, vol. 47, no. 2, pp. 207–217, 2021.
- [7] X. Tan, Y. Yang, J. Xu et al., "Luteolin exerts neuroprotection via modulation of the p62/Keap1/Nrf2 pathway in intracerebral hemorrhage," *Frontiers in Pharmacology*, vol. 10, p. 1551, 2020.
- [8] J. Xu, H. Wang, K. Ding et al., "Luteolin provides neuroprotection in models of traumatic brain injury via the Nrf2-ARE pathway," *Free Radical Biology & Medicine*, vol. 71, pp. 186–195, 2014.
- [9] S. Ahmad, M. H. Jo, M. Ikram, A. Khan, and M. O. Kim, "Deciphering the potential neuroprotective effects of luteolin against A $\beta$ 1–42-Induced Alzheimer's disease," *International Journal of Molecular Sciences*, vol. 22, no. 17, p. 9583, 2021.
- [10] J. R. Li, H. Z. Xu, S. Nie et al., "Fluoxetine-enhanced autophagy ameliorates early brain injury via inhibition of NLRP3 inflammasome activation following subarachnoid hemorrhage in rats," *Journal of Neuroinflammation*, vol. 14, no. 1, 2017.
- [11] W. Xu, T. Li, L. Gao et al., "Apelin-13/APJ system attenuates early brain injury via suppression of endoplasmic reticulum stress-associated TXNIP/NLRP3 inflammasome activation and oxidative stress in a AMPK-dependent manner after subarachnoid hemorrhage in rats," *Journal of Neuroinflammation*, vol. 16, no. 1, 2019.
- [12] K. Zhou, B. Enkhjargal, Z. Xie et al., "Dihydrolipoic acid inhibits lysosomal rupture and NLRP3 through lysosome-associated membrane protein-1/calcium/calmodulin-dependent protein kinase II/TAK1 pathways after subarachnoid hemorrhage in rat," *Stroke*, vol. 49, no. 1, pp. 175–183, 2018.
- [13] A. Shao, H. Wu, Y. Hong et al., "Hydrogen-rich saline attenuated subarachnoid hemorrhage-induced early brain injury in rats by suppressing inflammatory response: possible involvement of NF- $\kappa$ B pathway and NLRP3 inflammasome," *Molecular Neurobiology*, vol. 53, no. 5, pp. 3462–3476, 2016.
- [14] R. Baiyun, S. Li, B. Liu et al., "Luteolin-mediated PI3K/AKT/Nrf2 signaling pathway ameliorates inorganic mercury-induced cardiac injury," *Ecotoxicology and Environmental Safety*, vol. 161, pp. 655–661, 2018.
- [15] D. Yang, X. Tan, Z. Lv et al., "Regulation of Sirt1/Nrf2/TNF- $\alpha$  signaling pathway by luteolin is critical to attenuate acute mercuric chloride exposure induced hepatotoxicity," *Scientific Reports*, vol. 6, no. 1, 2016.
- [16] J. Lu, H. Jiang, B. Liu et al., "Grape seed procyanidin extract protects against Pb-induced lung toxicity by activating the AMPK/Nrf2/p62 signaling axis," *Food and Chemical Toxicology*, vol. 116, pp. 59–69, 2018.
- [17] X. Zhang, Q. Wu, Y. Lu et al., "Cerebroprotection by salvianolic acid B after experimental subarachnoid hemorrhage occurs via Nrf2- and SIRT1-dependent pathways," *Free Radical Biology & Medicine*, vol. 124, pp. 504–516, 2018.
- [18] G. Jia, S. Yu, W. Sun et al., "Hydrogen sulfide attenuates particulate matter-induced emphysema and airway inflammation through Nrf2-dependent manner," *Frontiers in Pharmacology*, vol. 11, 2020.
- [19] S. Li, C. Takasu, H. Lau et al., "Dimethyl fumarate alleviates dextran sulfate sodium-induced colitis, through the activation of Nrf2-mediated antioxidant and anti-inflammatory pathways," *Antioxidants*, vol. 9, no. 4, p. 354, 2020.
- [20] M. N. Lee, Y. Lee, D. Wu, and M. Pae, "Luteolin inhibits NLRP3 inflammasome activation via blocking ASC oligomerization," *The Journal of Nutritional Biochemistry*, vol. 92, p. 108614, 2021.
- [21] L. Zhao, Z. Zhou, C. Zhu, Z. Fu, and D. Yu, "Luteolin alleviates myocardial ischemia reperfusion injury in rats via Sirt1/NLRP3/NF- $\kappa$ B pathway," *International Immunopharmacology*, vol. 85, p. 106680, 2020.
- [22] X. S. Zhang, Y. Lu, T. Tao et al., "Fucoxanthin mitigates subarachnoid hemorrhage-induced oxidative damage via sirtuin 1-dependent pathway," *Molecular Neurobiology*, vol. 57, no. 12, pp. 5286–5298, 2020.
- [23] X. S. Zhang, Y. Lu, W. Li et al., "Cerebroprotection by dioscin after experimental subarachnoid haemorrhage via inhibiting NLRP3 inflammasome through SIRT1-dependent pathway," *British Journal of Pharmacology*, vol. 178, no. 18, pp. 3648–3666, 2021.
- [24] X. S. Zhang, Y. Lu, W. Li et al., "Astaxanthin ameliorates oxidative stress and neuronal apoptosis via SIRT1/NRF2/Prx2/ASK1/p38 after traumatic brain injury in mice," *British Journal of Pharmacology*, vol. 178, no. 5, pp. 1114–1132, 2021.
- [25] Y. Lu, X. S. Zhang, Z. H. Zhang et al., "Peroxiredoxin 2 activates microglia by interacting with toll-like receptor 4 after subarachnoid hemorrhage," *Journal of Neuroinflammation*, vol. 15, no. 1, 2018.
- [26] L. Cui, Q. Zhou, X. Zheng, B. Sun, and S. Zhao, "Mitoquinone attenuates vascular calcification by suppressing oxidative stress and reducing apoptosis of vascular smooth muscle cells via the Keap1/Nrf2 pathway," *Free Radical Biology & Medicine*, vol. 161, pp. 23–31, 2020.

- [27] Y. Lu, X. S. Zhang, X. M. Zhou et al., "Peroxiredoxin 1/2 protects brain against H<sub>2</sub>O<sub>2</sub>-induced apoptosis after subarachnoid hemorrhage," *The FASEB Journal*, vol. 33, no. 2, pp. 3051–3062, 2019.
- [28] T. Fumoto, M. Naraoka, T. Katagai, Y. Li, N. Shimamura, and H. Ohkuma, "The role of oxidative stress in microvascular disturbances after experimental subarachnoid hemorrhage," *Translational Stroke Research*, vol. 10, no. 6, pp. 684–694, 2019.
- [29] E. Atangana, U. C. Schneider, K. Blecharz et al., "Intravascular inflammation triggers intracerebral activated microglia and contributes to secondary brain injury after experimental subarachnoid hemorrhage (eSAH)," *Translational Stroke Research*, vol. 8, no. 2, pp. 144–156, 2017.
- [30] X. Zhang, Y. Lu, Q. Wu et al., "Astaxanthin mitigates subarachnoid hemorrhage injury primarily by increasing sirtuin 1 and inhibiting the Toll-like receptor 4 signaling pathway," *The FASEB Journal*, vol. 33, no. 1, pp. 722–737, 2019.
- [31] T. Tao, G. J. Liu, X. Shi et al., "DHEA attenuates microglial activation via induction of JMJD3 in experimental subarachnoid haemorrhage," *Journal of Neuroinflammation*, vol. 16, no. 1, 2019.
- [32] L. Y. Wu, B. Enkhjargal, Z. Y. Xie et al., "Recombinant OX40 attenuates neuronal apoptosis through OX40-OX40L/PI3-K/AKT signaling pathway following subarachnoid hemorrhage in rats," *Experimental Neurology*, vol. 326, p. 113179, 2020.
- [33] L. Y. Wu, Z. N. Ye, C. H. Zhou et al., "Roles of pannexin-1 channels in inflammatory response through the TLRs/NF-kappa B signaling pathway following experimental subarachnoid hemorrhage in rats," *Frontiers in Molecular Neuroscience*, vol. 10, p. 175, 2017.
- [34] N. Abu-Elsaad and A. El-Karef, "Protection against nonalcoholic steatohepatitis through targeting IL-18 and IL-1alpha by luteolin," *Pharmacological Reports*, vol. 71, no. 4, pp. 688–694, 2019.
- [35] X. B. Liu, F. Liu, Y. Y. Liang et al., "Luteolin delays photoreceptor degeneration in a mouse model of retinitis pigmentosa," *Neural Regeneration Research*, vol. 16, no. 10, pp. 2109–2120, 2021.
- [36] J. J. Kou, J. Z. Shi, Y. Y. He et al., "Luteolin alleviates cognitive impairment in Alzheimer's disease mouse model via inhibiting endoplasmic reticulum stress-dependent neuroinflammation," *Acta Pharmacologica Sinica*, 2021.
- [37] J. Wang, C. Jiang, K. Zhang et al., "Melatonin receptor activation provides cerebral protection after traumatic brain injury by mitigating oxidative stress and inflammation via the Nrf2 signaling pathway," *Free Radical Biology & Medicine*, vol. 131, pp. 345–355, 2019.
- [38] B. Han, S. Li, Y. Lv et al., "Dietary melatonin attenuates chromium-induced lung injury via activating the Sirt1/Pgc-1 $\alpha$ /Nrf2 pathway," *Food & Function*, vol. 10, no. 9, pp. 5555–5565, 2019.
- [39] T. Zhang, P. Wu, E. Budbazar et al., "Mitophagy reduces oxidative stress via Keap1 (Kelch-like epichlorohydrin-associated protein 1)/Nrf2 (nuclear factor-E2-related factor 2)/PHB2 (prohibitin 2) pathway after subarachnoid hemorrhage in rats," *Stroke*, vol. 50, no. 4, pp. 978–988, 2019.
- [40] A. Zolnourian, I. Galea, and D. Bulters, "Neuroprotective role of the Nrf2 pathway in subarachnoid haemorrhage and its therapeutic potential," *Oxidative Medicine and Cellular Longevity*, vol. 2019, Article ID 6218239, 21 pages, 2019.
- [41] C. Xiao, M. L. Xia, J. Wang et al., "Luteolin attenuates cardiac ischemia/reperfusion injury in diabetic rats by modulating Nrf2 antioxidative function," *Oxidative Medicine and Cellular Longevity*, vol. 2019, Article ID 2719252, 9 pages, 2019.
- [42] J. Wang and S. Dore, "Heme oxygenase-1 exacerbates early brain injury after intracerebral haemorrhage," *Brain*, vol. 130, no. 6, pp. 1643–1652, 2007.
- [43] N. Deng, H. Jiang, P. Wu et al., "Inhibition of the Nrf2/p38MAPK pathway involved in deltamethrin-induced apoptosis and fibrosis in quail kidney," *Food and Chemical Toxicology*, vol. 155, p. 112382, 2021.
- [44] W. Zhu, F. S. Cao, J. Feng et al., "NLRP3 inflammasome activation contributes to long-term behavioral alterations in mice injected with lipopolysaccharide," *Neuroscience*, vol. 343, pp. 77–84, 2017.
- [45] P. Xu, Y. Hong, Y. Xie et al., "TREM-1 exacerbates neuroinflammatory injury via NLRP3 inflammasome-mediated pyroptosis in experimental subarachnoid hemorrhage," *Translational Stroke Research*, vol. 12, no. 4, pp. 643–659, 2021.
- [46] Y. Cheng, M. Liu, H. Tang et al., "iTRAQ-based quantitative proteomics indicated Nrf2/OPTN-mediated mitophagy inhibits NLRP3 inflammasome activation after intracerebral hemorrhage," *Oxidative Medicine and Cellular Longevity*, vol. 2021, Article ID 6630281, 26 pages, 2021.
- [47] J. Cao, M. Lu, W. Yan, L. Li, and H. Ma, "Dehydroepiandrosterone alleviates intestinal inflammatory damage via GPR30-mediated NRF2 activation and NLRP3 inflammasome inhibition in colitis mice," *Free Radical Biology & Medicine*, vol. 172, pp. 386–402, 2021.
- [48] L. Kong, H. Zhang, C. Lu et al., "AICAR, an AMP-activated protein kinase activator, ameliorates acute pancreatitis-associated liver injury partially through Nrf2-mediated antioxidant effects and inhibition of NLRP3 inflammasome activation," *Frontiers in Pharmacology*, vol. 12, p. 724514, 2021.
- [49] J. J. Jhang, Y. T. Cheng, C. Y. Ho, and G. C. Yen, "Monosodium urate crystals trigger Nrf2- and heme oxygenase-1-dependent inflammation in THP-1 cells," *Cellular & Molecular Immunology*, vol. 12, no. 4, pp. 424–434, 2015.
- [50] T. Cheng, W. Wang, Q. Li et al., "Cerebroprotection of flavanol (-)-epicatechin after traumatic brain injury via Nrf2-dependent and -independent pathways," *Free Radical Biology & Medicine*, vol. 92, pp. 15–28, 2016.
- [51] B. Wegiel, Z. Nemeth, M. Correa-Costa, A. C. Bulmer, and L. E. Otterbein, "Heme oxygenase-1: a metabolic nuke," *Antioxidants & Redox Signaling*, vol. 20, no. 11, pp. 1709–1722, 2014.
- [52] N. Seiwert, S. Wecklein, P. Demuth et al., "Heme oxygenase 1 protects human colonocytes against ROS formation, oxidative DNA damage and cytotoxicity induced by heme iron, but not inorganic iron," *Cell Death & Disease*, vol. 11, no. 9, 2020.
- [53] W. Cui, J. Chen, F. Yu, W. Liu, and M. He, "GYY4137 protected the integrity of the blood-brain barrier via activation of the Nrf2/are pathway in mice with sepsis," *The FASEB Journal*, vol. 35, no. 7, 2021.
- [54] B. Liu, H. Yu, R. Baiyun et al., "Protective effects of dietary luteolin against mercuric chloride-induced lung injury in mice: Involvement of AKT/Nrf2 and NF- $\kappa$ B pathways," *Food and Chemical Toxicology*, vol. 113, pp. 296–302, 2018.
- [55] Q. Lu, Y. Shu, L. Wang et al., "The protective effect of *Veronica ciliata* Fisch. Extracts on relieving oxidative stress-induced



- liver injury via activating AMPK/p62/Nrf2 pathway,” *Journal of Ethnopharmacology*, vol. 270, p. 113775, 2021.
- [56] D. Yang, Q. Yang, N. Fu et al., “Hexavalent chromium induced heart dysfunction via Sesn2-mediated impairment of mitochondrial function and energy supply,” *Chemosphere*, vol. 264, p. 128547, 2021.
- [57] S. Li, X. Zheng, X. Zhang et al., “Exploring the liver fibrosis induced by deltamethrin exposure in quails and elucidating the protective mechanism of resveratrol,” *Ecotoxicology and Environmental Safety*, vol. 207, p. 111501, 2021.